

ASD-TDR-63-554

605185

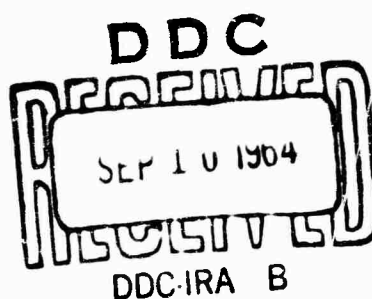
618-P

COPY	1	OF	3	Vol
HARD COPY	\$ . 9.20			
MICROFICHE	\$ . 2.50			

VOLUME I

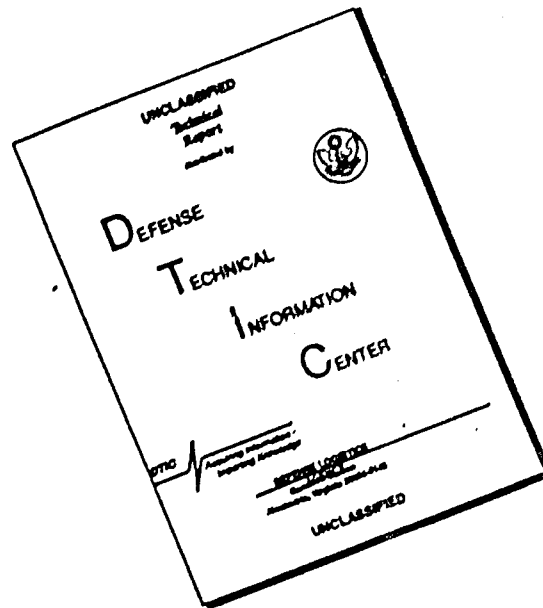
**SUMMARY OF LAMINAR BOUNDARY  
LAYER CONTROL RESEARCH**

TECHNICAL DOCUMENTARY REPORT ASD-TDR-63-554



Prepared under Contract No. AF33(616)-7564  
by Northrop Norair, A Division of  
Northrop Corporation, Hawthorne, California  
Author: Boundary Layer Research Section

# DISCLAIMER NOTICE



THIS DOCUMENT IS BEST QUALITY AVAILABLE. THE COPY FURNISHED TO DTIC CONTAINED A SIGNIFICANT NUMBER OF PAGES WHICH DO NOT REPRODUCE LEGIBLY.

ASD-TDR-63-554

S U M M A R Y   O F   L A M I N A R   B O U N D A R Y  
L A Y E R   C O N T R O L   R E S E A R C H

TECHNICAL DOCUMENTARY REPORT ASD-TDR-63-554

March 1964

Air Force Flight Dynamics Laboratory  
Aeronautical Systems Division  
Air Force Systems Command  
Wright-Patterson Air Force Base, Ohio

Project No. 1366, Task No. 136612

Prepared under Contract No. AF33(616)-7564  
by Northrop Norair, A Division of  
Northrop Corporation, Hawthorne, California  
Author: Boundary Layer Research Section

## NOTICES

When Government drawings, specifications, or other data are used for any purpose other than in connection with a definitely related Government procurement operation, the United States Government thereby incurs no responsibility nor any obligation whatsoever; and the fact that the Government may have formulated, furnished, or in any way supplied the said drawings, specifications, or other data, is not to be regarded by implication or otherwise as in any manner licensing the holder or any other person or corporation, or conveying any rights or permission to manufacture, use, or sell any patented invention that may in any way be related thereto.

Qualified requesters may obtain copies of this report from the Armed Services Technical Information Agency, (ASTIA), Arlington Hall Station, Arlington 12, Virginia.

This report has been released to the Office of Technical Services, U.S. Department of Commerce, Washington 25, D.C., in stock quantities for sale to the general public.

Copies of this report should not be returned to the Aeronautical Systems Division unless return is required by security considerations, contractual obligations, or notice on a specific document.



## FOREWORD

This report was prepared by the Boundary Layer Research Section under the direction of Dr. Werner Pfenninger, Northrop Norair, a Division of Northrop Corporation, Hawthorne, California, and covers research investigations performed from July 1959 through March 1963 under Contract AF33(616)-7564. This work was performed under Air Force Task No. 136612 of Project No. 1366, "Laminar Boundary Layer Control Research."

The work was administered under the direction of the Flight Dynamics Laboratory, Aeronautical Systems Division. Mr. Philip P. Antonatos and Mr. J. P. Nenni were project engineers for the Laboratory.

This abstract is unclassified

### ABSTRACT

At subsonic speeds, full length laminar flow and low drags were obtained up to high length Reynolds numbers on a thin straight, on a swept laminar suction wing and on a suction body of revolution. Moderately increased suction rates in the most critical region of a straight and a swept laminar suction wing enabled full chord laminar flow in the presence of external sound. Theoretical investigations are concerned with nonlinear boundary layer oscillations and stability investigations (assuming small disturbances) of a supersonic laminar boundary layer on a flat plate up to high supersonic speeds as well as on a highly swept supersonic low drag suction wing of low wave drag. On a supersonic flat laminar suction plate with and without weak incident shock waves, extensive laminar flow and low equivalent drags were obtained at  $M = 3$  up to length Reynolds numbers of  $26 \times 10^6$ . Further supersonic low drag suction experiments on a suction body of revolution, on a  $36^\circ$  supersonic yawing wing, as well as on a  $72^\circ$  supersonic yawing wing (swept behind the Mach cone) of low wave drag, are described. The latter wing showed full chord laminar flow with a subsonic type pressure distribution at  $M = 2$  and  $Re = 9 \times 10^6$ .

*to be given to you in 100*

This report has been reviewed and is approved.

*Alfred C. Berger*  
A. C. BERGER  
Asst. Dir.  
Flight  
Air Force

rat 107

## SUMMARY

## SUMMARY

### SECTION I--THEORETICAL INVESTIGATIONS

Chapter A of the theoretical investigations deals with the growth of boundary layer oscillations and the phenomena leading to transition, using the full nonlinear boundary layer disturbance equations. A theory is developed around the concept that, under certain frequent conditions and as a result of the nonlinearity of the equations, two partial oscillations of the whole motion can drive a third partial oscillation in a resonance-like manner to a large amplitude (Section I, Chapter A and Reference 1). The two driving oscillations can come from external disturbances--such as a roughness of the wall surface and a fluctuation of the external flow--or from the internal disturbance motions generated by preceding resonance-like interactions. For example, the following combinations of driving oscillations can produce significant amplifications: (1) an oscillation from surface roughness or surface vibration and an oscillation from external turbulence or sound, (2) either of these oscillations and an internal boundary layer oscillation, or (3) two internal boundary layer oscillations.

In deducing the theory, the whole motion is decomposed into a sequence of perturbations from a laminar flow, and then each perturbation is decomposed into a spectrum of Fourier components. The first perturbation is determined solely by the boundary irregularities at the wall surface and in the external flow, whereas each higher perturbation is determined mainly by the driving oscillations from the lower perturbations. Expressions for the resonance-like growth of the Fourier coefficients are derived, proceeding in a recursive manner from lower to higher perturbations. The role of these growths in producing transition phenomena is explained. Some aspects of the calculation techniques required to apply the theory also are discussed.

Chapter B of the theoretical investigations discusses calculations and results of the stability limit Reynolds number of the boundary layer on an insulated flat plate up to  $M = 5.8$  (also see Reference 2). The cases of constant stagnation temperature at various Mach numbers, corresponding essentially to wind tunnel conditions, and of constant static temperature at different Mach numbers, corresponding to flight conditions, have been analyzed. The full linearized stability equations of the compressible laminar boundary layer, as derived by Lees and Lin, have been integrated numerically from the wall to the outer edge of the boundary layer. The wave number  $\alpha$ , wave velocity  $C_r$  and boundary layer Reynolds number have been chosen such that the "inner" solution of the disturbance equation, as obtained from the integration through the boundary layer, is matched at the outer edge of the boundary layer with the "outer" solution beyond the outer edge of the boundary layer.

With increasing Mach number the stability limit Reynolds number of an insulated flat plate of zero pressure gradient first decreases slightly up to  $M \cong 1$  and rises again at supersonic speeds. For the case of constant static temperature, i.e., for flight conditions, the stability limit Reynolds number rises rapidly at higher Mach numbers. The corresponding rise of the stability limit Reynolds number of the compressible laminar boundary layer on an insulated flat plate at higher Mach numbers is considerably smaller for the case of constant stagnation temperature, corresponding essentially to wind tunnel conditions.

## SUMMARY (continued)

This difference is due to the variation of the properties of the air (viscosity, etc.) with temperature, which changes the boundary layer profile and the stability limit Reynolds number.

In view of the increased stability limit Reynolds numbers at supersonic speeds, it should basically be easier to maintain laminar flow at further increased length Reynolds numbers, as compared with the incompressible case, at least as long as interacting shock waves or boundary layer crossflow instability are not critical.

Boundary layer crossflow instability becomes particularly critical on highly swept supersonic laminar suction wings with subsonic type flow of low wave drag. At supersonic speeds the increased wall temperature causes a thicker laminar boundary layer with reduced kinetic energy close to the surface, resulting in a correspondingly stronger crossflow at supersonic speeds, under otherwise the same conditions. The crossflow stability limit Reynolds number of a supersonic laminar boundary layer on a  $65^\circ$  swept wing has been calculated in Section I, Chapter C at  $M = 1.8$  for the insulated wing and for the case of radiation cooling (also see Reference 3). The simplified Dunn and Lin stability equations for compressible flow were used. The calculations were repeated later with the complete Lees and Lin compressible stability equations.

For the same shape of the boundary layer crossflow profile the crossflow stability limit Reynolds number was slightly larger at  $M = 1.8$ , as compared with incompressible flow. At  $M = 1.8$  the Dunn-Lin equations gave results which closely agreed with those obtained from the more complete Lees-Lin equations.

The main effect of compressibility on boundary layer crossflow at supersonic speeds, such as in the case of highly swept supersonic low drag suction wings, is thus essentially a stronger crossflow caused by the thicker boundary layer at supersonic speeds due to the increased temperatures close to the surface. In contrast, the crossflow stability limit Reynolds number, at least at moderately high Mach numbers, is little affected by compressibility. Increased suction mass flow rates are required to avoid excessive boundary layer crossflow and thus to maintain laminar flow on supersonic swept wings, as compared with the case of incompressible flow.

Stuart (NPL) has shown (Reference 4) that the two disturbance equations of the laminar boundary layer in the direction tangential and normal to the potential flow streamline in the presence of boundary layer crossflow can be approximated by a single disturbance equation in the direction of the most critical disturbance wave fronts. These most critical disturbance waves are usually oriented at a small angle to the direction of the local potential flow. The question then arises concerning the angle between the most critical crossflow disturbance waves and the local potential flow and the variation of the crossflow stability limit Reynolds number with this angle. Chapter D of Section I (also Reference 5) presents results of crossflow stability calculations when the angle between the boundary layer disturbance waves and the potential flow direction is varied. A boundary layer crossflow profile in the rear part of a swept laminar suction wing was investigated. The disturbance equation for the resultant boundary layer flow in the direction normal to the

## SUMMARY (continued)

disturbance wave fronts was integrated as in References 6 and 7. The lowest stability limit Reynolds number for the above-mentioned crossflow profile close to the trailing edge of a swept wing was obtained when the disturbance vortices were aligned nearly parallel to the direction of the local potential flow. The corresponding wave velocity  $C_r$  was finite, indicating the existence of traveling crossflow disturbance vortices in the rear part of a swept laminar suction wing. For other angles between the disturbance wave fronts and the potential flow direction, the stability limit Reynolds number increased rather rapidly.

## SECTION II PART 1--EXPERIMENTAL AERODYNAMIC INVESTIGATIONS AT SUBSONIC SPEEDS

### A. Investigation of Swept Laminar Suction Wing

In view of the advantages of swept wings at high subsonic speeds, particular emphasis was given to the investigation of swept laminar suction wings. Section II, Part 1, Chapter A describes the experimental investigation of a  $30^\circ$  yawing, 12-percent-thick, symmetrical laminar suction wing of 7-foot chord and 7-foot span in the Ames 12-foot high-pressure tunnel (References 8, 9 and 10). Suction was applied through 93 fine slots located from 0.5-percent chord to 97-percent chord. In order to maintain fully developed spanwise flow in the test region of the model, auxiliary suction slots and chambers were added on both sides of the test area. Two-dimensional flow was maintained by shaping the endplates on both sides of the model according to the undisturbed streamlines around an infinitely long yawing wing of the same cross section and sweep working in infinite flow.

In the angle of attack range between  $\alpha = -1^\circ$  to  $+1^\circ$  full chord laminar flow was maintained at five atmospheres tunnel pressure up to a wing chord Reynolds number  $R_c = 28 \times 10^6$  to  $29 \times 10^6$ . The minimum total equivalent wing profile drag for both wing sides at  $\alpha = 1^\circ$  was  $C_{D_{\min}} = 0.00097$  at  $R_c = 28 \times 10^6$ , with a corresponding suction quantity coefficient  $C_{Q_{\text{opt}}} = 0.00070$ . At Reynolds numbers above  $R_c = 28 \times 10^6$  tunnel noise, rather than tunnel turbulence, seemed to contribute to the formation of turbulent bursts and a rising drag at  $\alpha$ 's between  $\pm 1^\circ$ . At  $\alpha = +1.5^\circ$  and  $-1.5^\circ$  full chord laminar flow was maintained up to  $R_c = 22 \times 10^6$  and  $24 \times 10^6$ , respectively, and up to  $21 \times 10^6$  at  $\alpha = -2^\circ$ . At the larger negative angles of attack the increased flow acceleration in the front part of the wing caused an increased boundary layer crossflow in this area, resulting in premature transition at higher Reynolds numbers. At  $\alpha = 1.5^\circ$  the occurrence of negative pressure peaks close to the leading edge followed by decelerated flow caused increased instability of the chordwise component of the boundary layer flow, resulting in premature transition at somewhat lower Reynolds numbers than at  $\alpha = +1^\circ$  to  $-1^\circ$ .

At higher wing chord Reynolds numbers the chordwise suction distributions at  $\alpha = +1^\circ$  to  $-1^\circ$  for minimum drag showed relatively high suction rates in the leading edge area, followed by weak suction in the region of the flat pressure distribution and relatively strong suction in the region of the rear pressure rise. An analysis of the boundary layer development in these cases (Section II, Part 1, Chapter A and References 9, 10 and 11) showed that the crossflow stability limit Reynolds number for the most critical disturbances

## SUMMARY (continued)

could be exceeded by approximately 80 percent at  $\alpha = 0^\circ$  in the region from the leading edge to the beginning of the rear pressure rise. At  $\alpha = +1$  and  $-1^\circ$  angles of attack and full chord laminar flow the crossflow stability limit Reynolds number at the downstream end of the area of the flat pressure distribution could be exceeded by approximately 30 percent and over 100 percent, respectively. In other words, when the chordwise boundary layer flow is less stable against Tollmien-Schlichting type of disturbances in the presence of decelerated chordwise flow, velocity fluctuations in the crossflow boundary layer appear to be amplified at a faster rate. Vice versa, when the chordwise flow is strongly accelerated and thus highly stable against Tollmien-Schlichting oscillations, the crossflow stability limit Reynolds number can be exceeded by a larger factor without causing premature transition. It thus appears that the growth of the disturbances in the crossflow component of the boundary layer is influenced by the growth of the chordwise boundary layer oscillations.

Toward the downstream end of the region of the rear pressure rise, where the chordwise component of the boundary layer flow is generally highly stable, the crossflow stability limit Reynolds number could be exceeded by over 100 percent without transition in the angle of attack range between  $\pm 1^\circ$ . In local areas, such as in the region of the leading edge at  $\alpha = -1^\circ$  or in the nonsuction region between 97 percent and 100 percent chord, the crossflow stability limit could be exceeded locally by considerably larger factors.

With the application of low drag suction to high subsonic speed jet-propelled airplanes the question arises concerning the influence of external sound, originating from the jet exhaust and the rotating components of the propulsion system, on the behavior of a swept laminar suction wing. In order to answer this question, low drag suction experiments were conducted in the Norair 7- by 10-foot low-turbulence tunnel on the above-described  $30^\circ$  swept low drag suction wing in the presence of longitudinal and transverse external sound of discrete frequencies as well as with a continuous spectrum. These investigations are described in Section II, Part 1, Chapter C and in Reference 12. Transition was caused by external sound and originated usually in the region of the flat pressure distribution. With the wing in smooth condition, i.e., with surface cavities such as static pressure orifices sealed, and with optimum suction for minimum drag in the absence of external sound, transition started at 120 to 126 db external sound pressure at wing chord Reynolds numbers between  $8 \times 10^6$  to  $12 \times 10^6$ .\* At  $R_c = 10^7$  the corresponding critical ratio of mean sound particle velocity  $u'$  to undisturbed velocity  $U_\infty$  was  $u'/U_\infty \approx 1.5 \times 10^{-3}$ . For the smooth wing the critical sound particle velocity ratio decreased at a somewhat slower rate than inversely proportional to the wing chord Reynolds number. Transition could be delayed to higher sound pressures by raising suction as a whole or locally in the area of the flat pressure distribution, where transition otherwise occurred. For example, at  $R_c = 10^7$ , the critical sound pressure could be raised to over 132 db, corresponding to  $(u'/U_\infty)_{crit} = 3 \times 10^{-3}$  to  $3.5 \times 10^{-3}$ , by increasing suction locally

\*The turbulence level of the Norair 7- by 10-foot tunnel enabled full chord laminar flow on this swept wing up to  $R_c = 13 \times 10^6$  without external sound.

## SUMMARY (continued)

in the region of the flat pressure distribution by 15 percent. The corresponding increase in equivalent wing profile drag was only 5 percent of the minimum profile drag. Raising suction as a whole required much larger increases in total suction quantity to prevent transition at higher sound pressures.

On the swept low drag suction wing transition was usually observed over a wide range of sound frequencies, and the variation of the critical sound pressure for transition with frequency was relatively small for the smooth wing. In the presence of open surface cavities such as nonsucking open or imperfectly sealed slots and open static pressure orifices the critical sound pressure at transition was reduced considerably to values as low as 110 db at higher sound frequencies within the frequency range for amplified Tollmien-Schlichting oscillations in the region of the open surface cavity in the front part of the wing.

According to naphthalene sublimation pictures, transition in the region of the flat pressure distribution in the presence of external sound was usually preceded by closely spaced chordwise striations, indicating the formation of chordwise disturbance vortices in the presence of external sound. (Without sound no striations were observed in the test Reynolds number range.) Apparently, in the presence of external sound, disturbance velocities are induced in the crossflow boundary layer by amplified boundary layer oscillations in other directions. These disturbance velocities are large compared with the maximum crossflow velocity. Due to the presence of the nonlinear terms in the stability equations, when the disturbance velocities are relatively large the crossflow stability limit Reynolds number is lower than the linearized stability theory would predict, and chordwise disturbance vortices are then generated in the presence of strong sound fields. With external sound hot wire measurements in the region of the flat pressure distribution indeed showed amplified boundary layer oscillations sufficiently strong to appreciably reduce the crossflow stability limit Reynolds number.

### B. Investigation of a Straight Laminar Suction Wing

In contrast to a swept laminar suction wing, where the nonlinear theory of the stability of the laminar boundary layer had to be used to understand transition in the presence of external sound, transition on a straight laminar suction wing could be correlated to a certain extent with the linearized boundary layer stability theory. Section II, Part 1, Chapter C and Reference 13 describe the experimental investigation of a 4-percent-thick straight symmetrical laminar suction wing of 17-foot chord at  $\alpha = 0^\circ$  in the Norair 7- by 10-foot low turbulence tunnel. Various disturbances such as external and internal sound, standing sound waves in the suction ducts, and mechanical vibrations of the external wing surface were superimposed. Suction was applied over the whole wing chord through a large number of fine slots. Previously, the same wing had been tested without sound in the Norair 7- by 10-foot tunnel with various chordwise pressure distributions induced by inserts in the tunnel wall (Section II, Part 1, Chapter B and Reference 14). Full chord laminar flow up to  $R_c = 26 \times 10^6$  and  $23 \times 10^6$  was maintained without inserts and with decelerated flow induced by inserts, respectively.

The investigation of this straight low drag suction wing in the presence of sound and surface vibration was conducted without tunnel wall inserts. Transition was caused by external sound, surface vibrations, and internal



## SUMMARY (continued)

noise in the suction ducts. These disturbances were particularly critical when their frequencies correlated with the frequencies for amplified chordwise boundary layer oscillations. With optimum suction ( $C_Q = 1.1 \times 10^{-4}$ ) for minimum drag in the absence of these disturbances the critical external sound pressure for transition at  $R_c = 20 \times 10^6$  was as low as 108 db, corresponding to a critical sound particle velocity ratio  $u'/U_\infty \cong 2.5 \times 10^{-4}$ . Transition due to external and internal sound and surface vibration could be delayed to increased disturbance levels by raising the suction quantities primarily in the most critical area, where the disturbance frequencies correlated with the frequencies for amplified chordwise boundary layer oscillations. Raising  $C_Q$  from  $1.1 \times 10^{-4}$  (for one wing surface) to  $1.8 \times 10^{-4}$  at  $R_c = 20 \times 10^6$  increased the critical external sound pressure for transition to over 130 db, corresponding to a critical sound particle velocity ratio  $u'/U_\infty = 2.7 \times 10^{-3}$ . Relatively small increases in suction rapidly raised the stability limit Reynolds number of the chordwise boundary layer flow and were thus highly effective in raising the critical sound pressure level for transition to much higher values.

With internal noise of certain discrete frequencies, originating from the suction compressor, standing sound waves of high intensity can develop along the suction duct. In this case transition at the higher internal sound pressures ( $> 140$  db at the peak of the standing sound waves) originated from the location of the suction holes underneath the suction slots in the form of turbulent wedges. The latter did not develop when the suction holes and the corresponding slot were sufficiently displaced in chordwise direction.

Internal sound in the suction duct was generally similarly critical with respect to transition as external sound. When external and internal sound were equally strong, the combination of both sound sources required a reduction of approximately three db of both sound sources to avoid transition. When internal sound was not critical, the critical sound pressure of the external sound was not measurably influenced by the presence of the weaker internal sound field, and vice versa.

### C. Investigation of Low Drag Suction Body of Revolution

With the drastic reduction of the friction drag on wings by means of boundary layer suction the parasite drag of the nonlaminarized turbulent fuselage, etc., becomes increasingly important. The question therefore arises as to the basic feasibility of full length laminar flow on three-dimensional bodies at high length Reynolds numbers by means of boundary layer suction. In order to partially answer this question, low drag suction experiments were conducted on a 12-foot long modified Sears-Haack body of revolution of fineness ratio 9 on which low drag boundary layer suction through 120 fine slots was applied (Section II, Part 1, Chapter D-a and Reference 15). In the Norair 7- by 10-foot low-turbulence tunnel full length laminar flow was maintained at  $\alpha = 0^\circ$  angle of attack up to  $R_L \cong 20 \times 10^6$  length Reynolds number, with a minimum equivalent total drag coefficient  $C_D = 0.00038$  (based on body wetted area). Tunnel turbulence and noise caused turbulent bursts and strongly increasing drag above  $R_L = 20 \times 10^6$ .

## SUMMARY (continued)

Practically full length laminar flow over most of the body wetted area was obtained at angles of attack up to  $5^\circ$  at length Reynolds numbers of  $15 \times 10^6$  to  $18 \times 10^6$ .

At further reduced turbulence levels, such as in the atmosphere in flight, considerably higher length Reynolds numbers with full length laminar flow should be feasible.

An analysis of the experimental data (Section II, Part 1, Chapter D-b) at  $\alpha = 0^\circ$  angle of attack showed a satisfactory agreement between the experimentally observed and the computed boundary layer profiles at the end of the body, at least on both sides and the bottom. The top rake at the end of the body often showed a transitional boundary layer profile with a somewhat larger momentum loss than the bottom and side rakes.

## SECTION II PART 2--EXPERIMENTAL AERODYNAMIC INVESTIGATIONS AT SUPERSONIC SPEEDS

### A. Investigation of Flat Plates with Suction with and without Incident Shock Waves

The theoretical investigations of the stability of the laminar boundary layer on a flat plate have shown a rapidly increasing stability limit Reynolds number at higher supersonic speeds. It should, therefore, be possible to maintain laminar flow by means of suction up to higher length Reynolds numbers than at subsonic speeds, as long as boundary layer crossflow is not critical. In order to verify this theoretical expectation, low drag suction experiments were conducted in the Tullahoma supersonic Tunnel A on a laminar flat suction plate, at  $\alpha = 0^\circ$ , with suction applied along the entire length of the plate through 76 slots (Section II, Part 2, Chapter A-a and Reference 16). The suction air was collected in eight suction chambers. At  $M = 3$  full length laminar flow was maintained up to  $R_L = 26.4 \times 10^6$  plate length Reynolds number, with a corresponding equivalent total drag and suction weight flow coefficient  $C_{D_t} = 4.50 \times 10^{-4}$  (including the equivalent suction drag) and  $C_{W_t} = 2.10 \times 10^{-4}$ , respectively. For comparison, the flat plate transition length Reynolds number in the same tunnel is 4.0 to  $4.5 \times 10^6$  at  $M = 3$ . At  $M = 3.5$  full length laminar flow was maintained up to  $R_L = 21.4 \times 10^6$ , and the corresponding total drag and suction weight flow coefficients were  $C_{D_t} = 5.65 \times 10^{-4}$  and  $C_{W_t} = 2.77 \times 10^{-4}$ , respectively. The maximum length Reynolds numbers with full chord laminar flow were limited by the maximum available tunnel pressure both at  $M = 3$  and 3.5. At  $M = 3$  and  $R_L = 26.4 \times 10^6$  the estimated ratio of mean particle velocity induced by the sound from the turbulent boundary layer of the wind tunnel test section to the undisturbed velocity is  $u'/U_\infty \approx 1.5$  to  $2.0 \times 10^{-3}$ . It is remarkable that laminar flow could be maintained up to these Reynolds numbers in the presence of the intense sound field in the test section of the tunnel. Thus, the experiments have verified the theoretical expectation that laminar flow by means of suction should be feasible at supersonic speeds up to quite high length Reynolds numbers, at least as long as boundary layer crossflow is not critical.

Weak incident shock waves at supersonic speeds may interact with the boundary layer of laminarized areas. The question then arises concerning

## SUMMARY (continued)

the feasibility of laminar flow in and downstream of regions of intersections with weak incident shock waves and, in particular, about the effectiveness of local boundary layer suction in the region of the shock intersection in raising the shock strength with laminar flow. In order to answer these questions, boundary layer suction experiments were conducted by the Northrop Norair Boundary Layer Research Section and I. Greber (MIT) on a flat plate (designed and built by the Northrop Norair Boundary Layer Research Section) at  $M = 2.0$  in the supersonic tunnel of the MIT Gas Turbine Laboratory (References 18 and 19). An incident shock was generated by an inclined flat plate. This shock intersected the test plate along a straight line in spanwise direction. Suction was applied in and downstream of the shock intersection region plate leading edge to the shock intersection position varied from 500,000 to 800,000; the total plate length Reynolds number was approximately twice as large.

The following results were obtained. At a length Reynolds number of 500,000 (based on length from the plate leading edge to the shock intersection) separation started at a shock strength (pressure ratio across shock in intersection region) of 1.20 without suction, as compared with a value of 1.62 with suction ( $C_Q$  was 0.0011, based on the area covered by the slots). Full length laminar flow to the plate trailing edge was observed with slightly stronger shocks. The Schlieren pictures showed a much thinner layer of separated flow with suction applied in the intersection region, as compared with the case without suction. As long as suction was effective in maintaining full length laminar flow on the plate, the pressure rise in the shock intersection region was steep but continuous and smooth, in contrast to the pressure rise without suction, which generally showed a flat pressure plateau in the separated region upstream of transition in the shock intersection area.

At higher length Reynolds numbers the critical shock strength with full length laminar flow decreased. For example, at a length Reynolds number of 800,000 (based on the plate length to the shock intersection or  $1.6 \times 10^6$ , based on total plate length) the critical shock strength with suction was 1.45.

In many cases oblique shock waves generated by three dimensional bodies may intersect the laminarized surfaces of a supersonic low drag suction airplane. The intersection of the shock with the laminarized surface is then a straight line under an oblique angle to the main flow. The question then arises concerning the maintenance of laminar flow by means of boundary layer suction on surfaces which are intersected by oblique weak incident shock waves. In order to answer this question, an inclined flat plate mounted normal to the above-described supersonic suction plate was used in Tullahoma Tunnel A to generate a weak shock which intersected the test area of the plate at the shock angle (Section II, Part 2, Chapter A-b and Reference 17). The test surface and the suction system were the same as during the previous plate experiments in the supersonic Tullahoma Tunnel A.

At  $M = 3$  full length laminar flow was maintained on the suction plate up to the test limit of Tullahoma Tunnel A, corresponding to  $R_L = 26.4 \times 10^6$  plate length Reynolds number, at shock pressure ratios of 1.10. The corresponding values for equivalent total drag and suction weight flow coefficient at  $M = 3$

## SUMMARY (continued)

and  $R_L = 26.4 \times 10^6$  were  $C_{D_t} = 0.00050$  and  $C_{W_t} = 0.00027$ , respectively. At lower plate length Reynolds numbers the shock pressure ratio for full length laminar flow on the plate increased; at  $M = 3$  and  $R_L = 11 \times 10^6$  laminar flow was maintained at shock pressure ratios up to 1.17.

These results are promising insofar as they basically prove the feasibility of laminar flow through and downstream of regions of intersections of incident shock waves at supersonic speeds by means of boundary layer suction.

### B. Investigations of a Supersonic Ogive Cylinder

In addition to supersonic low drag suction experiments on a flat plate and supersonic wings, an ogive of revolution with a cylindrical afterbody was tested in the 12- by 12-inch E-1 blowdown tunnel in Tullahoma (Section II, Part 2, Chapter B and Reference 20). Low drag boundary layer suction was applied through 29 suction slots connected to four individual suction chambers. (The small size of the model did not easily permit the installation of a larger number of slots.) Full length laminar flow at  $M = 2.5$  and 3 was maintained up to a length Reynolds number of  $16 \times 10^6$  and  $12 \times 10^6$ , respectively. The corresponding values for the equivalent total drag and suction weight flow coefficient (based on body wetted area) were at:

<u>M</u>	<u><math>R_L \times 10^{-6}</math></u>	<u><math>C_{D_t} \times 10^4</math></u>	<u><math>C_{W_t} \times 10^4</math></u>
2.5	15	5.1	2.0
3.0	12	6.1	1.8

The wave drag is not included in these drag figures. At higher Reynolds numbers tunnel noise, primarily from the blowdown valve, caused turbulent bursts and a rapidly rising drag with Reynolds number.

### C. Investigations of Swept Wings with Supersonic Leading Edges

The supersonic laminar flow suction experiments discussed thus far were concerned with two-dimensional boundary layers flowing in the direction of the undisturbed stream. The next item to be investigated was the effect of boundary layer crossflow at supersonic speeds. Since two different types of potential flow fields exist on swept wings, depending on whether they are swept ahead or aft of the Mach cone, two separate investigations were required.

A  $36^\circ$  swept wing of constant chord and a 3-percent-thick biconvex airfoil section (perpendicular to the leading edge) was selected for investigating the effects of boundary layer crossflow on a swept wing with a supersonic leading edge (Section II, Part 2, Chapter C-a and Reference 21). Suction experiments were conducted at the AEDC Tunnel A on a model of 39 inches chord (in flow direction) at Mach numbers between 2.5 and 3.5. Laminar flow was maintained up to the highest tunnel pressures, resulting in maximum length Reynolds numbers of the order of  $17$ ,  $25$  and  $20 \times 10^6$  at Mach numbers 2.5, 3.0 and 3.5, respectively. The Reynolds numbers are defined by chord length and velocity in flow direction. Two different suction systems were built for the

## SUMMARY (continued)

model, and two separate tests were conducted to cover the whole Mach and Reynolds number range. The model with the narrower slots provided better data at  $M = 2.5$ , while better data at  $M = 3.5$  was obtained with the wider slots. Two additional slots in front on the second suction system were required to cover the highest possible Reynolds numbers at  $M = 3.0$  and  $3.5$ . The tests showed a higher sensitivity of the laminar boundary layer to local suction quantities and slot widths than was observed on the previous models without crossflow. In general, high suction was required in the front half and low in the rear. Expressed in terms of the nondimensional inflow velocity coefficient,  $f_0^* > 2.0$  for  $x/c < 0.50$ ;  $f_0^* \sim 1.0 - 1.2$  near the trailing edge.

Computation of the laminar boundary layer development for such suction distributions gave values of crossflow Reynolds numbers at which full chord laminar flow was maintained:  $R_{0.1} < 180$  at 70 percent chord and  $R_{0.1} < 250$  near the trailing edge seem to be adequate design numbers. It was observed at  $M = 3.0$  and  $3.5$  that further reductions in total drag were possible by a further reduction of suction in the rear portion of the wing. Although the boundary layer profile became unstable, the increase in wake drag was less than the reduction in suction drag. In these cases, the theoretical laminar crossflow Reynolds number would have been of the order of 350.

The location of the first slot on the  $36^\circ$  swept suction wing was determined on account of the available test results on natural transition measurements. Most of the published data were obtained on swept wings with flat surfaces. A test program on boundary layer transition measurements on contoured swept wings was therefore initiated (Section II, Part 2, Chapter C-b and Reference 22). The model had the same cross section as the  $36^\circ$  swept suction wing; its sides were cut off in such a way that sweep angles of  $24$  and  $50^\circ$  could also be investigated. The model of 9.45-inch chord (perpendicular to the leading edge) was tested at the AEDC Tunnel E-1 at Mach numbers between 2.5 and 5.0. The main result of these measurements was that transition was affected predominantly by the bluntness of the leading edge. The crossflow from the swept cylindrical nose was more powerful than the crossflow which developed from the pressure distribution over the curved surface. The reduction of the transition Reynolds number due to sweep followed the trend observed in NASA experiments on blunt flat plate models.

### D. Investigation of a Highly Swept Supersonic Laminar Suction Wing, Swept Behind the Mach Cone

In order to obtain the maximum benefit from the application of low drag boundary layer suction to supersonic airplanes, it is desirable to reduce the supersonic wave drag, particularly due to lift, along with the reduction of the friction drag. The supersonic wave drag can be greatly reduced by distributing the aerodynamic lift over a relatively large wing span and, in addition, over a large length. In this respect, highly swept supersonic laminar suction wings with subsonic type flow over a large part of the wing appear attractive from the standpoint of low wave drag. The question then arises concerning the basic feasibility of full chord laminar flow of subsonic type on a highly swept wing at moderately high supersonic speeds. In order to answer this question, low drag suction experiments were conducted

## SUMMARY (continued)

in the 40- by 40-inch supersonic Tullahoma Tunnel A at  $M = 2.0$  and  $2.25$  on a  $72.5^\circ$  yawing cambered wing of constant chord. These experiments are described in Section II, Part 2, Chapter D and in Reference 23. The design of a highly swept supersonic laminar suction wing is strongly influenced by boundary layer crossflow consideration, particularly in the region of the steep rear pressure rise. Relatively strong suction must then be used in the rear part of the wing to maintain full chord laminar flow under these severe crossflow conditions. In order to approach area suction, which is aerodynamically optimum, a large number of closely spaced suction slots are required in this area of the wing. With the small scale of the model and the correspondingly high unit length Reynolds number, the slot spacing becomes very small in the rear part of the model, and the maximum wing chord Reynolds number with full chord laminar flow is then largely limited by the slot spacing and the size of the model. The model was therefore designed for wing chord Reynolds numbers between  $5$  and  $10 \times 10^6$ .

The experiments showed full chord laminar flow with a subsonic type pressure distribution of zero wave drag at  $M = 2$  and  $C_L = 0.065$  to  $0.07$  up to  $R_c = 9 \times 10^6$  wing chord Reynolds number. At  $M = 2.25$  and  $C_L \approx 0.08$  full chord laminar flow was observed with zero wave drag at  $R_c = 6.5 \times 10^6$ . The total equivalent wing profile drag for the upper wing surface at  $R_c = 8 \times 10^6$  and  $M = 2$  was  $C_{D\infty} \approx 0.0013$  (including the equivalent suction drag). This drag is relatively high due to the high suction quantities which are required to avoid transition from crossflow instability. In contrast to the upper surface, the rear pressure rise on the lower wing surface would be very small, and very much weaker suction should then be adequate to maintain laminar flow on the lower wing surface (the estimated equivalent profile drag of the lower wing surface would then be equal to approximately half of the value for the upper surface).

A supersonic low drag suction airplane with highly swept wings would most likely have tapered wings with considerably reduced wing sweep at the wing trailing edge, with the flow component normal to the isobars being sonic over the whole chord or slightly supersonic toward the trailing edge. With the reduced trailing edge sweep the crossflow in the most critical area of the rear pressure rise is then greatly alleviated, as compared with a wing of constant chord without taper, resulting in reduced suction quantities and further reduced wing profile drags.

### E. Pressure Drop in Tubes with Compressible Laminar Flow

At supersonic speeds the pressure drop through the components of the suction ducting system of a low drag suction airplane or model can become large compared to the absolute pressure. Compressible flow must then be assumed for the analysis of the pressure change in the components of the suction ducting system such as the suction slots, holes and ducts.

In order to provide data for the compressible laminar pressure drop in suction holes, the pressure distribution with laminar flow was measured along the inside of a circular tube of 0.244-inch inside diameter and 11.3-foot length for several inlet Mach numbers  $M_0$  and reservoir pressures  $p_k$  (Section II, Part 2, Chapter E and Reference 24). The pressure ratio  $p/p_k$

### SUMMARY (continued)

is presented versus the nondimensional tube length  $x/RR_R$  for various inlet Mach numbers.  $R_R = \bar{U}_0 R / \nu_0$  is the Reynolds number based on tube radius  $R$  and the mean velocity  $\bar{U}_0$  at the tube inlet. With increasing values of  $M_0$  and  $x/RR_R$  the density and static pressure decreased rapidly until choking occurred at pressures  $p \cong (0.20 \text{ to } 0.25)p_k$ , which are considerably lower than for one-dimensional tube flow. Boundary layer measurements showed supersonic flow in the center and subsonic flow toward the wall of the tube when choking occurred, with an average Mach number of approximately one.

The maximum tube length Reynolds number with laminar inlet flow was  $\bar{U}_0 x / \nu_0 = 26.1 \times 10^6$  at  $M_0 = 0.430$ .

## TABLE OF CONTENTS



# TABLE OF CONTENTS

	<u>Page</u>
FOREWORD.....	ii
ABSTRACT.....	iii
SUMMARY.....	iv

## SECTION I THEORETICAL INVESTIGATIONS

CHAPTER A. CURRENT STATUS OF RESONANCE THEORY OF TRANSITION.....	1
G. S. Raetz	
CHAPTER B. EXACT NUMERICAL SOLUTION OF THE COMPLETE LEES-LIN EQUATIONS FOR THE STABILITY OF COMPRESSIBLE FLOW.....	55
W. B. Brown	
CHAPTER C. CROSSFLOW STABILITY CALCULATIONS ON HIGHLY SWEEP (65° SWEEP) SUPERSONIC LOW DRAG BLC WING (MACH NUMBER 1.8) WITH AND WITHOUT COOLING.....	68
W. B. Brown	
CHAPTER D. INCOMPRESSIBLE CROSSFLOW STABILITY CALCULATIONS WITH VARIOUS ANGLES OF THE WAVE FRONTS WITH THE POTENTIAL FLOW DIRECTION.....	73
W. B. Brown	
LIST OF FIGURES FOR SECTION I.....	75
FIGURES FOR SECTION I.....	76

## SECTION II PART I EXPERIMENTAL AERODYNAMIC INVESTIGATIONS AT SUBSONIC SPEEDS

CHAPTER A. EXPERIMENTAL INVESTIGATION AND THEORETICAL ANALYSIS OF LAMINAR BOUNDARY LAYER SUCTION ON A 30° SWEEP, 12-PERCENT-THICK WING IN THE NASA AMES 12-FOOT PRESSURE WIND TUNNEL.....	96
L. W. Gross	
J. W. Bacon, Jr.	
V. L. Tucker	
CHAPTER B. EXPERIMENTAL INVESTIGATION OF A 4-PERCENT-THICK STRAIGHT LAMINAR SUCTION WING OF 17-FOOT CHORD IN THE NORAIR 7- BY 10-FOOT WIND TUNNEL.....	111
L. W. Gross	
CHAPTER C. INVESTIGATIONS OF A 30° SWEEP AND A 17-FOOT CHORD STRAIGHT SUCTION WING IN THE PRESENCE OF INTERNAL SOUND, EXTERNAL SOUND, AND MECHANICAL VIBRATIONS.....	120
J. W. Bacon, Jr.	
W. Pfenninger	
C. R. Moore	

CHAPTER D. LAMINARIZATION OF A SEARS-HAACK BODY OF REVOLUTION BY MEANS OF BOUNDARY LAYER SUCTION	
a. Investigation of a Laminar Suction Modified Sears-Haack Body of Revolution in the Norair 7- by 10-Foot Wind Tunnel.....	155
L. W. Gross	
b. Analysis of the Boundary Layer Development on a Modified Sears-Haack Suction Body of Revolution.....	166
Hartmut H. K. Bossel	
LIST OF TABLES FOR SECTION II PART 1.....	172
TABLES FOR SECTION II PART 1.....	173
LIST OF FIGURES FOR SECTION II PART 1.....	192
FIGURES FOR SECTION II PART 1.....	209

SECTION II PART 2  
EXPERIMENTAL AERODYNAMIC INVESTIGATIONS  
AT SUPERSONIC SPEEDS

CHAPTER A. INVESTIGATION OF A LAMINAR FLAT PLATE WITH SUCTION THROUGH MANY FINE SLOTS WITH AND WITHOUT WEAK INCIDENT SHOCK WAVES	
a. Low Drag Boundary Layer Suction Experiments on a Flat Plate at Mach Numbers 2.5, 3.0, and 3.5.....	428
E. E. Groth	
b. Boundary Layer Suction Experiments on a Slotted Flat Plate Model with Interfering Shock Waves.....	442
E. E. Groth	
CHAPTER B. LOW DRAG BOUNDARY LAYER SUCTION EXPERIMENTS AT SUPERSONIC SPEEDS ON AN OGIVE CYLINDER WITH 29 CLOSELY SPACED SLOTS.....	
E. E. Groth	
CHAPTER C. INVESTIGATIONS OF SWEEPED WINGS WITH SUPERSONIC LEADING EDGES	
a. Low Drag Boundary Layer Suction Experiments on a 36° Swept Wing at Mach Numbers 2.5, 3.0 and 3.5.....	464
E. E. Groth	
b. Boundary Layer Transition Measurements on Swept Wings at Supersonic Speeds.....	481
E. E. Groth	
CHAPTER D. INVESTIGATION OF LAMINAR FLOW CONTROL AIRFOILS SWEEPED BEHIND THE MACH ANGLE	
a. Low Drag Boundary Layer Suction Experiments on a 72° Swept Wing Model at Mach Number 2.0 and 2.25.....	487
J. Goldsmith	
b. Calculation of Compressible Flow Losses through Swept Suction Slots.....	509
J. Goldsmith	
CHAPTER E. PRESSURE DROP IN LAMINAR FLOW TUBES WITH COMPRESSIBLE FLOW..	
W. Pfenninger	
K. H. Rogers	

	<u>Page</u>
LIST OF TABLES FOR SECTION II PART 2.....	551
TABLES FOR SECTION II PART 2.....	552
LIST OF FIGURES FOR SECTION II PART 2.....	575
FIGURES FOR SECTION II PART 2.....	588

### SECTION III STRUCTURAL INVESTIGATIONS

CHAPTER A. STRUCTURAL ASPECTS OF LOW DRAG SUCTION AIRFOILS.....	794
J. Wieder	
W. Pfenninger	
CHAPTER B. SKIN DUCTING SYSTEM CONFIGURATION FOR LFC AIRCRAFT MAIN STRUCTURAL BOX.....	801
R. N. Worth	
CHAPTER C. EFFECT OF WEATHERING ON TYPICAL BONDED BOUNDARY LAYER CONTROL STRUCTURE.....	809
R. N. Worth	
LIST OF TABLES FOR SECTION III.....	821
TABLES FOR SECTION III.....	822
LIST OF FIGURES FOR SECTION III.....	829
FIGURES FOR SECTION III.....	831

### SECTION IV REFERENCES

LIST OF REFERENCES.....	858
-------------------------	-----

**SECTION I**  
**THEORETICAL INVESTIGATIONS**

## CHAPTER A. CURRENT STATUS OF RESONANCE THEORY OF TRANSITION

G. S. Raetz

### (A) Abstract

An improved form of the resonance theory of transition, first proposed by the author in 1959, is described. For simplicity, mainly a boundary layer generated on a flat wall by an unaccelerated flow of an incompressible fluid is considered. Also, as the conditions causing transition, mostly simple irregularities at the wall surface and in the adjoining flow are assumed. The main features of the resulting motion are deduced from the continuity and Navier-Stokes equations.

In this deduction, the whole motion first is decomposed into a basic flow, chosen as the laminar flow occurring in the absence of the boundary irregularities, and a sequence of perturbation flows. The basic flow satisfies a nonlinear but solvable differential system, whereas the perturbation flows all satisfy inhomogeneous linear differential systems. The first-perturbation flow, having just homogeneous differential equations, is determined solely by the boundary values representing the irregularities at the wall surface and in the adjoining flow. All higher-perturbation flows, having just trivial boundary values, are determined solely and recursively from lower-perturbation flows by inhomogeneous terms called driving functions in their differential equations. Thereby, the whole nonlinear disturbance motion is related directly and completely to the boundary irregularities themselves. Subsequently, each perturbation flow is decomposed into a general spectrum of Fourier components with aperiodically varying coefficients.

According to the theory, the main features of transition and also of turbulence are due to partial resonances of some Fourier components with the driving functions. The downstream growths of the coefficients of these Fourier components include variations like the exponential growths of ordinary linear stability theory and, more importantly, other variations which can be much faster and larger. As a result, the resonance theory seems to explain many properties of transition beyond the scope of linear theory and various other concepts.

Furthermore, the theory appears to offer a possible way of estimating transition motions and related phenomena, including the actual introduction of disturbances by boundary irregularities and perhaps certain properties of turbulence. Some aspects of such calculations as well as some generalizations of the theory to other flows are discussed.

### (B) Principal Notation

$a_k^*$	spacewise fundamental frequency
$a_k^\sigma$	spacewise harmonic frequency
$b_k$	spacewise growth factor
$c$	phase velocity

---

Manuscript released by the authors March 1964 for  
publication as an ASD Technical Documentary Report.

(B) Principal Notation (continued)

$c^*$	timewise fundamental frequency
$c^\sigma$	timewise harmonic frequency
$e_k^t$	bilinear norm component
$f_{jk}$	driving tensor component
$h^T$	resonance coefficient
$i$	unit imaginary number
$n_k$	unit outward normal component
$p$	pressure
$q$	pressure (in adjoining flow)
$r$	adjoint pressure
$s_j$	adjoint velocity component
$t$	time
$u_j$	velocity component
$v_j$	velocity component (at wall surface)
$w_j$	velocity component (in adjoining flow)
$x_k$	Cartesian coordinate
$x_k^0$	Cartesian coordinate (at wall surface)
$x_k^\infty$	Cartesian coordinate (in adjoining flow)
$z$	distance from wall surface
$\alpha$	principal frequency
$\beta$	frictional frequency
$\gamma$	normal frequency
$\delta_{jk}$	unit tensor component
$\epsilon$	perturbation parameter
$\zeta_{jk}$	adjoint velocity gradient component

(B) Principal Notation (continued)

$\tau_{jk}$	adjoint stress balance component
$\mu$	viscosity (shearing)
$\xi_{jk}$	adjoint momentum gradient component
$\rho$	density
$\varphi_{jk}$	velocity product component
$\psi_{jk}$	velocity gradient component
$\omega_{jk}$	stress balance component
$A_k$	spacewise complex frequency
$D$	transition domain
$E^\sigma$	phase function
$G$	growth function (initial or driving)
$H^T$	growth function (resonance)
$J_k^T$	integration constant
$K^T$	resonance kernel
$P^o$	pressure (basic flow)
$Q^o$	pressure (adjoining basic flow)
$R$	Reynolds number (local)
$U_j^o$	velocity component (basic flow)
$W_j^o$	velocity component (adjoining basic flow)
$\Lambda$	reference length
$U$	reference velocity

Subscripts\*:

$j, k, m, n$  tensor component indices

---

\*When the same index appears twice in a subscript, a summation of terms over the range of that index always is implied.

Subscripts: (continued)

,k co-variant derivative\* (with respect to  $x_k$ )  
,mn co-variant derivative\* (with respect to  $x_m$  and  $x_n$ )  
,t partial derivative (with respect to t)

Superscripts:

$\alpha$  harmonic index (injection flow)  
 $\beta$  harmonic index (fluctuation flow)  
 $\gamma$  harmonic index (resonance flow)  
 $\kappa$  amplitude coefficient (initial)  
 $\lambda$  amplitude coefficient (resonance)  
 $v, v_*$  perturbation component indices  
 $\sigma, \sigma_*$  harmonic component indices

T proper solution number

Miscellanea:

$d(x_m)$  volume differential  
 $O( )$  order of magnitude  
 $(\sim)$  complex conjugate value  
 $(\wedge)$  dimensionless value  
 $(\bar{\phantom{x}})$  fluctuation flow quantity  
 $(\underline{\phantom{x}})$  injection flow quantity

(C) Introduction

In the development and application of laminar flow control techniques, as well as in many other technical fields, a principal handicap always has been the lack of an adequate theory of boundary layer transition. In fact, in all laminar flow control projects undertaken so far, this obstacle has been overcome only by essentially empirical procedures, such as extrapolating experimental transition data by use of ordinary linear stability theory. Thus, notwithstanding the notable success attained in some of these projects, the actual mechanism of transition never has been fully understood, and progress has been hindered accordingly.

---

\*Identical to partial derivative (in Cartesian coordinates)



(C) Introduction (continued)

In an attempt to provide an adequate understanding and thereby to lay a foundation for greater progress in the future, the resonance theory of transition was conceived and developed. The original form of this theory first was presented by Raetz (Reference 1). Later, it was described briefly at the Tenth International Congress of Applied Mechanics by Stuart (Reference 53). Also, a feature of this form needing some clarification was pointed out at a meeting of the American Physical Society by Benney and Lin (Reference 27). At present, a substantially improved and extended form of the theory, believed to be useful as a basis for analyzing and predicting transition phenomena and for calculating some transition and turbulence motions as well, has been evolved. The basic elements of this form of the theory are explained here.

To simplify the analysis as much as feasible, just a relatively simple boundary layer development is examined in detail. Specifically, except for some generalizations indicated later, the boundary layer is assumed to be generated on a flat wall by an unaccelerated flow of an incompressible fluid. Thus, without irregularities at the wall surface and in the adjoining flow, the well-known Blasius laminar boundary layer would exist over the entire wall. To include elementary conditions that can cause transition, a weak simple injection of fluid through the wall surface and a weak simple fluctuation of the adjoining flow are assumed to occur. Otherwise, the wall surface is regarded as completely smooth, and the mean flow itself is regarded as uncurved and as parallel to the wall except for a slight deviation due to the boundary layer growth. For such conditions, a Cartesian coordinate system along with a Cartesian tensor notation is satisfactory and therefore is used, and a major boundary value problem associated with a rough wall is avoided.

In the analysis, a basic technique is to decompose each unknown (such as the pressure, velocity, or stress) into simple elements which, in general, can be investigated and calculated separately and relatively easily. Thus, after decomposing each unknown into its tensor components, each tensor component is decomposed into a basic component (chosen as the tensor component for completely laminar flow) and a sequence of perturbation components, and then each perturbation component is decomposed into a multi-dimensional spectrum of Fourier components (containing a mean component as well as oscillation components). To adequately cope with a nonlinearity of the problem, each Fourier component is represented by a product of a periodic phase function and an aperiodic Fourier coefficient which in turn is represented by a product of a growth function and an amplitude coefficient. The growth function includes any rapid variation along the wall surface, while the amplitude coefficient includes the rapid variation normal to that surface. Eventually, in the actual calculations, the amplitude coefficient in an approximate form would be decomposed into fundamental solutions of an ordinary linear differential system. The whole motion itself is constructed merely by recomposing the elements thus found. Although such motion often may appear to be exceptionally complicated, relatively few of the many possible elements usually need to be investigated and calculated. Due to the number of decompositions, though, the notation is tedious and must be carefully treated.

In a corresponding manner, the differential system for the whole motion, which includes the nonlinear Navier-Stokes equations, is decomposed into a basic system (identical to the nonlinear system for completely laminar flow) and a sequence of perturbation systems (all linear), and then each perturbation system is decomposed into a multi-dimensional spectrum of Fourier systems. In the first-perturbation systems, the differential equations are all homogeneous,

(C) Introduction (continued)

whereas in the higher-perturbation systems, the differential equations contain driving functions (inhomogeneous terms) that depend solely on products of lower-perturbation components. Consequently, the first-perturbation components are determined completely by the boundary values representing the injection at the wall surface and the fluctuation of the adjoining flow, and all higher-perturbation components are determined completely by their driving functions and thus recursively from lower-perturbation components. Thereby, all Fourier components are determined individually and explicitly in a sequence starting from the Fourier spectra of the boundary irregularities themselves. In these determinations, by extracting the phase and growth functions, the Fourier systems are reduced to amplitude coefficient systems, which in turn are approximated with sufficient accuracy by ordinary linear differential systems that are similar or, in many cases, identical to the well-known Orr-Sommerfeld system.

According to the resonance theory, the main features of transition and also of turbulence are due to partial resonances of some Fourier components with their driving functions. For example, two Fourier components, such as one from the fluid injection distribution and one from the adjoining flow fluctuation, may form driving functions having space and time frequencies which, over some part of the wall, happen to almost coincide with the natural frequencies of the driven Fourier component. In this case, over that part of the wall, the latter component will grow rapidly and greatly with downstream distance, although elsewhere it usually will grow or decay only slowly. Such variations are included in the applicable growth function, which therefore is especially important in the analysis. Likewise, over other parts of the wall, other partial resonances from other pairs of Fourier components of the same or other perturbations may occur. In the whole process, the mean components of some perturbations can become large, causing a large distortion of the whole mean flow, and certain oscillation components of various perturbations can become significant, producing a variety of oscillatory phenomena like those observed at transition and in turbulence. Conversely, over a part of the wall, for certain boundary values, motions resembling those predicted by ordinary linear stability theory can appear, and over other parts of the wall, motions resembling those of other theories evidently can occur insofar as such theories are valid. Thus, it appears that many correlations with experimental observations on transition, as well as with the verifiable parts of related theories, eventually can be established.

In more general boundary layers, various special phenomena can be caused by similar resonances. For example, when the wall surface is appropriately curved, Görtler vortices can be produced, and when the adjoining flow is sufficiently curved, crossflow vortices can be generated. In the resonance regions, the growth of these vortices with downstream distance will differ substantially from that predicted by ordinary linear stability theory, perhaps explaining a discrepancy between that theory and experiment. Also, the effect of wall vibration and external sound on the boundary layer development apparently can be explained satisfactorily by partial resonances. Moreover, it appears that the influence of wall roughness on transition and turbulence can be forecast once a suitable technique for handling an associated linear boundary-value problem is developed. Furthermore, analogous resonances can occur in compressible flows, probably explaining the principal features of transition at subsonic, supersonic, and even hypersonic speeds. Indeed, in still more general flows, important features of a variety of critical phenomena -- such as the combustion instability of rocket motors, the plasma instability of thermonuclear power devices, and the general circulation of the atmosphere -- probably can be explained and analyzed in terms of similar partial resonances.

(C) Introduction (continued)

Due to the large number of other investigations of transition that have been and are being conducted, a proper resume' of other transition theories delineating between seemingly valid and invalid aspects would be too lengthy to be practical here. However, some of the current theories and related work, as well as references to earlier research, are included in the papers listed as references. Needless to say, the present theory is indebted to these and other theories and investigations for some techniques and details and also for some hints as to promising and unpromising directions of search. Also, in developing this theory, the author personally was aided by many discussions with Dr. Werner Pfenninger. This assistance is acknowledged with gratitude.

(D) Differential Systems

To adequately explain the theory, several differential systems and some special quantities and concepts first must be introduced. The inherent complexity of transition seems to preclude a satisfactory simpler approach, at least in this preliminary exposition.

(1) General System

To represent the transition region, Cartesian coordinates  $x_k$  ( $k = 1, 2, 3$ ) are used, the boundary layer being generated on a wall surface at  $x_3 = 0$  by an adjoining flow at  $x_3 = \infty$ . When necessary to be more specific, the whole mean flow is regarded as in the positive  $x_1$ -direction. The velocity components  $u_j$  ( $j = 1, 2, 3$ ) and the pressure  $p$  vary with the coordinates and also the time  $t$ , whereas the density  $\rho$  and the viscosity  $\mu$  are constants. Co-variant derivatives, which in these coordinates are identical to partial derivatives, are denoted by a subscript comma followed by the subscript indices associated with the varied coordinates; for example,  $u_{j,k} = \partial u_j / \partial x_k$  and  $u_{j,mn} = \partial^2 u_j / \partial x_m \partial x_n$  ( $m, n = 1, 2, 3$ ). Similarly, timewise partial derivatives are denoted by a subscript comma followed by a subscript letter  $t$  for each differentiation; for example,  $u_{j,t} = \partial u_j / \partial t$ . Wherever the same index appears twice in a subscript, a summation of terms over the range of that index always is implied; for example,  $u_{j,j} = u_{1,1} + u_{2,2} + u_{3,3}$ . (This convention, though, is not extended to superscripts.)

In this notation, the differential equations of the whole motion, which include the incompressible continuity and Navier-Stokes equations, usually would be expressed in a form such as

$$u_{j,j} = 0$$

$$\rho(u_{j,t} + u_{j,k}u_k) = -p_{,j} + \mu u_{j,kk} \quad (1)$$

where  $j$  and  $k$  range over 1, 2, 3 (see, for example, Reference 25). Here, however, another form is more convenient and therefore is used. Thus, to confine the nonlinearity to a simple algebraic relation, the velocity product components  $\varphi_{jk} = u_j u_k$  are introduced, and to allow a first-order system the velocity

(1) General System (continued)

gradient components  $\psi_{jk} = u_{j,k}$  are included. Also, to arrive at shorter equations later, the stress balance components  $\omega_{jk} = \rho c_{jk} + p \delta_{jk} - \mu(\psi_{jk} + \psi_{kj})$  are used, where the unit tensor components  $\delta_{jk}$  equal 1 if  $j = k$  but equal 0 if  $j \neq k$ . Thus, the equations to be considered are

$$\begin{aligned} c_{jk} &= u_j u_k \\ \psi_{jk} &= u_{j,k} \\ \omega_{jk} &= \rho c_{jk} + p \delta_{jk} - \mu(\psi_{jk} + \psi_{kj}) \\ \psi_{jj} &= 0 \\ \rho u_{j,t} + \omega_{jk,k} &= 0 \end{aligned} \quad (2)$$

where  $j, k = 1, 2, 3$ . Equations (1) are regained merely by eliminating  $c_{jk}$ ,  $\psi_{jk}$ , and  $\omega_{jk}$ .

As will become apparent, several boundary conditions for these equations already are implied by the type of motion considered. Consequently, as boundary values, just the wall surface velocity components  $v_j$  ( $j = 1, 2, 3$ ) along with the adjoining flow velocity components  $w_j$  ( $j = 1, 2, 3$ ) and the adjoining flow pressure  $q$  are needed here. Thus, identifying coordinates at the wall surface and in the adjoining flow by the superscripts  $0$  and  $\infty$ , respectively, the boundary conditions to be imposed explicitly are

$$\begin{aligned} u_j(x_k^0, t) &= v_j \\ u_j(x_k^\infty, t) &= w_j \\ p(x_k^\infty, t) &= q \end{aligned} \quad (3)$$

where  $j, k = 1, 2, 3$  and  $v_j$ ,  $w_j$ ,  $q$  are given functions. As is essential,  $w_j$  and  $q$  are to satisfy Equations (1) or (2) within the adjoining flow itself.

(2) Perturbation Systems

To obtain a sequence of differential systems that can be solved in a convenient manner, all dependent variables are represented by perturbation series in a perturbation parameter  $\epsilon$ , which is stipulated later. Perturbation coefficients are distinguished by the superscript  $v$  (or  $v_*$ ) alone whereas parameter powers are indicated by parentheses with the superscript  $v$  attached. For example, the velocity components and the pressure are to be represented as

$$\begin{aligned} u_j &= \sum_0^\infty u_j^v(\epsilon)^v \\ p &= \sum_0^\infty p^v(\epsilon)^v \end{aligned} \quad (4)$$

## (2) Perturbation Systems (continued)

Substituting such series and equating coefficients of equal powers of  $\epsilon$ , Equations (2) and (3) decompose into the perturbation differential equations

$$\begin{aligned}\phi_{jk}^v &= \sum_0^v u_j^{v-v*} u_k^{v*} \\ \psi_{jk}^v &= u_{j,k}^v \\ \omega_{jk}^v &= \rho \phi_{jk}^v + p^v \delta_{jk} - \mu (\psi_{jk}^v + \psi_{kj}^v) \\ \psi_{jj}^v &= 0 \\ \rho u_{j,t}^v + u_{jk,k}^v &= 0\end{aligned}\tag{5}$$

and the perturbation boundary conditions

$$\begin{aligned}u_j^v(x_k^0, t) &= v_j^v \\ u_j^v(x_k^\infty, t) &= w_j^v \\ p^v(x_k^\infty, t) &= q^v\end{aligned}\tag{6}$$

where  $v = 0, 1, 2, \dots, \infty$  and  $v_j^v, w_j^v, q^v$  are given. These systems are to be solved, insofar as is necessary, separately but recursively (in the same order as their perturbation orders). In most cases, based on available evidence, the resulting series should converge satisfactorily. Otherwise, in exceptional cases not covered here, incorporation of some technique for summing slowly converging or diverging series (see, for example, References 35 and 36) might be desirable or necessary\*.

The singular perturbation component for  $v = 0$ , called the basic flow, is chosen to be the steady laminar flow that would occur if the wall surface irregularity and the adjoining flow fluctuation were absent. Thus, replacing lower by upper case letters for emphasis, the basic flow system is

$$\begin{aligned}\phi_{jk}^0 &= U_j^0 U_k^0 \\ \psi_{jk}^0 &= U_{j,k}^0 \\ \Omega_{jk}^0 &= \rho \phi_{jk}^0 + P^0 \delta_{jk} - \mu (\psi_{jk}^0 + \psi_{kj}^0) \\ \psi_{jj}^0 &= 0 \\ \Omega_{jk,k}^0 &= 0\end{aligned}\tag{7}$$

\*For example, a truly parallel flow, such as an asymptotic suction boundary layer, may entail questionable convergence.

(2) Perturbation Systems (continued)

and

$$\begin{aligned} U_j^0(x_k^0, t) &= 0 \\ U_j^0(x_k^\infty, t) &= W_j^0 \\ P^0(x_k^\infty, t) &= Q^0 \end{aligned} \quad (8)$$

where  $W_1^0$  and  $Q^0$  are given constants,  $W_2^0 = 0$ , and  $W_3^0$  need not be given. ( $W_3^0$  is ascertainable by substituting  $W_1^0$ ,  $W_2^0$ , and  $Q^0$  into Equations (7).) Due to the quadratic terms in the first equation, the basic flow system, unlike the other perturbation systems, is nonlinear. However, upon eliminating  $\phi_{jk}^0$ ,  $\psi_{jk}^0$ , and  $\omega_{jk}^0$ , Equations (7) reduce to the steady continuity and Navier-Stokes equations, which can be approximated satisfactorily by steady laminar boundary layer equations. In fact, as explained later, the resulting system yields merely the well-known Blasius laminar boundary layer as the basic flow.

After ascertaining the basic flow, the perturbation component for  $v = 1$  is obtained from the differential equations

$$\begin{aligned} \varphi_{jk}^1 &= u_j^1 u_k^0 + U_j^0 u_k^1 \\ \psi_{jk}^1 &= u_{j,k}^1 \\ \omega_{jk}^1 &= \rho \varphi_{jk}^1 + p^1 \delta_{jk} - \mu (\psi_{jk}^1 + \psi_{kj}^1) \\ \psi_{jj}^1 &= 0 \\ \rho u_{j,t}^1 + \omega_{jk,k}^1 &= 0 \end{aligned} \quad (9)$$

which are both linear and homogeneous. Thus, this component is determined solely by the boundary values representing the boundary irregularities. In fact, it is the sum of two simpler elements: one determined by the fluid injection distribution, called the injection flow and distinguished by an underline; and the other determined by the adjoining flow fluctuation, called the fluctuation flow and distinguished by an overline. In most of the analysis, just normalized injection and fluctuation flows are required, the appropriate boundary conditions therefore being

$$\begin{aligned} \underline{u}_j^1(x_k^0, t) &= \underline{v}_j^1 \\ \underline{u}_j^1(x_k^\infty, t) &= 0 \\ \overline{p}^1(x_k^\infty, t) &= 0 \end{aligned} \quad (10)$$

(2) Perturbation Systems (continued)

and

$$\begin{aligned}\bar{u}_j^1(x_k^0, t) &= 0 \\ \bar{u}_j^1(x_k^\infty, t) &= \bar{w}_j^1 \\ \bar{p}^1(x_k^\infty, t) &= \bar{q}^1\end{aligned}\tag{11}$$

where  $\bar{u}_j^1$ ,  $\bar{w}_j^1$ ,  $\bar{q}^1$  are normalized boundary values ascertained from the boundary irregularities. As is necessary,  $\bar{w}^1$  and  $\bar{q}^1$  are to satisfy Equations (9) with  $U_j^0$  replaced by  $W_j^0$ . Where required, the actual injection or fluctuation flow is obtained merely by multiplying the normalized flow by an injection parameter  $\underline{\epsilon}$  or a fluctuation parameter  $\bar{\epsilon}$ , respectively. Along with this normalization, the perturbation parameter itself is chosen as

$$\epsilon = (\bar{\epsilon}^2)^{1/2}\tag{12}$$

so that, as is appropriate,  $\epsilon$  depends solely on the magnitudes of the boundary irregularities. Correspondingly, the whole perturbation component is normalized by dividing its actual quantities by  $\epsilon$ .

With all boundary irregularities thus taken into account, each higher perturbation component, for  $v \geq 2$ , is determined solely by a driving tensor with the components

$$f_{jk} = \sum_1^{v-1} u_j^{v-1} u_k^{v-1} u_k^{v*}\tag{13}$$

which in turn are determined solely by lower perturbation components. Thus, the higher perturbation components are obtained recursively using this relation together with the inhomogeneous but linear differential equations

$$\begin{aligned}\varphi_{jk}^v &= u_j^v u_k^0 + u_j^0 u_k^v + f_{jk}^v \\ \psi_{jk}^v &= u_{j,k}^v \\ \omega_{jk}^v &= \rho \varphi_{jk}^v + p^v \delta_{jk} - \mu (\psi_{jk}^v + \psi_{kj}^v) \\ \psi_{jj}^v &= 0 \\ \rho u_{j,t}^v + \omega_{jk,k}^v &= 0\end{aligned}\tag{14}$$

and the trivial boundary conditions

(2) Perturbation Systems (continued)

$$\begin{aligned} u_j^v(x_k^0, t) &= 0 \\ u_j^v(x_k^\infty, t) &= 0 \\ p^v(x_k^\infty, t) &= 0 \end{aligned} \quad (15)$$

where  $v = 2, 3, \dots, \infty$ . Just normalized perturbation components must be and therefore are determined from this system, the recursive relationship yielding such components when just normalized first perturbation quantities are used in Equation (13). Where necessary, each actual perturbation component is obtained by multiplying the normalized component by a power of  $\epsilon$ , this power being equal to the perturbation order.

(3) Fourier Coefficient Systems

To adequately express the intricate motions of transition, each quantity of each perturbation component except the basic flow is represented by a complex Fourier series which extends over each coordinate and the time and also has aperiodically varying coefficients. The spacewise fundamental frequencies  $a_k^*$  ( $k = 1, 2, 3$ ) and the timewise fundamental frequency  $c^*$  are determined solely by the boundary irregularities. Specifically, these frequencies have the largest real values that enable an adequate representation of both the fluid injection distribution and the adjoining flow fluctuation. However, to encompass nonperiodic as well as periodic boundary irregularities, these frequencies may approach zero as a limit, the Fourier series then becoming Fourier integrals. Introducing a harmonic index  $\sigma$  with four components ( $\sigma^1, \sigma^2, \sigma^3, \sigma^4$ ) which each range over  $0, \pm 1, \pm 2, \dots, \pm \infty$ , the spacewise and timewise harmonic frequencies are  $a_k^\sigma = a_k^* \sigma^k$  ( $k = 1, 2, 3$ ) and  $c^\sigma = c^* \sigma^4$ , respectively. Designating the value  $(0, 0, 0, 0)$  by 0 and the value  $(-\sigma^1, -\sigma^2, -\sigma^3, -\sigma^4)$  by  $-\sigma$ , these frequencies obey the relations

$$\begin{aligned} a_k^0 &= 0 & c^0 &= 0 \\ a_k^{-\sigma} &= -a_k^\sigma & c^{-\sigma} &= -c^\sigma \\ a_k^{\sigma - \sigma^*} + a_k^{\sigma^*} &= a_k^\sigma & c^{\sigma - \sigma^*} + c^{\sigma^*} &= c^\sigma \end{aligned}$$

Each term of each Fourier series contains the phase function

$$E^\sigma = \exp i(a_k^\sigma x_k + c^\sigma t) \quad (16)$$



### (3) Fourier Coefficient Systems (continued)

with the important properties

$$E^0 = 1$$

$$E^{-\sigma} = \bar{E}^{\sigma}$$

$$E^{\sigma-\sigma^*} E^{\sigma^*} = E^{\sigma}$$

and

$$E_{,k}^{\sigma} = i a_k^{\sigma} E^{\sigma}$$

$$E_{,t}^{\sigma} = i c^{\sigma} E^{\sigma}$$

where  $i$  is the unit imaginary number and the overscript  $\sim$  denotes the complex conjugate value. Although timewise oscillations necessarily are encompassed, just spacewise variations of the coefficients themselves must be considered here (since the boundary layer is "equilibrated" in time). Thus, each coefficient is, at most, an aperiodic complex function of the coordinates alone. For example, the velocity components and the pressure of each perturbation component except the basic flow are represented as

$$\begin{aligned} u_j^v &= \sum u_j^{v\sigma}(x_k) E^{\sigma} \\ p^v &= \sum p^{v\sigma}(x_k) E^{\sigma} \end{aligned} \tag{17}$$

where the summation extends over the whole range of each harmonic index component. Finally, since all physical quantities are real, the two members of each pair of coefficients for each pair of values  $\pm\sigma$  necessarily are complex conjugates. For example, since  $p^v = \bar{p}^v$ ,

$$\begin{aligned} \sum p^{v\sigma} E^{\sigma} &= \sum \bar{p}^{v\sigma} \bar{E}^{\sigma} \\ &= \sum \bar{p}^{v\sigma} E^{-\sigma} \\ &= \sum \bar{p}^{v,-\sigma} E^{\sigma} \end{aligned}$$

whence, equating coefficients of equal phase functions,  $p^{v\sigma} = \bar{p}^{v,-\sigma}$ . (Superscript commas, unlike subscript commas, merely separate indices as necessary.)

In actual boundary layer developments, the boundary layer values at the wall surface and in the adjoining flow generally contain large spectra of influential Fourier components. In fact, even for the elementary boundary irregularities concerned here, the non-trivial boundary values of the first-perturbation component ordinarily would be

### (3) Fourier Coefficient Systems (continued)

$$\begin{aligned}\underline{v}_j^1 &= \sum \underline{v}_j^{1\sigma} E^\sigma \\ \underline{w}_j^1 &= \sum \underline{w}_j^{1\sigma} E^\sigma \\ \underline{q}^1 &= \sum \underline{q}^{1\sigma} E^\sigma\end{aligned}\tag{18}$$

where each component of  $\sigma$  may range over many integers and the Fourier coefficients  $\underline{v}_j^{1\sigma}$ ,  $\underline{w}_j^{1\sigma}$ ,  $\underline{q}^{1\sigma}$  may be aperiodic functions of the coordinates. However, in the analysis itself, many fundamental details can be explained adequately and simply in terms of just single Fourier components of relatively elementary types. Therefore, for the present, only such spectra are considered, generalizations to other spectra being discussed later. Specifically, except when otherwise indicated, the fluid injection distribution is to include just an exactly simple-harmonic stationary wave, distinguished by using the superscript  $1\alpha$  in place of other identification; and the adjoining flow fluctuation is to include just a nearly simple-harmonic traveling wave propagated parallel to the wall, distinguished by using the superscript  $1\beta$  in place of other identification. For such spectra, the whole motions at the wall surface and in the adjoining flow are

$$\begin{aligned}v_j &= \epsilon^{1\alpha} (v_j^{1\alpha} E^{1\alpha} + \tilde{v}_j^{1\alpha} \tilde{E}^{1\alpha}) \\ w_j &= W_j^0 + \epsilon^{1\beta} (w_j^{1\beta} E^{1\beta} + \tilde{w}_j^{1\beta} \tilde{E}^{1\beta}) \\ q &= Q^0 + \epsilon^{1\beta} (q^{1\beta} E^{1\beta} + \tilde{q}^{1\beta} \tilde{E}^{1\beta})\end{aligned}\tag{19}$$

where  $a_j^{1\alpha} = c^{1\alpha} = a_j^{1\beta} = 0$  and  $v_j^{1\alpha}$  are normalized constants while  $w_j^{1\beta}$  and  $q^{1\beta}$  are normalized weak aperiodic functions of the coordinates. For definiteness, the orders of magnitude of  $W_j^0$ ,  $Q^0$  and  $v_j^{1\alpha}$ ,  $w_j^{1\beta}$ ,  $q^{1\beta}$  are taken as unity--both  $\epsilon^{1\alpha}$  and  $\epsilon^{1\beta}$ , along with  $\epsilon = (\epsilon^{1\alpha} \epsilon^{1\beta})^{1/2}$ , therefore being much smaller than unity (since only weak boundary irregularities are involved).

For the boundary values under consideration, the normalized injection and fluctuation flows, being solutions of homogeneously linear differential equations, can be represented by two-term series such as

$$\begin{aligned}\underline{u}_j^1 &= u_j^{1\alpha} E^{1\alpha} + \tilde{u}_j^{1\alpha} \tilde{E}^{1\alpha} \\ \underline{p}^1 &= p^{1\alpha} E^{1\alpha} + \tilde{p}^{1\alpha} \tilde{E}^{1\alpha}\end{aligned}\tag{20}$$

### (3) Fourier Coefficient Systems (continued)

and

$$\begin{aligned}\bar{u}_j^1 &= u_j^{1E} E^{1\beta} + \bar{u}_j^{1\beta} \bar{E}^{1\beta} \\ \bar{p}^1 &= p^{1\beta} E^{1\beta} + \bar{p}^{1\beta} \bar{E}^{1\beta}\end{aligned}\quad (21)$$

respectively. Hence, substituting such expressions into Equations (9) and equating coefficients of equal phase functions, a single Fourier coefficient system for each flow is obtained. For the injection flow, the differential equations are

$$\begin{aligned}\varphi_{jk}^{1\alpha} &= u_j^{1\alpha} u_k^0 + u_j^0 u_k^{1\alpha} \\ v_{jk}^{1\alpha} &= i u_j^{1\alpha} a_k^{1\alpha} + u_{j,k}^{1\alpha} \\ \omega_{jk}^{1\alpha} &= \rho \varphi_{jk}^{1\alpha} + p^{1\alpha} \delta_{jk} - \mu (\dot{v}_{jk}^{1\alpha} + \dot{v}_{kj}^{1\alpha}) \\ \dot{v}_{jj}^{1\alpha} &= 0 \\ i \rho c u_j^{1\alpha} a_j^{1\alpha} + i \omega_{jk}^{1\alpha} a_k^{1\alpha} + \omega_{jk,k}^{1\alpha} &= 0\end{aligned}\quad (22)$$

with  $a_3^{1\alpha} = c^{1\alpha} = 0$ . For the fluctuation flow, the differential equations are the same as Equations (22) except with  $\alpha$  replaced by  $\beta$  and with  $a_3^{1\beta} = 0$ . The applicable boundary conditions are

$$\begin{aligned}u_j^{1\alpha}(x_k^0) &= v_j^{1\alpha} \\ u_j^{1\alpha}(x_k^\infty) &= 0 \\ p^{1\alpha}(x_k^\infty) &= 0\end{aligned}\quad (23)$$

and

$$\begin{aligned}u_j^{1\beta}(x_k^0) &= 0 \\ u_j^{1\beta}(x_k^\infty) &= w_j^{1\beta} \\ p^{1\beta}(x_k^\infty) &= q^{1\beta}\end{aligned}\quad (24)$$

where  $v_j^{1\alpha}$ ,  $w_j^{1\beta}$ ,  $q^{1\beta}$  are coefficients from Equations (19). Whereas  $v_j^{1\alpha}$  are to be constants,  $w_j^{1\beta}$  and  $q^{1\beta}$  are to be weak aperiodic functions of the coordinates

### (3) Fourier Coefficient Systems (continued)

satisfying Equations (22) with  $U_j^0$  replaced by  $W_j^0$ . The whole perturbation component for  $v = 1$  can be represented by four-term series such as

$$\begin{aligned} \epsilon u_j^1 &= \epsilon^{1\alpha} (u_j^{1\alpha} E^{1\alpha} + \tilde{u}_j^{1\alpha} \tilde{E}^{1\alpha}) + \epsilon^{1\beta} (u_j^{1\beta} E^{1\beta} + \tilde{u}_j^{1\beta} \tilde{E}^{1\beta}) \\ \epsilon p^1 &= \epsilon^{1\alpha} (p^{1\alpha} E^{1\alpha} + \tilde{p}^{1\alpha} \tilde{E}^{1\alpha}) + \epsilon^{1\beta} (p^{1\beta} E^{1\beta} + \tilde{p}^{1\beta} \tilde{E}^{1\beta}) \end{aligned} \quad (25)$$

obtained from Equations (20) and (21). Here, as well as for the more general boundary values, this perturbation component does not contain a mean Fourier component (with the phase function  $E^0$ ). If the boundary irregularities contained a mean Fourier component, it could and therefore would be included in the boundary values of the basic flow itself, always leaving the first-perturbation spectra without any mean component.

Substituting general Fourier series into Equations (13) and equating coefficients of equal phase functions, the general Fourier coefficient of the driving tensors is obtained as

$$f_{jk}^{v\sigma} = \sum_1^{v-1} (\sum u_j^{v-v_*, \sigma-\sigma_*} u_k^{v_*, \sigma_*}) \quad (26)$$

where  $v = 2, 3, \dots, \infty$  and each component of  $\sigma$  and  $\sigma_*$  may range over  $0, \pm 1, \pm 2, \dots, \pm \infty$ . Thus, each such coefficient, besides belonging to a generally large spectrum, involves a generally large sum of products of quantities from lower perturbation components. However, the actual value of these coefficients, being dependent on products of small actual quantities, usually are very small. In fact, in most boundary layers of practical interest, the Fourier components of the driving tensors can significantly affect the motion only at relatively infrequent conditions. These exceptional conditions, as elucidated later, are those allowing strong partial resonances between the driving and the driven Fourier components over long stretches of the boundary layer. Consequently, due to this fortunate feature, just a relatively small number of the Fourier coefficients of the driving tensors must be considered. Furthermore, in the sum for each of these coefficients, as will become evident, merely a few exceptional terms contribute significantly to the partial resonance and therefore must be retained. In the particular boundary layer concerned here, wherein the first perturbation component has just finite spectra, the driving tensor components also have just finite spectra and the sums are finite as well. Nevertheless, as will be explained, relatively few of even these coefficients and terms need to be analyzed.

In particular, the driving tensor for  $v = 2$  has the components

$$f_{jk}^2 = u_j^{11} u_k^{11}$$

and therefore, using Equations (25), just the Fourier components in the expression

### (3) Fourier Coefficient Systems (continued)

$$\epsilon^{1\alpha} \epsilon^{1\beta} f_{jk}^2 = [\epsilon^{1\alpha} (u_j^{1\alpha} E^{1\beta} + u_j^{-1\alpha} E^{-1\alpha}) + \epsilon^{1\beta} (u_j^{1\beta} E^{1\alpha} + u_j^{-1\beta} E^{-1\beta})] \\ \times [\epsilon^{1\alpha} (u_k^{1\alpha} E^{1\alpha} + u_k^{-1\alpha} E^{-1\alpha}) + \epsilon^{1\beta} (u_k^{1\beta} E^{1\beta} + u_k^{-1\beta} E^{-1\beta})]$$

Thus, in this case, each driving tensor component has only five distinct Fourier components, these being one real mean component with the phase function  $E^0$  and four complex oscillation components with the phase functions  $E^{1\alpha} E^{1\alpha}$ ,  $E^{1\alpha} E^{1\beta}$ ,  $E^{1\beta} E^{1\alpha}$ , and  $E^{1\beta} E^{1\beta}$ . Moreover, due to the restricted range of the natural frequencies of the driven Fourier components (see Part (G-3)), just one of these oscillation components has a possibility of yielding a significant partial resonance, this component being the one with the phase function  $E^{1\alpha} E^{1\beta}$  or  $E^{1\beta} E^{1\alpha}$ , depending on the particular harmonic frequencies involved. For definiteness, this exceptional component, to be distinguished by the superscript  $2\gamma$ , presently is assumed to have just the phase function

$$E^{2\gamma} = E^{1\alpha} E^{1\beta}$$

with the harmonic frequencies

$$a_k^{2\gamma} = a_k^{1\alpha} + a_k^{1\beta} \\ c^{2\gamma} = c^{1\alpha} + c^{1\beta} \quad (27)$$

where  $k = 1, 2, 3$ . Hence, for  $v = 2$ , just the mean components as evaluated from merely the dominant terms of the relations

$$\epsilon^{1\alpha} \epsilon^{1\beta} f_{jk}^{2,0} = \epsilon^{1\alpha} \epsilon^{1\alpha} (u_j^{1\alpha} u_k^{-1\alpha} + u_j^{-1\alpha} u_k^{1\alpha}) \\ + \epsilon^{1\beta} \epsilon^{1\beta} (u_j^{1\beta} u_k^{-1\beta} + u_j^{-1\beta} u_k^{1\beta}) \quad (28)$$

and just the oscillation components

$$f_{jk}^{2\gamma} = u_j^{1\alpha} u_k^{1\beta} + u_j^{1\beta} u_k^{1\alpha} \quad (29)$$

must be considered further. In fact, for this particular value of  $v$ , as will be explained, even the mean components usually should be negligible.

Similarly, the driving tensor for  $v = 3$  has the components

$$f_{jk}^3 = u_j^{1,2} u_k^{2,1} + u_j^{2,1} u_k^{1,2}$$

### (3) Fourier Coefficient Systems (continued)

of which relatively few Fourier components are important. In this case, a mean component is not included, the same being true for all other odd values of  $\nu$ . Any oscillation component of importance, as will become apparent, has a phase function  $E^{3\gamma}$  which is the product or quotient of  $E^{2\gamma}$  with either  $E^{1\alpha}$  or  $E^{1\beta}$ .

As in the case for  $\nu = 2$ , just the terms in the coefficient of  $E^{3\gamma}$  must be kept. Moreover, the driving tensor for  $\nu = 4$  has the components

$$f_{jk}^4 = u_j^1 u_k^3 + u_j^2 u_k^2 + u_j^3 u_k^1$$

of which few Fourier components must be retained. In this case, a mean component is involved, as is true for all other even values of  $\nu$ . Also, any oscillation component of importance now has a phase function  $E^{4\gamma}$  composed of the square of  $E^{2\gamma}$  or a combination of  $E^{3\gamma}$  with either  $E^{1\alpha}$  or  $E^{1\beta}$ . Hence, all terms except those in the coefficients of  $E^0$  and  $E^{4\gamma}$  can be omitted. Finally, the driving tensors for the higher values of  $\nu$  can be simplified in the same way.

Consequently, using the superscript  $\Delta$  to denote the relevant lower perturbation quantities and otherwise replacing lower by upper case letters for emphasis, the mean Fourier coefficients of the perturbation components for  $\nu = 2, 4, \dots, \infty$  are obtained from the mean driving coefficients

$$F_{jk}^\nu = u_j^\Delta \tilde{u}_k^\Delta \quad (30)$$

and the differential equations

$$\begin{aligned} \phi_{jk}^\nu &= U_j^\nu U_k^0 + U_j^0 U_k^\nu + F_{jk}^\nu \\ \psi_{jk}^\nu &= U_{j,k}^\nu \\ \Omega_{jk}^\nu &= \rho \phi_{jk}^\nu + P^\nu \delta_{jk} - \mu (\psi_{jk}^\nu + \psi_{kj}^\nu) \\ \psi_{jj}^\nu &= 0 \\ \Omega_{jk,k}^\nu &= 0 \end{aligned} \quad (31)$$

with the boundary conditions

$$\begin{aligned} U_j^\nu(x_k^0) &= 0 \\ U_j^\nu(x_k^\infty) &= 0 \\ P^\nu(x_k^\infty) &= 0 \end{aligned} \quad (32)$$

### (3) Fourier Coefficient Systems (continued)

Eventually, the whole mean motion could be expressed in perturbation series such as

$$\begin{aligned} U_j &= U_j^0 + \sum (U_j^\nu + \tilde{U}_j^\nu)(\epsilon)^\nu \\ P &= P^0 + \sum (P^\nu + \tilde{P}^\nu)(\epsilon)^\nu \end{aligned} \quad (33)$$

where  $\nu = 2, 4, \dots, \infty$ . However, in the boundary layer concerned here, besides the singular terms for  $\nu = 0$ , probably just the terms for  $\nu = 4$  will be large enough to merit consideration within the transition region.

Likewise, using the superscripts  $\delta$  and  $\epsilon$  to denote the relevant lower perturbation quantities, the oscillation Fourier coefficients of the perturbation components for  $\nu = 2, 3, \dots, \infty$  are obtained from the oscillation driving coefficients

$$f_{jk}^{\nu\gamma} = u_j^{\delta} u_k^{\epsilon} + u_j^{\epsilon} u_k^{\delta} \quad (34)$$

and the differential equations

$$\begin{aligned} c_{jk}^{\nu\gamma} &= u_j^{\nu} U_k^0 + U_j^0 u_k^{\nu\gamma} + f_{jk}^{\nu\gamma} \\ \dot{c}_{jk}^{\nu\gamma} &= i u_j^{\nu\gamma} a_k^{\nu\gamma} + u_{j,k}^{\nu\gamma} \\ \dot{u}_{jk}^{\nu\gamma} &= p_{jk}^{\nu\gamma} + p^{\nu\gamma} \delta_{jk} - \mu (c_{jk}^{\nu\gamma} + \dot{c}_{kj}^{\nu\gamma}) \\ \dot{c}_{jj}^{\nu\gamma} &= 0 \\ i p c^{\nu\gamma} u_j^{\nu\gamma} + i \dot{u}_{jk}^{\nu\gamma} a_k^{\nu\gamma} + u_{jk,k}^{\nu\gamma} &= 0 \end{aligned} \quad (35)$$

with the boundary conditions

$$\begin{aligned} u_j^{\nu\gamma}(x_k^0) &= 0 \\ u_j^{\nu\gamma}(x_k^\pi) &= 0 \\ p^{\nu\gamma}(x_k^\pi) &= 0 \end{aligned} \quad (36)$$

Ultimately, using the superscript  $\Gamma$  to denote the dominant terms of each perturbation component, the whole oscillatory motion, distinguished by the superscript  $*$ , could be expressed in perturbation series such as

$$\begin{aligned} u_j^* &= \sum (u_j^{\nu\Gamma} E^{\nu\Gamma} + \tilde{u}_j^{\nu\Gamma} \tilde{E}^{\nu\Gamma})(\epsilon)^\nu \\ p^* &= \sum (p^{\nu\Gamma} E^{\nu\Gamma} + \tilde{p}^{\nu\Gamma} \tilde{E}^{\nu\Gamma})(\epsilon)^\nu \end{aligned} \quad (37)$$

### (3) Fourier Coefficient Systems (continued)

where  $\nu = 1, 2, 3, \dots, \infty$ . Here, however, probably just some of the terms for  $\nu = 2, 3, 4$  will be large enough to be essential in these series. When the boundary irregularities include more Fourier components, the resulting motion is substantially more intricate. This property, rather than the higher perturbation components, probably accounts for much of the complicated appearance of most actual transitions. In some boundary layer developments, though, a few higher perturbation components may be significant. Also, such components may become important downstream of transition.

### (4) Amplitude Coefficient Systems

Although many rapid variations in the form of the phase functions already have been separated from the original quantities, other rapid variations in the form of special growth functions later will be extracted from the Fourier coefficients themselves. For this purpose, various quantities called the amplitude coefficients, which in the  $x_1$  and  $x_2$  directions vary as slowly as the basic flow itself, are needed. These coefficients now are defined by introducing their governing differential systems. Eventually, using approximations analogous to the conventional boundary layer assumptions, their systems will be reduced to dimensionless ordinary differential systems with the dimensionless  $x_3$ -coordinate as the independent variable. These approximate systems encompass the well-known Orr-Sommerfeld equation and can be solved satisfactorily by a technique that would be suitable for accurately integrating that equation.

Thus, the initial amplitude coefficients, denoted by the superscript  $n$ , are defined as the solutions of the homogeneously linear differential equations

$$\begin{aligned} u_{jk}^n &= u_j^{\nu} u_k^0 + u_j^0 u_k^n \\ v_{jk}^n &= i u_j^{\nu} A_k^n + u_{j,k}^n \\ \mu_{jk}^n &= \sigma_{jk}^n + p^{\nu} \delta_{jk} - \mu (\dot{u}_{jk}^n + v_{kj}^n) \\ i_{jj}^n &= 0 \\ i p c^{\nu} u_j^{\nu} + i \mu_{jk}^n A_k^n + \mu_{jk,k}^n &= 0 \end{aligned} \tag{38}$$

and the non-trivial boundary conditions

$$\begin{aligned} u_j^{\nu}(x_k^0) &= v_j^{\nu} \\ u_j^{\nu}(x_k^{\infty}) &= w_j^{\nu} \\ p^{\nu}(x_k^{\infty}) &= q^{\nu} \end{aligned} \tag{39}$$



(4) Amplitude Coefficient Systems (continued)

where the parameter  $c^k$  is a real constant but the parameters  $A_k^k$  and the boundary values  $v_j^k, w_j^k, q^k$  are complex constants. These coefficients include the injection amplitude coefficients, for which  $A_3^k = c^k = 0$  and  $w_j^k = q^k = 0$ , and the fluctuation amplitude coefficients, for which  $A_3^k = 0$  and  $v_j^k = 0$ . In the former case  $v_j^k$  can be arbitrary, but in the latter case  $w_j^k$  and  $q^k$  must satisfy Equations (38) with  $U_j^0$  replaced by  $W_j^0$ . In both cases, just normalized boundary values with an order of magnitude of unity are considered.

Next, the resonance amplitude coefficients, denoted by the superscript  $\lambda$ , are defined as the solutions of the homogeneously linear differential equations

$$\begin{aligned} \omega_{jk}^\lambda &= u_j^\lambda U_k^0 + U_j^0 u_k^\lambda \\ \psi_{jk}^\lambda &= i u_j^\lambda A_k^\lambda + u_{j,k}^\lambda \\ u_{jk}^\lambda &= \rho \omega_{jk}^\lambda + p^\lambda \delta_{jk} - \mu (\psi_{jk}^\lambda + \psi_{kj}^\lambda) \\ \psi_{jj}^\lambda &= 0 \\ i \rho c u_j^\lambda + i \omega_{jk}^\lambda A_k^\lambda + u_{jk,k}^\lambda &= 0 \end{aligned} \quad (40)$$

and the trivial boundary conditions

$$\begin{aligned} u_j^\lambda(x_k^0) &= 0 \\ u_j^\lambda(x_k^\infty) &= 0 \\ p^\lambda(x_k^\infty) &= 0 \end{aligned} \quad (41)$$

where the parameter  $c^\lambda$  is a real constant but the parameters  $A_k^\lambda$  necessarily are weak aperiodic complex functions of  $x_1$  and  $x_2$ . In the dimensionless approximate system deduced later, the parameters include just the local Reynolds number  $R = \rho \Lambda T / \mu$ , the dimensionless timewise frequency  $\hat{c}^\lambda = c^\lambda \Lambda / T$ , and the dimensionless spacewise frequencies  $\hat{A}_k^\lambda = A_k^\lambda \Lambda$ , where the reference length  $\Lambda$  and the reference velocity  $T$  characterize the local basic flow thickness and the adjoining flow velocity, respectively. Also, for given values of  $R$  and  $\hat{c}^\lambda$ , the dimensionless approximate system has non-trivial solutions, called the proper functions,

#### (4) Amplitude Coefficient Systems (continued)

if and only if the parameters  $\hat{A}_k^\lambda$  have certain singular values, called the proper values. Consequently, the dimensionless proper values depend on just  $R$  and  $\hat{C}^\lambda$ , and the dimensionless coefficients depend on just these parameters and the dimensionless  $x_3$ -coordinate. However, due to the variation of  $\Lambda$  and therefore  $R$  and  $\hat{C}^\lambda$  with  $x_1$  and  $x_2$ , both the dimensionless and dimensional parameters, as well as the dimensionless and dimensional coefficients, are weak aperiodic functions of  $x_1$  and  $x_2$ . The proper solutions, distinguished by the superscript  $T$ , are not unique but instead range over a sequence of discrete solutions. For convenience, as is probably true, the proper values of different solutions are assumed to be distinct in all cases, and the number of solutions is assumed to be infinite, although these properties neither have been proven nor are essential. Also, the solutions are regarded as ordered so that the absolute proper values

$$\left| A_k^{\lambda T} \right| = (A_k^{\lambda T} \bar{A}_k^{\lambda T})^{1/2}$$

form an ascending sequence, represented by the sequence  $T = 1, 2, \dots, \infty$ .

Although only real values of  $R$  exist in the physical problem under consideration, certain complex values of  $R$  appear in the mathematical representation of the partial resonances. In particular, the points in the complex  $R$ -plane where  $\hat{A}_k^{\lambda T}$  have specified real or nearly real values, while  $\hat{C}^\lambda/R$  has a specified real value, are involved. However, merely those points located on or near the real  $R$ -axis are important, since only such points are encountered in the significant partial resonances. As a result, usually just a single proper solution, which happens to be the same as the one considered in ordinary linear stability theory, is essential in the analysis. However, the present application of this solution, assumed to be the one for  $T = 1$ , differs greatly from its utilization in that theory.

Finally, the adjoint amplitude coefficients, denoted by  $\xi_{jk}^\lambda$ ,  $\eta_{jk}^\lambda$ ,  $\zeta_{jk}^\lambda$ ,  $r_j^\lambda$ , and  $s_j^\lambda$ , are needed. These coefficients are defined in the transition domain  $D$  enclosed by the boundary surface  $D_*$  on which the unit outward normal vector has the components  $n_k$  ( $k = 1, 2, 3$ ). Besides the whole transition region,  $D$  may include at least parts of the adjacent laminar and turbulent regions. The governing differential system is deduced by multiplying Equations (40) by  $\xi_{jk}^\lambda$ ,  $\eta_{jk}^\lambda$ ,  $\zeta_{jk}^\lambda$ ,  $r_j^\lambda$ , and  $s_j^\lambda$ , respectively, integrating the sum of the resulting scalars over  $D$ , rearranging terms using integrations by parts, and imposing conditions satisfying Equations (40) and (41). This process yields the scalar identity

(4) Amplitude Coefficient Systems (continued)

$$\begin{aligned}
 & \int_D \left\{ \xi_{jk}^\lambda (\varphi_{jk}^\lambda - u_j^\lambda u_k^0 - u_j^0 u_k^\lambda) + \eta_{jk}^\lambda (\psi_{jk}^\lambda - i u_j^\lambda A_k^\lambda - u_{j,k}^\lambda) \right. \\
 & \quad + \zeta_{jk}^\lambda [\omega_{jk}^\lambda - \rho \varphi_{jk}^\lambda - p^\lambda \delta_{jk} + \mu (\psi_{jk}^\lambda + \psi_{kj}^\lambda)] + r^\lambda \psi_{jj}^\lambda \\
 & \quad \left. + s_j^\lambda (i \rho c^\lambda u_j^\lambda + i \omega_{jk}^\lambda A_k^\lambda + \omega_{jk,k}^\lambda) \right\} d(x_m) \\
 & = \int_D \left\{ \varphi_{jk}^\lambda (\xi_{jk}^\lambda - \rho \zeta_{jk}^\lambda) + \psi_{jk}^\lambda [\eta_{jk}^\lambda + r^\lambda \delta_{jk} + \mu (\zeta_{jk}^\lambda + \zeta_{kj}^\lambda)] \right. \\
 & \quad + \omega_{jk}^\lambda (\zeta_{jk}^\lambda + i s_j^\lambda A_k^\lambda - s_{j,k}^\lambda) - p^\lambda \zeta_{jj}^\lambda \\
 & \quad \left. + u_j^\lambda [i \rho c^\lambda s_j^\lambda - (\xi_{jk}^\lambda + \xi_{kj}^\lambda) u_k^0 - i \eta_{jk}^\lambda A_k^\lambda + \eta_{jk,k}^\lambda] \right\} d(x_m) \\
 & \quad + \int_{D_\star} (s_j^\lambda \omega_{jk}^\lambda - u_j^\lambda \eta_{jk}^\lambda) n_k d_\star(x_m) \tag{42}
 \end{aligned}$$

where  $d(x_m)$  and  $d_\star(x_m)$  denote volume and area differentials, respectively ( $m = 1, 2, 3$ ). To satisfy Equations (40), the left member and therefore the right member of this relation must vanish. In the right member, this requirement is met if the coefficients of  $\varphi_{jk}^\lambda$ ,  $\psi_{jk}^\lambda$ ,  $\omega_{jk}^\lambda$ ,  $p^\lambda$ , and  $u_j^\lambda$  vanish in  $D$  and the coefficients of  $n_k$  vanish on  $D_\star$ . Thus, Equations (40) and (41) together are satisfied by imposing the homogeneously linear differential equations

$$\begin{aligned}
 \xi_{jk}^\lambda &= \rho \zeta_{jk}^\lambda \\
 \eta_{jk}^\lambda &= -r^\lambda \delta_{jk} - \mu (\zeta_{jk}^\lambda + \zeta_{kj}^\lambda) \\
 \zeta_{jk}^\lambda &= -i s_j^\lambda A_k^\lambda + s_{j,k}^\lambda \\
 \zeta_{jj}^\lambda &= 0 \\
 i \rho c^\lambda s_j^\lambda - (\xi_{jk}^\lambda + \xi_{kj}^\lambda) u_k^0 &= i \eta_{jk}^\lambda A_k^\lambda - \eta_{jk,k}^\lambda
 \end{aligned} \tag{43}$$

and the trivial boundary conditions

$$\begin{aligned}
 s_j^\lambda(x_k^0) &= 0 \\
 s_j^\lambda(x_k^\infty) &= 0 \\
 r^\lambda(x_k^\infty) &= 0
 \end{aligned} \tag{44}$$

#### (4) Amplitude Coefficient Systems (continued)

The parameters here are the same as those in Equations (40). Also, for given values of  $R$  and  $\hat{c}$ , the dimensionless approximate system has non-trivial solutions, again called proper functions, if and only if the parameters  $\hat{A}_k^\lambda$  equal the proper values of the corresponding system for Equations (40) and (41). As a result, both the dimensionless and the dimensional quantities are weak aperiodic functions of  $x_1$  and  $x_2$ . Moreover, the proper solutions, again distinguished by the superscript  $T$ , range over a sequence of discrete solutions, again represented by the sequence  $T = 1, 2, \dots, \infty$ . However, whereas the proper values are identical, the resonance and adjoint amplitude coefficients themselves are different. (Their differential systems, unlike the more familiar systems of the prevailing literature, are not self-adjoint.)

An important property here is the fact that, in the transition domain, each adjoint solution is orthogonal to all resonance solutions except the one with the same proper values. In particular, substitution of a resonance solution for  $T = T_1$  and an adjoint solution for  $T = T_2$  in Equation (42) yields the identity

$$e_k^{T_1 T_2} (\hat{A}_k^{T_1} - \hat{A}_k^{T_2}) = 0 \quad (45)$$

where the inner product components  $e_k^{T_1 T_2}$  are defined by

$$\int_D (s_j^{T_2 T_1} - u_j^{T_1 T_2}) d(x_m) = e_k^{T_1 T_2} \quad (46)$$

Consequently, if  $\hat{A}_k^{T_1} \neq \hat{A}_k^{T_2}$ ,  $e_k^{T_1 T_2}$  vanish -- meaning that the two solutions are orthogonal -- whereas, if  $\hat{A}_k^{T_1} = \hat{A}_k^{T_2}$ ,  $e_k^{T_1 T_2}$  do not all vanish. For convenience, the resonance and adjoint solutions, which each contain an arbitrary factor owing to the homogeneity of their differential systems, are regarded as normalized simultaneously. Specifically, the two arbitrary factors for each value of  $T$  are assumed to be chosen so that

$$e_k^T e_k^T = 1 \quad (47)$$

where the bilinear norm components  $e_k^T$  are defined by

$$\int_D (s_j^{T T} - u_j^{T T}) d(x_m) = e_k^T \quad (48)$$

[with  $\text{Re}(e_1^T) > 0$  when the mean flow is in the positive  $x_1$ -direction] and so that

$$e_1^T = 1 \quad (49)$$

#### (4) Amplitude Coefficient Systems (continued)

where the trilinear norm  $\theta^T$  is defined by

$$\int_D (u_j^{\lambda T} \xi_{jk}^{\lambda T} u_k^{\lambda T}) d(x_m) = \theta^T \quad (50)$$

As one result,  $e_k^{T_1 T_2}$  will satisfy the equations

$$\begin{aligned} e_k^{T_1 T_2} e_k^{T_1 T_2} &= 1 & (T_1 = T_2) \\ &= 0 & (T_1 \neq T_2) \end{aligned} \quad (51)$$

called the biorthonormality relations.

#### (E) Growth Functions

Having established the necessary foundation, some important properties of transition, expressed by various growth functions, now can be deduced. These growth functions include the amplitude and phase variations caused by the partial resonances of the driven with the driving Fourier components. Unlike the amplitude coefficients, they may vary rapidly with  $x_1$  and  $x_2$  over some parts of the wall but, for the particular boundary values under consideration, will be almost independent of  $x_3$ . The analysis now involves the expansion of each Fourier component as a sum of products of the growth functions and the amplitude coefficients, which include the rapid variations with  $x_3$ . In this respect, the technique amounts to an extension of the method of separation of variables, which often is used for linear partial differential equations in certain situations. Like the perturbation components, the growth functions are obtained recursively, starting with initial growth functions ascertained from the boundary irregularities themselves. The higher growth functions are established recognizing a requirement that all amplitude coefficients must be regular in the complex R-plane, at least on and near the real R-axis. This requirement leads to growths with  $x_1$  and  $x_2$  that can be much faster and larger than the amplifications predicted by ordinary linear stability theory, which overlooks such a requirement and therefore undoubtedly is incorrect for infinitesimal as well as finite oscillations. Like the driving Fourier components, though, relatively few of the growth functions will be important enough to require consideration. Insofar as has been observed, superposition of the terms with the dominant growth functions should yield motions which at least closely resemble actual transition motions.

The initial growth functions are determined from the differences between the boundary values of the Fourier coefficients of the first perturbation component and the boundary values of the initial amplitude coefficients. Thus, in the injection flow, the boundary values of both sets of coefficients are constants, yielding an injection growth function

(E) Growth Functions (continued)

$$G^{\kappa\alpha} = 1 \quad (52)$$

which is constant throughout the transition region. For this case, the parameters of Equations (38) have the values  $A_k^{\kappa\alpha} = a_k^{1\alpha}$  ( $k = 1, 2$ ) and  $A_3^{\kappa\alpha} = c^{\kappa\alpha} = 0$ . However, in the fluctuation flow, the boundary values of the Fourier coefficients, being weak functions of the coordinates, deviate slowly from those of the amplitude coefficients, which are constants. This difference leads to a fluctuation growth function

$$G^{\kappa\alpha} = \exp(b_k^{1\alpha} x_k) \quad (53)$$

in which the fluctuation growth factors  $b_k^{1\alpha}$  ( $k = 1, 2, 3$ ) are small negative real constants or zero throughout the transition region. In this case, if the mean flow is in the  $x_1$ -direction, the parameters of Equations (38) must have the values  $A_1^{\kappa\alpha} = a_1^{1\alpha} - ib_1^{1\alpha}$ ,  $A_2^{\kappa\alpha} = a_2^{1\alpha}$ ,  $A_3^{\kappa\alpha} = 0$ , and  $c^{\kappa\alpha} = c^{1\alpha}$ . Furthermore, their values also must satisfy the determinantal equation

$$\mu A_k^{\kappa\alpha} A_k^{\kappa\beta} + i\omega(w_k^{\alpha\beta} A_k^{\kappa\alpha} + c^{\kappa\beta}) = 0 \quad (54)$$

deduced by substituting adjoining flow quantities into Equations (22). Using the initial growth functions, all Fourier coefficients of the first perturbation component can be expressed by products such as

$$\begin{aligned} u_j^{1\alpha} &= u_j^{\kappa\alpha} G^{\kappa\alpha} \\ p^{1\alpha} &= p^{\kappa\alpha} G^{\kappa\alpha} \end{aligned} \quad (55)$$

for the injection flow and

$$\begin{aligned} u_j^{1\beta} &= u_j^{\kappa\beta} G^{\kappa\beta} \\ p^{1\beta} &= p^{\kappa\beta} G^{\kappa\beta} \end{aligned} \quad (56)$$

for the fluctuation flow. Substitution of such products into Equations (22) and (23) or (24) yields Equations (38) and (39).

All higher growth functions, for both the mean and the oscillation Fourier coefficients, are determined recursively from lower growth functions using essentially one general procedure. Several aspects of this procedure now are demonstrated on the oscillation Fourier coefficients of the second perturbation component, which are particularly important in transition. First, substituting Equations (55) and (56) into Equations (29) or (34), the oscillation driving coefficients are expressed as

(E) Growth Functions (continued)

$$f_{jk}^{\nu\gamma} = f_{jk}^{\alpha\beta} G^{\alpha\beta} \quad (57)$$

in terms of the driving amplitude coefficients

$$f_{jk}^{\alpha\beta} = u_j^{\kappa\alpha} u_k^{\kappa\beta} + u_j^{\kappa\beta} u_k^{\kappa\alpha} \quad (58)$$

and the driving growth function

$$G^{\alpha\beta} = G^{\kappa\alpha} G^{\kappa\beta} \quad (59)$$

Second, to adequately meet various requirements, the driven Fourier coefficients are expanded in series such as

$$\begin{aligned} u_j^{\nu\gamma} &= u_j^{\alpha\beta} G^{\alpha\beta} + \sum h^T u_j^{\lambda T} H^T \\ p^{\nu\gamma} &= p^{\alpha\beta} G^{\alpha\beta} + \sum h^T p^{\lambda T} H^T \end{aligned} \quad (60)$$

Here, the driven amplitude coefficients  $u_j^{\alpha\beta}$  and  $p^{\alpha\beta}$  may vary with  $x_1$  and  $x_2$  only slowly like the other amplitude coefficients, the resonance coefficients  $h^T$  are constants, and the resonance growth functions  $H^T$  may vary rapidly with  $x_1$  and  $x_2$ . Third, substituting such series into Equations (35) and (36) and recalling that  $u_j^{\lambda T}$  and  $p^{\lambda T}$  are defined by Equations (40) and (41), the following relations are obtained:

$$\begin{aligned} \varphi_{jk}^{\alpha\beta} - u_j^{\alpha\beta} u_k^{\alpha\beta} - u_j^{\alpha\beta} u_k^{\alpha\beta} &= f_{jk}^{\alpha\beta} \\ (\psi_{jk}^{\alpha\beta} - i u_j^{\alpha\beta} a_k^{\alpha\beta} - u_{j,k}^{\alpha\beta}) G^{\alpha\beta} - u_j^{\alpha\beta} G_{,k}^{\alpha\beta} \\ &= \sum h^T u_j^{\lambda T} [H_{,k}^T + i(a_k^{\alpha\beta} - A_k^{\lambda T}) H^T] \\ \omega_{jk}^{\alpha\beta} - p \omega_{jk}^{\alpha\beta} - p^{\alpha\beta} \delta_{jk} + \mu(\psi_{jk}^{\alpha\beta} + \psi_{kj}^{\alpha\beta}) &= 0 \\ \psi_{jj}^{\alpha\beta} &= 0 \\ (i p c^{\alpha\beta} u_j^{\alpha\beta} + i \omega_{jk}^{\alpha\beta} a_k^{\alpha\beta} + \omega_{jk,k}^{\alpha\beta}) G^{\alpha\beta} + \omega_{jk}^{\alpha\beta} G_{,k}^{\alpha\beta} \\ &= - \sum h^T \omega_{jk}^{\lambda T} [H_{,k}^T + i(a_k^{\alpha\beta} - A_k^{\lambda T}) H^T] \end{aligned} \quad (61)$$

(E) Growth Functions (continued)

and

$$\begin{aligned} u_j^{\alpha\beta}(x_k^0) &= 0 \\ u_j^{\alpha\beta}(x_k^\infty) &= 0 \\ p^{\alpha\beta}(x_k^\infty) &= 0 \end{aligned} \quad (62)$$

Here,  $a_k^{\alpha\beta} = a_k^{1\alpha} + a_k^{1\beta}$  and  $c^{\alpha\beta} = c^{1\beta}$  in accordance with Equations (27), whereas  $A_k^{\lambda T}$  are the proper values of Equations (40) and (41) for  $c^\lambda = c^{\alpha\beta}$ . Also, for the particular Fourier coefficients under consideration,

$$G_{,k}^{\alpha\beta} = b_k^{\alpha\beta} G^{\alpha\beta} \quad (63)$$

where  $b_k^{\alpha\beta} = b_k^{1\beta}$ , so that the left members of the second and fifth equations vary with  $x_1$  and  $x_2$  about as slowly as  $G^{\alpha\beta}$ . Fourth, recognizing that the right members of these equations also must vary with  $x_1$  and  $x_2$  about like  $G^{\alpha\beta}$ , the conditions

$$H_{,k}^T + i(a_k^{\alpha\beta} - A_k^{\lambda T})H^T = e_k^T G^{\alpha\beta} \quad (64)$$

are imposed, whereupon Equations (61) reduce to

$$\begin{aligned} \phi_{jk}^{\alpha\beta} - u_j^{\alpha\beta} u_k^0 - u_j^0 u_k^{\alpha\beta} &= f_{jk}^{\alpha\beta} \\ \psi_{jk}^{\alpha\beta} - i u_j^{\alpha\beta} A_k^{\alpha\beta} - u_{j,k}^{\alpha\beta} &= \sum h^T u_j^{\lambda T} e_k^T \\ \omega_{jk}^{\alpha\beta} - \rho \phi_{jk}^{\alpha\beta} - p^{\alpha\beta} \delta_{jk} + \mu(\psi_{jk}^{\alpha\beta} + \psi_{kj}^{\alpha\beta}) &= 0 \\ \psi_{jj}^{\alpha\beta} &= 0 \\ i \rho c^{\alpha\beta} u_j^{\alpha\beta} + i \omega_{jk}^{\alpha\beta} A_k^{\alpha\beta} + \omega_{jk,k}^{\alpha\beta} &= -\sum h^T \omega_{jk}^{\lambda T} e_k^T \end{aligned} \quad (65)$$

where  $A_k^{\alpha\beta} = a_k^{\alpha\beta} - i b_k^{\alpha\beta}$ . Fifth, to achieve another simplification, the driven amplitude coefficients themselves are expanded in series such as



(E) Growth Functions (continued)

$$\begin{aligned} u_j^{\alpha\beta} &= \sum g_j^T u_j^{\lambda T} \\ p^{\alpha\beta} &= \sum g_p^T \lambda^T \end{aligned} \quad (66)$$

where the driven coefficients  $g^T$  are slowly varying functions of  $x_1$  and  $x_2$  (or are constants\*). Sixth, substituting such series into Equations (65) and (62), neglecting the derivatives of  $g^T$  (if any), multiplying the resulting differential equations by the adjoint amplitude coefficients, integrating the sum of the resulting scalars over the transition domain, and applying Equations (42) through (51) as necessary, the following expression for  $g^T$  is derived:

$$i(A_k^{\alpha\beta} - A_k^{\lambda T}) e_k^T g^T = \int_D (\xi_{jk}^{\lambda T} f_{jk}^{\alpha\beta}) d(x_m) - h^T \quad (67)$$

Here, as already indicated,  $A_k^{\alpha\beta}$  along with  $c^{\alpha\beta}$  are constants determined by the boundary irregularities alone, whereas  $A_k^{\lambda T}$  vary with  $R$  which in turn varies with  $x_1$  and  $x_2$ . In particular, for each value of  $T$ ,  $A_k^{\lambda T}$  can equal  $A_k^{\alpha\beta}$  at some point in the complex  $R$ -plane, causing a pole in  $g^T$  unless the right member of Equation (67) vanishes at that point. Indeed, for the smaller values of  $T$  and various typical values of  $A_k^{\alpha\beta}$  and  $c^{\alpha\beta}$ , the pole could occur on or near the real  $R$ -axis, strongly contradicting the stipulation that  $g^T$  is slowly varying. Therefore, as the seventh step, to avoid the pole, the condition

$$h^T = \int_D (\xi_{jk}^{\lambda T} f_{jk}^{\alpha\beta}) d(x_m) \quad (68)$$

is imposed at the complex value of  $R$  where  $A_k^{\lambda T} = A_k^{\alpha\beta}$  (when  $c^\lambda = c^{\alpha\beta}$ ). Otherwise, the value of  $g^T$  is not considered further, since it generally should be small enough to be neglected. Indeed, just the value of  $h^T$  for  $T = 1$  probably will suffice. Applying Equations (49), (50), and (58), the resonance coefficient in the present case may be expressed as the ratio

$$h^T = \frac{\int_D (u_j^{\alpha\beta} \xi_{jk}^{\lambda T} u_k^{\alpha\beta} + u_j^{\alpha\beta} \xi_{jk}^{\lambda T} u_k^{\alpha\alpha}) d(x_m)}{\int_D (u_j^{\lambda T} \xi_{jk}^{\lambda T} u_k^{\lambda T}) d(x_m)} \quad (69)$$

\*At present, due to a lack of an appropriate expansion theorem for the proper functions, the possibility of these coefficients being constants is uncertain.

(E) Growth Functions (continued)

which probably will have an order of magnitude of unity at the lower values of  $T$ . Hence, the driven Fourier coefficients, expressed in full by Equations (60), probably will vary mostly like the single-term approximations

$$\begin{aligned} u_j^{yy} &\approx h^T u_j^T H^T \\ p^{yy} &\approx h^T p^T H^T \end{aligned} \quad (70)$$

where  $T = 1$  and  $h^T \sim O(1)$ .

In contrast to their inherently tedious derivation, the resonance growth functions display some important properties of transition in a simple way. For the case just considered, integrating Equations (64), these functions have the general forms

$$H^T(x_k) = e_k^T \left[ J_k^T - \int_0^{x_k} K^T(x_k^*) G^{qp}(x_k^*) dx_k^* \right]^{-1} K^T(x_k) \quad (71)$$

where the resonance kernel  $K^T$  is defined as

$$K^T(x_k) = \exp \left\{ i \int_0^{x_k} [a_k^2 - A_k^T(x_k^*)] dx_k^* \right\} \quad (72)$$

and the integration constants  $J_k^T$  are assigned so that  $H^T$  is bounded upstream from the transition region. Presently, to describe the principal properties of these functions, the variation of  $H^T$  with  $x_1$  along the line  $x_2 = x_3 = 0$ , with the mean flow in the positive  $x_1$ -direction, is considered. For convenience, the point  $x_1 = 0$  is located somewhere in the transition region, with the integration progressing from the laminar region at  $x_1 \rightarrow -\infty$  to the turbulent region at  $x_1 \rightarrow +\infty$ . To facilitate the integration, deformations of the contour in the complex  $x_1$ -plane and therefore in the complex  $R$ -plane are allowed. Under such conditions, Equations (71) and (72) reduce to

$$H^T(x_1) = e_1^T \left[ \int_{-\infty}^{x_1} K^T(x_1^*) G^{qp}(x_1^*) dx_1^* \right]^{-1} K^T(x_1) \quad (73)$$

and

$$K^T(x_1) = \exp \left\{ i \int_0^{x_1} [a_1^2 - A_1^T(x_1^*)] dx_1^* \right\} \quad (74)$$

(E) Growth Functions (continued)

while the driving growth function becomes

$$G^{\alpha\beta}(x_1) = \exp(b_1^{\alpha\beta} x_1) \quad (75)$$

Here,  $a_1^{\alpha\beta}$  and  $b_1^{\alpha\beta}$  are real constants determined by the boundary irregularities, whereas  $A_1^{\lambda T}$  is a complex function of  $R$  and thereby is a slowly varying complex function of  $x_1$ . Hence, depending on the integration contour,  $K^T$  usually is an oscillating function of  $R$  and thereby  $x_1$ . As is ordinarily true,  $b_1^{\alpha\beta}$  is assumed to be very small, allowing  $G^{\alpha\beta}$  to remain near unity throughout the transition region. Also, to concentrate on the most important situation, just the value of  $A_1^{\lambda T}$  for  $T = 1$  is considered further. Besides other distinctions, this value often can equal  $a_1^{\alpha\beta}$  on or near the real  $R$ -axis and therefore on or near the real  $x_1$ -axis, usually at two different points corresponding to the two branches of the neutral curve of ordinary linear stability theory. Because  $K^T$  usually is oscillatory, the first main contribution to the integral in Equation (73) occurs in the vicinity of the first saddle point of  $K^T$ , to be called the resonance point, which is the first point in the complex  $R$ -plane or the corresponding point in the complex  $x_1$ -plane where  $A_1^{\lambda T} = a_1^{\alpha\beta}$ . Close to this point,  $K^T$  remains almost constant, while the integral and therefore  $H^T$  often grows about as fast as  $x_1$  varies, causing a correspondingly fast growth of the driven Fourier component. In comparison, ordinary linear stability theory would predict a variation somewhat like  $[K^T(x_1)]^{-1}$  and therefore almost no growth in this region. Furthermore, because  $A^{\lambda T}$  varies only slowly with  $x_1$  and the resonance point often is located on or near the real  $x_1$ -axis, the fast growth often persists over a long interval of the real  $x_1$ -axis, yielding a much larger total growth in that region than would be indicated by ordinary linear stability theory. For example, the driven Fourier component sometimes can grow by a ratio of the order of 1000 near the resonance point alone, such growths evidently being the principal way that "disturbances" are "introduced" into the boundary layer. Immediately downstream of the resonance point, the integral remains relatively constant, allowing  $H^T$  to vary about like  $[K^T(x_1)]^{-1}$  and therefore somewhat like the variation considered in ordinary linear stability theory. However, even this resemblance to the latter theory usually will be obscure, since various other growth functions then will tend to dominate the motion. Further downstream, a second saddle point of  $K^T$ , where  $A_1^{\lambda T} = a_1^{\alpha\beta}$  for a second time, may be encountered. In this region, the integral in Equation (73) will begin to grow substantially again, while the factor  $[K^T(x_1)]^{-1}$  will begin to decay. Thereafter, as the net result,  $H^T$  will steadily decay and ultimately vanish, but at a slower rate than predicted by ordinary

(g) Growth Functions (continued)

linear stability theory. Along with all growths and decays, some phase variations and therefore frequency modifications also occur, affecting the Fourier synthesis of the whole motion and perhaps producing some appreciable phenomena of a subharmonic and/or superharmonic nature (in addition to the harmonic motions from other Fourier components). Ordinarily, the resonance growth functions of both two-dimensional and three-dimensional partial resonances, wherein

$a_2^{\alpha\beta} = 0$  and  $a_2^{\alpha\beta} \neq 0$ , respectively, are important. The former resonances tend to manifest first, since the two-dimensional neutral curve occurs first, whereas the latter resonances tend to amplify most, since the three-dimensional proper values vary most slowly with downstream distance.

Proceeding in the same way, the mean Fourier coefficients of the second perturbation component also can be estimated. However, these coefficients probably will be negligible in most boundary layers of interest. For example, substituting Equations (56) into Equation (30), the mean driving coefficients for  $\Delta = 1B$  are

$$F_{jk}^v = F_{jk}^s G^s \quad (76)$$

where

$$F_{jk}^s = u_j^{\alpha\beta} u_k^{\alpha\beta} \quad (77)$$

$$G^s = G^{\alpha\beta} G^{\alpha\beta} \quad (78)$$

Also, expanding the driven Fourier coefficients in series such as

$$\begin{aligned} U_j^v &= U_j^s G^s + \sum h^T u_j^{\lambda T} H^T \\ P^v &= P^s G^s + \sum h^T p^{\lambda T} H^T \end{aligned} \quad (79)$$

and substituting these series into Equations (31) and (32), the resonance coefficients

$$h^T = \int_D (\sum_{jk} \lambda^T F_{jk}^s) d(x_m) \quad (80)$$

eventually are deduced, which must be evaluated at the complex values of  $R$  where  $A_k^{\lambda T} = -i2b_k^{1s}$  (with  $c^\lambda = 0$ ). Moreover, the resonance growth functions become

$$H^T(x_k) = e_k^T \left[ J_k^T + \int_0^{x_k} K^T(x_k^*) G^s(x_k^*) dx_k^* \right] [K^T(x_k)]^{-1} \quad (81)$$

where

$$K^T(x_k) = \exp \left[ -i \int_0^{x_k} A_k^{\lambda T}(x_k^*) dx_k^* \right] \quad (82)$$

(E) Growth Functions (continued)

and  $J_k^T$  are constants chosen to keep  $H^T$  bounded upstream. Again, since  $G^B$  remains near unity, the main parts of  $H^T$  are acquired near the saddle points of  $K^T$ , which are at the complex values of  $R$  where  $A_k^{\lambda T} = 0$  (with  $c^\lambda = 0$ ). But now the saddle points probably are far from the applicable segment of the real  $R$ -axis or perhaps do not exist, leading to only small variations of  $H^T$  across the transition region. Starting from Equations (55), for  $\Delta = 1\alpha$ , similar relations are deduced, except that the resonance coefficients then must be evaluated where  $A_k^{\lambda T} = 0$  rather than where  $A_k^{\lambda T} = -12b_k^{1B}$ . (To fully clarify such details, actual calculations are desirable.)

In contrast, the mean Fourier coefficients of the fourth perturbation component apparently can be significant in many situations. In this case, considering just one dominant term of the second perturbation component, distinguished by the superscript  $T_0$ , the mean driving coefficients are

$$F_{jk}^v = F_{jk}^d G^d \quad (83)$$

where

$$F_{jk}^d = h_{T_0}^T \tilde{h}_{T_0}^{T_0} \lambda_{T_0}^T \tilde{u}_k^{\lambda T_0} \quad (84)$$

$$G^d = H_{T_0}^T \tilde{H}^{T_0} \quad (85)$$

while the driven Fourier coefficients have series such as

$$\begin{aligned} U_j^v &= U_j^d G^d + \sum h_{T_u}^T \lambda_{T_u}^T \tilde{H}^T \\ P^v &= P^d G^d + \sum h_{T_p}^T \lambda_{T_p}^T \tilde{H}^T \end{aligned} \quad (86)$$

However, in place of Equation (63), the driving growth function now has the gradient components

$$\begin{aligned} G_{,k}^d &= H_{,k}^T \tilde{H}^{T_0} + H_{T_0}^T \tilde{H}_{,k}^{T_0} \\ &= i(A_k^{\lambda T_0} - \tilde{A}_k^{\lambda T_0}) H_{T_0}^T \tilde{H}^{T_0} + \frac{T_0}{e_k} \alpha \tilde{H}^{T_0} + \frac{\tilde{T}_0}{e_k} \alpha \tilde{H}^{T_0} \end{aligned}$$

which can be approximated as

$$G_{,k}^d = i(A_k^{\lambda T_0} - \tilde{A}_k^{\lambda T_0}) G^d \quad (87)$$

(E) Growth Functions (continued)

since  $G^{OB}$  will be much smaller than  $H^{T0}$  in the important regions. Consequently, the resonance growth functions are required to satisfy

$$H_{,k}^T - iA_k^{\lambda T} H^T = e_k^T G^d \quad (88)$$

and the resonance coefficients become

$$h^T = \int_0^{\infty} (\xi_{jk}^{\lambda T} F_{jk}^d) d(x_m) \quad (89)$$

which are evaluated at the complex values of  $R$  where  $A_k^{\lambda T} = A_k^{\lambda T0} - \tilde{A}_k^{\lambda T0}$  (with  $c^\lambda = 0$ ). Finally, integrating Equation (88), the resonance growth functions have the general forms

$$H^T(x_k) = e_k^T [J_k^T + \int_0^{x_k} K^T(x_k^*) G^d(x_k^*) dx_k^*] [K^T(x_k)]^{-1} \quad (90)$$

where

$$K^T(x_k) = \exp \left[ -i \int_0^{x_k} A_k^{\lambda T}(x_k^*) dx_k^* \right] \quad (91)$$

and  $J_k^T$  are constants chosen to keep  $H^T$  bounded upstream. Here again, the saddle points of  $K^T$ , located at  $A_k^{\lambda T} = 0$  (with  $c^\lambda = 0$ ), probably are too far from the applicable segment of the real  $R$ -axis to be influential. However, unlike  $G^a$  in the preceding case,  $G^d$  may increase rapidly and greatly along that segment, apparently causing significant variations in  $H^T$  and therefore in the driven Fourier coefficients. (Again, for clarification, actual calculations are desirable.)

Similarly, the oscillation Fourier coefficients of the third, fourth, and perhaps higher perturbation components may be important. For example, considering the fourth perturbation quantities from two dominant terms of the second perturbation component with the indices 1 and 2, the oscillation driving coefficients are

$$f_{jk}^{vY} = f_{jk}^d G^d \quad (92)$$

(E) Growth Functions (continued)

where

$$f_{jk}^d = h^{T1} h^{T2} (u_j^{\lambda T1} u_k^{\lambda T2} + u_j^{\lambda T2} u_k^{\lambda T1}) \quad (93)$$

$$G^d = H^{T1} H^{T2} \quad (94)$$

Again, the driven Fourier coefficients have series such as

$$\begin{aligned} u_j^{pV} &= u_j^d G^d + \sum h^T u_j^{\lambda T} H^T \\ p^{pV} &= p^d G^d + \sum h^T p^{\lambda T} H^T \end{aligned} \quad (95)$$

while the driving growth function has the gradient components

$$\begin{aligned} G_{,k}^d &= H_{,k}^{T1} H^{T2} + H^{T1} H_{,k}^{T2} \\ &= i(A_k^{\lambda T1} + A_k^{\lambda T2} - a_k^{\alpha1\beta1} - a_k^{\alpha2\beta2}) H^{T1} H^{T2} + e_k^{T1} G^{\alpha1\beta1} H^{T2} + e_k^{T2} G^{\alpha2\beta2} H^{T1} \end{aligned}$$

which can be approximated as

$$G_{,k}^d = i(A_k^{\lambda T1} + A_k^{\lambda T2} - a_k^{\alpha1\beta1} - a_k^{\alpha2\beta2}) G^d \quad (96)$$

Thus, eventually, the resonance coefficients are evaluated as

$$h^T = \int_D (\xi_{jk}^{\lambda T} f_{jk}^d) d(x_m) \quad (97)$$

at the complex value of  $R$  where  $A_k^{\lambda T} = A_k^{\lambda T1} + A_k^{\lambda T2} - a_k^{\alpha1\beta1} - a_k^{\alpha2\beta2}$  (with  $c^{\lambda} = c^{\alpha1\beta1} + c^{\alpha2\beta2}$ ), and the resonance growth functions are expressed as

$$H^T(x_k) = e_k^T [J_k^T + \int_0^{x_k} K^T(x_k^*) G^d(x_k^*) dx_k^*] [K^T(x_k)]^{-1} \quad (98)$$

where

$$K^T(x_k) = \exp \left\{ i \int_0^{x_k} [a_k^{\alpha1\beta1} + a_k^{\alpha2\beta2} - A_k^{\lambda T}(x_k^*)] dx_k^* \right\} \quad (99)$$

(E) Growth Functions (continued)

and  $J_k^T$  are chosen to keep  $H^T$  bounded upstream. Here, as in the original example, the saddle points of  $K^T$ , located where  $A_k^{\lambda T} = a_k^{\alpha 1 \beta 1} + a_k^{\alpha 2 \beta 2}$  (with  $c^\lambda = c^{\alpha 1 \beta 1} + c^{\alpha 2 \beta 2}$ ), can occur on or near the real R-axis, greatly increasing the growth of  $H^T$ . Also, as in the preceding example,  $G^d$  itself can increase greatly along that axis. Hence, these tendencies together can yield an exceptionally large growth of  $H^T$  and therefore of the driven Fourier coefficients. However, the actual values of these coefficients, which contain the factor  $(\epsilon)^4$  where  $\epsilon$  is much smaller than unity, should remain within the same order of magnitude as the dominant lower perturbation quantities (at least in the transition region of the boundary layers of practical interest).

In general, the growth functions are bounded throughout the boundary layer. In fact, as easily seen, these functions can grow indefinitely only when some proper values have special constant values for unlimited downstream distances, which can happen only in certain truly parallel flows of unlimited length (such as certain Poiseuille flows and asymptotic suction boundary layers). Consequently, Fourier components with amplitudes increasing indefinitely with downstream distance, called secular terms, ordinarily are not encountered.\* As a result, the perturbation series used here generally should converge better than analogous series would in the more familiar problems of the classical theory of nonlinear oscillations, where secular terms often are encountered unless some other approximation scheme is utilized (which may entail an asymptotic series with uncertain convergence properties). Moreover, the perturbation series should apply particularly well to the initial phase of transition, which is the main objective in many analyses (especially those concerning laminar flow control techniques). For example, for very small boundary irregularities, just the first two perturbation components may be sufficient to describe the principal disturbance motions throughout both the laminar region and the beginning of transition and therefore to relatively large Reynolds numbers. (Such motions, though, will differ significantly from those predicted by ordinary linear stability theory.) Likewise, for somewhat larger boundary irregularities or Reynolds numbers, just a few more perturbation components may be adequate. Furthermore, the perturbation series should adapt well to automatic computation on an electronic computer, enabling a rather large number of perturbation components to be evaluated when needed. In particular, the growth functions, which are the principal elements, can be obtained recursively by rather simple numerical integrations. Thus, for many purposes, the perturbation series should be quite satisfactory.

However, in the final phase of transition and the ensuing turbulence, the computations become more complicated. In particular, as the perturbation order increases, the normalized growth functions increase (retarding the convergence), while the Reynolds numbers at which these functions appear also increase (assisting the convergence). Meanwhile, through a rather involved

---

\*Specifically, secular terms can occur only when, for an indefinite downstream distance, the space and time frequencies of one or more driving oscillations nearly equal those of one or more points on the neutral curve of ordinary linear stability theory. Hence, such terms may exist only if the Reynolds number is near or above the stability limit of that theory.



### (E) Growth Functions (continued)

sequence of relationships depending on the actual boundary irregularities, a partial counteraction of lower perturbation components by higher perturbation components eventually appears and then may prevail (furthering the convergence but hindering its evaluation). Nevertheless, additional analyses and actual calculations should clarify the computations and may suggest a more convenient series or expression. As one example, some information about the convergence, and perhaps some useful approximations, might be deduced by comparing the work available from the first perturbation component with the energy indicated by the perturbation series. (Perhaps, by this means, an approximation of the growth of turbulence energy with downstream distance, enabling an estimation of the skin friction, could be established.) As another example, further insight into the convergence, and into equilibrated turbulence as well, might be gained by extending an elementary turbulence model proposed by Raetz (Reference 1)\* so as to include one or more dominant forcing oscillations from the first perturbation component. Otherwise, an asymptotic series analogous to those utilized in the classical theory for weakly nonlinear oscillations might be obtainable and in some ways useful. However, such a series, besides covering the pertinent boundary irregularities, should apply to moderately large nonlinear oscillations. Thus, at the relevant conditions, it might diverge or at least converge too poorly to be desirable. Conjointly, it should be noted that any demand for an asymptotic series will be less compelling in a boundary layer of limited length than in processes of unlimited duration (which are the main subjects of the classical theory of nonlinear oscillations). Conversely, depending on the uniformity of the actual boundary irregularities, a reliable asymptotic series might be appropriate for a truly parallel flow, in which secular terms sometimes can occur. However, a suitable summation of the perturbation series already developed then might be obtained and managed more easily than an asymptotic series (especially since the classical theory has not yet been extended to three-dimensional motions of the kind concerned here). In particular, in a truly parallel flow with periodic boundary irregularities, the growth functions degenerate to quite simple expressions, suggesting that an approximate or exact summation of all nonsecular and secular terms might be established and investigated rather easily (especially with the aid of an automatic computer). Further exploration of such aspects of the theory are deferred for later papers.

### (F) Transition Mechanism

According to the resonance theory, the motion commonly called transition is merely a part of a sequence of partial resonances beginning in the laminar region and continuing in the turbulent region. In general, this sequence may be excited by any of a large variety of combinations of boundary irregularities at the wall surface and in the adjoining flow, and it altogether may contain numerous partial resonances of several different kinds, yielding a whole motion which is indeed diverse and complicated. Nevertheless, as already indicated, the individual partial resonances are quite simple and, in fact, can be analysed and calculated in a recursive manner by available techniques. In particular, the dominant motion from each significant partial resonance can be represented by just the product of three elementary variations, namely: an oscillation expressed by the phase function, an amplification and slight oscillation in the downstream direction expressed by the resonance growth function,

\*This model is an extension of instructive finite-disturbance models introduced by Meksyn and Stuart (Reference 43) and Stuart (Reference 51).

(F) Transition Mechanism (continued)

and a distribution across the boundary layer expressed by the resonance amplitude coefficient. Also, the overall magnitude and phase of this motion are determined by the product of the applicable power of the perturbation parameter and the applicable resonance coefficients. Furthermore, typical sequences of partial resonances, which might be adequate for analyzing and predicting transition in an approximate way, can be constructed from just a few suitably chosen partial resonances.

When the boundary irregularities have wide spectra of Fourier components, as in most actual boundary layers, the partial resonances generating the second perturbation motions tend to become noticeable somewhere near the critical Reynolds number of ordinary linear stability theory and thereafter to manifest more frequently and strongly. Initially, the dominant driven Fourier components are mainly two-dimensional, with wave fronts about normal to the mean flow direction; but eventually, they are mostly three-dimensional, with wave fronts in all directions. Somewhere after the beginning of such phenomena, the partial resonances yielding the third and fourth perturbation motions tend to become significant and thereafter to appear more frequently and strongly. In this case, the dominant driven Fourier components are mostly three-dimensional, and they also supplement the second perturbation motions, substantially increasing the intricacy of the whole motion. Further downstream, the partial resonances providing the higher perturbation motions may become important and further complicate the whole motion. Thus, in general, the partial resonances tend to manifest somewhat like a gradually developing avalanche, initially generating a few weak simple motions in the laminar region and eventually producing numerous strong complex motions in the turbulent region. Otherwise, within this overall trend, they tend to appear partially randomly owing to the randomness of the boundary irregularities. In the whole process, several mean Fourier components become significant, causing a rather gradual distortion of the mean flow. Also, the oscillation Fourier components often vary abruptly as a result of the rapid growths near the resonance points, causing burst-like phenomena. In the synthesis of the component motions, various other phenomena that are observed in experiments can be expected. For example, the non-exponential amplifications of partial oscillations reported by Klebanoff and Tidstrom (Reference 37) seem to be representable by merely superpositions of growths from successive perturbations. Likewise, considering the generality of the present theory, any special phenomena that are proposed and verified in other theories on instability, transition, and turbulence probably can be found. For example, insofar as they actually occur, the bent vortices suggested by Theodorsen (Reference 54) and the streamwise vortices hypothesized by Lin and Benney (Reference 42) probably are encompassed by the present theory.\*

Within this overall concept, ordinary linear stability theory pertains to just the simplest part of the second perturbation motion. In particular, that theory not only ignores the part of the second perturbation motion

---

\*Notwithstanding some resemblance, the Lin and Benney theory differs from the resonance theory in several respects. For example, the former theory involves fundamentally different perturbation and growth schemes. Also, it should be noted, some experimental observations suggesting streamwise vortices, including data cited by Lin and Benney in support of their theory, may be attributable instead to crossflow vortices caused by small crosswise pressure gradients.

(F) Transition Mechanism (continued)

representing the introducing of disturbances into the boundary layer but also misrepresents the eventual diminution of that motion and completely neglects all other perturbation motions. Also, the original form of the resonance theory introduced by Raetz (Reference 1) pertains mostly to that part of the fourth perturbation motion which is generated from the motions of the linear theory (by total rather than partial resonances). Moreover, an energy exchange mechanism claimed by Benney and Lin (Reference 27)\* mainly amounts to an eventual counteraction of a part of the second perturbation motion by a part of the sixth perturbation motion.

Conjointly, an implication by Benney and Niell (Reference 28) that such an energy exchange mechanism generally prevents individual partial resonances\*\* from being prominent appears to be inappropriate. Their analysis considers an elementary simulant differential system which, due basically to irrelevant boundary conditions, really resembles the differential system of a laminar boundary layer with a slight irregularity in the initial velocity profile but no irregularities at the wall surface and in the adjoining flow. As a result, the analysis involves just an autonomous system whereas, to properly typify the pertinent boundary irregularities, a non-autonomous system would be essential. In such a case, as known from various numerical integrations of the boundary layer equations, the distortion tends to decay quite rapidly in the downstream direction -- there being no noticeable partial resonances. In fact, this tendency has been utilized for calculating stagnation profiles of general boundary layers (Reference 45). Hence, although their analysis does indicate a suppression of certain partial resonances by an energy exchange mechanism, a similar suppression does not necessarily prevail at transition. Instead, a quite different and usually weaker interaction, manifesting sequentially like the higher perturbation motions and depending sensibly on the perturbation parameter, probably appertains. For example, an individual Fourier component of the second perturbation motion may grow considerably before any opposing Fourier component of a higher perturbation motion becomes significant, and the suppression then will depend substantially on the perturbation parameter (and various other quantities). Indeed, such a trend seems to be discernible in the streamwise growths and decays of partial oscillations measured by Kiebanoff and Tidstrom (Reference 37). Thus, in certain circumstances, individually strong partial resonances apparently are possible. Moreover, wherever discrete vortices are formed, such resonances evidently are important.

Since the partial resonances tend to become significant in a somewhat gradual manner, transition itself cannot be defined nor be located very distinctly. In most boundary layers, the so-called transition is merely a partially random succession of partial resonances that are stronger and more frequent than in the laminar flow but are weaker and less frequent than in the turbulent flow, these distinctions being quite arbitrary. Thus, in general, transition as commonly recognized does not involve a distinct change in the fundamental nature of the motion. However, in some boundary layers, a region where some higher perturbation component first becomes significant may be discernible, suggesting a distinct change. Otherwise, where a practical criterion is needed, transition can be regarded simply as the onset of an appreciable distortion of the mean flow. This criterion indicates the beginning of an appreciable increase in the shearing stress on the wall surface, which is a main consequence of the departure from laminar flow.

---

\*This claim appears to have been based on a doubtful argument published later by Benney and Niell, which is discussed in the next paragraph.

\*\*called apparent resonances in References 27 & 28.

(F) Transition Mechanism (continued)

In the preceding analysis, for simplicity, the boundary irregularities were assumed to include just a simple injection at the wall surface and a simple fluctuation in the adjoining flow. These irregularities introduced, respectively, a stationary and a traveling spectrum of Fourier components into the first perturbation component. As a result, the frequencies of some of the driving Fourier components formed from these spectra could resemble some of the natural frequencies or proper values of the driven Fourier components and thereby could yield some significant partial resonances. However, similar frequencies and thereby similar resonances also can result from any of a large variety of other combinations of boundary irregularities. For example, without altering the general nature of the whole motion, the injection spectrum can be replaced by a more general stationary spectrum representing injection or suction through discrete areas or slots or representing waviness or roughness of the wall surface. In this case, the main additional problem is the estimation of that spectrum, which requires only a linear superposition of products of the initial amplitude coefficients and the phase functions. Similarly, the fluctuation spectrum can be replaced by a more general traveling spectrum representing external turbulence or sound. In this case, also, the main additional problem requires only a linear superposition of basic functions, using compressible relations for the external sound.\* In fact, the injection and fluctuation spectra together can be replaced by a single traveling spectrum with certain space and time frequencies. Sometimes, just the spectrum from a vibrating wall surface can produce a sequence of significant partial resonances. Likewise, the spectrum from a vibrating ribbon within the boundary layer, such as used by Schubauer and Skramstad (Reference 48) may yield partial resonances like those at transition. However, by itself, neither a stationary spectrum from the wall surface nor a traveling spectrum from the adjoining flow can produce important partial resonances within boundary layers like that considered so far, due to the restricted ranges of the natural frequencies in such boundary layers.

Although generated in a similar way, the various dominant motions from a particular combination of boundary irregularities usually differ in several details. As one example, as already indicated, two-dimensional motions tend to appear first, whereas three-dimensional motions tend to grow most. As another example, the lower perturbation motions must occur first, but the higher perturbation motions may grow faster and also may become more numerous eventually. Along with such tendencies, the three-dimensional trends of the lower perturbation motions overlap the two-dimensional trends of the higher perturbation motions, diminishing any distinctness in the transition region. As a further example, special motions may result from the partial resonances in the more general boundary layers, such as Goertler vortices when the wall surface is curved and cross-flow vortices when the adjoining flow is curved. (Unlike most motions, these particular vortices can be excited by just a stationary spectrum of boundary irregularities at the wall surface.) Such special phenomena supplement the motions considered so far, and they may or may not be the more important, depending on their intensity. Also, as an interesting but unverified possibility, the

---

\*An, waviness or roughness of the wall surface complicates the boundary conditions for each perturbation. However, in some cases, as an approximation, this complication probably can be neglected in the second and higher perturbations. In other cases, a waviness might be handled conveniently as a periodic perturbation of the metrical coefficients of a curvilinear coordinate system.

(F) Transition Mechanism (continued)

resonance amplitude coefficients representing the distributions across the boundary layer perhaps may include abnormal as well as normal proper solutions (such as are used in ordinary linear stability theory). The abnormal proper solutions might exist for certain singular proper values encountered in three-dimensional motions, and they might account for some observations (see Part G-3).

When the basic flow itself is altered, several important changes can occur in the sequence of partial resonances. In the first place, the overall development of this sequence depends indirectly on the neutral curve of ordinary linear stability theory, which in turn depends greatly on the distribution of the basic flow velocity across the boundary layer. More specifically, an alteration of this distribution modifies the relationship of the proper values to the local Reynolds number and the timewise frequency -- thereby affecting the locations, durations, and strengths of the partial resonances and also the space and time frequencies of the dominant oscillations. In the second place, the strengths of the partial resonances further depend on the rate of variation of the local Reynolds number with downstream distance. Thus, as the local Reynolds number and thereby the proper values vary relatively slowly or rapidly, the total growths from the partial resonances become relatively large or small, respectively, shifting the position of transition accordingly. Such a trend apparently has been encountered in various experiments on bodies of revolution.\* On the forward, central and rearward parts of such bodies, transition has been observed at respectively lower, similar, and higher local Reynolds numbers than on essentially flat surfaces with locally similar basic flows, these discrepancies apparently being due in part to the differences in the rate of variation of the local Reynolds number.\*\* When transition is suppressed by suction through the wall surface, the same trend may diminish the effectiveness of the suction, insofar as the rate of variation of the local Reynolds number is decreased. However, unless the boundary irregularities including the suction variations are too large, this adverse trend ordinarily can be overcome merely by stronger suction, which otherwise tends to suppress the partial resonances. Furthermore, as already indicated, a concave curvature of the wall surface or a crosswise curvature of the adjoining flow may allow an additional class of proper solutions and thereby an additional

---

\*Also, such a trend evidently can aggravate any tendency toward transition near the leading edge of a swept wing. Specifically, if the nose radius is large enough to allow a sufficiently thick boundary layer in that region, the total growths along the stagnation line in the spanwise direction apparently can become excessive as a result of the slow variation of local Reynolds number and the long distance in that direction together with other adverse factors (such as a relatively small minimum Reynolds number on the applicable neutral curve, a roughness due to dust and insects, and usually an initial turbulence from a fuselage or other adjoining surface). Furthermore, such a trend may help explain an unresolved discrepancy between the observed and calculated stability limits for the crossflow vortices on a rotating disk. So far, the observed value has appeared to be much higher than the calculated value, perhaps partly because the Reynolds number varies too fast to allow detectable partial resonances to occur near the actual stability limit.

\*\*This trend also is influenced by differences in the neutral curves due to the differences in the wall curvature.

#### (F) Transition Mechanism (continued)

type of motion, in the form of Goertler or crossflow vortices, to exist. According to the resonance theory, such vortices grow downstream in a different way than in ordinary linear stability theory.

Insofar as the resonance theory is valid, the main techniques for preventing transition are quite obvious. In the first place, all boundary irregularities--including the wall waviness and roughness, the external turbulence and sound, any irregularities due to suction through discrete apertures, etc.--should be minimized. Thereby, all perturbation motions will have minimum magnitudes, the higher perturbation motions being suppressed the most. However, among the Fourier components of the boundary irregularities, just those with the frequencies allowing strong partial resonances need to be diminished, those with other frequencies being inconsequential. In the second place, the basic flow should be controlled so as to shift the local neutral curves and thereby the important partial resonances to the highest possible local Reynolds numbers, especially in those regions where transition otherwise tends to occur. In some cases, adequate control can be exercised merely by appropriately choosing the wall surface contour and the adjoining flow distribution. In certain cases, such control might be attained by coating the wall with a properly selected and sufficiently uniform viscoelastic layer so as to shift the strong partial resonances to higher local Reynolds numbers. In many cases, the best control is achieved by applying sufficiently strong and uniform suction through the wall surface. In the third place, as necessary and possible, the boundary layer thickness should be reduced so as to complete the prevention of strong partial resonances. In general, this reduction can be attained best by sufficiently strong suction. Such aspects of the theory, particularly the question of whether laminar flow can be maintained indefinitely in the streamwise direction, merit much further analysis.

#### (G) Calculation Techniques

To apply the resonance theory of transition, mainly the basic flow and amplitude coefficient systems must be solved, the remaining calculations being relatively minor. Since each of these systems contains several simultaneous partial differential equations with three independent variables and also entails either an elliptic boundary value or a proper value problem, exact solutions neither are possible nor would be practical by available techniques. However, the whole analysis purposely has been developed so as to exclude all rapid variations in the  $x_1$  and  $x_2$  directions from these systems. Consequently, merely by applying approximations analogous to the conventional boundary layer assumptions, each system can be reduced without excessive error to a much simpler system that can be solved in a practical manner.

##### (1) Basic Flow

The basic flow always must be ascertained first, since its velocity components  $U_j^0$  constitute the variable coefficients of the amplitude coefficient systems. Unlike the other systems, its differential system (Equations (7) and (8)) is nonlinear. However, upon eliminating  $\phi_{jk}^0$ ,  $\psi_{jk}^0$ , and  $\Omega_{jk}^0$ , Equations (7) reduce to the steady continuity and Navier-Stokes equations

$$U_{j,j}^0 = 0$$

$$\rho U_{j,k}^0 U_k^0 = -P_{,j}^0 + \mu U_{j,kk}^0$$

(100)

(1) Basic Flow (continued)

which can be approximated satisfactorily by steady laminar boundary layer equations. Thus, assigning the magnitudes

$$\begin{aligned} x_j &\sim O(\mu^{-1}) & x_3 &\sim O(1) \\ (\quad)_{,j} &\sim O(\mu) & (\quad)_{,3} &\sim O(1) \\ U_j^0 &\sim O(1) & U_3^0 &\sim O(\mu) \\ \rho &\sim O(1) & P^0 &\sim O(1) \end{aligned} \quad (101)$$

where  $j = 1, 2$  and  $\mu \ll 1$ , and retaining just the dominant terms, Equations (100) reduce to

$$\begin{aligned} U_{k,k}^0 &= 0 \\ \rho U_{j,k}^0 U_k^0 &= -P_{,j}^0 + \mu U_{j,33}^0 \\ P_{,3}^0 &= 0 \end{aligned} \quad (102)$$

where  $j = 1, 2$  and  $k = 1, 2, 3$ . When the pressure does not vary with  $x_1$  and  $x_2$  and the mean flow is in the  $x_1$ -direction, as was assumed in much of the preceding analysis, the whole approximate system is

$$\begin{aligned} U_{1,1}^0 + U_{3,3}^0 &= 0 \\ \rho(U_{1,1}^0 U_1^0 + U_{1,3}^0 U_3^0) &= \mu U_{1,33}^0 \end{aligned} \quad (103)$$

and

$$\begin{aligned} U_1^0 = U_3^0 &= 0 & (x_3 = 0) \\ U_1^0 = W_1^0 & & (x_3 = \infty) \end{aligned} \quad (104)$$

where  $W_1^0$  is a given positive constant.

In most of the preceding analysis, merely a dimensionless similarity solution of Equations (103) and (104) was involved. In this solution, if the boundary layer begins at  $x_1 = 0$ , the reference length and velocity are

$$\Lambda = x_1/R \quad (105)$$

$$T = W_1^0$$

where the local Reynolds number is

$$R = \rho \Lambda T / \mu = (\rho x_1 W_1^0 / \mu)^{1/2} \quad (106)$$

Also, the similarity coordinate  $z$  is

$$z = x_3 / \Lambda \quad (107)$$

and the similarity stream function  $X(z)$  is defined by

$$\begin{aligned} U_1^0 &= (\Lambda T X)_{,3} \\ U_3^0 &= -(\Lambda T X)_{,1} \end{aligned} \quad (108)$$



(1) Basic Flow (continued)

Substituting Equations (108) into Equations (103) and (104), the approximate system degenerates to the ordinary differential system

$$2X''' + XX'' = 0 \quad (109)$$

and

$$\begin{aligned} X(0) &= X'(0) = 0 \\ X'(\infty) &= 1 \end{aligned} \quad (110)$$

whose solution is the well-known Blasius profile (see, for example, Schlichting, Reference 47). In the resulting boundary layer, as evident from Equation (106),  $R$  varies like  $x_1^{1/2}$ , allowing the duration of the partial resonances to increase as  $x_1$  increases. As a result, the partial resonances tend to persist for relatively long distances in the transition region and even longer distances in the turbulent region, causing corresponding large amplifications.

(2) Initial Amplitude Coefficients

Knowing the basic flow, the initial amplitude coefficients are obtained from Equations (38) and (39), which constitute an inhomogeneous linear differential system with variable coefficients. Eliminating  $\phi_{jk}^n$ ,  $\psi_{jk}^n$ , and  $\omega_{jk}^n$ , Equations (38) reduce to

$$\begin{aligned} iu_{j,j}^n A_j^n + u_{j,j}^n &= 0 \\ i\rho u_j^n (A_k^n U_k^0 + c_k^n) + \rho(U_{j,k}^0 u_k^n + u_{j,k}^n U_k^0) + i p^n A_j^n + p_{,j}^n \\ &= \mu(u_{j,kk}^n + 12u_{j,k}^n A_k^n - u_j^n A_k^n A_k^n) \end{aligned} \quad (111)$$

where  $j, k = 1, 2, 3$ . These equations are simplified by observing Relations (101) and the additional magnitudes

$$\begin{aligned} A_m^n, c^n &\sim 0(1) \\ u_m^n, p^n &\sim 0(1) \end{aligned} \quad (112)$$

in most of the boundary layer while also necessarily allowing the alternative magnitudes

$$\begin{aligned} u_{j,3}^n &\sim 0(\mu^{-1/2}) & u_{3,3}^n &\sim 0(1) \\ u_{j,33}^n &\sim 0(\mu^{-1}) & u_{3,33}^n &\sim 0(\mu^{-1/2}) \end{aligned} \quad (113)$$



(2) Initial Amplitude Coefficients (continued)

in thin sublayers, where  $m = 1, 2, 3$  and  $j = 1, 2$ . Thus, retaining just dominant terms and some symmetrizing minor terms, the exact system degenerates to the approximate ordinary system

$$\begin{aligned} i u_m^{\wedge} A_m^{\wedge} + u_{3,3}^{\wedge} &= 0 \\ i \rho u_j^{\wedge} (A_k^{\wedge} U_k^{\circ} + c^{\wedge}) + \rho U_{j,3}^{\circ} u_3^{\wedge} + i p^{\wedge} A_j^{\wedge} \\ &= \mu (u_{j,33}^{\wedge} + 12 u_{j,3}^{\wedge} A_3^{\wedge} - u_j^{\wedge} A_m^{\wedge} A_m^{\wedge}) \end{aligned} \quad (114)$$

$$\begin{aligned} i \rho u_3^{\wedge} (A_k^{\wedge} U_k^{\circ} + c^{\wedge}) + p_{,3}^{\wedge} + i p^{\wedge} A_3^{\wedge} \\ = \mu (u_{3,33}^{\wedge} + 12 u_{3,3}^{\wedge} A_3^{\wedge} - u_3^{\wedge} A_m^{\wedge} A_m^{\wedge}) \end{aligned}$$

and

$$\begin{aligned} u_m^{\wedge}(x_n^{\circ}) &= v_m^{\wedge} \\ u_m^{\wedge}(x_n^{\infty}) &= w_m^{\wedge} \\ p^{\wedge}(x_n^{\infty}) &= q^{\wedge} \end{aligned} \quad (115)$$

where  $j, k = 1, 2$  and  $m, n = 1, 2, 3$ . The dimensionless quantities, distinguished by the overscript  $\wedge$ , are chosen as

$$\begin{aligned} \hat{\rho} &= \rho / \rho = 1 & \hat{\mu} &= \mu / \rho \Lambda T = R^{-1} \\ \hat{A}_m^{\wedge} &= A_m^{\wedge} \Lambda & \hat{c}^{\wedge} &= c^{\wedge} \Lambda / T \\ \hat{x}_m &= x_m / \Lambda & & \\ \hat{U}_m^{\circ} &= U_m^{\circ} / T & \hat{v}_m^{\wedge} &= v_m^{\wedge} / T \\ \hat{u}_m^{\wedge} &= u_m^{\wedge} / T & \hat{w}_m^{\wedge} &= w_m^{\wedge} / T \\ \hat{p}^{\wedge} &= p^{\wedge} / \rho T^2 & \hat{q}^{\wedge} &= q^{\wedge} / \rho T^2 \end{aligned} \quad (116)$$

Substituting these quantities and omitting the overscript, as done hereafter, a dimensionless system identical to Equations (114) and (115) is obtained.

For many purposes, an alternate form of Equations (114) and (115) is preferable. This form involves the parameters

(2) Initial Amplitude Coefficients (continued)

$$\begin{aligned}
 \alpha &= (A_1^* A_1^* + A_2^* A_2^*)^{1/2} \\
 \beta &= (\alpha^2 + i\rho\alpha c/\mu)^{1/2} \\
 \gamma &= A_3^* \\
 \alpha c &= A_1^* W_1^0 + A_2^* W_2^0 + c^*
 \end{aligned}
 \tag{117}$$

where  $\text{Re}(\alpha)$ ,  $\text{Re}(\beta) > 0$  and the new variables

$$\begin{aligned}
 \alpha u &= A_1^* (W_1^0 - U_1^0) + A_2^* (W_2^0 - U_2^0) \\
 \alpha \zeta &= A_2^* (W_1^0 - U_1^0) - A_1^* (W_2^0 - U_2^0) \\
 \omega &= iA_2^* u_1^* - iA_1^* u_2^* \\
 \varphi &= u_3^* \\
 p &= p^*
 \end{aligned}
 \tag{118}$$

which are regarded as functions of just the coordinate

$$z = x_3 \tag{119}$$

since Equations (114) have only  $x_3$ -derivatives. Thus, an elimination of  $u_1^*$ ,  $u_2^*$ , and  $p^*$  yields the principal equation

$$\begin{aligned}
 &\varphi^{iv} + 14\gamma\varphi''' - (\alpha^2 + \beta^2 + 6\gamma^2)\varphi'' \\
 &- i2\gamma(\alpha^2 + \beta^2 + 2\gamma^2)\varphi' + (\alpha^2 + \gamma^2)(\beta^2 + \gamma^2)\varphi \\
 &= -i(\rho\alpha/\mu) \left\{ u[\varphi'' + i2\gamma\varphi' - (\alpha^2 + \gamma^2)\varphi] - u''\varphi \right\}
 \end{aligned}
 \tag{120}$$

with the conditions

$$\begin{aligned}
 \varphi(0) &= v_3^* & \varphi'(0) &= -iA_m^* v_m^* \\
 \varphi(\infty) &= w_3^* & \varphi'(\infty) &= -iA_m^* w_m^*
 \end{aligned}
 \tag{121}$$

where  $m = 1, 2, 3$ . Likewise, another elimination of  $p^*$  alone supplies the supplemental equation

$$\omega'' + 12\gamma\omega' - (\beta^2 + \gamma^2)\omega + i(\rho\alpha/\mu)u\omega = -i(\rho\alpha/\mu)\zeta'\varphi \tag{122}$$

with the conditions

## (2) Initial Amplitude Coefficients (continued)

$$\begin{aligned} \omega(0) &= iA_2^x v_1^x - iA_1^x v_2^x \\ \omega(\infty) &= iA_2^x w_1^x - iA_1^x w_2^x \end{aligned} \quad (123)$$

Also, other eliminations provide the auxiliary relations

$$\begin{aligned} \alpha^2 u_1^x &= iA_1^x (\varphi' + i\gamma\varphi) - iA_2^x \omega \\ \alpha^2 u_2^x &= iA_2^x (\varphi' + i\gamma\varphi) + iA_1^x \omega \end{aligned} \quad (124)$$

Finally, the last members of Equations (114) and (115) are expressible as the equation

$$p' + i\gamma p = \mu [\varphi'' + i2\gamma\varphi' - (\beta^2 + \gamma^2)\varphi] + i\rho\alpha u\varphi \quad (125)$$

with the condition

$$p(\infty) = q^x \quad (126)$$

In this form,  $\varphi$  is obtained first, independently of all other unknowns, after which  $\omega$  and  $p$  and then  $u_1^x$  and  $u_2^x$  are evaluated as required. For some applications,  $u_m^x$  ( $m = 1, 2, 3$ ) but not  $p^x$  are needed, the system for  $p$  then being omissible.

## (3) Resonance Amplitude Coefficients

Applying similar simplifications, the resonance amplitude coefficients are evaluated from Equations (40) and (41), which constitute a homogeneous linear differential system with variable coefficients. In fact, replacing the superscript  $x$  by  $\lambda$  and the non-trivial boundary values by zeros, all relations of Part (2) above also can and therefore will be used for these coefficients. However, due to the difference in boundary values, the initial and resonance amplitude coefficients themselves differ in a fundamental way. In particular, the latter can be non-trivial functions, called the proper functions, only when their parameters have singular values, called the proper values. Furthermore, because the boundary values in the adjoining flow now vanish, the alternate system in Part (2) now can be simplified further merely by substituting the new variables

$$\begin{aligned} \varphi_* &= \varphi \exp(i\gamma z) \\ \omega_* &= \omega \exp(i\gamma z) \\ p_* &= p \exp(i\gamma z) \end{aligned} \quad (127)$$

### (3) Resonance Amplitude Coefficients (continued)

The resulting system with the asterisks omitted is identical to Equations (120) through (126) with  $\gamma$  equal to zero. Consequently,  $A_3^\lambda$  can have any real value, leaving at most just  $A_1^\lambda$  and  $A_2^\lambda$  with true proper values, which depend on just  $R$  and  $c^\lambda$ . In fact, if the basic flow is in the  $x_1$ -direction,  $A_2^\lambda$  itself can have any real value, leaving just  $A_1^\lambda$  with a true proper value, which in general must be complex. In that case, when  $\text{Re}(A_1^\lambda) = A_2^\lambda = 0$ , the proper values and functions represent streamwise vortices, which have not been adequately explored as yet.\*

When  $\gamma$  is equated to zero, or when  $A_3^\lambda$  actually is zero as in much of the preceding analysis, Equations (120) and (121) in the present case degenerate to

$$\begin{aligned} c^{iv} - (\alpha^2 + \beta^2)\varphi'' + \alpha^2\beta^2\varphi \\ = -i(\rho\alpha/\mu)[u(\varphi'' - \alpha^2\varphi) - u''\varphi] \end{aligned} \quad (128)$$

and

$$\begin{aligned} \varphi(0) = \varphi'(0) = 0 \\ \varphi(\infty) = \varphi'(\infty) = 0 \end{aligned} \quad (129)$$

which is merely the well-known Orr-Sommerfeld system in a convenient form. This system has been studied and solved extensively in ordinary linear stability theory, wherein  $\alpha$  and  $R$  but not  $c$  usually are regarded as real. Various results are included among the papers listed as references. When  $\alpha$  and  $R$  are the given parameters, the proper values are those values of  $c$ , denoted as  $c_*$ , for which non-trivial solutions exist. The familiar neutral curve of ordinary linear stability theory is merely the locus of  $\alpha$  versus  $R$  when  $c_*$  as well as  $\alpha$  and  $R$  are real. In boundary layers like the one considered in most of the preceding analysis, the inequality

$$0 < c_* < u(0) \quad (130)$$

exists on the neutral curve (see, for example, Schlichting, Reference 47), and a corresponding inequality exists elsewhere. This property, by restricting the ranges of the natural frequencies of the driven Fourier components, prevents a large class of partial resonances from becoming significant.

In principle, a technique that is suitable for accurately solving the Orr-Sommerfeld system also is adequate for solving Equations (120) through (126) for both non-trivial and trivial boundary values. However, the techniques available from ordinary linear stability theory neither meet this requirement fully nor are applicable directly. In the first place, the well-known approximate method of asymptotic expansions generally neglects all but the first term of an expansion which probably diverges, while the so-called

---

\*Apparently, based on observations by Gregory and Walker (Reference 33), such vortices (as included in the resonance theory) constitute the primary motions of turbulent wedges.

### (3) Resonance Amplitude Coefficients (continued)

exact method of numerical integration ordinarily entails an obscure but large accumulative error.\* Whereas such imprecision may not excessively affect the proper values, which are the main quantities in ordinary linear stability theory, it probably can adversely alter the proper functions and thereby the resonance coefficients, which are important in the present theory. Also, such imprecision would prevent a satisfactory exploration of the nature and role of the higher proper solutions (for  $T = 2, 3, \dots$ ), which may not always be negligible. In the second place, the techniques of ordinary linear stability theory generally apply to just real values of  $\alpha$  and  $R$ , whereas the present theory involves complex values of  $\alpha$  and  $R$  (as well as of  $c$ ). Moreover, the possible existence and importance of abnormal as well as normal proper solutions merit consideration. Specifically, the cases when  $\alpha$  and  $\beta$  differ by a multiple of a certain value, which may happen in the three-dimensional motions concerned here but not in the two-dimensional motions usually treated in ordinary linear stability theory, warrant investigation. For such values of  $\alpha$  and  $\beta$ , the fundamental solutions of the Orr-Sommerfeld equation have a singular nature\*\* that has not yet been assessed. Thus, despite the vast effort in ordinary linear stability theory, the Orr-Sommerfeld system hitherto has not been solved in an entirely satisfactory manner nor over the complete ranges of its parameters. For these reasons, as an initial step in the practical implementation of the present theory, a better technique of solving the Orr-Sommerfeld system and thereby the more general systems involved here was sought and eventually found. This improved technique has given excellent results in trial calculations on an electronic computer but still is being developed and therefore remains to be described in a later paper.

### (4) Adjoint Amplitude Coefficients

Continuing in an analogous manner, the adjoint amplitude coefficients are ascertained from Equations (43) and (44), which constitute another homogeneous linear differential system with variable coefficients.

Eliminating  $\xi_{jk}^\lambda$ ,  $\eta_{jk}^\lambda$ , and  $\zeta_{jk}^\lambda$ , Equations (43) reduce to

$$\begin{aligned} iA_j^\lambda s_j^\lambda - s_{j,j}^\lambda &= 0 \\ i p s_j^\lambda (A_k^\lambda U_k^0 + c^\lambda) + i A_j^\lambda (\rho s_k^\lambda U_k^0 + r^\lambda) - \rho (s_{j,k}^\lambda + s_{k,j}^\lambda) U_k^0 - r_{,j}^\lambda & \\ &= \mu (s_{j,kk}^\lambda - i 2 s_{j,k}^\lambda A_k^\lambda - s_j^\lambda A_k^\lambda A_k^\lambda) \end{aligned} \quad (131)$$

where  $j, k = 1, 2, 3$ . These equations are simplified by assigning the same magnitudes to  $s_j^\lambda$  and  $r^\lambda$  as to  $u_j^\lambda$  and  $p^\lambda$ , respectively, while observing Equations (101), (112), and (113). Thereby, the whole system reduces to

\*This error is due to a spurious solution of the differential equations which enters the numerical solution through truncation errors and then tends to grow excessively as the integration proceeds.

\*\*at least in some types of boundary layers.

(4) Adjoint Amplitude Coefficients (continued)

$$iA_m^{\lambda} s_m^{\lambda} - s_{3,3}^{\lambda} = 0$$

$$\begin{aligned} i\rho s_j^{\lambda}(A_k^{\lambda} U_k^0 + c^{\lambda}) + iA_j^{\lambda}(\rho s_k^{\lambda} U_k^0 + r^{\lambda}) \\ = \mu(s_{j,33}^{\lambda} - i2A_3^{\lambda} s_{j,3}^{\lambda} - s_{j,m}^{\lambda} A_m^{\lambda}) \end{aligned} \quad (132)$$

$$\begin{aligned} i\rho s_3^{\lambda}(A_k^{\lambda} U_k^0 + c^{\lambda}) + iA_3^{\lambda}(\rho s_k^{\lambda} U_k^0 + r^{\lambda}) - \rho s_{k,3}^{\lambda} U_k^0 - r_{,3}^{\lambda} \\ = \mu(s_{3,33}^{\lambda} - i2A_3^{\lambda} s_{3,3}^{\lambda} - s_{3,m}^{\lambda} A_m^{\lambda}) \end{aligned}$$

and

$$\begin{aligned} s_m^{\lambda}(x_n^0) &= 0 \\ s_m^{\lambda}(x_n^{\infty}) &= 0 \\ r^{\lambda}(x_n^{\infty}) &= 0 \end{aligned} \quad (133)$$

where  $j, k = 1, 2$  and  $m, n = 1, 2, 3$ . Substituting the dimensionless quantities

$$\begin{aligned} \hat{A}_m^{\lambda} &= A_m^{\lambda} \Lambda & \hat{c}^{\lambda} &= c^{\lambda} \Lambda / \mathcal{T} \\ \hat{s}_m^{\lambda} &= s_m^{\lambda} / \mathcal{T} & \hat{r}^{\lambda} &= r^{\lambda} / \rho \mathcal{T}^2 \end{aligned} \quad (134)$$

along with Equations (116) and omitting the overscript, the same relations are obtained as for the dimensional system.

As in the preceding case, an alternate form of Equations (132) and (133) often is preferable. This form involves Equations (117) through (119) with the superscript  $\kappa$  replaced by  $\lambda$  and also the new variables

$$\begin{aligned} \chi &= iA_2^{\lambda} s_1^{\lambda} - iA_1^{\lambda} s_2^{\lambda} \\ \psi &= s_3^{\lambda} \\ r &= \rho(s_1^{\lambda} U_1^0 + s_2^{\lambda} U_2^0) + r^{\lambda} \end{aligned} \quad (135)$$

which are regarded as functions of  $z$  alone. First, an elimination of  $r^{\lambda}$  alone supplies the supplementa' equation

$$\chi'' - i2\gamma\chi' - (\beta^2 + \gamma^2)\chi + i(\rho\alpha/\mu)u\chi = 0 \quad (136)$$

(4) Adjoint Amplitude Coefficients (continued)

with the conditions

$$\begin{aligned} X(0) &= 0 \\ X(\infty) &= 0 \end{aligned} \quad (137)$$

In the present problem, this system has just the trivial solution

$$X = 0 \quad (138)$$

which together with the first of Equations (132) leads to the auxiliary relations

$$\alpha^2 s_j^\lambda = -iA_j^\lambda(\psi' - i\gamma\psi) \quad (139)$$

and then to the identity

$$\alpha s_{j,3}^\lambda u_{j,3}^0 = i\gamma'(\psi' - i\gamma\psi) \quad (140)$$

where  $j = 1, 2$ . Next, an elimination of  $s_1^\lambda$ ,  $s_2^\lambda$ , and  $r^\lambda$  using Equation (140) yields the principal equation

$$\begin{aligned} &\psi^{iv} - i4\gamma\psi''' + (\alpha^2 + \beta^2 + 6\gamma^2)\psi'' \\ &+ 12\gamma(\alpha^2 + \beta^2 + 2\gamma^2)\psi' + (\alpha^2 + \gamma^2)(\beta^2 + \gamma^2)\psi \\ &= -i(\rho\alpha/\mu) \left\{ u[\psi'' - 12\gamma\psi' - (\alpha^2 + \gamma^2)\psi] + 2u'(\psi' - i\gamma\psi) \right\} \end{aligned} \quad (141)$$

with the conditions

$$\begin{aligned} \psi(0) &= \psi'(0) = 0 \\ \psi(\infty) &= \psi'(\infty) = 0 \end{aligned} \quad (142)$$

Finally, the last members of Equations (132) and (133) are expressible as the equation

$$\begin{aligned} r' - i\gamma r &= -\mu[\psi'' - 12\gamma\psi' - (\beta^2 + \gamma^2)\psi] \\ &- i\rho\alpha u\psi + i(\rho/\alpha)u'(\psi' - i\gamma\psi) \end{aligned} \quad (143)$$

and the condition

$$r(\infty) = 0 \quad (144)$$

From this form,  $\psi$  is obtained first, independently of all other unknowns, after which  $s_1^\lambda$  and  $s_2^\lambda$  and finally  $r^\lambda$  are evaluated as required. Sometimes,  $r^\lambda$  and

#### (4) Adjoint Amplitude Coefficients (continued)

therefore Equations (143) and (144) are not needed. Furthermore, substitution of the new variables

$$\begin{aligned}\psi_* &= \psi \exp(-i\gamma z) \\ r_* &= r \exp(-i\gamma z)\end{aligned}\tag{145}$$

yields an even simpler system, which with the asterisks omitted is identical to Equations (141) through (144) with  $\gamma$  equated to zero.

As would be expected, the principal resonance system given by Equations (120) and (121) for trivial boundary values and the principal adjoint system given by Equations (141) and (142) are adjoint to each other over the interval  $0 \leq z \leq \infty$ . Thus, the proper values of these systems are identical and could be ascertained from either system, although the principal resonance system seems to be slightly preferable for this purpose. When  $\gamma$  equals zero, Equations (141) and (142) degenerate to

$$\begin{aligned}\psi^{IV} - (\alpha^2 + \beta^2)\psi'' + \alpha^2\beta^2\psi \\ = -i(\rho\alpha/\mu)[u(\psi'' - \alpha^2\psi) + 2u'\psi']\end{aligned}\tag{146}$$

and

$$\begin{aligned}\psi(0) &= \psi'(0) = 0 \\ \psi(\infty) &= \psi'(\infty) = 0\end{aligned}\tag{147}$$

which is merely the adjoint of the Orr-Sommerfeld system.

Along with the reduction of the amplitude coefficient systems to ordinary differential systems, all three-dimensional integrals over the transition domain  $D$  are replaced by one-dimensional integrals over the interval  $0 \leq z \leq \infty$ . In effect, this interval is equivalent to a three-dimensional domain of unit lengths in the  $x_1$  and  $x_2$  directions.

#### (H) Generalizations

Although the analysis has pertained mostly to just a relatively simple boundary layer, the basic techniques and main results can be generalized directly to many other flows. First, besides the spacewise partial resonances considered so far, timewise partial resonances resulting from timewise aperiodic variations of the flow may be included. Second, the Cartesian tensor representation may be replaced by a curvilinear tensor representation, enabling curved wall surfaces and adjoining flows and also curvilinear phenomena like Goertler and crossflow vortices to be encompassed. Third, the original incompressible differential system may be replaced by a compressible system containing the continuity, momentum, and energy equations and the accompanying fluid property relationships. The latter system will permit supersonic transitions, and also the effect of external sound on subsonic transitions, to be investigated. However, that system ordinarily will have some nonquadratic terms



(H) Generalizations (continued)

which first must be reduced to more elementary forms. This reduction generally can be accomplished satisfactorily by approximating the fluid property relationships by finite power series as necessary and then defining various quadratic products as supplementary unknowns. Fourth, the underlying differential system may be generalized further so as to cover chemical and electromagnetical interactions including dissociation and ionization. This extension will pertain to hypersonic transitions and also a variety of other important phenomena -- such as combustion instability in rocket motors, plasma instability in thermonuclear power apparatuses, and certain features of the general circulation of the atmosphere. Again, the differential system could and therefore would be reduced to a form containing the unknowns just quadratically. Finally, several other extensions also are possible -- such as to deformable wall surfaces, foreign fluid injections, etc.

In each such generalization, the unknowns would be expressed by perturbation series in a perturbation parameter representing the magnitude of the boundary irregularities. Then, these series would be substituted into a quadratic differential system to obtain a sequence of perturbation differential systems. As in the preceding analysis, the zero-th or basic perturbation system would be nonlinear, whereas all other perturbation systems would be linear but inhomogeneous -- the first perturbation system having homogeneous differential equations and the higher perturbation systems having trivial boundary values. Again, the basic flow would be chosen as the laminar flow occurring in the absence of all boundary irregularities, while the first perturbation would be determined solely by the boundary irregularities, and the higher perturbations would be determined solely and recursively from lower perturbations. Thereby, in contrast to the formulations of other theories, the entire disturbance motion would be related directly and uniquely to the boundary irregularities themselves. Furthermore, by a process like that used earlier, the perturbation components of the unknowns would be expressed in Fourier series extending over all coordinates and the time. Next, these series would be substituted into the perturbation systems, yielding spectra of Fourier coefficient systems resembling those encountered earlier. Subsequently, the Fourier coefficients themselves would be decomposed into amplitude coefficients and growth functions. Again, the resulting amplitude coefficient systems would include a differential system resembling the one encountered in ordinary linear stability theory but possessing a greatly different interpretation and application. Also, by approximations corresponding to conventional boundary layer assumptions, the basic flow and amplitude coefficient systems eventually would be reduced to simpler differential systems that could be solved by available techniques. (For the basic flow in a boundary layer, a general calculation technique already has been developed (Reference 45)).

Even in these generalizations, the principal phenomena still would be simply the partial resonances between the driven and the driving Fourier coefficients. The resulting growths, expressed mainly by the growth functions, again would include not only variations like those deduced in ordinary linear stability theory but also diverse faster and larger variations. However, the forms of the elemental motions as represented by the products of the amplitude coefficients and the phase functions still would resemble those predicted by the linear theory. Moreover, the calculations involved would be similar to, though somewhat more general and complicated than, those required in that theory. In fact, after appropriate adaptation and re-interpretation, many results available

#### (H) Generalizations (continued)

from ordinary linear stability theory could be used for the more general phenomena concerned here -- insofar as such results are precise enough. However, upon synthesizing all of the constituent motions, a wide variety of critical phenomena not predicted nor explained by the linear theory would be obtained. Consequently, generalized analyses and calculations like those just indicated should yield a variety of new knowledge advancing the status of several engineering and scientific fields.

#### (I) Concluding Remarks

As formulated here, the resonance theory of transition seems to provide a reasonable explanation of instability, transition, and turbulence alike and also to offer a possible way of estimating such phenomena. In particular, this theory attributes the main features of each of these phenomena to a rather simple basic mechanism -- namely, the partial resonance that may occur between a driven and a driving Fourier component of the flow -- which can be calculated by available or attainable techniques. Moreover, unlike most other theories, the present theory relates the whole motion directly and uniquely to the conditions at the boundaries of the flow, this motion being synthesized from a basic motion and the elemental motions generated by a sequence of partial resonances that is excited by the boundary irregularities. Nevertheless, besides constituting a relatively simple solution of a formidable nonlinear mathematical problem, the theory can be generalized directly to a wide variety of fluid flows. Thus, altogether, the resonance theory appears to represent a substantial refinement and extension of several previous concepts of instability, transition, and turbulence.

However, to fully implement the theory, some new calculation methods are required. In the first place, precise and efficient techniques of solving the approximate amplitude coefficient systems are needed. As mentioned earlier, substantial progress in this direction already has been made. In the second place, suitable approximate or exact techniques of synthesizing the individual motions from the partial resonances should be developed. Also, the asymptotic form of the synthesized motion, representing fully developed turbulence, should be sought. For these purposes, incorporations of some techniques from the classical theory of non-linear oscillations may be helpful. In the third place, a feasible technique of determining each perturbation component for a rough or deformable wall surface is needed. Except for surface waves of infinitesimal height and slope, such a calculation requires the solution of a linear boundary value problem of a relatively difficult type. In the fourth place, after various details are clarified, convenient approximations for practical applications of the theory should be established.

Also, to ascertain the validity of the theory, careful and complete comparisons with experimental observations are essential. Unfortunately, despite their abundance, the existing experimental data are inadequate for this purpose. As a careful examination will reveal, these data generally do not include enough information to fully ascertain the boundary irregularities at the wall surface and in the adjoining flow. Moreover, the actual influential boundary irregularities usually have been quite random, preventing a simple comparison with theory. Therefore, some careful experiments with simple and known boundary irregularities, using refined and complete instrumentation, are needed.

CHAPTER B. EXACT NUMERICAL SOLUTION OF THE COMPLETE LEES-LIN EQUATIONS  
FOR THE STABILITY OF COMPRESSIBLE FLOW

W. Byron Brown

(A) Notation

	Dimensionless Quantities	Characteristic Measure
$\rho$	Gas Density	$\bar{\rho}_0^*$
$T$	Gas temperature	$\bar{T}_0^*$
$\mu$	First viscosity coefficient	$\bar{\mu}_{10}^*$
$\mu_2$	Second viscosity coefficient	$\bar{\mu}_{20}^*$
$\alpha$	Disturbance wave number	$\ell^{-1}$
$C$	Phase velocity of the disturbance	$\bar{u}_0^*$
$\gamma$	Specific heat ratio $C_p/C_v$	
$R$	Reynolds number	$\frac{\bar{\rho}_0^* \bar{u}_0^* \ell}{\bar{\mu}_{10}^*}$
$M$	Mach number	$\sqrt{\frac{\bar{u}_0^*}{\gamma \bar{T}_0^* R^*}}$
Prandtl number $\sigma = \frac{C_p \bar{\mu}_1^*}{k^*}$		
$k$	Thermal conductivity	$C_p \bar{\mu}_{10}^*$
$\ell$	Length unit $\frac{x^*}{R}$	
$x^*$	Distance from stagnation point	

(A) Notation (Continued)

	Dimensionless Quantities	Characteristic Measure
x	Nondimensional distance	$l$
y	Distance from wall	$l$
w	Undisturbed velocity in boundary layer	$\bar{u}_0^*$
f	Velocity disturbance amplitude in x direction	
	$u = w(y) + f(y)e^{i \alpha(x - Ct)}$	
$\phi$	Velocity disturbance amplitude in y direction	
	$v = \alpha \phi(y)e^{i \alpha(x - Ct)}$	
$\pi$	Disturbance amplitude of pressure	
t	Time	$l/\bar{u}_0^*$

A bar over a quantity denotes average value, a dart denotes fluctuation. Subscript o denotes freestream value, subscripts r and i denote real and imaginary parts.

(B) Introduction

At the Stresa Conference (Reference 57) Reshotko pointed out that at Mach numbers above 2, a number of terms depending on the temperature derivatives of the viscosity were no longer negligible on account of the large temperature changes in the boundary layer. For example, at Mach 5, the wall temperature is 5.3 times the free stream temperature if the wall is insulated. At Mach 3 it is 2.5 times.

In view of this, Pfenninger suggested a numerical solution that would include all the terms in the Lees-Lin equations (Reference 58), not only those suggested by Reshotko but all the others as well. This has been done in this report, and numerical solutions obtained for flat plate profiles with insulated walls for Mach numbers from .4 to 5.8 and with two air temperature conditions as in Reference 3. The first is a stagnation temperature in the air stream of 100°F, appropriate to common conditions in wind tunnel experiments. The second condition is a free stream temperature of -67°F, appropriate to flight at high altitudes. In most cases, the velocity and temperature profiles used were those given in Reference 59.

(C) Analysis

The stability equations for a compressible boundary are given in Reference 57 and 58 as follows in nondimensional notation.

(1) Lees-Lin Equations

$$\alpha \rho \left\{ i(w - c) f + w' \right\} = - \frac{i\alpha\pi}{\gamma M^2} + \frac{\mu}{R} \left\{ f'' + \alpha^2 (i\varphi' - 2f) \right\} + \frac{2}{3} \frac{\mu_2 - \mu_1}{R} \alpha^2 (i\varphi' - f) \quad (1)$$

$$+ \frac{1}{R} \left\{ m w'' + m' w' + \mu' (f' + i\alpha^2 \varphi) \right\}$$

$$\alpha^2 \rho \left\{ i(w - c) \varphi \right\} = - \frac{\pi'}{\gamma M^2} \frac{\mu\alpha}{R} \left\{ 2\varphi' + i f' - \alpha^2 \varphi \right\} + \frac{2\alpha}{3} \frac{\mu_2 - \mu_1}{R} \left\{ \varphi' + i f' \right\} \quad (2)$$

$$\frac{\alpha}{R} \left\{ i m \varphi' + 2\mu' \varphi' + \frac{2}{3} (\mu_2' - \mu_1') (\varphi' + i f) \right\}$$

$$\varphi' + i f - \frac{T'}{T} \varphi + i(w - c) \left( \pi - \frac{\varphi}{T} \right) = 0 \quad (3)$$

$$\alpha \rho \left\{ i(w - c) \theta + T' \varphi \right\} = - \alpha(\gamma - 1) \rho T (\varphi' + i f) + \frac{\gamma}{R\sigma} \left\{ \mu(\theta'' - \alpha^2 \theta) + (m T')' + \mu' \theta' \right\} \quad (4)$$

$$+ \frac{\gamma(\gamma - 1)}{R} M^2 \left\{ n w'^2 + 2\mu w' (f' + i\alpha^2 \varphi) \right\}$$

Boundary condition:  $f = \varphi = \theta = 0$  when  $y = 0$  and  $f, \varphi, \theta$  bounded as  $y \rightarrow \infty$  where

$$m = \theta \frac{d\mu}{dT} \quad \text{and} \quad (5)$$

$$\mu' = T' \frac{d\mu}{dT} \quad (6)$$

(C) Analysis (Continued)

$\mu_2$  may be eliminated by the relation

$$\mu_2 + \frac{2}{3} \mu_1 = 0 \quad (\text{Reference 60}) \quad (7)$$

Also the equation of state is  $1 = \rho T$  if the pressure is regarded as unchanged through the boundary layer thickness.

(2) Reduction to Normal Form

It is shown in Reference 58 that this set of four equations (three of the second order) can be expressed as a system of six linear first order equations. The dependent variables then become

$$\begin{aligned} z_1 &= f & z_2 &= f' & z_3 &= \psi \\ z_4 &= \frac{\pi}{M^2} & z_5 &= \theta & z_6 &= \theta' \end{aligned}$$

Thus the normal form for equations 1 to 4 becomes

$$z_i' = \sum_{j=1}^6 c_{ij} z_j \quad (i = 1, 2, \dots, 6) \quad (8)$$

where the  $c_{ij}$ 's are

$$c_{12} = 1$$

$$c_{21} = \frac{\alpha i (w - c) R}{\mu T} + \alpha^2$$

$$c_{22} = -\frac{1}{\mu} \frac{d\mu}{dT} T'$$

$$c_{23} = \frac{\alpha R}{\mu T} w' + \frac{i\alpha^2}{9} (\ln T)' - \frac{i\alpha^2}{\mu} \frac{d\mu}{dT} T'$$

$$c_{24} = \frac{i\alpha R}{\gamma \mu} + \frac{\alpha^2 (w - c) M^2}{9}$$

$$c_{25} = -\frac{1}{\mu} \frac{d\mu}{dT} w'' - \frac{w'}{\mu} T' \frac{d^2 \mu}{dT^2} - \frac{\alpha^2}{9} \frac{(w - c)}{T}$$

$$c_{26} = -\frac{w'}{\mu} \frac{d\mu}{dT}$$

(2) Reduction to Normal Form (Continued)

$$C_{31} = -i$$

$$C_{33} = (\ln T)'$$

$$C_{34} = -i(w - c)M^2$$

$$C_{35} = \frac{i(w - c)}{T}$$

$$C_{41} = \frac{1}{a_{44}} \left[ -\frac{8}{9} (\ln T)' i - 2(\ln T)' \frac{T}{\mu} \frac{d\mu}{dT} i \right]$$

$$C_{42} = \frac{1}{a_{44}} [-i]$$

$$C_{43} = \frac{1}{a_{44}} \left[ \frac{8}{9} (\ln T)'' + \frac{8}{9} \{(\ln T)'\}^2 - \alpha^2 - \frac{\alpha R i (w - c)}{\mu T} + \frac{8}{9} \{(\ln T)'\}^2 \frac{T}{\mu} \frac{d\mu}{dT} \right]$$

$$C_{44} = \frac{1}{a_{44}} \left[ -\frac{8}{9} w' M^2 i - \frac{8}{9} (\ln T)' i (w - c) M^2 - \frac{8}{9} i (w - c) M^2 (\ln T)' \frac{T}{\mu} \frac{d\mu}{dT} \right]$$

$$C_{45} = \frac{1}{a_{44}} \left[ \frac{8}{9} \left( \frac{w - c}{T} \right)' i + \frac{8}{9} (\ln T)' \frac{w - c}{T} i + \frac{i w'}{\mu} \frac{d\mu}{dT} + \frac{8}{9} (\ln T)' \frac{w - c}{\mu} \frac{d\mu}{dT} i \right]$$

$$C_{46} = \frac{1}{a_{44}} \frac{8}{9} i \frac{(w - c)}{T}$$

$$\text{where } a_{44} = \frac{R}{\mu \alpha \gamma} + \frac{8}{9} i (w - c) M^2$$

$$C_{56} = 1$$

$$C_{62} = -2(\gamma - 1) M^2 \sigma w'$$

$$C_{63} = \frac{\alpha \sigma R}{\mu} (\ln T)' - 2(r - 1) M^2 w' \alpha^2 \sigma i$$

$$C_{64} = (r - 1) (w - c) \alpha \frac{M^2 \sigma R}{\gamma \mu} i$$

$$C_{65} = \frac{i \alpha R \sigma (w - c)}{\mu T} + \alpha^2 - \frac{T''}{\mu} \frac{d\mu}{dT} - \frac{T'^2}{\mu} \frac{d^2 \mu}{dT^2} - \frac{\sigma (\gamma - 1) M^2}{\mu} \frac{d\mu}{dT} w'^2$$

(2) Reduction to Normal Form (Continued)

$$C_{66} = - \frac{2T'}{\mu} \frac{d\mu}{dT}$$

The boundary conditions in terms of the Z's are, when  $y = 0$ ,

$$Z_1 = Z_3 = Z_5 = 0 \quad \text{and}$$

$$Z_1, Z_3, Z_5 \text{ bounded as } y \rightarrow \infty$$

The condition  $Z_5 = 0$  when  $y = 0$  is the usual one for high frequencies (Reference 58).

(3) Boundary Condition at  $y = \delta$

A significant difference between the conditions when  $y < \delta$  and those when  $y > \delta$  is that in the former region the velocity, density, temperature, viscosity, thermal conductivity, etc., all vary from wall values to freestream values, i.e., they are functions of the wall distance  $y$ . In the freestream, these physical quantities are constants (at a fixed value of  $x_1$  the distance from the stagnation point). Thus where  $y > \delta$ , all the  $C_{ij}$ 's become constants, say  $C_{ij}^*$ 's.

The system of equations (8) becomes the system

$$Z_i' = \sum_{j=1}^6 C_{ij}^* Z_j \quad (i = 1, 2, 3, 4, 5, 6) \quad (9)$$

whose solution is well known.

If  $Z_i = k_i \exp(\lambda y)$  is substituted into the above system equation (9) in the usual way, it can be shown that the characteristic determinant can be expressed as

$$F(\lambda) = f(\lambda^2) = (\lambda^2)^3 + A_1 (\lambda^2)^2 + A_2 \lambda^2 + A_3$$

where

$$-A_1 = C_{21}^* + C_{65}^* + C_{24}^* C_{42}^* + C_{34}^* C_{43}^* + C_{46}^* C_{64}^*$$

$$A_2 = C_{21}^* C_{46}^* C_{64}^* - C_{35}^* C_{43}^* C_{64}^* - C_{25}^* C_{42}^* C_{64}^* + C_{21}^* C_{65}^* \\ + C_{34}^* C_{43}^* C_{61}^* + C_{24}^* C_{42}^* C_{65}^* + C_{21}^* C_{34}^* C_{43}^* - C_{24}^* C_{31}^* C_{43}^*$$

$$A_3 = C_{21}^* C_{35}^* C_{43}^* C_{64}^* - C_{25}^* C_{31}^* C_{43}^* C_{64}^* - C_{21}^* C_{34}^* C_{43}^* C_{65}^* \\ + C_{24}^* C_{31}^* C_{43}^* C_{65}^*$$



(3) Boundary Condition at  $y = \delta$  (Continued)

If the roots of  $F(\lambda) = 0$  are denoted by

$$\pm \Lambda_i, \quad i = 1, 2, 3$$

where real part  $\Lambda_i > 0$

then

$$\lambda_1 = -\Lambda_1$$

$$\lambda_2 = -\Lambda_2$$

$$\lambda_3 = -\Lambda_3$$

$$\lambda_4 = +\Lambda_1$$

$$\lambda_5 = +\Lambda_2$$

$$\lambda_6 = +\Lambda_3$$

and the general solution of equation (9) may be written

$$Z_i = \sum_{j=1}^6 k_{ij} \exp(\lambda_j y) \quad (i = 1, 2, 3, 4, 5, 6) \quad (y \geq \delta)$$

Of the 36 constants  $k_{ij}$  only six may be chosen independently.

The remainder are determined by substitution into the differential equations (9). Thus it is found that when

$$\begin{aligned} k_{1s} &= \lambda_s \left[ C_{24}^* (\lambda_s^2 - C_{65}^*) + C_{25}^* C_{64}^* \right] K_s \\ &= \bar{k}_{1s} K_s \quad s = (1, 2, 3, 4, 5, 6) \end{aligned}$$

$$\bar{k}_{1s} = \lambda_s \left[ C_{24}^* (\lambda_s^2 - C_{65}^*) + C_{25}^* C_{64}^* \right]$$

and

$$\bar{k}_{2s} = \lambda_s \bar{k}_{1s}$$

$$\begin{aligned} \bar{k}_{3s} &= C_{34}^* (\lambda_s^2 - C_{21}^*) (\lambda_s^2 - C_{65}^*) + C_{35}^* C_{64}^* (\lambda_s^2 - C_{21}^*) \\ &\quad + C_{31}^* \left[ C_{24}^* (\lambda_s^2 - C_{65}^*) + C_{25}^* C_{64}^* \right] \end{aligned}$$

$$\bar{k}_{4s} = \lambda_s (\lambda_s^2 - C_{21}^*) (\lambda_s^2 - C_{65}^*)$$

$$\bar{k}_{5s} = \lambda_s C_{64}^* (\lambda_s^2 - C_{21}^*)$$

$$\bar{k}_{6s} = \lambda_s \bar{k}_{5s}$$

### (3) Boundary Condition at $y = \delta$ (Continued)

Thus the general solution of (9) is

$$Z_1 = \sum_{j=1}^6 k_{1s} K_s e^{\lambda_s y} \quad (11)$$

The stated boundary conditions as  $y \rightarrow \infty$  are that  $Z_1, Z_2, Z_3$ , remain bounded. The implication is that the coefficients of  $e^{\lambda_s y}$  must vanish for  $y \geq \delta$  when the real part of  $\lambda_s$  is positive i.e., when  $s = 4, 5, 6$ .

Since equations (11) applied at  $y = \delta$ , form a system of simultaneous linear equations for evaluating the 6  $K_s$ 's, upon solving and setting  $K_s = 0, s = 4, 5, 6$ , three homogeneous linear functionals in the  $Z_1$ 's result, which must be satisfied when  $y = \delta$ .

To obtain these functionals, let  $\bar{k}^{1j}$  be the cofactor of  $\bar{k}_{1j}$  in the  $\bar{k}_{1j}$  matrix and let  $\bar{k} = \det \bar{k}_{1j}$ . Then

$$K_j = e^{-\lambda_j \delta} \sum_{i=1}^6 \frac{\bar{k}^{1j}}{\bar{k}} Z_i(\delta) \quad j = 1, 2, 3, 4, 5, 6 \quad (12)$$

The factor  $\frac{\bar{k}^{1j}}{\bar{k}} = (\bar{k}_{1j})^{-1}$  and can be found by inverting the  $\bar{k}_{1j}$  matrix. Thus the boundary conditions when  $y = \delta$  are given by

$$\sum_{i=1}^6 (\bar{k}_{1j})^{-1} Z_i(\delta) = 0 \quad i = 4, 5, 6. \quad (13)$$

### (4) Fundamental Numerical Solutions

When  $y < \delta$ , the coefficients are variable and a numerical solution is required. In Reference 61 it is shown that the general solution of a system of linear equations can be expressed in terms of a set of fundamental solutions defined by their initial conditions. Thus, if

$$Z_1^{(j)}(0) = \delta_{1j}$$

the general solution of (8) may be written

$$Z_1 = \sum_{j=1}^6 C_j Z_1^{(j)} \quad (14)$$

where the  $C_j$  are constants to be determined.

#### (4) Fundamental Numerical Solutions (Continued)

Substitution of the initial conditions yields

$$z_1(0) = c_1 z_1^{(1)}(0) = c_1 = 0$$

$$z_3(0) = c_3 z_3^{(3)}(0) = c_3 = 0$$

$$z_5(0) = c_5 z_5^{(5)}(0) = c_5 = 0$$

Hence the general solution becomes

$$z_i = c_2 z_i^{(2)} + c_4 z_i^{(4)} + c_6 z_i^{(6)} \quad (15)$$

Let  $c_2 = 1$ . Then the problem is to determine  $c_4$  and  $c_6$  and any two of the real parameters  $\alpha$ ,  $R$ ,  $C_r$  and  $C_i$  from the conditions at  $y = \delta$ ,  $K_4 = K_5 = K_6 = 0$  i.e., at  $y = \delta$ .

$$\sum_{j=1}^6 (\bar{k}_{ij})^{-1} z_j^{(2)} + c_4 \sum_{j=1}^6 (\bar{k}_{ij})^{-1} z_j^{(4)} + c_6 \sum_{j=1}^6 (\bar{k}_{ij})^{-1} z_j^{(6)} = 0 \quad (16)$$

$$i = 4, 5, 6.$$

For convenience, let

$$K_i^* = \sum_{j=1}^6 (\bar{k}_{ij})^{-1} z_j(\delta) \quad \text{and} \quad (17)$$

$$K_i^*(p) = \sum_{j=1}^6 (\bar{k}_{ij})^{-1} z_j^{(p)}(\delta) \quad (18)$$

Then (16) becomes

$$K_i^* = K_i^{*(2)} + c_4 K_i^{*(4)} + c_6 K_i^{*(6)} = 0 \quad i = 4, 5, 6. \quad (19)$$

By setting  $K_4^* = K_5^* = 0$ , two equations can be found containing  $c_4$  and  $c_6$ . Solution of these two simultaneously yields values for  $c_4$  and  $c_6$ . These values substituted in (19) yield a value for  $K_6^*$ . Then  $\alpha$ ,  $R$ ,  $C_r$  and  $C_i$  must be adjusted so that  $K_6^* = 0$ .

#### (4) Fundamental Numerical Solutions (Continued)

For values of  $\alpha R > 45$  it is difficult to ascertain sufficiently accurate values of  $C_4$  and  $C_6$  from the fundamental solutions (which are oscillatory with high amplification). In this event a method of employing differential corrections to  $C_4$  and  $C_6$  is used. After  $C_4$  and  $C_6$  have been found approximately from equation (19)  $i = 4, 5$ , an integration is carried out with initial conditions.

$$\begin{aligned} Z_1 &= 0 & Z_4 &= C_4 \\ Z_2 &= C_2 = 1 & Z_5 &= 0 \\ Z_3 &= 0 & Z_6 &= C_6 \end{aligned} \quad (20)$$

Denote by  $C_4^{(1)}$  and  $C_6^{(1)}$ , the solution of  $K_4^* = K_5^* = 0$  and by  $Z_{i(1)}$  the particular solution based on these initial values.

The values of the linear functions  $K_i^*$  calculated from the  $Z_{i(1)}$  will be denoted by  $K_{i(1)}^*$  i.e.,

$$K_{i(1)}^* = \sum_{j=1}^6 (\bar{k}_{ij})^{-1} Z_j(\delta) = K_i^* [C_4^{(1)}, C_6^{(1)}] \quad (21)$$

If  $K_{4(1)}^*$  and  $K_{5(1)}^*$  are not exactly zero,  $C_4^{(1)}$  and  $C_6^{(1)}$  must be corrected to make them so. Because the  $K_{4(1)}^*$  and  $K_{5(1)}^*$  are functions of  $C_4$  and  $C_6$ , they may be expanded in a Taylor's Series.

$$\begin{aligned} K_i^* (C_4, C_6) &= K_i^* [C_4^{(1)}, C_6^{(1)}] + [C_4 - C_4^{(1)}] \left. \frac{\partial K_i^*}{\partial C_4} \right|_{\substack{C_4 = C_4^{(1)} \\ C_6 = C_6^{(1)}}} \\ &\quad + [C_6 - C_6^{(1)}] \left. \frac{\partial K_i^*}{\partial C_6} \right|_{\substack{C_4 = C_4^{(1)} \\ C_6 = C_6^{(1)}}} \end{aligned} \quad (22)$$

Because  $K_i^* [C_4, C_6] = 0 \quad i = 4, 5$

$$\begin{aligned} -K_{i(1)}^* &= \Delta C_4 \left. \frac{\partial K_i^*}{\partial C_4} \right|_{\substack{C_4 = C_4^{(1)} \\ C_6 = C_6^{(1)}}} + \Delta C_6 \left. \frac{\partial K_i^*}{\partial C_6} \right|_{\substack{C_4 = C_4^{(1)} \\ C_6 = C_6^{(1)}}} \quad i = 4, 5 \end{aligned} \quad (23)$$

#### (4) Fundamental Numerical Solutions (Continued)

where

$$\begin{aligned} C_4^{(2)} &= C_4^{(1)} + \Delta C_4 \\ C_6^{(2)} &= C_6^{(1)} + \Delta C_6 \end{aligned}$$

will give improved values of  $C_4$  and  $C_6$ .

The partial derivatives in (22) and (23) may be approximated by

$$\frac{\partial K_1^*}{\partial C_4} \approx \frac{K_1^* [C_4^{(1)} + \delta C_4, C_6^{(1)}] - K_1^* [C_4^{(1)}, C_6^{(1)}]}{\delta C_4}$$

(24)

$$\frac{\partial K_1^*}{\partial C_6} \approx \frac{K_1^* [C_4^{(1)}, C_6^{(1)} + \delta C_6] - K_1^* [C_4^{(1)}, C_6^{(1)}]}{\delta C_6}$$

The entire process may then be repeated until satisfactory convergence is attained.

Finally, after the  $n$ th boundary values  $K_{1(n)}^*$  have been computed and the corrections  $\Delta C_k = C_k^{(n+1)} - C_k^{(n)}$  found, a final improved estimate of  $K_6^* [C_4^{(n+1)}, C_6^{(n+1)}]$  may be obtained from its Taylor expansion.

$$K_6^* [C_4^{(n+1)}, C_6^{(n+1)}] = K_6^*(n) + \Delta C_4 \frac{\partial K_6}{\partial C_4} + \Delta C_6 \frac{\partial K_6}{\partial C_6} \quad (25)$$

#### (D) Calculations

The method described has been used to compute neutral stability curves for two series of flat plate profiles from  $M = 0$  to  $M = 5.0$ . The two series are those whose velocity and temperature profiles have been published in Reference 59. In the first series, the stagnation temperature of the air stream was taken as  $100^\circ\text{F}$ , appropriate to many wind tunnel experiments. In the second series, the freestream static temperature was taken as  $-67^\circ\text{F}$ , appropriate to high flying airplanes. In addition, some calculations have been made for  $M = 5.8$  (stagnation temperature  $225^\circ\text{F}$  and  $Eu = +.0019$ ) to compare with the data of Reference 62.

Another series of experiments was carried out at  $M = 5.8$  (Reference 62). In order to compare these results with the theoretical solutions, velocity and temperature profiles were computed for this case by the method of Reference 45.

### (E) Results and Discussion

The velocity and temperature profiles are plotted in Figure 1 and Figure 2 in nondimensional coordinates. All the profiles are for the insulated flat plate case except  $M = 5.8$ , where the Euler number was  $+0.0019$  and the stagnation temperature  $225^{\circ}\text{F}$  to match the experimental conditions in Reference 62.

A comparison between this theory and the experimental results of Reference 63 is shown in Figures 3 and 4. In Figure 3 ( $M = 1.6$ ) there is good agreement with the experimental data in both branches.

In Figure 4 ( $M = 2.2$ ) agreement between theory and experiment is good in the lower branch, but not so good in the upper branch.

The theoretical curve of Figure 4 ( $M = 2.2$ ) has been compared in Figure 5 with another theoretical curve presented in Reference 64, the agreement here is very close on both branches.

Figure 6 shows a comparison of theory with experiment at  $M = 5.8$ . The data points are from Reference 62. At this Mach number there is still good agreement in the lower branch. Again there is disagreement in the upper branch, but not in the same sense. Here the computed points are above the data points whereas at  $M = 2.2$ , Figure 4, the computed points are below the experimental points.

A comparison at  $M = 2.2$  is made between the neutral stability curves given by a numerical solution of the Lees-Lin equations (this report) and the Dunn-Lin equations. The critical Reynolds number for the Dunn-Lin solution is about 25 percent less than for the Lees-Lin. The unstable region is larger for the Dunn-Lin.

Figure 8 shows a similar comparison between the neutral curves computed by the Lees-Lin and Dunn-Lin equations when the Mach number is increased to 5. Here the difference between the critical Reynolds numbers has increased to 62 percent instead of 25 percent at  $M = 2.2$ . Both are below Demetriades data at  $M = 5.8$ .

Figure 9 shows a series of neutral curves near the critical Reynolds number in each case for Mach numbers from 0 to 5 when the freestream stagnation temperature is  $100^{\circ}\text{F}$  and the surface is an insulated flat plate. The velocity and temperature profiles used were those of Reference 59.

A similar series of neutral curves was computed and plotted in Figure 10 for the other set of profiles computed in Reference 59, those where the freestream temperature is taken as  $-67^{\circ}\text{F}$ .

These two series of neutral curves are compared in Figure 11, where critical Reynolds number  $R_{cr}$  is plotted as ordinate against Mach number  $M$  as abscissa. This comparison shows a large divergence at high Mach numbers. When the flight airstream condition is used (stream temperature  $-67^{\circ}\text{F}$ ) considerably more stability is indicated than when the wind tunnel test condition is used, stagnation temperature  $= 100^{\circ}\text{F}$ .

(F) Conclusions

To a Mach number of about 1.6, the Lees-Lin equations agree very closely with observed stability data in both upper and lower branches of the neutral stability curve. From there up to 5.8, neutral stability calculations with the Lees-Lin equations agree well with the experimental data for the lower branch of the neutral curve. The calculations do not agree with the data in the upper branch. A possible remedy for this is being studied. Up to about 1.8, the Dunn-Lin equations give a good approximation. Above that Mach number, they diverge rapidly from the Lees-Lin equations as the Mach number increases. At Mach 5, the Dunn-Lin critical Reynolds number is 62 percent below the Lees-Lin number.

CHAPTER C. CROSSFLOW STABILITY CALCULATIONS ON HIGHLY SWEPT (65° SWEEP)  
SUPERSONIC LOW DRAG BLC WING (MACH NUMBER 1.8) WITH AND  
WITHOUT COOLING

W. Byron Brown

(A) Notation

	<u>Nondimensional Quantities</u>	<u>Reference Quantities</u>
Distance normal to wing	$y$	$\delta = \text{boundary layer unit}$
Time	$t$	$\delta/Q'$
Velocity components		
Crossflow parallel to wall	$w(y) + f(y) e^{i\alpha(z-ct)}$	$Q'$
Crossflow perpendicular to wall	$v(y) + (y) e^{i\alpha(x-ct)}$	$Q'$
Density	$\rho + r(y) e^{i\alpha(x-ct)}$	$\bar{\rho}_1^*$
Pressure	$p(y) + r(y) e^{i\alpha(x-ct)}$	$\bar{p}_1^*$
Temperature	$T(y) + \theta(y) e^{i\alpha(x-ct)}$	$\bar{T}_1^*$
Viscosity coefficient	$\mu n(y) + \frac{d\mu}{dT} \theta(y) e^{i\alpha(x-ct)}$	$\bar{\mu}_1^*$
Wave number of disturbance	$\alpha$	$1/\delta$
Wave velocity of disturbance	$c$	$Q'$
Specific heat at constant pressure	$\gamma$	$C_p$
Specific heat at constant volume	$1$	$C_v$
Reynolds number	$Re = \frac{\bar{\rho}_1^* Q' \delta}{\bar{\mu}_1^*} = \sqrt{R}$	
Reynolds number	$R = \frac{\bar{\rho}_1^* Q' L_o'}{\bar{\mu}_1^*}$	
Prandtl number	$\sigma = \frac{C_p \bar{\mu}_1^*}{k^*}$	



(A) Notation (Continued)

Mach number  $M = \frac{Q'}{\sqrt{\gamma R^* T_1^*}}$

Thermal conductivity  $k = \frac{\mu(y)}{\sigma(y)} + \frac{d}{dT} \frac{\mu}{\sigma} \theta(y) e^{i\alpha(x-ct)}$

A bar (—) denotes a mean value.

The nondimensional quantities  $w, f, \theta, \pi, T, r, \theta$  are considered functions of  $y$  alone.

The quantities  $\mu, \gamma, \sigma, \rho$  are functions of  $T$  only.

For moderate Mach numbers as here,  $\gamma$  and  $\sigma$  are considered as constants equal to freestream values.

$$\delta = L_0' \cdot R^{-1/2}$$

$L_0'$  = chord measured perpendicular to the leading edge.

$Q'$  = resultant potential velocity at edge of boundary layer.

$\rho_1^*, P_1^*, T_1^*, \mu_1^*$ , etc., are dimensional values at edge of the boundary layer.

The primes (') indicate differentiation with respect to  $y$ .

(B) Introduction

It has been found by Reshotko (Reference 65) that (for Mach numbers below 2) the terms used in the Dunn-Lin equations (Reference 66) are sufficient for stability calculations of a compressible laminar boundary layer. This simplified version of the complete Lees-Lin equations (Reference 58) has been used, therefore, to compute the stability of the crossflow profiles on a highly swept (65-degree sweep) supersonic low drag BLC wing at a Mach number of 1.86 with and without cooling.

(C) Analysis

The analysis is the same as in Reference 7) except that the values of the  $C_{ij}$ 's are simpler. In this case they are as follows:

$$C_{12} = 1$$

$$C_{21} = \frac{Re}{\mu T} i\alpha (w-c)$$

(C) Analysis (Continued)

$$C_{22} = 0$$

$$C_{23} = \frac{\text{Re } \alpha w'}{\mu T}$$

$$C_{24} = \frac{\text{Re } i\alpha}{\mu \gamma}$$

$$C_{31} = -i$$

$$C_{33} = (\ln T)'$$

$$C_{34} = -i M^2 (w-c) T$$

$$C_{35} = \frac{i (w-c)}{T}$$

$$a_{44} = \frac{\text{Re}}{\mu \alpha \gamma} + M^2 i (w-c)$$

$$C_{41} = \frac{-i (\ln T)'}{a_{44}}$$

$$C_{42} = \frac{-i}{a_{44}}$$

$$C_{43} = \frac{1}{a_{44}} \left\{ - \frac{\text{Re } i\alpha (w-c)}{\mu T} + (\ln T)'' + [(\ln T)']^2 \right\}$$

$$C_{44} = \frac{1}{a_{44}} \left\{ - (\ln T)' [M^2 i (w-c)] - [M^2 i (w-c)]' \right\}$$

$$C_{45} = \frac{1}{a_{44}} \left\{ \left[ \frac{i (w-c)}{T} \right]' + (\ln T)' \left[ \frac{i (w-c)}{T} \right] \right\}$$

$$C_{46} = \frac{1}{a_{44}} \frac{i (w-c)}{T}$$

$$C_{63} = \frac{\text{Re } \sigma \alpha}{\mu} (\ln T)'$$

$$C_{64} = - \frac{\text{Re } \sigma M^2 (\gamma-1)}{\mu \gamma} i \alpha (w-c)$$

$$C_{65} = \frac{\alpha \text{Re } \sigma i (w-c)}{\mu T}$$

#### (D) Calculations

Two crossflow profiles were considered. These profiles were computed by the method described in Reference 45. The angle of sweep was 65 degrees and the local Mach number was 1.86 in both cases. The velocity profiles are shown in Figure 12 and the corresponding temperature profiles in Figure 13.

Four neutral stability curves were computed, two for each profile. Because the boundary condition at the wall is different for high and low disturbance frequencies (as explained fully in Reference 66), each condition was computed for each profile. Reference 66 shows that when the disturbance frequency is high (the usual case with a metal surface), the boundary condition at the wall is  $\theta(0) = 0$ . When the disturbance frequency is very low the condition reduces to

$$\theta'(0) + \left[ \frac{1}{k} \frac{dk}{dT} \frac{\partial T}{\partial y} \right]_{y=0} \theta(0) = 0$$

Thus in the insulated profile  $\frac{\partial T}{\partial y} = 0$  at the wall so that  $\theta' = 0$ . When the surface was cooled by radiation,  $\left[ \frac{1}{k} \frac{dk}{dT} \frac{\partial T}{\partial y} \right]_{y=0} = .08666$  in this case so that the low frequency condition was

$$\theta'(0) + .08666 \theta(0) = 0$$

For comparative purposes the Orr-Sommerfeld equation was applied to the two velocity profiles, the temperature profiles being neglected.

#### (E) Results and Discussion

The four neutral curves are shown in Figure 14, the solid curves representing the two high frequency cases and the dotted curves the low frequency cases.

Though most practical cases are close to the condition  $\theta(0) = 0$ , the other extreme (very low frequency) would not alter the results much, especially in the adiabatic case when it alters the critical Reynolds number 1.6 percent.

The compressible and the Orr-Sommerfeld solutions are compared in Figure 15. The Orr-Sommerfeld approximation is lower than the compressible one by an amount which appears to depend on the wall temperature. In Figure 16 the ratio of the critical Reynolds number computed by the Dunn-Lin compressible equation to that computed by the Orr-Sommerfeld equation is plotted against the ratio of wall to stream temperature. Over this range the results are represented by the curve

$$\frac{R_{cc}}{R_{co}} = T^{0.47}$$

### (E) Results and Discussion (Continued)

For design purposes, a few compressible solutions covering the temperature range expected should determine a curve enabling routine results to be found by the Orr-Sommerfeld equation, which can be integrated with less time and expense.

Figure 17 shows the correlation plotted in Reference 67 but suggested by Gregory (Reference 68) between a shape parameter Reynolds number  $\chi$  and a shape factor  $\eta''$ .  $\chi$  is defined as the maximum velocity of the profile multiplied by a boundary layer thickness when the velocity has decreased to 10 percent of its maximum value, divided by the kinematic viscosity  $\nu$ .  $\eta''$  is the wall value of the second derivative of the velocity profile. In our notation

$$\chi_{crit} = \bar{U}_{max} Z_{\Delta} Re_{cr}$$

and

$$\eta'' = \frac{\partial^2 \left( \frac{\bar{U}}{\bar{U}_{max}} \right)}{\partial \left( \frac{Z}{Z_{\Delta}} \right) \bigg|_{Z=0}}$$

The equation of the straight line is

$$\chi_{crit} = 58.8 + .7077 \eta'' \text{ (Reference 67).}$$

When the two points found from the compressible neutral curves (Figure 14) are plotted in Figure 17, they are found to lie quite near the correlation line determined from incompressible calculations.

CHAPTER D. INCOMPRESSIBLE CROSSFLOW STABILITY CALCULATIONS WITH VARIOUS ANGLES OF THE WAVE FRONTS WITH THE POTENTIAL FLOW DIRECTION

W. Byron Brown

(A) Notation

L	wing chord
R	flight Reynolds number = $\frac{U_o L}{\nu}$
Re	boundary layer Reynolds number = $\sqrt{R}$
$U_o$	freestream velocity component perpendicular to the wing leading edge
w	velocity component parallel to the surface in any of the given planes
y	nondimensional wall distance
$\alpha$	wave number of disturbance (always real, nondimensional)
$\epsilon$	angle between given plane and the transverse plane
$\nu$	kinematic viscosity

(B) Introduction

Stuart, in Reference 4, stated that if the plane in which a two-dimensional boundary layer profile on a swept wing is computed is shifted from a direction transverse to the main flow both ways, then a series of boundary layer profiles results, as is shown in Figure 18. Each profile will have a neutral stability curve which can be computed by integrating the Orr-Sommerfeld equation. One of these should have the lowest Reynolds number of the group.

In the present report four of the suction profiles on a swept wing close to the wing trailing edge have been computed and used, in turn, to compute four neutral stability curves. Among these four, the transverse profile has the lowest value for the critical Reynolds number.

(C) Analysis

If the dimensionless velocity normal to the potential streamline is called N and that along the potential streamline is called T, then in any other direction, obviously,

$$\frac{w}{U_o} = N \cos \epsilon - T \sin \epsilon \quad (1)$$

if  $\epsilon$  is the angle between the given plane and the transverse plane. This equation was used to compute the velocity profiles in a direction  $\epsilon$ .

(D) Calculations

Four profiles were computed by eq (1) and plotted in Figure 18. The four values of  $\epsilon$  were  $-7^\circ 40'$ ,  $0$ ,  $7^\circ 40'$  and  $15^\circ 20'$ .

Four neutral stability curves were computed by the method of Reference 6. These stability curves are shown in Figure 19.

(E) Results and Discussion

The curves of Figure 19 show that both the critical Reynolds number and the range of wave numbers in which amplification is possible depends on  $\epsilon$ , which measures the direction of the profile plane.

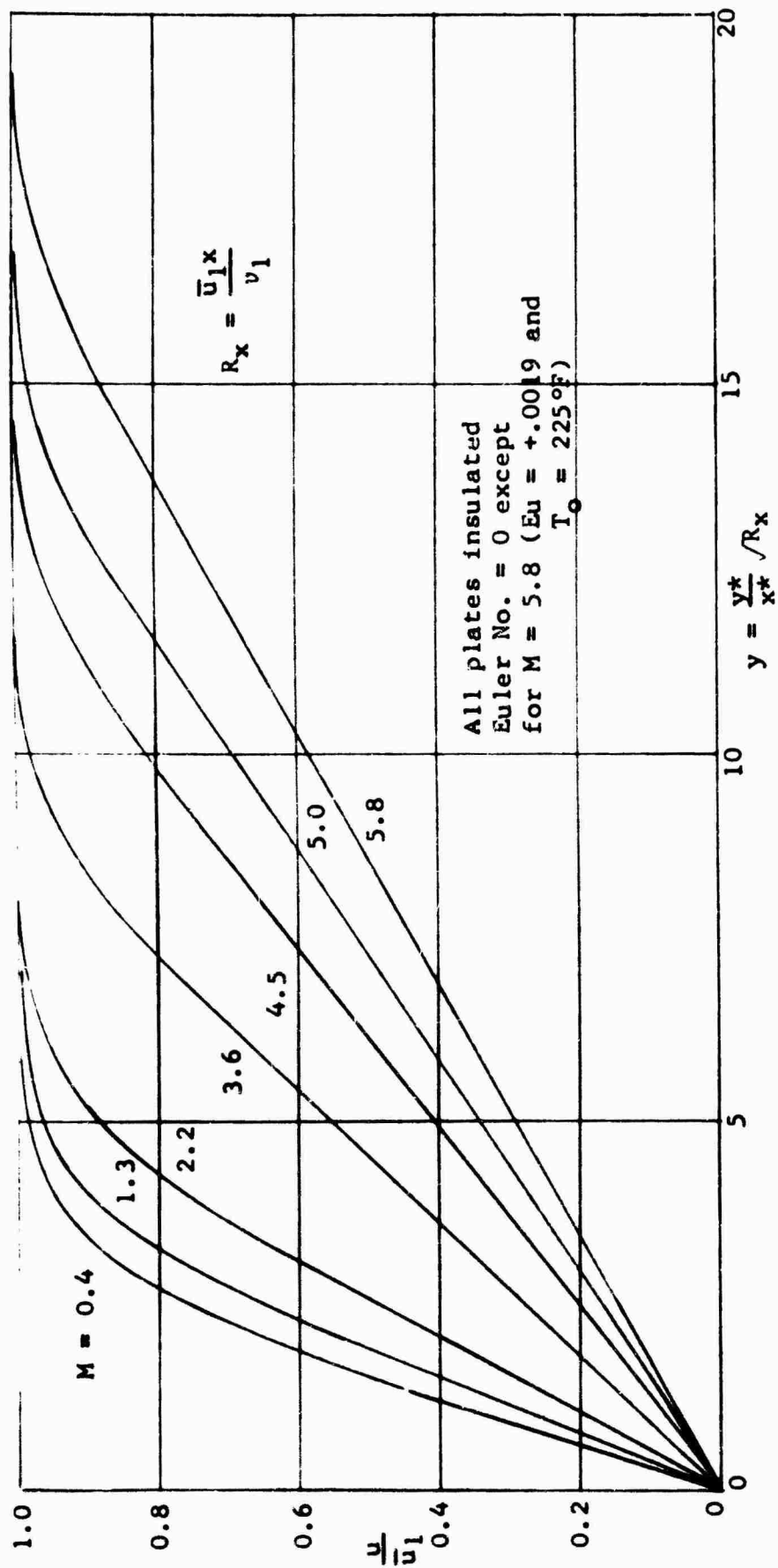
If the critical Reynolds numbers are read from the curves of Figure 20 and plotted against values of  $\epsilon$ , then Figure 20 results. The lowest point of the curve does not appear to be exactly at the transverse plane, but it is so near it that the value of  $Re$  critical for the transverse plane is not far from the minimum for any plane.

(F) Conclusions

The critical Reynolds number computed from the transverse boundary layer profile at a station close to the trailing edge of a swept laminar suction wing is within about ten percent of the lowest value for any plane profile.

# LIST OF FIGURES FOR SECTION I

<u>Figure No.</u>	<u>Figure Title</u>	<u>Page</u>
1	VELOCITY PROFILES, STAGNATION TEMPERATURE = 100°F.....	76
2	TEMPERATURE PROFILES, STAGNATION TEMPERATURE, 100°F.....	77
3	THEORETICAL AND EXPERIMENTAL NEUTRAL STABILITY CURVES AT M = 1.6.....	78
4	THEORETICAL AND EXPERIMENTAL NEUTRAL STABILITY CURVES AT M = 2.2.....	79
5	NEUTRAL STABILITY CURVE.....	80
6	THEORETICAL AND EXPERIMENTAL NEUTRAL STABILITY CURVES AT M = 5.8.....	81
7	NEUTRAL STABILITY CURVES M = 2:2 STAGNATION TEMP 100°F.....	82
8	NEUTRAL STABILITY CURVES M = 5 STAGNATION TEMP 100°F.....	83
9	NEUTRAL STABILITY CURVES FOR 100°F STAGNATION TEMP MACH NOS. 0 TO 5.....	84
10	NEUTRAL STABILITY CURVES FOR -67°F FREE STREAM TEMP MACH NOS. 0 TO 5.....	85
11	CRITICAL REYNOLDS NUMBER $R_{cr}$ VERSUS MACH NUMBER M FOR TWO TEMPERATURE CONDITIONS OF THE AIR INSULATED FLAT PLATE.....	86
12	CROSSFLOW VELOCITY PROFILES.....	87
13	CROSSFLOW TEMPERATURE PROFILES.....	88
14	NEUTRAL STABILITY CURVES FOR CROSSFLOW COMPRESSIBLE PROFILES.....	89
15	COMPARISON OF ORR-SOMMERFELD AND COMPRESSIBLE SOLUTIONS.....	90
16	CRITICAL REYNOLDS NUMBER RATIO VERSUS TEMPERATURE RATIO.....	91
17	$X_{crit}$ VERSUS $\eta''$ .....	92
18	VELOCITY PROFILES NORMAL TO THE POTENTIAL STREAMLINE AND MAKING SMALL ANGLES WITH THE NORMAL DIRECTION.....	93
19	NEUTRAL STABILITY CURVES FOR PROFILES AT VARIOUS ANGLES WITH TRANSVERSE PLANE.....	94
20	EFFECT ON THE CRITICAL REYNOLDS NUMBER OF CHANGING THE PROFILE PLANE.....	95



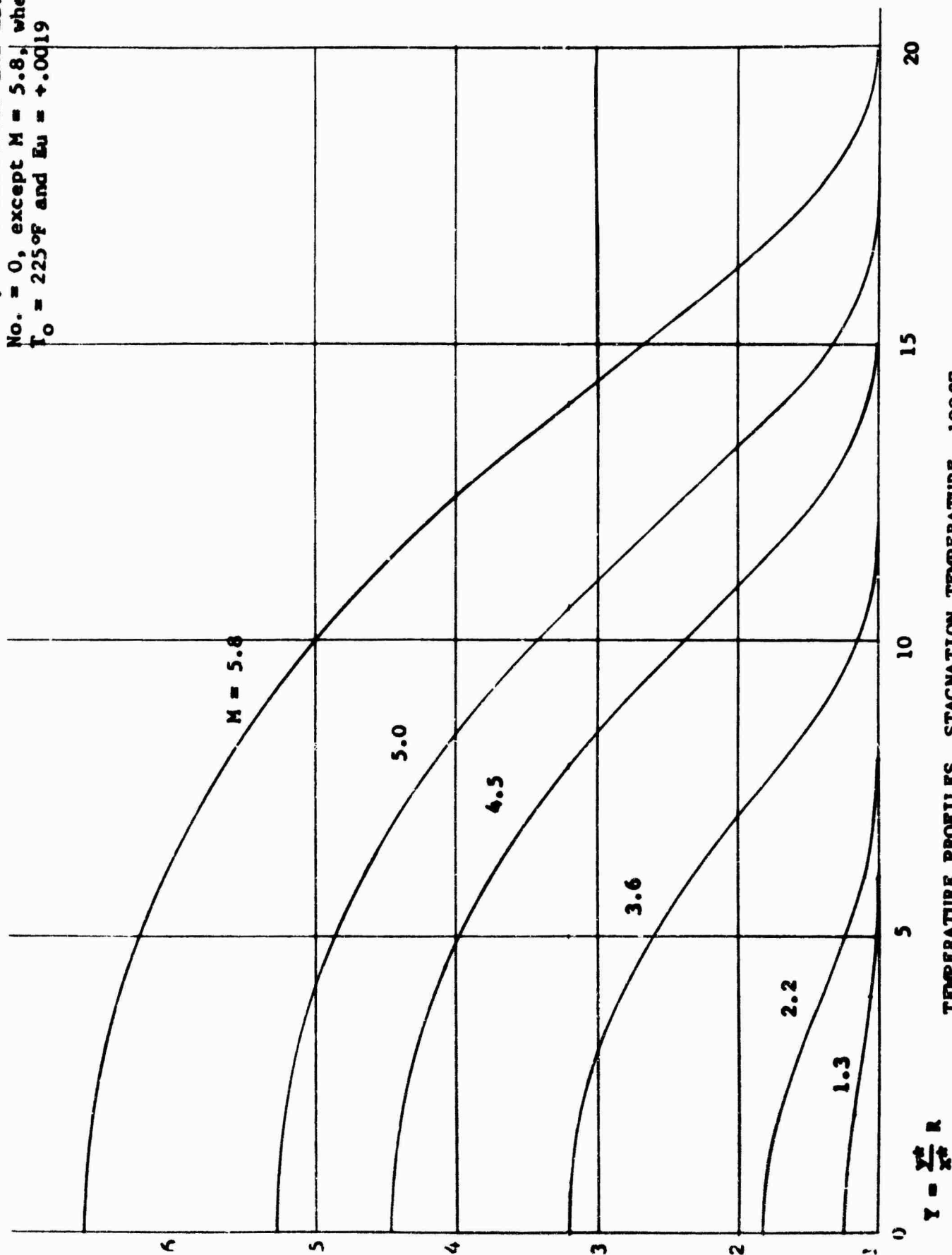
VELOCITY PROFILES, STAGNATION TEMPERATURE =  $100^\circ\text{F}$

FIGURE 1



$$R = \sqrt{\frac{\bar{U}_1 \kappa}{v_1}}$$

All plates insulated and Euler No. = 0, except  $M = 5.8$ , where  $T_0 = 225^\circ\text{F}$  and  $Eu = +0.0019$



TEMPERATURE PROFILES, STAGNATION TEMPERATURE,  $100^\circ\text{F}$   
FIGURE 2

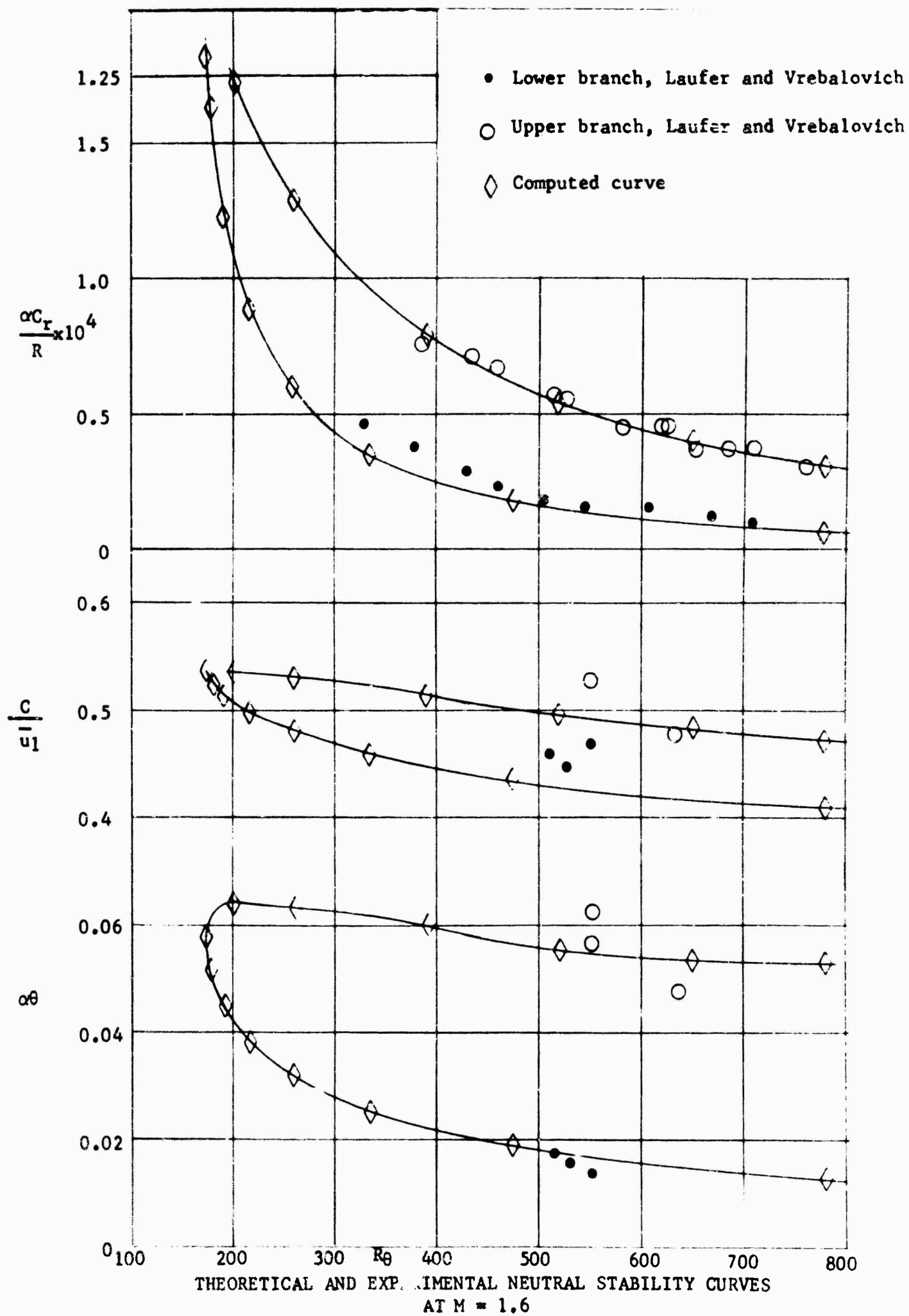
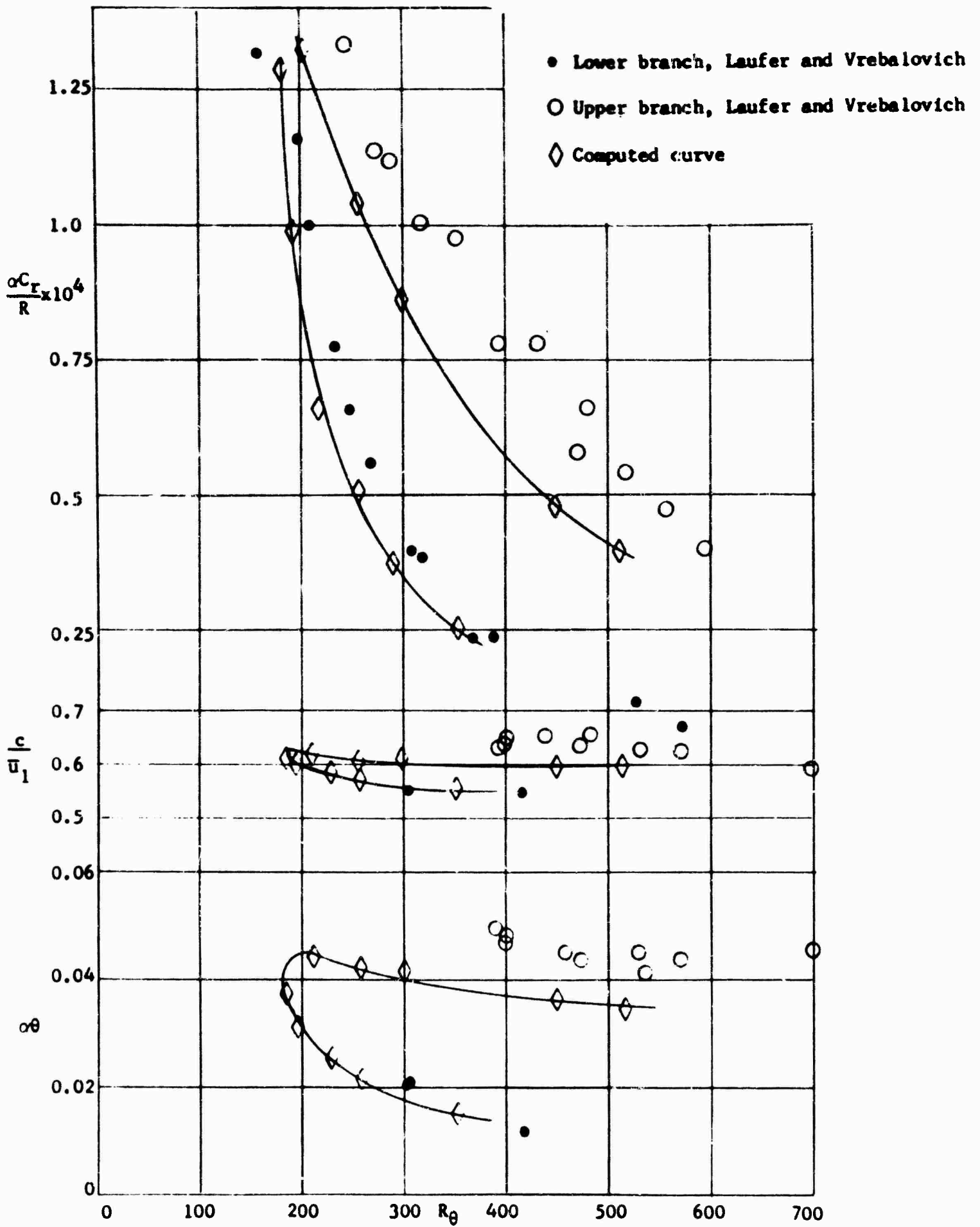


FIGURE 3



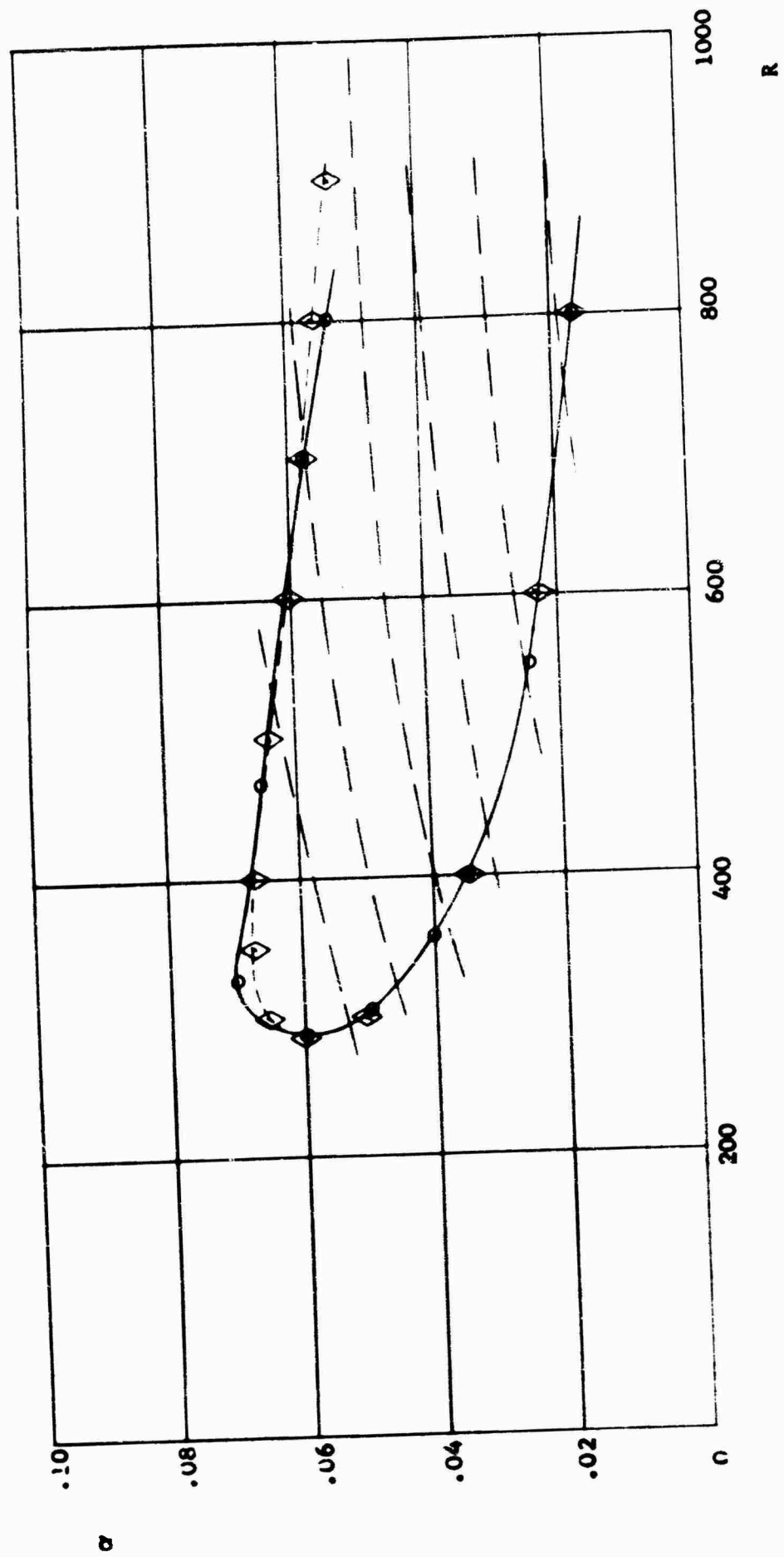
THEORETICAL AND EXPERIMENTAL NEUTRAL STABILITY CURVES AT  
 $M = 2.2$

FIGURE 4

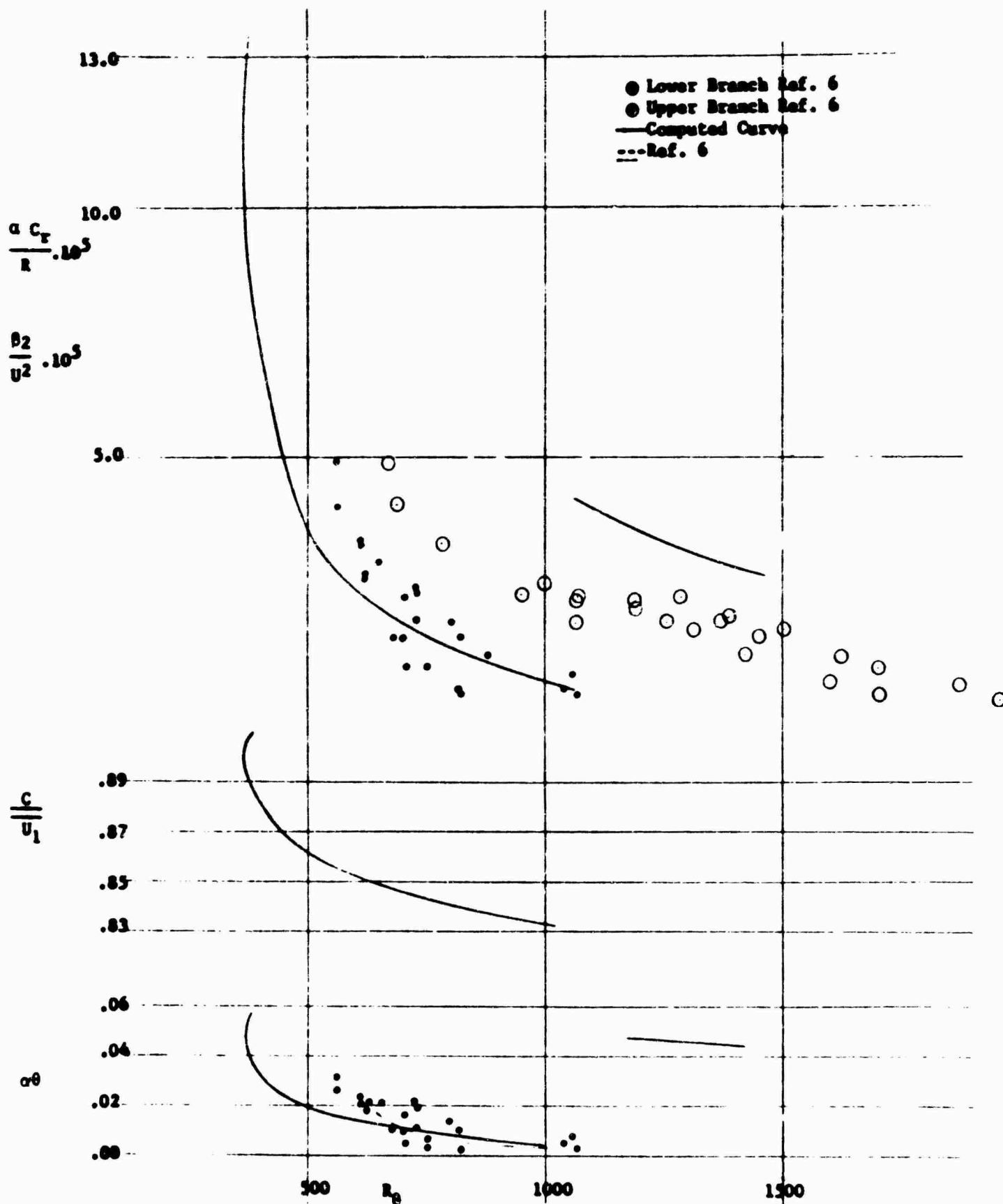
$M = 2.2$

$\theta = .64244$

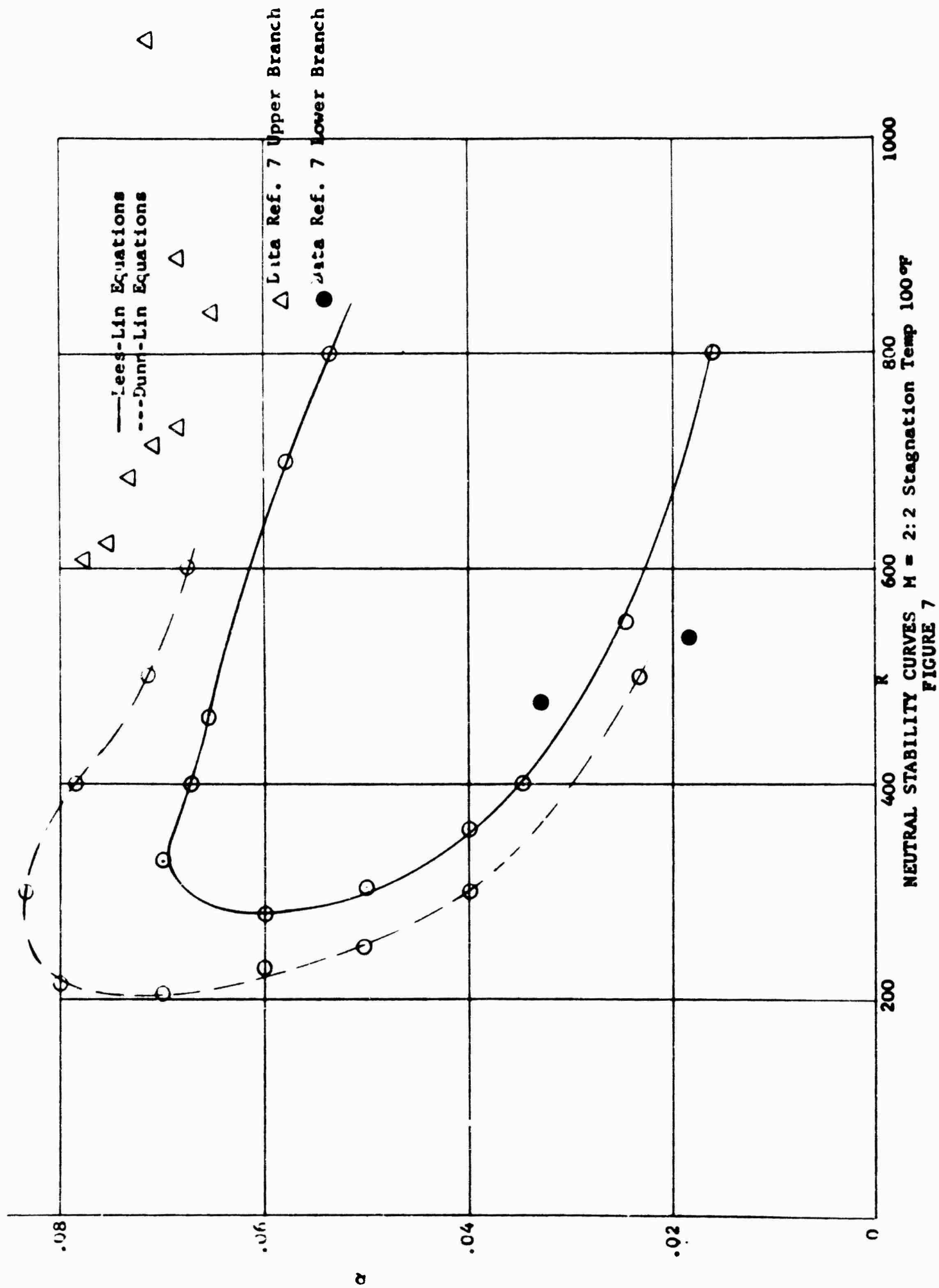
$\circ$  —  $\circ$  Mr. Brown  
 $\diamond$  —  $\diamond$  Dr. Mack

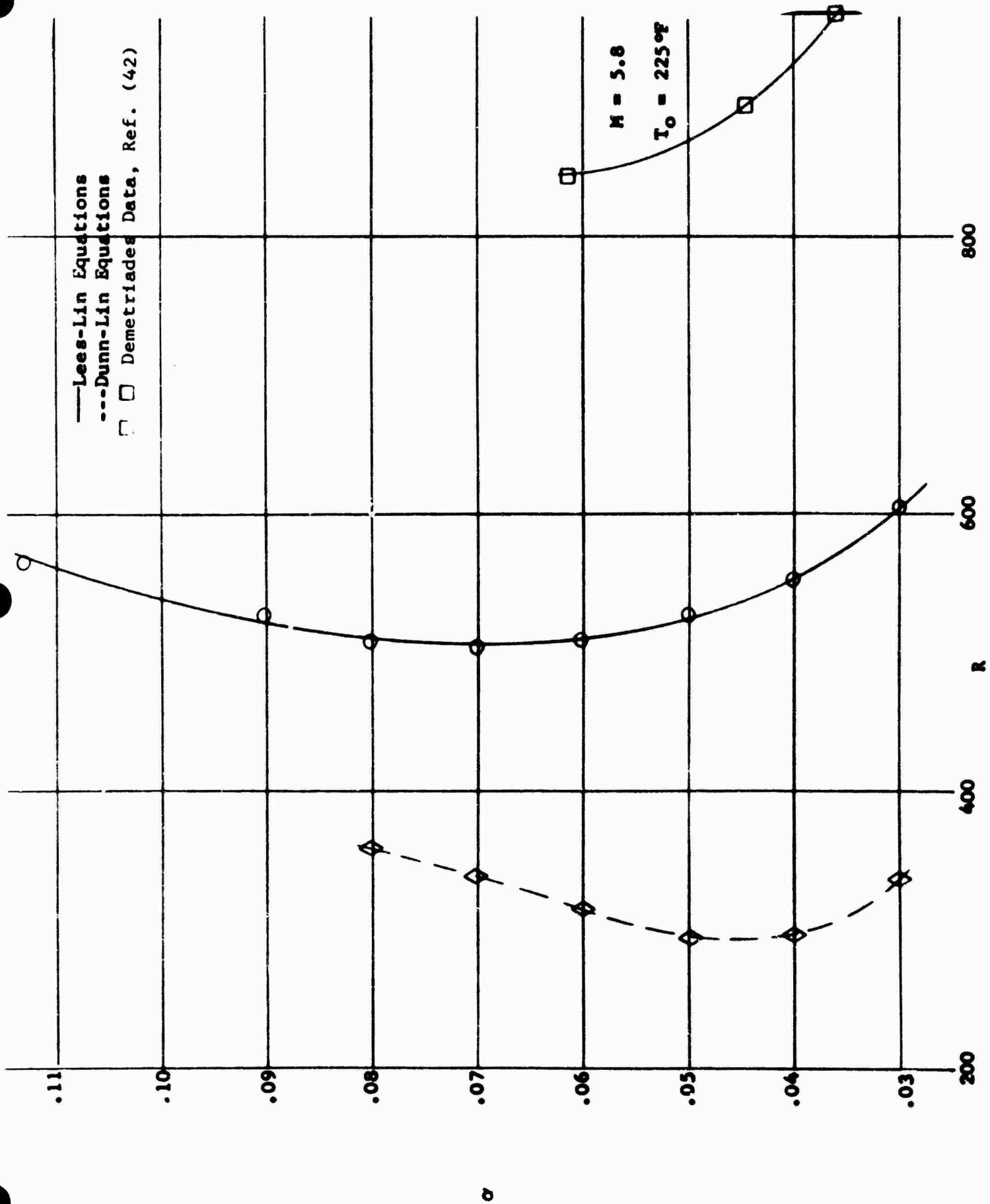


NEUTRAL STABILITY CURVE  
FIGURE 5



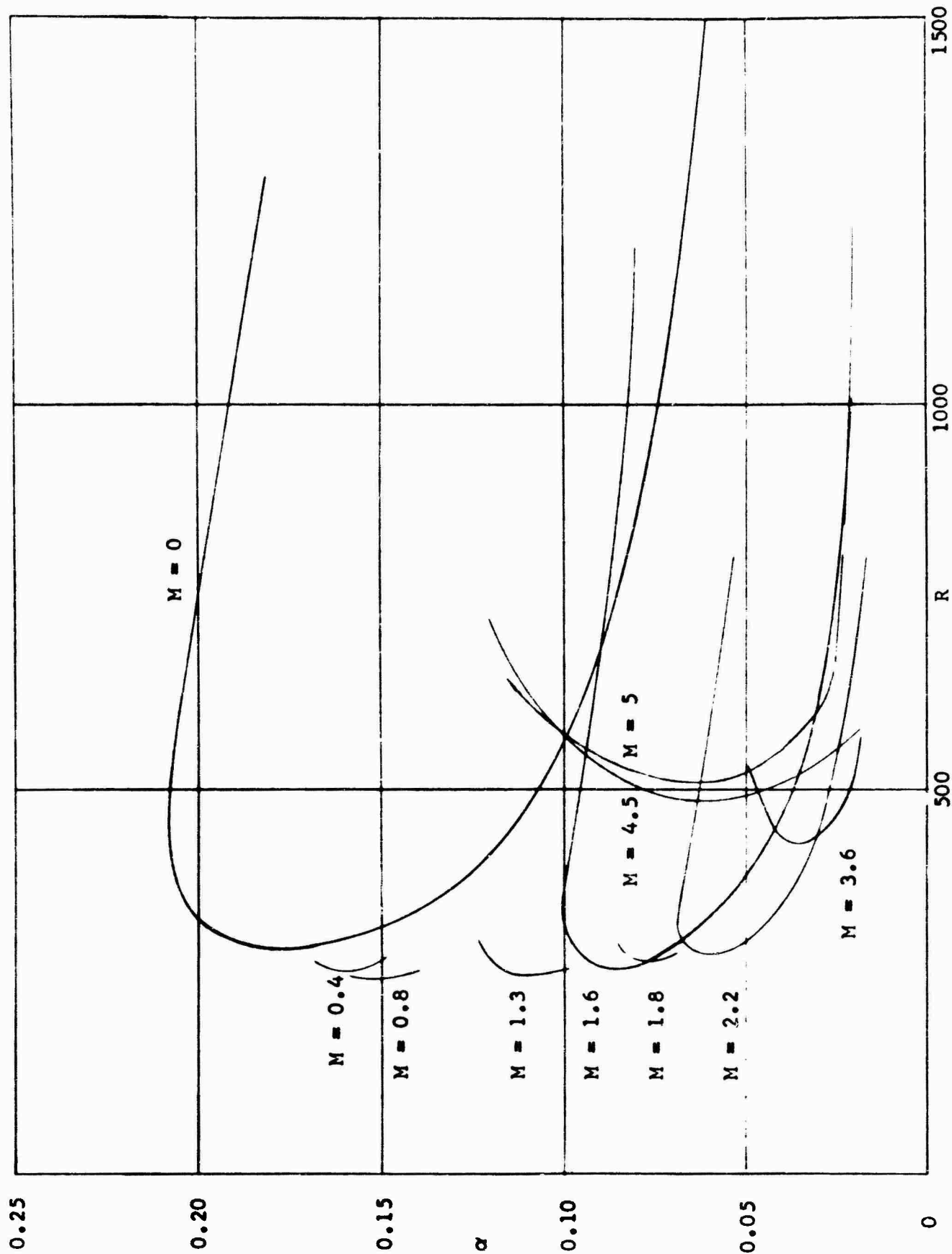
THEORETICAL AND EXPERIMENTAL NEUTRAL STABILITY CURVES AT  $M = 5.8$   
 FIGURE 6





NEUTRAL STABILITY CURVES  $M = 5$  STAGNATION TEMP.  $100^\circ\text{F}$

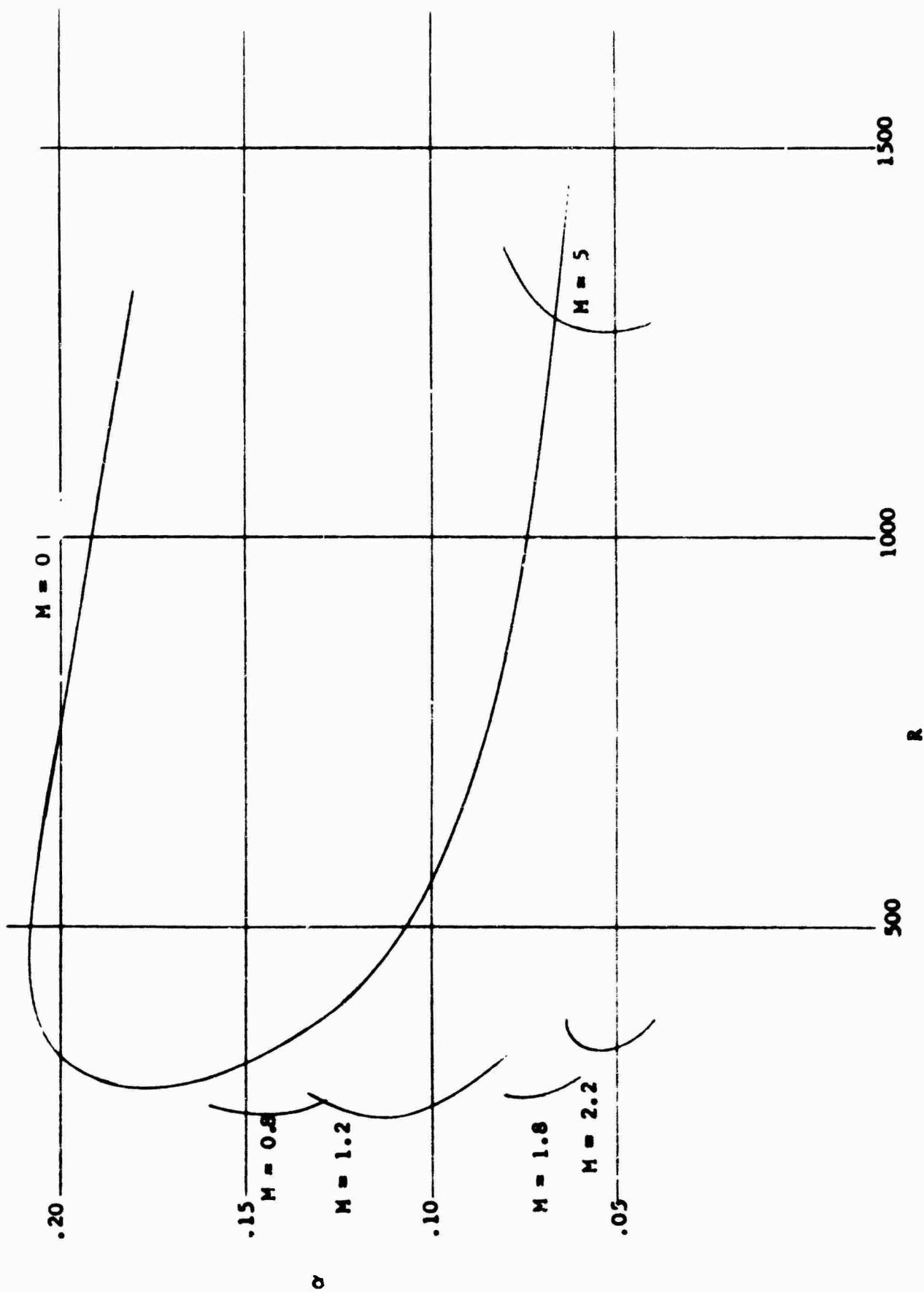
FIGURE 8



NEUTRAL STABILITY CURVES FOR 100°F STAGNATION TEMPERATURE, MACH NOS. 0 TO 5

FIGURE 9





NEUTRAL STABILITY CURVES FOR  $-67^{\circ}\text{F}$  FREE STREAM TEMPERATURE MACH NOS 0 to 5

FIGURE 10

X Stagnation Temperature = 100°F  
 O Stream Temperature = -67°F

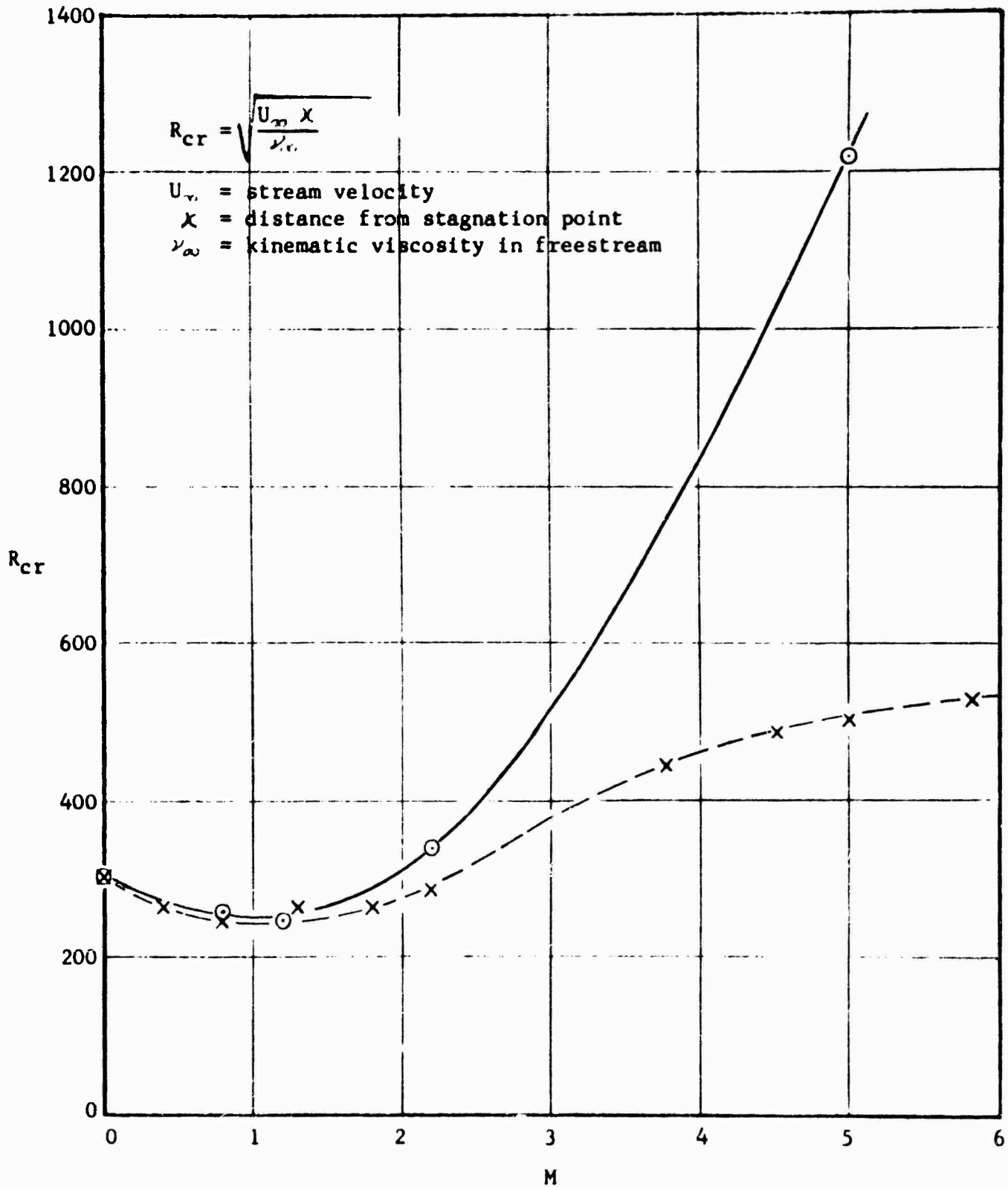


FIGURE 11  
 CRITICAL REYNOLDS NUMBER  $R_{cr}$  VERSUS MACH NUMBER  $M$   
 FOR TWO TEMPERATURE CONDITIONS OF THE AIR  
 INSULATED FLAT PLATE

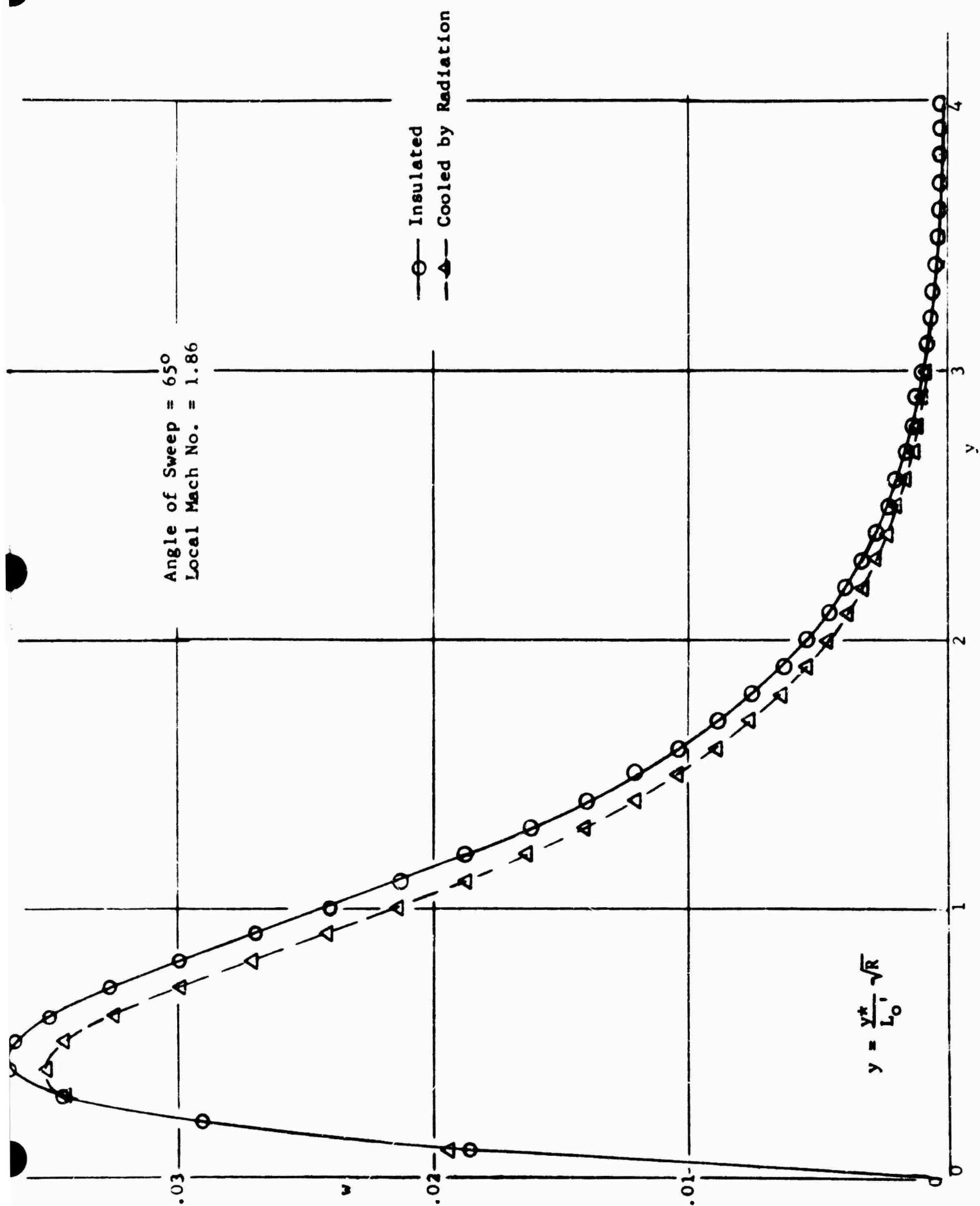


FIGURE 12  
CROSSFLOW VELOCITY PROFILES

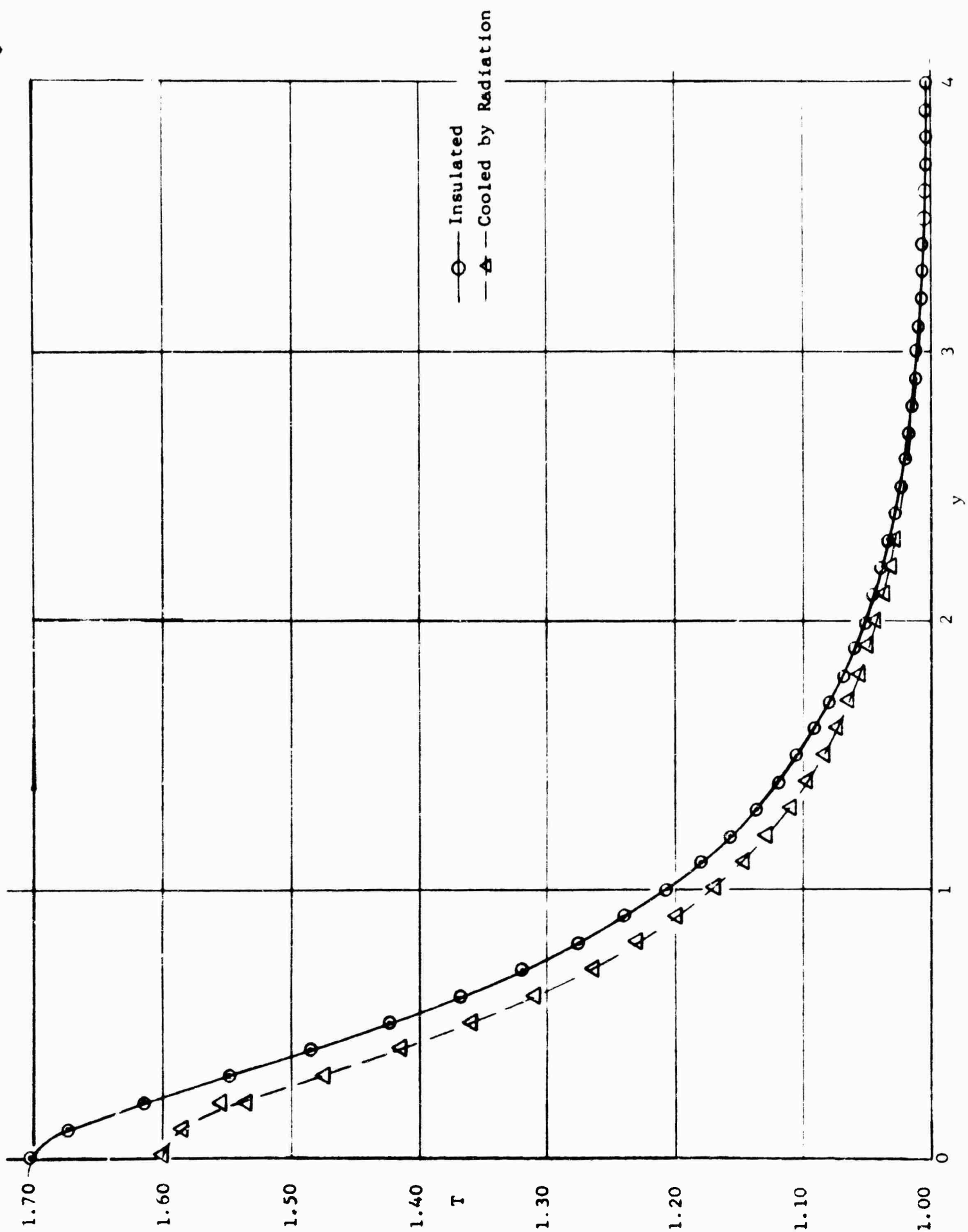


FIGURE 13  
CROSSFLOW TEMPERATURE PROFILES

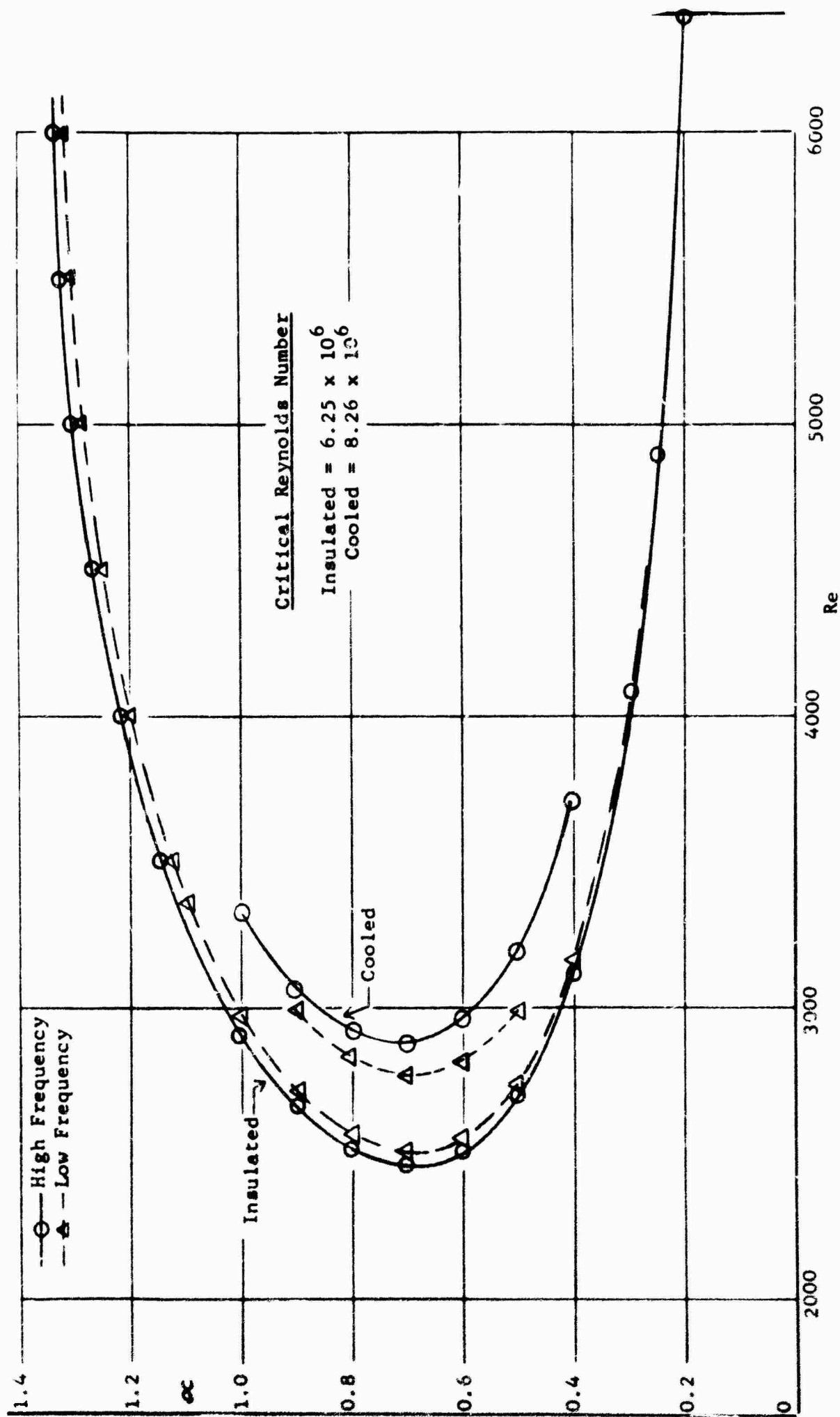


FIGURE 14  
NEUTRAL STABILITY CURVES FOR CROSSFLOW COMPRESSIBLE PROFILES

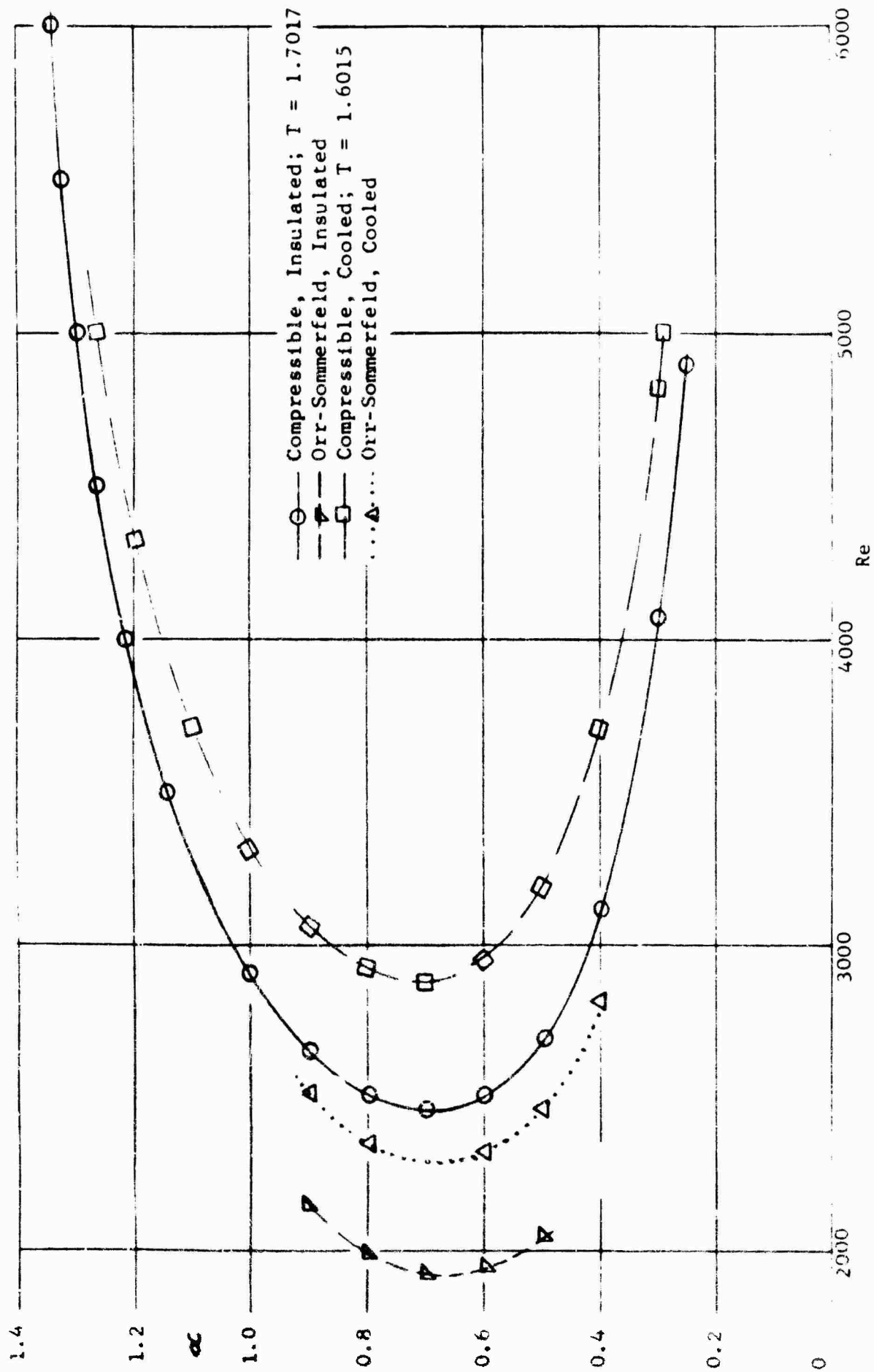


FIGURE 15

COMPARISON OF ORR-SOMMERFELD AND COMPRESSIBLE SOLUTIONS

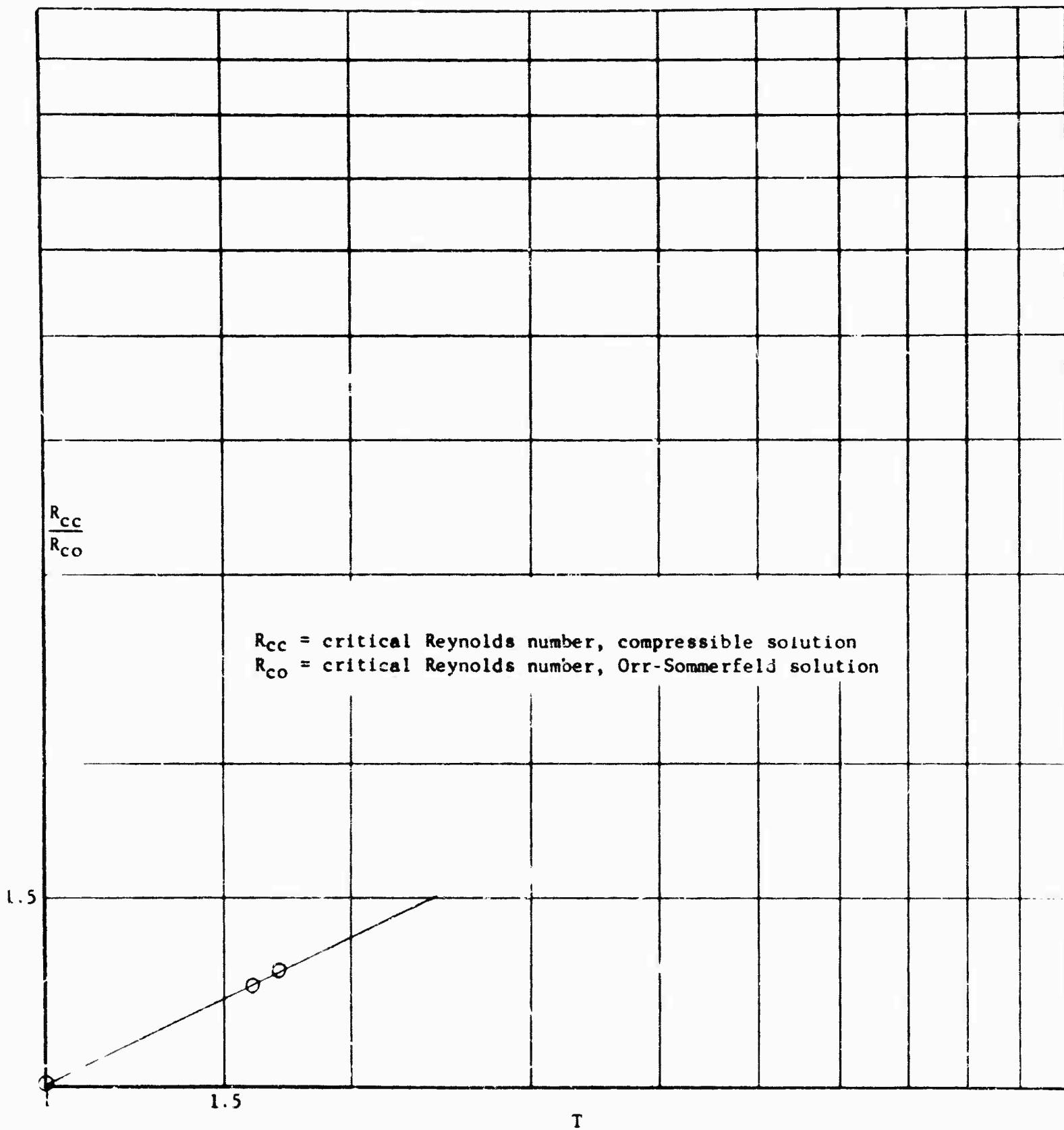


FIGURE 16

CRITICAL REYNOLDS NUMBER RATIO VERSUS TEMPERATURE RATIO

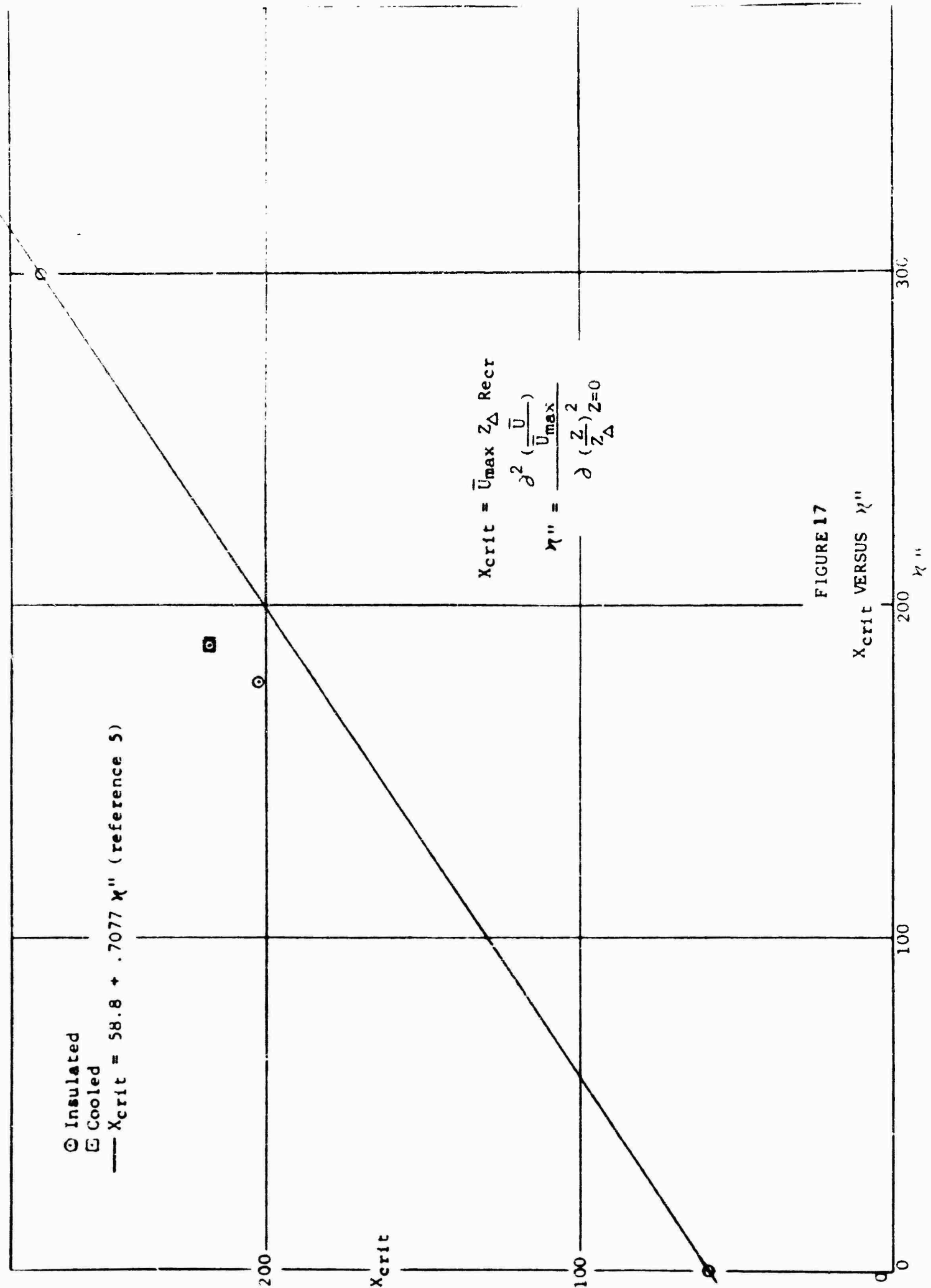
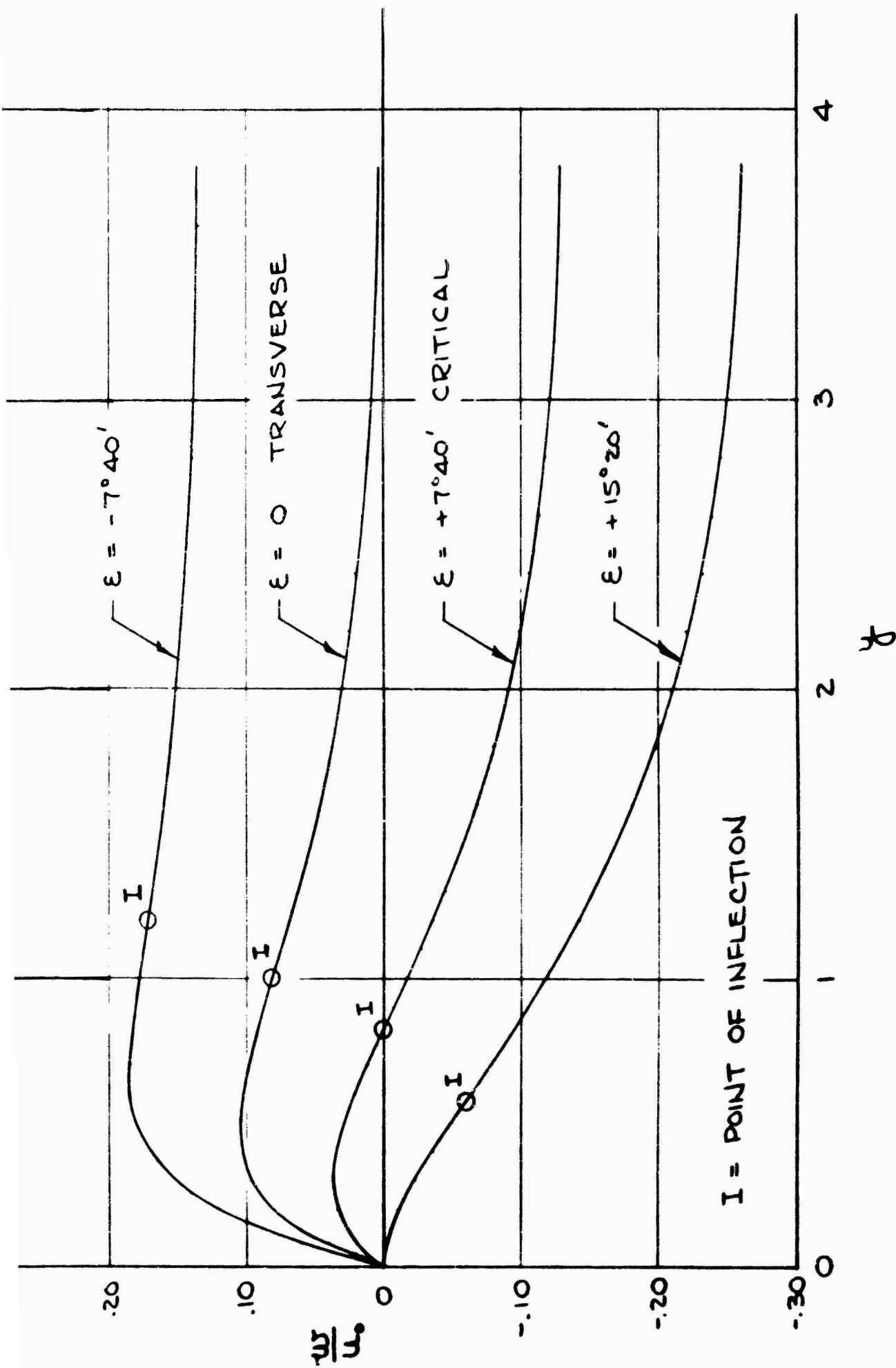
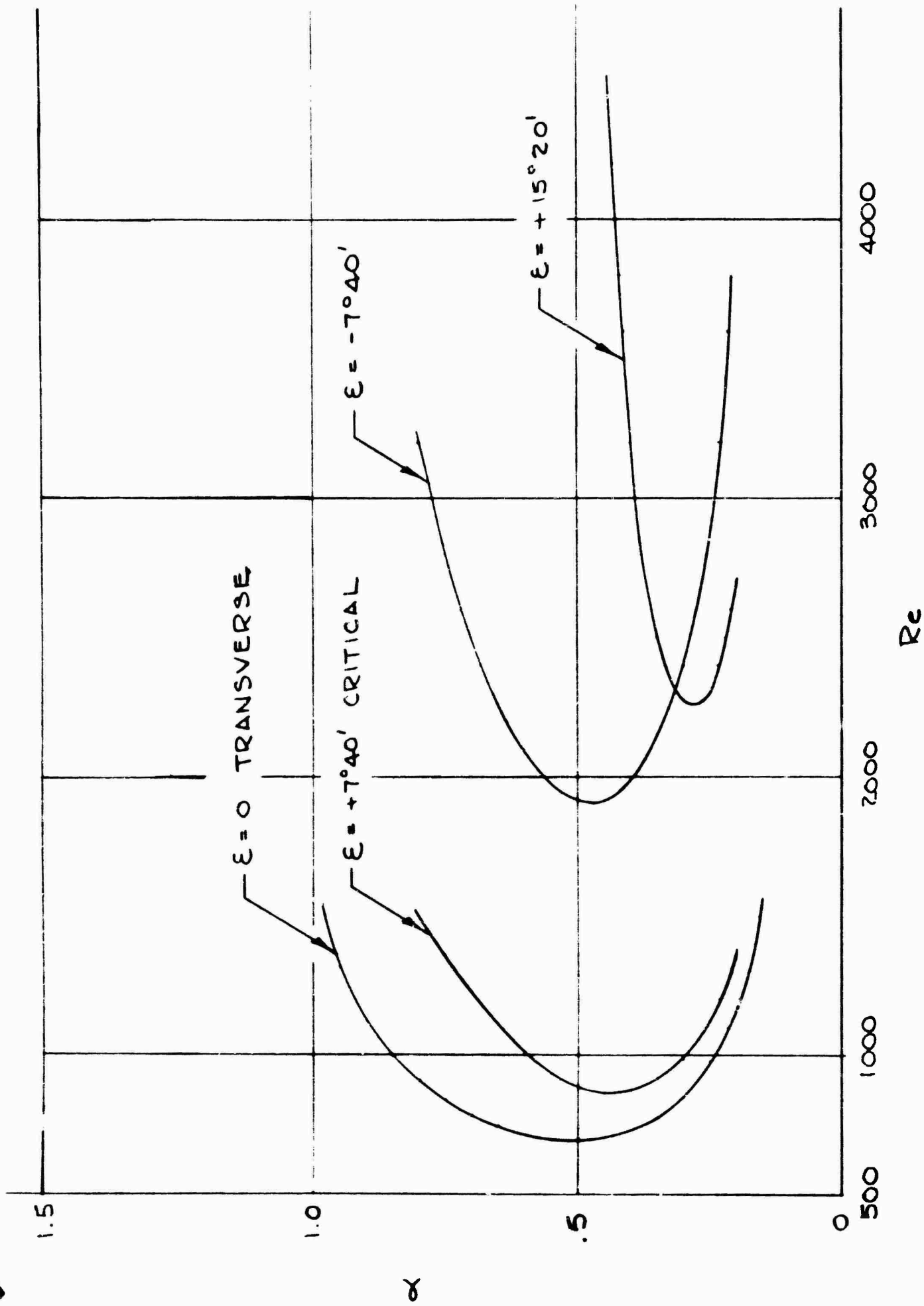


FIGURE 17  
 $X_{crit}$  VERSUS  $\eta''$



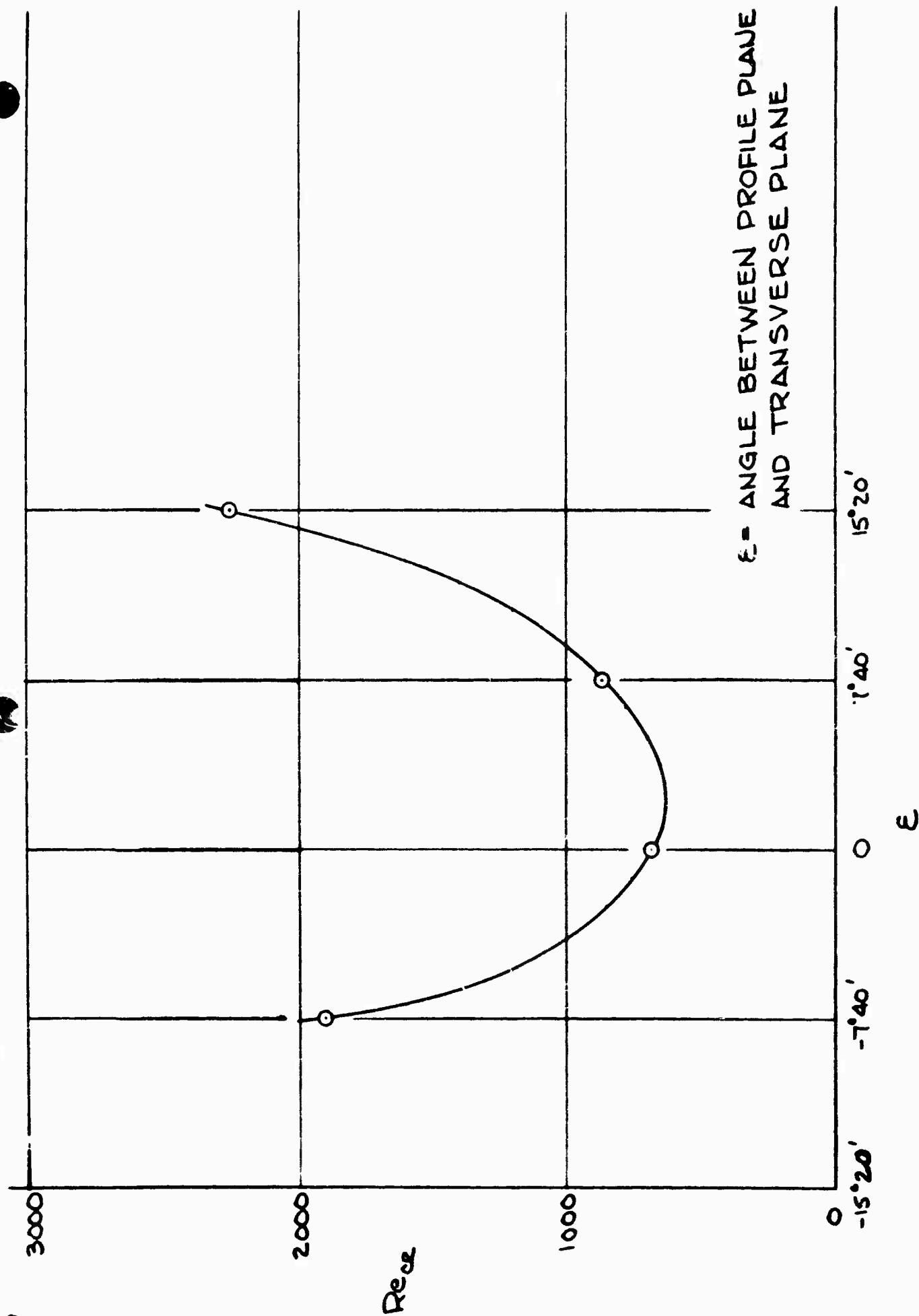


VELOCITY PROFILES NORMAL TO THE POTENTIAL STREAMLINE  
AND MAKING SMALL ANGLES WITH THE NORMAL DIRECTION  
FIGURE 18



NEUTRAL STABILITY CURVES FOR PROFILES AT VARIOUS ANGLES WITH TRANSVERSE PLANE

FIGURE 19



$\epsilon$  - ANGLE BETWEEN PROFILE PLANE  
AND TRANSVERSE PLANE

EFFECT ON THE CRITICAL REYNOLDS NUMBER  
OF CHANGING THE PROFILE PLANE

FIGURE 20

SECTION II PART 1  
EXPERIMENTAL AERODYNAMIC INVESTIGATIONS  
AT SUBSONIC SPEEDS

SECTION II PART 1

CHAPTER A. EXPERIMENTAL INVESTIGATION AND THEORETICAL ANALYSIS OF LAMINAR BOUNDARY LAYER SUCTION ON A 30° SWEEP, 12-PERCENT-THICK WING IN THE NASA AMES 12-FOOT PRESSURE WIND TUNNEL

L. W. Gross  
J. W. Bacon, Jr.  
V. L. Tucker

(A) Acknowledgements

The support of the NASA Ames Research Center during the experiments is greatly appreciated. The authors are indebted, in particular, to D. Gault, Ames project aerodynamicist, and to the staff of the Ames 12-foot tunnel. In addition, the authors express their appreciation for the help of B. H. Carmichael, formerly with Norair, during the experiments at Ames.

(B) Summary

Low drag boundary layer suction experiments were conducted at high Reynolds numbers in the Ames 12-foot pressure tunnel on the Norair 30° swept, 12-percent-thick, symmetrical laminar suction wing at  $\alpha = 0, \pm 1, \pm 1.5$  and  $-2^\circ$  angles of attack. At five atmospheres tunnel pressure full chord laminar flow was maintained up to a wing chord Reynolds number  $R_c = 29 \times 10^6$  within an angle of attack range of  $\alpha = \pm 1^\circ$ , with a minimum equivalent total drag coefficient at  $R_c = 27 \times 10^6$  of  $C_{D_{t_{min}}} = .00097$  for both wing surfaces (including equivalent suction drag) and a corresponding optimum suction quantity coefficient  $C_{Q_{opt}} = .00070$ . At  $\alpha = \pm 1.5^\circ$  full chord laminar flow was maintained up to  $R_c = 22 \times 10^6$  and  $24 \times 10^6$ , respectively.

With increasing wing chord Reynolds numbers higher values of the nondimensional suction quantity  $C_Q \sqrt{R_c}$  were required to maintain the boundary layer sufficiently stable under the crossflow conditions due to sweep. As a result, the profile drag decreased with Reynolds number at a considerably slower rate than the laminar friction drag of a flat plate.

With increasing wing chord Reynolds numbers suction had to be extended further forward toward the leading edge, and increasing local suction rates  $(v_o/U_\infty) \sqrt{R_c}$  (for equivalent area suction) were then required over the wing chord, particularly in the leading edge region.

Calculation of the boundary layer development for several test points at angles of attack  $\alpha = 1^\circ, 0^\circ, +1^\circ$  indicate that the laminar boundary layer on a swept laminar suction wing is affected by both the stability of the tangential flow and the crossflow in the boundary layer. It appears that the crossflow stability limit Reynolds number cannot be exceeded as much without transition when the tangential flow is less stable, and vice versa. At  $\alpha = 0^\circ$  and  $R_c = 23 \times 10^6$  the minimum stability limit

(B) Summary (Continued)

Reynolds number for the crossflow was exceeded by approximately 80 percent over a large percentage of the wing chord.

Premature transition, as observed at the higher Reynolds numbers, was probably caused (1) by the wind tunnel disturbance level (due to turbulence and noise) and (2) by the fact that most of the suction slots and suction holes were too wide for the high Reynolds number tests since the model was originally designed for much lower wing chord Reynolds numbers. The same fact probably was responsible for the frequently observed loss of full chord laminar flow with over-suction at the higher wing chord Reynolds numbers. At lower Reynolds numbers oversuction did not cause premature transition.

(C) Notation

b            average span of test region (measured normal to the free-stream direction) (ft)

c            model chord (measured in the freestream direction) (ft.)

$C_D$         =  $\frac{D}{q_\infty S}$ ; coefficient of drag, based on body wetted area S.

$C_{D_s}$        =  $\sum_{\text{all chambers}} C_{Qa} (1 - C_{p_{ga}})$ ; coefficient of drag due to suction power required to accelerate the suction air to undisturbed velocity and pressure without losses

$C_{D_t}$        =  $C_{D_s} + C_{D_w}$ ; coefficient of equivalent total drag

$C_{D_{t_{\min}}}$    minimum equivalent total drag coefficient

$C_{D_w}$        wake drag coefficient

$C_f$         laminar flat plate friction coefficient

$C_p$         =  $\frac{p - p_\infty}{q_\infty}$ ; pressure coefficient with respect to ambient static pressure  $p_\infty$

$C_{p_{ga}}$        =  $\frac{p_a - p_\infty}{q_\infty}$ ; pressure coefficient of individual suction chamber with respect to ambient static pressure  $p_\infty$

$C_{Qa}$        =  $\frac{Q_a}{U_\infty S}$ ; suction coefficient of individual suction based on body wetted area S

(C) Notation (Continued)

$C_{Qopt}$	optimum total suction coefficient corresponding to minimum equivalent total drag
$C_{Qt}$	$= \sum_{\text{all chambers}} C_{Qa}$ ; total suction coefficient
$D$	drag (lb.)
$H$	$= \frac{\delta^*}{\theta}$ ; boundary layer shape parameter
$\bar{H}$	average boundary layer shape parameter between the value at the wing trailing edge and the value at infinity
$H_{TE}$	boundary layer shape parameter at the wing trailing edge
$p$	static pressure (lb/ft <sup>2</sup> )
$p_a$	static pressure in individual suction chamber (lb/ft <sup>2</sup> )
$p_{\infty}$	undisturbed freestream static pressure (lb/ft <sup>2</sup> )
$q_{\infty}$	$= \frac{1}{2} \rho_{\infty} U_{\infty}^2$ undisturbed freestream dynamic pressure (lb/ft <sup>2</sup> )
$Q_a$	suction quantity of individual suction chamber (ft <sup>3</sup> /sec)
$r_h$	radius of metering hole (ft.)
$R_c$	$= \frac{\rho U_{\infty} c}{\mu}$ ; Reynolds number based on model chord
$R_h$	$= \frac{\rho \bar{u}_h r_h}{\mu}$ ; Reynolds number of suction flow metering hole
$R_s$	$= \frac{\rho \bar{u}_s \Delta/2}{\mu}$ ; Reynolds number of suction slot
$R_{SL}$	minimum crossflow Reynolds number below which all boundary layer disturbances are damped
$R_{0.1}$	$= \frac{\rho w_{max} y_{w=0.1} w_{max}}{\mu}$ ; crossflow Reynolds number
$R_{\theta}$	$= \frac{\rho U \theta}{\mu}$ ; Reynolds number based on boundary layer momentum thickness

(C) Notation (Continued)

s	distance along airfoil surface (ft.)
S	= b x c; area of test region (ft <sup>2</sup> )
u	velocity in boundary layer (at height y) tangential to the streamline at the outer edge of the boundary layer (ft/sec)
$\bar{u}_h$	average velocity through suction flow metering hole (ft/sec)
$\bar{u}_s$	average velocity through suction slot (ft/sec)
U	velocity at outer edge of boundary layer (ft/sec)
$U_{TE}$	potential flow velocity at the wing trailing edge (ft/sec)
$U_\infty$	undisturbed freestream velocity (ft/sec)
$v_o$	suction velocity for equivalent area suction (ft/sec)
$v_o^*$	= $\frac{v_o}{U_\infty} \sqrt{R_c}$ ; nondimensional suction velocity for equivalent area suction
w	crossflow velocity in boundary layer (at height y) normal to the streamline at the outer edge of the boundary layer (ft/sec)
$w_{max}$	maximum crossflow velocity (ft/sec)
x	distance along airfoil chord line (ft.)
y	distance normal to the airfoil surface (ft.)
$\alpha$	angle of attack
$\delta$	boundary layer thickness (ft.)
$\delta^*$	= $\int_0^\delta (1 - \frac{u}{U}) dy$ ; boundary layer displacement thickness (ft.)
$\delta_{TE}^*$	boundary layer displacement thickness at the wing trailing edge (ft.)
$\Delta$	slot width measured normal to the wing element lines (ft.)
$\theta$	= $\int_0^\delta \frac{u}{U} (1 - \frac{u}{U}) dy$ ; boundary layer momentum thickness (ft.)



(C) Notation (Continued)

$\delta_{TE}$	boundary layer momentum thickness at the wing trailing edge (ft.)
$\delta_{\infty}$	wake momentum thickness far behind the model (ft.)
$\mu$	absolute viscosity (lb-sec/ft <sup>2</sup> )
$\rho$	density (lb-sec <sup>2</sup> /ft <sup>4</sup> )

(D) Introduction

On a swept laminar suction wing spanwise pressure gradients deflect the boundary layer air, which has lost part of its energy, toward the regions of low static pressure. As a result, the flow path of the boundary layer particles on a swept laminar suction wing differs from the potential flow streamline, and a boundary layer crossflow develops in the direction normal to the potential flow streamline. The boundary layer crossflow profiles in this direction show inflection points and are thus dynamically highly unstable against external disturbances at high wing chord Reynolds numbers. The boundary layer crossflow becomes unstable beyond the crossflow stability limit Reynolds number (Reference 6), and the question then arises whether laminar flow can be maintained by means of boundary layer suction through discrete slots up to high wing chord Reynolds numbers.

Full chord laminar flow was maintained on a 30° swept 12-percent-thick symmetrical laminar suction wing by means of suction through many fine slots up to  $R_c = 13 \times 10^6$  in the Michigan 5- by 7-foot tunnel (References 69 and 70) and in the Norair 7- by 10-foot tunnel. According to theory, full length laminar flow should have been feasible up to higher wing chord Reynolds numbers

with somewhat larger nondimensional suction velocities  $v_o^* = \frac{v_o}{U_{\infty}} \sqrt{R_c}$ , particularly in the front part of the wing, provided the external turbulence was further reduced.

The purpose of the present experiments is the verification of full chord laminar flow on the 30° swept 12-percent-thick symmetrical low drag suction wing of Reference 2 at further increased Reynolds numbers in the Ames 12-foot pressure tunnel.

In order to correlate the actual crossflow Reynolds number of the tests on the 30-degree swept laminar suction wing with the theoretical stability limit Reynolds number for the boundary layer crossflow (Reference 6), the boundary layer development over the model was calculated at several test points by the method of Reference 45. The results of these calculations are presented in the second part of this report.

The model used in the wind tunnel experiments was designed for operation at a length Reynolds number  $R_c = 10^7$ . During the experiments, length

#### (D) Introduction (Continued)

Reynolds numbers of  $28 \times 10^6$  were attained with full chord laminar flow. In order to ascertain the effects of operating so far from the design point, calculations were made to determine the inflow of each slot near the trailing edge at the highest length Reynolds numbers attained. The results of these calculations are also included in this report.

#### (E) Experimental Investigation

##### (1) Experimental Setup

Figure 1 shows the installation of the model in the NASA Ames 12-foot pressure tunnel. The model, of seven-foot chord and seven-foot span, was mounted between endplates and was supported by struts extending from the endplates to the wind tunnel floor and ceiling. Two-dimensional flow along the wing span was maintained by shaping the inner walls of the endplates according to the undisturbed streamlines around an infinitely long yawing wing of the same cross section and sweep, working in infinite flow at  $\alpha = 0^\circ$ .

Figure 2 and Tables I and II give the cross section of the wing with details of the suction skin and chambers. The suction air passed through ninety-three fine slots of 0.004 to 0.005-inch width (located from 0.005 c to 0.97 c) into small spanwise grooves and holes, located underneath the slots, into various suction chambers (Figure 2). The slots were cut with a diamond slitting saw into a 0.030-inch-thick outer skin which was bonded onto a 0.25-inch-thick continuous inner skin. In order to be able to adjust the suction distribution in the front part of the wing within a wide range for various angles of attack and wing chord Reynolds numbers, individual suction chambers were provided for the first five slots, located from 0.005 c to 0.13 c. The remaining eighty-eight slots were connected to twelve suction chambers. From the various chambers, the suction air was ducted through individual flow measuring nozzles and tubes, passing through the lower support strut, into a common suction box (Figure 1) and through a long pipe and a sonic throat into the atmosphere. Since the experiments were conducted at five atmospheres tunnel pressure, suction could be operated by bleeding the suction air into the atmosphere. The total rate of suction was controlled by remotely varying the cross section of the sonic throat. The individual suction quantities of the various suction chambers were remotely controlled by means of adjustable needle valves located at the inlet to the common suction box.

In order to maintain uniform flow conditions in the test area with fully developed spanwise flow in the boundary layer, auxiliary suction slots and chambers were added to both sides of the test area. The length of the auxiliary slots on the upstream side of the wing was chosen according to an analysis by Raetz (Reference 45) of the spanwise extent over which the boundary layer crossflow is not yet fully developed. The three suction tubes from each measuring chamber and its two corresponding auxiliary chambers were connected upstream of the common suction box in such a manner that the spanwise suction rate in the area of the auxiliary chambers was the same as in the measuring region.

## (1) Experimental Setup (Continued)

A surface waviness of 1/3000 inch per inch wave length or less was maintained. The test surface was sanded with No. 600 grade sandpaper and polished with silicone wax. Dust was removed with a "tack-rag."

## (2) Measurements and Evaluation

The objective of this investigation was the study of the behavior of the laminar boundary layer on a swept wing with suction through many fine slots and the determination of the drag characteristics and suction requirements of this swept wing at various angles of attack  $\alpha$  and Reynolds numbers  $R_c$ . At each of the various Reynolds numbers and angles of attack the suction quantities were varied over a range that included the point of minimum drag. The following measurements were taken.

The pressure drop across the calibrated flow measuring nozzles located at the downstream end of the various suction chambers was measured to evaluate the suction quantities  $Q_a$  of the various suction chambers. The corresponding chamber static pressures were taken at the downstream end of the suction chambers. The lengthwise pressure distribution was recorded by means of twenty-four static pressure orifices located from 0.8 to 100 percent of the chord  $c$ .

The boundary layer profile at the model trailing edge was measured by means of a boundary layer rake, consisting of seven flattened total pressure tubes, and by a static pressure orifice located at the same chord station but displaced by 0.5 inch in the spanwise direction.

The state of the boundary layer in the test area was observed by means of microphones, connected to various wall static pressure orifices, and from the boundary layer measurements at the model trailing edge.

The static pressures in the measuring nozzle, suction chambers and on the external wing surface and the total pressures from the boundary layer rake were displayed on a U-tube manometer panel. The pressure data were recorded photographically on 70-mm roll film, which was then read on a film reading machine. The final recording was on keypunched cards suitable for use on an IBM 704 digital computer.

The undisturbed freestream static and dynamic pressures  $p_\infty$  and  $q_\infty$  were evaluated by a comparison of the measured and theoretical wing pressure distributions. At angle of attack,  $p_\infty$  and  $q_\infty$  were selected so as to cause agreement of the measured wing pressure distributions at the trailing edge. In addition, it was checked that the variation of the measured pressure at a given orifice location was linear with angle of attack.

From the measured suction quantities  $Q_a$  of the various suction chambers the suction quantity coefficients  $C_{Q_a} = Q_a / U_\infty bc$  of the individual chambers and the total suction quantity coefficient  $C_{Q_t} = \sum_{\text{all chambers}} C_{Q_a}$  were

## (2) Measurements and Evaluation (Continued)

evaluated. With the nondimensional coefficient of the pressure rise across the suction compressor  $C_{p_{ga}} = (p_a - p_\infty)/q_\infty$  to accelerate the suction air isentropically to freestream pressure and velocity the equivalent suction drag coefficient is

$$C_{Ds} = \sum_{\text{all chambers}} C_{Qa} (1 - C_{p_{ga}}).$$

The wake drag coefficient was evaluated from the measured momentum thickness  $\theta_{TE}$  of the boundary layer at the wing trailing edge according to Squire and Young:

$$C_{Dw} = \frac{2\theta_\infty}{c} = \frac{2}{c} \theta_{TE} \left( \frac{U_{TE}}{U_\infty} \right)^{\bar{H}+2}$$

where  $\bar{H}$  is the value of  $H = (\delta^*/\theta)$  in the wake between the trailing edge and infinity;  $H = 1.4$  and  $1.0$  shortly downstream of the wing trailing edge and at infinity, respectively, so that  $\bar{H} + 2 = 3.2$  and

$$C_{Dw} = \frac{2\theta_{TE}}{c} \left( \frac{U_{TE}}{U_\infty} \right)^{3.2}$$

The equivalent total drag coefficient of the wing is, then,

$$C_{Dt} = C_{Dw} + C_{Ds}.$$

## (3) Experimental Results

The pressure distributions measured at various angles of attack  $\alpha$  are shown in Figure 4. In Figures 5 through 10 are shown representative variations of the equivalent suction drag  $C_{Ds}$ , wake drag  $C_{Dw}$  and equivalent total drag  $C_{Dt}$  with total suction coefficient  $C_{Qt}$  for various angles of attack  $\alpha$  and wing chord Reynolds numbers  $R_c$ . The figures illustrate the two regimes of flow characteristic of the variation of the equivalent total drag coefficient with increasing rate of suction flow. The low-suction regime of flow is characterized by rapidly decreasing wake drag as increasing suction stabilizes the boundary layer and reduces the number of occurrences of turbulent bursts. As suction is increased further, and turbulent bursts are eliminated entirely the laminar boundary layer is merely thinned by additional suction. Since the decrease of wake drag due to the thinning of the laminar boundary layer is inadequate to compensate for the additional equivalent drag due to suction the equivalent total drag increases. Thus, a minimum equivalent total drag  $C_{Dt_{min}}$  occurs at a given optimum total suction flow coefficient  $C_{Q_{opt}}$ .

### (3) Experiment Results (Continued)

The variation with wing chord Reynolds number  $R_c$  of the minimum equivalent total drag  $C_{D_{t_{min}}}$  of the upper wing surface at angles of attack  $\alpha = 0$  and  $\pm 1^\circ$  is shown in Figure 11 and the variation of the corresponding optimum total suction flow coefficient  $C_{Q_{opt}}$  with  $R_c$  is shown in Figure 12. Previous results from tests in the University of Michigan 5- by 7-foot wind tunnel (Reference 70) and the Norair 7- by 10-foot wind tunnel are also shown. The variation of  $C_{D_{t_{min}}}$  with  $R_c$  at  $\alpha = \pm 1.5, -2^\circ$  is shown in Figure 13.

Figure 14 shows faired plots of the experimental values  $C_D \sqrt{R_c}$  for different angles of attack and Reynolds numbers. Chordwise distributions of the nondimensional equivalent area suction velocity

$v_o^* = \frac{v_o}{U_\infty} \sqrt{R_c}$  are shown in Figure 15 for various representative Reynolds numbers at the angles of attack studied.

#### (F) Theoretical Analysis

##### (1) Computational Procedure

###### (a) Boundary Layer Development

The particular test points (run numbers) chosen for study are listed in Table III. Angles of attack  $\alpha = -1, 0$  and  $+1$  degrees, at which full chord laminar flow was maintained up to  $25 \times 10^6$  to  $29 \times 10^6$  wing chord Reynolds numbers were selected. Various Reynolds numbers were chosen at each angle of attack. At a given Reynolds number and angle of attack the test point having a suction coefficient closest to or somewhat larger than the optimum (i.e., the suction coefficient for minimum equivalent total drag) was selected. Finally, the test points of highest suction coefficient at the maximum and minimum Reynolds numbers were included to give an indication of the effect of oversuction.

Development of the boundary layer for the selected test runs was calculated by means of Raetz's method (Reference 45) on an IBM 704 high speed digital computer. The method calculates boundary layer profiles at a large number of chordwise steps by a difference method. Numerical data defining the boundary conditions is required at each point. For computational stability, these data must be smooth and consistent, and their derivatives are restricted in magnitude so that the differences between points are not too large. Figure 16 is a comparison of the measured pressure distributions and the approximations used for the calculations. The nondimensional inflow velocity distribution used for a given run is illustrated along with the summary of results for the run. Total suction quantity of the distributions used for the calculations agreed with the measured total suction quantities within plus or minus 1 percent.

### (a) Boundary Layer Development (Continued)

Since the model was originally designed to be tested at a wing chord Reynolds number  $R_C = 10^7$  and was actually tested up to  $R_C = 28 \times 10^6$ , the chordwise suction inflow distribution at the high Reynolds number would not be uniform. Preliminary calculations showed that it would be of a "sawtooth" nature, as shown in Figure 24. Such a distribution would be very difficult to approximate in the manner required by the program, and the large differences involved would strain the accuracy of the computations (especially toward the rear of the airfoil).

### (b) Off-Design Suction Inflow

Calculation of the effects of operating the model under conditions far from those for which it was designed required determination of the suction flow through each individual slot. The model geometry is given in Table II and the external flow conditions are the experimental values. The pressure drops through the model slot and hole combinations were determined by plotting surface and suction chamber pressure coefficients. The suction flow rate could then be evaluated from existing data on the pressure drop through slots and holes as a function of flow rate (Reference 73, pages 307 and 310). This method requires an iterative calculation procedure. Slot Reynolds numbers  $R_s$  (based on the average velocity through the slot and the half width of the slot) and hole Reynolds numbers  $R_h$  (based on the average velocity through the hole and the hole radius) were calculated directly, once the suction flow rate through the slot and hole combination was known.

## (2) Computation Results

### (a) Boundary Layer Development

A representative example of the computed development of the laminar boundary layer is given in Figures 17 and 18. Figure 17 summarizes the development of the boundary layer crossflow as represented by the crossflow Reynolds number  $R_{0.1}$  (based on the maximum crossflow velocity  $w_{max}$  and the height of the crossflow boundary layer where the crossflow velocity  $w = 0.1 w_{max}$ ). Also included is the minimum stability limit Reynolds number  $R_{SL}$  (below which all boundary layer disturbances are damped) as defined by the calculations in Reference 6 and a Reynolds number that is 67 percent greater than  $R_{SL}$ . The associated distribution of the nondimensional suction velocity  $v_o^*$  for equivalent area suction is included in this figure.

Figure 17 shows an apparent break in the crossflow development at the wing position of minimum pressure and the beginning of the rear pressure rise at approximately 65 percent chord. Due to the change in sign of the pressure gradient in this region, the boundary layer crossflow, which is directed inboard in the region of decreasing pressure, changes direction downstream of 65 percent chord and flows toward the wing tip in the region of increasing pressure. At the beginning of the rear pressure rise the crossflow profile develops a double loop, the stability of which is, as yet, undefined. The crossflow Reynolds number is defined only in its absolute magnitude in this report.

### (a) Boundary Layer Development (Continued)

Figure 18 illustrates the development of the tangential boundary layer flow as represented by the momentum thickness Reynolds number  $R_\theta$  (based on local potential velocity  $U$  and boundary layer momentum thickness  $\theta$ ) and the shape parameter  $H = \delta^*/\theta$ , where  $\delta^*$  = displacement thickness of the boundary layer.

Figures 19, 20 and 21 show the variation of the ratio of the crossflow Reynolds number  $R_{0.1}$  to the minimum stability limit Reynolds number  $R_{SL}$  along the chord length for  $\alpha = 0, -1$  and  $+1$  degrees angle of attack. These figures illustrate the amount by which the stability limit Reynolds number was exceeded during the Ames experiments on the 30-degree swept laminar suction wing.

Comparison of the calculated trailing edge boundary layer velocity profile with the measured velocities is given in Figure 22 for the case whose boundary layer development was illustrated in Figures 17 and 18. In Table III the calculated momentum thickness  $\theta$  is compared with the momentum thickness as determined from the measured velocity points for all the cases studied theoretically. The effect of the boundary layer crossflow velocity is not included in the velocity profiles as drawn. Since the crossflow velocity, under the conditions studied, is small when compared to the tangential boundary layer velocity component (Reference 6), the resulting error is usually small.

### (b) Off-Design Suction Inflow

Calculations of the detailed suction inflow characteristics of the model at off-design conditions were performed for six test points that represent the furthest deviation from design conditions. Figure 23 is a representative superposition of the suction chamber pressure coefficients on a plot of the external wing surface pressure distribution. Like figures were used in the cases studied to evaluate the local suction velocities for equivalent area suction. Calculations were performed for the last four chambers in each case, providing an adequate illustration of the effect of the off-design conditions.

Figure 24 shows the variation of the local inflow velocity along the chord for the case whose pressure distribution was illustrated in Figure 23. Table IV lists, for this particular case, the non-dimensional suction velocity  $v_o^*$  for equivalent area suction, the Reynolds numbers  $R_s$  of the flow through the slots and the Reynolds numbers  $R_h$  of the flow through the metering holes. In addition, the computed and measured suction coefficients  $C_{Qa}$  for the various suction chambers are listed.

### (G) Discussion

At angles of attack  $\alpha = 0$  and  $\pm 1^\circ$ , full length laminar flow was observed on a  $30^\circ$  swept laminar suction wing in the NASA Ames 12-foot

(G) Discussion (Continued)

pressure wind tunnel up to a wing chord Reynolds number  $R_c = 29 \times 10^6$ , with a minimum wing equivalent total drag coefficient  $C_{D_{t_{min}}} = 0.00097$  (including equivalent suction drag) for both wing surfaces together at  $\alpha = 1^\circ$  and  $R_c = 28 \times 10^6$  (Figures 11, 12 and 13). The corresponding suction quantity coefficient was  $C_{Q_{opt}} = 0.00070$  (for both wing surfaces). At Reynolds numbers above  $28 \times 10^6$  tunnel noise, rather than tunnel turbulence seemed to cause turbulent bursts and a rising drag at  $\alpha = 0$  and  $\pm 1^\circ$ .\* At  $\alpha = +1.5$  and  $-1.5^\circ$  full chord laminar flow was maintained up to  $R_c = 22 \times 10^6$  and  $24 \times 10^6$ , respectively, and up to  $21 \times 10^6$  at  $\alpha = 2^\circ$ . The drag was somewhat higher at these angles of attack than at  $\alpha = 0$  and  $-1^\circ$ . At the larger negative angles of attack the increased flow acceleration over the front part of the wing (see chordwise pressure distributions, Figure 4) caused an increased spanwise pressure gradient with a correspondingly stronger boundary layer cross-flow in this area, which reduced the maximum Reynolds number with full chord laminar flow.

At  $\alpha = 1.5^\circ$  the occurrence of a negative pressure peak close to the leading edge followed by local flow deceleration probably caused increased instability of the boundary layer against Tollmien-Schlichting disturbances, causing transition and drag rise at somewhat lower Reynolds numbers than at  $\alpha = 0$  and  $\pm 1^\circ$ .

From the far red plots of  $C_D/\sqrt{R_c}$  and  $C_Q/\sqrt{R_c}$  for different angles of attack and Reynolds numbers (Figure 14), it can be seen that in order to maintain laminar flow on a swept wing under crossflow conditions, increasingly higher minimum values of  $C_Q/\sqrt{R_c}$  were required with increasing Reynolds numbers, as predicted by theory (Chapter 13 of Reference 47). For this reason the drag decreased with increasing Reynolds number at a considerably slower rate than the laminar friction drag of a flat plate.

In order to maintain full chord laminar flow at Reynolds numbers up to  $R_c = 11 \times 10^6$  and  $\alpha = 0$  and  $1^\circ$ , no suction had been previously required upstream of the 0.25 chord station (first University of Michigan experiments, Reference 69), and weak suction was adequate in the region of the flat pressure distribution, followed by stronger suction in the region of the rear pressure rise. With increasing Reynolds numbers, however, suction had to be applied further forward toward the leading edge, and higher nondimensional equivalent area suction velocities  $v_o^*$  were required over the whole wing chord

---

\*An analysis of the noise level of the Ames 12-foot pressure wind tunnel (Reference 71) at  $R_c = 28 \times 10^6$  and five atmospheres tunnel pressure gave a ratio of root mean square value of mean particle velocity to undisturbed flow velocity  $\overline{u'^2}/U_\infty = 2.4 \times 10^{-4}$  due to acoustical vibrations, as compared with  $\overline{u'^2}/U_\infty \leq 10^{-4}$  due to tunnel turbulence (Reference 71).



(G) Discussion (Continued)

(Figure 15), particularly in the front part of the wing, in order to achieve full chord laminar flow, as predicted by theory.

At greater angles of attack higher nondimensional equivalent area suction velocities  $v_0^*$  had to be applied on the whole upper wing surface and especially in the area of the negative pressure peak close to the leading edge at  $\alpha = 1.5^\circ$ . At larger negative angles of attack, increasingly stronger suction was necessary in the area of the strong flow acceleration in the front part of the wing to prevent excessive crossflow instability in this area. On the other hand, the rear pressure rise toward the trailing edge decreased somewhat at larger negative angles of attack, resulting in correspondingly smaller suction quantities in this area.

In the region of the flat pressure distribution upstream of the location of minimum pressure, the ratio of crossflow Reynolds number  $R_{0.1}$  to the minimum stability limit Reynolds number  $R_{SL}$  was quite consistent as Reynolds number was varied at a given angle of attack (Figures 19, 20 and 21). In general, the crossflow Reynolds number was greater than the minimum stability limit Reynolds number by 50 to 70 percent in the nose region (up to approximately 5 percent in this case) and seems to be independent of angle of attack. Downstream of this region, between 5 and 60 percent chord, the ratio of the crossflow Reynolds number to the stability limit Reynolds number seems to be a function of angle of attack. At an angle of attack  $\alpha = 0$  degree (Figure 19),  $R_{0.1}$  increased until it exceeded  $R_{SL}$  by approximately 100 percent; at  $\alpha = -1$  degree the ratio of  $R_{0.1}$  to  $R_{SL}$  increased to approximately 2.5 (Figure 20); and at  $\alpha = +1$  degree  $R_{0.1}$  decreased until it was approximately equal to the stability limit Reynolds number at the 60 percent chord station. At the low wing chord Reynolds number and angles of attack  $\alpha = 0$  and  $-1$  degrees, the trends as just described were surpassed locally. Specifically, at  $\alpha = 0$  degree and  $R_c = 13.9 \times 10^6$  (Figure 19) the minimum stability limit Reynolds number  $R_{SL}$  was exceeded by as much as 150 percent over part of the forward portion of the model, but this ratio was reduced by additional suction to 100 percent by the time the location of minimum pressure was reached. At an angle of attack  $\alpha = -1$  degree (Figure 20) and Reynolds number  $14.1 \times 10^6$  the minimum stability limit Reynolds number was exceeded by 140 percent at the nose of the model, followed by increased suction which rapidly reduced the ratio  $R_{0.1}/R_{SL}$  to values somewhat below those achieved at higher Reynolds numbers.

In the region of the model downstream of the location of minimum pressure there was no such systematic variation either with angle of attack or with wing chord Reynolds number at a given angle of attack. The majority of the cases studied showed an increase of the crossflow Reynolds number until  $R_{0.1}$  was approximately 100 to 150 percent greater than the minimum stability limit Reynolds number at the trailing end of the suction region.

(G) Discussion (Continued)

According to Table III the momentum thickness of the boundary layer velocity profiles as calculated and measured at the model trailing edge agreed fairly closely, in most cases. However, the agreement between the calculated and measured velocity profiles was not good in many of the cases. On the model the total pressure rake used to measure the final boundary layer profile was fitted to the model at the trailing edge. The last slot was at 97 percent chord and slot spacing was 0.55 percent chord. Thus, the trailing edge rake was about 5.5 slot spacing lengths aft of the last slot. An attempt was made to approximate the effect of this nonsuction area by rapidly reducing the suction aft of 97 percent chord in the calculations. It can be seen in Figures 19 through 21 that the effect of reducing suction in this area was to decrease the minimum stability limit Reynolds number  $R_{SL}$ . Thus, in the physical case,  $R_{Q,1}$  rapidly surpassed  $R_{SL}$  to such an extent that transition occurred in the vicinity of the wing trailing edge; turbulent bursts were, in fact, observed close to the trailing edge of the wing during the tests in question at those runs near minimum drag.

Figure 24 illustrates the "sawtooth" suction inflow velocity distribution (for equivalent area suction) caused by off-design operation of the model at high Reynolds numbers, and, in fact, indicates outflow from the first slots of three chambers. The calculations (see Table IV for representative results) showed that the Reynolds numbers (based on average velocity through the slot and half of the slot width) of the slots at the aft end of the suction chambers ranged from  $R_s = 65$  to 92 with the slots having Reynolds numbers greater than 80 in many cases. The corresponding hole Reynolds numbers ranged from  $R_h = 600$  to 850

In Reference 74 (page 136), Schiller reports that vortices were formed at the entrance of a sharp-inlet tube at a tube Reynolds number

$\frac{\bar{u} \cdot R}{\nu} = 280$ . Schiller's experiments were conducted with water that had been allowed to settle for several hours in order to ensure steady flow conditions at the entrance of the tube. During similar tube experiments Davies and White (Reference 74 page 151) used strongly disturbed water and reported the formation of similar vortices at the beginning of a sharp-inlet tube at Reynolds numbers one-half of those reported for Schiller's experiments. In Reference 75 Rogers showed that the flow through holes of small length-to-diameter ratio detaches from the surface of the hole at its inlet. As a result, unsteady flow may develop in the hole at hole Reynolds numbers  $R_h = 600$  to 800 for the range of length-to-diameter ratios of interest, as long as the hole inlet is sharp.

If it is assumed that a slot and hole of equal hydraulic radius and with sharp inlets exhibit similar flow characteristics, the flow phenomena as discussed above for holes will occur at slot Reynolds numbers  $R_s$  (based on average slot velocity and one-half width) equal to one-half of the corresponding hole Reynolds numbers  $R_h$ . Therefore, vortices may develop at the leading edge of a slot at a Reynolds number  $R_s = 75$ , as long as the leading edge of the suction slot is sharp (as during the present experiments).

(G) Discussion (Continued)

From the above it appears that inlet vortices and subsequent unsteady flow may have occurred in the slots at the aft end of the suction chambers and almost certainly in the holes. The outflow in the forward portions of the suction chambers and the unsteady flow through the slots and holes at the aft portion of the suction chambers due to off-design operation of the model at high chord Reynolds numbers may thus have generated disturbances in the boundary layer, particularly in the case of oversuction.

The results shown present essentially the overall development of the boundary layer along the chord, using equivalent area suction. Further refined calculations would be required to evaluate the local boundary layer development, such as in the vicinity of the wing leading edge, etc. In order to obtain the local boundary layer development from slot to slot, suction through individual slots would have to be used, taking into account sink effects at the slots.

CHAPTER B. EXPERIMENTAL INVESTIGATION OF A 4-PERCENT-THICK STRAIGHT LAMINAR SUCTION WING OF 17-FOOT CHORD IN THE NORAIR 7- BY 10-FOOT WIND TUNNEL

L. W. Gross

(A) Acknowledgements

The author wishes to thank all those of the Norair Boundary Layer Group who contributed to the completion of this work. In particular, appreciation is due J. Wada for the mechanical design of the model and fairings; J. James, E. Meyer, R. Heiss and others of the Boundary Layer Research Laboratory for their efforts in building the model; and V. L. Tucker for her contributions to the preparation of the report.

The author is also indebted to the staff of the Norair 7- by 10-foot wind tunnel, J. Killian of Photographic Services, and R. C. Skinner and V. Rockefeller of the Data Analysis Group for their services during the course of the tests and data evaluation.

(B) Summary

Full chord laminar flow and very low wing equivalent total drags were maintained on a 4-percent-thick unswept suction wing of 17-foot chord up to a wing chord Reynolds number of  $26 \times 10^6$  by means of suction through 100 fine slots. Without tunnel wall fairings, the minimum wing equivalent total drag coefficient for one wing surface (including the equivalent suction drag) was  $C_{D_{t_{min}}} = .000375$  at  $R_c \approx 25 \times 10^6$  and  $\alpha = 0$  degree angle of attack; the corresponding suction quantity coefficient (based on wing projected area) was  $C_{Q_{opt}} = .000130$ . The maximum wing chord Reynolds number with full chord laminar flow was twice as large as that measured in the same tunnel on a 30-degree swept laminar suction wing of 7-foot chord and was probably limited by wind tunnel noise as well as by the number of suction slots used. The maximum attainable wing chord Reynolds number with full chord laminar flow was only slightly influenced by moderate changes of the external pressure distribution. These changes were obtained by varying the angle of attack and by putting fairings on the tunnel walls opposite the model. An increased overall flow acceleration along the wing chord resulted in somewhat higher wing chord Reynolds numbers with full chord laminar flow and, conversely, the maximum wing chord Reynolds number with 100 percent laminar flow was somewhat reduced when the flow was more strongly decelerated along the chord, as compared with the model at  $\alpha = 0$  degree angle of attack without tunnel wall fairings present.

(C) Notation

c            chord length

$C_{D_s} = \sum_{\text{all chambers}} C_{Q_a} (1 - C_{p_{ga}})$ ; equivalent drag due to suction power required to accelerate the suction air without losses to undisturbed velocity and pressure

(C) Notation (Continued)

$C_{Dt}$	$= C_{Ds} + C_{Dw}$ ; equivalent total drag coefficient
$C_{Dt_{min}}$	minimum equivalent total drag coefficient
$C_{Dw}$	wake drag coefficient
$C_p$	$= \frac{p - p_\infty}{q_\infty}$ ; pressure coefficient
$C_{p_{g_a}}$	$= \frac{p_a - p_\infty}{q_\infty}$ ; pressure coefficient of individual suction chamber with respect to $p_\infty$
$C_{Q_a}$	$= \frac{Q_a}{U_\infty S_c}$ ; suction coefficient of individual suction chamber
$C_{Qt}$	$= \sum_{\text{all chambers}} C_{Q_a}$ ; total suction coefficient
$C_{Q_{opt}}$	total suction coefficient corresponding to minimum equivalent total drag
$b$	span of suction chamber
$p$	static pressure, with respect to $p_\infty$
$p_a$	static pressure in suction chamber, with respect to $p_\infty$
$p_\infty$	undisturbed freestream static pressure
$q_\infty$	$= 1/2 \rho_\infty U_\infty^2$ ; undisturbed freestream dynamic pressure
$Q_a$	suction quantity of each suction chamber
$R_c$	$= \frac{\rho_\infty U_\infty c}{\mu}$ ; Reynolds number based on chord
$S$	area of test portion of model
$S_c$	$= b \cdot c$
$u$	boundary layer velocity at height $y$
$U$	velocity at outer edge of boundary layer

(C) Notation (Continued)

$U_{\infty}$	velocity of flow at infinity
$v_o$	equivalent area suction velocity
$v_o^*$	$= \frac{v_o}{U_{\infty}} / R_c$ , nondimensional equivalent area suction velocity
$x$	distance along chord
$y$	distance normal to surface of model
$Y$	model ordinate
$\alpha$	angle of attack
$\rho$	density
$\mu$	absolute viscosity

(D) Introduction

In connection with the application of low drag boundary layer suction to large airplanes, the question arises concerning the feasibility of full chord laminar flow on the wings of such airplanes at high Reynolds numbers by means of boundary layer suction. According to theory (Reference 47), suction will increase the stability limit Reynolds number of the boundary layer and reduce the amplification of oscillations introduced into the boundary layer; at the same time its thickness is reduced. As a result the application of area suction should enable full length laminar flow to very high length Reynolds numbers (Reference 47), provided external disturbances due to turbulence, sound, etc., are minimized. How far the stability limit Reynolds number of the boundary layer can be exceeded without transition to turbulent flow is critically dependent on the magnitude of the external disturbances. Theories describing the growth of boundary layer oscillations (Reference 1) give an improved physical insight into the phenomena leading to transition.

In order to verify how effective area suction is in maintaining full chord laminar flow at high Reynolds numbers in the absence of large external pressure gradients, a 4-percent-thick symmetrical straight laminar suction wing of 17-foot constant chord and 7-foot span was investigated in the Norair 7- by 10-foot low turbulence wind tunnel.

(E) Experimental Setup

The airfoil selected was a 4-percent-thick symmetrical section interpolated between a biconvex wing and an NACA 66-004 airfoil in such a manner that the test section closely resembles a biconvex wing. A large wing chord of 17 feet was chosen in order to achieve high wing chord Reynolds numbers at relatively low tunnel speeds and correspondingly reduced external disturbances from tunnel turbulence and sound. The maximum permissible wing chord (17 feet) was dictated by the length of the wind tunnel test section

### (E) Experimental Setup (Continued)

and by the spread of the turbulent wedges on the wing on both sides of the model test area. The span of the vertically mounted wing was seven feet.

A thin wing (4-percent-thickness ratio) was selected in order to minimize chordwise pressure gradients on the test surface during the first phase of the investigation. Figure 25 shows the cross section of the wing with details of the suction system. During the second phase fairings of various shapes (contour and coordinates of the fairings are shown in Figure 28 and Table VII) were inserted on both side walls of the wind tunnel test section in the region of the test wing to increase the chordwise pressure gradients on the model. The minimum pressure peaks on the wing with fairings numbered 1 and 2 were located at approximately 45 and 20 percent of the wing chord, respectively. Figure 35 compares the chordwise pressure distributions at an angle of attack  $\alpha = 0^\circ$  as measured during the tests.

Area suction was closely approached by means of suction through 100 fine slots located from 1 to 97.2 percent of the wing chord in the laminarized test area outside the turbulent wedges on the wing, originating from the junctures between the wing leading edge and the tunnel floor and ceiling (Figure 26). The span of the slots decreased from 77.4 inches for slot 1 to 15.2 inches for slot 100, close to the wing trailing edge.

The suction air was ducted through the slots, cut into a thin outer skin which was bonded to a thicker inner skin, into spanwise grooves and through metering holes (drilled through the inner skin) into 16 suction chambers (Figure 25) and through flow measuring nozzles and tubes into a common suction box and finally to the suction compressor. The suction quantities of the various chambers could be adjusted individually by means of needle valves at the entrance to the common suction box. The total rate of suction could be varied by changing the rpm of the suction compressor. In addition, bleed air could be ducted into the common suction box to change the overall suction quantity and avoid surge of the suction compressor.

The design of the suction system was based on boundary layer calculations with suction, using Raetz's method (Reference 76), for a design wing chord Reynolds number  $R_c = 25 \times 10^6$  at  $\alpha = 0.25$  degree angle of attack, with the chordwise pressure distribution as calculated by Theodorsen's method (Reference 80). At  $\alpha = 0.25$  degree the occurrence of a slight negative pressure peak close to the wing leading edge required suction forward to 1 percent of the wing chord to avoid laminar separation and transition in the front part of the wing. In the region of the rather flat pressure distribution from approximately 5 to 60 percent chord relatively weak suction was found to be adequate to maintain laminar flow with suction slots of approximately 2 percent chord spacing and 0.004- to 0.005-inch width. In the region of the rear pressure rise downstream of 60 percent chord increased suction is necessary to avoid premature transition in this area, requiring more closely spaced slots of 0.005- to 0.008-inch width.

## (F) Measurements and Evaluation

The objective of this investigation was the study of the behavior of the laminar boundary layer at high Reynolds numbers on a thin laminar suction wing with suction through many fine slots and the determination of the drag characteristics and suction requirements of this wing (with and without tunnel wall fairings) at various angles of attack  $\alpha$  and wing chord Reynolds numbers  $R_c$ . For the various Reynolds numbers and angles of attack the suction quantities were varied. The following measurements were made.

The pressure drop across calibrated flow measuring nozzles located at the downstream end of the various suction chambers was measured to evaluate the suction quantities  $Q_a$  of the various suction chambers. The corresponding chamber static pressures were taken at the downstream end of the suction chambers. The boundary layer profile at the wing trailing edge was measured by means of a trailing edge rake, consisting of twelve flattened total pressure tubes, and by a static pressure orifice located at the same chord station but displaced by 0.5 inch in spanwise direction. The chordwise pressure distribution was recorded by means of twenty-six static pressure orifices located from 0.2 to 99.75 percent chord. In order to provide sufficient test points in the front part of the wing at angles of attack, six orifices were located within the first 4 percent of the wing chord.

The state of the boundary layer in the test area was observed by means of microphones, connected to the various wall static pressure orifices, and from the boundary layer measurements at the wing trailing edge.

The static pressures in the measuring nozzles, suction chambers and on the external wing surface were displayed on a first U-tube manometer panel. The trailing edge readings (total and static pressures) were recorded on a second, separate U-tube manometer board. In this manner fluctuations of the trailing edge total pressures did not influence the remaining pressure readings. The pressure data were recorded photographically on 70-mm. microfilm, which was then read on an automatic film-reading machine. The final recording was on keypunched cards suitable for use on an IBM 704 digital computer.

The undisturbed freestream static and dynamic pressures  $p_\infty$  and  $q_\infty$ , for the wing without tunnel wall fairings, were evaluated from calculations of the tunnel wall corrections (Reference 81). In the case of the model with fairings an arbitrary minimum static pressure coefficient  $C_{p_{min}}$  was specified on the model at the location of minimum pressure. The pressure distribution would then correspond to that around a thicker airfoil.  $p_\infty$  and  $q_\infty$  were then evaluated from  $C_{p_{min}}$  and the freestream total pressure in the test section of the tunnel.

From the measured suction quantities  $Q_a$  in the various suction chambers the suction quantity coefficients  $C_{Q_a} = \frac{Q_a}{U_\infty b c}$  of the individual



(F) Measurements and Evaluation (Continued)

chambers and the total suction quantity coefficient  $C_{Qt} = \sum_{\text{all chambers}} C_{Qa}$  were

evaluated. With the nondimensional coefficient of the pressure rise across the suction compressor  $C_{p_{ga}} = (p_a - p_\infty)/q_\infty$  to accelerate the suction air isentropically to freestream velocity and pressure the equivalent suction drag coefficient is

$$C_{Ds} = \sum_{\text{all chambers}} C_{Qa} (1 - C_{p_{ga}}).$$

The wake drag coefficient was evaluated from the measured momentum thickness  $\theta_{TE}$  of the boundary layer at the wing trailing edge according to Squire and Young:

$$C_{Dw} = \frac{2 \theta_\infty}{c} = \frac{2}{c} \theta_{TE} \left( \frac{U_{TE}}{U_\infty} \right)^{\bar{H}+2}$$

where  $\bar{H}$  is the value of  $H = \left( \frac{\delta^*}{\theta} \right)$  in the wake between the trailing edge and infinity;  $H_{TE} = 1.4$  and  $1.0$  shortly downstream of the wing trailing edge and at infinity, respectively, so that  $\bar{H} + 2 = 3.2$  and

$$C_{Dw} = \frac{2 \theta_{TE}}{c} \left( \frac{U_{TE}}{U_\infty} \right)^{3.2}$$

The equivalent total drag coefficient of the wing is, then,

$$C_{Dt} = C_{Dw} + C_{Ds}.$$

(G) Experimental Results

The pressure distributions of the basic model in the wind tunnel with no fairings on the walls are given in Figures 29 and 30. The pressure distributions for the case of the model with Fairing Number 1 installed on the wind tunnel walls are given in Figures 31 and 32 and comparable information for the case of the model with Fairing Number 2 is given in Figures 33 and 34. In Figure 35 the pressure distributions at an angle of attack  $\alpha = 0^\circ$  are shown for the three cases studied to allow a comparison between them.

Figures 36 through 42 present representative examples of the variation of the equivalent suction drag coefficient  $C_{Ds}$ , wake drag coefficient  $C_{Dw}$ , and equivalent total drag coefficient  $C_{Dt}$  as functions of total suction volume coefficient  $C_{Qt}$ . The figures were all chosen from the case of the model with no fairing but illustrate the behavior of these parameters in the other cases as well.

## (G) Experimental Results (Continued)

The variation of the minimum equivalent total drag coefficient  $C_{D_{t_{min}}}$  (including equivalent suction drag) and the corresponding suction coefficient for minimum equivalent total drag  $C_{Q_{opt}}$  with wing chord Reynolds number  $R_c$  at given angles of attack  $\alpha$  are shown in Figures 43 and 44, respectively, for the case of the model with no fairing. For the case of the model with Fairing Number 1 installed, the variations of  $C_{D_{t_{min}}}$  and  $C_{Q_{opt}}$  with  $R_c$  are given in Figures 45 and 46, while for the case of the model with Fairing Number 2 installed the same information is given in Figures 47 and 48.

In Figures 49 through 55 are shown representative chordwise distributions of the nondimensional suction velocity  $v_o^*$  for equivalent area suction. The distributions shown were computed from the suction quantities of the test points closest to minimum equivalent total drag coefficient  $C_{D_{t_{min}}}$ . Figures 49, 50 and 51 show the  $v_o^*$  distributions for the three cases studied (basic model and with Fairings Number 1 and 2) at an angle of attack  $\alpha = 0^\circ$  and for several chord Reynolds numbers  $R_c$ . In Figures 52, 53 and 54 the  $v_o^*$  distributions are shown at a given Reynolds number,  $R_c \approx 21 \times 10^6$ , and for several angles of attack  $\alpha$ . Finally, the  $v_o^*$  distributions of the three models at the angle of attack  $\alpha = 0^\circ$  and Reynolds number  $R_c \approx 21 \times 10^6$  are compared in Figure 55. This illustrates the differences of suction velocity distribution required by the different pressure distributions of the three cases.

Boundary layer velocity profiles as measured at the trailing edge of the test model under the three conditions studied are presented in Figures 56 through 63 for varying Reynolds numbers at an angle of attack  $\alpha = 0^\circ$ . The boundary layer velocity profiles of Figures 56, 57, and 58, correspond to the suction velocity  $v_o^*$  distributions of Figures 49, 50, and 51, respectively.

In order to illustrate the effect of increasing suction at a given angle of attack  $\alpha$  and Reynolds number  $R_c$  on the trailing edge boundary layer velocity profiles, selected series of test points were chosen from the case of the test with Fairing Number 2. These velocity profiles are shown in Figures 59 through 63.

## (H) Discussion

### (1) Basic Model

At an angle of attack  $\alpha = 0$  degree full chord laminar flow was maintained up to a wing chord Reynolds number  $R_c$  of approximately  $28 \times 10^6$  (Figures 43 and 44). At this Reynolds number, however, external disturbances (tunnel turbulence and noise) were of sufficient magnitude to cause turbulent bursts. As a result, increased suction quantities were required to maintain extensive laminar flow and, as a consequence, the equivalent total drag coefficient was substantially higher than the minimum at this angle of attack.

#### (H) Discussion (Continued)

Minimum equivalent total drag coefficient at an angle of attack  $\alpha = 0$  degree occurred at a Reynolds number  $R_c = 26 \times 10^6$ , the equivalent total drag coefficient (including equivalent suction drag)

$C_{D_{t_{min}}} = 3.75 \times 10^{-4}$  being achieved at a total suction coefficient

$C_{Q_{opt}} = 1.3 \times 10^{-4}$  (for one wing surface). Negative angles of attack exhibited progressively lower drag coefficients, the lowest being  $C_{D_{t_{min}}} = 3.07 \times 10^{-4}$  at  $R_c = 28 \times 10^6$  and  $C_{Q_{opt}} = 0.9 \times 10^{-4}$  for an angle of attack  $\alpha = -1.5$  degrees.

Due to the very small leading edge radius of the model ( $R = 0.05$  inch), a negative pressure peak was present at the leading edge of the model for all positive angles of attack investigated (chordwise pressure distributions are shown in Figures 29 and 31). At an angle of attack  $\alpha = 0.26$  degree a pressure rise of  $0.195 q_\infty$  was present over the first 4 percent chord. At  $\alpha = 0.4$  degree and  $0.5$  degree this front pressure rise increased to  $0.276 q_\infty$  and  $0.377 q_\infty$ , respectively. With suction applied from 1 percent chord, full chord laminar flow was maintained at an angle of attack  $\alpha = 0.26$  degree up to a Reynolds number  $R_c = 25.5 \times 10^6$  with  $C_{D_{t_{min}}} = 4.0 \times 10^{-4}$  and  $C_{Q_{opt}} = 1.45 \times 10^{-4}$ . The strong negative pressure peak limited the maximum attainable Reynolds number with full chord laminar flow to  $R_c = 23.5 \times 10^6$  for  $\alpha = 0.4$  degree and  $R_c = 11 \times 10^6$  for  $\alpha = 0.5$  degree.

#### (2) Model with Fairing Number 1

Compared with the basic model, Fairing Number 1 induced more highly accelerated flow over the forward portion of the model, followed by stronger decelerated flow over the aft portion of the model and a lower overall pressure. From Figures 45 and 46 the minimum equivalent total drag coefficient (including equivalent suction drag) at an angle of attack  $\alpha = 0$  degree was  $C_{D_{t_{min}}} = 4.15 \times 10^{-4}$  at a Reynolds number  $R_c = 26 \times 10^6$  and a suction coefficient  $C_{Q_{opt}} = 1.65 \times 10^{-4}$  (for one wing surface). Overall equivalent total

drag level was 10 percent greater than that of the basic model. The increased equivalent total drag results from additional suction requirements necessary to stabilize the boundary layer in the region of the increased flow deceleration that are not compensated for by the decreased requirements in the region of stronger flow acceleration. In addition, the reduced static pressure level on the surface of the model reduces the suction chamber pressures, which increases the equivalent suction drag coefficient.

At an angle of attack  $\alpha = 0.26$  degree the maximum Reynolds number attained was  $24 \times 10^6$ , and at an angle of attack  $\alpha = 0.4$  degree the maximum Reynolds number was  $R_c = 13 \times 10^6$ . The local pressure rises in the region of the nose at  $\alpha = 0.26$  and  $0.4$  degree were  $0.185 q_\infty$  and  $0.295 q_\infty$ , respectively.

(ii) Discussion (Continued)

(3) Model with Fairing Number 2

Fairing Number 2 was designed to induce a flat or adverse pressure gradient over as long a portion of the model chord as possible. Compared with the pressure gradients induced by Fairing Number 1 (see Figure 35), the adverse pressure gradient over the aft 50 percent of the model was similar. However, in the region from 20 to 50 percent chord the pressure was constant or slightly increasing, whereas with Fairing Number 1 the pressure in this area was decreasing. From Figures 47 and 48 it is apparent that the effect of the increased region of constant or increasing pressure was to limit the maximum attainable Reynolds number slightly and to increase the total drag coefficient by approximately five percent. At an angle of attack  $\alpha = 0$  degree the maximum attainable Reynolds number was  $R_c = 23.5 \times 10^6$ . Minimum equivalent total drag coefficient  $C_{D_{t_{min}}} = 4.7 \times 10^{-4}$  occurred at a Reynolds number of approximately  $R_c = 21 \times 10^6$ .

At an angle of attack  $\alpha = 0.26$  degree the shape of the  $C_{D_{t_{min}}}$  vs  $R_c$  curve is similar to that of the other angles of attack and thus the effect of the nose pressure peak is not as apparent as in the other cases. At an angle of attack  $\alpha = 0.4$  degree minimum drag occurred at a Reynolds number  $R_c = 13 \times 10^6$ . The pressure rise downstream of the minimum pressure peak close to the leading edge was  $0.23 q_\infty$  for  $\alpha = 0.26$  degree and  $0.3 q_\infty$  for  $\alpha = 0.4$  degree.

**CHAPTER C. INVESTIGATIONS OF A 30° SWEEP AND A 17-FOOT CHORD STRAIGHT SUCTION WING IN THE PRESENCE OF INTERNAL SOUND, EXTERNAL SOUND, AND MECHANICAL VIBRATIONS**

J. W. Bacon, Jr.  
W. Pfenninger  
C. R. Moore

**(A) SUMMARY**

A 4-percent-thick straight laminar suction wing of 17-foot chord and a 30° swept, 12-percent-thick laminar suction wing of seven-foot chord were investigated in the Nasa 7- by 10-foot low turbulence wind tunnel at  $\alpha = 0^\circ$  angle of attack in the presence of external sound (longitudinal and transverse sound waves). The 4 percent-thick straight wing was tested, in addition, with internal sound and panel vibration. The external and internal sound consisted of discrete frequencies and octave bands of random noise in the 150 to 4000 cps frequency range, while the vibration frequencies were 100, 190, and 1240 cps. The critical sound pressure or panel vibration at transition could be increased considerably by increasing the suction quantities either as a whole over the entire wing chord or in the area critical to the applied disturbance. From the standpoint of total suction quantity and drag, it was much more economical to increase suction locally in the region where transition occurred.

The straight wing showed a frequency dependence of transition with external sound that correlates with the stability theory for amplified Tollmien-Schlichting oscillations.

On the swept laminar suction wing under the influence of external sound, however, transition occurred over a wide range of frequencies. In the presence of open surface cavities, such as nonsucking open slots, static pressure orifices, or imperfectly sealed slots, the critical sound pressure at transition was reduced considerably, particularly at higher sound frequencies.

For the swept wing in smooth condition the critical sound particle velocity ratio at transition generally decreased at a somewhat slower rate than inversely proportional to the wing chord Reynolds number. In the presence of open surface cavities, however, or with marginal suction the critical sound particle velocity ratio for transition often decreased at a much faster rate with increasing Reynolds number.

Naphthalene sublimation pictures of transition with external sound on the straight wing had two-inch wide streaks, the typical pattern for breakdown of laminar flow on a flat plate (Reference 38). For the swept wing, naphthalene sublimation pictures with external sound showed that transition generally occurred in the region of the flat pressure distribution and was usually preceded by the formation of closely spaced chordwise striations, indicating the presence of chordwise disturbance vortices in the presence of external sound. The formation of these vortices can probably be explained by the fact that the external disturbances superimposed on the crossflow boundary layer in the presence of external sound are of such a large magnitude (as compared with the mean crossflow velocity) that the stability limit Reynolds number of the boundary layer crossflow in the area of the flat pressure distribution is reduced to considerably lower values, as compared with the case of infinitely small external disturbances.

(A) Summary (continued)

Hot wire measurements on the swept wing verified amplified boundary layer oscillations in the region of the flat pressure distribution which appear sufficiently strong to reduce appreciably the crossflow stability limit Reynolds number in the presence of strong external sound fields.

When the chordwise flow in the boundary layer in the front part of the wing was not too stable, the swept wing exhibited a similar streak pattern at transition in the flat pressure distribution area as the straight 4-percent-thick wing in the presence of external sound. Even when the two-dimensional breakdown pattern appeared on the swept wing, the closely spaced striations were also evident in the transition region.

(B) Notation

$c$	wing chord
$C_{Ds}$	equivalent suction drag coefficient
$C_{Dw}$	wake drag coefficient
$C_{D\infty}$	equivalent wing profile drag coefficient
$C_p$	$= (p - p_\infty) / q_\infty$
$C_Q$	suction quantity coefficient
$f$	sound frequency (cycles per second, cps)
$H$	$= \delta^* / \theta$
$p$	static pressure on external wing surface with respect to the ambient static pressure $p_\infty$
$P_a$	static pressure in suction chamber with respect to $p_\infty$
$q_\infty$	$= \frac{\rho}{2} U_\infty^2$ , undisturbed dynamic pressure
$Q_a$	suction quantity
$R_c$	$U_\infty c / \nu$ , wing chord Reynolds number
SPL	sound pressure level (decibel), 0 db = 0.0002 dyne/cm <sup>2</sup>
$s'$	internal sound disturbance velocity
$u', v', w'$	external sound disturbance velocities in x-, y-, and z-directions, respectively ( $v'$ also is peak velocity of vibration skin panel)

(B) Notation (continued)

$U$	local potential flow velocity
$U_{\infty}$	undisturbed velocity at infinity
$v_o$	suction velocity for equivalent area suction
$v_o^*$	$= \frac{v_o}{U_{\infty}} \sqrt{R_c}$
$x$	coordinate in undisturbed flow direction
$y$	coordinate normal to the wing surface
$z$	coordinate in spanwise direction normal to the direction of the undisturbed flow
$\alpha$	angle of attack
$\hat{\sigma}_r$	$= 2\pi f$ , angular frequency of sound or disturbance
$\delta^*$	boundary layer displacement thickness
$\theta$	boundary layer momentum thickness

(C) Introduction and Formulation of the Problem

Boundary layer transition under the influence of external sound was reported in References 48, 83 and 84. In the presence of sound from a loudspeaker Schubauer and Skramstad (Reference 48) observed amplified oscillations in the laminar boundary layer of a flat plate at  $R_{\delta^*} = 1200$  to 2800, leading to premature transition with the proper combination of sound intensity and frequency. In general, the maximum amplification of the boundary layer oscillations on the flat plate in the presence of external sound occurred in the vicinity of the upper branch of the neutral stability curve. On a glider wing with boundary layer suction through a perforated surface Carmichael and Raspet (Reference 83) observed amplified boundary layer oscillations and premature transition in flight at  $R_c = 1.5$  to  $5 \times 10^6$  under the influence of external sound from a loudspeaker when its frequency coincided with that of the amplified boundary layer oscillations. Similar results have been published by the NLL (Reference 84) at wing chord Reynolds numbers  $R_c \approx 10^5$ . During low drag suction experiments on a 15-percent-thick slotted low drag suction wing in the NACA TDT tunnel, the second author observed a considerable increase in wake drag at  $R_c = 16.3 \times 10^6$  with optimum suction for minimum drag when a blowdown tunnel was started in the vicinity of the TDT tunnel (Reference 77). At lower wing chord Reynolds numbers ( $R_c \leq 13 \times 10^6$ ) the sound from the blowdown tunnel no longer affected transition on the model. It appeared that the noise from this blowdown tunnel caused transition on the rear part of the wing, resulting in a correspondingly higher wake drag, when the suction model was tested close to the maximum wing chord Reynolds number with full chord laminar flow.

(C) Introduction and Formulation of the Problem (continued)

Afterburner operation during flight experiments on an F-94 wing glove with suction through many fine slots generally caused premature transition beyond  $R_c = 30 \times 10^6$  wing chord Reynolds number (Reference 85). Noise from the propulsion system and possibly from the turbulent boundary layer of the fuselage may have been partially responsible for the fact that laminar flow could not be maintained on the F-94 glove in the nonsuction region from the leading edge to the 40 percent chord station at lift coefficients beyond  $C_L \approx 0.37$  (Reference 85). From transition experiments on three-dimensional bodies, flat plates and wings in the Ames 12-foot low turbulence pressure tunnel, NASA Ames concluded that acoustical disturbances were primarily responsible for transition in this tunnel (Reference 71). Similarly, the maximum wing chord Reynolds number with full chord laminar flow on a  $30^\circ$  swept low drag suction wing in the Ames 12-foot pressure tunnel was partially limited by acoustical disturbances in this tunnel (Reference 9). During transition experiments in the inlet length of laminar flow tubes, the second author observed premature transition when standing waves in the tube were induced by the exhaust noise of Diesel truck engines (Reference 86).

Boundary layer oscillations on the wetted surfaces of a low drag suction airplane under the influence of external sound, generated by the airplane itself, can be sufficiently amplified to cause transition at high Reynolds numbers. The noise from a low drag suction airplane can originate from the jet exhaust and the rotating components of its propulsion system, including the drive system, as well as from the turbulent boundary layer of the nonlaminarized areas. The noise spectrum of the rotating components of the propulsion system, such as the main engine compressor and turbine, the ducted fan and suction compressor, largely consists of peaks of discrete frequencies. In contrast, the jet exhaust and turbulent boundary layer noise has a continuous spectrum ("white" noise). The question then arises concerning the permissible sound pressure level with laminar flow and the mechanism of transition on laminar suction surfaces in the presence of external sound with discrete frequencies and with a continuous spectrum. In view of the advantages of swept wings at high subsonic speeds, a designer of a high subsonic speed low drag suction airplane will be particularly interested in the behavior of swept laminar suction wings under the influence of external sound and in methods which enable full chord laminar flow on swept suction wings at further increased sound pressure levels. At the same time, the investigation of a straight wing in the presence of external sound fields is required for a clear understanding of the swept wing results.

The question then arises in what manner disturbances from external sound influences the boundary layer on straight and swept laminar suction wings. On straight wings the chordwise component and on swept wings both the chordwise component and the crossflow component of the boundary layer flow can become unstable under the influence of external disturbances. As a result, disturbance vortices in the laminar boundary layers of low drag suction wings can develop in chordwise direction for both straight and swept wings and in the crossflow direction normal to the potential flow streamlines for swept wings. These disturbance vortices are then oriented essentially along the wing span and wing chord, respectively. According to experimental observations (Reference 87), the crossflow disturbance vortices are stationary with respect to the swept wing in the region of the flat pressure distribution. In the region of the rear pressure rise, however, they travel in the direction of the boundary layer crossflow with a finite



(C) Introduction and Formulation of the Problem (continued)

wave velocity (Reference 69). At high wing chord Reynolds numbers the behavior of the laminar boundary layer on a swept low drag suction wing is generally critically influenced by the dynamic instability of the boundary layer crossflow, particularly in the region of the rear pressure rise where the boundary layer crossflow is most pronounced. The chordwise component of the boundary layer in the rear part of the swept wing is usually highly stable as a result of the locally increased suction quantities which are required to avoid transition due to the instability of the boundary layer crossflow in this area. In contrast, considerably smaller suction quantities are usually adequate to maintain laminar flow in the region of the flat pressure distribution both on the unswept and the swept laminar suction wings. The boundary layer is, then, not stabilized very much by means of suction both on the straight wing and in the flat pressure distribution area of the swept wing. Under the influence of external disturbances amplified boundary layer oscillations in chordwise direction may then lead to transition on the straight wing and, in certain cases, on the swept wing when the chordwise boundary layer in the region of the flat pressure distribution is not too stable. In addition, the swept wing can develop stationary chordwise disturbance vortices in the region of the leading edge and the flat pressure distribution under the influence of strong external disturbances when the crossflow stability limit Reynolds number is exceeded.

With external sound as the source of the external disturbance, boundary layer crossflow disturbance vortices on the swept wing might be induced and amplified by transverse sound waves traveling in the direction normal to the potential flow streamline. In the region of the rear pressure rise the most critical frequency of the transverse sound waves would be evaluated from the particular combination of wave velocity and wave length which amplifies the crossflow disturbance vortices in the boundary layer most. In the region of the flat pressure distribution the swept wing crossflow disturbance vortices are stationary, i.e., the corresponding wave velocity and time frequency are then zero. For this reason, based on the ordinary stability theory of the boundary layer crossflow for infinitely small disturbances, no amplification of crossflow disturbances would be expected in the area of the flat pressure distribution under the influence of external sound.

Tollmien-Schlichting type disturbance waves in the boundary layer, traveling in chordwise direction, can be excited by longitudinal sound waves traveling in this direction. Throughout the straight wing and in the region of the flat pressure distribution of a swept laminar suction wing, where the chordwise boundary layer is only moderately stable, longitudinal sound waves may cause amplified boundary layer oscillations in chordwise direction when the sound frequency coincides with the frequency of the most strongly amplified chordwise boundary layer oscillations.

At low wing chord Reynolds numbers, when the boundary layer crossflow in the area of the flat pressure distribution can be stabilized with very small suction rates, the frictional instability of the chordwise component of the boundary layer flow on the swept wing may lead to premature transition in the presence of strong longitudinal sound. In contrast, on the rear part of a swept laminar suction wing with full chord laminar flow, the chordwise boundary layer flow generally appears sufficiently stable to avoid strongly amplified boundary layer oscillations in chordwise direction.

### (C) Introduction and Formulation of the Problem (continued)

The question, of course, arises as to whether or not boundary layer stability theory, assuming infinitely small disturbances, will be adequate in predicting the behavior of the boundary layer on laminar suction wings in the presence of strong external sound fields. The sound particle velocity will generally be small as compared with the tangential velocity component of the boundary layer of straight and swept wings; it will be of a similar order of magnitude, however, as the swept wing crossflow component of the boundary layer, particularly in the region of the flat pressure distribution. For this reason, it appears that nonlinear theory of the stability of the boundary layer crossflow on a swept laminar suction wing will eventually have to be used to understand the behavior of a swept laminar suction wing in the presence of strong external sound fields.

### (D) Experimental Setup

In order to answer the questions raised in Part (C), a straight wing model and a  $30^\circ$  swept wing model mounted vertically in the wind tunnel test section were investigated in the Norair 7- by 10-foot low turbulence wind tunnel at  $\alpha = 0^\circ$  angle of attack in the presence of external white noise and noise of discrete frequencies. The straight wing was also subjected to internal sound in one suction chamber and to mechanically excited wing surface panel vibrations. The 4-percent-thick straight symmetrical laminar suction wing of 17-foot chord\* and installation details are shown on Figures 64, 65 and 66. Its airfoil ordinates and the locations of the 100 fine suction slots and 16 suction chambers are shown in Tables V and VI. The seven-foot chord,  $30^\circ$  swept symmetrical laminar suction model of 12-percent-thickness\*\* and the installation are shown on Figures 67, 68 and 69. The streamwise ordinates for the modified NACA 66-012 symmetrical section appear in Table I. In order to excite boundary layer disturbance vortices both in chordwise and crossflow direction, longitudinal sound waves of discrete frequencies and with a continuous spectrum, traveling essentially in undisturbed flow direction, were generated by means of an air-modulated transducer located upstream of the nozzle and damping screens of the wind tunnel (Figure 69). In addition, during the investigation of the swept wing, transverse sound waves traveling essentially along the wing span normal to the tunnel axis were generated by a second air-modulated transducer located on top of the wind tunnel test section (Figure 69). The design of the acoustical part of the experimental setup was conducted by K. Eldred and J. Christoff of Western Electro-Acoustic Laboratories (WEAL).

The electropneumatic transducer, Ling Electronics Model Altec 6786, is based on the principle of producing sound by interrupting a compressed air jet with an annular valve. A speaker coil that is integral with the annular valve in a permanent magnet field gives a low distortion output up to 500 acoustical watts of power in the 200 to 1200 cps frequency range. In order to provide the longitudinal sound field, the transducer was coupled to an exponential horn and mounted in a fiberglass aerodynamic fairing with a parachute cloth-covered

\*Previously tested in the Norair 7- by 10-foot wind tunnel (Reference 14).

\*\*Previously tested in the 5- by 7-foot Michigan and 7- by 10-foot Norair tunnels and the 12-foot, low-pressure Ames tunnel (References 8, 9, 69 and 70).

(D) Experimental Setup (continued)

tail cone over the horn opening. The paired transducer assembly was attached on centerline of the tunnel to the turning vanes upstream of the wind tunnel test section. For the production of the transverse sound field, the transducer and horn assembly was located above the wind tunnel test section with a transition duct to bring the sound through openings in the wind tunnel ceiling along the swept wing upper surface.

During the first phase of the swept wing experiments, the transverse sound was produced by ten permanent magnet speakers, James B. Lansing Model D-131, 30-watt. The ten speakers were mounted in a sound-treated box and connected to the test section ceiling fairings by a transition duct. Six of the same speakers were used in another sound-treated box with connecting duct to supply a sound field inside suction chamber number 9 of the straight wing.

A Barber Colman permanent magnet, d.c. motor-driven, reciprocating mass shaker developed by the Norair Flight Test group was used as an exciter for the panel vibration experiments on the straight wing. Because of the small size of this shaker unit, it was possible to mount it in a wing spar cutout between chamber numbers 8 and 9 (Figure 65). The attachments to the closing ribs and the bottom skin of the straight wing model for this spar and the one immediately aft were removed to facilitate the panel vibration. With the exception of the installation of the sound and vibration generating equipment, the experimental setup for the straight wing and the swept wing were the same as described in References 9 and 14.

In order to minimize reflected sound waves in the test section in the region of the model, the walls of the test section and part of the wind tunnel nozzle, as well as the wind tunnel turning vanes downstream of the test section, were acoustically lined. The acoustical lining in the test section (Figure 69) consisted of a fiberglass insulation of 2- to 3-inch thickness mounted between the tunnel wall and a fiberglass cloth and an outer perforated metal sheet (one-eighth-inch diameter holes, 50 percent open area).

Two-dimensional flow in the test area of the swept wing model was maintained by shaping the walls of the test section according to the undisturbed streamlines around an infinitely long yawing wing of the same cross section working in infinite flow at  $\alpha = 0^\circ$  angle of attack.

The straight wing and swept wing chordwise pressure distributions  $C_p$  versus  $x/c$  are shown in Figures 70 and 71.

(E) Measurements and Evaluation

(1) Investigation of the Sound Field in the Wind Tunnel Test Section

The sound field in the wind tunnel test section was determined under various conditions by traversing one of the WEAL condenser microphones on a rail-mounted carriage which traveled longitudinally along the tunnel from behind the wing trailing edge to a point in front of the leading edge of the model. This microphone was flush-mounted on a laminar flow body of revolution of two

(1) Investigation of the Sound Field in the Wind Tunnel  
Test Section (continued)

inches diameter and twenty inches length. Laminar flow on the microphone body was verified by stethoscope and hot wire observations. The microphone was located 7.5 inches downstream of the nose of the microphone body. The sound pressure in the test section of the wind tunnel was recorded in the presence of longitudinal and transverse sound of discrete frequencies and with various bands of white sound at several distances from the model and tunnel floor and at different tunnel speeds (including zero). The microphone output was measured by a General Radio Company or a Brüel and Kjaer level recorder and was recorded on an oscilloscope and on magnetic tape.

The first sound measurements during the swept wing investigation were conducted with the acoustical lining in the test section extending upstream to the beginning of the wind tunnel nozzle. In this condition strong fluctuations of the sound pressure in spanwise and chordwise direction were observed on the front part of the wing, indicating the presence of strong standing sound waves between the tunnel walls. In order to minimize these standing waves, the acoustical lining was extended further upstream into the wind tunnel nozzle as far as practical (Figures 66 and 69).

The reference sound pressure was measured by means of a second WEAL condensor microphone, which was flush-mounted on a laminar flow body of revolution. For the straight wing test the reference microphone was located opposite 69 percent chord, 25 inches above the tunnel floor and seven inches from the wing surface. The reference microphone for the swept wing was located opposite the 15.6 percent chord station, with reference to the wing section at the center-line of the measuring region, at a distance of 7-1/8 inches from the wing surface and 25 inches above the floor of the wind tunnel test section. Ideally, the sound pressure should be measured as closely as possible to the model to minimize errors due to standing waves between the model and the side walls of the tunnel. However, in such a close vicinity to the model, the microphone body would induce a disturbance flow field of sufficient magnitude to cause non-uniform local suction and premature transition.

Both the reference microphone and the movable microphone were calibrated in the anechoic chamber of WEAL and were frequently checked during the experiments with the aid of a calibration coupler. The microphone signal was read through a WEAL microphone amplifier complement and voltmeter.

The flush-mounted microphone recorded, in addition to the external sound, pressure fluctuations in the laminar boundary layer on the microphone body caused by boundary layer oscillations. In order to obtain an idea about the corresponding possible error in the sound pressure measurement, the velocity fluctuations in the laminar boundary layer of the microphone body were recorded for several cases by means of hot wires. The velocity fluctuations observed at the reference microphone location were considerably larger than those due to the external sound alone. For this reason the somewhat higher sound pressure recorded by the reference microphone is generally attributed to the presence of boundary layer oscillations on the microphone body. For the evaluation of the sound experiments the error in the measurement of the reference sound pressure caused by laminar boundary layer oscillations on the reference microphone body was neglected.

(1) Investigation of the Sound Field in the Wind Tunnel Test Section (continued)

In order to investigate to which degree two-dimensional sound fields were obtained in the test section with the individual sound sources, the components in x-, y- and z-directions,  $u'$ ,  $v'$  and  $w'$ , of the sound particle velocity in the wind tunnel test section were measured by means of hot wires under different conditions at both the edge of the boundary layer on the swept wing and one inch off the reference microphone body. V-wires were used for the measurement of  $v'$  and  $w'$ . At the same time a comparison could be made with the sound pressure as recorded with the reference microphone by adding vectorially the three components  $u'$ ,  $v'$  and  $w'$  of the sound particle velocity, assuming that they were in phase and that the sound waves were plane. Longitudinal as well as transverse sound waves of discrete frequencies and various bands of white noise were investigated.

For the evaluation of the ratio of the signal of the external sound to the noise of the disturbances from tunnel turbulence and tunnel noise, the latter were measured at different tunnel speeds by means of a hot wire and microphone. Figure 72 shows a plot of the tunnel turbulence  $u'/U_\infty$  versus undisturbed velocity  $U_\infty$  of the Norair 7- by 10-foot low turbulence tunnel.\*  $u'$  is the rms turbulent velocity fluctuations in the wind tunnel test section. The same figure presents a plot of the sound pressure of the tunnel (expressed in decibels and as a ratio of sound particle velocity to tunnel velocity, assuming plane sound waves) for various tunnel speeds.

(2) Standard Measurements on Low Drag Suction Wings and Their Evaluation

The following standard measurements were taken at various wing chord Reynolds numbers with external and internal sound of discrete frequencies and different bands of white noise and with panel vibration:

- (a) Static pressure distribution on the external wing surface by means of 0.020-inch diameter static pressure orifices;
- (b) Static pressures in the individual suction chambers by means of static pressure orifices;
- (c) Suction flow quantities in the individual suction chambers as evaluated from the pressure drop across calibrated flow measuring nozzles connected to the individual suction chambers;
- (d) Boundary layer profile at the wing trailing edge by means of a boundary layer total pressure rake and a local static pressure tube;
- (e) Boundary layer profiles at various chordwise stations by means of hot wires.

\*A more detailed description of the Norair 7- by 10-foot low-turbulence wind tunnel is given in Reference 14.

(2) Standard Measurements on Low Drag Suction Wings and Their Evaluation (continued)

The wake drag coefficient  $C_{D_w}$  was determined according to Squire and Young from the measured boundary layer momentum thickness at the wing trailing edge. The coefficient  $C_{D_s}$  of the equivalent suction drag to accelerate the suction air isentropically to freestream velocity was evaluated from the static pressures and the suction quantities in the various individual suction chambers. The coefficient  $C_{D_\infty}$  of the equivalent wing profile drag is, then, the sum of  $C_{D_w}$  and  $C_{D_s}$ :

$$C_{D_\infty} = C_{D_w} + C_{D_s}$$

where

$$C_{D_w} = \frac{2\theta}{c} = \frac{2}{c} \theta_{TE} \left( \frac{U_{TE}}{U_\infty} \right)^{\bar{H}+2}_{wake}$$

Index TE refers to the trailing edge station and  $\infty$  to the location at infinity.

$$\bar{H}_{wake} = \frac{H_{turbTE} + H_\infty}{2}$$

With  $H_{turbTE} = 1.4$  and  $H_\infty = 1$ :

$$C_{D_w} = \frac{2}{c} \theta_{TE} \left( \frac{U_{TE}}{U_\infty} \right)^{3.2};$$

$$C_{D_s} = \sum_{\text{all chambers}} C_{Q_i} C_{p_{g_i}}, \quad C_Q = \sum_{\text{all chambers}} C_{Q_i}$$

with

$$C_{Q_i} = \frac{Q_{a_i}}{U_\infty bc}, \quad C_{p_{g_i}} = 1 - \frac{p_{a_i} - p_\infty}{q_\infty}$$

i refers to each individual suction chamber.

In order to obtain a better understanding of the mechanism of transition on a swept low drag suction wing under the influence of external sound, the state of the boundary layer and location of transition were observed under different conditions by means of microphones, connected to the wall static pressure orifices, and by spraying the test surfaces with naphthalene. The latter sublimates at a much faster rate in the presence of a turbulent boundary layer

(2) Standard Measurements on Low Drag Suction Wings and Their Evaluation (continued)

with its high surface shear stress as compared to a laminar boundary layer. As a result, the laminar areas appear white in contrast to the clear areas where the boundary layer is turbulent.

During the first phase of the experiments the critical sound pressure level at which transition occurred was determined for various conditions. For example, at a given wing chord Reynolds number and chordwise suction distribution the sound pressure level, for a certain sound frequency, was slowly increased until transition was observed. In other cases, when transition occurred under the influence of external sound, internal sound or panel vibration, suction was increased as a whole or locally upstream of the transition region until full chord laminar flow was re-established. Furthermore, under otherwise the same conditions, the frequency of the disturbance was varied. The influence of surface disturbances such as open static pressure orifices, etc., in the presence of sound was investigated.

(3) Measurements of the Velocity Fluctuations in the Laminar Boundary Layer in the Suction Area in the Presence of External Sound

In order to investigate whether or not transition under the influence of external sound was caused by amplified boundary layer oscillations, the velocity fluctuations  $u'$  and  $w'$  in the laminar boundary layer of the test area of the swept wing were measured at  $R_c = 8.1 \times 10^6$  at several chordwise stations ( $x/c = 0.37, 0.44, 0.45, 0.58$  and  $0.90$ ) with sound of various discrete frequencies and with white noise of different frequency bands by means of hot wires. The sound pressure level and chordwise suction distribution were varied. Since amplified oscillations in the boundary layer of a swept laminar suction wing can develop under the influence of external sound both in tangential and crossflow directions, the velocity fluctuations in the boundary layer were measured in tangential as well as in crossflow direction by means of ordinary  $u'$ -wires and  $V$ -wires, respectively. The hot wires used were platinum wires of 0.05-inch length and 0.00015-inch diameter for the straight wing and platinum iridium wires of 0.1-inch length and 0.00028-inch diameter for the swept wing. The velocity fluctuations  $u'$  and  $w'$  in the boundary layer were evaluated from King's equation for the rate of heat loss from heated wires in an airflow (Reference 85). The wires were calibrated in a 4- by 4-inch low-turbulence tunnel, and the hot wire data were recorded with a modified four-channel Tele-Wright hot wire set. Preceding quantitative hot wire readings, a series of oscilloscope pictures were taken at various chordwise locations in the boundary layer of the test wing for different suction distributions and external sound fields on the swept wing.

On both models, strong velocity fluctuations were observed in the laminar boundary layer of the test wing at low frequencies below 30 cps. These low frequency fluctuations, which have no apparent effect on the laminar boundary layer, may have been caused by unsteady flow in the first wind tunnel diffuser and upstream of the wind tunnel fan. During the hot wire measurements in the boundary layer, these low frequency oscillations were filtered out. High frequencies (above 4800 or 10,000 cps) that were predominantly amplifier noise were also filtered.



## (F) Results and Discussion

### (1) Sound Field in the Wind Tunnel Test Section

The sound field in the wind tunnel test section was investigated with the swept wing installed. Figure 73 shows a typical plot of the sound pressure, as measured with a traveling WEAL condenser microphone, along the tunnel axis at the height of the centerline of the swept wing model at a distance of six inches from the maximum thickness of the model. The plotted circles show the comparison values of the hot wire measurements at one inch above the wing surface where the components of  $u'$ ,  $v'$  and  $w'$  were combined, assuming that all components are in phase. The double circle represents the reading on the reference microphone. Longitudinal and transverse sound of discrete frequencies and with a continuous spectrum of different frequency bands was applied.

The mean sound pressure on the model, as measured with the traveling microphone at the centerline of the model, was generally slightly higher than the corresponding reading of the reference microphone, especially with longitudinal sound. At the higher tunnel speeds and wing chord Reynolds numbers the variation of the sound pressure along the tunnel axis was small with transverse sound of discrete frequencies and with a continuous spectrum. With longitudinal sound the sound pressure often decreased slowly in downstream direction from the leading edge toward the trailing edge of the model, particularly at the lower frequencies, probably caused by the attenuation of sound waves, reflected from the tunnel walls and the model, in the acoustical lining of the test section.

The periodic variations of the sound pressure observed with the traveling microphone were probably caused by standing sound waves between the walls of the test section and the model. At lower tunnel speeds and wing chord Reynolds numbers these periodic variations of the sound pressure became much more pronounced, and vice versa.

Similar chordwise traverses of the sound field at various heights in the wind tunnel test section as well as at other distances from the model showed similar fluctuations of the sound pressure in the wind tunnel test section in vertical and horizontal directions. These fluctuations of the sound pressure also probably resulted from standing sound waves between the tunnel walls and the model.

It thus appeared that the formation of standing sound waves in the test section caused considerable fluctuations of the sound pressure in the test region, especially at the lower sound frequencies. The question then arose as to which sound pressure reading should be used for the evaluation and analysis of the experimental data. Ideally, for the analysis of the data, the sound pressure somewhat upstream of the transition region close to the model would have been most meaningful. Transition, according to naphthalene sublimation observations, generally occurred in the region of the flat pressure distribution of the swept wing in spanwise areas where the sound pressure was highest. For this reason an attempt was first made to correlate the data with the local sound pressure in the transition area with various external sound fields. Since the spanwise and chordwise positions of transition with these different sound fields varied considerably, an excessively large number of chordwise sound traverses would have been required to determine accurately the sound pressure



(1) Sound Field in the Wind Tunnel Test Section (continued)

in and upstream of the transition area for these varied conditions. In view of these difficulties, this attempt was finally abandoned, and the sound pressure at the reference microphone was used for the evaluation and analysis of the experimental data.

The agreement between the sound pressure as measured with the traveling microphone and evaluated from hot wire measurements of the sound particle velocity components  $u'$ ,  $v'$  and  $w'$  was generally satisfactory with transverse sound (white noise and sound of discrete frequencies) and with longitudinal white sound. With longitudinal sound of discrete frequencies the agreement was less satisfactory at 800 cps.

(a) Critical Sound Pressure and Sound Particle Velocity Ratio  $(u'/U_\infty)_{crit}$  at Transition under Various Conditions

With optimum suction for minimum drag external sound caused transition on the straight laminar suction wing at rather low sound pressures (108 db at  $R_c \approx 20 \times 10^6$  and  $C_Q = 1.1 \times 10^{-4}$ ). The critical sound pressure for transition could be raised to considerably higher values by increasing suction either as a whole by raising the level of suction or by increasing the suction locally in the areas where transition occurred. For example, by increasing suction from  $C_Q = 1.1 \times 10^{-4}$  to  $1.8 \times 10^{-4}$  at  $R_c = 20 \times 10^6$  raised the critical sound pressure to over 130 db. A definite dependence of the transition on the frequency of the acoustic disturbance was apparent on the straight wing. Figures 74 to 77 graphically illustrate this dependence. These figures show the required suction distribution without external sound and the additional increments of suction required to re-establish laminar flow in the presence of strong external sound fields of various frequencies. For example, on these figures, the 600/1200 octave band of random noise input needed additional suction in the forward part of the wing to maintain full chord laminar flow; the 300/600 suction increment needed an increase through the midportion of the wing; while suction had to be increased primarily in the rear part of the wing with white noise of 150/300 cps. Similarly, the discrete sound frequencies on Figure 76 show the same pattern where the lower sound frequencies required additional suction to the rear and the higher frequencies required additional suction forward for the maintenance of full chord laminar flow. From this data the conclusion is drawn that the forward, middle and aft portions of the wing are more sensitive to frequencies in the 800, 400 and 200 cycle range, respectively. It appears that transition occurred at particularly low critical sound pressures when the sound frequencies correlated with the frequencies for amplified chordwise boundary layer oscillations.

In Figures 78 to 82  $(u'/U_\infty)_{crit}$  at transition is plotted versus sound frequency for a given Reynolds number to show the effect of suction level on transition with external sound. The crossed line represents the maximum sound pressure field available so that a point on the crossed line indicates that there was no transition up to the maximum available sound pressure level. To obtain these data, the suction distribution was first set at the required level for no transition at the maximum sound field for each of the frequencies at the stated Reynolds number. Then, the suction level was reduced in steps to the

(a) Critical Sound Pressure and Sound Particle Velocity Ratio  $(u'/U_\infty)_{crit}$  at Transition under Various Conditions (continued)

minimum value for full chord laminar flow. The great improvement in value of  $(u'/U_\infty)_{crit}$  for transition at 800 cps with higher forward suction (run 129) compared to run 117 (Figure 73 ) again supports the earlier observation that sound of 800 cps would be critical forward. Again, in Figure 81 a suction increase in the front part of the wing raised the critical sound particle velocity ratio  $(u'/U_\infty)_{crit}$  for transition progressively with increasing sound frequency.

Figures 83 and 84 illustrate the increase in total suction quantity and equivalent wing profile drag for the 17-foot chord, 4-percent-thick wing with full chord laminar flow in the presence of external sound of increasing sound pressure and sound particle velocity. These two figures show that the increase in suction and the corresponding equivalent wing profile drag required to maintain full chord laminar flow on a thin straight laminar suction wing were not unreasonable in the presence of strong external sound fields.

The increase of the equivalent wing profile drag  $C_{D_\infty}$  at increasing sound pressure level with the suction quantity held constant was also investigated. Figures 85 to 88 show the variation of  $C_{D_\infty}$  versus  $u'/U_\infty$  for several external sound frequencies. In general, the equivalent wing profile drag approximately doubled for a value of  $u'/U_\infty$  equal to twice the value at initial drag rise. The initial drag rise for a given frequency was strongly influenced by the suction distribution and level. For example, on Figure 87 the substandard amount of suction on chamber number 9 (45 to 52 percent chord) led to early transition for 442 and 300/600 cps, some transition for 150/300 cps, but no transition at 660, 810 or 600/1200 cps. Here again, a frequency dependence of amplified oscillations corresponding to stability theory is evident in that the 300/500 cps disturbances were amplified in this region of the wing while disturbances of higher and lower frequencies were amplified less or not at all. This example emphasizes the need of providing adequate suction along the entire wing chord when external disturbances from sound and other sources cover a wide range of frequencies.

A set of runs where only the forward static pressure orifices were sealed at the surface, with the rear static pressure orifices still open at the wing surface\* (Figure 88 ), brings out another interesting point. In this instance the two suction distributions tested corresponded to the same total suction quantity,  $C$ , but the distribution of suction for runs 65 to 69 was lower from 20 to 40 percent chord and higher from 40 to 80 percent chord than runs 60 to 64. These data show that the drag rise due to premature transition in the presence of sound was delayed to higher sound pressure levels when suction was relatively higher in the region of the open wing surface static pressure orifices. Suction was, then, beneficial to the maintenance of laminar flow in the presence of the disturbance caused by the interaction between a strong external field and open static pressure orifices.

---

\*Airtight otherwise.

(a) Critical Sound Pressure and Sound Particle Velocity Ratio  $(u'/U_\infty)_{crit}$  at Transition under Various Conditions (continued)

A correlation for the straight wing of  $(u'/U_\infty)_{crit}$  versus  $C_Q$  for all octave band noise data under the influence of external sound is presented in Figure 89. The slope of the straight lines  $(\frac{\partial u'_{crit}/\partial U_\infty}{\partial C_Q})$  is equal to approximately 48 for all three octave bands. The white noise data were chosen for the correlation because the corresponding sound field was more uniform over the model than with sound of discrete frequencies.

(3) Variation of the Critical Sound Pressure for Transition on a Swept Laminar Suction Wing under Various Conditions

(a) Influence of Sound Frequency on Transition

Figures 90 and 91 show the variation with sound frequency of the critical sound pressure and the corresponding values for the critical sound particle velocity ratio  $(u'/U_\infty)_{crit}$  (assuming plane sound waves) for the start of transition in the presence of longitudinal and transverse sound of various discrete frequencies and bands of white noise at several wing chord Reynolds numbers. "Minimum" suction, closely corresponding to the optimum suction distribution for minimum drag in the absence of external sound, was applied in most cases shown in Figures 90 and 91 ( $C_Q \approx 3.5 \times 10^{-4}$  to  $3.70 \times 10^{-4}$ ). Slightly increased suction rates ( $C_Q \approx 3.70 \times 10^{-4}$  to  $3.9 \times 10^{-4}$ ) correspond to low suction, and still stronger suction ( $C_Q \approx 4.2 \times 10^{-4}$ ) is designated as medium suction. The first fifteen surface static pressure orifices up to the beginning of the rear pressure rise were sealed when the experiments with the transverse sound generated by loudspeakers started. The remaining static pressure orifices in the region of the rear pressure rise were sealed during run 46 and were kept sealed for the remaining part of the investigation. During part of the runs, suction was applied through all slots from 0.5 to 97 percent chord. Since no suction was really required in the front part of the swept suction wing at the test wing chord Reynolds numbers up to  $R_c \approx 11 \times 10^6$ , no suction was applied during part of the runs in some of the front slots. These slots were then either sealed with clay or purposely left open (see notes on Figures 90 and 91). Test runs 47a, 48a and 49 were conducted in the presence of small pinholes in an imperfectly sealed front slot.

At higher sound frequencies the maximum sound power of the speakers and of the transducers was limited, and the sound wave became increasingly distorted at these higher sound power levels at high frequencies. For this reason reliable data for the critical sound pressure level could not be established on the smooth wing at sound frequencies beyond 1500 cps with sound of discrete frequencies, particularly with increased suction rates. On the smooth wing full chord laminar flow could generally be maintained at these higher sound frequencies up to the maximum available sound power level.

(a) Influence of Sound Frequency on Transition (continued)

In the presence of longitudinal and transverse sound of discrete frequencies the critical sound pressure on the smooth wing at wing chord Reynolds numbers of  $8 \times 10^6$  to  $11.5 \times 10^6$  decreased from a value of 125 to 130 db at low sound frequencies (below 1000 cps) to approximately 120 to 125 db at higher sound frequencies (1000 to 1500 cps). With white noise the critical sound pressure level decreased slightly at the higher frequency ranges. At  $R_c \approx 10^7$  the minimum critical sound pressure was usually observed in the 1200/2400 cps frequency band with longitudinal as well as transverse sound. On the smooth wing with minimum suction, transition with white noise in the 1200/2400 cps frequency range started at a sound pressure of 120 to 125 db, with suction applied either through all slots or from 15 to 96 percent chord and with the nonsucking front slots carefully sealed. The frequency range of 1200/2400 cps correlates with that for amplified chordwise boundary layer oscillations in the front part of the wing. Contrary to the straight wing results and to ordinary boundary layer stability theory, which would predict a frequency dependence of the critical sound pressure, the relatively small variation of the critical sound pressure and  $(u'/U_\infty)_{crit}$  with sound frequency on the smooth swept wing was somewhat unexpected.

Figures 92 and 93 show the only case where transition on the swept wing due to external sound could be correlated with the Tollmien-Schlichting stability theory of the tangential boundary layer flow in a similar manner as on a 17-foot chord straight laminar suction wing. Suction was applied over the rear half of the wing chord only, and the front half of the wing with the suction slots was covered with paper. Under such conditions the instability of the tangential component of the boundary layer becomes critical in the front nonsuction area of the wing at somewhat lower Reynolds numbers ( $R_c \leq 7 \times 10^6$ ). The instability of the boundary layer crossflow component becomes rapidly less critical at these low wing chord Reynolds numbers. Figure 92 illustrates, at a wing chord Reynolds number  $R_c = 7 \times 10^6$ , a strong reduction of the critical sound pressure at sound frequencies of 400 to 850 cps, corresponding to the frequency range for amplified Tollmien-Schlichting oscillations at 50 percent chord. At 600 cps transition was observed at quite low sound pressures (109 db). Figure 93 presents the correlation of the observed critical sound frequencies with the frequencies of amplified Tollmien-Schlichting oscillations of the tangential component of the boundary layer at the midchord station.

Under marginal conditions, for example, with marginal suction rates, particularly in the front half of the wing, at higher wing chord Reynolds numbers, the critical sound pressure for transition dropped considerably. Figures 90 and 91 illustrate the variation of the critical sound pressure with sound frequency at  $R_c = 11.2 \times 10^6$ \* with marginal suction rates in the most critical part of the wing slightly below the minimum suction distribution in the absence of sound as well as with increased suction rates closer to the optimum distribution. With marginal suction transition occurred at approximately 5 db lower sound pressure levels, as compared with the case of the more optimum suction distribution.

\*The maximum wing chord Reynolds number with full chord laminar flow on the  $30^\circ$  swept laminar suction wing mounted in the smooth test section of the Nasa 7- by 10-foot tunnel was  $1.3 \times 10^6$ .

(b) Influence of Suction Quantity and Chordwise Suction Distribution on the Swept Wing

In order to investigate the influence of suction in the region of the flat pressure distribution, where transition started, a series of runs (Figure 94) were conducted varying the suction quantity in chamber 8 ( $x/c = 0.33$  to  $0.41$ ) from zero to high suction in the presence of longitudinal and transverse sound of 800 cps. The critical values  $(u'/U_\infty)_{crit}$  for various suction quantities in chamber 8 are shown in Figure 94, indicating a rapid increase of  $(u'/U_\infty)_{crit}$  with the suction quantity in chamber 8.

A corresponding sequence increasing suction as a whole over the entire wing chord is shown in Figure 95. The wing chord Reynolds number was  $R_c = 5.8 \times 10^6$ . Some of the front slots were imperfectly sealed (pinholes).  $(u'/U_\infty)_{crit}$  increases with larger suction quantities at a relatively slow rate, and quite large suction quantities were required to maintain full chord laminar flow at higher sound pressure levels, as compared with the case when suction was increased only locally in the region of the flat pressure distribution where transition started. Figure 96 shows, as an example, the variation of the critical sound particle velocity ratio at  $R_c = 4.1 \times 10^6$  with increasing suction in the forward region of the flat pressure distribution, with the suction distribution in the region of the rear pressure rise held constant (static pressure orifices open).

Another increasing overall suction level sequence at  $R_c = 8 \times 10^6$  and the corresponding critical sound particle velocity ratios  $(u'/U_\infty)_{crit}$  at transition for the smooth wing are shown in Figure 97. Even a 45 percent increase in overall suction did not prevent transition at all frequencies below the maximum available sound level. Insufficient suction was applied in the forward chambers to avoid transition. The importance of raising the suction rates in the region of the flat pressure distribution upstream of the 60 percent chord station and the inefficiency of an overall suction increase previously encountered (Figures 95 and 97) is confirmed in Figures 98 and 99. Run 130 (Figure 98) represents the minimum amount of suction for full chord laminar flow without sound. At  $R_c = 9.8 \times 10^6$  this suction distribution is adequate to maintain full chord laminar flow at  $(u'/U_\infty)_{crit} = 10 \times 10^{-4}$ . In order to increase the critical sound particle velocity ratio to  $(u'/U_\infty)_{crit} = 25 \times 10^{-4}$ , suction in the front part of the wing had to be raised such that the total suction quantity was increased by 15 percent, as compared to more than 41 percent when suction was raised as a whole over the entire wing chord. A comparison of the top and lower suction distribution plots (Figure 98) shows even more clearly that the critical sound pressure and the corresponding ratios  $(u'/U_\infty)_{crit}$  depend essentially only on the suction rates ahead of the 60 percent chord station. For example, runs 128 and 131 showed approximately the same critical sound pressure level when their suction rates  $v_o^*$  ahead of 60 percent chord were practically the same. In Figure 99 suction was first set for no transition without sound (run 82) and then increased to a level required for transition with maximum sound (run 86). In order to maintain full chord laminar flow at  $R_c = 11.5 \times 10^6$  with the

(b) Influence of Suction Quantity and Chordwise Suction Distribution on the Swept Wing (continued)

maximum external sound field (run 86), suction upstream of the 60 percent chord station had to be increased by 49 percent. This increase represents but a small percentage of the total suction quantity.

Summarizing, on the swept wing the critical sound pressure and the corresponding sound particle velocity ratio  $(u'/U_\infty)_{crit}$  could generally be increased to the maximum available level by increasing the suction quantities either as a whole over the entire wing chord or locally in the critical area of the flat pressure distribution, where transition otherwise occurred. From the standpoint of total suction quantity and wing profile drag it was much more economical to increase suction locally in the critical region of the flat pressure distribution. As an example, the critical sound pressure at transition could be increased by approximately 8 to 10 db with a 15 percent larger suction quantity when suction was locally increased in the most critical area, with an increase in wing profile drag of approximately 5 percent.

At the higher wing chord Reynolds numbers increased suction had to be applied, particularly to the forward part of the swept wing, to reduce the growth of boundary layer oscillations in the area of the flat pressure distribution and thus to delay transition to higher sound pressures.

(c) Influence of Wing Chord Reynolds Number on the Swept Wing

Figures 100 and 101 show, in log-log plots, the variation of the critical sound particle velocity ratio  $(u'/U_\infty)_{crit}$  at transition with wing chord Reynolds number under various conditions (smooth model without surface cavities with minimum and increased suction as well as with open static pressure orifice holes and nonsucking open slots in the front part of the wing). For minimum suction the critical sound pressure level at transition generally increased slightly with increasing wing chord Reynolds number. The corresponding critical sound particle velocity ratio  $(u'/U_\infty)_{crit}$  then decreased at a somewhat slower rate than inversely proportional to the wing chord Reynolds number.

The reduction of the critical sound pressure and  $(u'/U_\infty)_{crit}$  for transition with open surface cavities such as static pressure orifices, imperfectly sealed slots with pinholes, nonsucking open slots, etc., was generally observed over the whole test Reynolds number range up to  $R_c = 12 \times 10^6$  except at the lowest test Reynolds numbers,  $R_c \leq 4 \times 10^6$  (Figures 100 and 101).

(4) Critical Sound Pressure for Transition with Open Surface Cavities on Both Straight and Swept Wings

During the experiments premature transition under the influence of external sound was often observed downstream of open surface cavities such as static pressure orifices, nonsucking slots or imperfectly sealed suction slots. Leakage of air from these cavities to the external surface was prevented, and full chord laminar flow was achieved without external sound. In the presence of strong external sound, according to naphthalene sublimation studies, turbulent wedges

(4) Critical Sound Pressure for Transition with Open Surface Cavities on Both Straight and Swept Wings (continued)

were observed downstream of static pressure orifices and pinholes in an imperfectly sealed slot. When the static pressure orifices and nonsucking slots were properly sealed at the wing surface such local turbulent wedges did not develop. The straight wing values of  $(u'/U_\infty)_{crit}$  for transition are shown in Figure 82

for the case where individual static pressure orifices were open at the surface but sealed at the manometer end of the pressure line. With the orifices sealed at the surface and the same suction applied, no transition existed at the maximum sound pressure. The  $-\Delta u'/U_\infty$  ordinate (Figure 82) represents the decrease in  $(u'/U_\infty)_{crit}$  due to opening a static pressure orifice. Figure 82 shows that the 15 percent chord orifice location was least sensitive and the 46 percent chord orifice was most sensitive to external sound. The suction comparison at the right of Figure 82 shows that the local suction in excess of minimum drag requirements was greatest at 15 percent chord and least at 46 percent chord. Apparently, suction was again not only beneficial to the maintenance of laminar flow with open orifices under the influence of external sound, but also explains the differences in critical disturbance velocity  $(u'/U_\infty)_{crit}$  at various chordwise orifice locations. Another important feature of Figure 82 is that transition occurred at all frequencies for each chordwise orifice location, while other transitions due to external sound have shown a frequency dependence that correlated with stability theory. Therefore, the two-dimensional small disturbance theory did not apply to the straight wing transition in the case of the interaction of the open static pressure orifice and the external sound field.\* The transition mechanism for open orifices and external sound fields was probably not associated with amplified Tollmien-Schlichting waves but a three-dimensional flow phenomena similar to that described in the chapter on internal sound (Part 9).

Figures 90 and 91 show the critical sound pressure on the swept wing at transition and the corresponding critical sound particle velocity ratio in the presence of small pinholes in an improperly sealed front suction slot with external sound of various discrete frequencies and bands of white noise (minimum suction). At  $R_c = 9.8 \times 10^6$  and sound frequencies between 1200 to 2400 cps (with white noise and sound of discrete frequencies) the critical sound pressure with this imperfectly sealed front slot was approximately 8 to 12 db lower than for the smooth model with properly sealed front slots or with suction applied through slots. Figures 90 and 91 illustrate the reduction of the critical sound pressure for various sound frequencies with some of the forward nonsucking slots open. At  $R_c = 9.8 \times 10^6$  and sound frequencies between 1200 to 2000 cps, transition was observed at 5 to 10 db lower sound pressures with the nonsucking slots open. The critical sound pressure level for transition with open surface cavities (pinholes in one of the imperfectly sealed front suction slots, nonsucking open slots in the front part of the wing) was particularly low in a range of sound frequencies which correlated with the frequencies for amplified chordwise boundary layer oscillations in the front part of the wing in the region of the open surface cavity. The smooth wing showed a considerably smaller reduction in critical sound pressure at higher frequencies as compared to the

\*At the same time, the lack of a frequency dependence indicates that the surface cavities did not act as Helmholtz resonators.



(4) Critical Sound Pressure for Transition with Open Surface Cavities on Both Straight and Swept Wings (continued)

model with open surface cavities (Figures 90 and 91). The only example when transition was observed at low sound pressures and at rather distinct frequencies (1900 to 4500 cps) was the case when the static pressure orifices in the region of the rear pressure rise were left open (Figure 91). The remaining static pressure orifices and nonsucking slots were sealed. In this case the rear static pressure orifices may have acted like Helmholtz resonators. Closing the static pressure orifices in the region of the rear pressure rise or sucking through these orifices by lowering the reservoir of the manometer bank raised the critical sound pressure at the higher sound frequencies (between 1500 and 5000 cps) to and beyond the maximum available sound pressure.

It thus can be concluded that small open cavities on the external surface can appreciably reduce the permissible sound pressure for full chord laminar flow, even though such cavities are closed inside the wing. In order to avoid premature transition due to open surface cavities in the presence of external sound, all static pressure orifices and nonsucking slots were carefully sealed during the major phases of the investigations. Naphthalene sublimation studies were conducted to check whether or not the test surface was sufficiently smooth to prevent premature transition from surface disturbances such as surface cavities, roughness, etc. It might be suspected that other surface disturbances such as surface roughness, steps, etc., might also be more critical in the presence of strong external sound. A preliminary experiment with a relatively large surface roughness showed local transition downstream of the roughness in the presence of strong external sound. Without sound full chord laminar flow was observed. The smooth wing without roughness was laminar to the trailing edge in the presence of the external sound. This experiment indicates that the maximum permissible height of a surface roughness and possibly other surface disturbances for full chord laminar flow may be reduced by the presence of strong external sound fields.

(5) Observations of the State of the Boundary Layer and Transition with External Sound by Means of Naphthalene Sublimation Studies for Straight and Swept Wings

Figures 102 to 126 show representative naphthalene sublimation photographs of the test surface of the wing with external sound. When a saturated solution of naphthalene in petroleum ether is sprayed on the model surface, a thin white layer of naphthalene particles remains on the surface after the ether evaporates. As the air flow passes over the model the higher shear stress where the boundary layer is turbulent removes the white naphthalene powder by sublimation. The resulting development shows white areas where the boundary layer remains laminar and clear areas where the boundary layer is turbulent.

On the straight wing several attempts were made to check the nature of transition under the influence of external sound by naphthalene spray flow visualization. In general, transition on the 17-foot chord, 4-percent-thick straight wing was too gradual to obtain sharp sublimation pictures. There are, moreover, paint-filled regions on the wing opposite the joints in the under skin panels that confuse the flow visualizations. As a result of these difficulties, only a few sublimations were obtained. Figure 102 is the clearest of the flow



(5) Observations of the State of the Boundary Layer and Transition with External Sound by Means of Naphthalene Sublimation Studies for Straight and Swept Wings (continued)

visualization photographs. The flow direction over the wing is from right to left and the model spans the test section from floor to ceiling. The vertical white band adjacent to the signboard is paint filling, as is the similar spanwise band at left center. For this sublimation picture, the spray was applied from just behind the front paint stripe to the extreme left of the picture. The turbulent region is shown by the dark area extending from the center of the picture downstream (to the left). Transition for the external sound field of 125 db at 863 cps occurred at 12 percent chord with turbulent streaks about two inches apart. This forward portion of the wing had already been found to be critical to frequencies in the above 800 cycle region. The two-inch streak transition pattern corresponds to that described in Reference 38 for the laminar boundary layer breakdown on a flat plate following amplified Tollmien-Schlichting waves.

During the early phase of the swept wing experiments premature transition in the presence of external sound was often experienced in the region downstream of surface static pressure orifices or open nonsucking slots and similar surface cavities, even though leakage out of the wing surface had been prevented and no transition was observed in the absence of sound. As an example, the naphthalene sublimation pictures show turbulent wedges downstream of a static pressure orifice and a small hole in an improperly sealed slot when external sound was applied (Figures 103 and 104). Without sound these turbulent wedges did not develop. During the later stages of the investigation the critical sound pressure for transition was raised considerably by carefully sealing the surface static pressure orifices and nonsucking slots. Local surface disturbances which might cause premature transition in the presence of external sound were periodically checked by naphthalene sublimation observations and eliminated whenever they occurred.

With the swept wing model in clean condition, i.e., with the static pressure orifices and nonsucking slots sealed, the following observations were made when external sound was applied. Under the influence of longitudinal and transverse sound of discrete frequencies and different bands of white noise transition was generally observed in the region of the flat pressure distribution and at the beginning of the rear pressure rise. With moderately strong sound of discrete frequencies the naphthalene pictures (Figures 105 to 114) show that transition in this case was often preceded by the formation of chordwise striations of one-eighth to one-tenth of an inch spacing. These striations became rapidly more pronounced in downstream direction until transition started. Their location varied for different sound inputs and frequencies. Figure 105 [run 292, transverse sound (speakers) of 127 db sound pressure and 200 cps at  $R_c = 4.1 \times 10^6$ , striations between 45 and 49 percent chord]; Figure 106 [run 315, transverse sound (speakers) of 121 db and 365 cps at  $R_c = 5.8 \times 10^6$ , striations between 46 and 50 percent chord]; and Figure 107 [run 304, transverse sound (speakers) of 129.5 db and 667 cps at  $R_c = 5.8 \times 10^6$ , striations between 63 and 67 percent chord] are examples of the striation pattern in the midchord region of the wing.\* The

\*The persistence of some naphthalene downstream (left) of the transition region in Figure 105 is due to the establishment of a laminar sublayer in the turbulent boundary layer and should not be misinterpreted as a return to laminar flow.

(5) Observations of the State of the Boundary Layer and Transition with External Sound by Means of Naphthalene Sublimation Studies for Straight and Swept Wings (continued)

striations were usually more clearly defined at lower Reynolds numbers, between  $R_c = 6 \times 10^6$  to  $8 \times 10^6$ ; they were observed, however, up to the maximum test Reynolds number of  $12 \times 10^6$ . The existence of striations at other spanwise locations is illustrated in Figure 108 [run 286, longitudinal sound (transducer) of 133 db and 400 cps at  $R_c = 4.1 \times 10^6$ , transition at 46 percent chord in the upper and at 49 percent chord in the lower part of the wing, respectively].

The striations and transition probably developed first in a spanwise area of maximum sound output. Figures 105, 108, 113 and 114 show quite different transition locations, depending on the external sound field.

The longest striations, of 11 percent chord length, are recorded in Figure 109 [run 290, transverse sound (speakers) of 125 db and 400 cps at  $R_c = 4.1 \times 10^6$ , striations between 45 and 56 percent chord].

Without external sound full chord laminar flow was maintained with the front slots open but without suction. In the presence of external sound, however, striations and transition were observed quite far forward on the wing, as illustrated in Figure 110 (run 447, longitudinal sound of 128.5 db and 1000 cps at  $R_c = 8.1 \times 10^6$ , transition at 9 percent chord) and Figure 111 & 112 [run 999, transverse sound (transducer) of 130 db and 1000 cps at  $R_c = 8.1 \times 10^6$ , transition at 34 percent chord]. The most rearward location of transition caused by chordwise striations are presented in Figure 113 (run 474, longitudinal sound of 130 db and 1000 cps at  $R_c = 8.1 \times 10^6$ , transition at 68 percent chord) and Figure 114 (run 460, longitudinal sound of 134.5 db and 781 cps at  $R_c = 8.1 \times 10^6$ , transition at 70 percent chord).

The observed striations closely resemble those observed by the British (References 87 and 89) and later by NASA Ames in the front part of swept wings at high Reynolds numbers. Without external sound full chord laminar flow existed without striations within the test Reynolds number range. It thus appears that transition in the region of the flat pressure distribution on a swept laminar suction wing under the influence of external sound of discrete frequencies was often preceded and probably caused by the development of closely spaced stationary chordwise disturbance vortices which apparently cause the observed striations.

In many cases, especially with strong sound fields of higher frequencies (800 to 1000 cps at  $R_c = 8.2 \times 10^6$  and sound pressures above 130 db) and with relatively weak suction in the front part of the wing, rather regularly spaced turbulent wedges, or stripes, of approximately three-quarters-inch spanwise spacing developed in the transition area (Figures 114 to 119). The stripes bear a marked resemblance to the ultimate breakdown of two-dimensional flow on the straight wing, Figure 102. The stripes were particularly well developed at sound frequencies which roughly coincided with the frequencies for amplified oscillations in the tangential boundary layer flow upstream of transition, i.e., with increasing wing chord Reynolds numbers, these stripes were generally more

(5) Observations of the State of the Boundary Layer and Transition with External Sound by Means of Naphthalene Sublimation Studies for Straight and Swept Wings (continued)

pronounced at the higher sound frequencies, and vice versa. A series of runs at increasing sound pressure levels of 125, 127, 130 and 133 db with the longitudinal transducer sound source at 800 cps and  $R_c = 8.1 \times 10^6$  with transition at 50, 49, 48 and 44 percent chord, respectively, are shown on Figures 115 to 118. Coexistent stripes and striations are shown in Figure 119 (longitudinal transducer, 134 db, 785 cps,  $R_c = 8.1 \times 10^6$ , striations at 63 to 66 percent chord above, stripes at 44 to 49 percent chord below, run 335). This stripe pattern transition on the swept wing is not fully identical, however, to the straight wing transition because the stripes were preceded by chordwise striations of one-eighth to one-tenth inch spanwise spacing (Figure 112), indicating the simultaneous existence of closely spaced chordwise disturbance vortices.

Under the influence of external sound, according to transition observations by means of naphthalene sublimation studies and hot wire measurements, transition started in the swept wing boundary layer at a considerable distance from the wing surface when transition resulted from the instability of boundary layer crossflow. In other words, transition due to boundary layer crossflow instability occurred somewhat earlier in the outer regions of the boundary layer than the naphthalene sublimation pictures would indicate. This same observation was previously made during the first low drag suction experiments on the same 30° swept low drag suction wing in the Michigan 5- by 7-foot low-turbulence wind tunnel (Reference 69). Similarly, on a rotating disc, where transition is caused by the instability of boundary layer crossflow, the second author observed the beginning of transition (by means of stethoscope) at a considerable distance from the wall. The start of transition in a crossflow boundary layer at such relatively large distances from the wall is probably a result of the strong amplification of boundary layer oscillations in the critical layer of the crossflow boundary layer in the vicinity of the inflection point of the crossflow profile (Reference 6).

Transition usually was not observed on the swept wing in the region of the rear pressure rise in the presence of external sound, except at high sound frequencies (3500 to 4000 cps) with the rear surface static pressure orifices open, or with marginal suction in the region of the rear pressure rise when premature transition in the rear part of the wing had already occurred without sound. When suction between 63 and 72.5 percent chord was considerably reduced below the minimum for full chord laminar flow, transition occurred between 90 and 94 percent chord both with and without external sound (Figure 124). In this case transition in the rear part of the swept wing was not appreciably affected by the external sound field.

With optimum suction for minimum drag, regular chordwise streaks of approximately one-third to one-half inch spanwise spacing at  $R_c = 8.1 \times 10^6$  and  $5.8 \times 10^6$ , respectively, were observed between the wing trailing edge and approximately the 75 percent chord station (Figures 120 and 121). These streaks developed with and without external sound on the swept wing but were not observed on the straight wing. No external sound field was applied for Figure 122. With increasing sound pressure there was a tendency for turbulent wedges to develop from the more pronounced streaks (Figures 120

(5) Observations of the State of the Boundary Layer and Transition with External Sound by Means of Naphthalene Sublimation Studies for Straight and Swept Wings (continued)

and 121). At 121 db (Figure 123) striations and transition occurred around 50 percent chord in the center of the wing, while the one-half inch spaced streaks are still visible in the upper portion of the wing. With increased suction in the region of the rear pressure rise the streaks disappeared.

Transition with white sound occurred without developing any chordwise striations or regularly spaced turbulent wedges. For example, Figure 125 shows a naphthalene sublimation picture for the swept wing with longitudinal sound of 300/600 cps and 129.5 db sound pressure (run 310) at a wing chord Reynolds number  $R_C = 5.8 \times 10^6$ . Transition occurred at 63 percent chord.

Under certain conditions transition occurred in a different manner, as discussed previously. The naphthalene sublimation picture, Figure 126, shows chordwise striations of one-quarter inch spacing between 6 and 9 percent chord originating from the location of the suction holes in the inner wing skin located directly underneath the third suction slot at the 5 percent c chord station. Transverse sound of 800 cps and 134 db sound pressure was applied at  $R_C = 8.1 \times 10^6$ . No suction was applied through the forward slots, which were left open. The transition pattern was probably caused by the action of intermittent in and out flow of the suction holes from the chamber underneath. When the suction holes were displaced in chordwise direction with respect to the corresponding slot, no striations were observed downstream of these holes in the presence of sound. This appears to duplicate the effect recorded with strong internal sound fields on Figures 149 to 152 and discussed in the chapter on internal sound (Part 9).

(6) Hot Wire Observations on the Straight Wing

Although voltmeter readings were often taken, most of the hot wire readings were recorded by means of photographs of the oscilloscope traces. Hot wire photographs from the forward portion of the wing for runs without suction for various wing chord Reynolds numbers and chord stations are presented in Figure 127. Each photograph contains three sets of traces. The clean sine wave trace is the reference frequency of 500 or 100 cps and the superimposed irregular trace is the hot wire signal, proceeding from left to right. The amplifier noise causes the very short period oscillations on the hot wire signal that are particularly evident in the low Reynolds number data where a higher amplifier gain was necessary to make the boundary layer fluctuations evident. By comparison to the frequency reference signals, the boundary layer oscillations are found to correspond to:

<u>Frequency, cps</u>	<u>Percent Chord</u>	<u>Chord Reynolds number</u>
330	11.4	$8.4 \times 10^6$
320	12.9	$8.4 \times 10^6$
310	15.7	$8.4 \times 10^6$
445	15.7	$11.5 \times 10^6$
750	11.4	$14.2 \times 10^6$
850	11.4	$16.4 \times 10^6$

(6) Hot Wire Observations on the Straight Wing (continued)

On Figure 128 the nondimensional frequency was plotted versus the boundary layer Reynolds number for these data points. The solid line curve on Figure 128 is the neutral curve for the Blasius flat plate profile, according to Brown (Reference 6). For the present case, the flow acceleration over the nose of the 4-percent wing gives a more stable profile. The dotted line neutral curve on Figure 128 was estimated to be applicable to the present data. As one would expect, the oscillations measured in the boundary layer fall in the maximum amplification portion of the instability region. These laminar boundary layer oscillations have a distinct resemblance to the laminar boundary layer oscillations on a flat plate as recorded in Figures 9 and 10 (Reference 48). The stabilizing power of suction was clearly demonstrated when these boundary layer oscillations disappeared completely upon the application of very small amounts of suction.

The hot wire data for the straight wing under the influence of external sound are presented in Figures 129 to 138. Figures 129, 130 and 131 show oscillograph records for hot wires in the boundary layer at a height of 0.073-inch with a 248 cps, 105, 110, and 115 db external sound field for various chord locations from 46.5 to 74.8 percent c.\* For this 248 cycle case the variation of amplification with time was particularly pronounced, giving the hot wire response the overall appearance of a modulated wave. As the flow was observed at higher external sound pressures or further downstream, the areas of high amplification grew rapidly to the characteristic turbulent spots that precede transition. In this case, full transition occurred very soon after the formation of turbulent spots. The turbulent regions appeared as blanks in the hot wire trace because the amplitudes and frequencies were too great to show at the oscilloscope settings used. The suction distribution used for these runs was adjusted for no transition ahead of 45 percent chord with external sound, for no transition without sound at 45 to 52 percent chord, and at a medium suction level from 52 percent chord aft. The resulting suction (Figure 132) was, then, weakest from 45 to 52 percent chord. As evidenced on the last photograph of Figure 130, particularly, the oscillations that did not grow enough to cause turbulent spots in the weak suction region were rapidly damped further downstream. To illustrate this point, the values of  $u'/U_\infty$  for the various sound pressure levels of external sound available at 248 cps were plotted versus  $x/c$  on Figure 133. The solid lines on the figure show the values for the most amplified portions of the hot wire signal, while the dotted curves are taken from the average signal levels between the peaks. The discontinuance of a solid curve represents the formation of the first turbulent burst, while the discontinuance of a dotted curve (before 70 percent c) indicates fully turbulent flow. The interesting feature of this figure is that the laminar oscillations in the boundary layer were strongly damped beyond about 65 percent chord. The damping was probably due to a combination of the increased suction behind 52 percent chord and the evidence of Figures 121 to 124, supporting the stability theory prediction that 248 cps fluctuations would be damped in the aft portion of the wing.

The last photograph of Figure 130, depicting intermittent turbulent bursts spaced by unamplified laminar oscillations, is now clearly interpreted as a typical hot wire record of a partially laminar boundary in a stable

\*In these and the remaining oscilloscope photographs the reference frequency trace appears below the hot wire signal and the second and third records are shown at a much slower sweep rate to give a longer record of the varying response.

(6) Hot Wire Observations on the Straight Wing (continued)

region that is downstream from a critical region where turbulent spots have developed.\* In addition to 248 cps, all other sound frequencies that gave any transition were run for the suction distribution of Figure 132. Since the transitions at other frequencies were similar to the 248 cps except for the fact that they occurred at a higher sound pressure level, the oscilloscope photographs are not included in this report. Figure 134, however, shows the critical sound particle velocity ratio  $(u'/U_\infty)_{crit}$  with external sound required to cause transition plotted against chord station for these other frequencies. The untagged symbols represent transition positions as determined by the total head rake and the tagged symbols by hot wire observations. The same data are presented again in the form of  $(u'/U_\infty)_{crit}$  to cause transition vs sound frequency in Figure 135.

The discrete frequency curve here suggests that a frequency below 248 cps might be more critical. Discrete frequencies at 200 cps and below have generally been avoided, however, because they seemed to cause an increase in the wind tunnel turbulence level that lasted for a matter of several minutes. Nevertheless, in view of the octave band random noise data which consistently showed earlier transition on Figure 135 for the 300/600 band than for the 150/300 band, transition occurring below 248 cps must have developed at a generally higher level of external sound pressure. From the data on Figure 135, one concludes that the midchord portion of the wing was again most sensitive to a frequency range of about 200 to 500 cps.

Chordwise traverses from 9.2 to 28.8 percent chord were also conducted with the hot wire located at a distance of 0.044 inch above the surface for  $R_c = 14.2 \times 10^6$  with medium suction forward and high suction over the rest of the wing. Under these conditions it was possible to obtain transition over a frequency range from 384 to 1005 cps for the existing boundary layer conditions. Figure 136 shows the external disturbance level  $(u'/U_\infty)_{crit}$  required to cause transition as a function of chordwise location of transition. The frequency dependence of transition is presented in Figure 137, where the critical disturbance level was plotted vs frequency. Although the dependence of transition on frequency was not strong on Figure 137, transition did occur at lower external sound disturbance levels for 500 to 900 cps.

Figure 138 shows pictures of the boundary layer oscillations for 120 db of 775 cps external sound. The amplified laminar oscillations on Figure 138 were uniform within 15 percent of the mean value. Both this uniform type and the modulated type of amplified oscillations (Figures 129 to 131) occurred on the swept wing as well as on the straight wing without any apparent dependency on frequency or chord location. Since the slots in this forward portion of the straight wing were more than 2 percent chord -- or four inches -- apart (Table 1A), the boundary layer oscillations can be expected to appear alternately grown or damped on Figure 138, according to whether they were observed ahead of or behind a slot. As a result, Figure 138 is not necessarily a reliable indication of the local chordwise amplitude trend of the boundary layer oscillations. In addition, the oscillograph records were too short to give an adequate

\*Also see the swept wing hot wire record (Figure 140) and discussion in the next chapter (Part 7).

(6) Hot Wire Observations on the Straight Wing (continued)

record of the frequency for the occurrence of turbulent spots. For example, although the photographs for 15.6 and 28.8 percent chord appeared to show more frequent turbulent bursts than at 19.8 and 24.6 percent chord, concurrent visual observations indicated the same frequency of bursts downstream of 15.6 percent chord and no bursts at 9.2 or 12.1 percent chord. The two significant features of Figure 138 are that the turbulent spots occurred between 12.1 and 15.6 percent chord and that the spots were spreading out by 28.8 percent chord under the influence of the 120 db, 775 cps external sound field. The chordwise location of transition for this 775 cps external sound case, Figure 136, at low sound pressure levels, Figure 139, was thus the result of spreading turbulent spots from a critical region upstream.

(7) Hot Wire Observations on the Swept Wing

Before any swept wing quantitative hot wire readings were made, a series of oscilloscope pictures were taken at various locations in the wing boundary layer for a wide variation of suction and boundary layer conditions. Figure 139 is an oscilloscope photograph of the hot wire signal superimposed on the constant amplitude input sound field signal. This particular record is from a u' wire at 0.55 c in a 449-cycle sound field for sound pressure levels of 125 db at the top, 126 db in the middle and 127 db at the bottom of Figure 139. Low suction was applied at  $R_c = 5.8 \times 10^6$  ( $C_Q = 3.69 \times 10^{-4}$ ) with the first five slots sealed. This particular picture is of interest because the bottom record at 127 db caught the changing phase of an amplifying oscillation. A longer record at this condition would characteristically show amplified oscillations of increasing and decreasing magnitude without any transition. As the sound level was increased, amplified oscillations exceeded a critical magnitude and turbulent spots were observed in the boundary layer. At still higher sound levels the turbulent spots merged together, and fully developed turbulent flow was then observed with the hot wire.

The scope traces on Figure 140 were obtained with a hot wire located at the 0.9 c station and are typical of the start of transition in the region of the rear pressure rise. Here, the trace is again from left to right, but the sweep rate has been decreased to obtain a longer time interval record. At the 0.9 c chord location the disturbances in the boundary layer were turbulent spots which were not preceded by locally amplified boundary layer oscillations. These spots presumably had their origin in the occasional occurrence of an amplified boundary layer oscillation in the midchord region of the wing while the intermediate amplified oscillations were damped out by the relatively strong suction in the region of the rear pressure rise (see Figure 130, also).

As the external sound field was increased above that of Figure 140, more turbulent spots originated in the region of the flat pressure distribution, and the existing spots spread until the flow was completely turbulent. The above suggestion that the cause of transition on the aft wing is a result of amplified oscillations in the midchord region is supported by the experimentally observed fact that laminar flow can be re-established by stabilizing the boundary layer in the region of the flat pressure distribution by means of increased suction in the 0.2 to 0.6 c portion of the wing.



(7) Hot Wire Observations on the Swept Wing (continued)

Figure 141 shows a typical plot of the velocity fluctuation  $u'/U$  in the laminar boundary layer versus the distance from the surface for various stations  $x/c$  at  $R_c = 8.1 \times 10^6$  in the presence of longitudinal sound of 400 cps frequency with minimum suction. Here the sound pressure was increased until transition started. In the region of the flat pressure distribution of 45 percent chord the ratio  $u'/U$  of the tangential velocity fluctuations  $u'$  reached maximum values of one percent of the local potential flow velocity  $U$  in the vicinity of the wing surface. The maximum values  $w'/U$  of the velocity fluctuation  $w'$  in the crossflow direction were generally somewhat smaller than the corresponding ratios  $u'/U$ . With increasing distance  $y$  from the wing surface,  $u'$  decreased rapidly to the approximate values for the sound particle velocity. It is not certain whether or not the fluctuations toward the edge of the boundary layer were  $180^\circ$  out of phase with the fluctuations close to the wall.

As a result of the presence of standing waves in the test section, the sound pressure at the hot wire location evaluated from the hot wire readings did not always correlate with the reference sound pressure as measured by the reference microphone.

The fluctuation measurements of  $u'$  and  $w'$  in the boundary layer in the region of the rear pressure rise at 90 percent chord showed similar results as at the 45 percent chord station. The observed velocity fluctuations at this location, however, were considerably smaller than those in the region of the flat pressure distribution, particularly at high sound frequencies. At the 90 percent chord station the strongest velocity fluctuations were usually observed at rather low sound frequencies (150/300 cps). At lower frequencies increasing suction did not appreciably change the velocity fluctuations in the boundary layer at the 90 percent chord station. At higher sound frequencies  $u'/U$  and  $w'/U$  decreased somewhat with increasing suction.

(8) Influence of Internal Sound in a Suction Duct on the Straight Wing

Boundary layer transition may be caused by internal noise and standing sound waves in the suction duct. In order to investigate the influence of internal sound on the behavior of an unswept laminar suction wing, preliminary experiments were conducted on the influence of internal sound disturbances, generated in a suction chamber of the 17-foot chord straight laminar suction wing, on the behavior of the boundary layer on this wing. Sound from six speakers was introduced into chamber number 9, which includes seven suction slots located from  $x/c = 0.456$  to  $0.518$  (Figure 66).<sup>\*</sup> The internal sound field was surveyed by moving a microphone attached to a long rod along the suction chamber. At discrete frequencies of 228, 582, 1221, 1611 and 4147 cps strong standing sound waves existed due to reflection from the end bulkhead, which was perpendicular to the suction chamber axis. For octave bands of white noise the sound pressure level was quite uniform along the duct. The reference microphone reading for internal sound was taken at a station which indicated a peak sound pressure level for the discrete frequencies.

<sup>\*</sup>This experimental setup was designed by T. R. Rooney, Norair Dynamics group.



(9) Influence of Internal Sound in a Suction Duct on the Straight Wing (continued)

The data for runs with internal sound in chamber 9 are presented in Figures 142 to 152. The critical sound pressure and the corresponding critical sound particle velocity ratio  $(s'/U_\infty)_{crit}$  (assuming plane sound waves) for transition were plotted versus sound frequency for various wing chord Reynolds number and chordwise suction distributions on Figures 142 to 148. These figures indicate that the critical sound pressure level for transition had a minimum in the frequency range from 100 to 600 cycles. This critical frequency band for the midchord portion of the wing correlates with the external sound field results and with the frequencies for amplified chordwise boundary layer oscillations. As with external noise, increased suction had a powerful stabilizing effect, rapidly raising to higher values the critical sound pressure for transition.

On Figures 142 to 145 the overall suction level has been raised to maintain laminar flow under the influence of internal sound disturbances, while Figures 146 to 148 show the local suction increases necessary for the maintenance of full chord laminar flow in the presence of increased internal sound. For a practical case where all ducts would have comparable sound pressure levels, the increased overall suction level (Figures 142 to 145) would generally give a better indication of the suction requirements than the locally increased suction (Figures 146 to 148).

Very high peak sound pressure levels were attained with sound of discrete frequencies as a result of standing waves. With these strong standing waves the effectiveness of increased suction was reduced to the point where a large increase in suction was necessary to maintain full chord laminar flow. A sublimation check at 150 db, 582 cps (Figures 149 and 150) gave visual representation of the transition pattern for this very strong standing wave disturbance. Transition originated in the regions of maximum sound pressure of the standing wave opposite the one-half inch spaced row of holes that provided a passage from the small plenum chambers under the slots into the suction chambers (Figure 65). Opposite each hole there were two streaks that developed into turbulent wedges further downstream in the same manner as transition from three-dimensional roughness particles. These streaks that are attributed to trailing vortex pairs were observed by Goldsmith and Meyer to originate from sucking or pulsating flow through a hole (Reference 97). In one case during the swept wing acoustical tests (Figure 126), transition also originated from the holes under the slot for very strong external sound disturbances when the slot and holes were in line. The holes under the 0.005-inch slots in chamber 9 were 0.031-inch in diameter for the forward slot and 0.029-inch for the rest. The transition zones at the bottom, middle and top of Figures 149 and 150 initiated from slots 28, 29 and 30, which are in line with the drilled holes.

Figures 151 and 152 were taken at internal sound pressure levels of 146 and 159 db for 200 cps. Transition was clearly similar to Figures 149 and 150. For the very high SPL of Figure 152 some interesting additional features appear. Transition in the midspan portion of the wing initiated from the first slot in chamber 9 (slot number 24), which has the holes displaced a little more than the hole radius from the slot centerline. With the aligned slot and hole pattern of slots 28 and 29 (Figure 151) transition existed at 146 db. For this particular case, then, offsetting a hole by one radius allowed a

(8) Influence of Internal Sound in a Suction Duct on the Straight Wing (continued)

13 db increase in disturbance level. In addition, at the bottom of the picture, some vortex streaks initiated from slot number 23, the last slot of the upstream chamber (number 8), which did not have any directly introduced internal sound disturbance. The holes at slot 23 were again directly below the slot in the region of transition. At the same time, there is no transition in the lower region from slots 24, 25, 26 and 27, which are in chamber 9, but have holes offset by at least one hole radius. Finally, downstream of the lower transition pattern the disturbances from the holes toward the bottom of slots 28 and 29 are evident in the thin film of naphthalene remaining in the laminar sublayer. The conclusion from Figures 149 to 152 is that at the extremely high disturbance levels, where direct transition due to pumping action through the holes and slots occurred, transition was delayed considerably when the drilled holes were offset from the corresponding slot. Although this direct transition is at an internal sound level well above any that would probably be allowed in an actual design, the hole offset effect very likely influenced transition due to internal sound at lower pressure levels. In any case, in the construction of laminar flow surfaces, the holes and slots should be offset whenever there is a possibility of strong sound fields and standing waves.

(9) Influence of Mechanical Vibrations of the External Wing Surface on Transition on a Straight Low Drag Suction Wing

Considerations of the type of structure contemplated and a survey of existing data on flying airplanes indicated that peak panel accelerations of about 10g in the 100 to 1000 cycle frequency range could be expected. The question then arises as to the influence of mechanical vibrations of the external wing surface on the behavior of a laminar suction wing. In order to answer this question for an unswept laminar suction wing, low drag suction experiments were conducted to check the feasibility of exciting panel vibrations on the present 17-foot chord wing. After the two spars adjacent to chamber number 9 were disconnected from the supporting structure to provide a more flexible wing structure, the wing vibration modes were obtained in the BLC shop, using a standard vibration exciter. Since nearly two-dimensional panel modes of more adequate acceleration were obtained, a high-speed, d.c. motor-driven, reciprocating mass shaker was installed in a cutout in the spar web immediately upstream of chamber number 9. The acceleration was controlled by using shafts of different eccentricity to drive the oscillating mass while the frequency was set by regulating the supply voltage to the d.c. motor. The motor power-limited the shaker to about 260 cps frequency and 46g peak panel acceleration for intermittent operation. For the high accelerations (large shaft eccentricity) the wave forms were reasonably sinusoidal, but for the allayed excitation in the case for 10g at 100 cps (small shaft eccentricity) the accelerometer response had a large content of higher harmonics. Although, for the above reasons, the test-measured values of acceleration and frequency are somewhat nebulous, the values did correspond to repeatable conditions of model response because the internal vibrator speed settled out at the natural frequencies of the structure. Although mode shapes were again determined with the internal shaker prior to model installation in the tunnel, the frequencies were not repeatable with the model mounted in the wind tunnel. For the wind tunnel experiment, then, the accelerations were determined by searching out the peaks with a roving accelerometer pickup, and no time was available to redefine the complete mode shapes. According to this brief survey, modes of vibration at 100, 190 and 240 cps were reasonably two-dimensional.

(9) Influence of Mechanical Vibrations of the External Wing Surface on Transition on a Straight Low Drag Suction Wing  
(continued)

The data for these preliminary experimental investigations on the influence of surface vibration on transition are presented in Figures 153 to 157. In all instances of 10g peak acceleration or more, suction had to be increased above the minimum drag value to maintain full chord laminar flow. Figure 153 shows the increase in suction quantity and drag that applied to the 4-percent-thick straight wing when full chord laminar flow was re-established in the presence of surface vibrations by raising the suction level over the whole wing, whereas Figures 154 to 157 give the same data for cases where the suction distribution was locally adjusted. In the case of vibration excitation, in contrast to the internal sound case, the disturbance was transmitted through the structure to the forward part of the wing to require suction increases well upstream of point of excitation as evidenced on Figures 154 to 157. For a peak panel velocity ratio  $v'/U_\infty = 20 \times 10^{-4}$ , the maintenance of full chord laminar flow by raising suction level required a 24 percent increase in suction coefficient  $C_Q$  and a corresponding 5 percent increase in equivalent drag,  $C_{D_t}$ , compared to a case with no vibration (Figure 153). With the suction applied on individual chambers as required, the suction quantity and equivalent drag increased an average of about 5 percent and 1 percent, respectively. Since panel velocity ratios,  $v'/U_\infty$ , in the order of  $2 \times 10^{-3}$  are possible, the present preliminary vibration investigation indicates that some additional suction might be required for thin straight wing laminar suction aircraft.

(10) Effects of Combined Internal Sound, External Sound, and Surface Vibration on a Straight Wing

Figures 158 and 159 show the combined disturbance effects of internal sound, external sound, and panel vibration. Up to this point internal sound, external sound, and vibration had been applied to the straight wing model separately to note their influence on transition. Of course, the model response to each of the input disturbances involves, to a lesser degree, the modes of the other two disturbances. For example, the external sound caused internal noise in the duct and excited some panel vibration, etc. Figure 158 shows in block diagram form the increase in suction level above minimum drag suction required to maintain laminar flow at various levels and combinations of the three different disturbances. Several features of combined effects are evident here. First, where one disturbance was predominant, the required suction to maintain laminar flow for the combined effects was practically the same as that required for the major disturbance alone. This appears on the bars labeled 3 and 4 where the vibration alone and the vibration combined with internal and external disturbances are laminar for the same suction quantity. Secondly, superposition of two or three equally critical disturbances required much less than the proportional suction increases to maintain laminar flow. For example, Figure 159 shows that an average suction increase of 23 percent was required to stabilize for one disturbance, while an average of 6 percent had to be added to stabilize against a combination of any two of the equally critical disturbances. Moreover, the suction quantity required to stabilize the boundary layer for any two of the equally critical disturbances was generally adequate for all three disturbances combined (external noise plus internal noise plus surface vibrations).

(10) Effects of Combined Internal Sound, External Sound, and Surface Vibration on a Straight Wing (continued)

The results obtained on the 4-percent-thick straight wing with internal noise and surface vibrations are applicable to unswept low drag suction wings; they are not generally applicable, however, to swept laminar suction wings.

(G) Hypothesis of the Mechanism of Transition on a Swept Laminar Suction Wing under the Influence of External Sound

While the frequency dependence and mechanism of transition on the straight laminar suction wing under the influence of external sound correlated to Tollmien-Schlichting wave amplifications and observed breakdown, the transition on the swept wing in the presence of external sound was not generally explained by small-disturbance theory.

The naphthalene flow pictures showed that transition under the influence of external sound in the area of the flat pressure distribution was usually preceded by the formation of closely spaced chordwise striations of approximately one-eighth to one-tenth inch spacing. These striations became rapidly more pronounced as transition was approached. Without external sound no striations were observed at the test Reynolds numbers. The observed striations resemble those experienced by the British (References 87 and 88) and later by NASA Ames at high Reynolds numbers in the front part of swept wings, indicating the existence of stationary chordwise disturbance vortices. Thus, in the presence of external sound, transition on a swept laminar suction wing generally occurred in the region of the flat pressure distribution and was preceded by closely spaced chordwise disturbance vortices which caused the observed fine striations. The question then arises as to the origin of these chordwise disturbance vortices observed on a swept laminar suction wing in the region of the flat pressure distribution under the influence of external sound.

The ordinary stability theory of the boundary layer crossflow, assuming infinitely small disturbances (Reference 6), would predict approximately neutrally stable boundary layer crossflow in the region of the flat pressure distribution at the test Reynolds numbers. Furthermore, for stationary disturbance vortices of zero wave velocity, no meaningful time frequency of the external disturbances can be formed. In order to understand the formation of the observed striations, corresponding to chordwise disturbance vortices, and the mechanism of transition on a swept laminar suction wing in the presence of external sound, it is evident that the stability theory of the boundary layer on a swept laminar suction wing must be further refined.

In the region of the swept wing flat pressure distribution the maximum crossflow velocity is only one to two percent of the freestream velocity. Under these conditions, in the presence of strong external sound fields with mean sound particle velocity ratios  $u'/U_\infty = 0.001$  to  $0.003$ , it appears questionable to neglect higher order terms in the disturbance equations for the boundary layer crossflow, as is done in ordinary stability theory, which assumes infinitely small disturbances. According to Stuart (Reference 53), a shear flow or a laminar boundary layer which is neutrally stable against infinitely small disturbances can become unstable in the presence of large external disturbances. Under such conditions, according to suggestions by G. Raetz, the Reynolds stresses

(G) Hypothesis of the Mechanism of Transition on a Swept Laminar Suction Wing under the Influence of External Sound (continued)

in an oscillating boundary layer may distort the mean boundary layer crossflow profile in such a manner as to lower its stability limit Reynolds number in the presence of large external disturbances. On a flat plate, similar and quite pronounced distortions of the Blasius boundary layer profile in the presence of strong velocity fluctuations were observed by Klebanoff, Tidstrom and Sargent at the National Bureau of Standards (Reference 38). An analysis by Raetz indicates that the distortion of the mean boundary layer crossflow profile by external sound alone (acoustic streaming) would be insufficient to appreciably change the crossflow stability limit, unless disturbances in the boundary layer were amplified under the action of external sound. The existence of amplified boundary layer oscillations in the presence of external sound on the present swept laminar suction wing, particularly in the region of the flat pressure distribution, was verified by velocity fluctuation measurements in the boundary layer with hot wires. The observed velocity fluctuations in the boundary layer in the direction tangential and normal to the potential flow were generally considerably larger than due to acoustic streaming alone, particularly in the region of the flat pressure distribution preceding transition. The observed velocity fluctuations, however, were not sufficiently strong to cause transition directly; much stronger velocity fluctuations,  $u'/U_\infty \geq 0.05$  were observed by Dryden, Schubauer, Klebanoff and others in the laminar boundary layer of a flat plate preceding transition (References 38 and 90). In the presence of external sound, with the observed velocity fluctuations, the mean crossflow boundary layer profile in the area of the flat pressure distribution is then probably sufficiently distorted to lower appreciably its stability limit Reynolds number, causing the formation of chordwise disturbance vortices and, finally, transition.

The question now arises as to the cause of the amplified oscillations observed in the boundary layer under the influence of external sound. Boundary layer velocity fluctuations can be induced by sound in the direction of the sound particle velocity vector. When the boundary layer in this direction is unstable, these boundary layer oscillations will be amplified. According to the hot wire measurements of the components of the sound particle velocity, the sound field in the test section was generally three-dimensional. As an example, when the sound particle velocity vector is perpendicular to the swept wing leading edge, sound can induce amplified oscillations into the boundary layer in the direction normal to the wing leading edge. At the moderately high wing chord Reynolds numbers of the experiments, relatively weak suction in the leading edge area and in the region of the flat pressure distribution was generally adequate to avoid transition due to the instability of the boundary layer crossflow. Under such conditions, in the region of the flat pressure distribution, the chordwise boundary layer is not too stable. Chordwise boundary layer oscillations induced by sound can then be amplified in this part of the wing. The component of these velocity fluctuations in the direction normal to the potential flow introduces, then, velocity fluctuations into the crossflow boundary layer, as observed with hot wires, which may be sufficiently strong to distort the mean crossflow profile in such a manner as to lower appreciably its stability limit Reynolds number. Increasing suction in the region of the flat pressure distribution, before transition will otherwise occur, reduces the local crossflow Reynolds number and at the same time increases the stability of the chordwise boundary layer. As a result, the chordwise boundary layer oscillations are less amplified, and the component of these oscillations in the crossflow direction is

(G) Hypothesis of the Mechanism of Transition on a Swept Laminar Suction Wing under the Influence of External Sound (continued)

correspondingly reduced. Increasing suction in the region of the flat pressure distribution will thus delay the start of transition on a swept laminar suction wing in the region of the flat pressure distribution to higher sound pressure levels, as verified experimentally.

When the chordwise boundary layer in the front half of the swept wing was less stable, i.e., when no suction was applied in the front part of the wing, chordwise boundary layer oscillations probably were sufficiently amplified in the presence of strong external sound fields to become nonlinear and three-dimensional, as observed on a laminar flat plate when the originally two-dimensional oscillations had grown to large amplitudes (Reference 38). Transition then started at regularly spaced selective spanwise stations where the chordwise boundary layer oscillations had grown most, thus explaining the formation of the rather regularly spaced turbulent wedges in the region of the flat pressure distribution with strong external sound. In many cases the local crossflow stability limit Reynolds number was sufficiently reduced by the presence of these strong chordwise boundary layer oscillations to form closely spaced chordwise disturbance vortices, indicated by fine striations in the naphthalene sublimation pictures, preceding transition (Figure 112 ).

When the pressure drop through a suction slot is small (i.e., at low flow velocities through a relatively wide slot), acoustical disturbances can induce a pulsating flow through the slot of such a magnitude that the resulting chordwise boundary layer oscillations downstream of the slot are sufficiently amplified to cause premature transition. Higher local suction rates must then be applied in such slots to increase the pressure drop through the suction skin and to reduce the amplification of boundary layer oscillations downstream of the slot, thus delaying the beginning of transition to higher sound pressures. This experience was gained on the present swept wing model with relatively weak suction through some of the front suction slots. These slots were relatively wide, and the pressure drop through the wing skin was correspondingly small. At  $R_c \approx 10^7$  transition was observed at 120 db (with white noise of 1200/2400 cps). Increasing suction in these front slots raised the critical sound pressure for transition to 124 db, under otherwise the same conditions. (Sealing the front slots raised the critical sound pressure to 123 to 125 db.)

With increasing wing chord Reynolds numbers, in order to avoid transition due to the instability of boundary layer crossflow, higher nondimensional suction velocities  $v_0/U_\infty \sqrt{R_c}$  (for equivalent area suction) are required, particularly in the region of the flat pressure distribution and especially toward the wing leading edge. The chordwise boundary layer then becomes increasingly more stable at higher wing chord Reynolds numbers. As a result, the chordwise boundary layer oscillations are less amplified and the component of these oscillations in the direction normal to the potential flow streamline is correspondingly reduced. On a swept laminar suction wing one might therefore expect a relatively slow decrease of the critical sound particle velocity ratio  $(u'/U_\infty)_{crit}$  at transition with increasing Reynolds number. With minimum suction the experiments showed a slightly increasing critical sound pressure at transition with wing chord Reynolds number, as long as marginal suction was not too closely approached; i.e.,  $(u'/U_\infty)_{crit}$  decreased with wing chord Reynolds number at a somewhat slower



(G) Hypothesis of the Mechanism of Transition on a Swept Laminar Suction Wing under the Influence of External Sound (continued)

rate than inversely proportional to the latter  $[(u'/U_\infty)_{crit} \sim R_c^{-0.75}$  with minimum suction].

In the region of the rear pressure rise of a swept low drag suction wing where the boundary layer crossflow is most pronounced, one might expect transition in the presence of sound to be caused by amplified boundary layer oscillations traveling in crossflow direction. The experiments, however, rarely showed transition in the region of the rear pressure rise except in the case of marginal suction when transition would already have occurred without external sound. This result can probably be explained by the fact that the maximum crossflow velocity increases rapidly toward the wing trailing edge. For a disturbance wave traveling in crossflow direction with a given wave velocity  $c_r$  the ratio of this wave velocity to the local maximum crossflow velocity then decreases considerably toward the wing trailing edge. Under such conditions, in the neutral stability diagram of the boundary layer crossflow, disturbances are strongly amplified only during a short time over a small chordwise extent in the region of the rear pressure rise. In the remaining part of the area of the rear pressure rise the ratio of wave velocity to maximum crossflow velocity (for a given sound frequency and a constant wave velocity) is either too high or too low to cause a strong amplification of oscillations in the crossflow boundary layer. In addition, with the strong suction required in the rear pressure rise of the swept wing model to prevent crossflow instability, the chordwise component of the boundary layer is highly stable against chordwise disturbances. Chordwise boundary layer oscillations and the component in crossflow direction then never grow to large amplitudes, and the reduction of the crossflow stability limit Reynolds number by the nonlinear terms in the disturbance equations is then much less in the region of the rear pressure rise, as compared with the area of the flat pressure distribution.

CHAPTER D. LAMINARIZATION OF A SEARS-HAACK BODY OF REVOLUTION BY MEANS OF BOUNDARY LAYER SUCTION

a. INVESTIGATION OF A LAMINAR SUCTION MODIFIED SEARS-HAACK BODY OF REVOLUTION IN THE NORAIR 7- BY 10-FOOT WIND TUNNEL

L. W. Gross

(A) Summary

Full length laminar flow with very low friction and equivalent total drags was maintained on a 9-to-1 fineness ratio laminar suction modified Sears-Haack body of revolution of 142-inch length up to a length Reynolds number  $R_L = 20.1 \times 10^6$  by means of suction through 120 fine slots. The coefficient of equivalent total drag (based on wetted area and including the equivalent suction drag) at an angle of attack  $\alpha = 0^\circ$  was 1.18 times the laminar flat plate friction coefficient up to  $R_L = 19.6 \times 10^6$  with a corresponding suction quantity coefficient (based on wetted area)  $C_{Q_t} = 1.75 \times 10^{-4}$ .

At an angle of attack  $\alpha = 2^\circ$  the minimum equivalent total drag coefficient varied from 1.18 times the laminar flat plate friction coefficient  $C_f$  at a Reynolds number  $R_L = 6.3 \times 10^6$  up to  $1.45 C_f$  at  $R_L = 16.19 \times 10^6$ . An equivalent total drag coefficient  $C_{D_t} = 4.8 \times 10^{-4}$  was measured at  $R_L = 16.19 \times 10^6$  requiring a total suction quantity coefficient  $C_{Q_t} = 1.95 \times 10^{-4}$ . Full length laminar flow at  $\alpha = 2^\circ$  was observed up to a length Reynolds number  $R_L = 18.55 \times 10^6$ .

(B) Notation

$c_{D_w}(\varphi)$  local drag contribution of boundary layer momentum thickness at a given radial angle  $\varphi$

$C_D = \frac{D}{q_\infty S}$ ; coefficient of drag, based on body wetted area  $S$

$C_{D_s} = \sum_{\text{all chambers}} C_{Q_a}(1 - C_{p_{ga}})$ ; coefficient of drag due to suction power required to accelerate the suction air to undisturbed velocity and pressure without losses

$C_{D_t} = C_{D_s} + C_{D_w}$ ; coefficient of equivalent total drag

$C_{D_{tmin}}$  minimum equivalent total drag coefficient

$C_{D_w} = \int_0^{2\pi} c_{D_w}(\varphi) d\varphi$ ; coefficient of wake drag

$C_f$  laminar flat plate friction coefficient



(B) Notation (Continued)

$C_p = \frac{p - p_\infty}{q_\infty}$ ; pressure coefficient with respect to ambient static pressure  $p_\infty$

$C_{p_{sa}} = \frac{p_a - p_\infty}{q_\infty}$ ; pressure coefficient of individual suction chamber with respect to ambient static pressure  $p_\infty$

$C_{Qa} = \frac{Q_a}{U_\infty S}$ ; suction coefficient of individual suction chamber based on body wetted area  $S$

$C_{Qt} = \sum_{\text{all chambers}} C_{Qa}$ ; total suction coefficient

$C_{Q_{opt}}$  optimum total suction coefficient corresponding to minimum equivalent total drag

$D$  drag (lb)

$H = \frac{\delta^*}{\theta}$ ; boundary layer shape parameter

$\bar{H}$  average boundary layer shape parameter between the value at the rearmost station of the model and the value at infinity

$H_{TE}$  boundary layer shape parameter at the rearmost station of the model

$L$  model length to the rearmost station of the model (ft)

$L'$  length of basic model before addition of sting (ft)

$p$  static pressure (lb/ft<sup>2</sup>)

$p_a$  static pressure in suction chamber (lb/ft<sup>2</sup>)

$p_\infty$  freestream undisturbed static pressure (lb/ft<sup>2</sup>)

$q_\infty = \frac{1}{2} \rho_\infty U_\infty^2$ ; freestream undisturbed dynamic pressure (lb/ft<sup>2</sup>)

$Q_a$  suction quantity of each suction chamber (ft<sup>3</sup>/sec)

$r$  body radius at axial station  $x$

$r_{TE}$  body radius at rearmost station of the model = 3.132 in.

$R_L = \frac{U_\infty L}{\nu}$ ; Reynolds number based on model length

(B) Notation (Continued)

$R_\theta$	$= \frac{U\theta}{\nu}$ ; Reynolds number based on boundary layer momentum thickness
$R_\theta(0^\circ)$	Reynolds number based on boundary layer momentum thickness measured by top rake
$R_\theta(90^\circ)$	Reynolds number based on boundary layer momentum thickness measured by side rake
$S$	wetted surface area of model = 35.44 ft <sup>2</sup>
$u$	velocity in the boundary layer at height $y$ (ft/sec)
$U$	velocity at outer edge of boundary layer (ft/sec)
$U_{TE}$	potential flow velocity at the rearmost station of the model (ft/sec)
$U_\infty$	undisturbed freestream velocity (ft/sec)
$v_o$	suction velocity for equivalent area suction (ft/sec)
$v_o^*$	$= \frac{v_o}{U_\infty} \sqrt{R_L}$ ; nondimensional suction velocity for equivalent area suction
$x$	distance along axis of model (ft)
$y$	distance normal to the surface of the model (ft)
$\alpha$	angle of attack (degrees)
$\delta$	boundary layer thickness
$\delta^*$	$= \int_0^\delta (1 - \frac{u}{U}) (1 + \frac{y}{r}) dy$ ; boundary layer displacement thickness (ft)
$\delta_{TE}^*$	boundary layer displacement thickness at the rearmost station of the model (ft)
$\theta$	$= \int_0^\delta \frac{u}{U} (1 - \frac{u}{U}) (1 + \frac{y}{r}) dy$ ; boundary layer momentum thickness (ft)
$\theta_{TE}$	boundary layer momentum thickness at the rearmost station of the model (ft)
$\theta_\infty$	wake momentum thickness far behind the model (ft)

(B) Notation (Continued)

$\mu$	absolute viscosity (lb-sec/ft <sup>2</sup> )
$\nu$	$= \frac{\mu}{\rho}$ ; kinematic viscosity (ft <sup>2</sup> /sec)
$\rho$	density (lb-sec <sup>2</sup> /ft <sup>4</sup> )
$\theta$	radian angle (degrees)

(C) Introduction

In connection with the application of low-drag laminar boundary layer control to airplanes, the question arises as to the feasibility of maintaining extended regions of laminar flow on components that are essentially bodies of revolution (such as the fuselage and engine nacelles). Specifically, the ability of suction to stabilize the laminar boundary layer on bodies of revolution up to very high Reynolds numbers should be demonstrated. In addition, it is desirable to establish data from which the limits of the parameters significant to laminar boundary layer stability on a body can be deduced for design purposes.

Investigation of natural boundary layer transition on bodies of revolution (Reference 92) has shown that boundary layer stability is affected by the three-dimensional nature of bodies. When the body radius is increasing, the boundary layer momentum thickness Reynolds number  $R_\theta$  at transition is lower than that of an equivalent two-dimensional surface; i.e., the stability limit is decreased. In like manner, the stability limit is increased above that of the equivalent two dimensional surface when the body radius is decreasing. It appears that the boundary layer in the front part of a body is less stable than on a wing due to the stretching of disturbance vortices in the region of increasing body radius and due to fluctuations of the front stagnation point (Reference 93).

Low drag boundary layer suction was applied to an ellipsoid of revolution of fineness ratio 9:1 and tested in the Norair 8- by 11-foot wind tunnel and in the University of Michigan 5- by 7-foot wind tunnel (Reference 94 ). The model was of 142-inch length and had nineteen suction slots arranged from 10.5 percent to 96 percent length. Slot widths varied from 0.004 to 0.014 inch. As reported in Reference 94, the minimum equivalent total drag coefficient based on wetted area (including equivalent drag due to suction) was 1.24 times the laminar flat plate friction coefficient up to a length Reynolds number  $R_l = 12 \times 10^6$  and full length laminar flow was maintained with slightly higher values of minimum total drag up to a length Reynolds number  $R_L = 15 \times 10^6$ .

On the basis of these experiments and experience with other low drag suction models at high Reynolds numbers, a laminar suction body of revolution was designed for tests at high length Reynolds numbers (design length Reynolds number  $R_L = 49 \times 10^6$  for test conditions similar to the Ames 12 foot pressure tunnel at a unit Reynolds number  $U_\infty/\nu = 4.15 \times 10^6$  per foot). In

### (C) Introduction (Continued)

order to gain experience with the model and to establish experimental data at the lower end of the anticipated Reynolds number range, the model was first tested in the Norair 7- by 10-foot wind tunnel. This report describes these investigations.

### (L) Experimental Setup

The body shape chosen was a 9:1 fineness ratio Sears-Haack body modified to have a rounded nose of small radius of curvature (Figure 160). This shape was chosen on the basis of the investigation of Reference 33 and gives as large an extent of natural laminar flow as possible while retaining adequate internal volume. The length of the Norair model was limited to approximately 156 inches by the available lathe. It was desired to retain a 9:1 fineness ratio and after allowing for an adequate mounting length of the sting the basic body length became  $L' = 139.5$  inches giving a maximum diameter of 15.5 inches. The model was mounted on a sting of 6.5-inch diameter which provided space for the suction air. The body shape was faired smoothly into the sting from 85 to 103 percent of the body length. The final contour is illustrated in Figure 160.

For the design of the suction system, the boundary layer development along the body was calculated (Figure 166) by means of Raetz's method (Reference 45), using the theoretical suction distribution shown in Figure 166. The potential flow pressure distribution used for the design calculations was taken from Reference 92 and is shown in Figure 165.

Figure 160 shows the model and details of the suction system. The position of the first slot was selected on the basis of the investigation of natural transition on the body by Groth (Reference 92). The spacing of the 0.003 inch slots was determined from the theoretical boundary layer development (Figure 166) to be two inches in the region from 4.84 to 75 percent of the basic body length  $L'$  and one-half inch in the region of the rear pressure rise, from 75 percent to 100.4 percent for a total of 120 slots.

The slot width was chosen approximately equal to the thickness of the sucked layer at a design length Reynolds number of  $49 \times 10^6$ .\* Considerable attention was given to avoiding any local flow separation in the suction slots and holes underneath the slots by restricting the flow Reynolds numbers in these slots and holes to sufficiently low values.

The model was built up of an inner shell composed of eight machined tubes bolted together, a nose piece, and outer rings shrunk-fit to the inner shell. Suction air passage through the inner shell was provided by drilled holes which also acted as metering holes to compensate for variations of the external pressure field. Details of the slot and hole system are given in Table IX. Suction plenum chambers were turned into the outer rings. During assembly, the outer rings were forced together as they were shrunk-fit onto the inner shell and the slots were subsequently turned into the joint between

---

\*Assuming test conditions similar to those in the Ames 12-foot pressure tunnel.

#### (D) Experimental Setup (Continued)

the rings to provide positive control of the slot width. Compartmentation of the model into thirteen suction chambers was accomplished by means of sealed bulkheads. Calibrated suction flow measuring nozzles were mounted on the face of the bulkheads.

The Norair 7- by 10-foot wind tunnel and its auxiliary air supply are described in Appendix B of Reference 14. Figures 162 and 163 show the model mounted in the wind tunnel test section and a schematic drawing of the installation is given as Figure 161. The model was held in a tube which was, in turn, supported from the test section floor by two columns, the rearward of which was adjustable in length so that the model could be pitched through an angle of attack range of  $4^\circ$ . The support system was faired with sheet metal and wooden blocks so as to minimize flow disturbances.

The suction air was drawn from the boundary layer on the surface of the model, through the slots, plenum chambers and holes and into the thirteen independent suction chambers. The suction air was then ducted from each suction chamber, by means of aluminum tubing, to the exterior of the model by way of the sting. Flexible tubing led the air through the model support structure and to a common suction box. The suction quantities of the various chambers could be adjusted individually by means of remotely controlled needle valves at the entrance to the common suction box. The total rate of suction could be varied by introducing bleed air into the suction box. The suction air was then drawn from the suction box by the wind tunnel auxiliary air exhaust system described in Appendix B of Reference 14.

#### (E) Measurements and Evaluation

The objective of this investigation was the study of the behavior of the laminar boundary layer on a body of revolution with suction through many fine slots and the determination of the drag characteristics and suction requirements of this body at various angles of attack  $\alpha$  and Reynolds numbers  $R_L$ . At each of the various Reynolds numbers and angles of attack, the suction quantities were varied over a range that included the point of minimum drag.

The coordinate system is shown in Figure 164. The following measurements were taken.

The pressure drop across the calibrated flow measuring nozzles located at the downstream end of the various suction chambers was measured to evaluate the suction quantities  $Q_a$  of the various suction chambers. The corresponding chamber static pressures were taken at the downstream end of the suction chambers. The lengthwise pressure distribution was recorded by means of twenty-two static pressure orifices located from 1 to 100 percent of the basic body length  $L'$ . The locations of the static pressure orifices are given in Table X. In order to properly set the model at an angle of attack  $\alpha = 0^\circ$ , four pressure taps arranged 90 degrees from each other were provided at a position 5 percent of the basic body length  $L'$  from the nose.

(E) Measurements and Evaluation (Continued)

The boundary layer profiles at the rear end of the model were measured by means of two boundary layer rakes located on the top and side of the sting. The measuring plane of the rakes was a length  $L = 142$  inches from the nose so the Reynolds number  $Re_L$  and other performance characteristics of the model were based on this length (as opposed to the basic body length  $L' = 139.5$  inches). The top boundary layer rake consisted of fourteen and the side rake of twelve flattened total pressure tubes. Each of the rakes had two static pressure tubes displaced one-half inch from the plane of the total pressure tubes.

The state of the boundary layer was observed from the boundary layer velocity profile measurements at the rear end of the body and from the response of 9 microphones connected to surface static pressure orifices along the length of the body.

The static pressures in the measuring nozzles, suction chambers and on the external body surface were displayed on a first U-tube manometer panel. The boundary layer rake readings (total and static pressures) were recorded on a second, separate U-tube manometer board. In this manner, fluctuations of the total pressure readings from the rakes did not influence the remaining pressure readings. The pressure data were recorded photographically on 70 mm microfilm, which was then read on a film reader machine. The recording was done on punched cards suitable for use on an IBM 7090 digital computer.

The freestream undisturbed static and dynamic pressure  $p_\infty$  and  $q_\infty$  were determined from calculations of the tunnel wall corrections given by Lock and presented in Reference 95 and from the wind tunnel calibration curves given in Appendix B of Reference 14. The resultant minimum pressure coefficients showed a scatter of 0.4 percent of freestream dynamic pressure.

From the measured suction quantities  $Q_a$  in the various suction

chambers, the suction quantity coefficients  $C_{Qa} = \frac{Q_a}{U_\infty S}$  of the individual

chambers and the total suction quantity coefficient  $C_{Qt} = \sum_{\text{all chambers}} C_{Qa}$  were

evaluated. With the non-dimensional coefficient  $C_{pga} = \frac{p_a - p_\infty}{q_\infty}$  of the pressure

rise across a suction compressor necessary to accelerate the suction air isentropically to freestream velocity and ambient static pressure, the equivalent suction drag coefficient is:

$$C_{Ds} = \sum_{\text{all chambers}} C_{Qa} (1 - C_{pga})$$

### (E) Measurements and Evaluation (Continued)

Due to the surface curvature of the body at the rake location, a pressure gradient normal to the body was present. This pressure gradient was measured by the two static pressure probes mounted on each rake. A linear variation of static pressure was assumed for the determination of the velocity distribution in the boundary layer at the rake location.

For the evaluation of the wake drag it was assumed that the measured boundary layer profile is first accelerated over a short distance to a constant static pressure equal to the value at the edge of the boundary layer at the rake location. This new fictitious boundary layer profile at constant static pressure can be determined from the continuity equation and the Bernoulli equation (i.e., assuming constant total pressure along streamlines). The wake momentum loss at infinity, which determines the wake drag, can be evaluated from the momentum thickness of this fictitious boundary layer at constant static pressure according to Squire and Young:

$$C_{Dw} = \frac{2}{S} \int_0^{2\pi} r \theta_{TE} d\varphi = \left( \frac{U_{TE}}{U_{\infty}} \right) \bar{H} + 2 \int_0^{2\pi} \frac{2 r_{TE} \theta_{TE}}{S} d\varphi$$

where  $r_{TE}$  is the body radius at the measuring station,  $U_{TE}$  is the potential flow velocity at the edge of the boundary layer,  $\bar{H}$  is the value of  $H = \left( \frac{\delta^*}{\theta} \right)$  in the wake between the rearmost station and infinity and

$$\theta_{TE} = \int_0^{\delta} \frac{u}{U} \left( 1 - \frac{u}{U} \right) \left( 1 + \frac{y}{r_{TE}} \right) dy$$

$$\delta_{TE}^* = \int_0^{\delta} \left( 1 - \frac{u}{U} \right) \left( 1 + \frac{y}{r_{TE}} \right) dy$$

$H_{TE} = 1.4$  shortly downstream of the rear end of the model and  $H = 1.0$  at infinity; therefore  $\bar{H} + 2 = 3.2$ , and

$$C_{Dw} = \left( \frac{U_{TE}}{U_{\infty}} \right)^{3.2} \int_0^{2\pi} \frac{2 r_{TE} \theta_{TE}}{S} d\varphi$$

For the determination of the total wake drag the momentum thickness as measured by each boundary layer rake was determined and a local wake drag  $c_{Dw}(\varphi)$  at the radial angle of the rake was defined as

$$c_{Dw}(\varphi) = \left( \frac{U_{TE}}{U_{\infty}} \right)^{3.2} \times \frac{2 r_{TE} \theta_{TE}}{S}$$

#### (E) Measurements and Evaluation (Continued)

At an angle of attack  $\alpha = 0^\circ$  it was assumed that the circumferential distribution of the partial drag was sinusoidal so that

$$C_{D_w} = 2\pi \times \frac{c_{D_w}(0^\circ) + c_{D_w}(90^\circ)}{2}$$

where the subscripts t and s refer to the top and side rakes respectively. This assumes that the boundary layer diametrically opposite a given rake would be the same as the boundary layer at the rake. At an angle of attack this procedure is incorrect and must be modified as follows. The nose of the model was elevated to the proper angle, the test conditions were established and data were taken over a range of total suction quantity. After stopping the wind tunnel the nose of the model was depressed to the negative value of the chosen angle and the previous test conditions were re-established. For the determination of the total wake drag coefficient a sinusoidal distribution of the partial drag measured at plus and minus  $\alpha$  was assumed at a given total suction quantity. Thus

$$C_{D_w} = 2\pi \times \left\{ \frac{[c_{D_w}(0) + c_{D_w}(90)]_{+\alpha} + [c_{D_w}(180) + c_{D_w}(90)]_{-\alpha}}{4} \right\} Q_t = \text{const}$$

The total equivalent drag is then the sum of the wake and equivalent suction drags:

$$C_{D_t} = C_{D_w} + C_{D_s}$$

#### (F) Experimental Results

The pressure distributions measured at angles of attack  $\alpha = 0$  and  $2^\circ$  are shown in Figure 167. The given pressure distributions for an angle of attack  $\alpha = 2^\circ$  are those of the upper and lower meridians only.

Figures 168 through 170 show representative local wake drag coefficients  $c_{D_w}(\phi)$  (defined in (E) above) at an angle of attack  $\alpha = 0^\circ$  as calculated from the measurements of the boundary layer rakes at the aft end of the model. The total wake drag coefficients  $C_{D_w}$  resulting from the integration of the local wake drag coefficients  $c_{D_w}(\phi)$  of the chosen samples are shown in Figures 171 through 173, along with the equivalent suction drag  $C_{D_s}$  and the equivalent total drag coefficient  $C_{D_t}$ , as a function of suction flow coefficient  $C_{Q_t}$ .

According to Figures 168 through 170 the local drag measured by the top rake  $c_{D_w}(0^\circ)$  was consistently higher than that of the side rake  $c_{D_w}(90^\circ)$ . In the analytical section of this report Bossel's calculations show good agreement between the theoretical boundary layer velocity profile at the measuring station and the profile measured by the side rake. Therefore, it appears reasonable to include a study of the drag assuming that only the measurements of the side rake were valid. The wake drag was defined as  $C_{D_w} = 2\pi c_{D_w}(90^\circ)$  and



## (F) Experimental Results (Continued)

samples are shown as a function of total suction coefficient  $C_{Qt}$  in Figures 174 through 176. Also included in Figures 174 through 176 are the equivalent suction drags  $C_{Ds}$  and the equivalent total drag coefficient  $C_{Dt}$  that results from this definition of  $C_{Dw}$ .

Representative local wake drags measured at an angle of attack  $\alpha = 2^\circ$  are shown in Figures 177 through 179. For simplicity of presentation, it was assumed that the measurements at  $\alpha = -2^\circ$  were the equivalent of measurements of two additional rakes (located at the bottom and side of the model) at  $\alpha = +2^\circ$ . Therefore, in Figures 177 through 179 the notation  $C_{Dw}(180^\circ)$  is introduced to identify the local drag measured by the top rake at  $\alpha = -2^\circ$ .

The total wake drag coefficients  $C_{Dw}$  at an angle of attack  $\alpha = 2^\circ$  are shown in Figures 180 through 182 as a function of total suction flow coefficient  $C_{Qt}$ . The same figures include the equivalent suction drag coefficients  $C_{Ds}$  and the equivalent total drag coefficient  $C_{Dt}$ .

Figures 183 and 184 show the variation of the minimum equivalent drag coefficient  $C_{Dt_{min}}$  and the corresponding optimum suction quantity coefficient at minimum equivalent total drag  $C_{Q_{opt}}$  with length Reynolds number  $R_L$  at an angle of attack  $\alpha = 0^\circ$ . Figure 183 shows the results when the wake drag was taken as the average of the partial drags of both top and side rakes and Figure 184 shows the effect of determining the wake drag from the partial drag of the side rake alone.  $C_{Dt_{min}}$  and  $C_{Q_{opt}}$  as functions of  $R_L$  for  $\alpha = 2^\circ$  are shown in Figure 185.

The lengthwise distributions of the nondimensional equivalent area suction velocity  $v_o^*$  as evaluated for several test runs at angle of attack  $\alpha = 0^\circ$  are shown in Figure 186. These suction velocity distributions correspond to the test points that gave the lowest values of  $C_{Dt}$  during each test run and are compared to the design suction velocity distribution taken from Figure 166. The boundary layer velocity profiles that correspond to the experimental suction velocity distributions of Figure 186 are shown in Figures 187a and 187b.

The variation of the boundary layer velocity profiles, as measured by the boundary layer rakes, with total suction coefficient  $C_{Qt}$  are shown in Figures 188a through 190b. Figures 188a, 189a and 190a show the velocity profiles measured by the top rake whereas Figures 188b, 189b and 190b show those measured by the side rake.

## (G) Discussion

At an angle of attack  $\alpha = 0^\circ$  full length laminar flow was maintained on the modified Sears-Haack low drag suction body of revolution to a

(G) Discussion (Continued)

length Reynolds number  $R_L = 20.1 \times 10^6$  (see Figure 184). The minimum equivalent total drag coefficient (based on wetted area and including equivalent suction drag) at  $\alpha = 0^\circ$  and  $R_L = 19.6 \times 10^6$  was  $C_{D_{t_{min}}} = 3.6 \times 10^{-4}$  and the corresponding total suction coefficient was  $C_{Q_{opt}} = 1.75 \times 10^{-4}$ . At length Reynolds number below  $R_L = 19.6 \times 10^6$  the minimum equivalent total drag was approximately 1.18 times the friction drag of a laminar flat plate.

The above results were based on the wake drag as determined from the boundary layer measurements of the side rake alone. If the boundary layer measurements of both top and side rakes are used to determine the wake drag, then the level of the minimum equivalent total drag coefficient is raised to 1.34 times the laminar flat plate friction coefficient (Figure 183). Since the boundary layer profiles measured by the top rake are consistently thicker than those of the side rake it is felt that, although the nose of the model was known to be aligned with the wind tunnel airflow, the rear end of the model was at a slight angle of attack such that the airflow was from the bottom of the model toward the top. This induced angle of attack might have been due to slightly asymmetric flow in the wind tunnel or the asymmetry of the mounting system. If the increased partial drag of the top rake was due to the rear of the model being at a slight angle of attack then it is reasonable to assume that the boundary layer over the lower portion of the model would be thinner and thus give a lower drag. The lower drag over the underside of the model would tend to compensate for the increased drag of the upper portion and thus the overall drag would approach the results given by the side rake alone.

The lowest equivalent total drag coefficient measured at an angle of attack  $\alpha = 2^\circ$  was  $C_{D_{t_{min}}} = 4.8 \times 10^{-4}$  at a Reynolds number  $R_L = 16.19 \times 10^6$  (Figure 185). The total suction quantity at minimum equivalent total drag was  $C_{Q_t} = 1.95 \times 10^{-4}$ . This equivalent total drag is 1.44 times the laminar flat plate friction drag. At lower Reynolds numbers the ratio of the equivalent total drag to the friction drag of a laminar flat plate decreased. At a Reynolds number  $R_L = 6.3 \times 10^6$  the minimum equivalent total drag was 1.18 times the laminar flat plate friction coefficient. At this Reynolds number the actual minimum equivalent total drag coefficient  $C_{D_{t_{min}}} = 6.25 \times 10^{-4}$  occurred at a total suction coefficient  $C_{Q_t} = 1.24 \times 10^{-4}$ .

b. ANALYSIS OF THE BOUNDARY LAYER DEVELOPMENT ON A MODIFIED SEARS-HAACK SUCTION BODY OF REVOLUTION

Hartmut B. K. Bessel

(A) Summary

The laminar boundary layer development in incompressible flow over a modified Sears-Haack low drag suction body of revolution of 142-inch length was computed by means of Raetz's method (Reference 45). The theoretical data obtained are compared with experimental data for eight test points at length Reynolds numbers from  $6.3$  to  $19.6 \times 10^6$ .

The theoretical data are in satisfactory agreement with the experimental data although they are not exactly comparable, since pure axisymmetric flow was not achieved during the experiments.

(B) Notation

$\bar{r}$  nondimensional body radius =  $r/L'$

$\bar{x}$  =  $x/L'$  = nondimensional distance along body axis

$\bar{z}$  =  $(z/L)\sqrt{R_L}$  = nondimensional distance normal to surface

$\bar{\delta}$  =  $(\delta/L)\sqrt{R_L}$  = nondimensional boundary layer thickness  
( $u/U = 0.999$ )

$\bar{\delta}^*$  =  $(\delta^*/L)\sqrt{R_L}$  = nondimensional boundary layer displacement thickness

$\bar{\theta}$  =  $(\theta/L)\sqrt{R_L}$  = nondimensional boundary layer momentum thickness

Bars denote nondimensional quantities. All other symbols are defined in the notation given in Chapter D-a.

(C) Introduction

This report is concerned with the computation of the boundary layer development along a modified Sears-Haack suction body of revolution in axisymmetric incompressible flow and comparison with test results.

The Sears-Haack low drag suction body was designed for operation at very low turbulence levels at length Reynolds numbers up to  $49 \times 10^6$ . Area suction was closely approached by means of suction through 120 fine slots. The model was tested in the Norair low turbulence 7- by 10-foot wind tunnel at Reynolds numbers between  $6$  and  $20 \times 10^6$  (see Section II, Part 1, Chapter D-a). About 400 test runs were obtained, of which eight are analyzed in this report. Data for these eight runs are given in Tables XI through XIV. The shape of the body and its velocity distribution are shown in Figure 191. This velocity distribution was obtained by averaging the pressure readings for run numbers 41, 46, 52, 66, 76 and 78.

### (C) Introduction (Continued)

During the wind tunnel tests, the measured velocity distribution in the boundary layer at the end of the model (at a station 142 inches from the nose of the model) was not uniform along the circumference of the model. The boundary layer measured at the side of the model was thinner than that at the top. The shape of the top rake velocity profile indicated transitional flow in most cases. Increased suction tended to bring both rake readings to closer agreement.

The boundary layer development along the body was computed for incompressible flow by means of Raetz's method (Reference 45) on a high speed electronic IBM 7090 computer. Area suction was assumed for the calculation. The experimental suction distributions were approximated by analytical expressions. Figure 192 shows an example of this approximation for run number 66. The resulting differences in the total suction flow coefficients are tabulated in Table XIV.

### (D) Results

#### (1) Boundary Layer Development

The computed boundary layer development for each of the eight test runs is given in Figures 193 through 200. Momentum thickness Reynolds number  $R_\theta = U\theta/\nu$ , nondimensional momentum thickness  $\bar{\theta} = (\theta/L) \sqrt{R_L}$ , nondimensional displacement thickness  $\bar{\delta}^* = (\delta^*/L) \sqrt{R_L}$ , and shape parameter  $H = \delta^*/\theta$  are plotted vs  $\bar{x} = x/L$ . The nondimensional suction inflow velocity\*  $v_o^*$  is added to the figures to show the effect of varying suction.

#### (2) Velocity Distribution in the Boundary Layer at the Rake Position

The computed nondimensional velocity distribution in the boundary layer at the position of the rakes ( $\bar{x} = 1.0179$ ) is plotted in Figures 201 through 208. Experimental points from the side and top rakes are added for comparison. The nondimensional height  $\bar{z}$  above the surface may be converted to the actual height  $z$  (in.) by using the relation

$$z = \frac{\bar{z}L}{\sqrt{R_L}} \text{ (in.)}; \text{ where } L = 142 \text{ inches.}$$

The following table gives the conversion factors.

Run Number	41	46	52	66	76	78	397	421
$L/\sqrt{R_L}$	.0565	.0564	.0480	.0386	.0370	.03705	.0342	.0321

The computed velocity profiles are compared in Figure 209 with the experimental data. The profile for run number 421 lies between those for run numbers 41, 66, and 397. It has been omitted for the sake of clarity.

\*For equivalent area suction.

(D) Results (Continued)

(3) Characteristic Values at the Rake Position

In Figures 210 through 212 the computed and experimental values of the displacement thickness  $\bar{\delta}^*$ , the momentum thickness  $\bar{\theta}$ , and the shape parameter  $H$  are plotted as functions of the total suction flow coefficient  $C_{Qt}$ .

The effect of suction on the boundary layer Reynolds number can be compared by plotting  $R_\theta/\sqrt{R_L}$  vs  $C_{Qt}$  (Figure 213). Since the momentum thickness Reynolds number  $R_\theta$  is proportional to the dimensionless momentum thickness times the square root of the length Reynolds number,  $R_\theta/\sqrt{R_L}$  is constant for equal nondimensional suction distributions  $v_o^*(\bar{x})$ .

The influence of suction on the wake drag coefficient  $C_{D_w}$  can be seen from Figure 214, where  $C_{D_w}/\sqrt{R_L}$  has been plotted vs  $C_{Qt}$ . Since  $C_{D_w}$  is proportional to  $\bar{\theta}/\sqrt{R_L}$ ,  $C_{D_w}/\sqrt{R_L}$  must be constant for constant  $\bar{\theta}$ .

A summary of the experimental and computed data for the eight points is given in Table XIII.

(E) Discussion

(1) Boundary Layer Development

The laminar boundary layer thickness on a body of revolution is influenced mainly by two things:

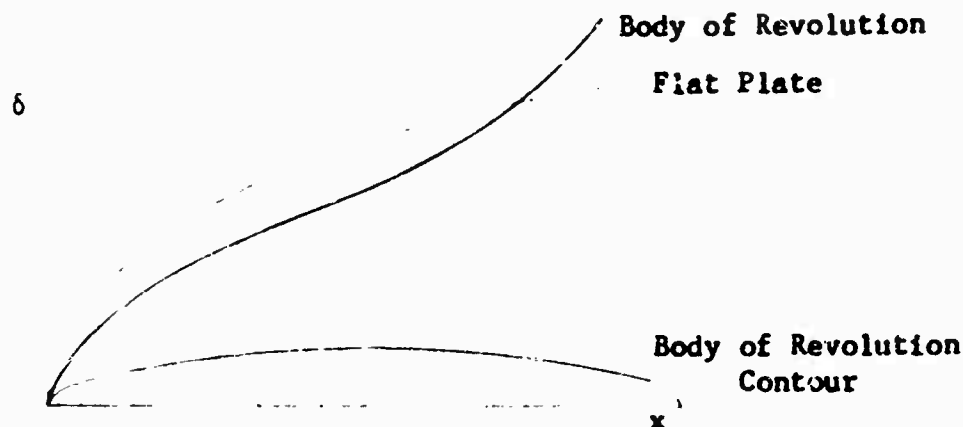
- (a) it tends to become thicker with  $\sqrt{x}$ ;
- (b) as the body diameter changes with  $x$ , the boundary layer is expanded and contracted accordingly. Its thickness thus tends to change inversely proportional to  $r$ .

We thus have

$$\delta \sim \frac{\sqrt{x}}{r} \quad (\text{laminar region}).$$

This causes the boundary layer to grow in thickness more slowly in regions of increasing  $r$  compared to the two-dimensional case and to grow faster in regions of decreasing  $r$ . The overall effect is sketched below (assuming laminar flow, which cannot be maintained much beyond maximum thickness without suction at higher Reynolds numbers).

## (1) Boundary Layer Development (continued)



This general tendency is shown in Figures 193 through 200 for the displacement and momentum thicknesses  $\delta^*$  and  $\bar{\theta}$  and the momentum thickness Reynolds number  $R_\theta$ .

Increasing suction decreases the boundary layer displacement and momentum thicknesses  $\delta^*$  and  $\bar{\theta}$ , the boundary layer momentum thickness Reynolds number  $R_\theta$ , and the boundary layer shape parameter  $H$ . This effect is especially pronounced for the cases of strong suction (runs 46 and 78).

The nondimensional boundary layer thickness  $\bar{\delta}$  is proportional to the square root of the length Reynolds number  $R_L$ . Displacement and momentum thicknesses  $\delta^*$  and  $\bar{\theta}$  and momentum thickness Reynolds number  $R_\theta$  are therefore higher for higher length Reynolds numbers.

Forward suction must be increased with higher length Reynolds numbers since the stability limit Reynolds number is reached farther forward. This may be seen from Figure 215 where the "center of gravity" coordinate  $\bar{x}_{c.g.}$  of the suction inflow velocity distribution ( $v_o^*$ ) has been plotted vs  $R_L$ . The  $v_o^*_{c.g.}$  coordinate has also been plotted. It is dependent upon the total suction flow coefficient  $C_{Qt}$  and upon the form of the inflow velocity distribution. The lower values for runs 421 and 397 may explain the highly transitional flow for these two runs at the top rake position.

## (2) The Boundary Layer at the Rake Position

Stronger suction causes fuller velocity profiles. This can be seen from Figures 201 through 208, and from Figure 209, where seven boundary layer velocity profiles are compared. The profiles for weak suction ( $C_{Qt} \approx 1.8$  to  $2 \times 10^{-4}$ ) closely resemble each other. The dimensionless total boundary layer thickness  $\bar{\delta}$  lies around  $\bar{z} = 8$  to 9.

The test points for the top and side rakes (Figures 200 through 208) are not in agreement, indicating that the flow around the test body was not axisymmetric. The computed velocities lie between the two extremes, agreeing better with the points measured at the side rake. This agreement is

## (2) The Boundary Layer at the Rake Position (Continued)

even better in the case of increased suction (e.g., run numbers 46 and 78). The top rake test points for all runs except 46 and 78 indicate transitional flow.

Inspection of Figures 210 through 214 shows a dependence of  $\bar{\delta}^*$ ,  $\bar{\theta}$ ,  $H$ ,  $R_0$  and  $C_{D_w}$  on the total suction flow coefficient  $C_{Q_t}$ . The computed points for  $\bar{\theta}$ ,  $R_0/\sqrt{R_L}$  and  $C_{D_w}/\sqrt{R_L}$  (Figures 211, 213 and 214) agree fairly well with the test results for the side rake while the agreement for  $\bar{\delta}^*$  and  $H$  and the top rake points is less satisfactory.

The plots for  $\bar{\theta}$ ,  $C_{D_w}/\sqrt{R_L}$  and  $R_0/\sqrt{R_L}$  vs  $C_{Q_t}$  are similar since

$$\bar{\theta} \sim C_{D_w}/\sqrt{R_L} \sim R_0/\sqrt{R_L}.$$

Computed points and side rake points are in relatively close agreement for these values (Figures 211, 213 and 214), while the top rake points are higher. The points representing top rake measurements for run numbers 41, 52, 66, 397, and 421 are not in consistent relationship to those for run numbers 46, 76, and 78, which are cases of stronger suction. Inspection of Figures 201 through 208 indicates transitional flow for run numbers 41, 52, 66, 397 and 421.

The fuller the velocity profile, the smaller is the displacement thickness

$$\bar{\delta}^* = \frac{\sqrt{R_L}}{L} \int_{z=0}^{\delta} (1 - \frac{u}{U}) dz$$

The computed displacement thicknesses on Figure 210 are between those for the top and side rakes. The agreement for the cases of higher suction (46 and 78) is much better than for those of lower suction.

The computed shape parameters  $H$  (Figure 212) are higher than those for the side and top rakes. They show an almost linear dependence on  $C_{Q_t}$ , while the test points are more scattered.

The shape parameters measured at the top and side rakes are smaller than those computed. The reasons are:

- (a) for the side rake  $\bar{\delta}^*$  is smaller than computed, while  $\bar{\theta}$  is about the same;
- (b) for the top rake  $\bar{\delta}^*$  is higher, but  $\bar{\theta}$  is also much higher, with the overall result of a lower  $H$ .

(F) Conclusion

The laminar boundary layer development along a 142-inch long modified Sears-Haack body of revolution was computed and compared with test results for Reynolds numbers from 6.3 to  $19.6 \times 10^6$  (see Section II, Part 1, Chapter D-a).

Six cases of minimum suction ( $C_{Q_t} = 1.75$  to  $2.02 \times 10^{-4}$ ) and two cases of higher suction ( $C_{Q_t} = 2.66$  and  $3.68 \times 10^{-4}$ ) were considered. Area suction was assumed and approximated analytically. The resulting average difference of the total inflow coefficient  $C_{Q_t}$  was 0.59 percent, with a maximum deviation of 1.54 percent.

The computations showed the computed values to lie between those measured at the top and the side rakes. The differences must be attributed to asymmetric flow during the experiments.

The measured displacement thickness  $\delta^*$  at the side rake (top rake) was 68 to 88 percent (109 to 140 percent) of the computed value, while measured momentum thickness  $\theta$  and wake drag coefficient  $C_{D_w}$  at the side rake (top rake) were 89 to 102 percent (135 and 179 percent) of the computed values. The computed wake drag coefficients  $C_{D_w}$  ranged from 0.000179 to 0.000386.



# LIST OF TABLES FOR SECTION II, PART 1

<u>Table No.</u>	<u>Table Title</u>	<u>Page</u>
I	30° SWEEP WING MODEL AIRFOIL COORDINATE PERPENDICULAR TO LEADING EDGE.....	173
II	POSITION OF SLOTS AND CHAMBERS, SLOT WIDTHS.....	174
III	SUMMARY OF TEST POINTS CHOSEN FOR ANALYTICAL STUDY OF BOUNDARY LAYER DEVELOPMENT.....	176
IV	OFF-DESIGN SUCTION INFLOW INTO THE AFT FOUR CHAMBERS AT HIGH REYNOLDS NUMBER.....	177
V	MODEL COORDINATES 17-FOOT CHORD STRAIGHT LAMINAR SUCTION WING.....	178
VI	CHARACTERISTICS OF MODEL SLOT AND METERING HOLE DESIGN 17-FOOT CHORD STRAIGHT LAMINAR SUCTION WING.....	179
VII	FAIRING ORDINATES 17-FOOT CHORD STRAIGHT LAMINAR SUCTION WING.....	182
VIII	MODEL COORDINATES MODIFIED SEARS-HAACK LAMINAR SUCTION BODY OF REVOLUTION.....	183
IX	CHARACTERISTICS OF MODEL SLOT AND METERING HOLE DESIGN MODIFIED SEARS-HAACK LAMINAR SUCTION BODY OF REVOLUTION.....	184
X	STATIC PRESSURE ORIFICE AND MICROPHONE LOCATIONS MODIFIED SEARS-HAACK LAMINAR SUCTION BODY OF REVOLUTION..	187
XI	SUMMARY OF TEST POINTS CHOSEN FOR ANALYTICAL STUDY OF BOUNDARY LAYER DEVELOPMENT.....	188
XII	CHORDWISE SUCTION INFLOW VELOCITY DISTRIBUTION - $v_o^*$ VS $\bar{x}$ MODIFIED SEARS-HAACK LAMINAR SUCTION BODY OF REVOLUTION.....	189
XIII	SUMMARY OF COMPUTED AND EXPERIMENTAL DATA AT THE RAKE POSITION MODIFIED SEARS-HAACK LAMINAR SUCTION BODY OF REVOLUTION.....	190
XIV	COMPARISON OF EXPERIMENTAL AND COMPUTED TOTAL SUCTION FLOW COEFFICIENT $C_{Q_t}$ MODIFIED SEARS-HAACK LAMINAR SUCTION BODY OF REVOLUTION.....	191

TABLE I

30° SWEEP WING MODEL

AIRFOIL COORDINATE PERPENDICULAR TO LEADING EDGE

Chord in perpendicular direction  $C' = 72.96$  in.  
Leading edge radius  $R_0/C' = .81\%$

Abscissa X % C'	Ordinate Y % C'
0	0
.5482	$\pm .9745$
.8224	$\pm 1.1636$
1.2335	$\pm 1.3939$
2.4671	$\pm 1.9312$
5.2786	$\pm 2.8506$
7.7713	$\pm 3.4768$
10.2641	$\pm 4.0072$
15.2494	$\pm 4.8607$
20.2347	$\pm 5.5129$
25.2200	$\pm 6.0163$
30.2054	$\pm 6.3962$
35.1907	$\pm 6.6664$
40.1760	$\pm 6.8319$
45.1613	$\pm 6.8917$
50.1467	$\pm 6.8508$
55.1320	$\pm 6.6973$
60.1173	$\pm 6.3992$
65.1026	$\pm 5.8588$
70.0881	$\pm 5.1269$
75.0734	$\pm 4.2694$
80.0587	$\pm 3.3661$
85.0440	$\pm 2.4605$
90.0294	$\pm 1.5404$
95.0147	$\pm .6880$
100	0

TABLE II

## POSITION OF SLOTS AND CHAMBERS, SLOT WIDTHS

SLOT NO.	SLOT WIDTH INCHES	SLOT POSITION % PROJECTED CHORD	CHAMBER NO.	SLOT NO.	SLOT WIDTH INCHES	SLOT POSITION % PROJECTED CHORD	CHAMBER NO.
101	0.004	0.52	101	30	0.005	66.29	5
102		2.07	102	31		66.84	5
103		4.97	103	32		67.39	5
104		8.92	104	33		67.94	6
105		12.96	105	34		68.48	
106		16.98	106	35		69.03	
107		20.50	106	36		69.58	
1		25.00	1	37		70.13	
2		29.85	1	38		70.68	
3		33.31	2	39		71.23	
4		36.16		40		71.77	
5		38.54		41		72.32	6
6		40.60	2	42		72.87	7
7		42.49	3	43		73.42	
8		44.31		44		73.97	
9		45.99		45		74.52	
10		47.57		46		75.06	
11		49.04		47		75.61	
12		50.41		48		76.16	
13		51.75	3	49		76.71	
14		53.02	4	50		77.26	7
15		54.20		51		77.81	8
16		55.34		52		78.36	
17		56.39		53		78.90	
18		57.43		54		79.45	
19		58.46		55		80.00	
20		59.46		56		80.55	
21		60.45		57		81.10	
22		61.41		58		81.65	
23	0.004	62.33	4	59		82.19	8
24	0.005	63.00	5	60		82.74	9
25		63.55		61		83.29	
26		64.10		62		83.84	
27		64.65		63		84.39	
28		65.19		64		84.94	
29	0.005	65.74	5	65	0.005	85.48	9

TABLE II (Continued)

POSITION OF SLOTS AND CHAMBERS, SLOT WIDTHS

SLOT NO.	SLOT WIDTH INCHES	SLOT POSITON % PROJECTED CHORD	CHAMBER NO.
66	0.005	86.03	9
67		86.58	
68		87.13	9
69		87.68	10
70		88.23	
71		88.77	
72		89.32	
73		89.87	
74		90.42	
75		90.97	
76		91.52	
77		92.07	10
78		92.61	11
79		93.16	
80		93.71	
81		94.26	
82		94.81	
83		95.36	
84		95.90	
85		96.45	
86	0.005	97.00	11

TABLE III

SUMMARY OF TEST POINTS CHOSEN FOR ANALYTICALSTUDY OF BOUNDARY LAYER DEVELOPMENT

Run Number	$\alpha$	$R_c \times 10^{-6}$	$C_{Qt} \times 10^4$	$C_{Qt}/C_{Qopt}$	$\theta_{test}$ (in.)	$\theta_{calc}$ (in.)	$\theta_{calc}/\theta_{test}$
12	0°	23.795	3.963	1.086	.00541	.00449	0.830
13		23.607	3.842	1.050	.00523	.00441	0.843
24		17.881	3.659	1.028	.00742	.00751	1.012
33		18.836	3.479	0.980	.00965	.00758	0.785
73		13.943	3.256	0.935	.00906	.00963	1.063
75		13.938	4.073	1.170	.00826	.00801	0.970
85	-1°	14.093	3.534	0.986	.00884	.00901	1.019
86		14.118	3.991	1.115	.00814	.00890	1.093
90		19.546	3.389	1.010	.00690	.00704	1.020
100		23.706	3.486	1.006	.00593	.00639	1.078
104		27.211	3.354	1.020	.00553	.00590	1.067
109		27.172	3.586	1.093	.00512	.00582	1.137
154	+1°	28.577	3.668	0.987	.00571	.00511	0.895
155		28.567	3.972	1.068	.00438	.00429	0.979
178		18.659	3.381	1.000	.00844	.00814	0.964
184		13.417	4.124	1.102	.00844	.00879	1.041
186		13.417	3.931	1.050	.00912	.00873	0.957
187		23.349	3.789	1.041	.00684	.00583	0.852

TABLE IV  
OFF-DESIGN SUCTION INFLOW INTO THE  
AFT FOUR CHAMBERS AT HIGH REYNOLDS NUMBER

Run Number	Chamber Number	Slot Number	Slot -v <sub>0</sub> *	R <sub>s</sub>	R <sub>h</sub>	10 <sup>4</sup> x Chamber C <sub>Qc</sub> (calc.)	10 <sup>4</sup> x Chamber C <sub>Qm</sub> (meas.)	( $\frac{C_{Qc}}{C_{Qm}} - 1$ ) (%)
154	8	51	-0.573	7.32	60.54	.33978	.32306	-5.18
		52	1.545	19.73	167.50			
		53	2.672	34.12	297.56			
		54	3.559	45.45	401.86			
		55	4.200	53.63	487.75			
		56	4.767	60.88	561.68			
		57	5.239	66.89	626.25			
		58	5.624	71.81	682.32			
	9	59	5.992	76.51	738.04	.35184	.37905	-7.18
		60	0.000	0.00	0.00			
		61	1.636	20.89	174.97			
		62	2.785	35.56	305.90			
		63	3.624	46.28	403.59			
		64	4.218	53.86	482.91			
		65	4.818	61.51	559.44			
		66	5.298	67.65	624.18			
	10	67	5.734	73.21	685.36	.34378	.36694	-6.31
		68	6.084	77.69	738.23			
		69	-1.290	16.47	134.44			
		70	1.026	13.10	109.73			
		71	2.368	30.23	256.56			
		72	3.370	43.03	375.26			
		73	4.291	54.79	484.45			
		74	4.935	63.01	573.03			
	11	75	5.674	72.45	668.42	.35644	.41182	-13.45
		76	6.220	79.43	743.64			
		77	6.820	87.08	827.44			
		78	-1.385	17.68	144.29			
		79	1.516	19.36	162.20			
		80	2.936	37.49	318.20			
		81	3.956	50.51	440.47			
		82	4.537	57.93	512.23			
		83	5.154	65.81	590.08			
		84	5.553	70.90	644.80			
		85	6.022	76.90	709.52			
		86	6.355	81.14	759.62			

**TABLE V****MODEL COORDINATES****17-FOOT CHORD STRAIGHT LAMINAR SUCTION WING**

<u>x ( c )</u>	<u>y ( <math>\frac{1}{2}</math> c )</u>
0	0
0.4	0.1549
0.8	0.2240
1.2	0.2779
1.6	0.3250
2.0	0.3652
2.5	0.4142
3.0	0.4598
4.0	0.5471
5.0	0.6289
7.5	0.8142
10.0	0.9800
15.0	1.2632
20.0	1.4931
25.0	1.6770
30.0	1.8181
35.0	1.9181
40.0	1.9789
45.0	2.0000
50.0	1.9789
55.0	1.9181
60.0	1.8181
65.0	1.6770
70.0	1.4971
75.0	1.2730
80.0	1.0240
85.0	0.7461
90.0	0.4642
95.0	0.2044
100.00	0

TABLE VI

CHARACTERISTICS OF MODEL SLOT AND METERING HOLE DESIGN17-FOOT CHORD STRAIGHT LAMINAR SUCTION WING

Hole Spacing = 0.50 inch

Chamber Number	Slot Number	Location (% c)	Slot Width (in.)	Hole Diameter (in.)
1	1	1.000	0.004	0.0350
2	2	3.000		0.0350
3	3	5.130		0.0350
↑	4	7.323		0.0320
3	5	9.529		0.0320
4	6	11.735		0.0292
↑	7	13.941		0.0310
↓	8	16.147		0.0320
4	9	18.353	0.004	0.0350
5	10	20.559	0.005	0.0292
↑	11	22.765		0.0310
5	12	24.971		0.0310
6	13	27.177		0.0310
↑	14	29.749		0.0320
↓	15	32.320		0.0320
6	16	34.180		0.0320
↑	17	35.910		0.0320
↓	18	37.540		0.0320
8	19	39.070		0.0310
↑	20	40.520		0.0310
↓	21	41.890		0.0310
8	22	43.190		0.0310
↑	23	44.430		0.0292
9	24	45.610		0.0310
↑	25	46.750		0.0292
↓	26	47.840		0.0292
↑	27	48.890		0.0292
↓	28	49.900		0.0292
9	29	50.890		0.0292
↑	30	51.840		0.0292
10	31	52.770		0.0292
↑	32	53.680		0.0292
↓	33	54.530		0.0292
↑	34	55.370		0.0292
↓	35	56.190		0.0292
↑	36	56.990		0.0280
10	37	57.770	0.005	0.0280



**TABLE VI (Continued)**

Chamber Number	Slot Number	Location (% c)	Slot Width (in.)	Hole Diameter (in.)
11	38	58.530	0.005	0.0292
	39	59.268		0.0292
11	40	59.995		0.0292
	41	60.708		0.0292
12	42	61.405		0.0280
	43	62.088		0.0280
12	44	62.755		0.0280
	45	63.408		0.0280
12	46	64.045		0.0292
	47	64.670		0.0292
13	48	65.285	0.005	0.0280
	49	65.898		0.0280
13	50	66.511		0.0280
	51	67.124		0.0280
13	52	67.737		0.0280
	53	68.350		0.0280
13	54	68.963		0.0260
	55	69.576		0.0260
13	56	70.189		0.0310
	57	70.802		0.0292
14	58	71.415	0.006	0.0292
	59	72.028		0.0292
14	60	72.641		0.0280
	61	73.254		0.0280
14	62	73.867		0.0280
	63	74.480		0.0280
14	64	75.093		0.0280
	65	75.706		0.0260
14	66	76.319		0.0320
	67	76.932		0.0310
15	68	77.545	0.006	0.0310
	69	78.158		0.0310
15	70	78.771		0.0292
	71	79.384		0.0292
15	72	79.997		0.0292
	73	80.610		0.0280
15	74	81.223		0.0280
	75	81.836		0.0280
15	76	82.449		0.0330
	77	83.062		0.0320
15	78	83.675	0.007	0.0320
	79	84.288		0.0310
15	80	84.901		0.0310
	81	85.514		0.0292
15	82	86.127		0.0292
	83	86.740		0.0292
15	84	87.353		0.0280

**TABLE VI (Continued)**

Chamber Number	Slot Number	Location (% c)	Slot Width (in.)	Hole Diameter (in.)
15	85	87.966	0.007	0.0280
16	86	88.579		0.0350
↑	87	89.192		0.0330
	88	89.805		0.0320
	89	90.418		0.0320
	90	91.031	0.008	0.0310
	91	91.644		0.0310
	92	92.257		0.0292
	93	92.870		0.0292
	94	93.483		0.0292
	95	94.096		0.0280
	96	94.709		0.0280
	97	95.322		0.0280
	98	95.935		0.0260
	99	96.548		0.0260
	100	97.161		0.0250
16			0.008	

TABLE VII

FAIRING ORDINATES

17-FOOT CHORD STRAIGHT LAMINAR SUCTION WING

Abscissa x Measured from Airfoil Nose (in.)	Ordinate y Fairing No. 1 (in.)	Ordinate y Fairing No. 2 (in.)
-30.000		0
-20.000		5.903
-10.000		7.467
-6.919	0	- -
0	1.005	7.920
10.000	2.206	7.719
20.000	3.173	7.433
30.000	3.944	7.112
40.000	4.549	6.786
50.000	5.013	6.470
60.000	5.356	6.163
70.000	5.594	5.867
80.000	5.740	5.580
90.000	5.800	5.304
100.000	5.780	5.037
110.000	5.680	4.781
120.000	5.500	4.534
130.000	5.240	4.297
140.000	4.900	4.042
150.000	4.480	3.696
160.000	3.980	3.248
170.000	3.410	2.708
180.000	2.810	2.094
190.000	2.210	1.428
200.000	1.610	0.734
210.000	1.010	0.330
210.479	- -	0
220.000	0.410	
226.833	0	

TABLE 'III

MODEL COORDINATES

MODIFIED SEARS-HAACK LAMINAR SUCTION BODY OF REVOLUTION

<u>x/L'</u>	<u>r/L'</u>
0	0
.005	.00433
.010	.00638
.030	.01239
.050	.01714
.075	.02189
.100	.02664
.150	.03412
.200	.04017
.250	.04505
.300	.04892
.350	.05186
.400	.05392
.450	.05515
.500	.05556
.550	.05515
.600	.05392
.650	.05186
.700	.04892
.750	.04505
.800	.04017
.850	.03412
.900	.02798
.950	.02342
1.000	.02097
1.030	.02050

TABLE IX

CHARACTERISTICS OF MODEL SLOT AND METERING HOLE DESIGNMODIFIED SEARS-HAACK LAMINAR SUCTION BODY OF REVOLUTION

All slot widths = 0.003 inch

<u>Chamber Number</u>	<u>Slot Number</u>	<u>Slot Position (% Length)</u>	<u>Hole Diameter (Inch)</u>	<u>Number Of Holes (Per Inch)</u>
1	1	.0556	.0260	5.23
	2	.0699	.0260	6.80
	3	.0842	.0292	6.98
1	4	.0986	.0465	4.42
2	5	.1129	.0260	4.88
	6	.1272	.0260	5.32
	7	.1416	.0260	5.82
	8	.1559	.0260	6.77
	9	.1703	.0292	6.04
2	10	.1846	.0320	5.28
3	11	.1989	.0260	5.50
	12	.2133	.0260	5.78
	13	.2276	.0260	5.96
	14	.2419	.0260	5.87
	15	.2563	.0280	5.56
	16	.2706	.0292	5.20
	17	.2849	.0310	4.78
	18	.2993	.0320	4.48
	19	.3136	.0330	4.23
	20	.3280	.0260	5.06
	21	.3423	.0260	5.12
	22	.3566	.0260	4.92
	23	.3710	.0280	4.72
	24	.3853	.0280	4.54
	25	.3996	.0280	4.35
	26	.4140	.0292	4.23
	27	.4283	.0292	4.00
4	28	.4427	.0310	4.00
	29	.4570	.0250	4.48
	30	.4713	.0260	4.39
	31	.4857	.0280	4.26
	32	.5000		4.15
	33	.5143		4.02
	34	.5287	.0280	4.00
	35	.5430	.0292	4.00
	36	.5573		
	37	.5717		
5	38	.5860	.0292	
6	39	.6004	.0292	4.00
	40	.6147	.0292	4.00
	41	.6290		
6	42	.6434	.0292	4.00

**TABLE IX (Continued)**

<u>Chamber Number</u>	<u>Slot Number</u>	<u>Slot Position (% Length)</u>	<u>Hole Diameter (Inch)</u>	<u>Number Of Holes (Per Inch)</u>
6	43	.6577	.0280	4.00
	44	.6720	.0280	4.00
	45	.6864	.0260	4.19
	46	.7007		4.00
	47	.7151		3.66
	48	.7294		3.31
	49	.7437		2.89
	50	.7509	.0260	8.56
7	51	.7545	.0310	9.12
	52	.7581	.0292	9.56
	53	.7616	.0280	9.98
	54	.7652	.0260	9.62
	55	.7688		9.04
	56	.7724		8.58
	57	.7760		8.14
	58	.7796		7.76
	59	.7832	.0260	7.44
	60	.7867	.0350	7.44
8	61	.7903	.0320	8.28
	62	.7939	.0292	8.92
	63	.7975	.0280	9.78
	64	.8011	.0260	10.05
	65	.8047		9.42
	66	.8082		8.76
	67	.8118		8.24
	68	.8154		7.82
	69	.8190	.0260	7.44
	70	.8226	.0410	6.37
9	71	.8262	.0350	7.44
	72	.8297	.0230	8.32
	73	.8333	.0292	9.04
	74	.8369	.0260	9.74
	75	.8405		9.70
	76	.8441		8.98
	77	.8477		8.40
	78	.8513		7.86
	79	.8548	.0260	7.44
	80	.8584	.0410	6.48
10	81	.8620	.0350	7.56
	82	.8656	.0310	8.44
	83	.8692	.0280	9.20
	84	.8728	.0260	9.90
	85	.8763	.0260	9.56
	86	.8799	.0260	8.86
	87	.8799	.0260	8.86
	88	.8871		7.84
	89	.8907	.0260	7.44

TABLE IX (Continued)

<u>Chamber Number</u>	<u>Slot Number</u>	<u>Slot Position (% Length)</u>	<u>Hole Diameter (Inch)</u>	<u>Number Of Holes (Per Inch)</u>
11	90	.8943	.0330	7.72
	91	.8978	.0310	8.48
	92	.9014	.0292	9.14
	93	.9050	.0260	9.72
	94	.9086		9.82
	95	.9122		9.20
	96	.9158		8.64
	97	.9194		8.18
	98	.9229		7.80
11	99	.9265	.0260	7.44
12	100	.9301	.0330	7.84
	101	.9337	.0310	8.48
	102	.9373	.0292	9.00
	103	.9409	.0280	9.78
	104	.9444	.0260	9.98
	105	.9480		9.66
	106	.9516		9.18
	107	.9552	.0260	8.86
	108	.9588	.0260	8.60
12	109	.9624	.0260	8.30
13	110	.9660	.0330	7.84
	111	.9695	.0320	8.28
	112	.9731	.0310	8.62
	113	.9767	.0292	8.94
	114	.9803	.0280	9.24
	115	.9839	.0280	9.78
	116	.9875	.0260	9.82
	117	.9910	.0260	10.05
	118	.9946	.0260	9.84
13	119	.9982		9.52
	120	1.0018	.0260	9.24

TABLE X

STATIC PRESSURE ORIFICE AND MICROPHONE LOCATIONS

MODIFIED SEARS-HAACK LAMINAR SUCTION BODY OF REVOLUTION

<u>Static Orifice Number</u>	<u>Position (% Length)</u>	<u>Microphone Number</u>	<u>Position (% Length)</u>
1	1.00	1	8.96
2	3.00	2	30.82
3a, b, c, d	5.00	3	57.89
4	7.50	4	73.48
5	10.04	5	77.78
6	14.50	6	81.36
7	19.50	7	88.17
8	25.00	8	91.76
9	29.50	9	95.34
10	35.00		
11	39.50		
12	45.00		
13	55.00		
14	59.50		
15	65.00		
16	69.50		
17	74.91		
18	79.93		
19	84.95		
20	89.96		
21	94.98		
22	100.00		



TABLE XI

SUMMARY OF TEST POINTS CHOSEN FOR  
ANALYTICAL STUDY OF BOUNDARY LAYER DEVELOPMENT

<u>Run Number</u>	<u>Length Reynolds Number <math>R_L</math></u>
41	6,302,360
46	6,337,120
52	8,754,970
66	13,585,310
76	14,742,850
78	14,708,310
397	17,228,480
421	19,583,940

TABLE XII

CHORDWISE SUCTION INFLOW VELOCITY DISTRIBUTION -  $v_o^*$  VS  $\bar{x}$ 

MODIFIED SEARS-HAACK LAMINAR SUCTION BODY OF REVOLUTION

Run Number $\bar{x}$	41	46	52	66	76	78	397	421
0.0484	0	0	0	0	0	0	0	0
0.1058	0	0	0	0	0	0	0.5272	0.8880
0.1918	0	0	0	0.5022	0.6504	0.8696	0.6420	0.7151
0.3208	0	0	0.0920	0.4642	0.5530	0.7362	0.6239	0.6739
0.4499	0.2671	0.5182	0.3036	0.3956	0.4865	0.6482	0.5687	0.6349
0.5932	0.2576	0.4905	0.2621	0.3717	0.4383	0.5908	0.4962	0.5600
0.7473	0.2817	0.5205	0.2515	0.3424	0.4329	0.5743	0.4896	0.5305
0.7850	2.0760	3.8562	2.0235	2.0411	2.5263	3.4568	1.5745	1.5586
0.8208	2.0419	3.5376	1.8460	1.8687	2.3113	3.0644	1.5886	1.2857
0.8566	1.9418	3.4733	1.8969	1.9834	2.4586	3.1430	1.8550	1.5579
0.8925	1.6846	3.2067	1.5430	1.7413	2.0079	2.6941	1.9107	1.8570
0.9283	1.7440	3.1706	1.5980	1.5921	2.0770	2.6430	1.6836	1.5142
0.9642	1.4163	2.6565	1.2659	1.5951	1.2351	1.7671	1.4984	1.3470
1.0036	1.5875	2.7020	1.3224	1.1475	0.9209	1.0884	1.3134	1.2769
1.0179	0	0	0	0	0	0	0	0

189

# SUMMARY OF COMPUTED AND EXPERIMENTAL DATA AT THE RAKE POSITION

## MODIFIED SEARS-HAACK LAMINAR SUCTION BODY OF REVOLUTION

Run Number	41	46	52	66	76	78	397	421
$\delta^*$ (in.)								
Comp	0.11185	0.06509	0.09861	0.07443	0.06438	0.05036	0.06329	0.06118
Side	0.09094	0.05705	0.07158	0.05380	0.04535	0.03666	0.04314	0.04149
Top	0.15546	0.07901	0.13826	0.09088	0.07101	0.05484	0.08278	0.07928
$\delta_{side}^*/\delta_{comp}^*$	0.814	0.877	0.727	0.723	0.705	0.729	0.683	0.679
$\delta_{top}^*/\delta_{comp}^*$	1.390	1.215	1.403	1.220	1.103	1.090	1.310	1.295
$\theta$ (in.)								
Comp	0.05533	0.03660	0.04766	0.03634	0.03186	0.02609	0.03106	0.02954
Side	0.05367	0.03728	0.04298	0.03393	0.02882	0.02458	0.02755	0.02667
Top	0.08471	0.05055	0.07064	0.05477	0.04305	0.03612	0.05445	0.05288
$\theta_{side}/\theta_{comp}$	0.972	1.020	0.900	0.935	0.906	0.943	0.888	0.904
$\theta_{top}/\theta_{comp}$	1.530	1.380	1.440	1.510	1.350	1.284	1.755	1.790
H								
Comp	2.0214	1.7785	2.0693	2.0484	2.0207	1.9304	2.0379	2.0712
Side	1.6945	1.5304	1.5653	1.5858	1.5738	1.4917	1.5660	1.5559
Top	1.8352	1.5629	1.9573	1.6593	1.6494	1.5181	1.5203	1.4993
$R_\theta$								
Comp	2355	1565	2808	3320	3160	2582	3600	3890
Side	2290	1595	2525	3110	2860	2425	3200	3520
Top	3610	2160	4160	5020	4270	3575	6310	6960
$C_{D_v}$ $\times 10^3$								
Comp	0.38559	0.25305	0.32602	0.24566	0.21823	0.17874	0.20752	0.20284
Side	0.37019	0.25773	0.29522	0.23899	0.19882	0.17472	0.18945	0.17740
Top	0.56701	0.35011	0.50275	0.38492	0.29857	0.24970	0.36231	0.33605

TABLE XIV  
COMPARISON OF EXPERIMENTAL AND COMPUTED TOTAL SUCTION FLOW COEFFICIENT  $C_{Qt}$   
MODIFIED SEARS-HAACK LAMINAR SUCTION BODY OF REVOLUTION

Run Number	41	46	52	66	76	78	397	421
$C_{Qtcomp} \times 10^4$	2.0127	3.6608	1.8378	1.7613	2.0069	2.6801	1.8237	1.7778
$C_{Qtexp} \times 10^4$	2.0173	3.6791	1.8362	1.7521	1.9983	2.6576	1.8091	1.7508
$\frac{C_{Qtcomp} - C_{Qtexp}}{C_{Qtcomp}}$	-0.023%	-0.501%	+0.089%	+0.527%	+0.432%	+0.847%	+0.805%	+1.540%

TABLE XIII

SUMMARY OF COMPUTED AND EXPERIMENTAL

# LIST OF FIGURES FOR SECTION II, PART 1

<u>Figure No.</u>	<u>Figure Title</u>	<u>Page</u>
1	MODEL INSTALLATION (SCHEMATIC) .....	209
2	WING CROSS SECTION WITH DETAILS OF SUCTION CHAMBERS & SUCTION SLOTS .....	210
3	30° SWEPT, 12% THICK LAMINAR SUCTION WING MODEL .....	211
4	PRESSURE DISTRIBUTION $\Delta p/q_\infty$ VERSUS $x/c$ FOR $\alpha = +1.5^\circ$ , $+1^\circ$ , $0^\circ$ , $-1^\circ$ , $-1.5^\circ$ , $-2^\circ$ ANGLE OF ATTACK .....	212
5	DRAG $C_D$ VERSUS SUCTION QUANTITY $C_{Qt}$ FOR VARIOUS REYNOLDS NUMBERS $R_c$ AND ANGLES OF ATTACK $\alpha$ .....	213
6	DRAG $C_D$ VERSUS SUCTION QUANTITY $C_{Qt}$ FOR VARIOUS REYNOLDS NUMBERS $R_c$ AND ANGLES OF ATTACK $\alpha$ .....	214
7	DRAG $C_D$ VERSUS SUCTION QUANTITY $C_{Qt}$ FOR VARIOUS REYNOLDS NUMBERS $R_c$ AND ANGLES OF ATTACK $\alpha$ .....	215
8	DRAG $C_D$ VERSUS SUCTION QUANTITY $C_{Qt}$ FOR VARIOUS REYNOLDS NUMBERS $R_c$ AND ANGLES OF ATTACK $\alpha$ .....	216
9	DRAG $C_D$ VERSUS SUCTION QUANTITY $C_{Qt}$ FOR VARIOUS REYNOLDS NUMBERS $R_c$ AND ANGLES OF ATTACK $\alpha$ .....	217
10	DRAG $C_D$ VERSUS SUCTION QUANTITY $C_{Qt}$ FOR VARIOUS REYNOLDS NUMBERS $R_c$ AND ANGLES OF ATTACK $\alpha$ .....	218
11	30° SWEPT LAMINAR SUCTION WING, MIN WING EQUIVALENT TOTAL DRAG (INCLUDING EQUIVALENT SUCTION DRAG) VS. $R_c$ FOR UPPER WING SURFACE .....	219
12	30° SWEPT LAMINAR SUCTION WING OPTIMUM SUCTION QUANTITY, $C_{Q_{opt}}$ VS. $R_c$ FOR UPPER WING SURFACE .....	220
13	30° SWEPT LAMINAR SUCTION WING MIN WING EQUIVALENT TOTAL DRAG (INCLUDING EQUIVALENT SUCTION DRAG) VS. $R_c$ FOR UPPER WING SURFACE .....	221
14	30° SWEPT LAMINAR SUCTION WING MEASURED DRAG COEFFICIENTS ( $C_{Ds}/R_c$ , $C_{Dt}/R_c$ ) VS. SUCTION CO- EFFICIENT ( $C_Q/R_c$ ) AT VARIOUS $\alpha$ AND $R_c$ .....	222
15	30° SWEPT LAMINAR SUCTION WING SUCTION VELOCITY $-v_o^*$ VS. CHORD ( $X/C$ ) .....	223

LIST OF FIGURES FOR SECTION II, PART 1 (Continued)

<u>Figure No.</u>	<u>Figure Title</u>	<u>Page</u>
16	COMPARISON BETWEEN MEASURED VELOCITY DISTRIBUTION AND APPROXIMATE VELOCITY DISTRIBUTION USED FOR CALCULATIONS OF BOUNDARY LAYER DEVELOPMENT .....	224
17	VARIATION OF CROSSFLOW REYNOLDS NUMBER WITH CHORD--30° SWEEP LAMINAR SUCTION WING MODEL IN NASA-AMES 12-FT. PWT .....	225
18	VARIATION OF MOMENTUM THICKNESS REYNOLDS NUMBER AND SHAPE PARAMETER WITH CHORD--30° SWEEP LAMINAR SUCTION WING MODEL IN NASA-AMES 12-FT. PWT .....	226
19	COMPARISON OF CROSSFLOW REYNOLDS NUMBER WITH STABILITY LIMIT REYNOLDS NUMBER AT SEVERAL LENGTH REYNOLDS NUMBERS, SUCTION COEFFICIENTS AND ANGLES OF ATTACK, $\alpha = 0^\circ$ .....	227
20	COMPARISON OF CROSSFLOW REYNOLDS NUMBER WITH STABILITY LIMIT REYNOLDS NUMBER AT SEVERAL LENGTH REYNOLDS NUMBERS, SUCTION COEFFICIENTS AND ANGLES OF ATTACK, $\alpha = -1^\circ$ .....	228
21	COMPARISON OF CROSSFLOW REYNOLDS NUMBER WITH STABILITY LIMIT REYNOLDS NUMBER AT SEVERAL LENGTH REYNOLDS NUMBERS, SUCTION COEFFICIENTS AND ANGLES OF ATTACK, $\alpha = 1^\circ$ .....	229
22	COMPARISON OF MEASURED AND CALCULATED TRAILING EDGE BOUNDARY LAYER VELOCITY PROFILES .....	230
23	COMPARISON OF CHORDWISE PRESSURE DISTRIBUTION AND SUCTION CHAMBER PRESSURE COEFFICIENTS .....	231
24	CHORDWISE DISTRIBUTION OF NONDIMENSIONAL SUCTION VELOCITY COEFFICIENT $v_o^*$ IN AFT FOUR SUCTION CHAMBERS .....	232
25	MODEL CROSS SECTION WITH DETAILS OF SUCTION CHAMBERS AND SUCTION SLOTS .....	233
26	INSTALLATION DRAWING 17-FOOT CHORD LAMINAR SUCTION WING IN NORAIR 7- BY 10-FOOT WIND TUNNEL .....	234
27	17-FOOT CHORD LAMINAR SUCTION WING IN NORAIR 7- BY 10-FOOT WIND TUNNEL WITH FAIRING NO. 1 INSTALLED .....	235
28	CROSS SECTIONS - WIND TUNNEL WALL FAIRINGS .....	236
29	PRESSURE DISTRIBUTIONS AT VARYING ANGLES OF ATTACK .....	237

LIST OF FIGURES FOR SECTION II, PART 1 (Continued)

<u>Figure No.</u>	<u>Figure Title</u>	<u>Page</u>
30	PRESSURE DISTRIBUTIONS AT VARYING ANGLES OF ATTACK .....	238
31	PRESSURE DISTRIBUTIONS AT VARYING ANGLES OF ATTACK .....	239
32	PRESSURE DISTRIBUTIONS AT VARYING ANGLES OF ATTACK .....	240
33	PRESSURE DISTRIBUTIONS AT VARYING ANGLES OF ATTACK .....	241
34	PRESSURE DISTRIBUTIONS AT VARYING ANGLES OF ATTACK .....	242
35	COMPARISON OF PRESSURE DISTRIBUTIONS AT ANGLE OF ATTACK $\alpha = 0^\circ$ OF THE THREE CASES INVESTIGATED .....	243
36	DRAG $C_D$ VERSUS SUCTION QUANTITY $C_{Qt}$ FOR VARIOUS REYNOLDS NUMBERS $R_c$ AND ANGLES OF ATTACK $\alpha$ .....	244
37	DRAG $C_D$ VERSUS SUCTION QUANTITY $C_{Qt}$ FOR VARIOUS REYNOLDS NUMBERS $R_c$ AND ANGLES OF ATTACK $\alpha$ .....	245
38	DRAG $C_D$ VERSUS SUCTION QUANTITY $C_{Qt}$ FOR VARIOUS REYNOLDS NUMBERS $R_c$ AND ANGLES OF ATTACK $\alpha$ .....	246
39	DRAG $C_D$ VERSUS SUCTION QUANTITY $C_{Qt}$ FOR VARIOUS REYNOLDS NUMBERS $R_c$ AND ANGLES OF ATTACK $\alpha$ .....	247
40	DRAG $C_D$ VERSUS SUCTION QUANTITY $C_{Qt}$ FOR VARIOUS REYNOLDS NUMBERS $R_c$ AND ANGLES OF ATTACK $\alpha$ .....	248
41	DRAG $C_D$ VERSUS SUCTION QUANTITY $C_{Qt}$ FOR VARIOUS REYNOLDS NUMBERS $R_c$ AND ANGLES OF ATTACK $\alpha$ .....	249
42	DRAG $C_D$ VERSUS SUCTION QUANTITY $C_{Qt}$ FOR VARIOUS REYNOLDS NUMBERS $R_c$ AND ANGLES OF ATTACK $\alpha$ .....	250
43	VARIATION OF MINIMUM TOTAL DRAG COEFFICIENT $C_{Dt}$ (INCLUDING EQUIVALENT SUCTION DRAG) WITH REYNOLDS NUMBER $R_c$ FOR SEVERAL ANGLES OF ATTACK $\alpha$ .....	251
44	VARIATION OF OPTIMUM SUCTION COEFFICIENT $C_{Qt\text{opt}}$ WITH REYNOLDS NUMBER $R_c$ FOR SEVERAL ANGLES OF ATTACK $\alpha$ .....	252
45	VARIATION OF MINIMUM TOTAL DRAG COEFFICIENT $C_{Dt}$ (INCLUDING EQUIVALENT SUCTION DRAG) WITH REYNOLDS NUMBER $R_c$ FOR SEVERAL ANGLES OF ATTACK $\alpha$ .....	253

LIST OF FIGURES FOR SECTION II, PART 1 (Continued)

<u>Figure No.</u>	<u>Figure Title</u>	<u>Page</u>
46	VARIATION OF OPTIMUM SUCTION COEFFICIENT $C_{Q_{opt}}$ WITH REYNOLDS NUMBER $R_c$ FOR SEVERAL ANGLES OF ATTACK $\gamma$ .....	254
47	VARIATION OF MINIMUM TOTAL DRAG COEFFICIENT $C_{D_t}$ (INCLUDING EQUIVALENT SUCTION DRAG) WITH REYNOLDS NUMBER $R_c$ FOR SEVERAL ANGLES OF ATTACK $\gamma$ .....	255
48	VARIATION OF OPTIMUM SUCTION COEFFICIENT $C_{Q_{opt}}$ WITH REYNOLDS NUMBER $R_c$ FOR SEVERAL ANGLES OF ATTACK $\gamma$ .....	256
49	NONDIMENSIONAL EQUIVALENT AREA SUCTION VELOCITY $v_o^*$ DISTRIBUTION NEAR OPTIMUM SUCTION COEFFICIENT $C_{Q_{opt}}$ FOR SEVERAL REYNOLDS NUMBERS $R_c$ .....	257
50	NONDIMENSIONAL EQUIVALENT AREA SUCTION VELOCITY $v_o^*$ DISTRIBUTION NEAR OPTIMUM SUCTION COEFFICIENT $C_{Q_{opt}}$ FOR SEVERAL REYNOLDS NUMBERS $R_c$ .....	258
51	NONDIMENSIONAL EQUIVALENT AREA SUCTION VELOCITY $v_o^*$ DISTRIBUTION NEAR OPTIMUM SUCTION COEFFICIENT $C_{Q_{opt}}$ FOR SEVERAL REYNOLDS NUMBERS $R_c$ .....	259
52	NONDIMENSIONAL EQUIVALENT AREA SUCTION VELOCITY $v_o^*$ DISTRIBUTION NEAR OPTIMUM SUCTION COEFFICIENT $C_{Q_{opt}}$ FOR SEVERAL ANGLES OF ATTACK $\alpha$ AT A REYNOLDS NUMBER $R_c$ OF APPROXIMATELY $21 \times 10^6$ .....	260
53	NONDIMENSIONAL EQUIVALENT AREA SUCTION VELOCITY $v_o^*$ DISTRIBUTION NEAR OPTIMUM SUCTION COEFFICIENT $C_{Q_{opt}}$ FOR SEVERAL ANGLES OF ATTACK $\alpha$ AT A REYNOLDS NUMBER $R_c$ OF APPROXIMATELY $21 \times 10^6$ .....	261
54	NONDIMENSIONAL EQUIVALENT AREA SUCTION VELOCITY $v_o^*$ DISTRIBUTION NEAR OPTIMUM SUCTION COEFFICIENT $C_{Q_{opt}}$ FOR SEVERAL ANGLES OF ATTACK $\gamma$ AT A REYNOLDS NUMBER $R_c$ OF APPROXIMATELY $21 \times 10^6$ .....	262
55	COMPARISON OF NONDIMENSIONAL EQUIVALENT AREA SUCTION VELOCITY $v_o^*$ DISTRIBUTION NEAR OPTIMUM SUCTION COEFFICIENT $C_{Q_{opt}}$ AT ANGLE OF ATTACK $\gamma = 0^\circ$ AND REYNOLDS NUMBER $R_c$ OF APPROXIMATELY $21 \times 10^6$ FOR THE THREE PRESSURE DISTRIBUTIONS STUDIED .....	263



# LIST OF FIGURES FOR SECTION II, PART 1 (Continued)

<u>Figure No.</u>	<u>Figure Title</u>	<u>Page</u>
56	TRAILING EDGE BOUNDARY LAYER VELOCITY PROFILES NEAR OPTIMUM SUCTION COEFFICIENT $C_{Qopt}$ FOR SEVERAL REYNOLDS NUMBERS $R_c$ .....	264
57	TRAILING EDGE BOUNDARY LAYER VELOCITY PROFILES NEAR OPTIMUM SUCTION COEFFICIENT $C_{Qopt}$ FOR SEVERAL REYNOLDS NUMBERS $R_c$ .....	265
58	TRAILING EDGE BOUNDARY LAYER VELOCITY PROFILES NEAR OPTIMUM SUCTION COEFFICIENT $C_{Qopt}$ FOR SEVERAL REYNOLDS NUMBERS $R_c$ .....	266
59	VARIATION OF TRAILING EDGE BOUNDARY LAYER VELOCITY PROFILES WITH SUCTION COEFFICIENT $C_Q$ .....	267
60	VARIATION OF TRAILING EDGE BOUNDARY LAYER VELOCITY PROFILES WITH SUCTION COEFFICIENT $C_Q$ .....	268
61	VARIATION OF TRAILING EDGE BOUNDARY LAYER VELOCITY PROFILES WITH SUCTION COEFFICIENT $C_Q$ .....	269
62	VARIATION OF TRAILING EDGE BOUNDARY LAYER VELOCITY PROFILES WITH SUCTION COEFFICIENT $C_Q$ .....	270
63	VARIATION OF TRAILING EDGE BOUNDARY LAYER VELOCITY PROFILES WITH SUCTION COEFFICIENT $C_Q$ .....	271
64	17 FT CHORD WING ACOUSTICAL TESTS IN NORAIR 7 x 10 WIND TUNNEL .....	272
65	17 FT CHORD SUCTION MODEL .....	273
66	ACOUSTICAL INSTALLATION .....	274
67	INVESTIGATION OF A 30° SWEEP SUCTION WING UNDER THE IN- FLUENCE OF SOUND MODEL INSTALLED IN NORAIR 7 x 10 WIND TUNNEL .....	275
68	30° SWEEP LAMINAR SUCTION WING MODEL WING CROSS SECTION WITH DETAIL OF SUCTION CHAMBERS AND SUCTION SLOTS .....	276
69	INVESTIGATION OF A 30° SWEEP SUCTION WING UNDER THE INFLUENCE OF SOUND ACOUSTICAL INSTALLATION .....	277
70	MEASURED AIRFOIL PRESSURE DISTRIBUTION, 17 FT CHORD STRAIGHT WING .....	278
71	PRESSURE COEFFICIENT $C_p$ VS CHORD $x/c$ 30° SWEEP SUCTION WING UNDER THE INFLUENCE OF SOUND, $\alpha = 0^\circ$ .....	279

LIST OF FIGURES FOR SECTION II, PART 1 (Continued)

<u>Figure No.</u>	<u>Figure Title</u>	<u>Page</u>
72	NORAIR 7- BY 10-FOOT WIND TUNNEL TURBULENCE AND NOISE LEVELS WITH MODEL AND ACOUSTICAL WALL TREATMENT INSTALLED 30° SWEEP SUCTION WING UNDER THE INFLUENCE OF SOUND .....	280
73	COMPARISON OF SOUND FIELD TRAVERSES AT MIDSPAN 6 INCHES AWAY FROM WING MAXIMUM THICKNESS, $R_c = 9.8 \times 10^6$ (WITH HOT WIRE READINGS AT EDGE OF BOUNDARY LAYER, $R_c = 8.1 \times 10^6$ ) .....	281
74	ADDITIONAL SUCTION, $-\Delta v_o^*$ , REQUIRED TO MAINTAIN LAMINAR FLOW AT VARIOUS FREQUENCIES AND EXTERNAL SOUND PRESSURE LEVELS, $R_c = 11.4 \times 10^6$ .....	282
75	ADDITIONAL SUCTION, $-\Delta v_o^*$ , REQUIRED TO MAINTAIN LAMINAR FLOW AT VARIOUS FREQUENCIES AND EXTERNAL SOUND PRESSURE LEVELS, $R_c = 16.4 \times 10^6$ .....	283
76	ADDITIONAL SUCTION $-\Delta v_o^*$ , REQUIRED TO MAINTAIN LAMINAR FLOW AT VARIOUS FREQUENCIES AND EXTERNAL SOUND PRESSURE LEVELS, $R_c = 20.2 \times 10^6$ .....	284
77	ADDITIONAL SUCTION, $-\Delta v_o^*$ , REQUIRED TO MAINTAIN LAMINAR FLOW AT VARIOUS FREQUENCIES AND EXTERNAL SOUND PRESSURE LEVELS, $R_c = 21.5 \times 10^6$ .....	285
78	EFFECT OF VARIATION OF SUCTION LEVEL ON TRANSITION WITH EXTERNAL SOUND, $R_c = 11.5 \times 10^6$ .....	286
79	EFFECT OF VARIATION OF SUCTION LEVEL ON TRANSITION WITH EXTERNAL SOUND, $R_c = 16.4 \times 10^6$ .....	287
80	EFFECT OF VARIATION OF SUCTION LEVEL ON TRANSITION WITH EXTERNAL SOUND, $R_c = 21.5 \times 10^6$ .....	288
81	EFFECT OF FORWARD SUCTION ON TRANSITION WITH EXTERNAL SOUND, $R_c = 11.5 \times 10^6$ .....	289
82	EFFECT OF SINGLE OPEN STATIC PRESSURE ORIFICE ON TRANSITION WITH EXTERNAL SOUND, $R_c = 16.5 \times 10^6$ .....	290
83	DRAG EFFECT OF INCREASING SUCTION QUANTITY TO MAINTAIN LAMINAR FLOW WITH EXTERNAL SOUND, $R_c = 11.5 \times 10^6$ .....	291
84	DRAG EFFECT OF INCREASING SUCTION QUANTITY TO MAINTAIN LAMINAR FLOW WITH EXTERNAL SOUND, $R_c = 20.2 \times 10^6$ .....	292
85	VARIATION OF TOTAL DRAG WITH EXTERNAL SOUND AT CONSTANT SUCTION QUANTITY, $R_c = 16.5 \times 10^6$ .....	293
86	VARIATION OF TOTAL DRAG WITH EXTERNAL SOUND AT CONSTANT SUCTION QUANTITY, $R_c = 16.5 \times 10^6$ .....	294

LIST OF FIGURES FOR SECTION II, PART 1 (Continued)

<u>Figure No.</u>	<u>Figure Title</u>	<u>Page</u>
87	VARIATION OF TOTAL DRAG WITH EXTERNAL SOUND AT CONSTANT SUCTION QUANTITY (SUCTION LOW ON CHAMBER NO. 9, $x/c = 0.45$ TO $0.523$ ), $R_c = 16.4 \times 10^6$ .....	295
88	VARIATION OF TOTAL DRAG WITH EXTERNAL SOUND AT CONSTANT SUCTION QUANTITY (STATICS OPEN BEHIND 40 PERCENT C), $R_c = 16.4 \times 10^6$ .....	296
89	VELOCITY FLUCTUATION OF EXTERNAL SOUND FIELD TO CAUSE TRANSITION VS SUCTION QUANTITY AT VARIOUS CHORD REYNOLDS NUMBERS.....	297
90	SOUND PRESSURE LEVEL FOR TRANSITION AS A FUNCTION OF FREQUENCY $30^\circ$ SWEPT SUCTION WING UNDER THE INFLUENCE OF SOUND .....	298
91	SOUND PRESSURE LEVEL FOR TRANSITION AS A FUNCTION OF FREQUENCY $30^\circ$ SWEPT SUCTION WING UNDER THE INFLUENCE OF SOUND .....	299
92	SOUND OF DISCRETE FREQUENCIES ALONG TUNNEL AXIS WITH SUCTION FROM $0.5c$ to $0.95c$ , FRONT SLOTS AND STATIC PRESSURE ORIFICES SEALED (No suction upstream of $0.5c$ , $R_c = 7 \times 10^6$ ).....	300
93	TOLLMIEN -SCHLICHTING INSTABILITY AGAINST 2 DIMENSIONAL DISTURBANCES (DISTURBANCE WAVE FRONTS ALONG WING SPAN).....	301
94	TRANSITION LIMIT WITH INCREASING SUCTION ON ONE CHAMBER $30^\circ$ SWEPT SUCTION WING UNDER THE INFLUENCE OF SOUND, $R_c = 5.8 \times 10^6$ .....	302
95	TRANSITION LIMIT WITH INCREASING SUCTION LEVEL $30^\circ$ SWEPT SUCTION WING UNDER THE INFLUENCE OF SOUND, $R_c = 5.8 \times 10^6$ ... ..	303
96	TRANSITION LIMIT WITH INCREASING FORWARD SUCTION $30^\circ$ SWEPT SUCTION WING UNDER THE INFLUENCE OF SOUND, $R_c = 4.1 \times 10^6$ ... ..	304
97	TRANSITION LIMIT WITH INCREASING SUCTION LEVEL $30^\circ$ SWEPT SUCTION WING UNDER THE INFLUENCE OF SOUND, $R_c = 8.1 \times 10^6$ ... ..	305
98	TRANSITION LIMIT WITH INCREASING FORWARD SUCTION AND INCREASING SUCTION LEVEL $30^\circ$ SWEPT SUCTION WING UNDER THE INFLUENCE OF SOUND, $R_c = 9.8 \times 10^6$ .....	306
99	TRANSITION LIMIT WITH INCREASING FORWARD SUCTION $30^\circ$ SWEPT SUCTION WING UNDER THE INFLUENCE OF SOUND, $R_c = 11.5 \times 10^6$ .. ..	307

LIST OF FIGURES FOR SECTION II, PART 1 (Continued)

<u>Figure No.</u>	<u>Figure Title</u>	<u>Page</u>
100	VELOCITY FLUCTUATION, $\frac{u'}{U_\infty}$ , FOR TRANSITION WITH SMOOTH WING AND PINHOLE IMPERFECTIONS AS A FUNCTION OF CHORD REYNOLDS NUMBER $30^\circ$ SWEEP SUCTION WING UNDER THE INFLUENCE OF SOUND..	308
101	VELOCITY FLUCTUATION, $\frac{u'}{U_\infty}$ , FOR TRANSITION WITH SINGLE AND MULTIPLE SLOTS OPEN WITHOUT SUCTION AS A FUNCTION OF CHORD REYNOLDS NUMBER $30^\circ$ SWEEP SUCTION WING UNDER THE INFLUENCE OF SOUND .....	309
102	TRANSITION SHOWN BY NAPHTHALENE SPRAY TECHNIQUE EXTERNAL SOUND, 125 DB, 863 CPS, $R_c = 14.2 \times 10^6$ , STRIPS STARTING AT 12% CHORD, RUN 156 .....	310
103	TRANSITION SHOWN BY NAPHTHALENE SPRAY TECHNIQUE TRANS- VERSE, TRANSDUCER, 122 DB, 800 CPS, $R_c = 11.2 \times 10^6$ , WEDGE AT 17% C FROM UNSEALED STATIC PRESSURE AT 3.7%, RUN 532 .....	311
104	TRANSITION SHOWN BY NAPHTHALENE SPRAY TECHNIQUE LONGI- TUDINAL, TRANSDUCER, 115 DB, 800 CPS, $R_c = 5.8 \times 10^6$ , WEDGES AT 30% C TOP AND AT 35% C BOTTOM FROM IMPERFECTLY SEALED FORWARD SLOTS, RUN 221 .....	312
105	TRANSITION SHOWN BY NAPHTHALENE SPRAY TECHNIQUE TRANS- VERSE, SPEAKERS, 127 DB, 200 CPS, $R_c = 4.1 \times 10^6$ , STRIATIONS AT 45 AND 49% C, RUN 292 .....	313
106	TRANSITION SHOWN BY NAPHTHALENE SPRAY TECHNIQUE TRANS- VERSE, SPEAKERS, 121 DB, 365 CPS, $R_c = 5.8 \times 10^6$ , STRIATIONS AT 46 AND 50% C, RUN 315 .....	314
107	TRANSITION SHOWN BY NAPHTHALENE SPRAY TECHNIQUE TRANS- VERSE, SPEAKERS, 129.5 DB, 667 CPS, $R_c = 5.8 \times 10^6$ , STRIATIONS AT 63 AND 67% C, RUN 304 .....	315
108	TRANSITION SHOWN BY NAPHTHALENE SPRAY TECHNIQUE LONGI- TUDINAL, TRANSDUCER, 133 DB, 400 CPS, $R_c = 4.1 \times 10^6$ , TRANSITION AT 46% C TOP AND AT 49% C BOTTOM, RUN 286 .....	316
109	TRANSITION SHOWN BY NAPHTHALENE SPRAY TECHNIQUE TRANS- VERSE, SPEAKERS, 125 DB, 400 CPS, $R_c = 4.1 \times 10^6$ , STRIATIONS AT 45 AND 56% C, RUN 290 .....	317

# LIST OF FIGURES FOR SECTION II, PART 1 (Continued)

<u>Figure No.</u>	<u>Figure Title</u>	<u>Page</u>
110	TRANSITION SHOWN BY NAPHTHALENE SPRAY TECHNIQUE LONGI- TUDINAL, TRANSDUCER, 128.5 DB, 1000 CPS, $R_c = 8.1 \times 10^6$ , TRANSITION AT 9% C, RUN 447 .....	318
111	TRANSITION SHOWN BY NAPHTHALENE SPRAY TECHNIQUE TRANS- VERSE, TRANSDUCER, 130 DB, 1000 CPS, $R_c = 8.1 \times 10^6$ , TRANSITION AT 34% C, RUN 999 .....	319
112	TRANSITION SHOWN BY NAPHTHALENE SPRAY TECHNIQUE TRANS- VERSE, TRANSDUCER, 130 DB, 1000 CPS, $R_c = 8.1 \times 10^6$ , TRANSITION AT 34% C, RUN 999 .....	320
113	TRANSITION SHOWN BY NAPHTHALENE SPRAY TECHNIQUE LONGI- TUDINAL, TRANSDUCER, 130 DB, 1000 CPS, $R_c = 8.1 \times 10^6$ , TRANSITION AT 68% C, RUN 474 .....	321
114	TRANSITION SHOWN BY NAPHTHALENE SPRAY TECHNIQUE LONGI- TUDINAL, TRANSDUCER, 134.5 DB, 781 CPS, $R_c = 8.1 \times 10^6$ , TRANSITION AT 70% C, RUN 460 .....	322
115	TRANSITION SHOWN BY NAPHTHALENE SPRAY TECHNIQUE LONGI- TUDINAL, TRANSDUCER, 125 DB, 800 CPS, $R_c = 8.1 \times 10^6$ , TRANSITION AT 50% CHORD, RUN 921 .....	323
116	TRANSITION SHOWN BY NAPHTHALENE SPRAY TECHNIQUE LONGI- TUDINAL, TRANSDUCER, 127 DB, 800 CPS, $R_c = 8.1 \times 10^6$ , TRANSITION AT 49% C, RUN 920 .....	324
117	TRANSITION SHOWN BY NAPHTHALENE SPRAY TECHNIQUE LONGI- TUDINAL, TRANSDUCER, 130 DB, 800 CPS, $R_c = 8.1 \times 10^6$ , TRANSITION AT 48% C, RUN 919 .....	325
118	TRANSITION SHOWN BY NAPHTHALENE SPRAY TECHNIQUE LONGI- TUDINAL, TRANSDUCER, 133 DB, 800 CPS, $R_c = 8.1 \times 10^6$ , TRANSITION AT 44% C, RUN 918 .....	326
119	TRANSITION SHOWN BY NAPHTHALENE SPRAY TECHNIQUE LONGI- TUDINAL, TRANSDUCER, 134 DB, 785 CPS, $R_c = 8.1 \times 10^6$ , STRIATIONS AT 63 TO 66% C ABOVE, STRIPES AT 44 TO 49% C BELOW, RUN 335 .....	327

LIST OF FIGURES FOR SECTION II, PART 1 (Continued)

<u>Figure No.</u>	<u>Figure Title</u>	<u>Page</u>
120	TRANSITION SHOWN BY NAPHTHALENE SPRAY TECHNIQUE TRANS- VERSE SPEAKERS, 117 DB, 365 CPS, $R_c = 5.8 \times 10^6$ , 1/2-INCH STREAKS AT 75 TO 100% C, RUN 324 .....	328
121	TRANSITION SHOWN BY NAPHTHALENE SPRAY TECHNIQUE TRANS- VERSE, SPEAKERS, 118 DB, 365 CPS, $R_c = 5.8 \times 10^6$ , 1/2-INCH STREAKS AT 75 TO 100% C, RUN 316 .....	329
122	TRANSITION SHOWN BY NAPHTHALENE SPRAY TECHNIQUE NO SOUND INPUT, $R_c = 5.8 \times 10^6$ , 1/2-INCH STREAKS AT 75 TO 100% C, RUN 327 .....	330
123	TRANSITION SHOWN BY NAPHTHALENE SPRAY TECHNIQUE TRANS- VERSE, SPEAKERS, 121 DB, 365 CPS, $R_c = 5.8 \times 10^6$ , TRANSITION AT 50% C AND 1/2-INCH STREAKS, RUN 315 .....	331
124	TRANSITION SHOWN BY NAPHTHALENE SPRAY TECHNIQUE NO SOUND INPUT, $R_c = 8.1 \times 10^6$ , TRANSITION AT 90 TO 94% C (COMING FROM STREAKS) RUN 453 .....	332
125	TRANSITION SHOWN BY NAPHTHALENE SPRAY TECHNIQUE LONGI- TUDINAL, TRANSDUCER, 129 DB, 300/600 CPS, $R_c = 5.8 \times 10^6$ , TRANSITION AT 63% C, RUN 310 .....	333
126	TRANSITION SHOWN BY NAPHTHALENE SPRAY TECHNIQUE LONGI- TUDINAL, TRANSDUCER, 134 DB, 800 CPS, $R_c = 8.1 \times 10^6$ , TRANSITION AT 6 TO 9% C, RUN 455 .....	334
127	TOLLMIE-SCHLICHTING BOUNDARY LAYER OSCILLATIONS, NO APPLIED SUCTION, NO APPLIED SOUND, $y = 0.018$ INCH .....	335
128	NONSUCTION AMPLIFIED OSCILLATION FREQUENCY DEPENDENCE .....	336
129	CHORDWISE HOT WIRE TRAVERSE, SPL = 105 DB, $f = 248$ CPS, $R_c = 14.2 \times 10^6$ , $y = 0.073$ INCH .....	337
130	CHORDWISE HOT WIRE TRAVERSE, SPL = 110 DB, $f = 248$ CPS, $R_c = 14.2 \times 10^6$ , $y = 0.073$ INCH .....	338
131	CHORDWISE HOT WIRE TRAVERSE, SPL = 115 DB, $f = 248$ CPS, $R_c = 14.2 \times 10^6$ , $y = 0.073$ INCH .....	339
132	CHORDWISE SUCTION DISTRIBUTION .....	340

LIST OF FIGURES FOR SECTION II, PART 1 (Continued)

<u>Figure No.</u>	<u>Figure Title</u>	<u>Page</u>
133	BOUNDARY LAYER FLUCTUATIONS AT VARIOUS CHORD LOCATIONS, $f = 248$ CPS, $R_c = 14.2 \times 10^6$ , PROBE AT $y = 0.073$ INCH .....	341
134	EXTERNAL SOUND LEVEL TO CAUSE TRANSITION AS A FUNCTION OF CHORD, $R_c = 14.2 \times 10^6$ .....	342
135	EXTERNAL SOUND LEVEL TO CAUSE TRANSITION AT VARIOUS CHORDWISE STATIONS AS A FUNCTION OF FREQUENCY, $R_c = 14.2 \times 10^6$ .....	343
136	EXTERNAL SOUND LEVEL TO CAUSE TRANSITION AS A FUNCTION OF CHORDWISE LOCATION OF TRANSITION, $R_c = 14.2 \times 10^6$ .....	344
137	EXTERNAL SOUND LEVEL TO CAUSE TRANSITION AS A FUNCTION OF FREQUENCY, $R_c = 14.2 \times 10^6$ .....	345
138	CHORDWISE HOT WIRE TRAVERSE, SPL = 120 DB, $f = 775$ CPS, $R_c = 14.2 \times 10^6$ $y = 0.044$ INCH .....	346
139	OSCILLOSCOPE PHOTOGRAPH OF HOT WIRE SIGNAL SUPERIMPOSED ON REFERENCE SIGNAL FOR $u'$ WIRE AT 55% C IN A 449 CPS SOUND FIELD; 125 DB TOP, 126 DB MIDDLE, 127 DB BOTTOM (SWEEP CHANGED BETWEEN TOP AND MIDDLE TRACES) .....	347
140	OSCILLOSCOPE PHOTOGRAPH OF HOT WIRE SIGNAL FOR $u'$ WIRE LOCATED AT 90% C IN 449 CPS, 130 DB SOUND FIELD (TRACE FROM LEFT TO RIGHT) .....	348
141	LONGITUDINAL VELOCITY FLUCTUATIONS AT 45% CHORD $30^\circ$ SWEPT SUCTION WING UNDER THE INFLUENCE OF SOUND $R_c = 8.1 \times 10^6$ .....	349
142	EFFECT OF SUCTION LEVEL INCREASE ON TRANSITION WITH INTERNAL SOUND, $R_c = 11.5 \times 10^6$ .....	350
143	EFFECT OF INCREASING SUCTION LEVEL ON TRANSITION WITH INTERNAL SOUND, $R_c = 16.4 \times 10^6$ .....	351
144	EFFECT OF INCREASING SUCTION LEVEL ON TRANSITION WITH INTERNAL SOUND, $R_c = 18.9 \times 10^6$ .....	352

LIST OF FIGURES FOR SECTION III, PART 1 (Continued)

<u>Figure No.</u>	<u>Figure Title</u>	<u>Page</u>
145	EFFECT OF SUCTION LEVEL INCREASE ON TRANSITION WITH INTERNAL SOUND, $R_c = 19.3 \times 10^6$ .....	353
146	EFFECT OF LOCAL SUCTION INCREASE ON TRANSITION WITH INTERNAL SOUND, $R_c = 16.4 \times 10^6$ .....	354
147	EFFECT OF LOCAL SUCTION INCREASE ON TRANSITION WITH INTERNAL SOUND, $R_c = 19.3 \times 10^6$ .....	355
148	EFFECT OF SUCTION ON TRANSITION WITH INTERNAL SOUND, $R_c = 14.2 \times 10^6$ .....	356
149	TRANSITION SHOWN BY NAPHTHALENE SPRAY TECHNIQUE, INTERNAL SOUND, 150 DB, 582 CPS, $R_c = 11.5 \times 10^6$ , SUCTION RUN 205 .....	357
150	TRANSITION SHOWN BY NAPHTHALENE SPRAY TECHNIQUE, INTERNAL SOUND, 150 DB, 582 CPS, $R_c = 11.5 \times 10^6$ , SUCTION RUN 205 .....	358
151	TRANSITION SHOWN BY NAPHTHALENE SPRAY TECHNIQUE, INTERNAL SOUND, 146 DB, 200 CPS, $R_c = 11.5 \times 10^6$ . SUCTION RUN 205, TRANSITION AT 50% CHORD, RUN 15 .....	359
152	TRANSITION SHOWN BY NAPHTHALENE SPRAY TECHNIQUE, INTERNAL SOUND, 159 DB, 200 CPS, $R_c = 11.5 \times 10^6$ , SUCTION RUN 205, TRANSITION AT ABOUT 45%, RUN 17 .....	360
153	DRAG EFFECT OF INCREASING SUCTION LEVEL TO MAIN- TAIN LAMINAR FLOW WITH FORCED PANEL VIBRATION, $R_c = 18.9 \times 10^6$ .....	361
154	DRAG EFFECT OF INCREASING SUCTION LOCALLY TO MAIN- TAIN LAMINAR FLOW WITH FORCED PANEL VIBRATION, $R_c = 11.5 \times 10^6$ .....	362
155	DRAG EFFECT OF INCREASING SUCTION LOCALLY TO MAIN- TAIN LAMINAR FLOW WITH FORCED PANEL VIBRATION, $R_c = 14.2 \times 10^6$ .....	363
156	DRAG EFFECT OF INCREASING SUCTION LOCALLY TO MAIN- TAIN LAMINAR FLOW WITH FORCED PANEL VIBRATION, $R_c = 16.4 \times 10^6$ .....	364



# LIST OF FIGURES FOR SECTION III, PART 1 (Continued)

<u>Figure No.</u>	<u>Figure Title</u>	<u>Page</u>
157	DRAW EFFECT OF INCREASING SUCTION LOCALLY TO MAINTAIN LAMINAR FLOW WITH FORCED PANEL VIBRATION, $R_c = 18.9 \times 10^6$ .....	365
158	SUCTION REQUIREMENTS FOR LAMINAR FLOW WITH VARIOUS COMBINATIONS OF EXTERNAL SOUND, INTERNAL SOUND AND VIBRATION, $R_c = 18.9 \times 10^6$ .....	366
159	SUCTION REQUIREMENTS FOR LAMINAR FLOW WITH EQUAL STRENGTH COMBINATIONS OF EXTERNAL SOUND, INTERNAL SOUND AND VIBRATION, $R_c = 18.9 \times 10^6$ .....	367
160	MODIFIED SEARS-HAACK BODY OF REVOLUTION MODEL CROSS SECTION WITH DETAILS OF SUCTION SLOTS .....	368
161	MODIFIED SEARS-HAACK BODY OF REVOLUTION INSTALLATION DRAWING .....	369
162	BOUNDARY LAYER CONTROL SEARS-HAACK BODY OF REVOLUTION .....	370
163	BOUNDARY LAYER CONTROL SEARS-HAACK BODY OF REVOLUTION .....	371
164	MODIFIED SEARS-HAACK BODY OF REVOLUTION COORDINATE SYSTEM .....	372
165	PRESSURE DISTRIBUTION OF SIMILAR, NON-SUCTION MODEL MEASURED IN NORAIR 8 x 11 FOOT WIND TUNNEL (FROM REFERENCE 33) .....	373
166	DESIGN AREA SUCTION VELOCITY DISTRIBUTION AND THEORETICAL BOUNDARY LAYER DEVELOPMENT $R_L = 49 \times 10^6$ .....	374
167	PRESSURE DISTRIBUTIONS AT ANGLES OF ATTACK $\alpha = 0$ AND $2^\circ$ ....	375
168	PARTIAL DRAG $c_{Dw}$ VERSUS SUCTION QUANTITY $C_{Qt}$ FOR VARIOUS REYNOLDS NUMBERS $R_L$ AND ANGLES OF ATTACK $\alpha$ .....	376
169	PARTIAL DRAG $c_{Dw}$ VERSUS SUCTION QUANTITY $C_{Qt}$ FOR VARIOUS REYNOLDS NUMBERS $R_L$ AND ANGLES OF ATTACK $\alpha$ .....	377
170	PARTIAL DRAG $c_{Dw}$ VERSUS SUCTION QUANTITY $C_{Qt}$ FOR VARIOUS REYNOLDS NUMBERS $R_L$ AND ANGLES OF ATTACK $\alpha$ .....	378
171	DRAG $C_D$ VERSUS SUCTION QUANTITY $C_{Qt}$ FOR VARIOUS REYNOLDS NUMBERS $R_c$ AND ANGLES OF ATTACK $\alpha$ .....	379

LIST OF FIGURES FOR SECTION III, PART 1 (Continued)

<u>Figure No.</u>	<u>Figure Title</u>	<u>Page</u>
172	DRAG $C_D$ VERSUS SUCTION QUANTITY $C_{Qt}$ FOR VARIOUS REYNOLDS NUMBERS $R_c$ AND ANGLES OF ATTACK $\alpha$ .....	380
173	DRAG $C_D$ VERSUS SUCTION QUANTITY $C_{Qt}$ FOR VARIOUS REYNOLDS NUMBERS $R_c$ AND ANGLES OF ATTACK $\alpha$ .....	381
174	DRAG $C_D$ VERSUS SUCTION QUANTITY $C_{Qt}$ FOR VARIOUS REYNOLDS NUMBERS $R_c$ AND ANGLES OF ATTACK $\alpha$ .....	382
175	DRAG $C_D$ VERSUS SUCTION QUANTITY $C_{Qt}$ FOR VARIOUS REYNOLDS NUMBERS $R_c$ AND ANGLES OF ATTACK $\alpha$ .....	383
176	DRAG $C_D$ VERSUS SUCTION QUANTITY $C_{Qt}$ FOR VARIOUS REYNOLDS NUMBERS $R_c$ AND ANGLES OF ATTACK $\alpha$ .....	384
177	PARTIAL DRAG $c_{Dw}$ VERSUS SUCTION QUANTITY $C_{Qt}$ FOR VARIOUS REYNOLDS NUMBERS $R_L$ AND ANGLES OF ATTACK $\alpha$ .....	385
178	PARTIAL DRAG $c_{Dw}$ VERSUS SUCTION QUANTITY $C_{Qt}$ FOR VARIOUS REYNOLDS NUMBERS $R_L$ AND ANGLES OF ATTACK $\alpha$ .....	386
179	PARTIAL DRAG $c_{Dw}$ VERSUS SUCTION QUANTITY $C_{Qt}$ FOR VARIOUS REYNOLDS NUMBERS $R_L$ AND ANGLES OF ATTACK $\alpha$ .....	387
180	DRAG $C_D$ VERSUS SUCTION QUANTITY $C_{Qt}$ FOR VARIOUS REYNOLDS NUMBERS $R_c$ AND ANGLES OF ATTACK $\alpha$ .....	388
181	DRAG $C_D$ VERSUS SUCTION QUANTITY $C_{Qt}$ FOR VARIOUS REYNOLDS NUMBERS $R_c$ AND ANGLES OF ATTACK $\alpha$ .....	389
182	DRAG $C_D$ VERSUS SUCTION QUANTITY $C_{Qt}$ FOR VARIOUS REYNOLDS NUMBERS $R_c$ AND ANGLES OF ATTACK $\alpha$ .....	390
183	VARIATION OF MINIMUM EQUIVALENT TOTAL DRAG $C_{Dtmin}$ AND SUCTION COEFFICIENT AT MINIMUM EQUIVALENT TOTAL DRAG $C_{Qopt}$ WITH LENGTH REYNOLDS NUMBER $R_L$ , $\alpha = 0^\circ$ .....	391
184	VARIATION OF MINIMUM EQUIVALENT TOTAL DRAG $C_{Dtmin}$ AND SUCTION COEFFICIENT AT MINIMUM EQUIVALENT TOTAL DRAG $C_{Qopt}$ WITH LENGTH REYNOLDS NUMBER $R_L$ , $\alpha = 0^\circ$ . SIDE RAKE DATA ONLY .....	392

# LIST OF FIGURES FOR SECTION III, PART 1 (Continued)

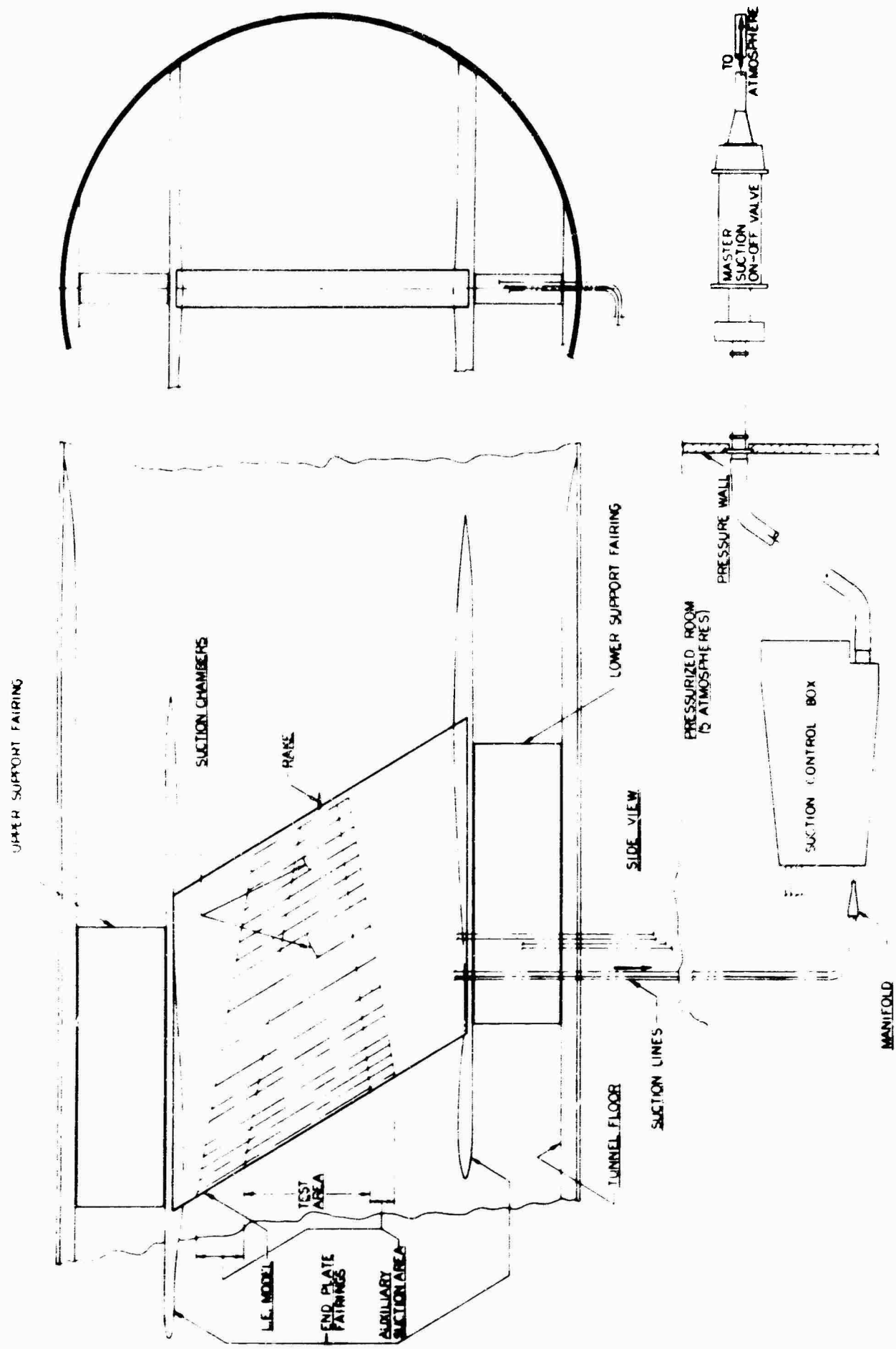
<u>Figure No.</u>	<u>Figure Title</u>	<u>Page</u>
185	VARIATION OF MINIMUM EQUIVALENT TOTAL DRAG $C_{D_{tmin}}$ AND SUCTION COEFFICIENT AT MINIMUM EQUIVALENT TOTAL DRAG $C_{Q_{opt}}$ WITH LENGTH REYNOLDS NUMBER $R_L$ , $\alpha = 2^\circ$ .....	393
186	LENGTHWISE DISTRIBUTION OF EQUIVALENT AREA SUCTION $v_o^*$ FOR SEVERAL REYNOLDS NUMBERS $R_L$ COMPARED TO DESIGN SUCTION VELOCITY DISTRIBUTION .....	394
187a	BOUNDARY LAYER VELOCITY PROFILES MEASURED NEAR MINIMUM EQUIVALENT TOTAL DRAG $C_{D_{tmin}}$ AT SEVERAL REYNOLDS NUMBERS $R_L$ , $\alpha = 0^\circ$ .....	395
187b	BOUNDARY LAYER VELOCITY PROFILES MEASURED NEAR MINIMUM EQUIVALENT TOTAL DRAG $C_{D_{tmin}}$ AT SEVERAL REYNOLDS NUMBERS $R_L$ , $\alpha = 0^\circ$ .....	396
188a	VARIATION OF AFT END BOUNDARY LAYER VELOCITY PROFILE WITH SUCTION COEFFICIENT $C_{Q_t}$ $R_L = 6.303 \times 10^6$ $\alpha = 0^\circ$ .....	397
188b	VARIATION OF AFT END BOUNDARY LAYER VELOCITY PROFILE WITH SUCTION COEFFICIENT $C_{Q_t}$ $R_K = 6.303 \times 10^6$ $\alpha = 0^\circ$ .....	398
189a	VARIATION OF AFT END BOUNDARY LAYER VELOCITY PROFILE WITH SUCTION COEFFICIENT $C_{Q_t}$ $R_L = 13.585 \times 10^6$ $\alpha = 0^\circ$ .....	399
189b	VARIATION OF AFT END BOUNDARY LAYER VELOCITY PROFILE WITH SUCTION COEFFICIENT $C_{Q_t}$ $R_L = 13.585 \times 10^6$ $\alpha = 0^\circ$ .....	400
190a	VARIATION OF AFT END BOUNDARY LAYER VELOCITY PROFILE WITH SUCTION COEFFICIENT $C_{Q_t}$ $R_L = 19.592 \times 10^6$ $\alpha = 0^\circ$ .....	401
190b	VARIATION OF AFT END BOUNDARY LAYER VELOCITY PROFILE WITH SUCTION COEFFICIENT $C_{Q_t}$ $R_L = 19.592 \times 10^6$ $\alpha = 0^\circ$ .....	402
191	SEARS-HAACK SUCTION BODY CONTOUR AND CHORDWISE VELOCITY DISTRIBUTION .....	403
192	COMPARISON OF EXPERIMENTAL AND ANALYTICAL CHORDWISE SUCTION INFLOW VELOCITY DISTRIBUTION FOR RUN NUMBER 66 .....	404

LIST OF FIGURES FOR SECTION III, PART 1 (Continued)

<u>Figure No.</u>	<u>Figure Title</u>	<u>Page</u>
193	VARIATION OF DISPLACEMENT THICKNESS $\bar{\delta}^*$ , MOMENTUM THICKNESS $\bar{\theta}$ , SHAPE PARAMETER H, MOMENTUM THICKNESS REYNOLDS NUMBER $R_\theta$ AND NONDIMENSIONAL SUCTION INFLOW VELOCITY $v_o^*$ WITH CHORD .....	405
194	VARIATION OF DISPLACEMENT THICKNESS $\bar{\delta}^*$ , MOMENTUM THICKNESS $\bar{\theta}$ , SHAPE PARAMETER H, MOMENTUM THICKNESS REYNOLDS NUMBER $R_\theta$ AND NONDIMENSIONAL SUCTION INFLOW VELOCITY $v_o^*$ WITH CHORD .....	406
195	VARIATION OF DISPLACEMENT THICKNESS $\bar{\delta}^*$ , MOMENTUM THICKNESS $\bar{\theta}$ , SHAPE PARAMETER H, MOMENTUM THICKNESS REYNOLDS NUMBER $R_\theta$ AND NONDIMENSIONAL SUCTION INFLOW VELOCITY $v_o^*$ WITH CHORD .....	407
196	VARIATION OF DISPLACEMENT THICKNESS $\bar{\delta}^*$ , MOMENTUM THICKNESS $\bar{\theta}$ , SHAPE PARAMETER H, MOMENTUM THICKNESS REYNOLDS NUMBER $R_\theta$ AND NONDIMENSIONAL SUCTION INFLOW VELOCITY $v_o^*$ WITH CHORD .....	408
197	VARIATION OF DISPLACEMENT THICKNESS $\bar{\delta}^*$ , MOMENTUM THICKNESS $\bar{\theta}$ , SHAPE PARAMETER H, MOMENTUM THICKNESS REYNOLDS NUMBER $R_\theta$ AND NONDIMENSIONAL SUCTION INFLOW VELOCITY $v_o^*$ WITH CHORD .....	409
198	VARIATION OF DISPLACEMENT THICKNESS $\bar{\delta}^*$ , MOMENTUM THICKNESS $\bar{\theta}$ , SHAPE PARAMETER H, MOMENTUM THICKNESS REYNOLDS NUMBER $R_\theta$ AND NONDIMENSIONAL SUCTION INFLOW VELOCITY $v_o^*$ WITH CHORD .....	410
199	VARIATION OF DISPLACEMENT THICKNESS $\bar{\delta}^*$ , MOMENTUM THICKNESS $\bar{\theta}$ , SHAPE PARAMETER H, MOMENTUM THICKNESS REYNOLDS NUMBER $R_\theta$ AND NONDIMENSIONAL SUCTION INFLOW VELOCITY $v_o^*$ WITH CHORD .....	411
200	VARIATION OF DISPLACEMENT THICKNESS $\bar{\delta}^*$ , MOMENTUM THICKNESS $\bar{\theta}$ , SHAPE PARAMETER H, MOMENTUM THICKNESS REYNOLDS NUMBER $R_\theta$ AND NONDIMENSIONAL SUCTION INFLOW VELOCITY $v_o^*$ WITH CHORD .....	412
201	COMPARISON OF MEASURED AND CALCULATED BOUNDARY LAYER VELOCITY PROFILES AT THE RAKE POSITION .....	413
202	COMPARISON OF MEASURED AND CALCULATED BOUNDARY LAYER VELOCITY PROFILES AT THE RAKE POSITION .....	414
203	COMPARISON OF MEASURED AND CALCULATED BOUNDARY LAYER VELOCITY PROFILES AT THE RAKE POSITION .....	415

LIST OF FIGURES FOR SECTION III, PART 1 (Continued)

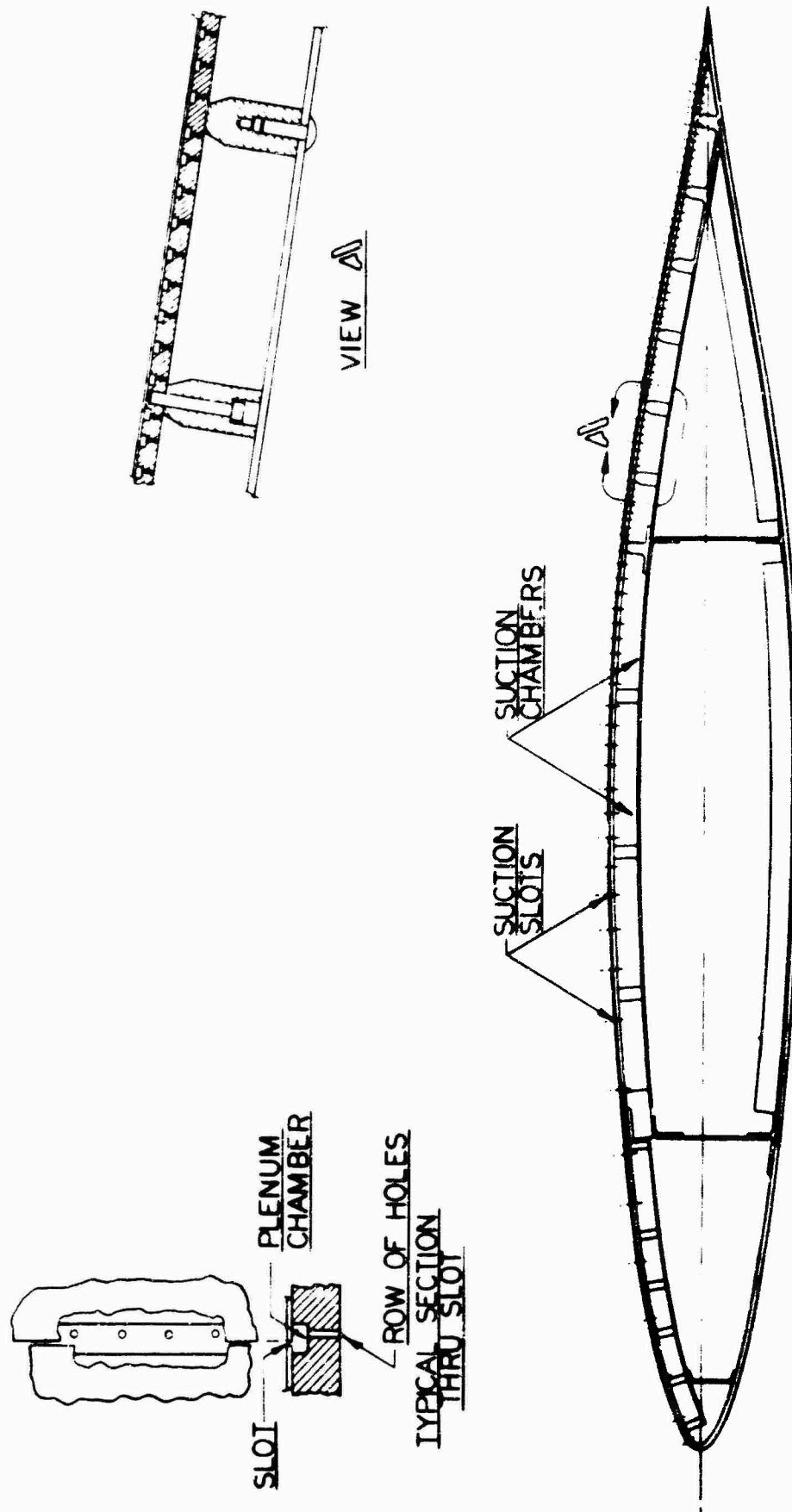
<u>Figure No.</u>	<u>Figure Title</u>	<u>Page</u>
204	COMPARISON OF MEASURED AND CALCULATED BOUNDARY LAYER VELOCITY PROFILES AT THE RAKE POSITION .....	416
205	COMPARISON OF MEASURED AND CALCULATED BOUNDARY LAYER VELOCITY PROFILES AT THE RAKE POSITION .....	417
206	COMPARISON OF MEASURED AND CALCULATED BOUNDARY LAYER VELOCITY PROFILES AT THE RAKE POSITION .....	418
207	COMPARISON OF MEASURED AND CALCULATED BOUNDARY LAYER VELOCITY PROFILES AT THE RAKE POSITION .....	419
208	COMPARISON OF MEASURED AND CALCULATED BOUNDARY LAYER VELOCITY PROFILES AT THE RAKE POSITION .....	420
209	COMPARISON OF COMPUTED BOUNDARY LAYER VELOCITY DISTRIBUTIONS AT THE RAKE POSITION .....	421
210	VARIATION OF EXPERIMENTAL AND COMPUTED DIS- PLACEMENT THICKNESS $\delta^*$ AT THE RAKE POSITION WITH TOTAL SUCTION FLC. COEFFICIENT $C_{Qt}$ .....	422
211	VARIATION OF EXPERIMENTAL AND COMPUTED MOMENTUM THICKNESS $\bar{\theta}$ AT THE RAKE POSITION WITH TOTAL SUCTION FLOW COEFFICIENT $C_{Qt}$ .....	423
212	VARIATION OF EXPERIMENTAL AND COMPUTED SHAPE PARAMETER $\eta$ AT THE RAKE POSITION WITH TOTAL SUCTION FLOW COEFFICIENT $C_{Qt}$ .....	424
213	VARIATION OF EXPERIMENTAL AND COMPUTED $R_\theta / \sqrt{R_L}$ AT THE RAKE POSITION WITH TOTAL SUCTION FLOW COEFFICIENT $C_{Qt}$ .....	425
214	VARIATION OF EXPERIMENTAL AND COMPUTED $C_{Dw} \sqrt{R_L}$ AT THE RAKE POSITION WITH TOTAL SUCTION FLOW COEFFICIENT $C_{Qt}$ .....	426
215	VARIATION OF CENTER OF GRAVITY POSITION OF SUCTION INFLOW VELOCITY DISTRIBUTION WITH LENGTH REYNOLDS NUMBER $R_L$ AND TOTAL SUCTION FLOW COEFFICIENT $C_{Qt}$ .....	427



MODEL INSTALLATION (SCHEMATIC)

FIGURE 1

FIGURE 3 30° SWEPT, 12% THICK LAMINAR SUCTION WING MODEL



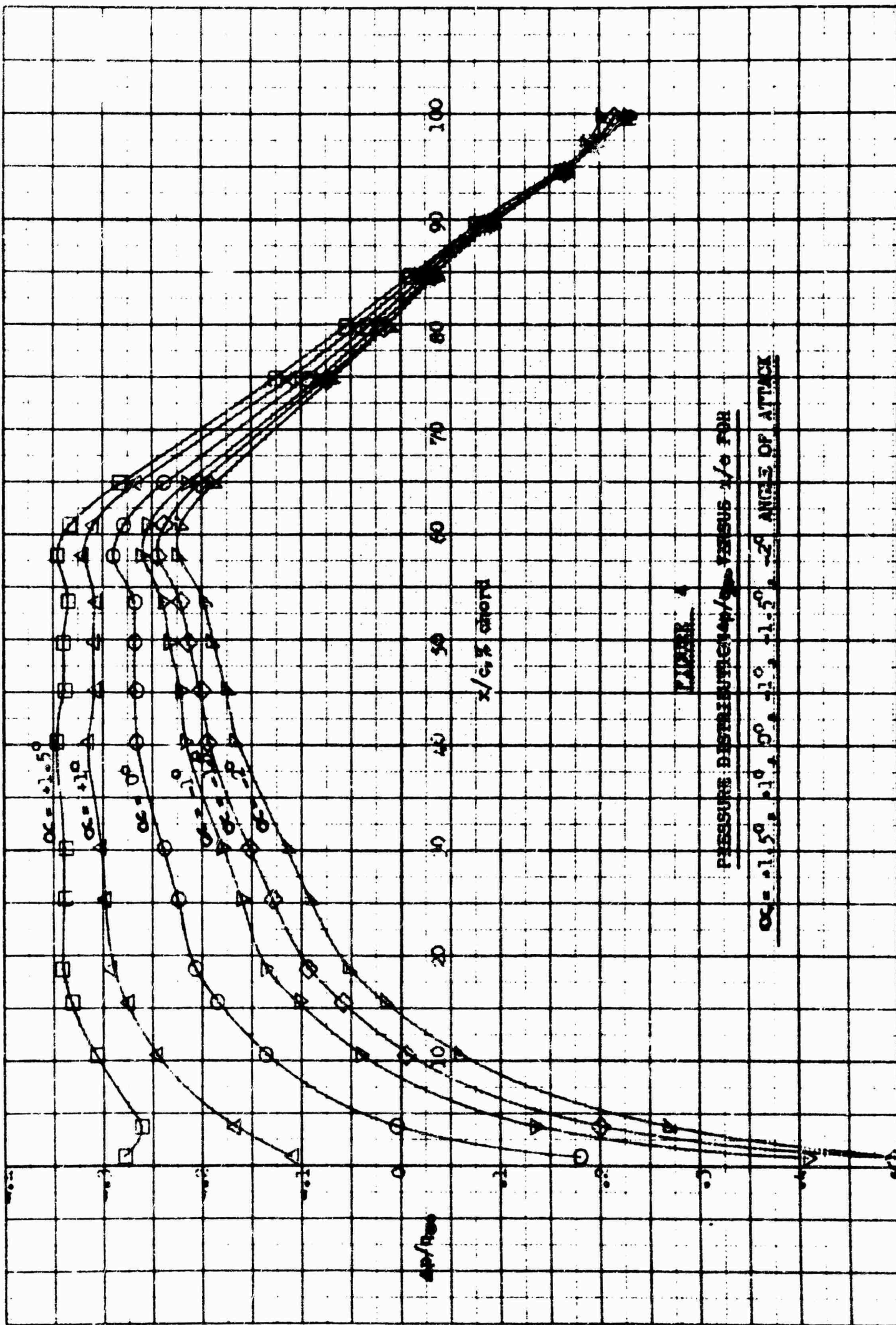
WING CROSS SECTION WITH DETAILS OF SUCTION CHAMBERS & SUCTION SLOTS

FIGURE 2



FIGURE 2 202 CURVE





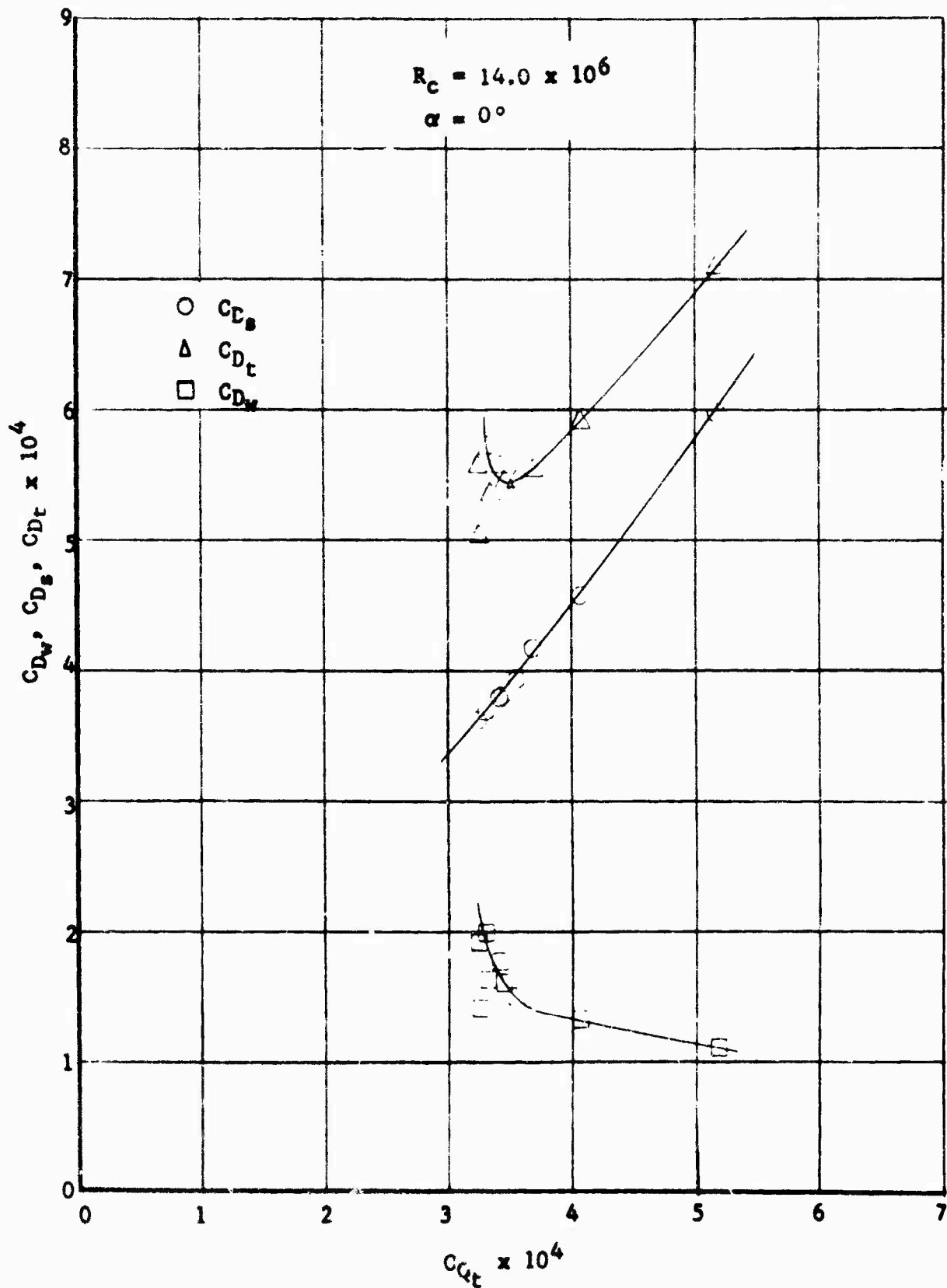


FIGURE 5 DRAG  $C_D$  VERSUS SUCTION QUANTITY  $C_{Qt}$  FOR VARIOUS REYNOLDS NUMBERS  $R_c$  AND ANGLES OF ATTACK  $\alpha$

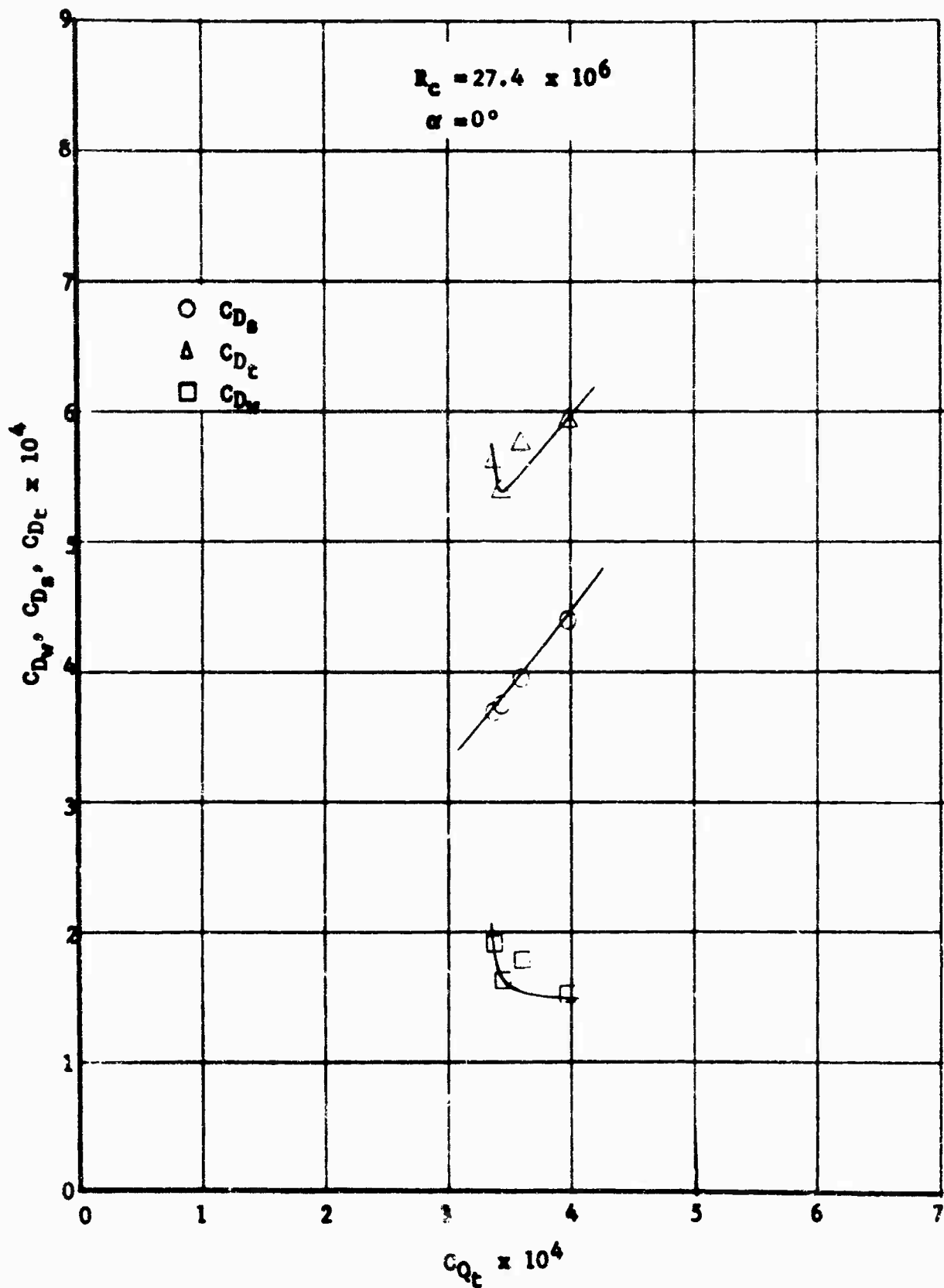


FIGURE 6 DRAG  $C_D$  VERSUS SUCTION QUANTITY  $C_{Q_t}$  FOR VARIOUS REYNOLDS NUMBERS  $R_e$  AND ANGLES OF ATTACK  $\alpha$

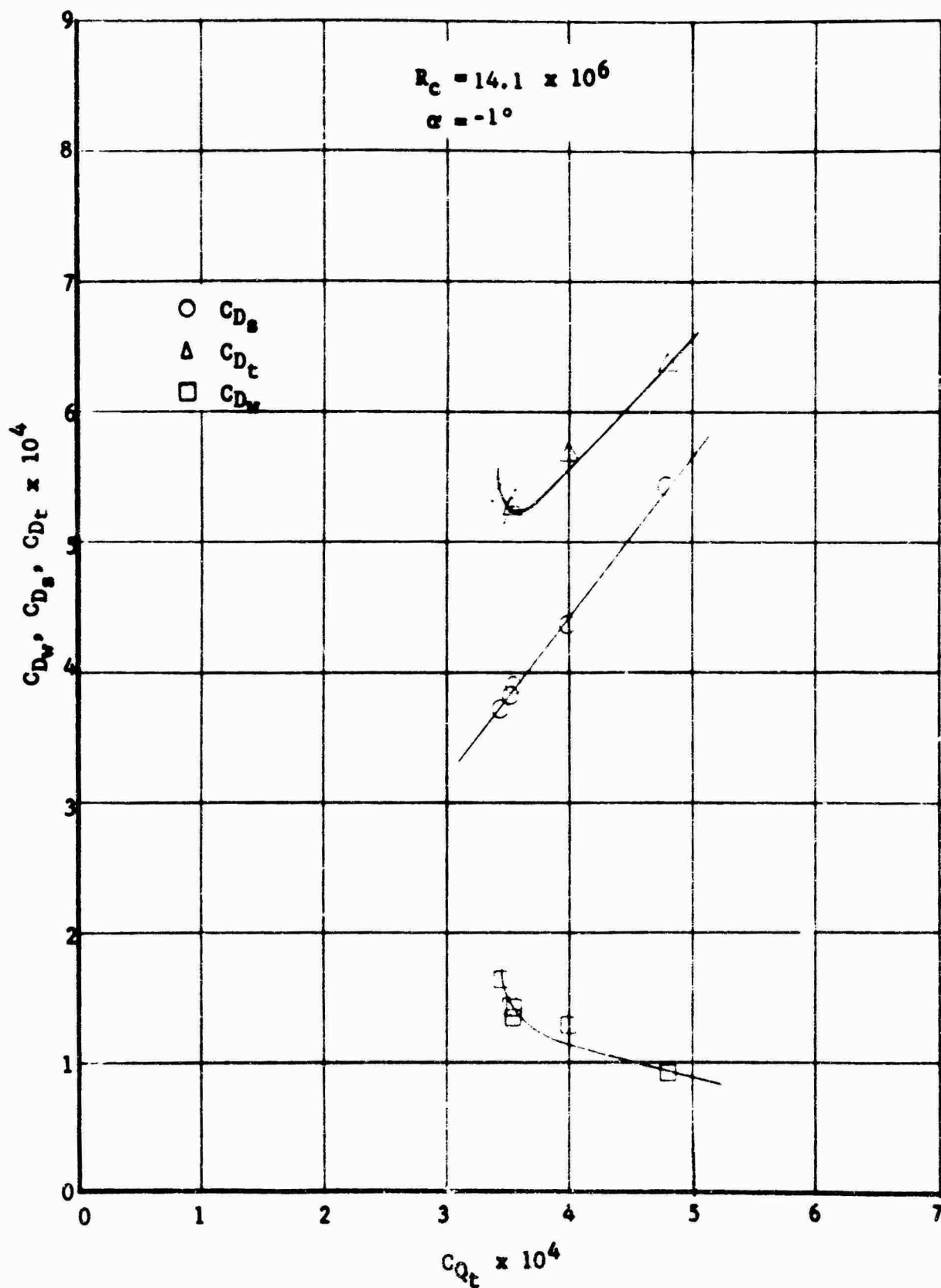


FIGURE 7 DRAG  $C_D$  VERSUS SUCTION QUANTITY  $C_{Q_t}$  FOR VARIOUS REYNOLDS NUMBERS  $R_c$  AND ANGLES OF ATTACK  $\alpha$

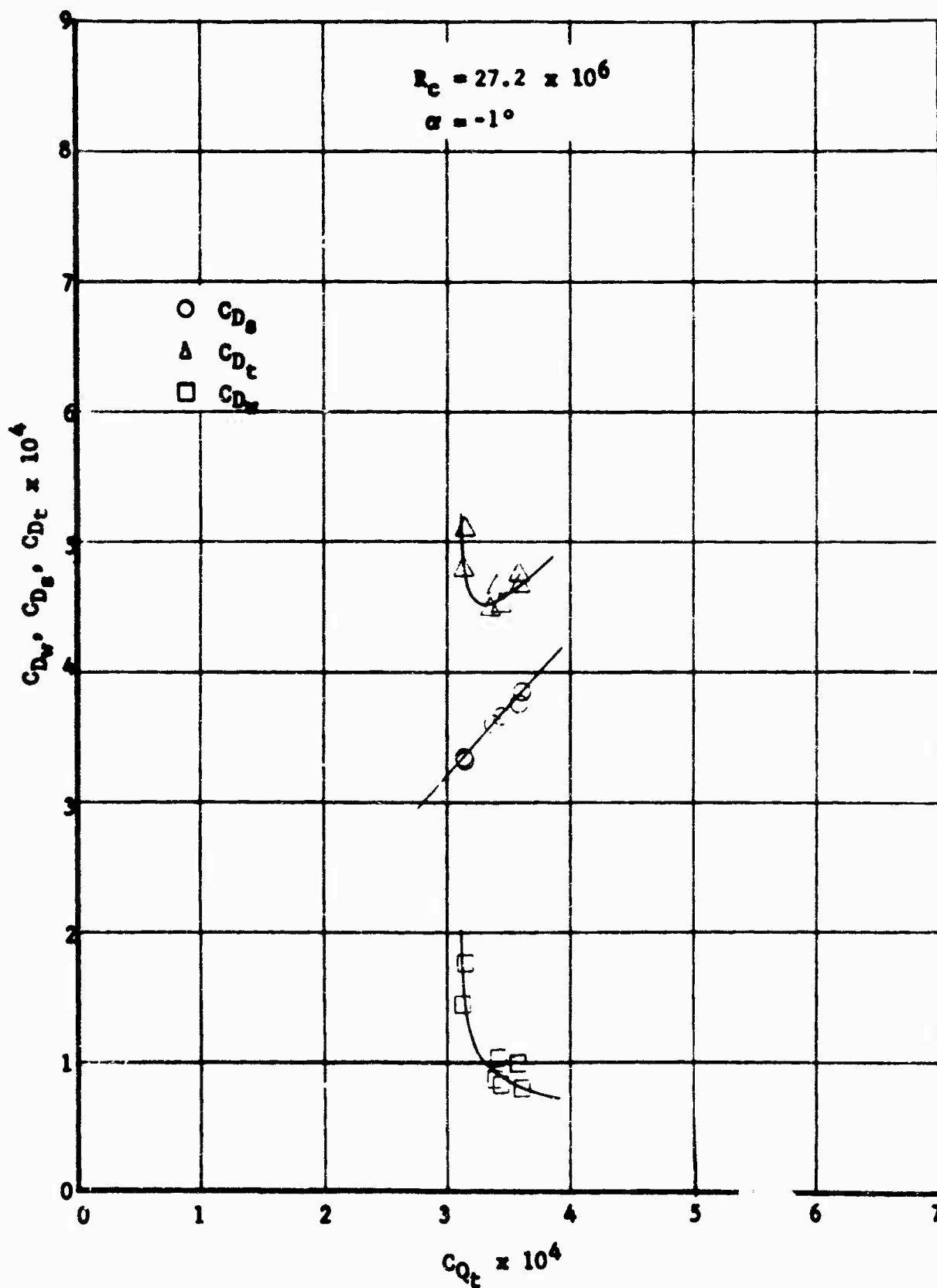


FIGURE 8 DRAG  $C_D$  VERSUS SUCTION QUANTITY  $C_{Qt}$  FOR VARIOUS REYNOLDS NUMBERS  $R_c$  AND ANGLES OF ATTACK  $\alpha$

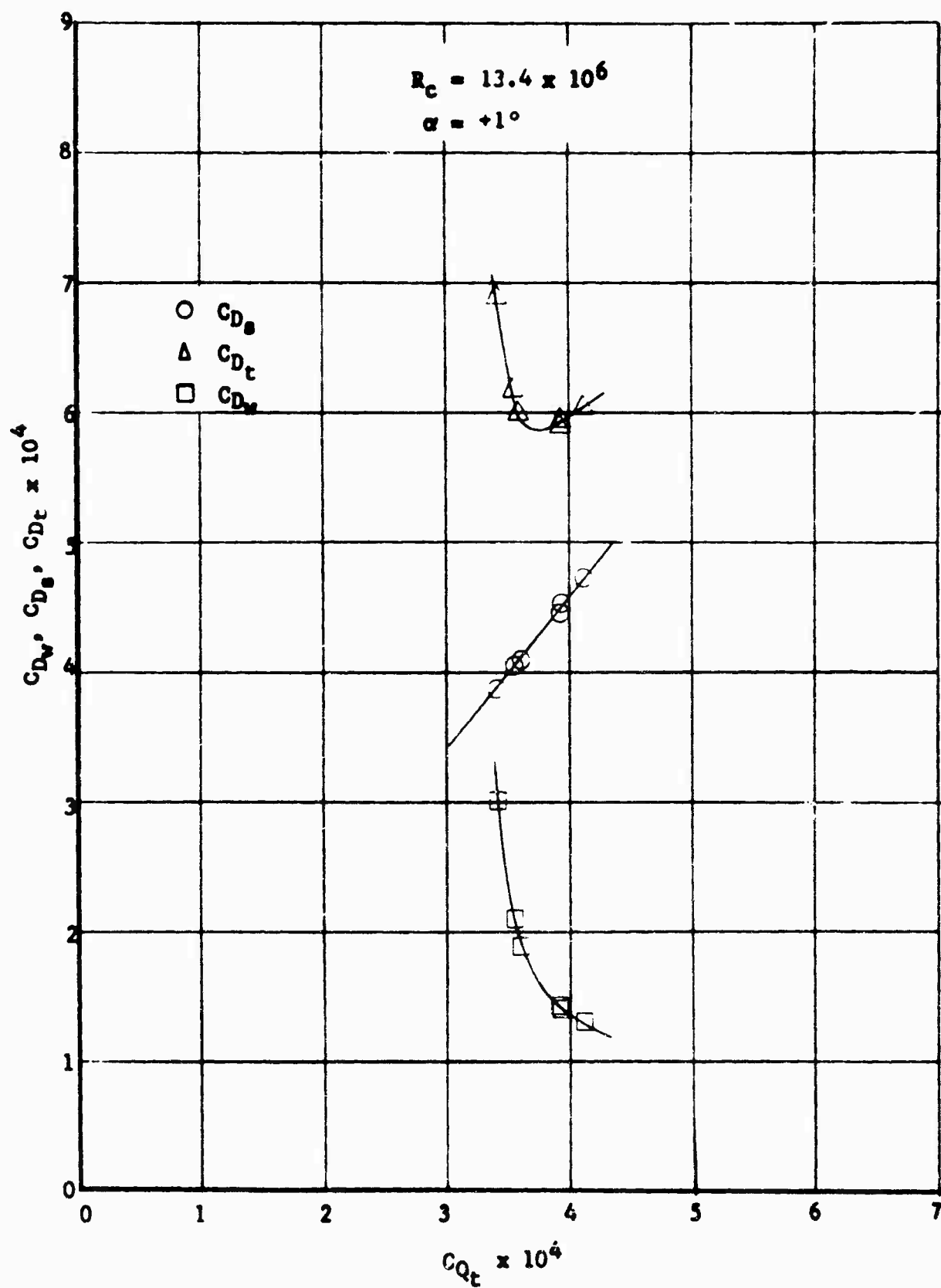


FIGURE 9 DRAG  $C_D$  VERSUS SUCTION QUANTITY  $C_{Q_t}$  FOR VARIOUS REYNOLDS NUMBERS  $R_c$  AND ANGLES OF ATTACK  $\alpha$

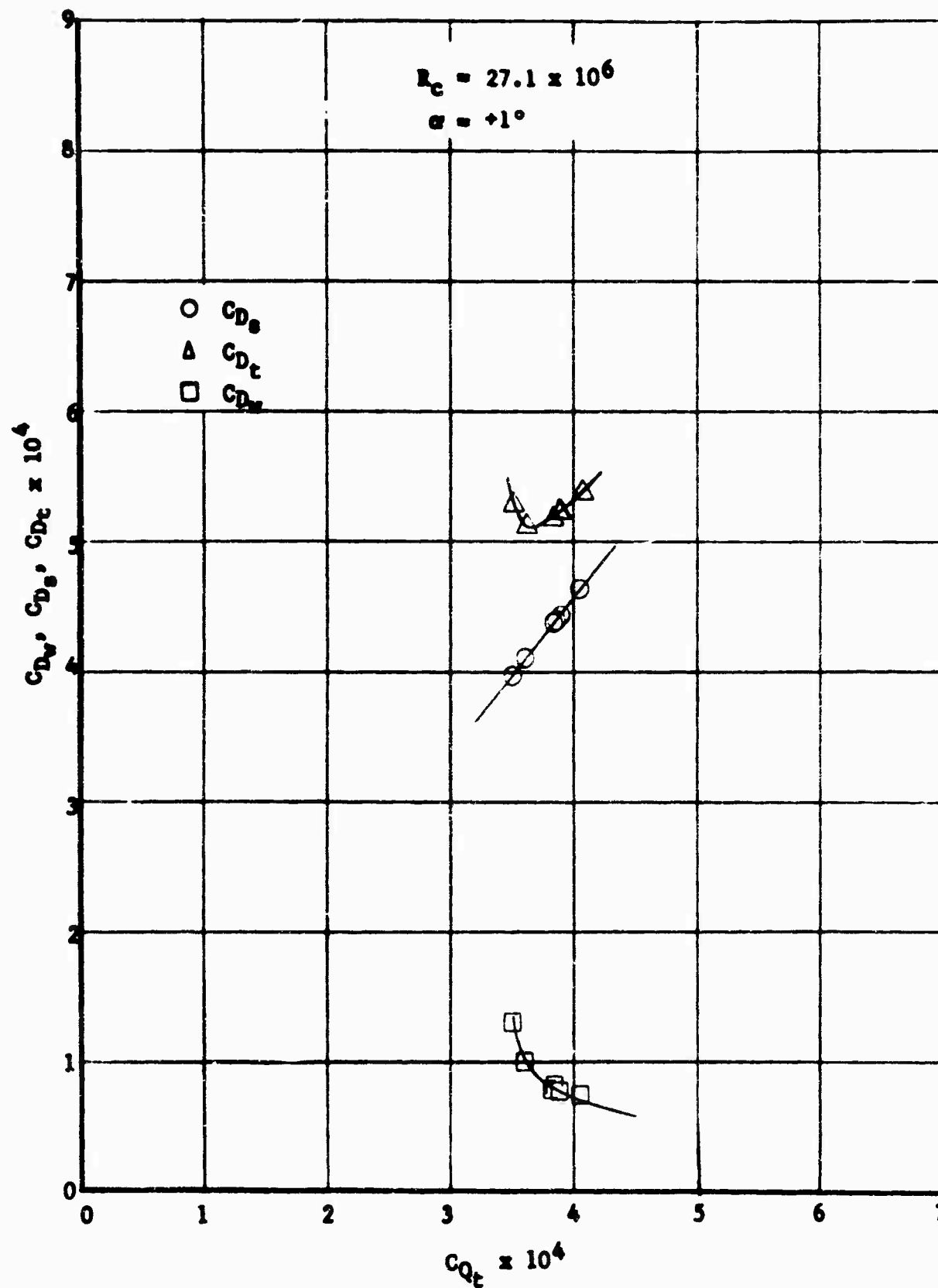
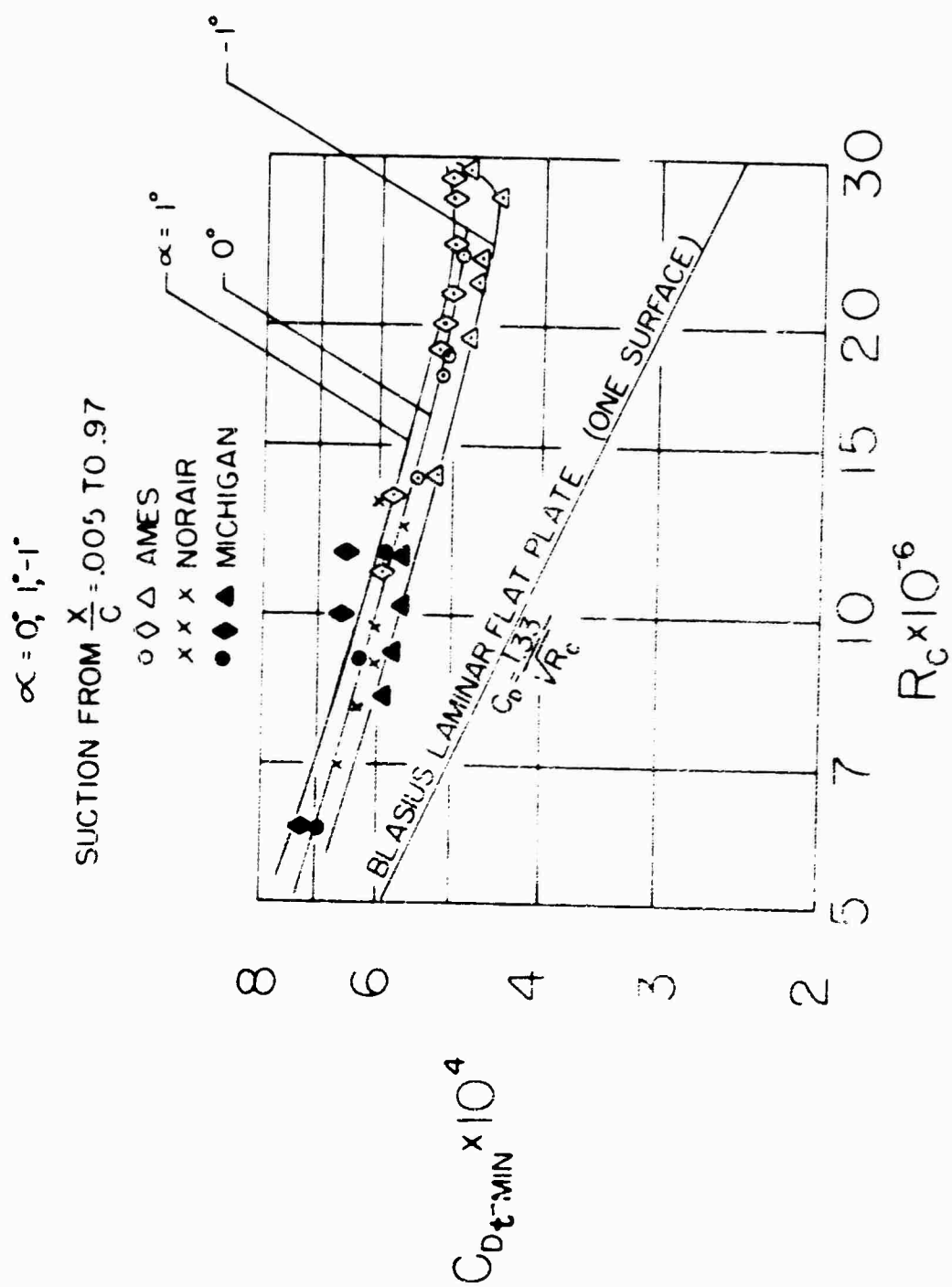


FIGURE 10 DRAG  $C_D$  VERSUS SUCTION QUANTITY  $C_{Qt}$  FOR VARIOUS REYNOLDS NUMBERS  $R_c$  AND ANGLES OF ATTACK  $\alpha$



30° SWEEP LAMINAR SUCTION WING, MIN. WING EQUIVALENT TOTAL DRAG (INCLUDING EQUIVALENT SUCTION DRAG) VS.  $R_c$  FOR UPPER WING SURFACE

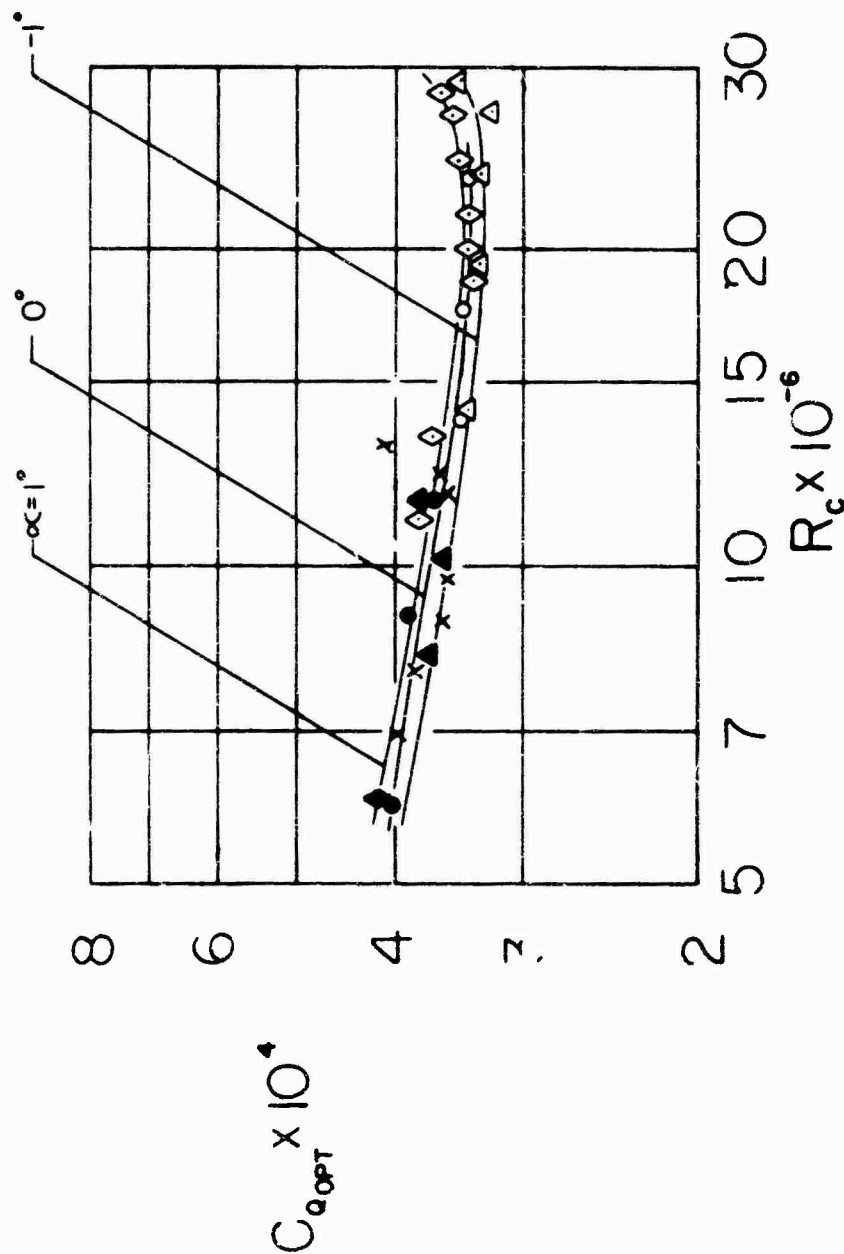
FIGURE 11

212



FIGURE 13 221

- ◇△ AME<sup>c</sup>
- ××× NORAIR
- ◆▲ MICHIGAN

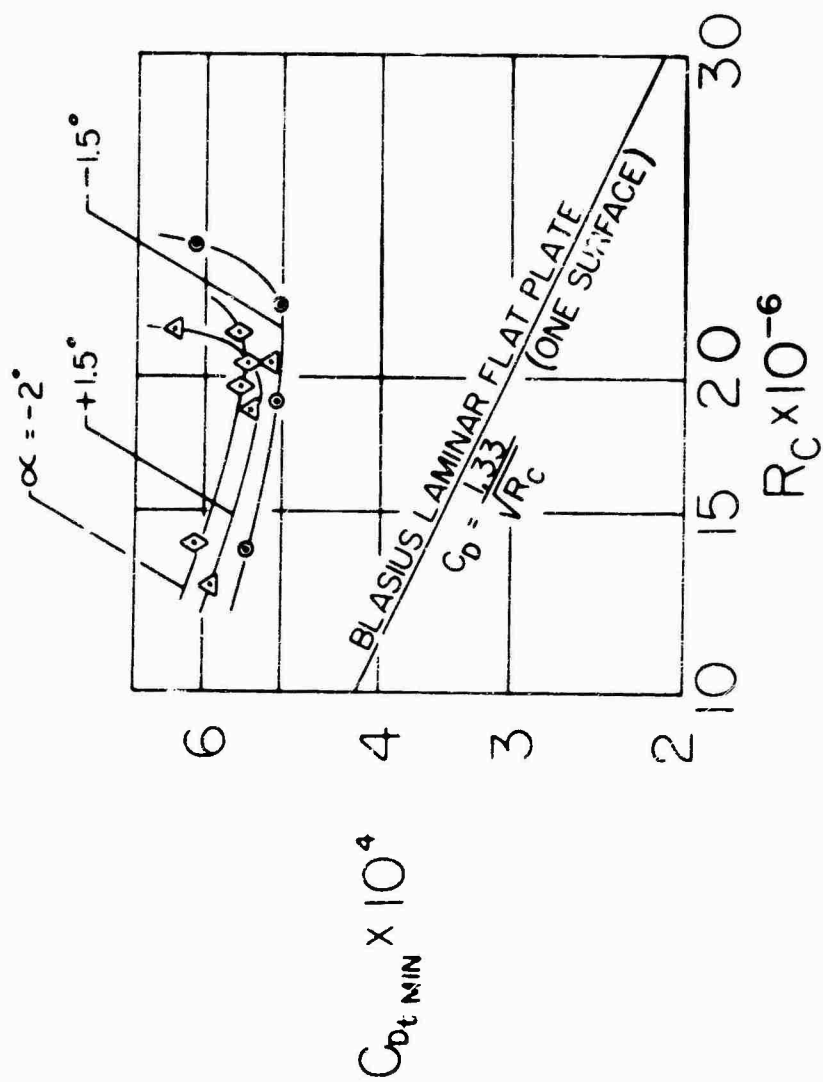


30° SWEEP LAMINAR SUCTION WING OPTIMUM SUCTION QUANTITY,  $C_{q_{opt}}$  VS.  $R_c$   
FOR UPPER WING SURFACE

FIGURE 12

220

AMES TESTS, @  $\alpha = 1.5^\circ, -1.5^\circ, -2.0^\circ$

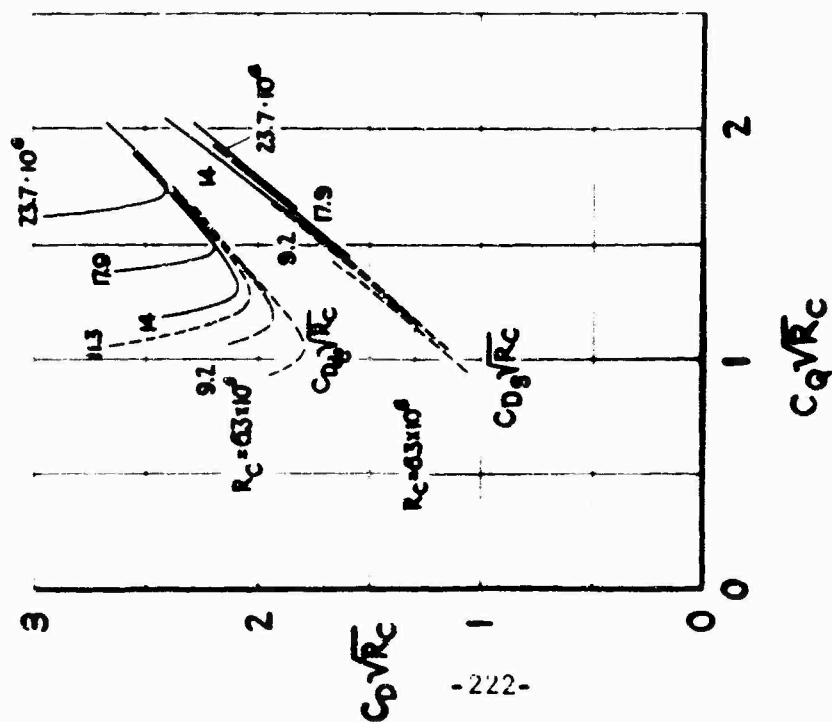


30° SWEEP LAMINAR SUCTION WING MIN WING EQUIVALENT TOTAL DRAG INCLUDING EQUIVALENT SUCTION DRAG VS.  $R_c$  FOR UPPER WING SURFACE

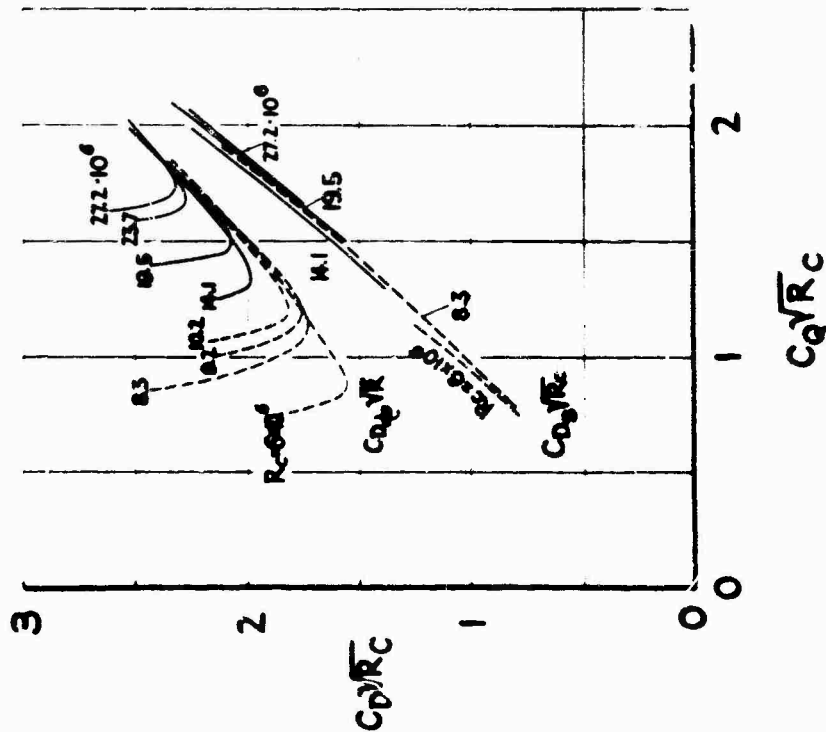
FIGURE 13

AMES TESTS  
MICHIGAN TESTS

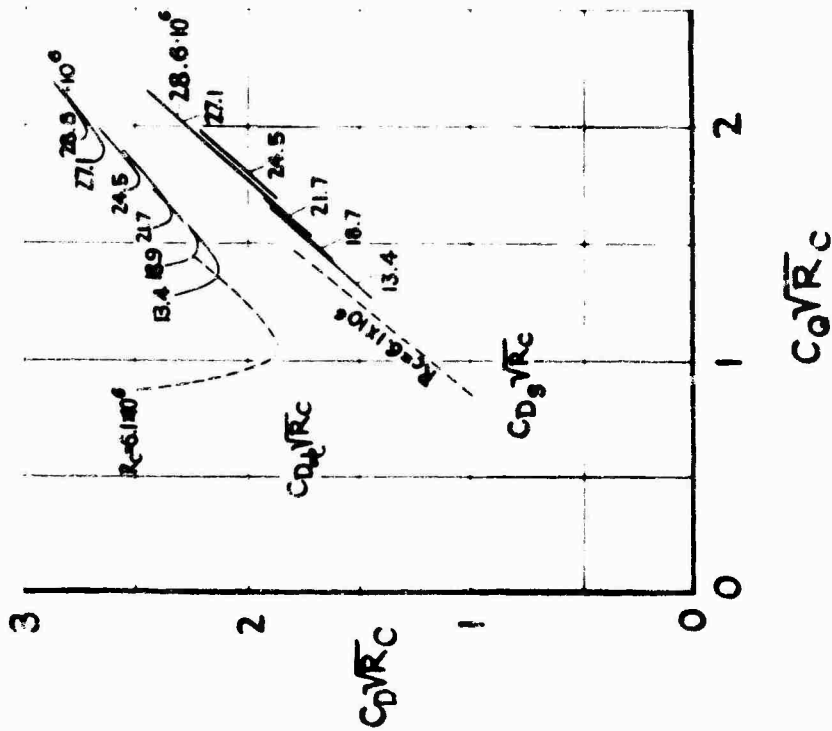
$\alpha = 0^\circ$



$\alpha = -1^\circ$

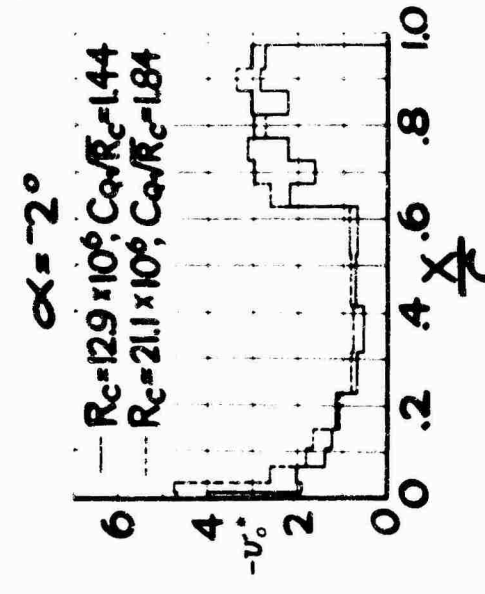
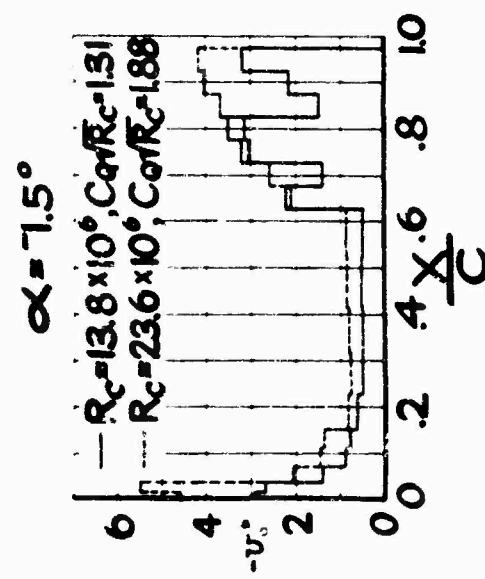
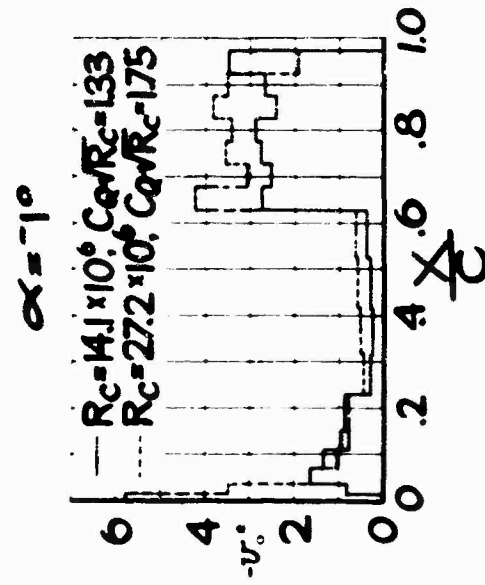
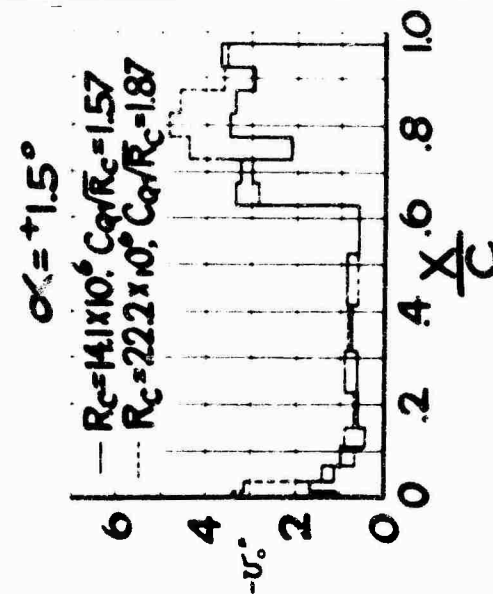
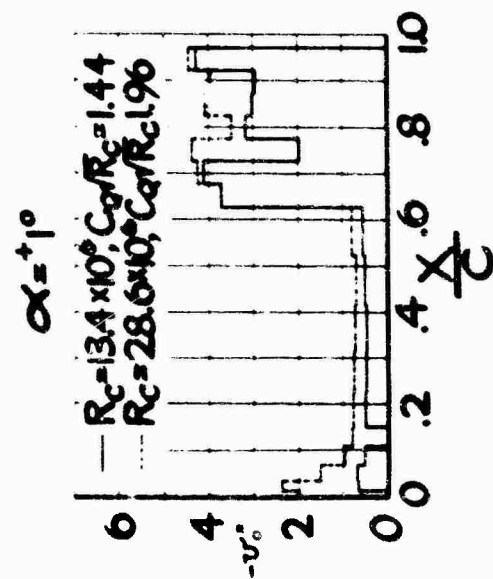
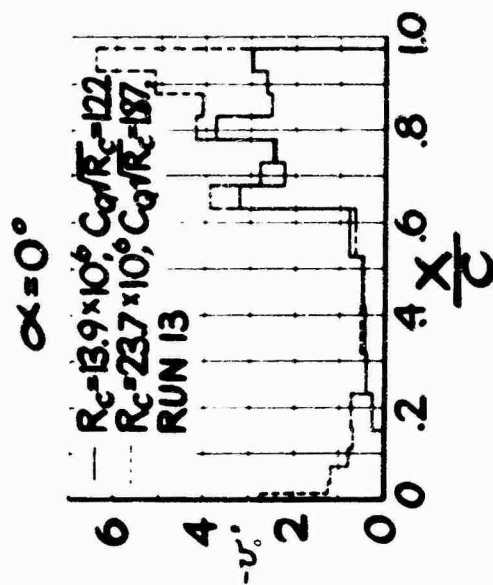


$\alpha = +1^\circ$



30° SWEEP LAMINAR SUCTION WING MEASURED DRAG COEFFICIENTS ( $C_{D_s}/R_c$ ,  $C_{D_t}/R_c$ )  
VS SUCTION COEFFICIENT ( $C_Q/R_c$ ) AT VARIOUS  $\alpha$  AND  $R_c$

FIGURE 14



30° SWEEP LAMINAR SUCTION WING SUCTION VELOCITY  $-v_o$  VS. CHORD ( $X/C$ )

FIGURE 15

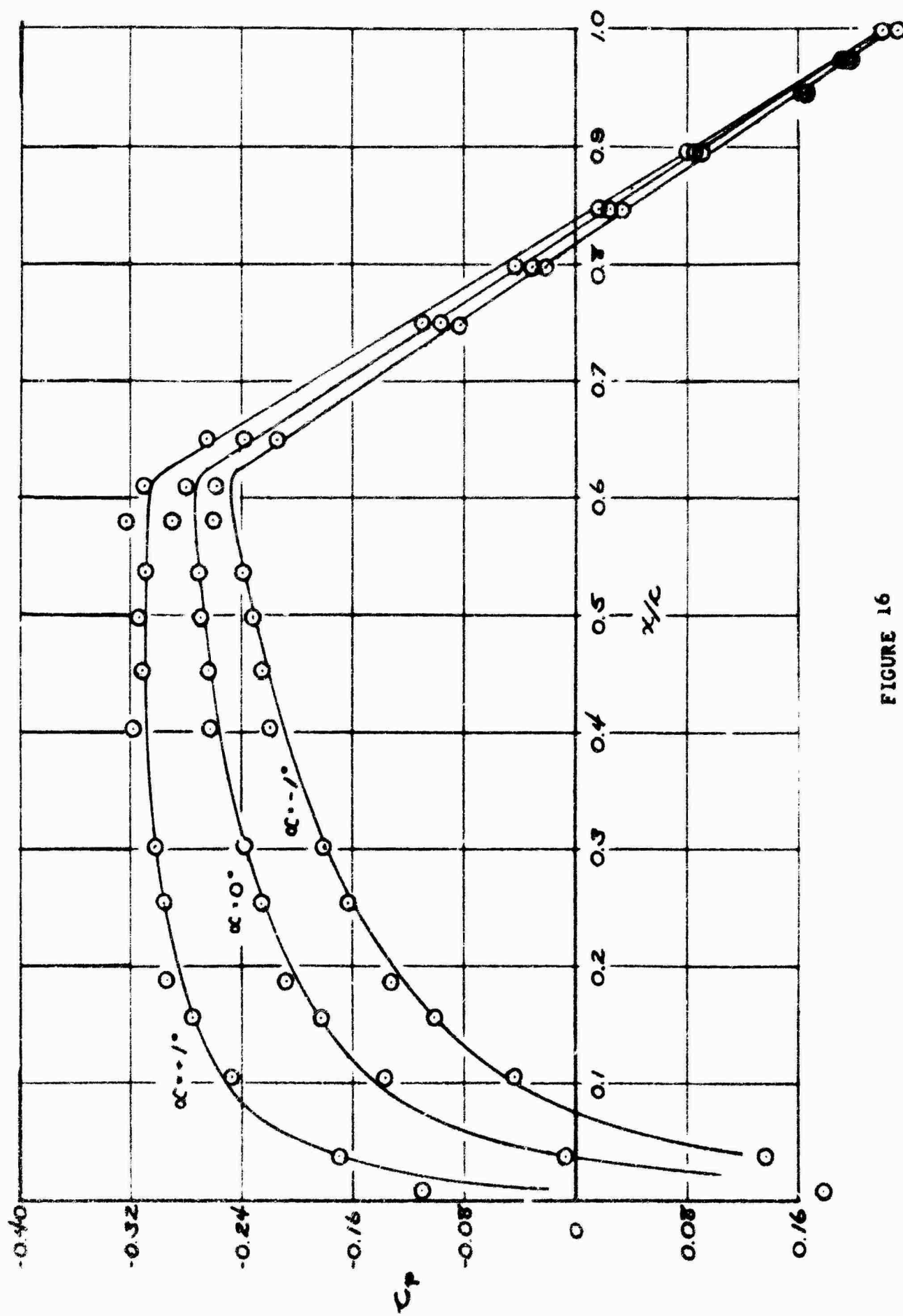


FIGURE 16

COMPARISON BETWEEN MEASURED VELOCITY DISTRIBUTION AND APPROXIMATE  
VELOCITY DISTRIBUTION USED FOR CALCULATIONS OF BOUNDARY LAYER DEVELOPMENT

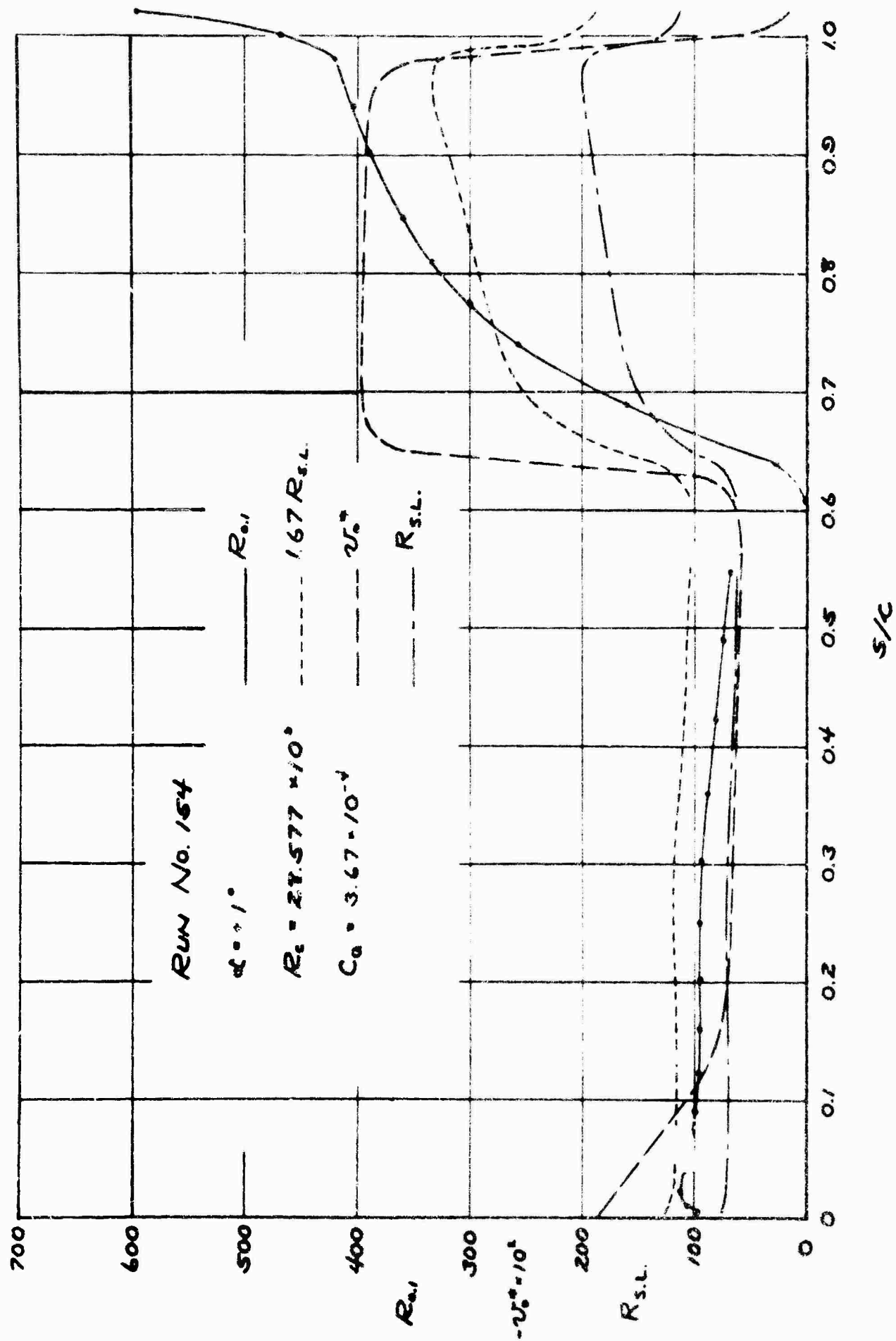


FIGURE 17

VARIATION OF CROSSFLOW REYNOLDS NUMBER WITH CHORD-- $30^\circ$  SWEEP LAMINAR SUCTION WING MODEL  
IN NASA-AMES 12-FT. PWT

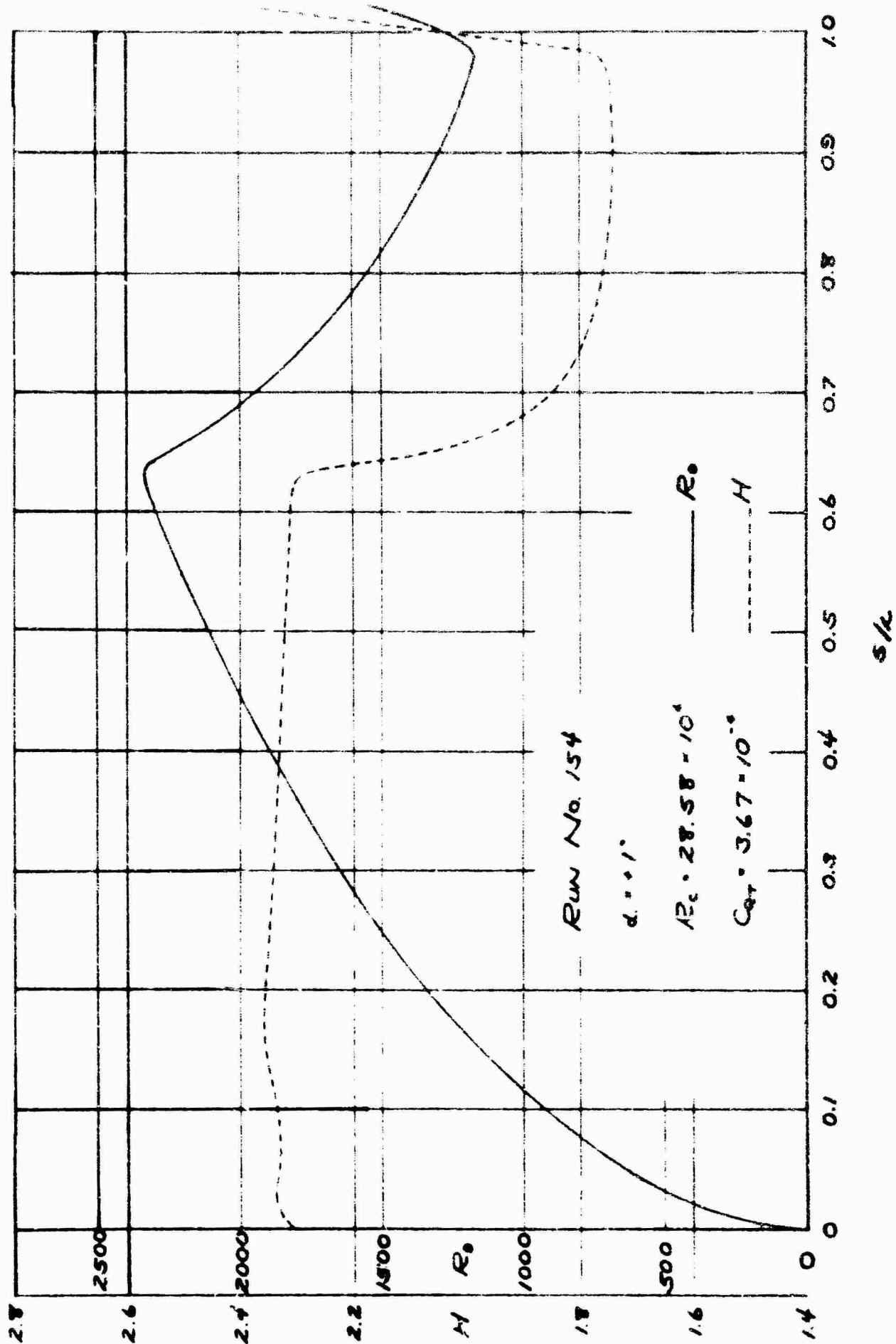


FIGURE 18

VARIATION OF MOMENTUM THICKNESS REYNOLDS NUMBER AND SHAPE PARAMETER WITH CHORD--30° SWEEP LAMINAR SUCTION WING MODEL IN NASA-AMES 12-FT. PWT

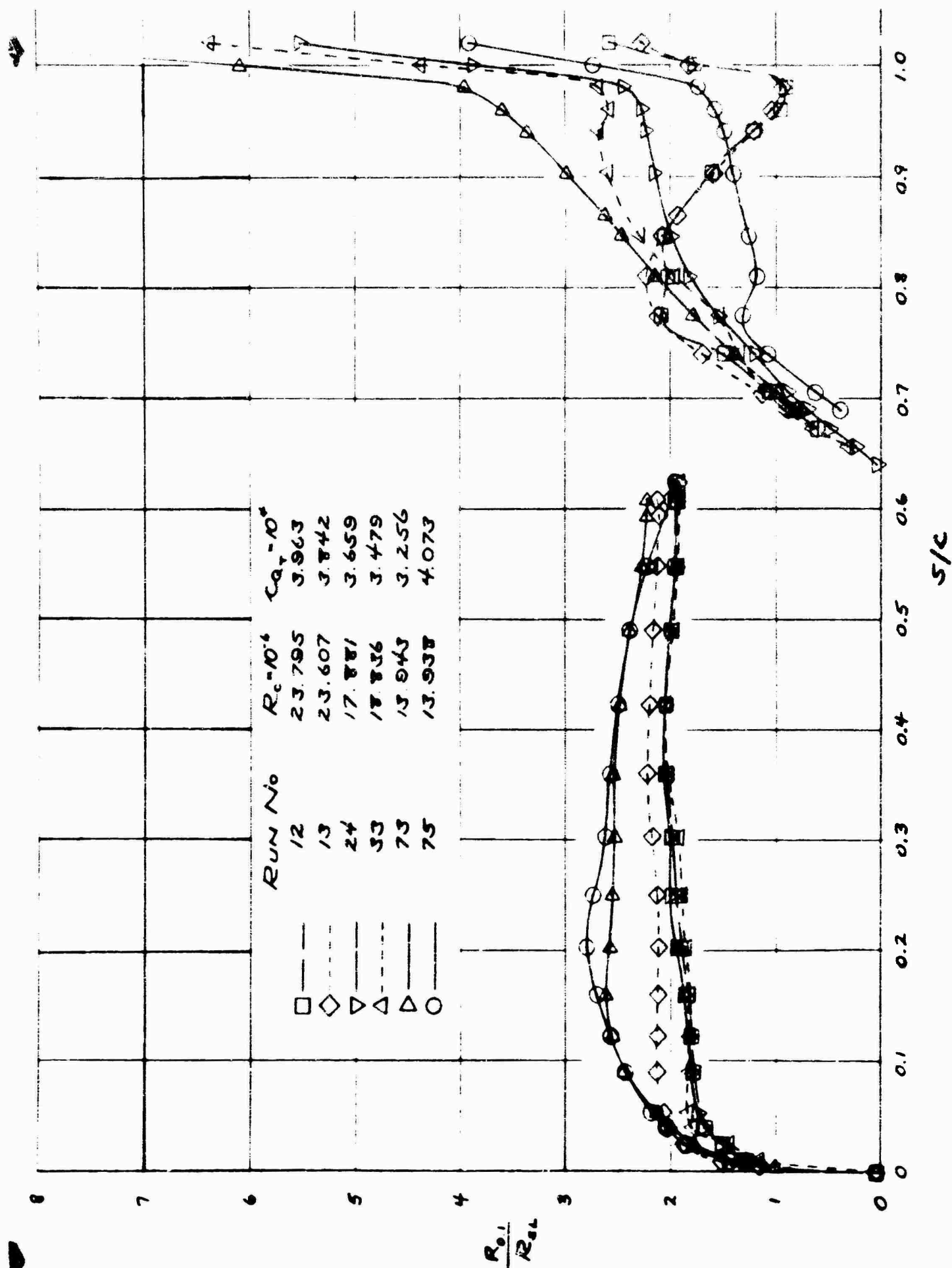


FIGURE 19  
COMPARISON OF CROSSFLOW REYNOLDS NUMBER WITH STABILITY LIMIT REYNOLDS NUMBER AT  
SEVERAL LENGTH REYNOLDS NUMBERS, SUCTION COEFFICIENTS AND ANGLES OF ATTACK  
 $\alpha = 0^\circ$



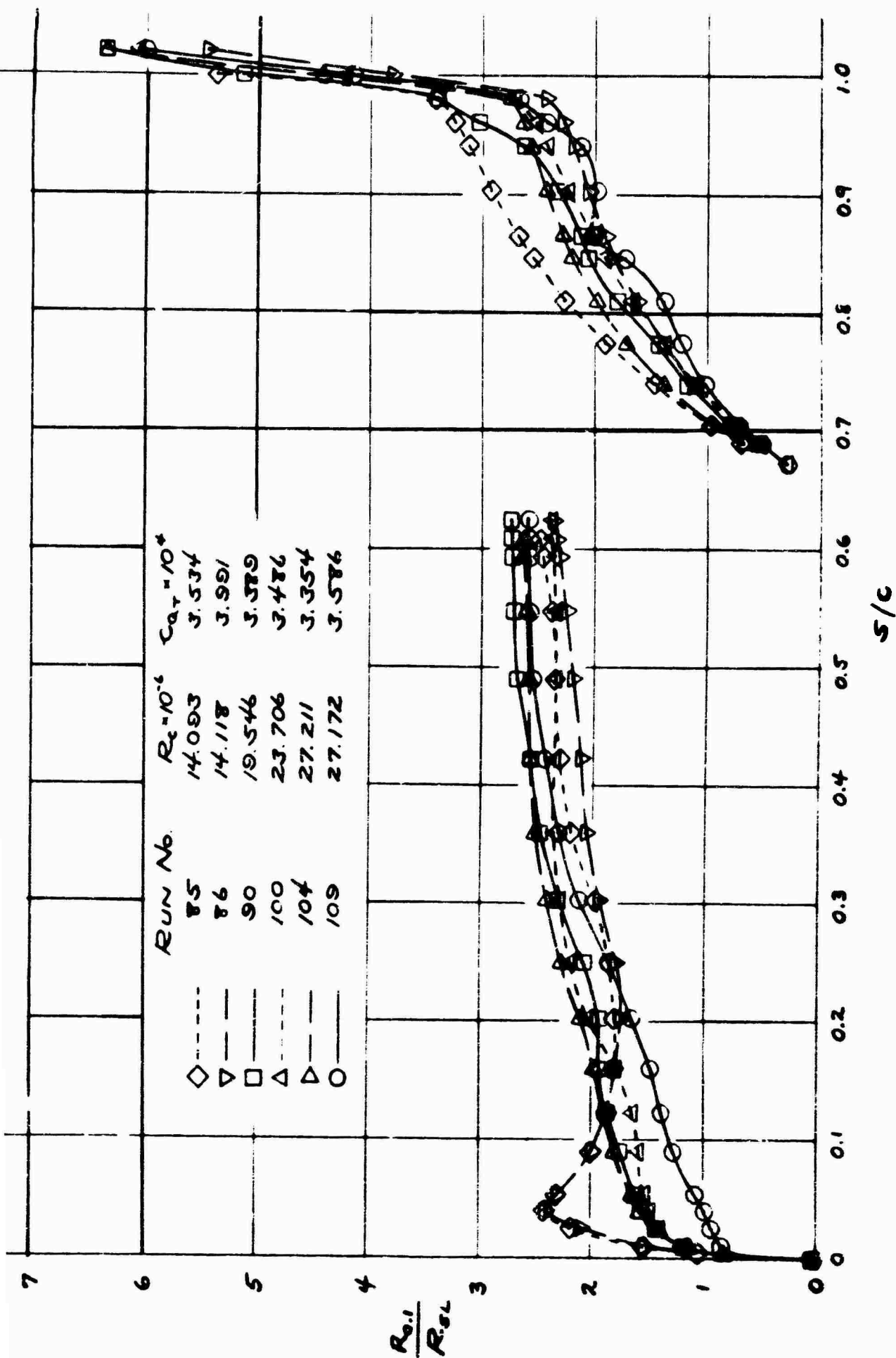


FIGURE 20  
COMPARISON OF CROSSFLOW REYNOLDS NUMBER WITH STABILITY LIMIT REYNOLDS NUMBER AT  
SEVERAL LENGTH REYNOLDS NUMBERS, SUCTION COEFFICIENTS AND ANGLES OF ATTACK  
 $\alpha = -1^\circ$

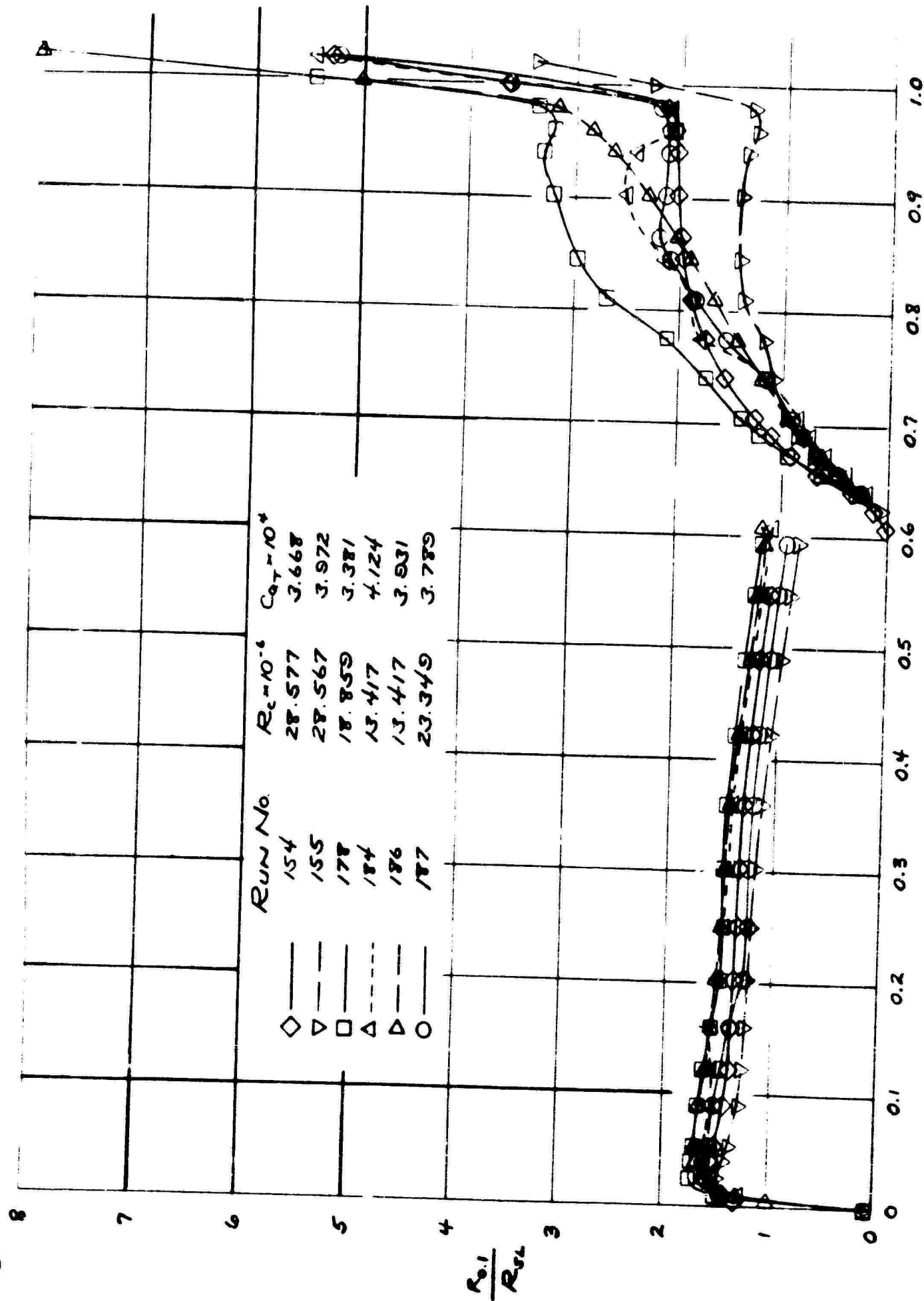


FIGURE 21  
 $5/c$

COMPARISON OF CROSSFLOW REYNOLDS NUMBER WITH STABILITY LIMIT REYNOLDS NUMBER AT  
SEVERAL LENGTH REYNOLDS NUMBERS, SUCTION COEFFICIENTS AND ANGLES OF ATTACK

$\alpha = 1^\circ$

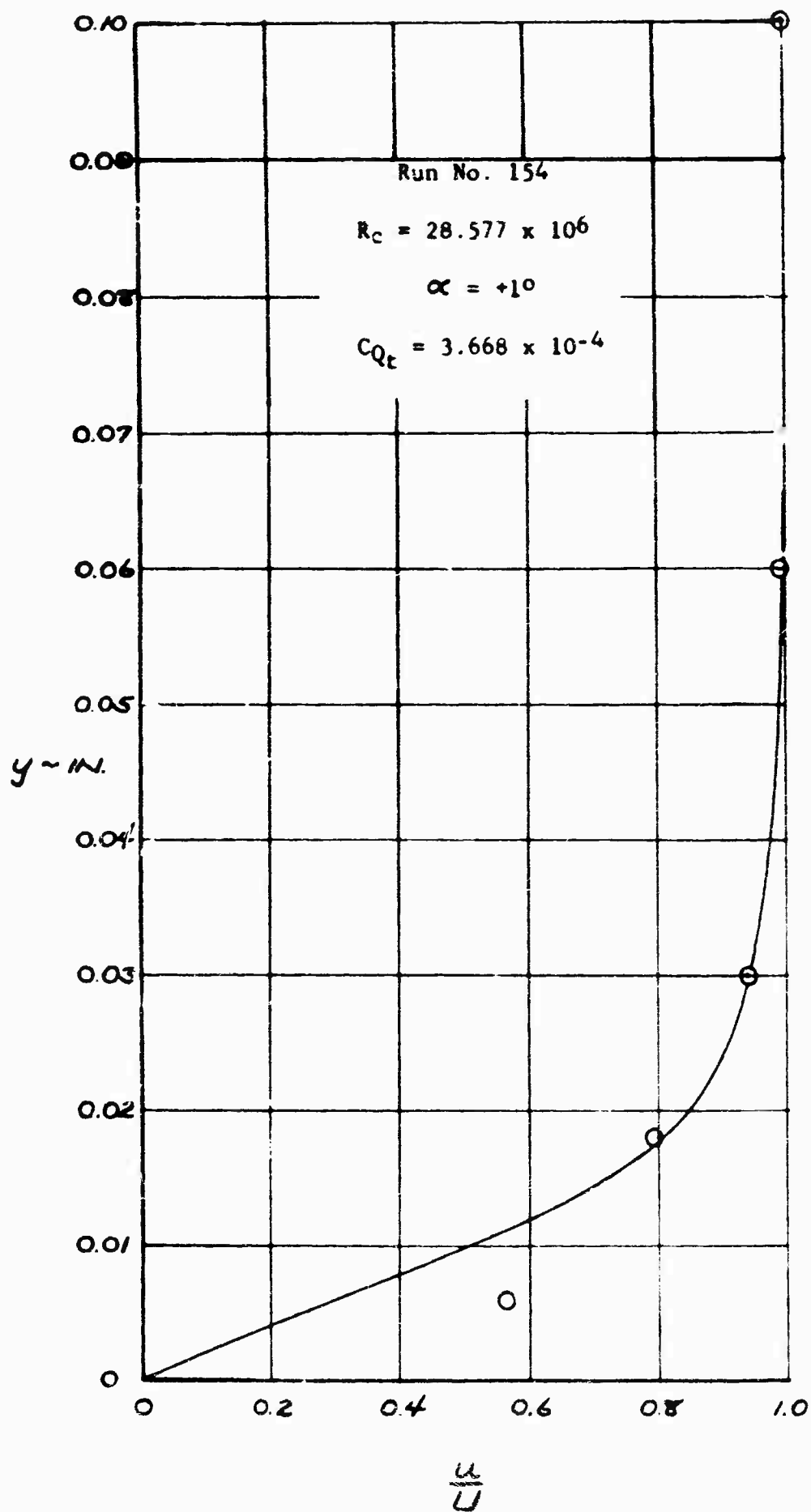


FIGURE 22

COMPARISON OF MEASURED AND CALCULATED TRAILING EDGE  
BOUNDARY LAYER VELOCITY PROFILES

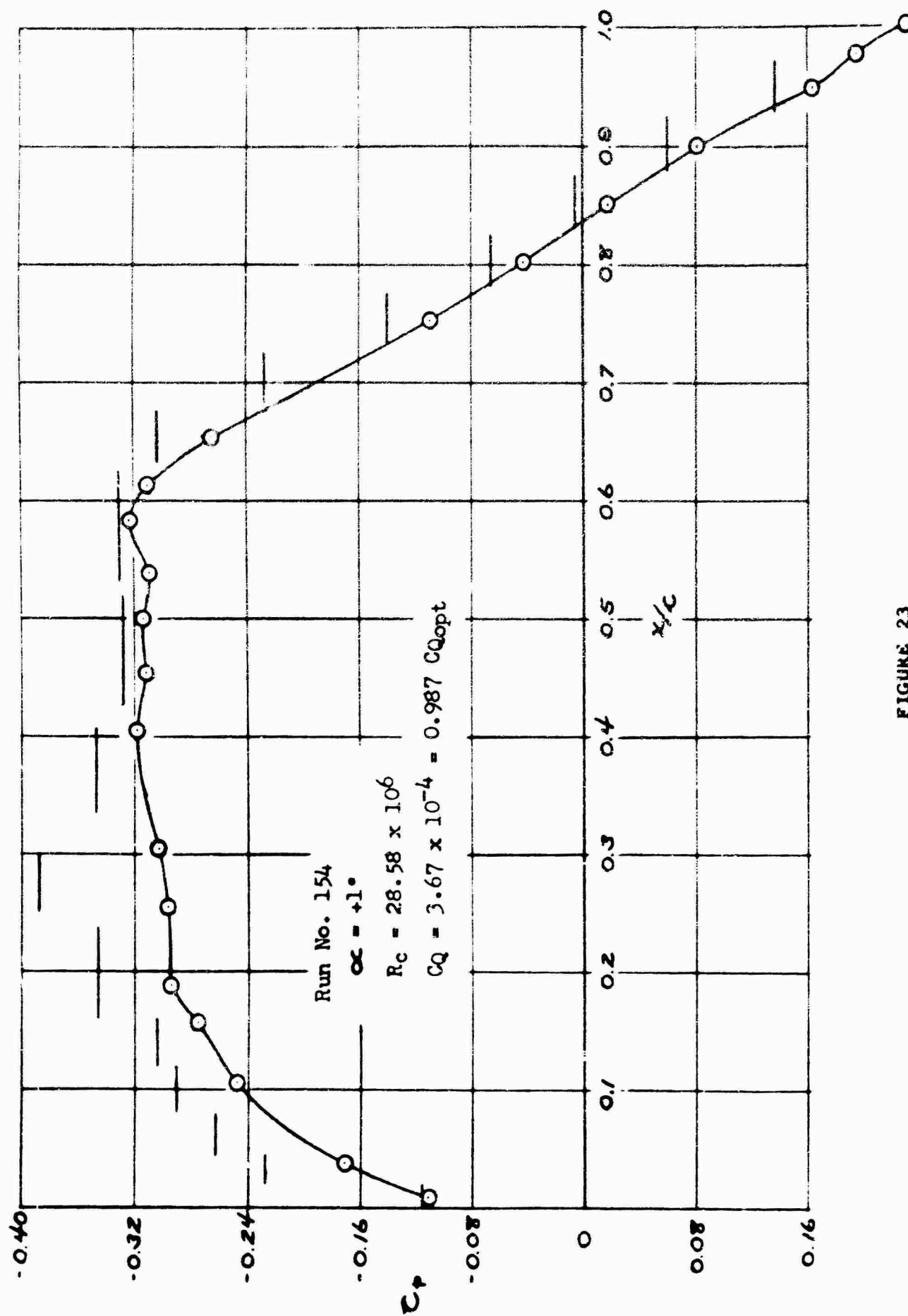


FIGURE 23  
 COMPARISON OF CHORDWISE PRESSURE DISTRIBUTION  
 AND SUCTION CHAMBER PRESSURE COEFFICIENTS

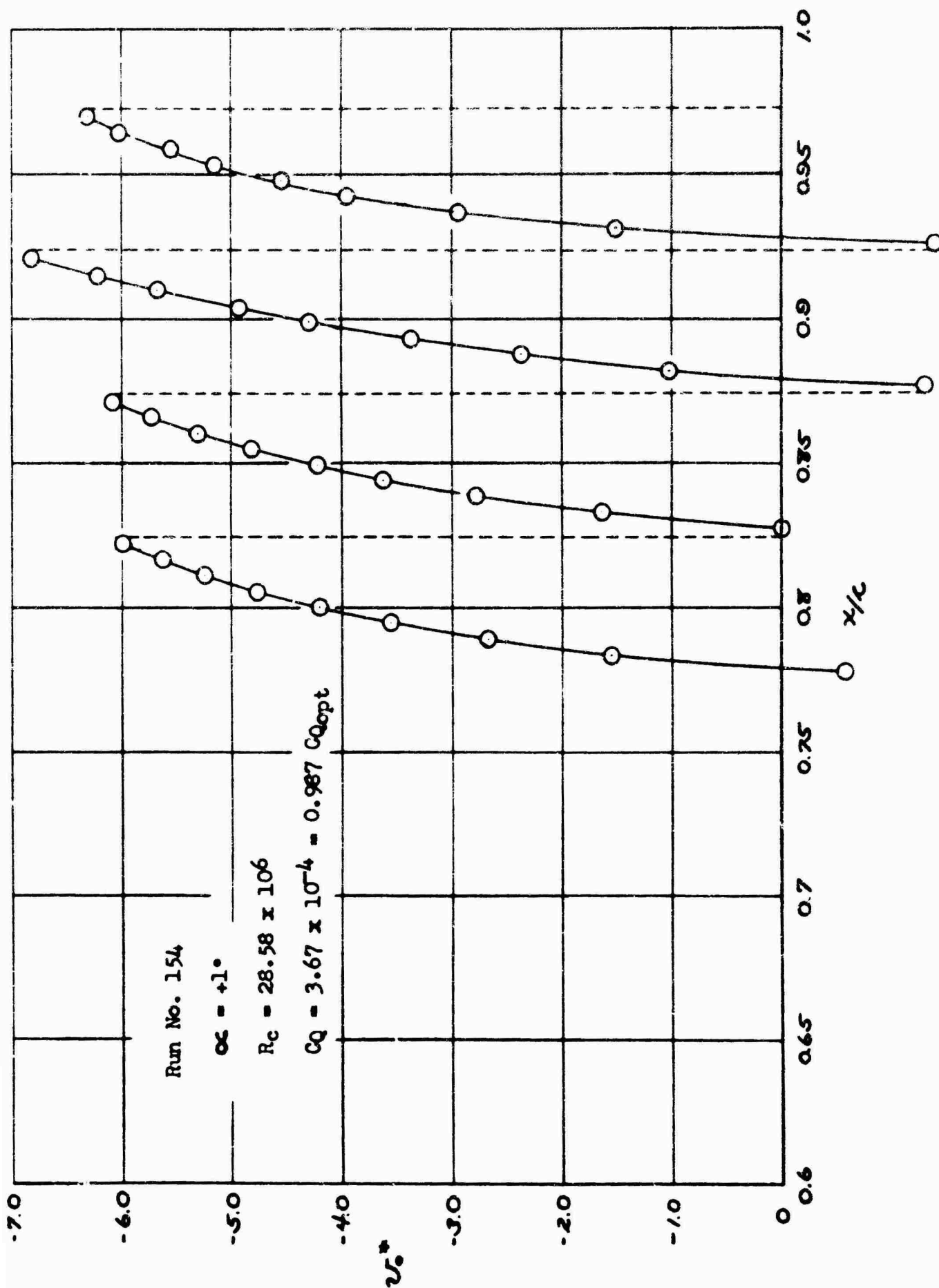
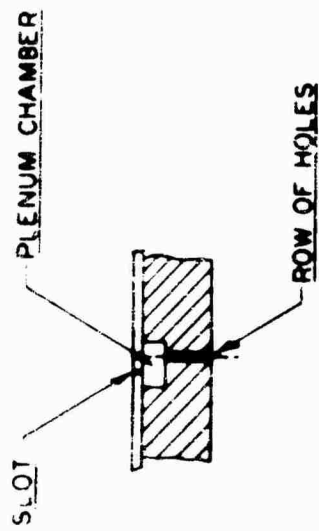
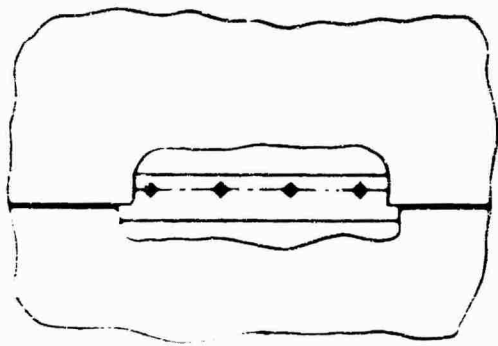
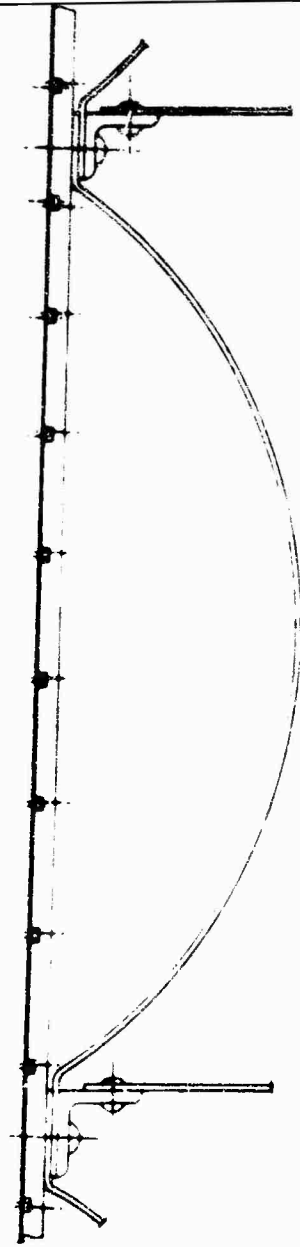


FIGURE 24  
 CHORDWISE DISTRIBUTION OF NONDIMENSIONAL SUCTION  
 VELOCITY COEFFICIENT  $v_o^*$  IN AFT FOUR SUCTION CHAMBERS



TYPICAL SECTION THRU SLOT



VIEW A

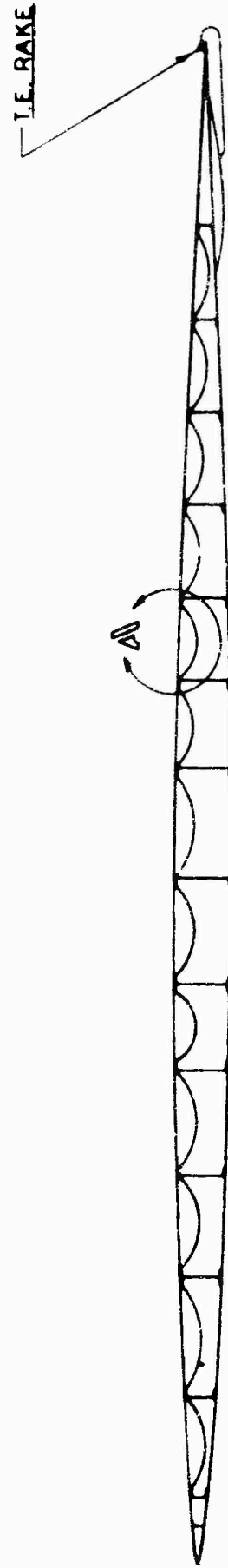


FIGURE 25 MODEL CROSS SECTION WITH DETAILS OF SUCTION CHAMBERS AND SUCTION SLOTS

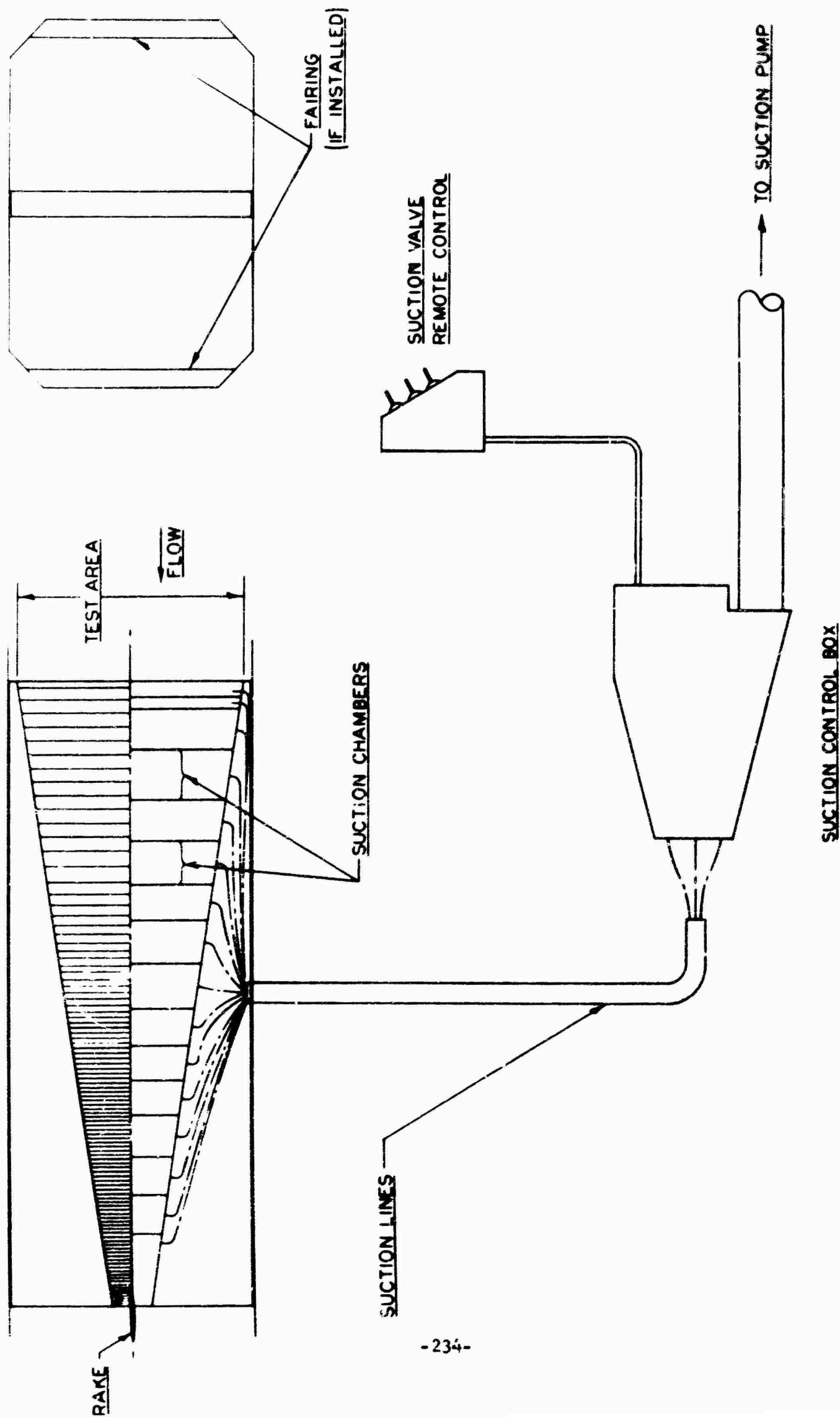


FIGURE 26 INSTALLATION DRAWING 17-FOOT CHORD LAMINAR SUCTION WING IN NORAIR 7- BY 10-FOOT WIND TUNNEL

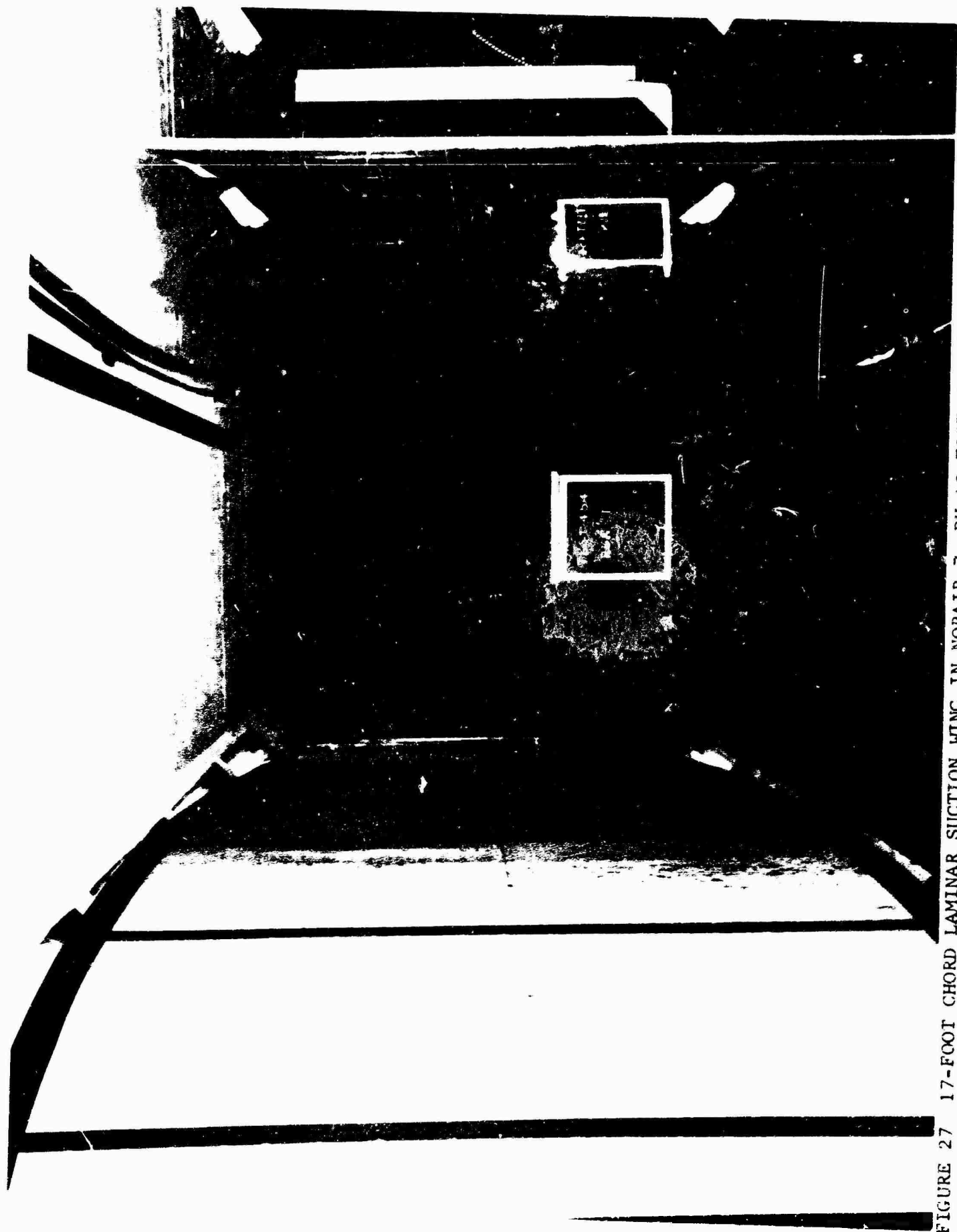
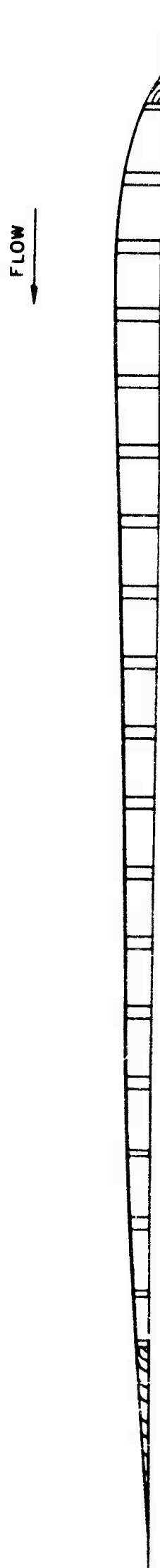
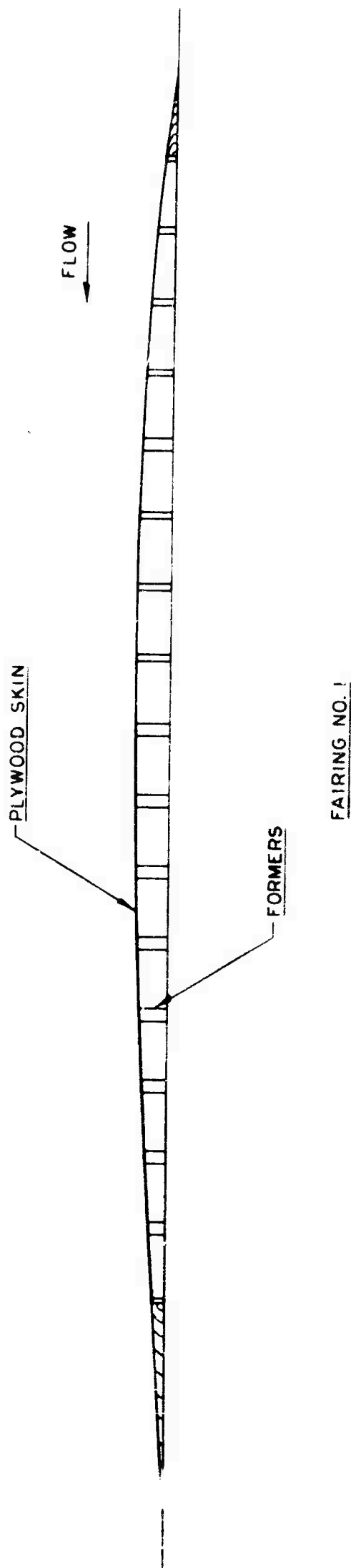


FIGURE 27 17-FOOT CHORD LAMINAR SUCTION WING IN NORAIR 7- BY 10-FOOT WIND TUNNEL WITH FAIRING NO. 1 INSTALLED





FAIRING NO. 2

FIGURE 28 CROSS SECTIONS - WIND TUNNEL WALL FAIRINGS

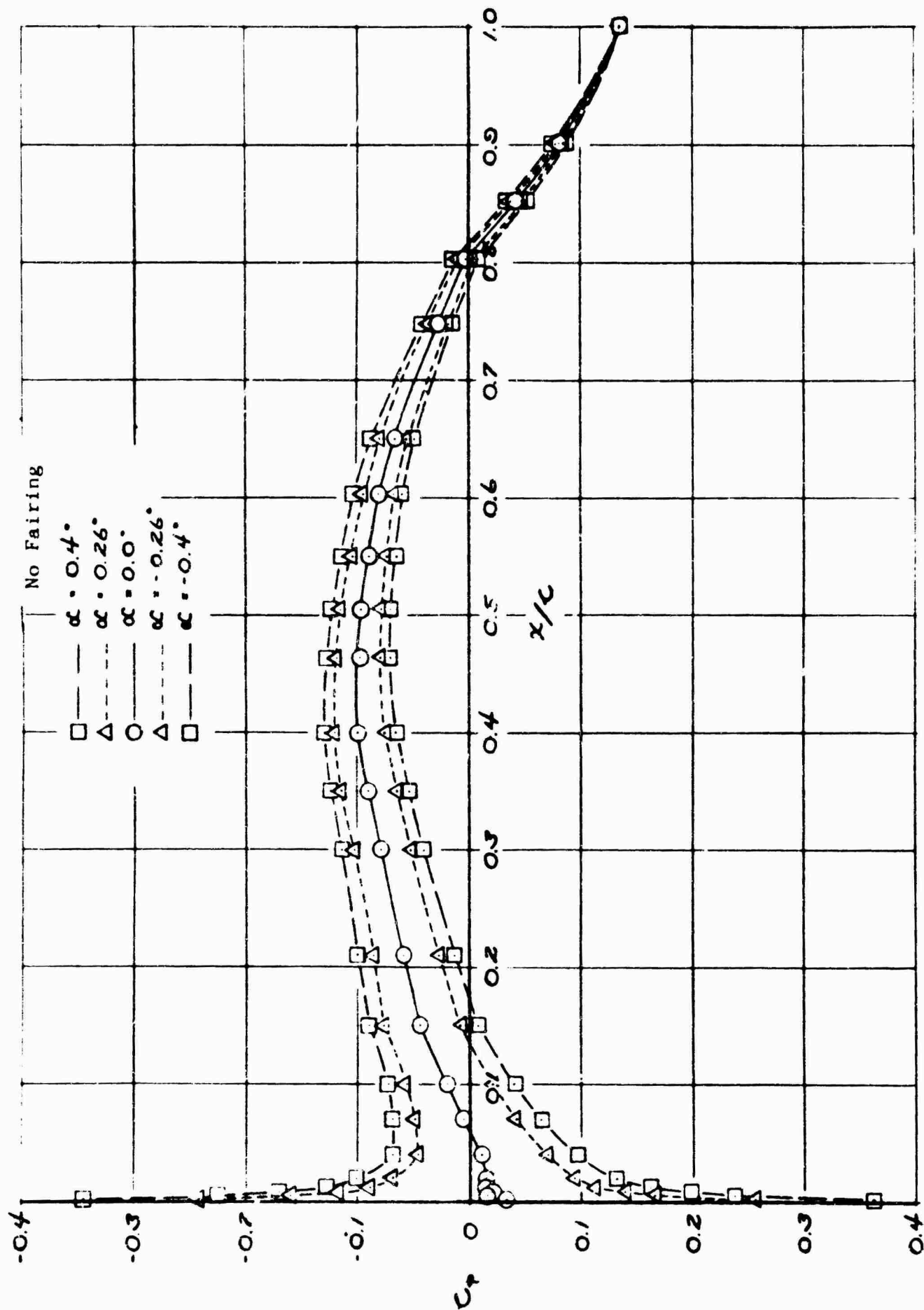


FIGURE 29 PRESSURE DISTRIBUTIONS AT VARYING ANGLES OF ATTACK

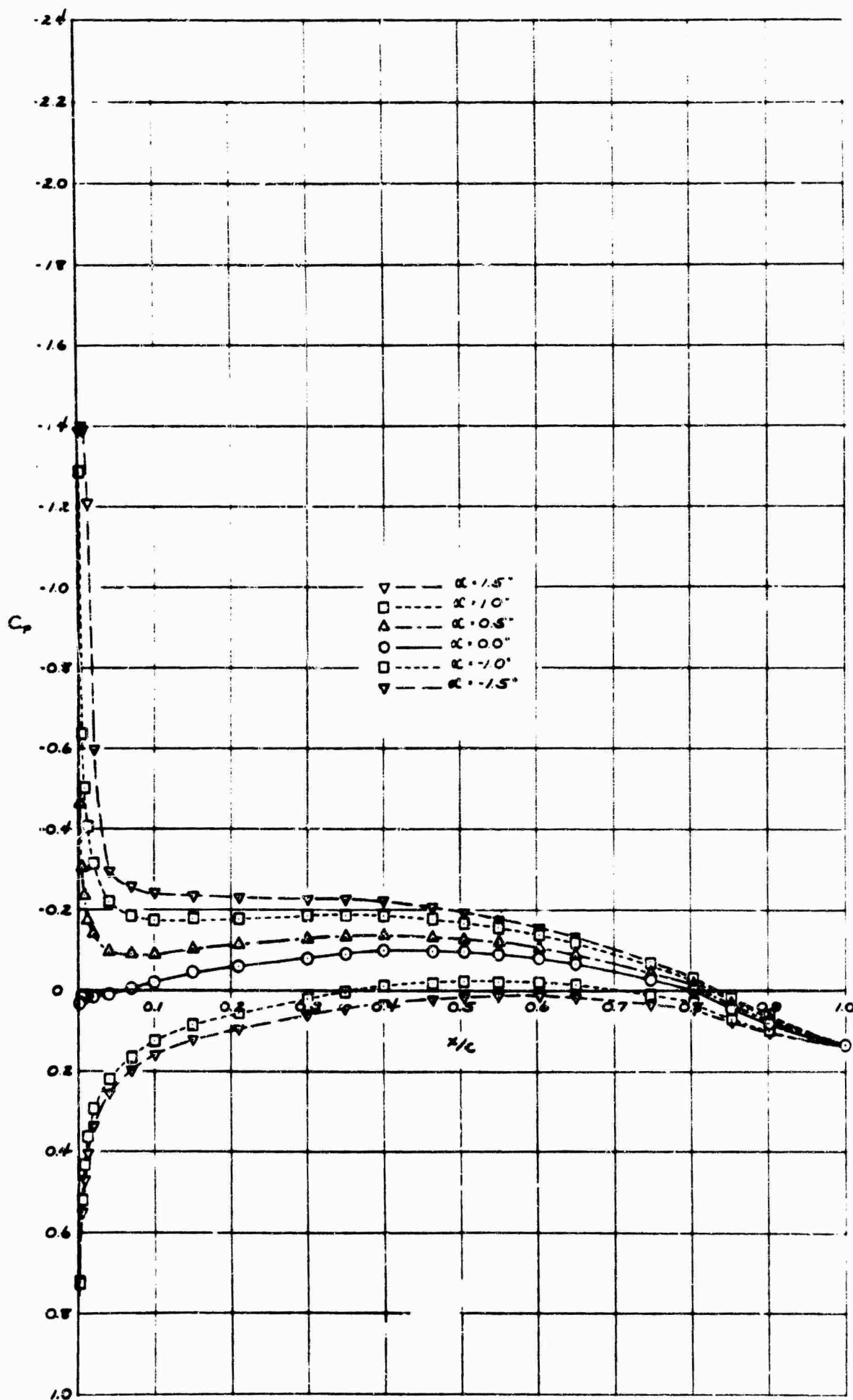


FIGURE 30 PRESSURE DISTRIBUTIONS AT VARYING ANGLES OF ATTACK

No Fairing

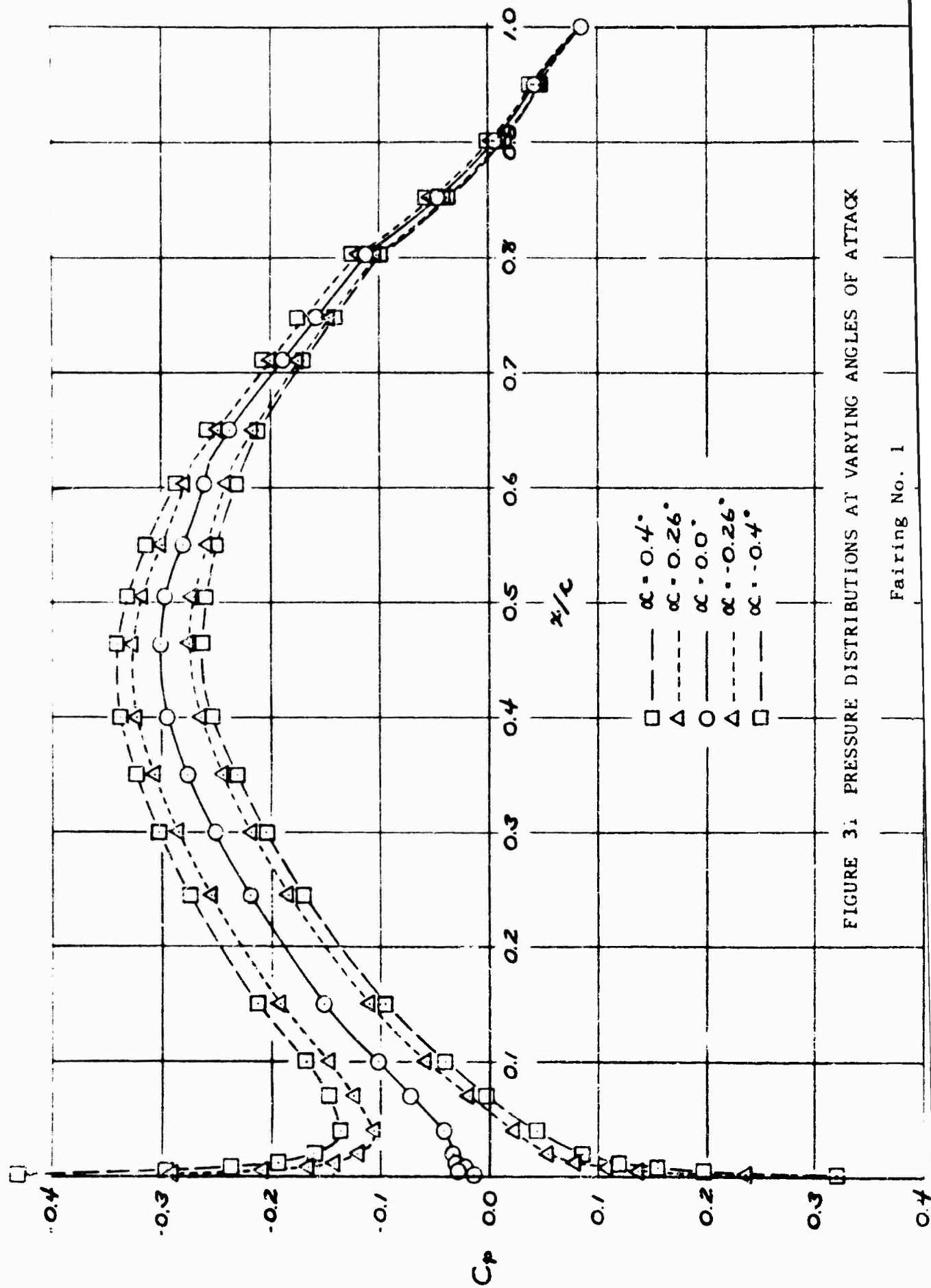


FIGURE 31. PRESSURE DISTRIBUTIONS AT VARYING ANGLES OF ATTACK

Fairing No. 1

FIGURE 3.5 PRESSURE DISTRIBUTIONS AT VARYING ANGLES OF ATTACK

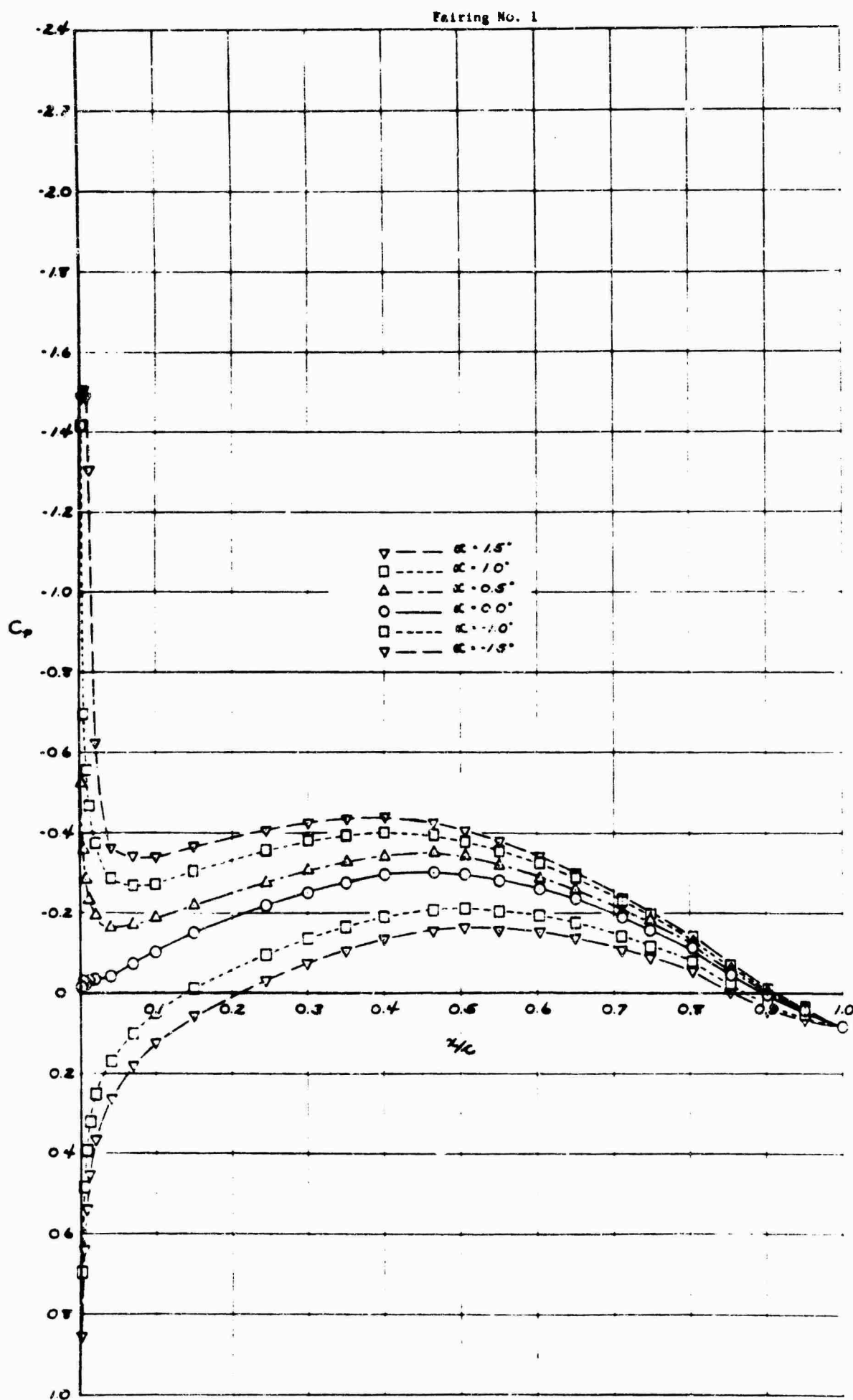


FIGURE 3.2 PRESSURE DISTRIBUTIONS AT VARYING ANGLES OF ATTACK

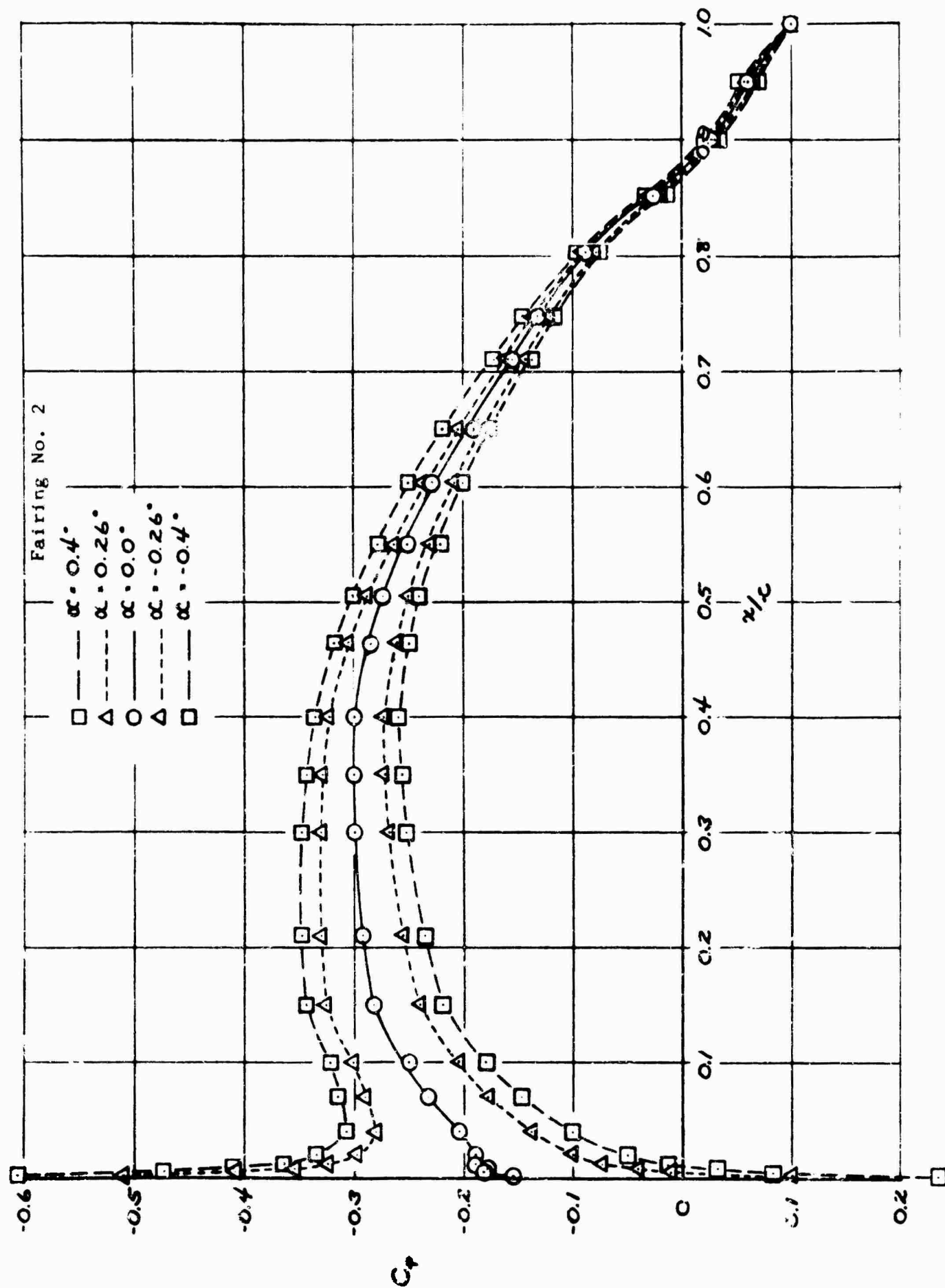


FIGURE 33 PRESSURE DISTRIBUTIONS AT VARYING ANGLES OF ATTACK

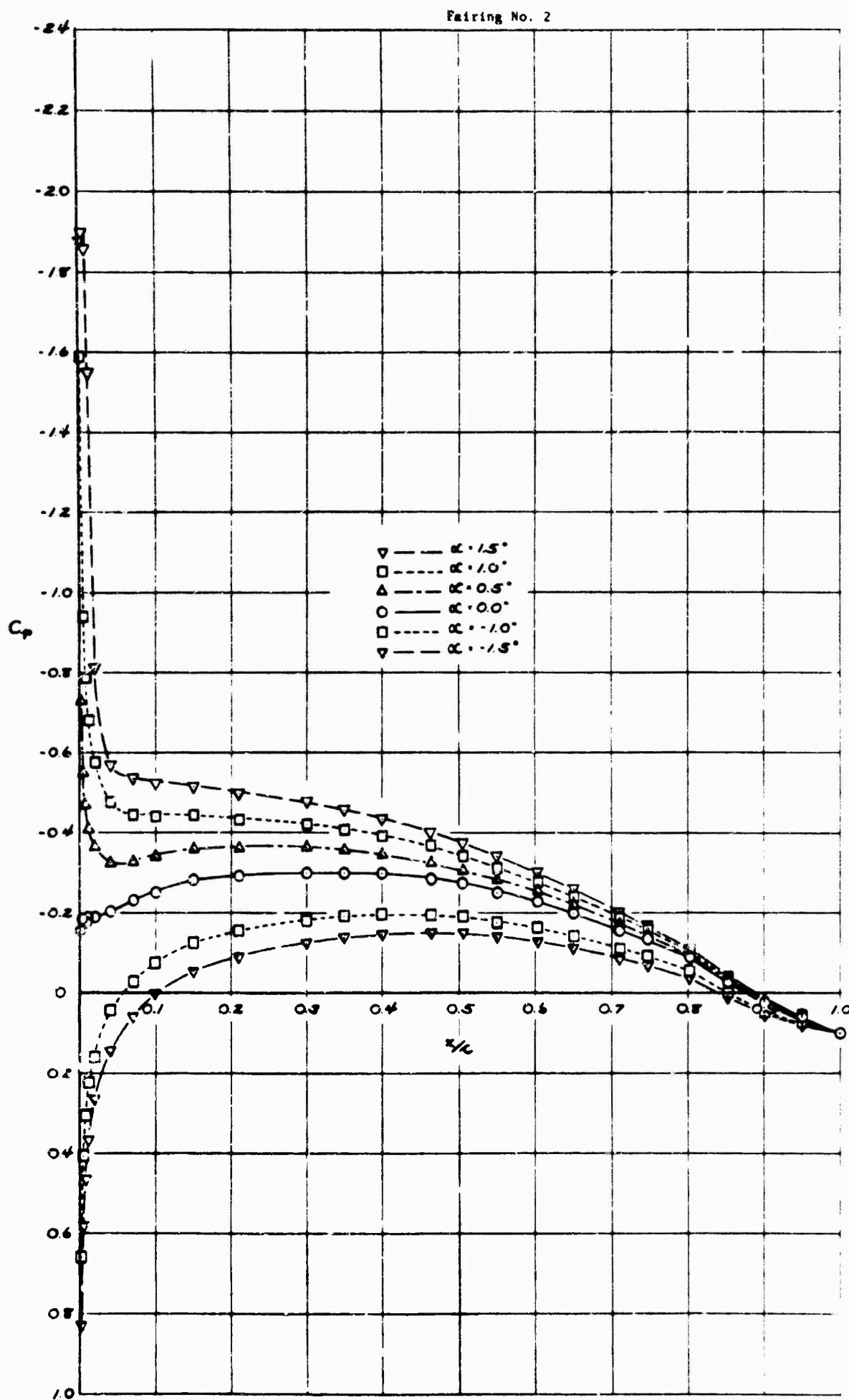
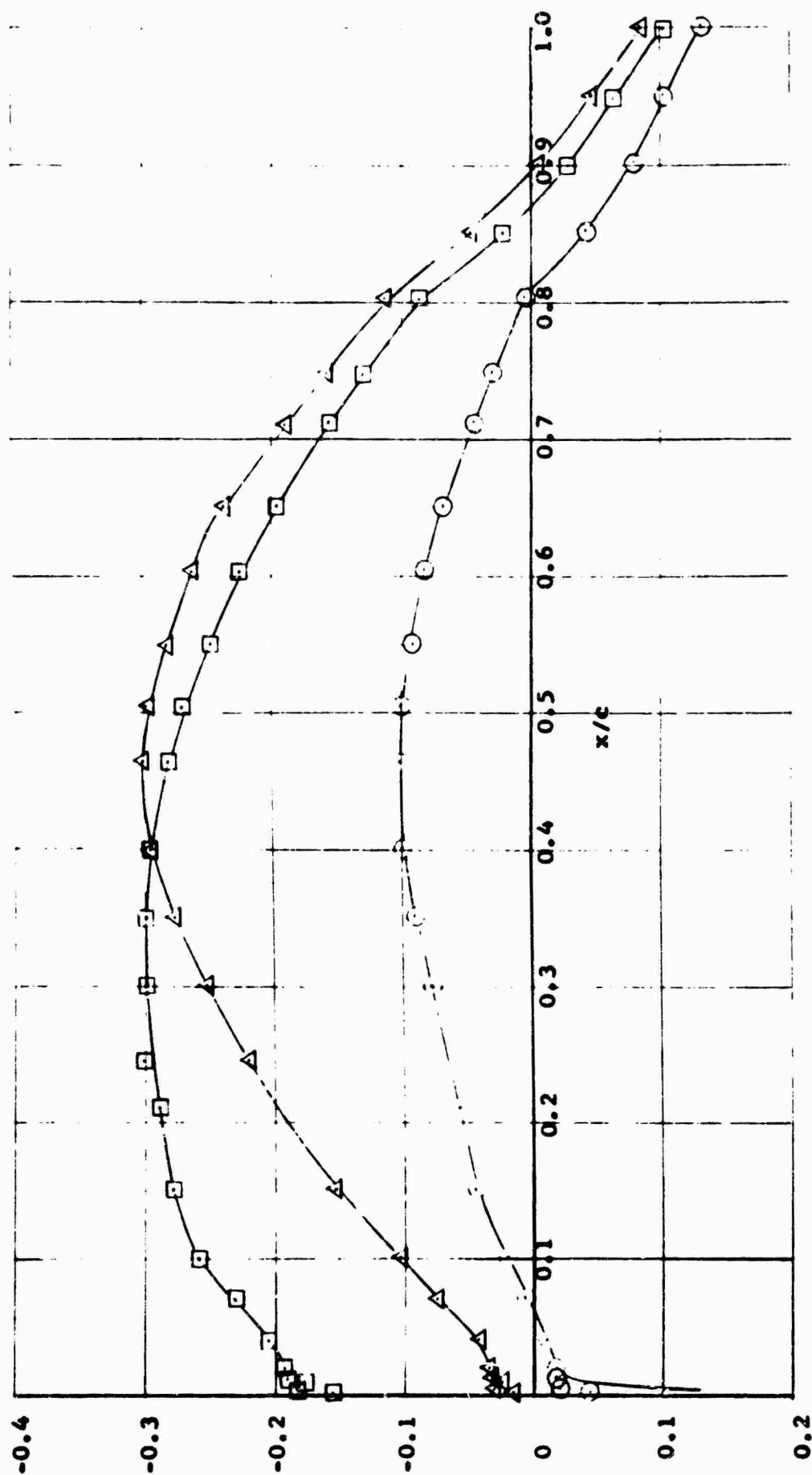


FIGURE 34 PRESSURE DISTRIBUTIONS AT VARYING ANGLES OF ATTACK

○ No Fairing  
 △ Fairing No. 1  
 □ Fairing No. 2



COMPARISON OF PRESSURE DISTRIBUTIONS AT ANGLE OF ATTACK  $\alpha = 0^\circ$   
OF THE THREE CASES INVESTIGATED

FIGURE 35



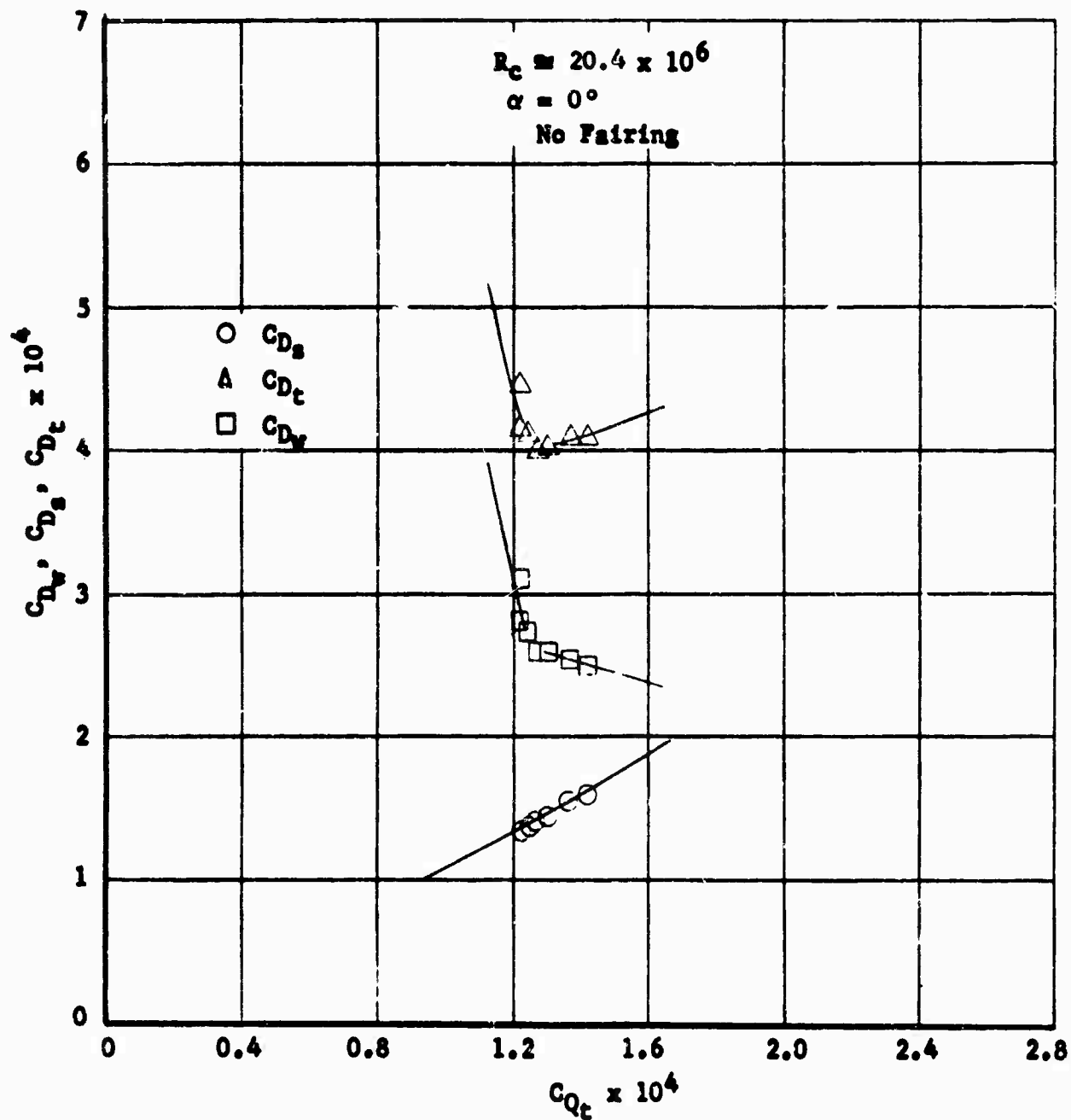


FIGURE 36 DRAG  $C_D$  VERSUS SUCTION QUANTITY  $C_{Qt}$  FOR VARIOUS REYNOLDS NUMBERS  $R_e$  AND ANGLES OF ATTACK  $\alpha$

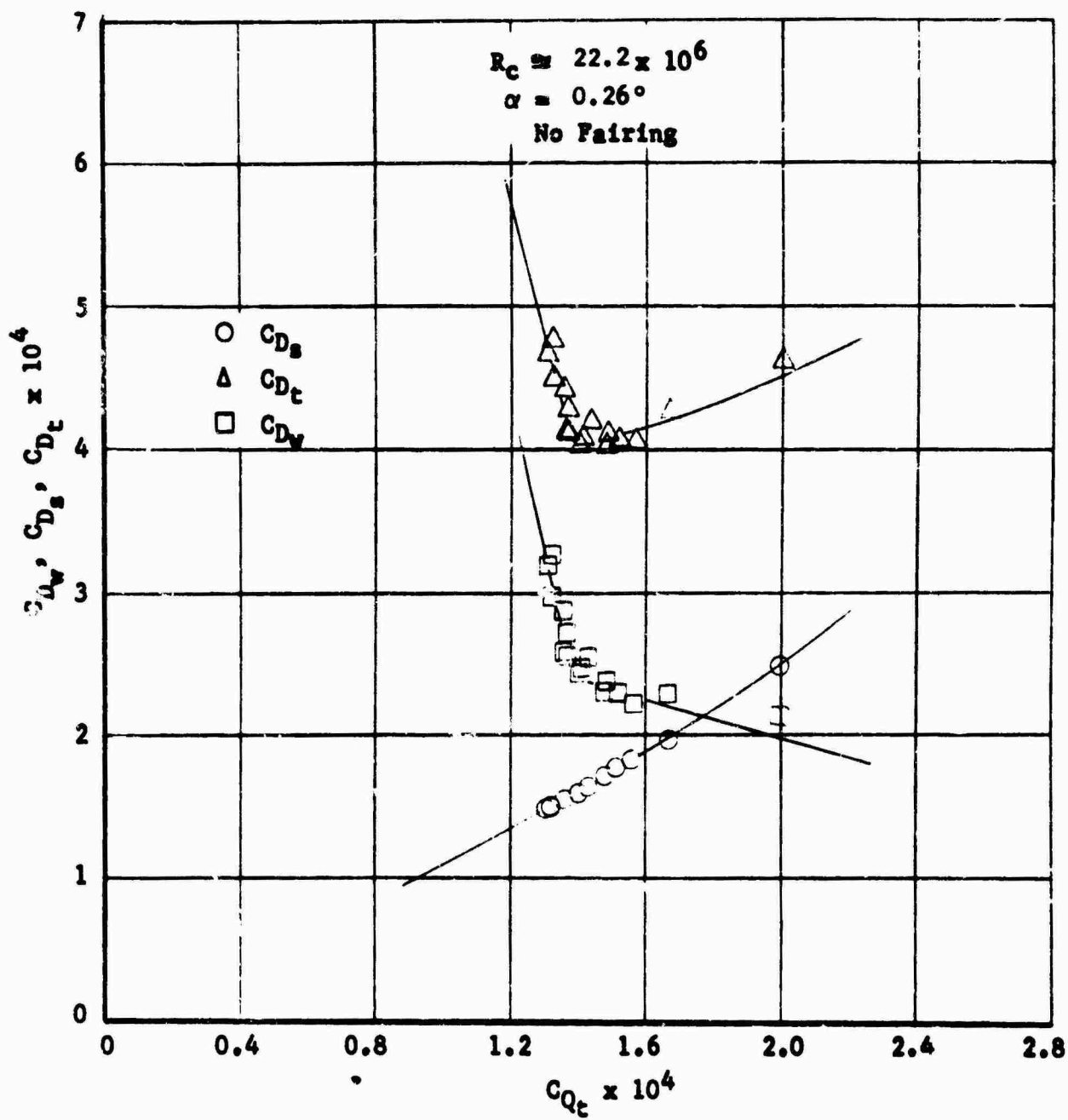


FIGURE 37 DRAG  $C_D$  VERSUS SUCTION QUANTITY  $C_{Qt}$  FOR VARIOUS REYNOLDS NUMBERS  $R_c$  AND ANGLES OF ATTACK  $\alpha$

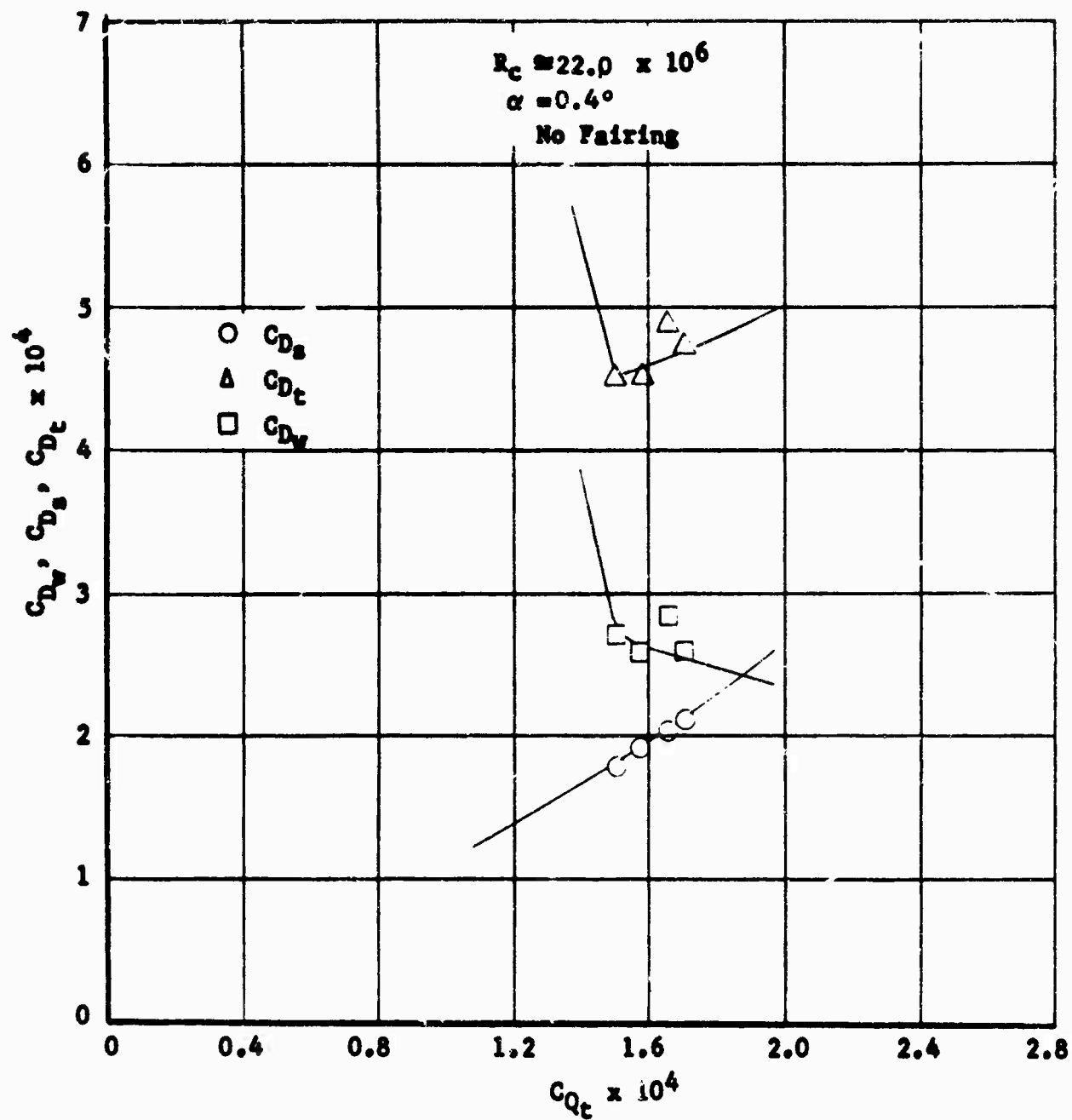


FIGURE 38 DRAG  $C_D$  VERSUS SUCTION QUANTITY  $C_{Q_c}$  FOR VARIOUS REYNOLDS NUMBERS  $R_e$  AND ANGLES OF ATTACK  $\alpha$

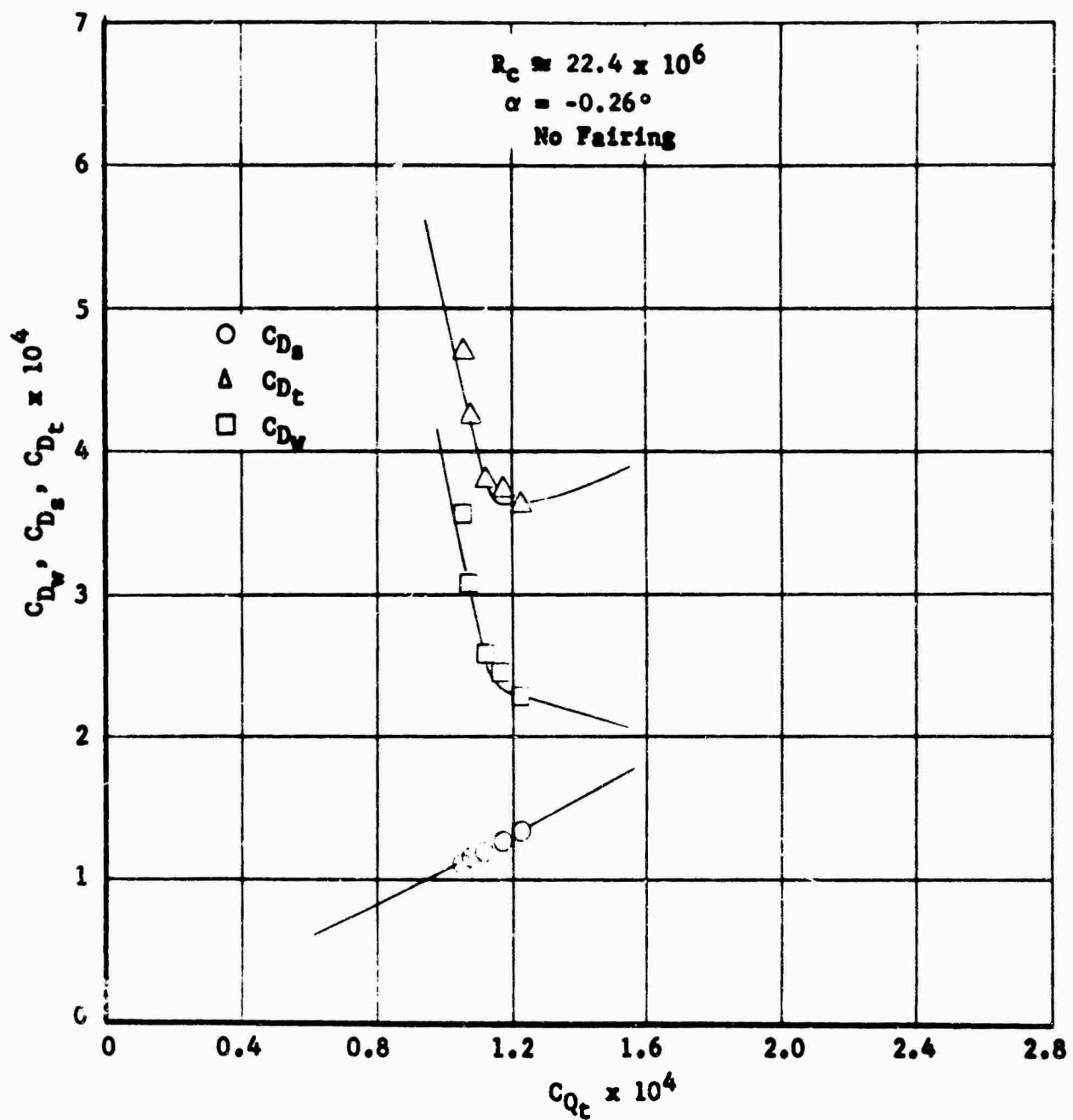


FIGURE 39 DRAG  $C_D$  VERSUS SUCTION QUANTITY  $C_{Qt}$  FOR VARIOUS REYNOLDS NUMBERS  $R_c$  AND ANGLES OF ATTACK  $\alpha$

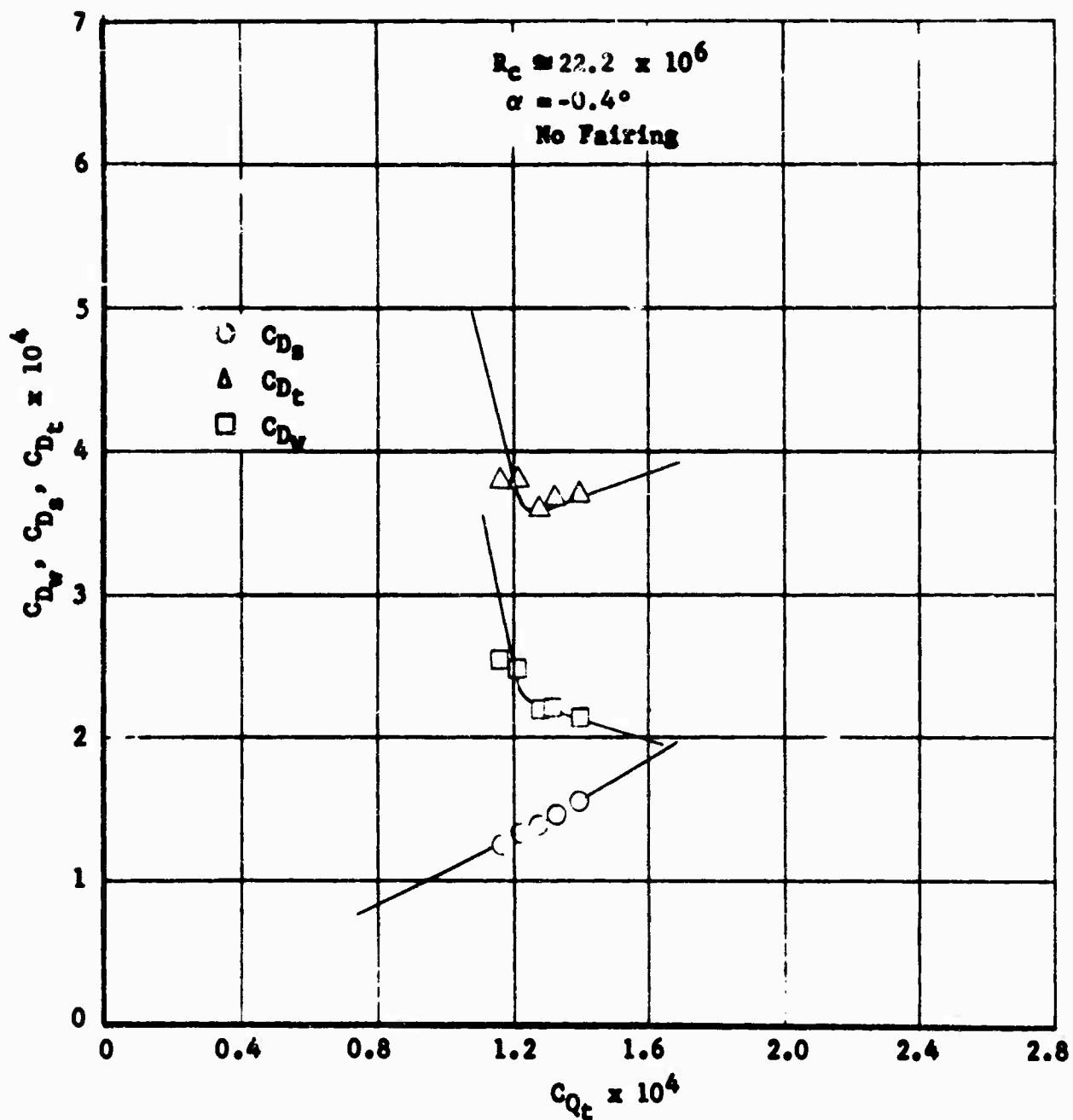


FIGURE 40 DRAG  $C_D$  VERSUS SUCTION QUANTITY  $C_{Qt}$  FOR VARIOUS REYNOLDS NUMBERS  $R_c$  AND ANGLES OF ATTACK  $\alpha$

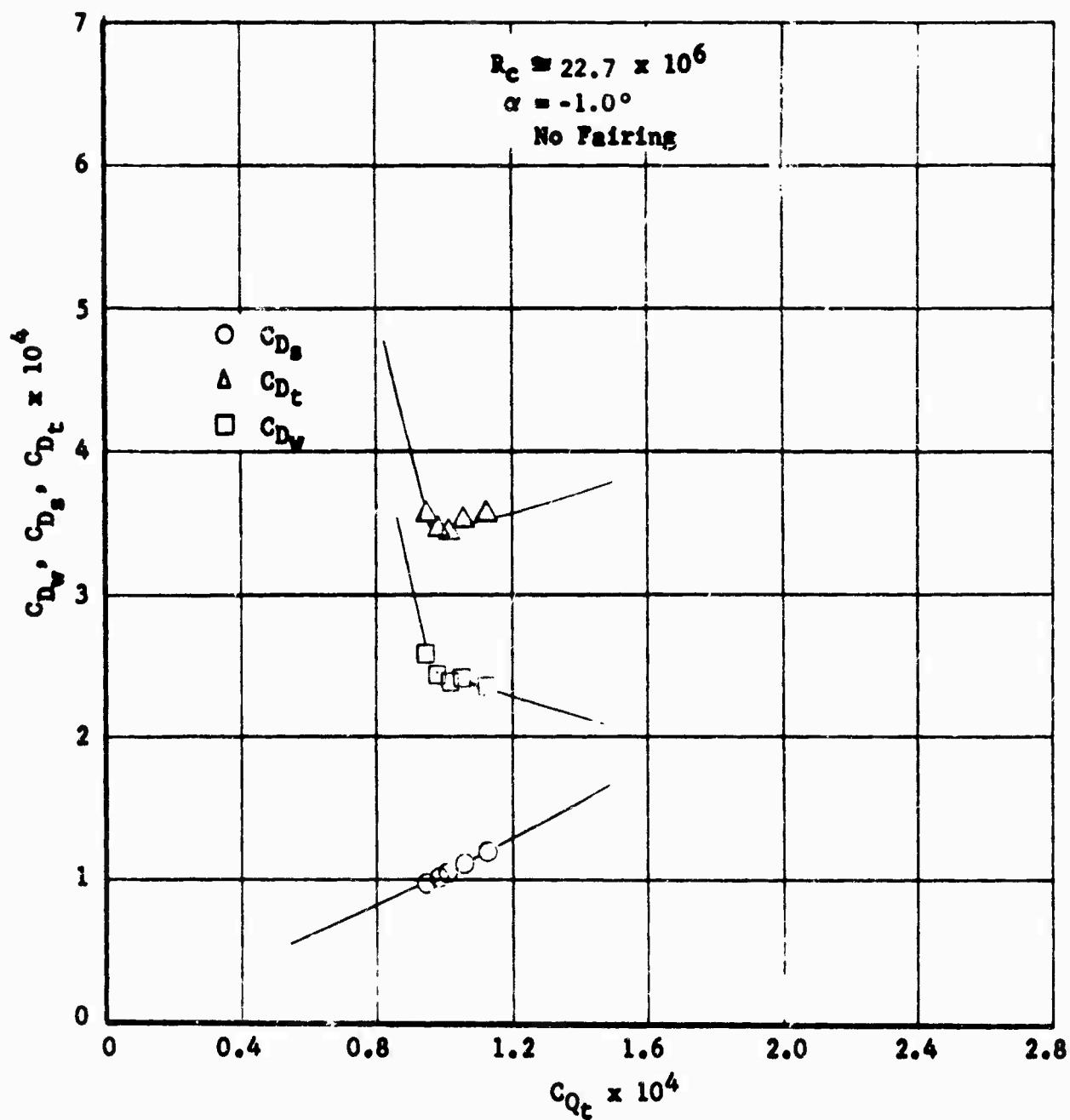


FIGURE 41 DRAG  $C_D$  VERSUS SUCTION QUANTITY  $C_{Q_t}$  FOR VARIOUS REYNOLDS NUMBERS  $R_c$  AND ANGLES OF ATTACK  $\alpha$

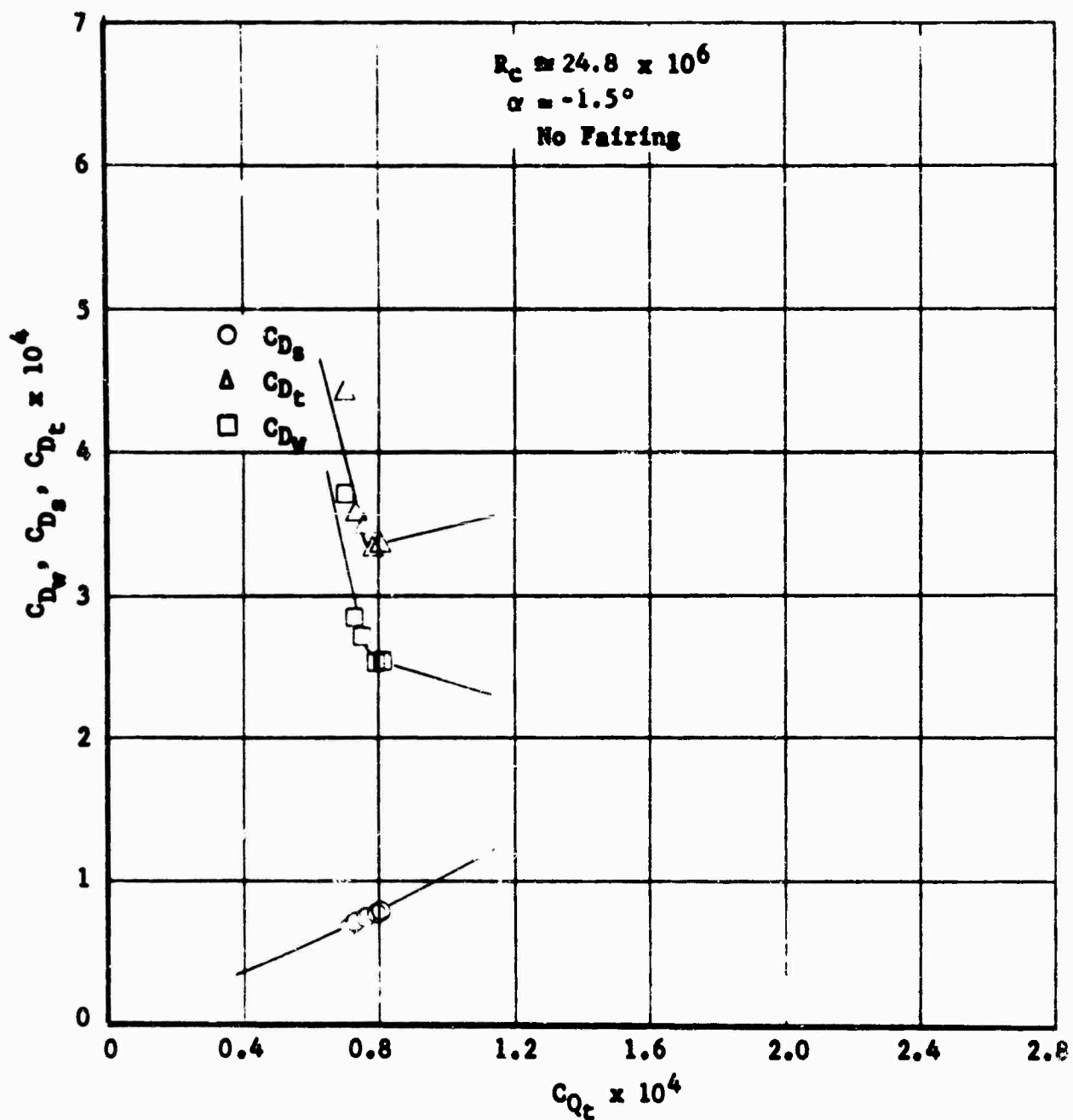


FIGURE 42 DRAG  $C_D$  VERSUS SUCTION QUANTITY  $C_{Q_t}$  FOR VARIOUS REYNOLDS NUMBERS  $R_e$  AND ANGLES OF ATTACK  $\alpha$

No Fairing

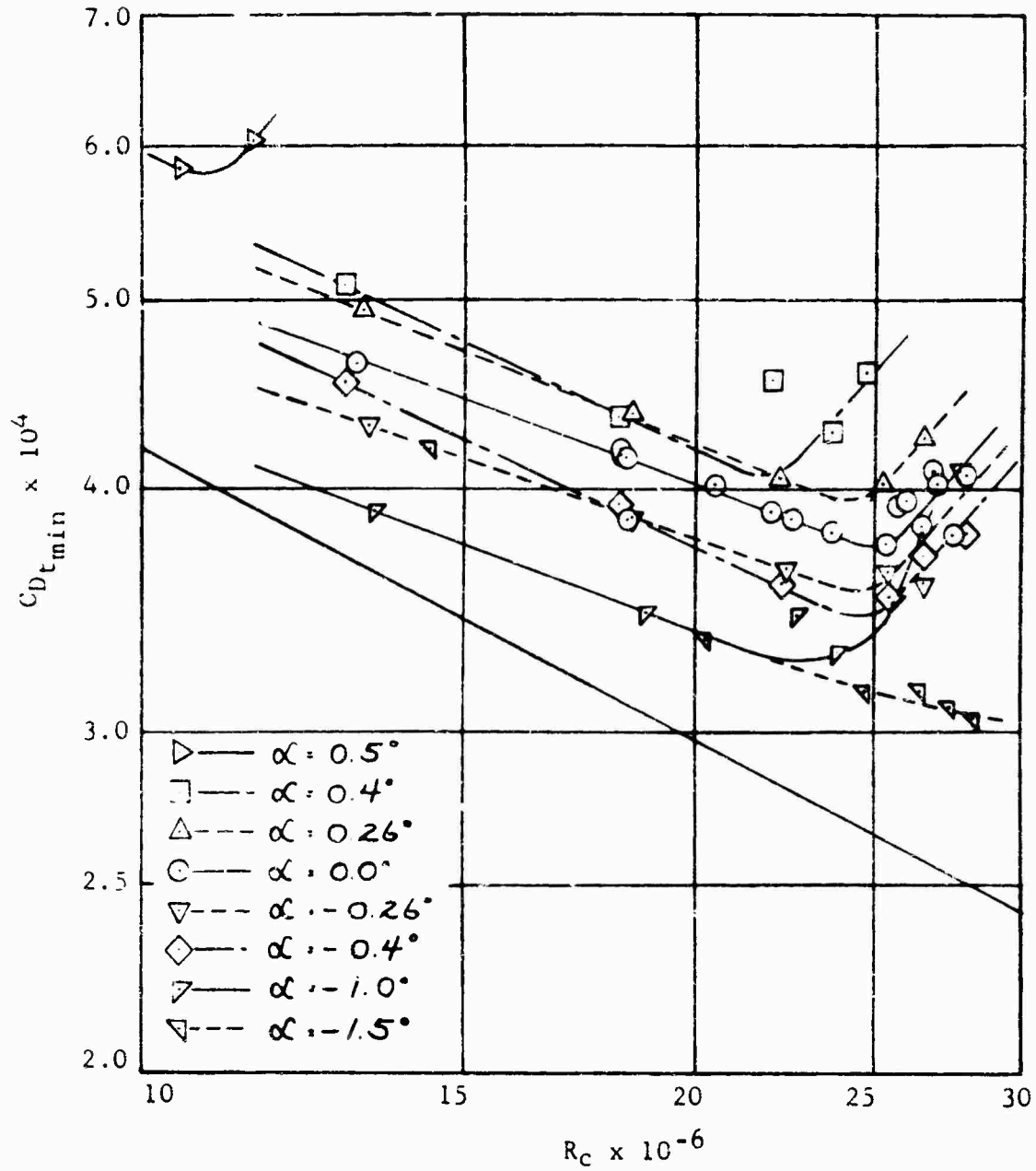


FIGURE 43 VARIATION OF MINIMUM TOTAL DRAG COEFFICIENT  $C_{D_t}$  (INCLUDING EQUIVALENT SUCTION DRAG) WITH REYNOLDS NUMBER  $R_c$  FOR SEVERAL ANGLES OF ATTACK  $\alpha$



No Fairing

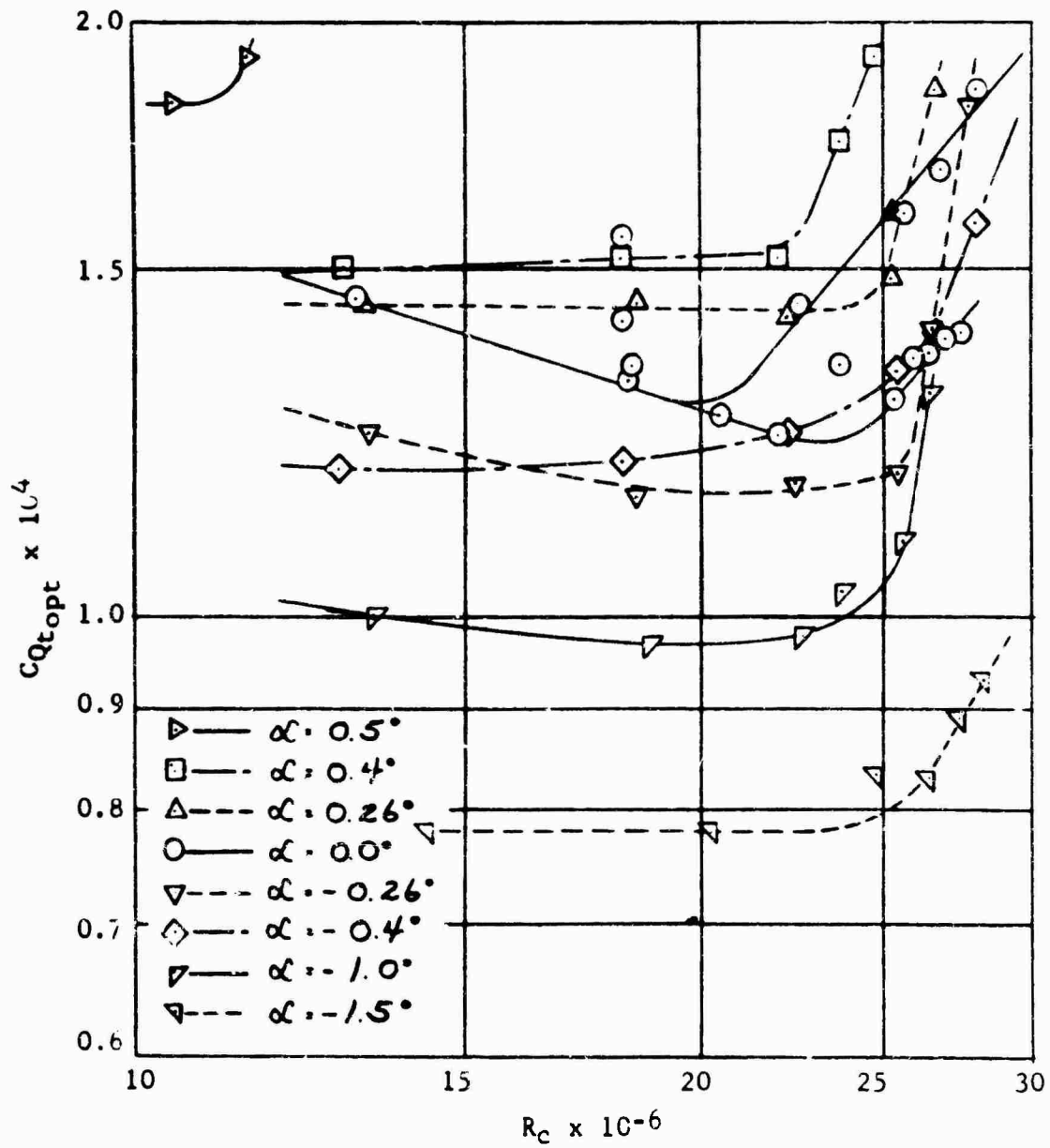


FIGURE 44 VARIATION OF OPTIMUM SUCTION COEFFICIENT  $C_{Qt_{opt}}$  WITH REYNOLDS NUMBER  $R_c$  FOR SEVERAL ANGLES OF ATTACK  $\alpha$

Fairing No. 1

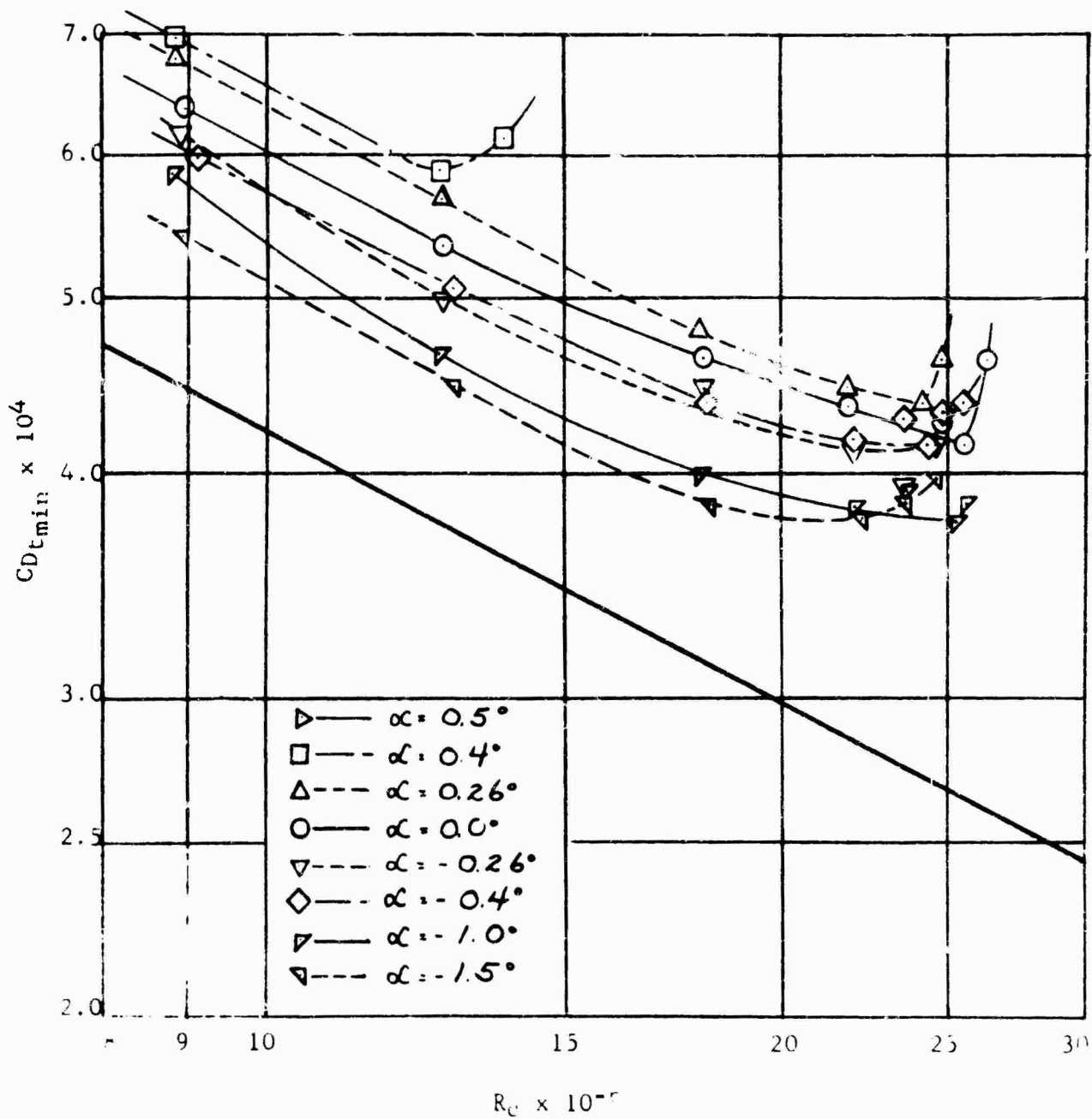


FIGURE 45 VARIATION OF MINIMUM TOTAL DRAG COEFFICIENT  $CD$ ,  
(INCLUDING EQUIVALENT SUCTION DRAG) WITH REYNOLDS  
NUMBER  $Re$  FOR SEVERAL ANGLES OF ATTACK  $\alpha$

Fairing No. 1

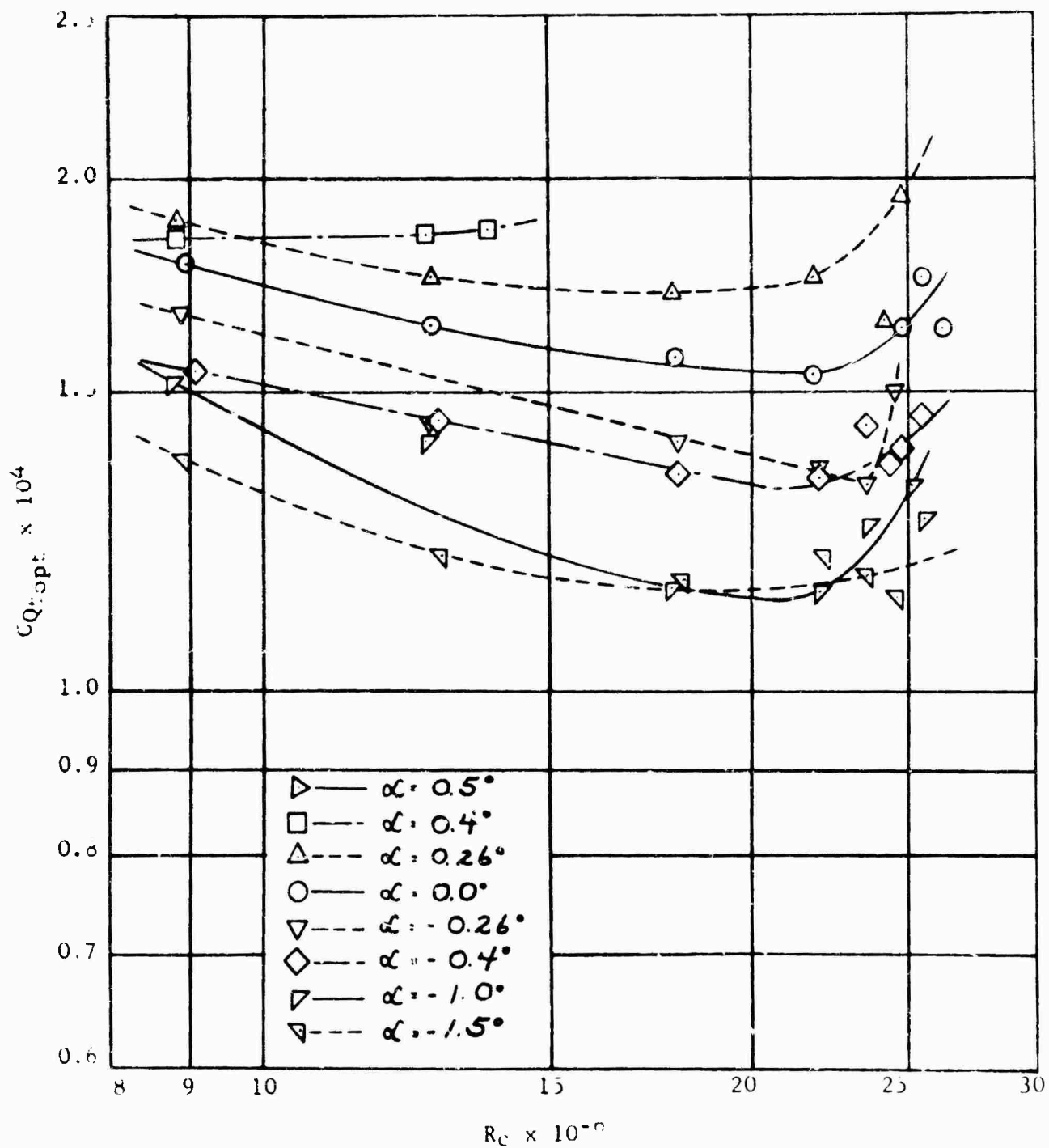


FIGURE 46 VARIATION OF OPTIMUM SUCTION COEFFICIENT  $C_{Qt_{opt}}$  WITH REYNOLDS NUMBER  $R_c$  FOR SEVERAL ANGLES OF ATTACK  $\alpha$

Fairing No. 2

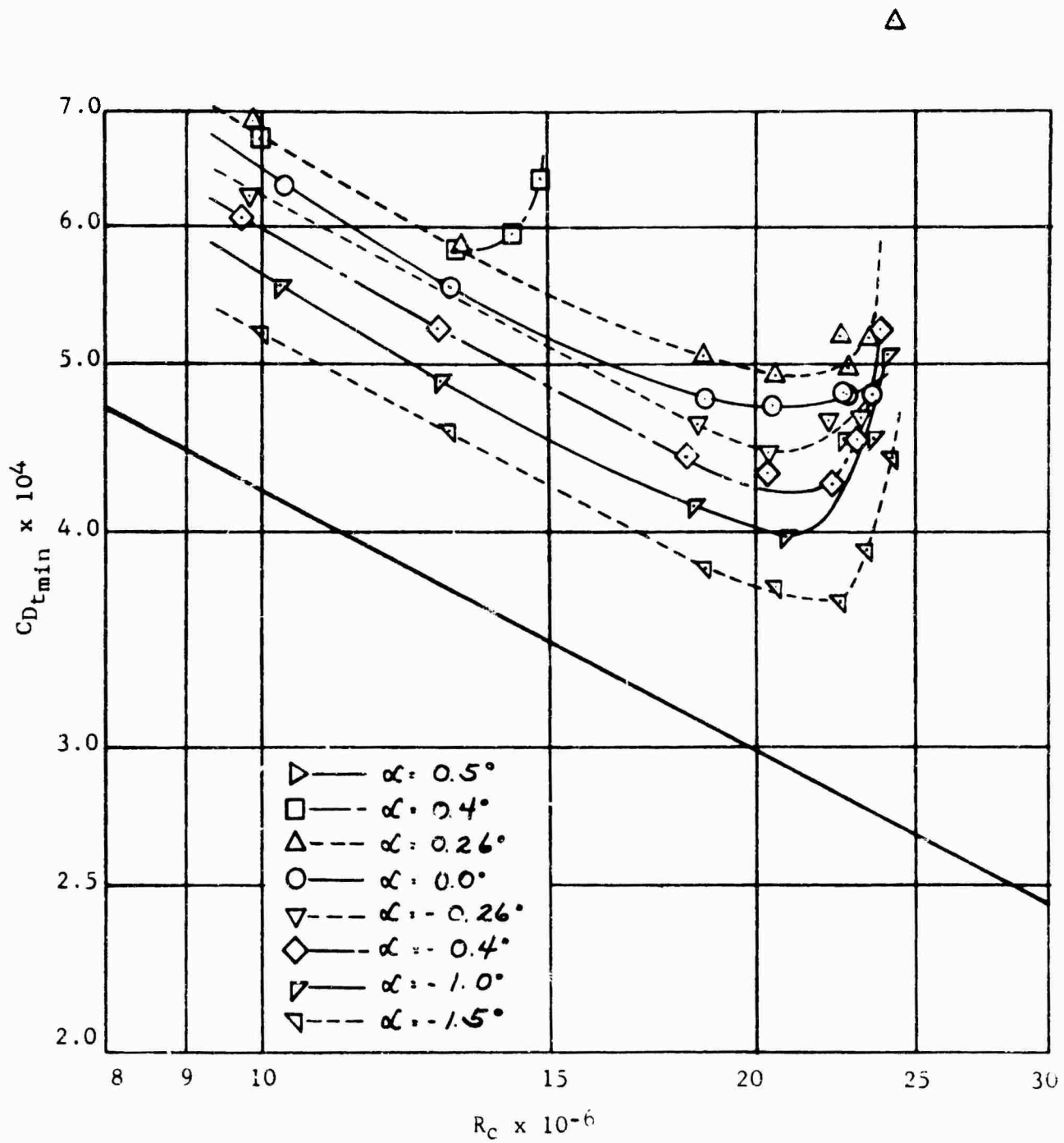
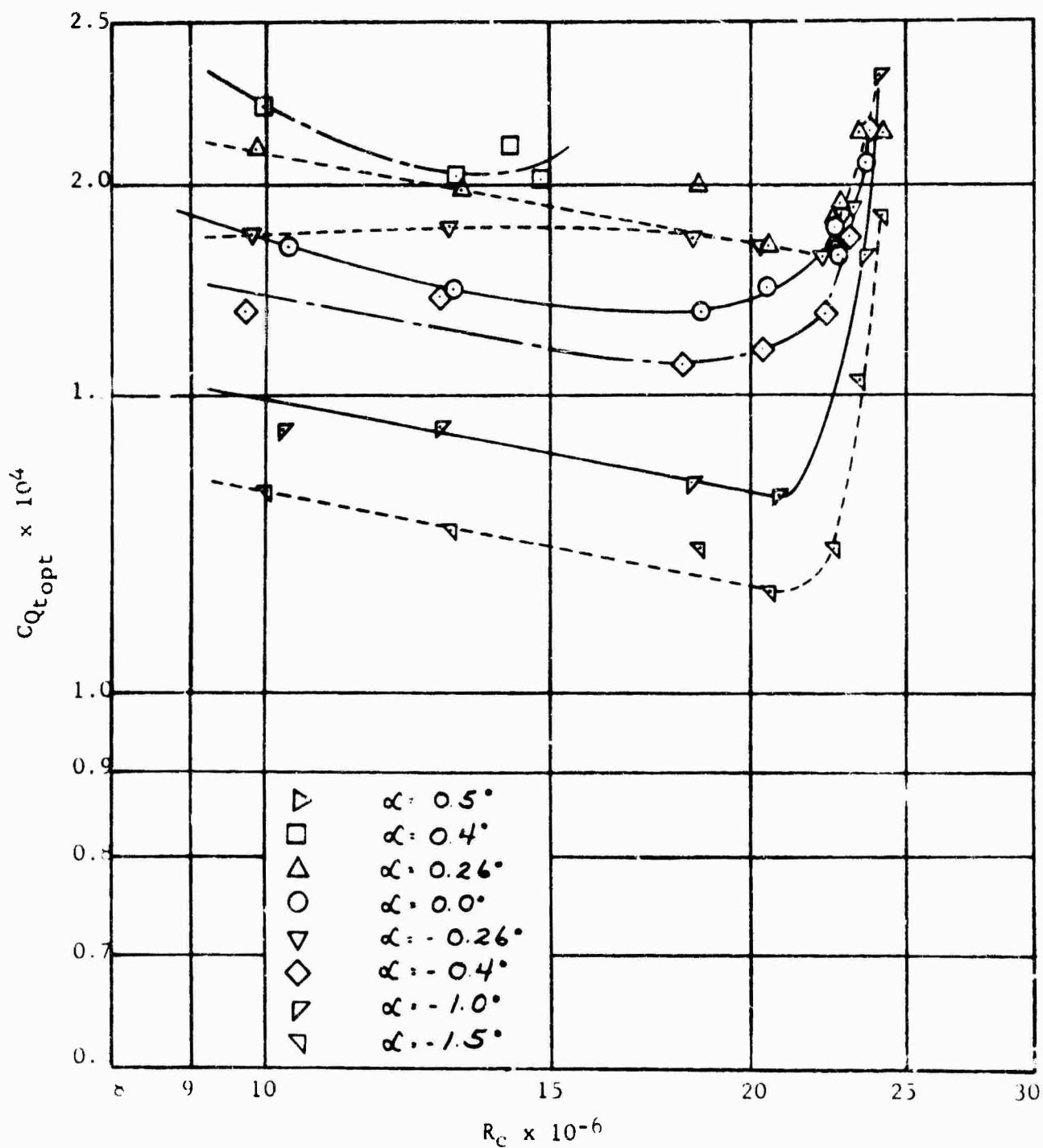


FIGURE 47 VARIATION OF MINIMUM TOTAL DRAG COEFFICIENT  $C_{Dt}$   
(INCLUDING EQUIVALENT SUCTION DRAG) WITH REYNOLDS  
NUMBER  $R_c$  FOR SEVERAL ANGLES OF ATTACK  $\alpha$



VELOCITY SUCTION COEFFICIENT  $C_{Q_{opt}}$  FOR SEVERAL REYNOLDS NUMBERS  $R_c$   
 $\alpha = 0^\circ$   
 No Fairing

FIGURE 48 VARIATION OF OPTIMUM SUCTION COEFFICIENT  $C_{Qt_{opt}}$  WITH REYNOLDS NUMBER  $R_c$  FOR SEVERAL ANGLES OF ATTACK  $\alpha$

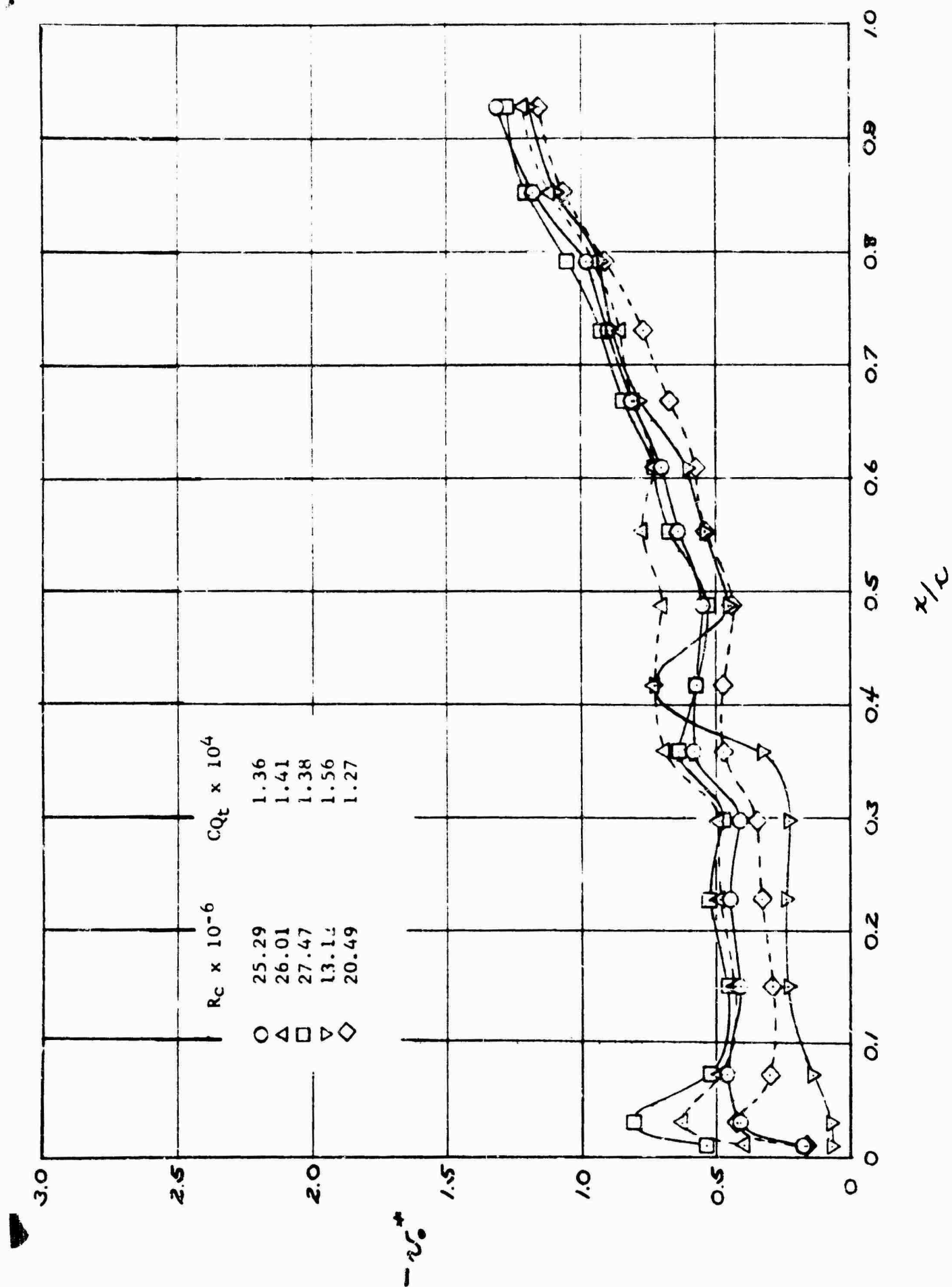


FIGURE 49 NONDIMENSIONAL EQUIVALENT AREA SUCTION VELOCITY  $v_o^*$  DISTRIBUTION NEAR OPTIMUM SUCTION COEFFICIENT  $C_{Q_{opt}}$  FOR SEVERAL REYNOLDS NUMBERS  $R_c$

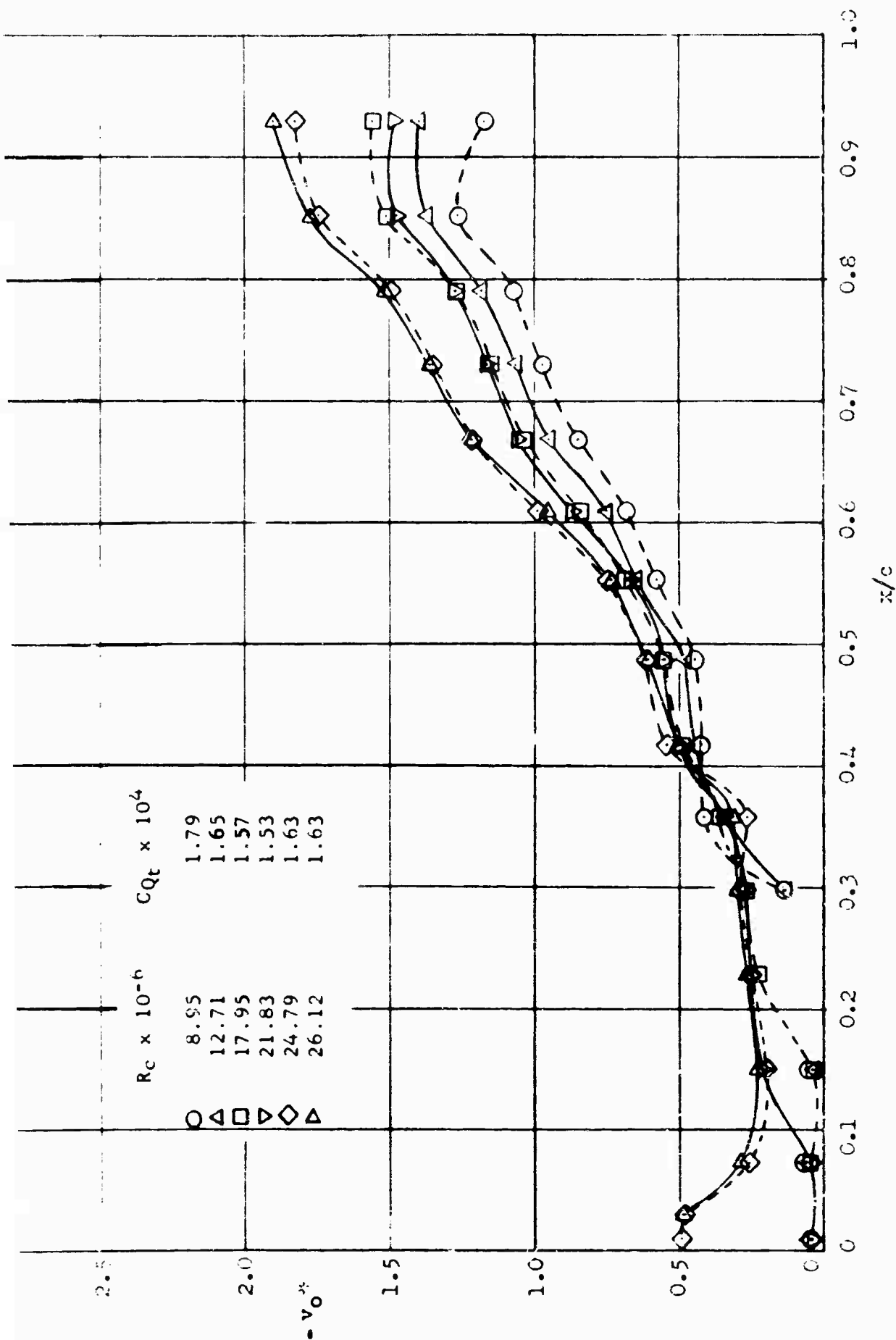


FIGURE 50 NONDIMENSIONAL EQUIVALENT AREA SUCTION VELOCITY  $v_0^*$  DISTRIBUTION NEAR  
OPTIMUM SUCTION COEFFICIENT  $CQ_{opt}$  FOR SEVERAL REYNOLD NUMBERS  $R_C$

Falling No. 1

$\alpha = 0^\circ$

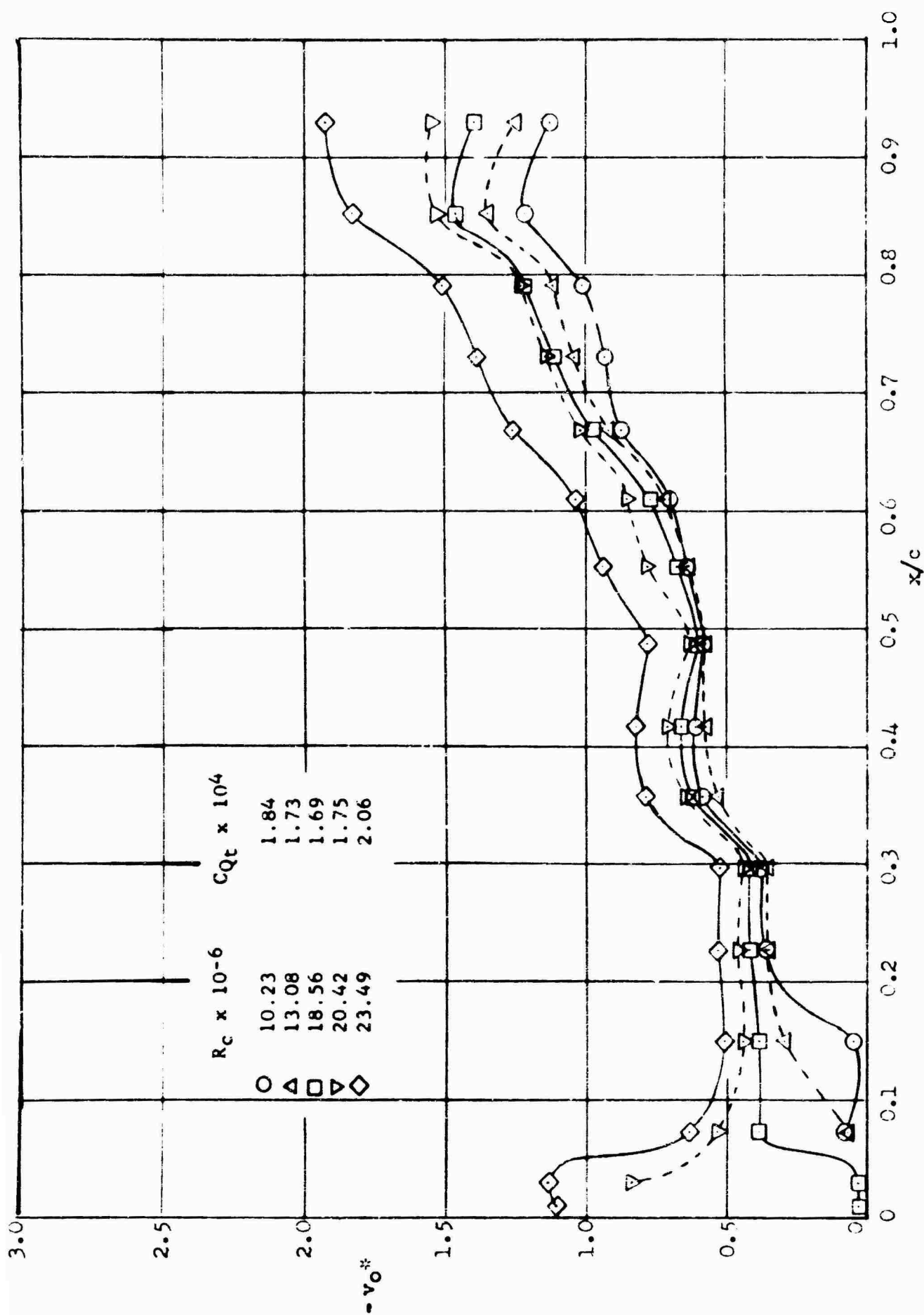


FIGURE 51 NONDIMENSIONAL EQUIVALENT AREA SUCTION VELOCITY  $v_o^*$  DISTRIBUTION NEAR OPTIMUM SUCTION COEFFICIENT  $C_{Q_{opt}}$  FOR SEVERAL REYNOLDS NUMBERS  $R_c$

Fairing No. 2



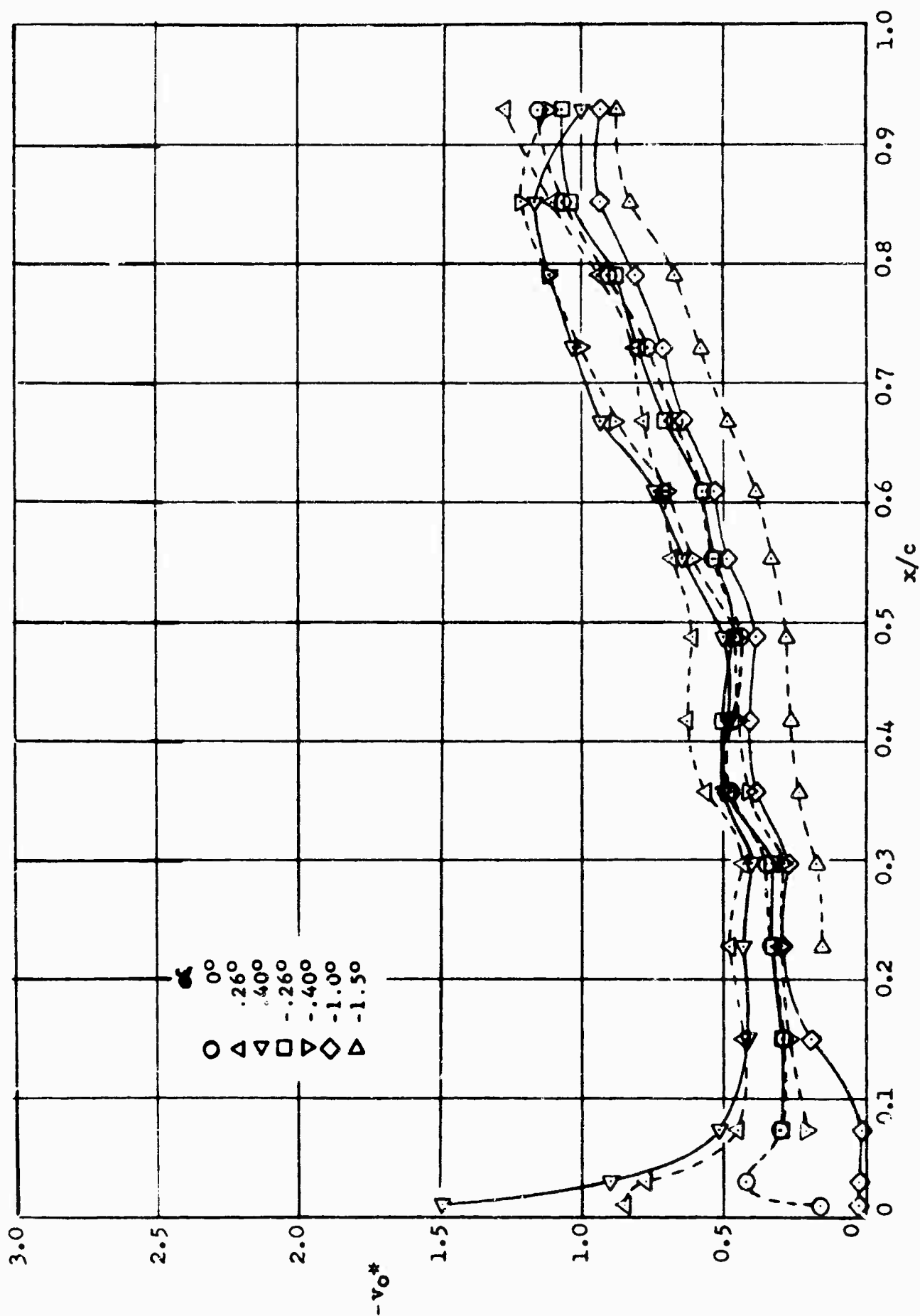


FIGURE 52 NONDIMENSIONAL EQUIVALENT AREA SUCTION VELOCITY  $v_o^*$  DISTRIBUTION NEAR

OPTIMUM SUCTION COEFFICIENT  $C_{Q_{opt}}$  FOR SEVERAL ANGLES OF ATTACK  $\alpha$  AT

A REYNOLDS NUMBER  $R_c$  OF APPROXIMATELY  $21 \times 10^6$

No Fairing

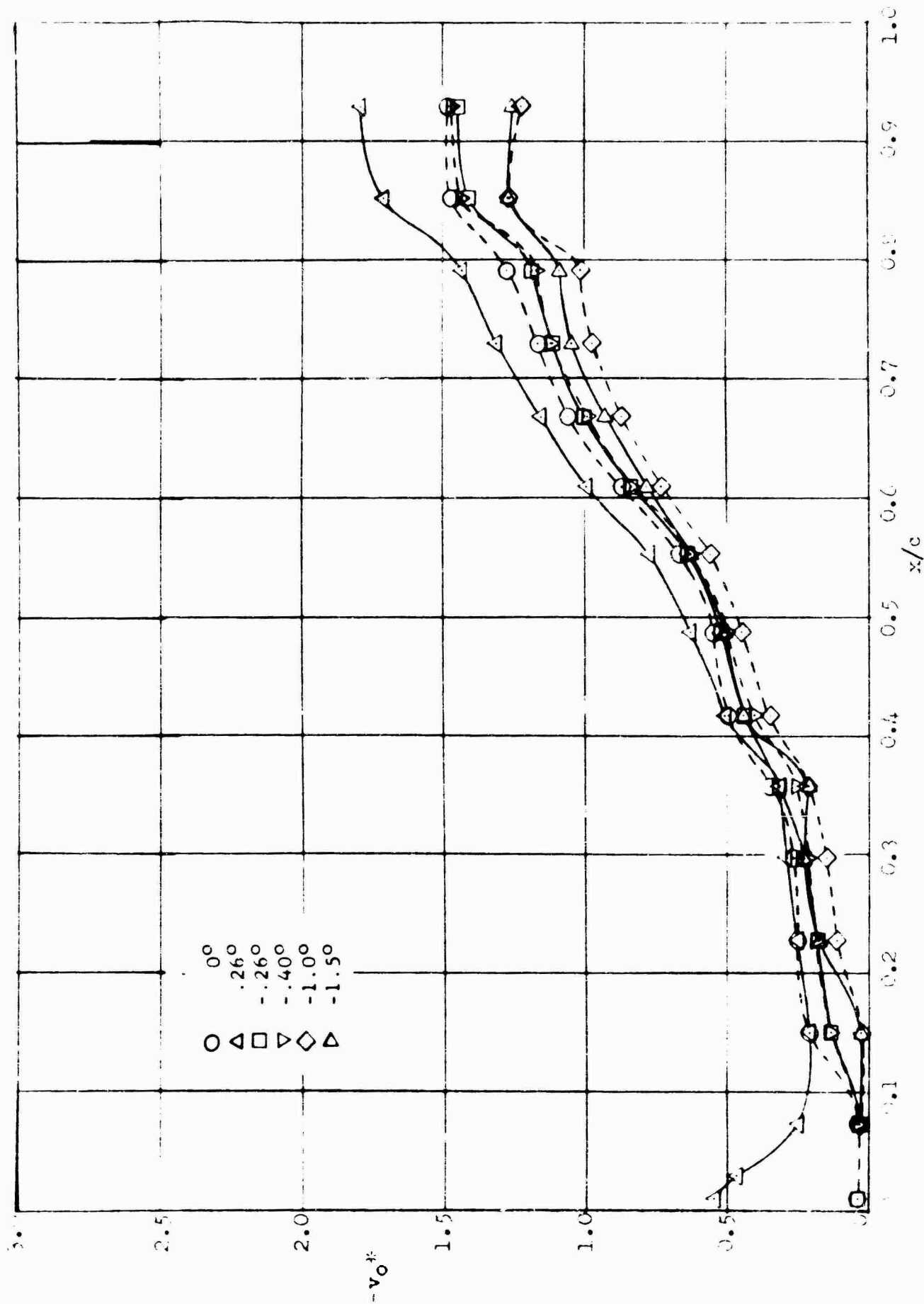


FIGURE 53 NONDIMENSIONAL EQUIVALENT AREA SUCTION VELOCITY  $v_O^*$  DISTRIBUTION NEAR  
OPTIMUM SUCTION COEFFICIENT  $C_{Q_{opt}}$  FOR SEVERAL ANGLES OF ATTACK  $\alpha$  AT  
A REYNOLDS NUMBER  $R_c$  OF APPROXIMATELY  $21 \times 10^6$

Fairing No. 1

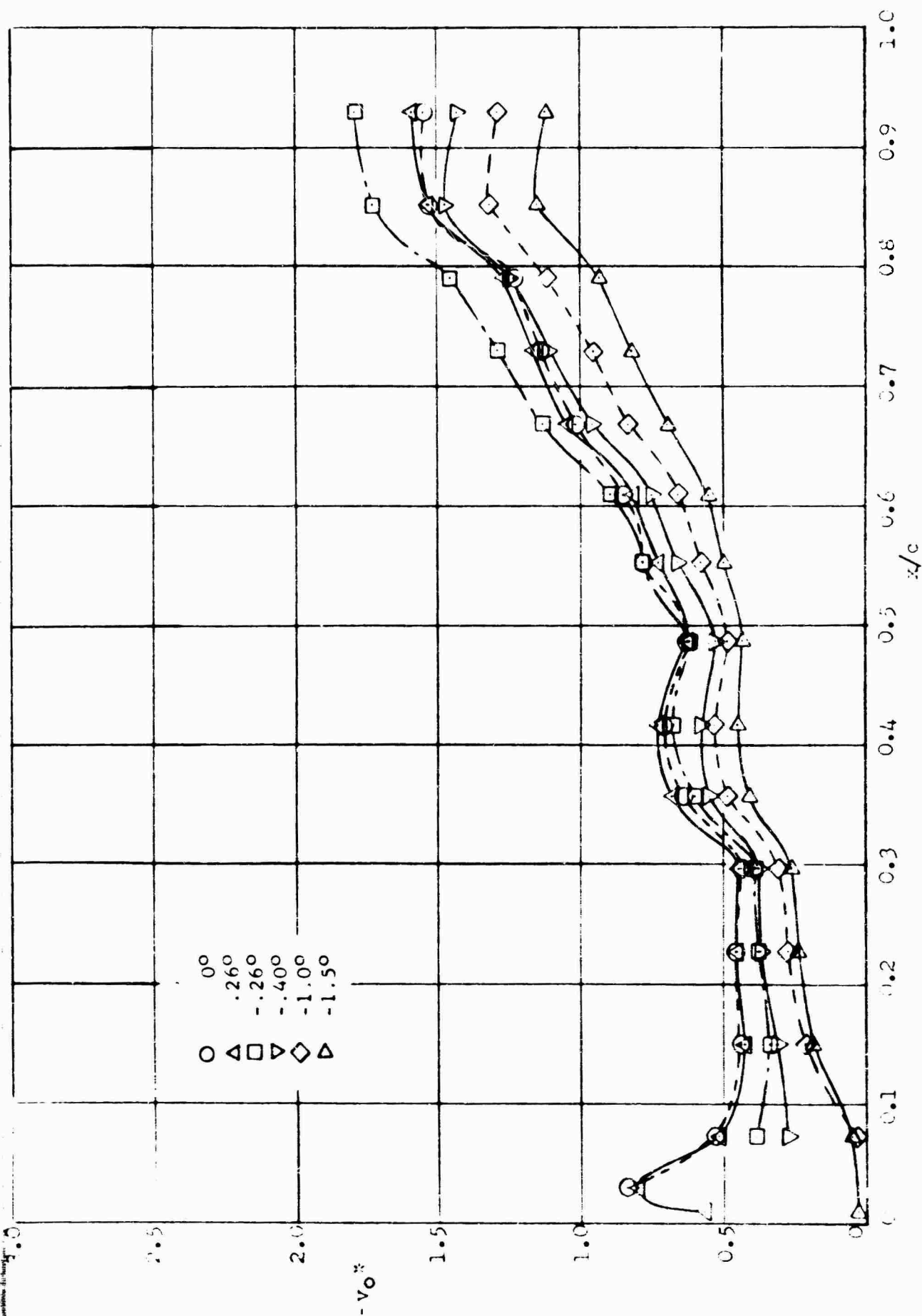


FIGURE 54 NONDIMENSIONAL EQUIVALENT AREA SUCTION VELOCITY  $v_o^*$  DISTRIBUTION NEAR

OPTIMUM SUCTION COEFFICIENT  $C_{Qopt}$  FOR SEVERAL ANGLES OF ATTACK  $\alpha$  AT

A REYNOLDS NUMBER  $R_c$  OF APPROXIMATELY  $21 \times 10^6$

Fairing No. 2

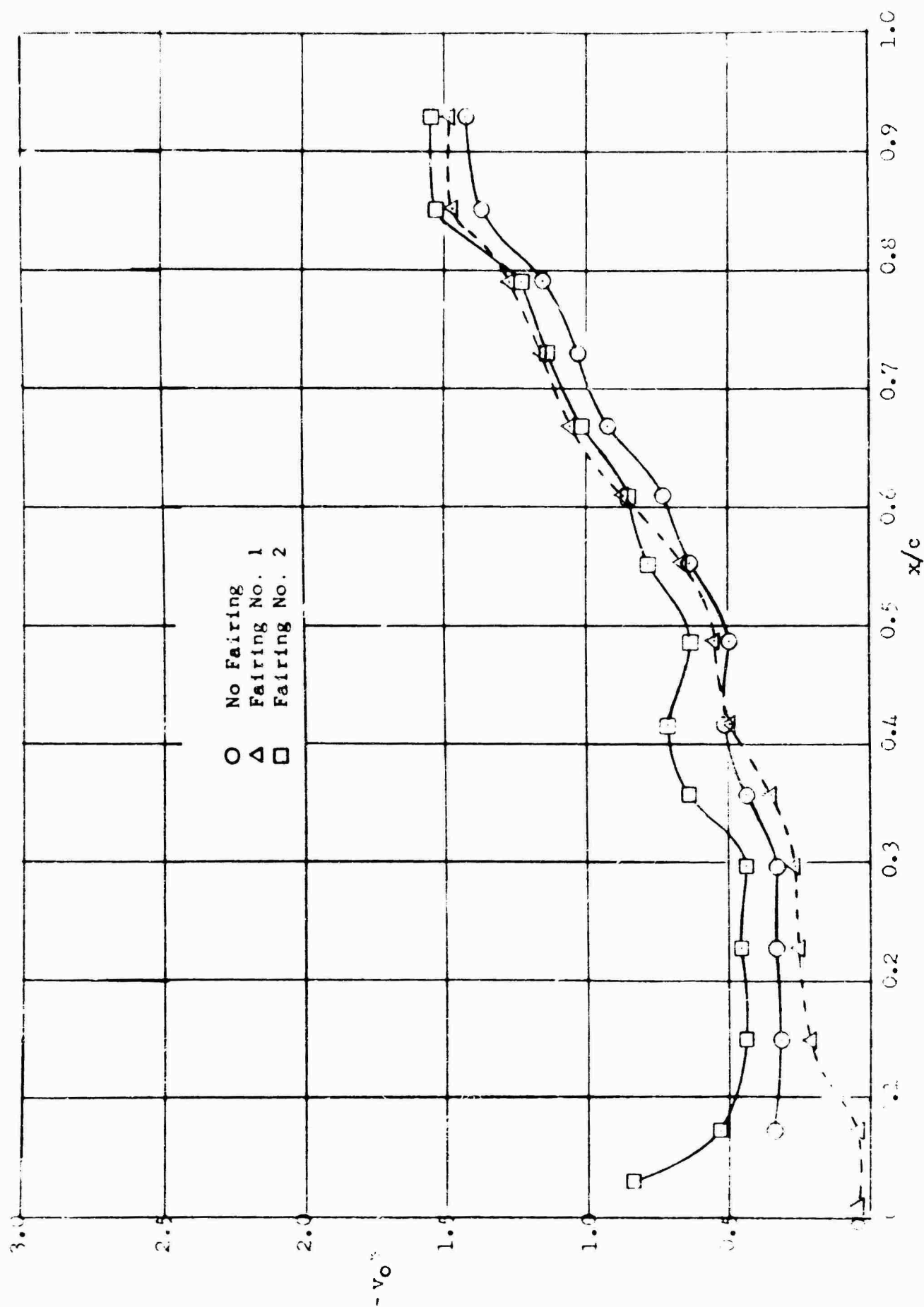
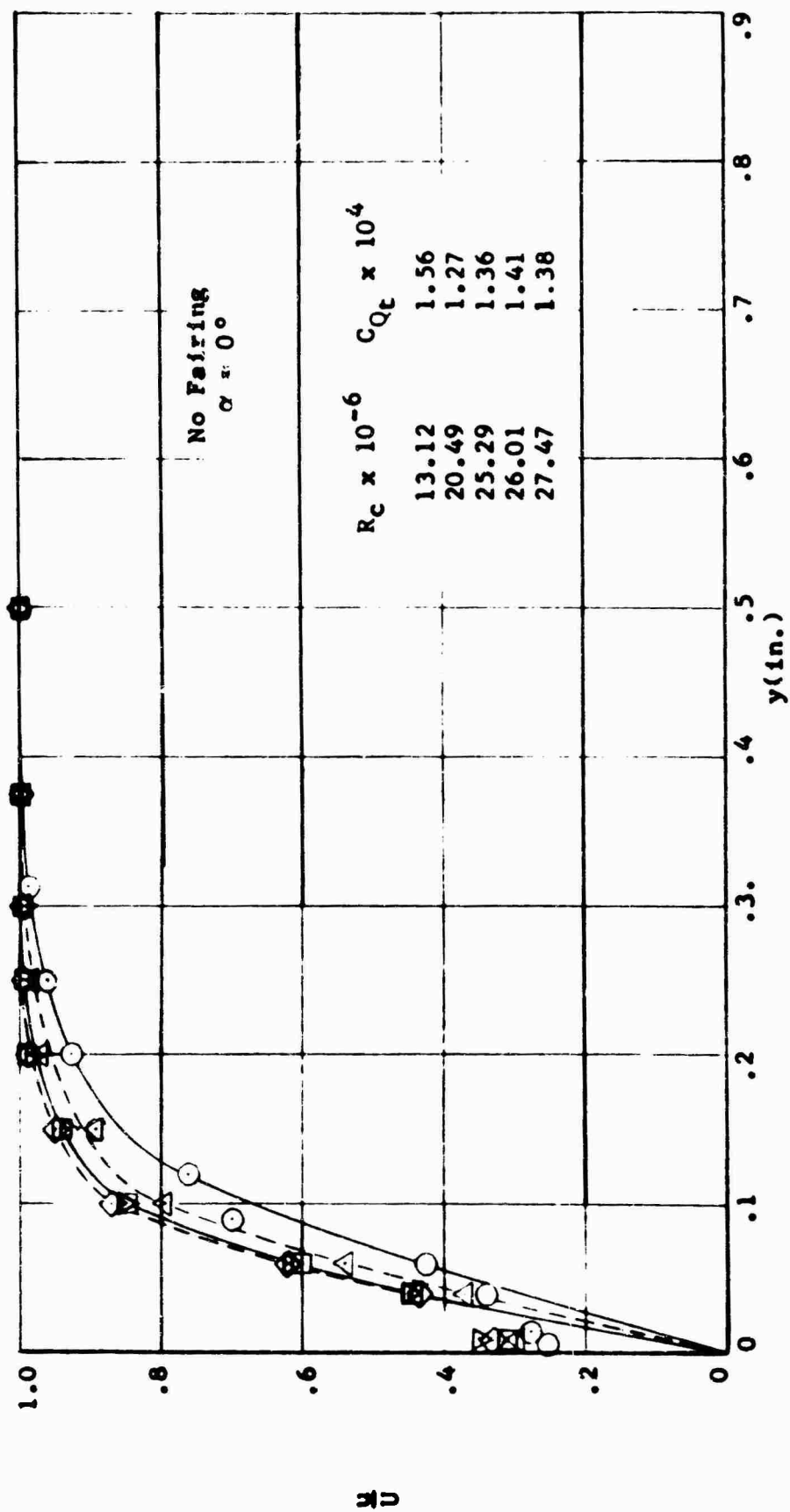


FIGURE 55 COMPARISON OF NONDIMENSIONAL EQUIVALENT AREA SUCTION VELOCITY  $v_0^*$

DISTRIBUTION NEAR OPTIMUM SUCTION COEFFICIENT  $C_{Qopt}$  AT ANGLE OF

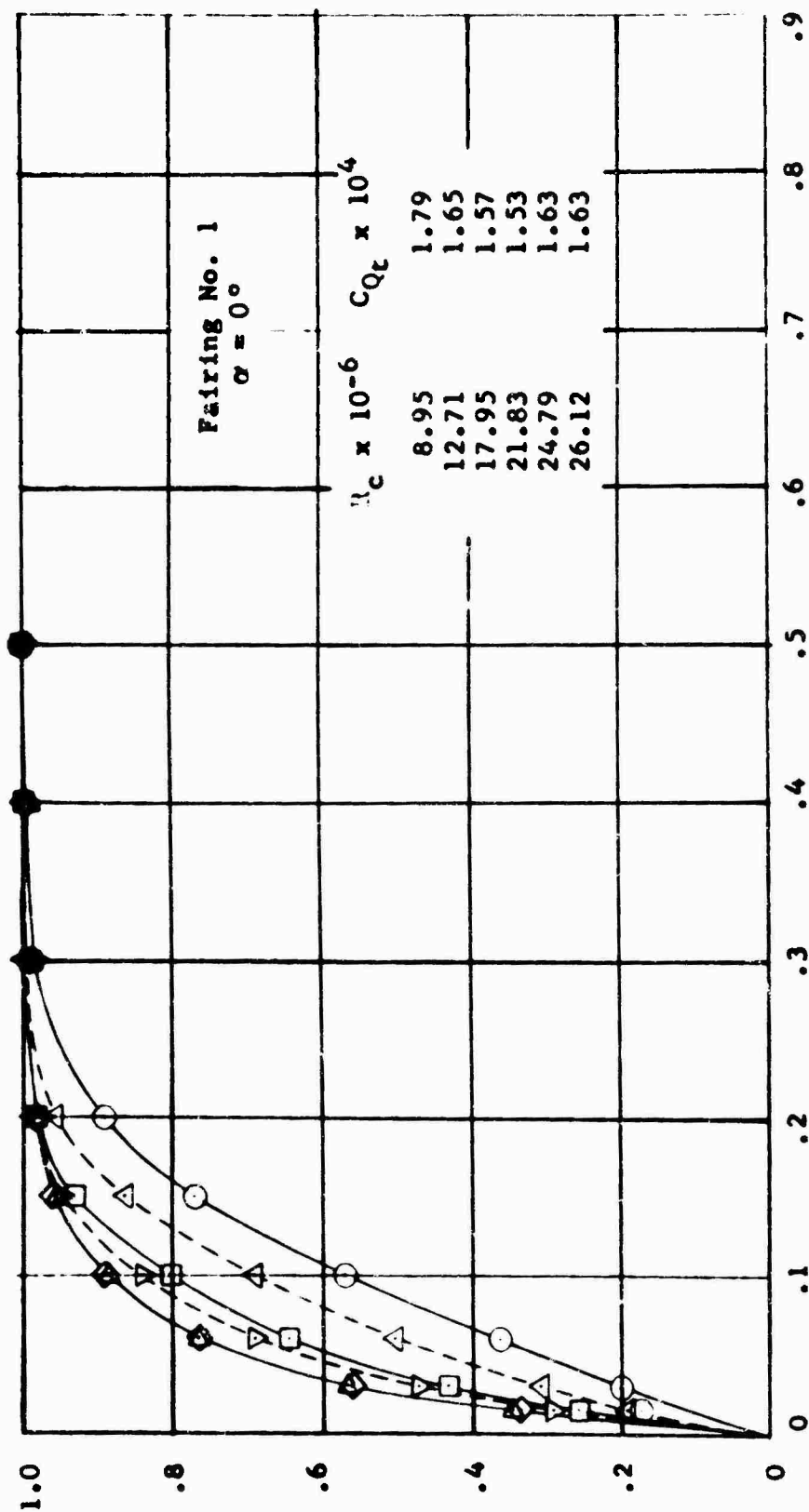
ATTACK  $\alpha = 0^\circ$  AND REYNOLDS NUMBER  $R_c$  OF APPROXIMATELY  $21 \times 10^6$

FOR THE THREE PRESSURE DISTRIBUTIONS STUDIED



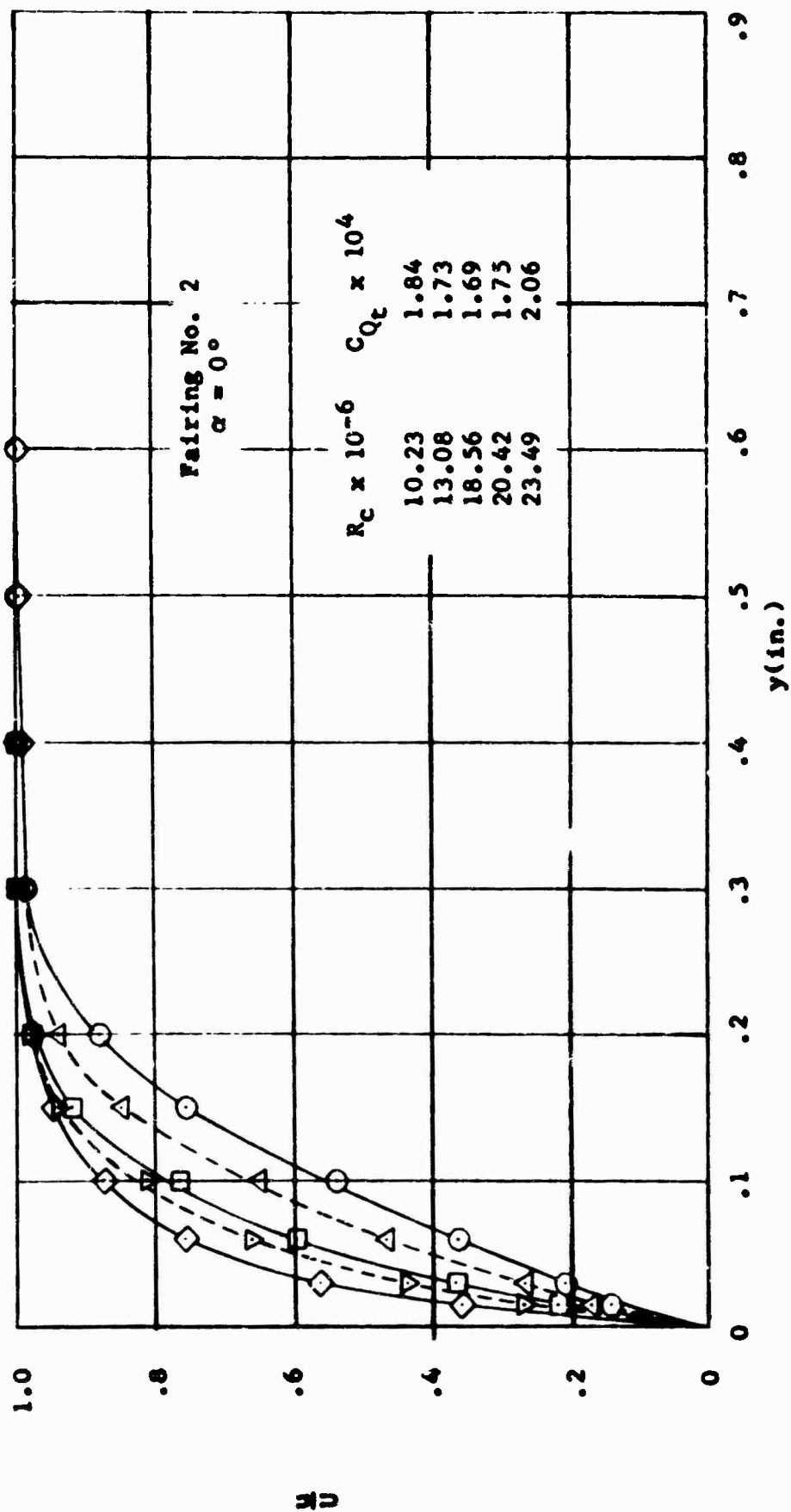
TRAILING EDGE BOUNDARY LAYER VELOCITY PROFILES NEAR  
OPTIMUM SUCTION COEFFICIENT  $C_{Qt}$  FOR SEVERAL  
REYNOLDS NUMBERS  $R_c$

FIGURE 56



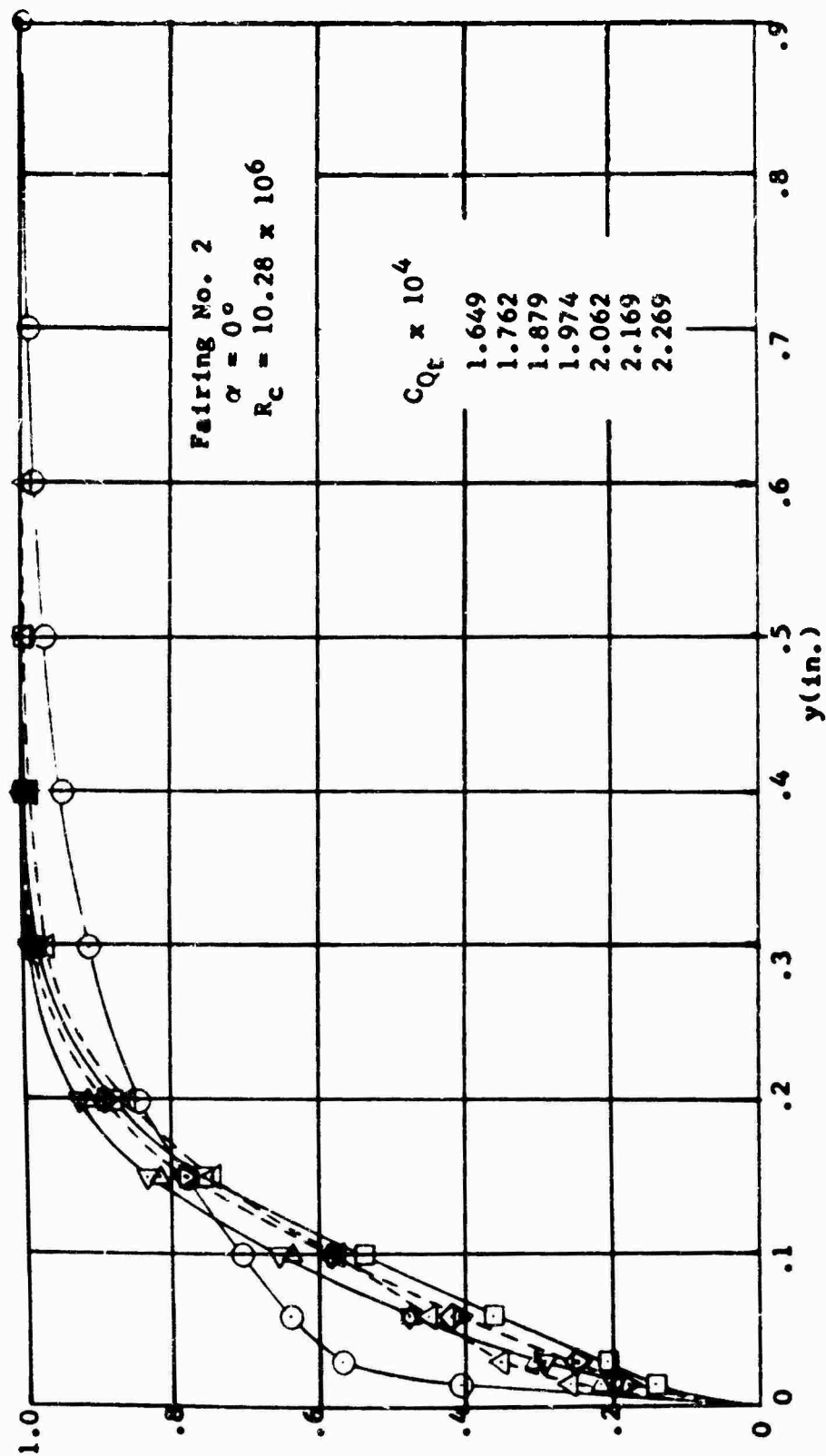
TRAILING EDGE BOUNDARY LAYER VELOCITY PROFILES NEAR  
OPTIMUM SUCTION COEFFICIENT  $C_{Q_{opt}}$  FOR SEVERAL  
REYNOLDS NUMBERS  $R_c$

FIGURE 57



TRAILING EDGE BOUNDARY LAYER VELOCITY PROFILES NEAR  
OPTIMUM SUCTION COEFFICIENT  $C_{Q_{opt}}$  FOR SEVERAL  
REYNOLDS NUMBERS  $R_c$

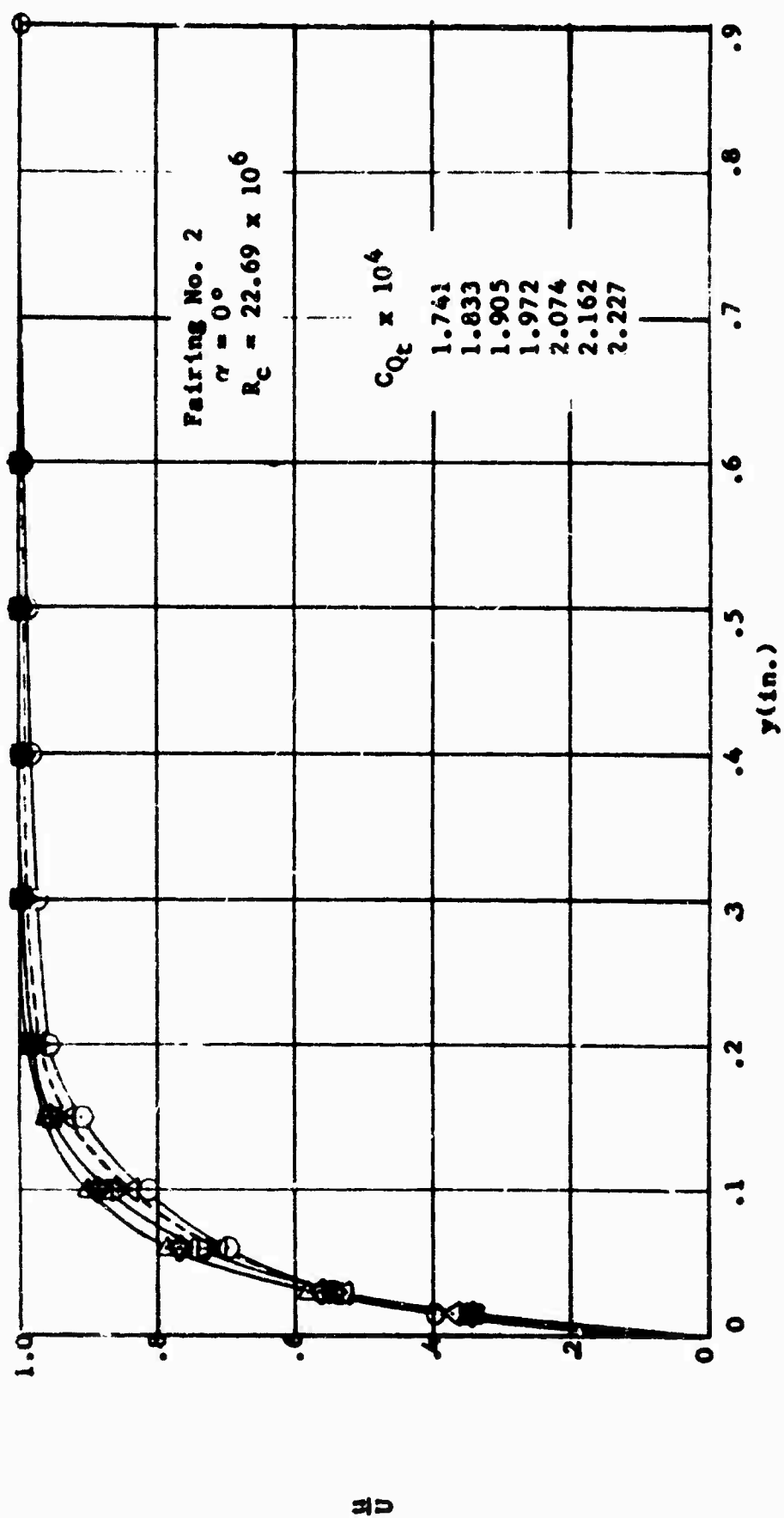
FIGURE 58



VARIATION OF TRAILING EDGE BOUNDARY LAYER VELOCITY  
 PROFILES WITH SUCTION COEFFICIENT  $C_Q$

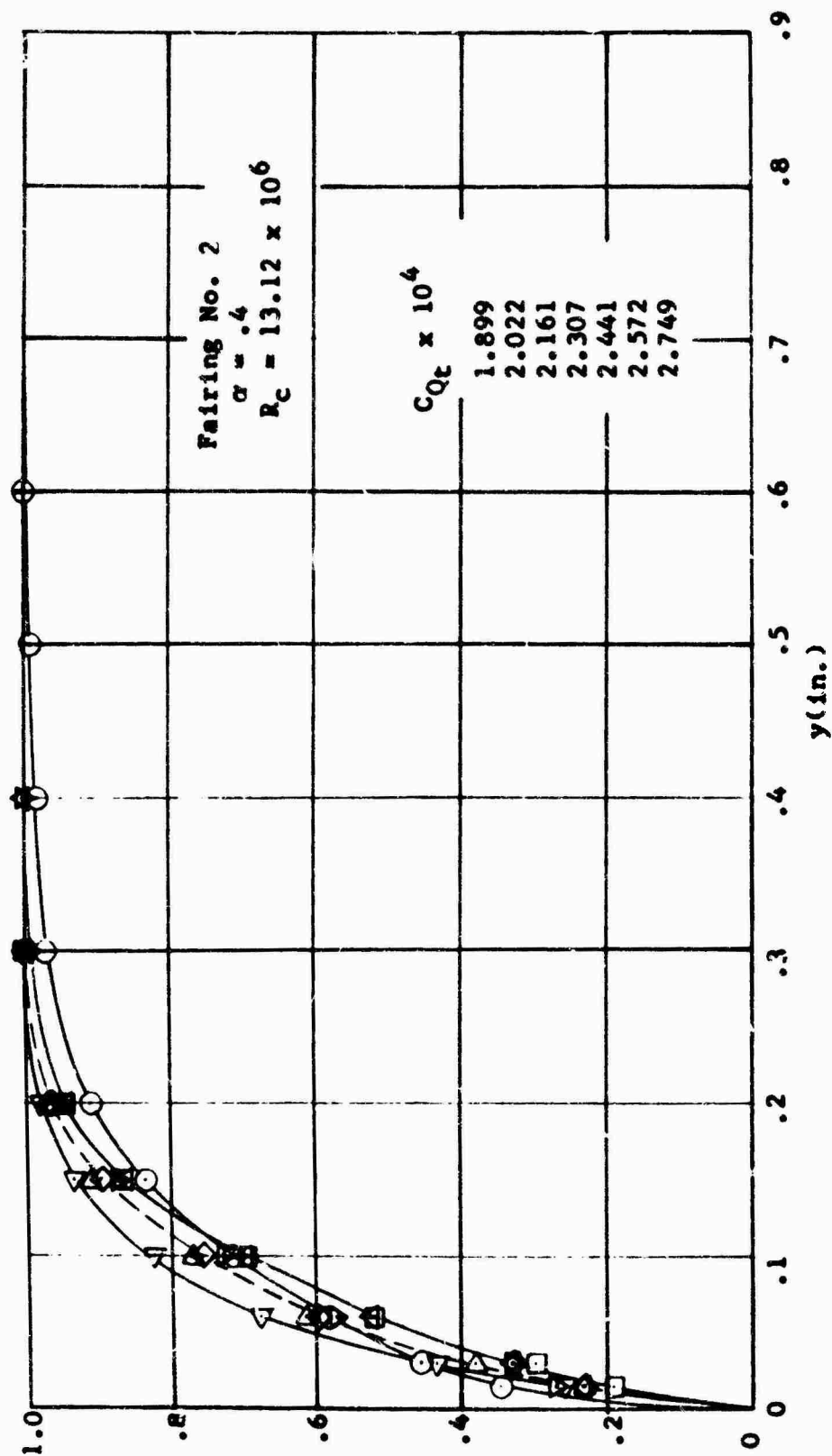
FIGURE 59





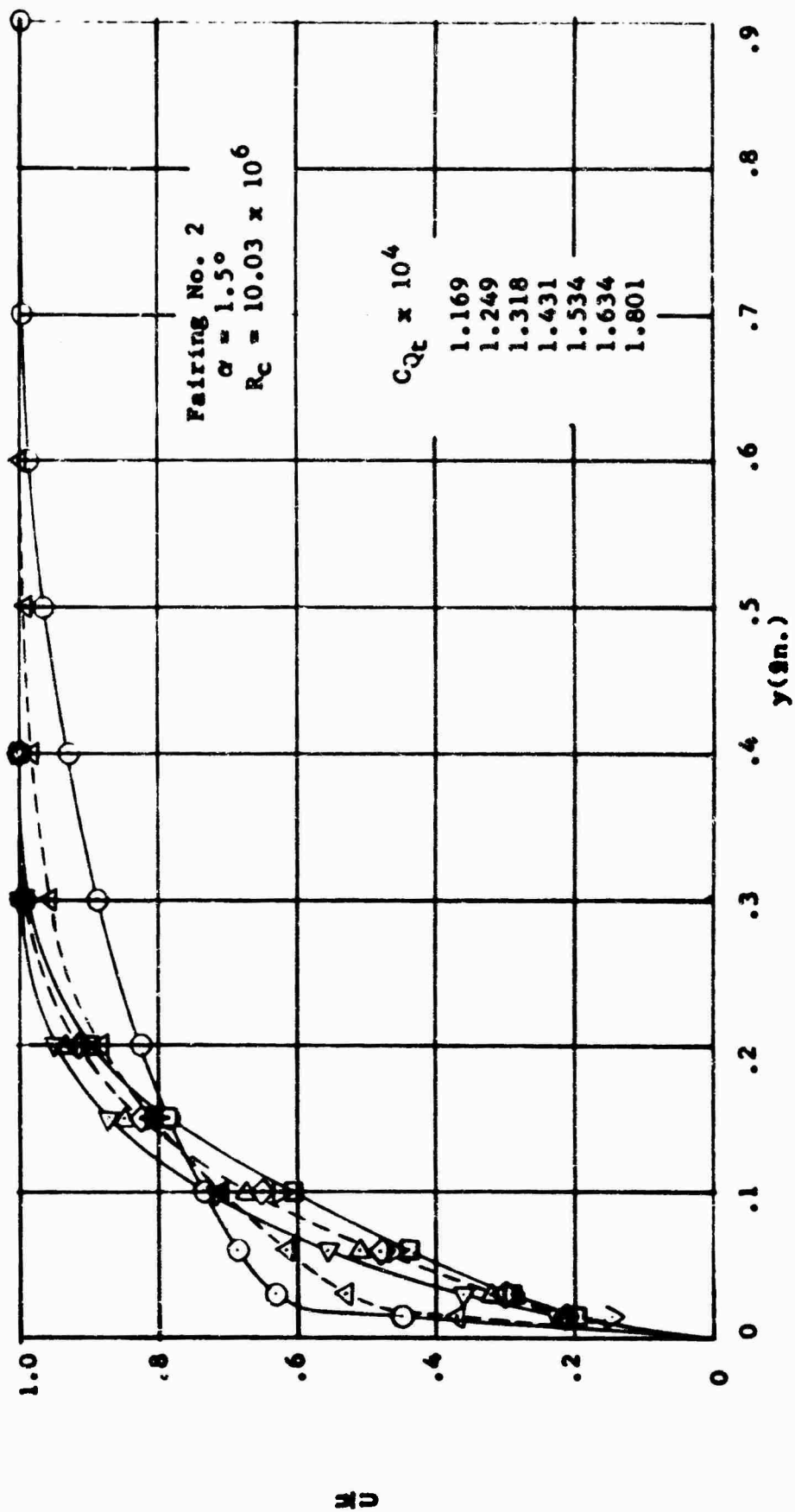
VARIATION OF TRAILING EDGE BOUNDARY LAYER VELOCITY  
 PROFILES WITH SUCTION COEFFICIENT  $C_Q$

FIGURE 60



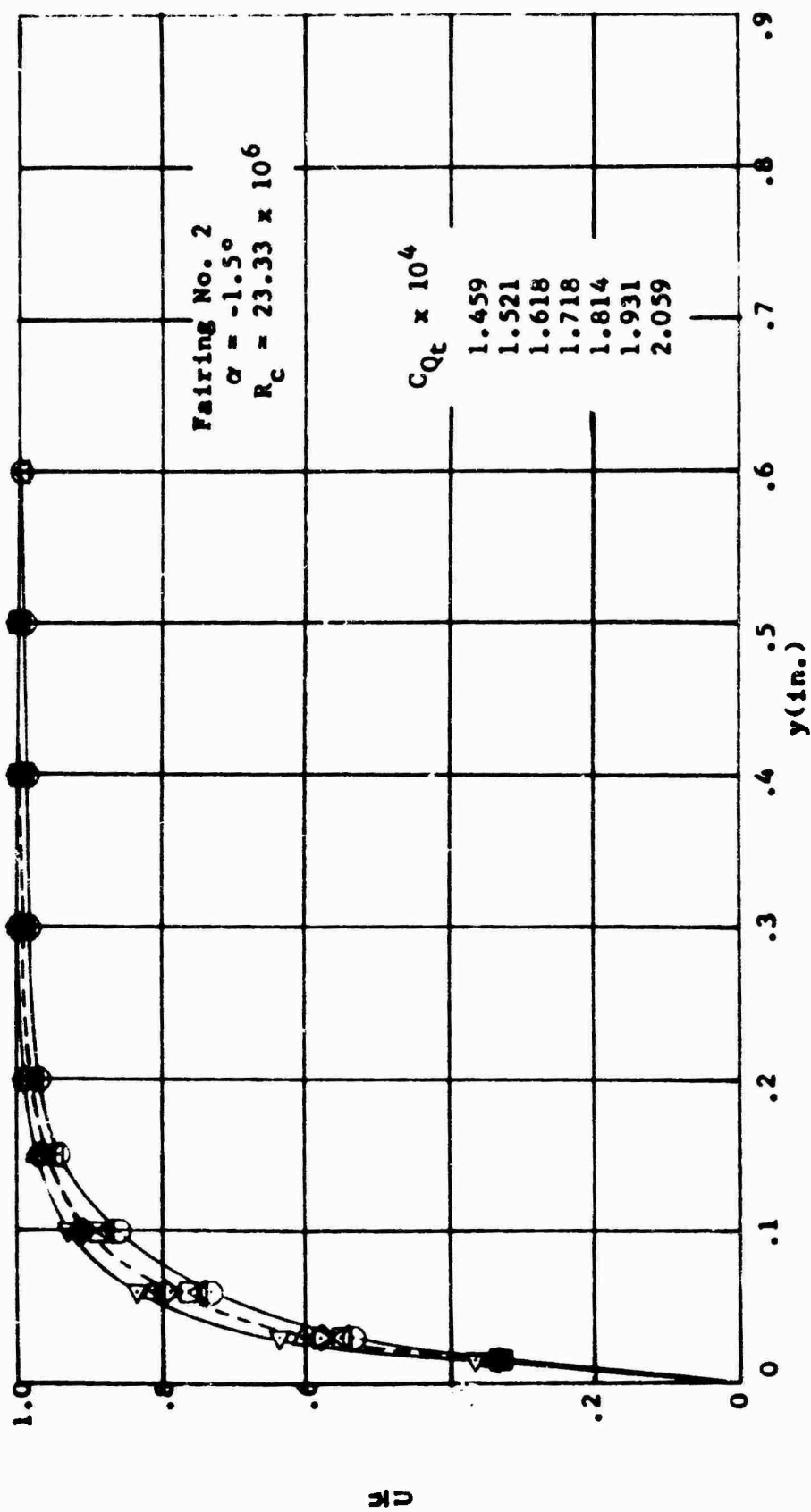
VARIATION OF TRAILING EDGE BOUNDARY LAYER VELOCITY  
 PROFILES WITH SUCTION COEFFICIENT  $C_Q$

FIGURE 61



VARIATION OF TRAILING EDGE BOUNDARY LAYER VELOCITY  
 PROFILES WITH SUCTION COEFFICIENT  $C_q$

FIGURE 62



VARIATION OF TRAILING EDGE BOUNDARY LAYER VELOCITY  
 PROFILES WITH SUCTION COEFFICIENT  $C_q$

FIGURE 63

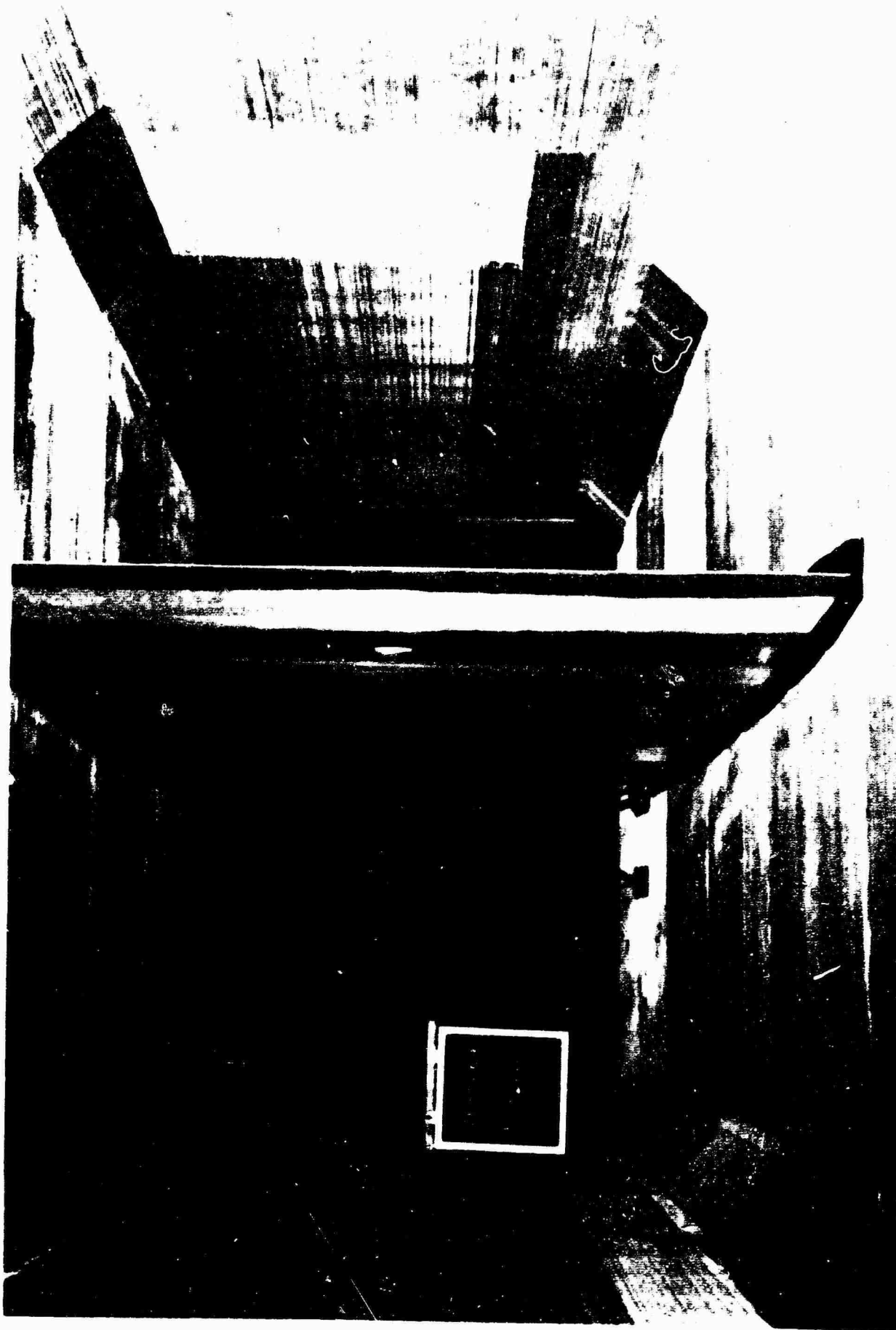


FIGURE 64 17 FT CHORD WING ACOUSTICAL TESTS IN NORAIR 7 x 10 FT WIND TUNNEL

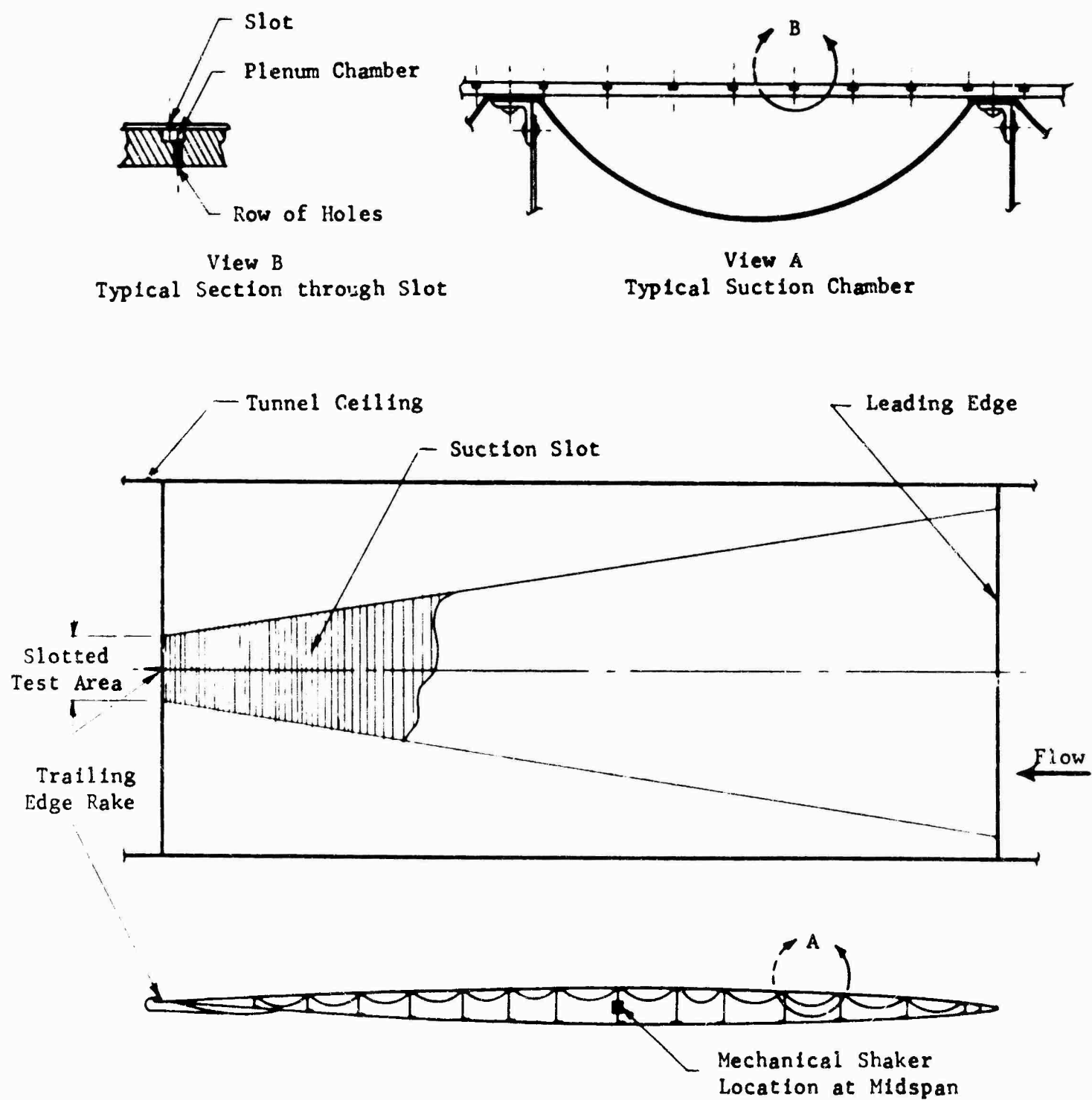


FIGURE 65 17-FOOT CHORD SUCTION MODEL

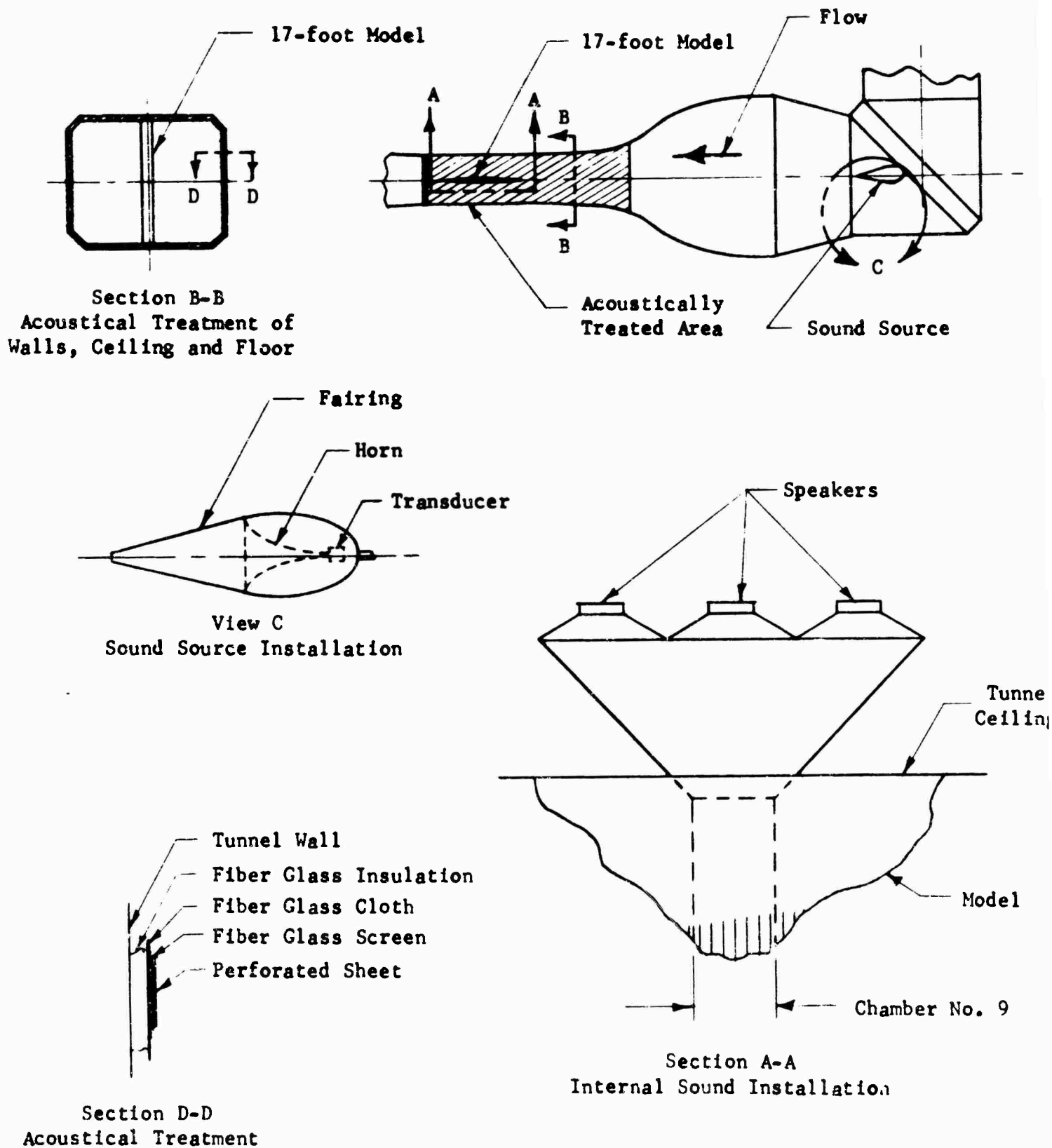


FIGURE 66 ACOUSTICAL INSTALLATION

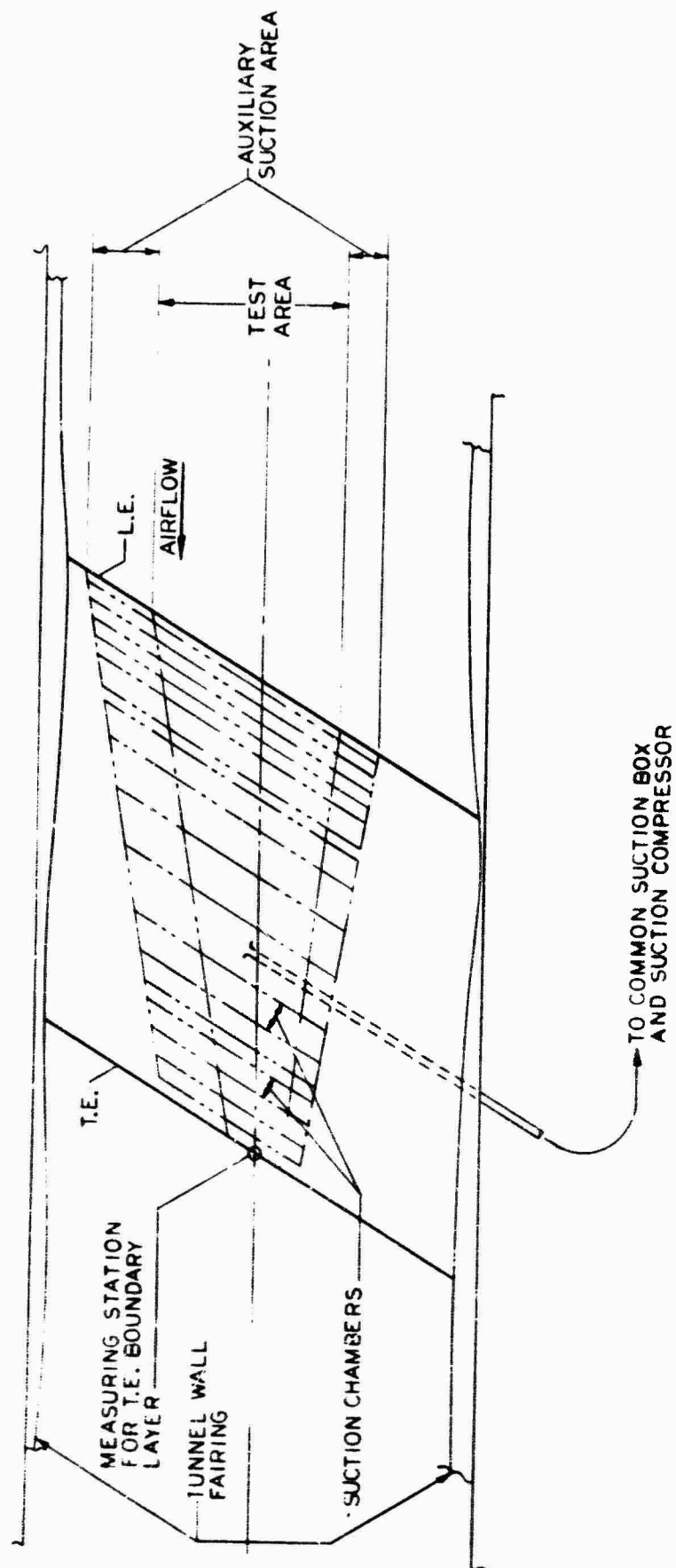


FIGURE 67

INVESTIGATION OF A 30° SWEEP SUCTION WING UNDER THE INFLUENCE OF SOUND  
MODEL INSTALLED IN NORAIR 7 x 10 WIND TUNNEL



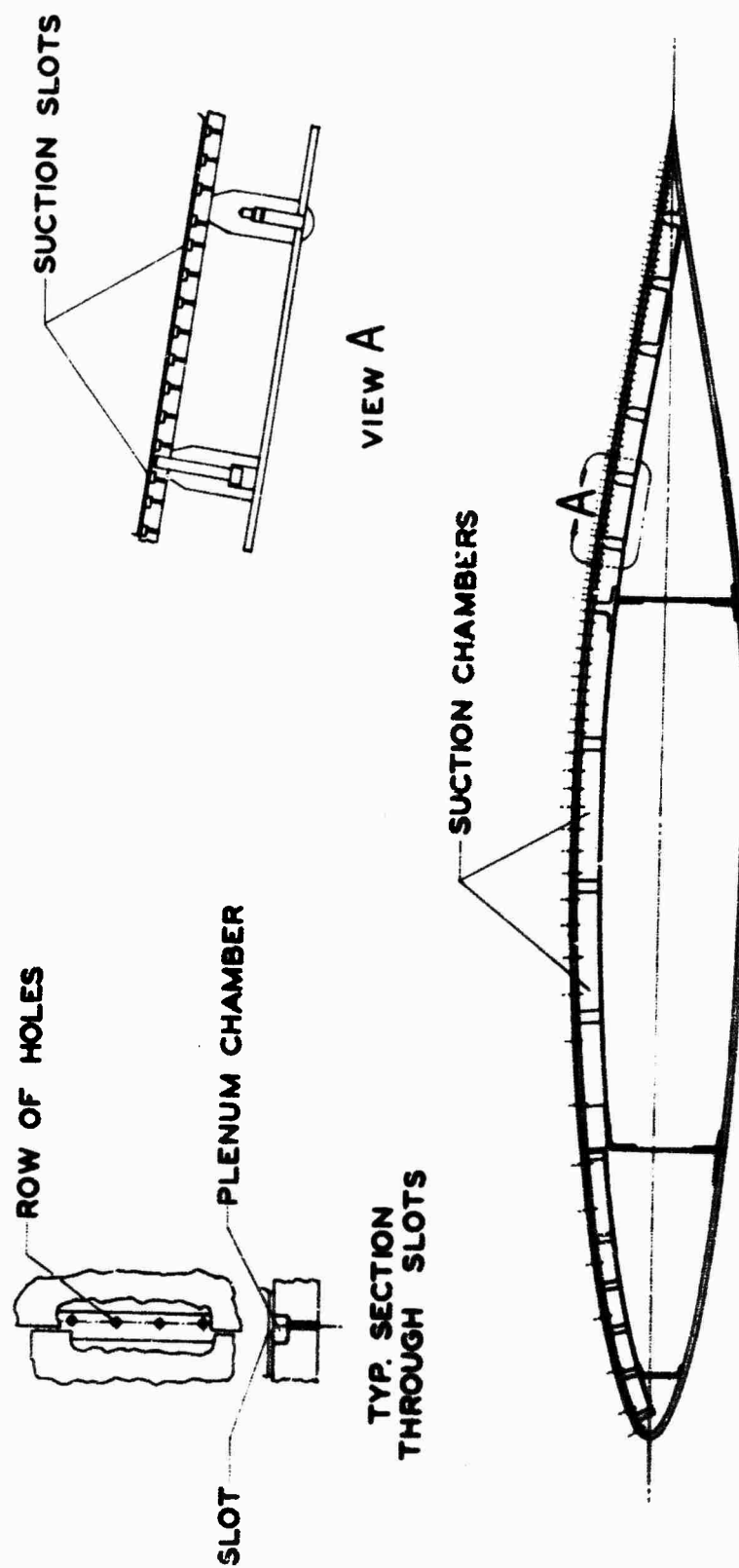


FIGURE 68

30° SWEEP LAMINAR SUCTION WING MODEL WING CROSS SECTION WITH DETAIL  
OF SUCTION CHAMBERS AND SUCTION SLOTS

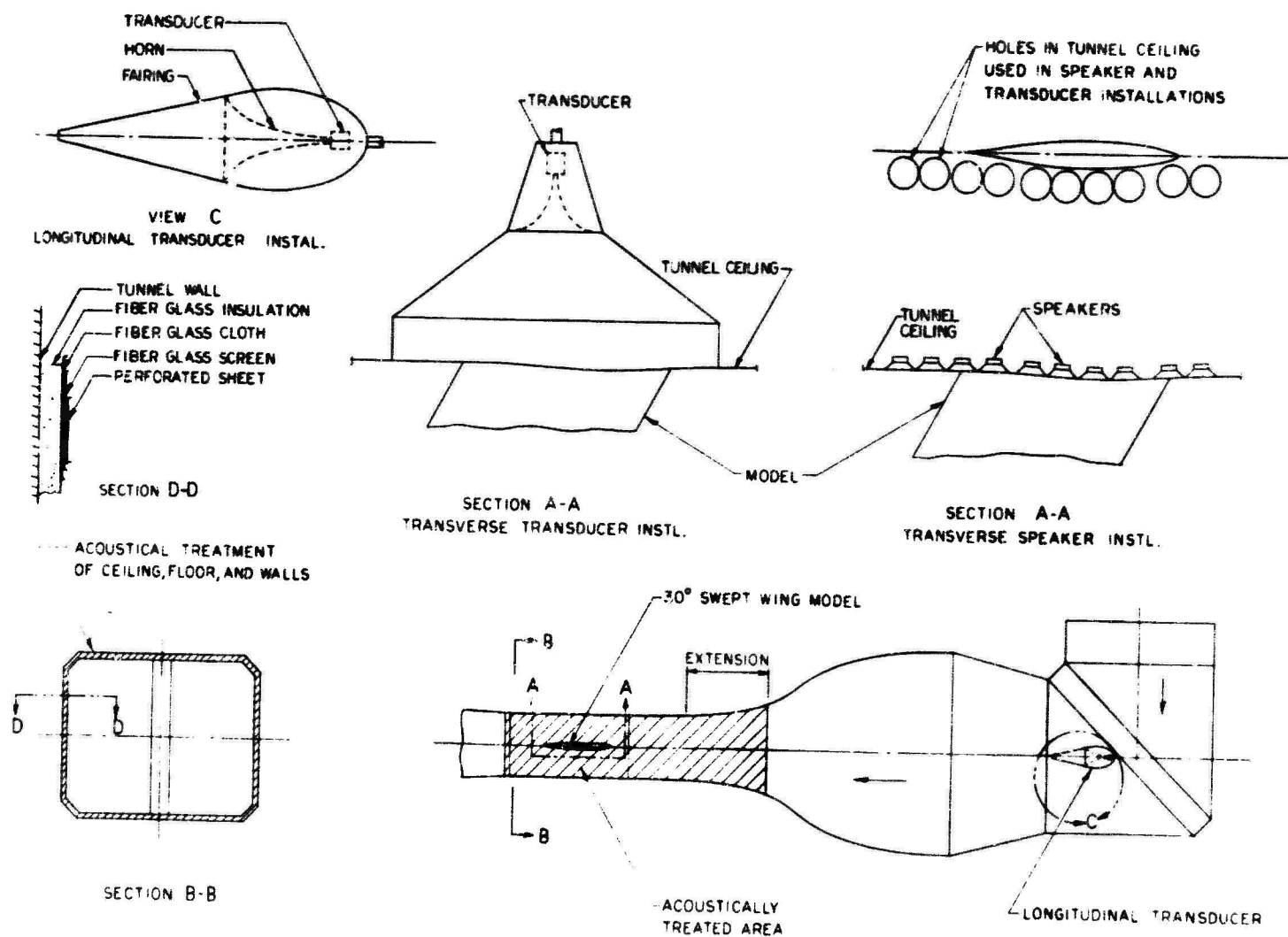


FIGURE 69  
INVESTIGATION OF A 30° SWEEP SUCTION WING UNDER THE INFLUENCE  
OF SOUND ACOUSTICAL INSTALLATION

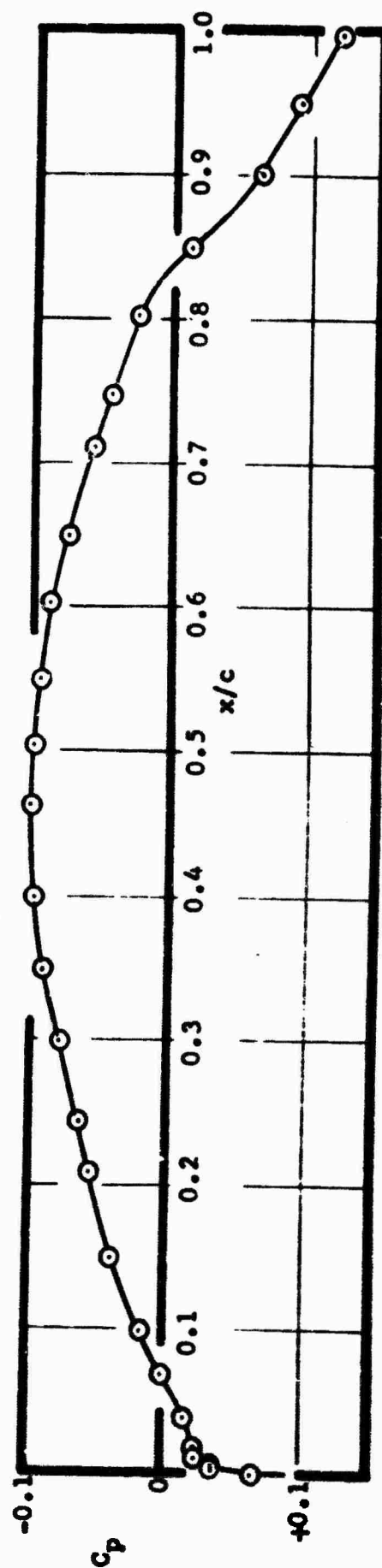


FIGURE 70 MEASURED AIRFOIL PRESSURE DISTRIBUTION, 17-FOOT CHORD STRAIGHT WING

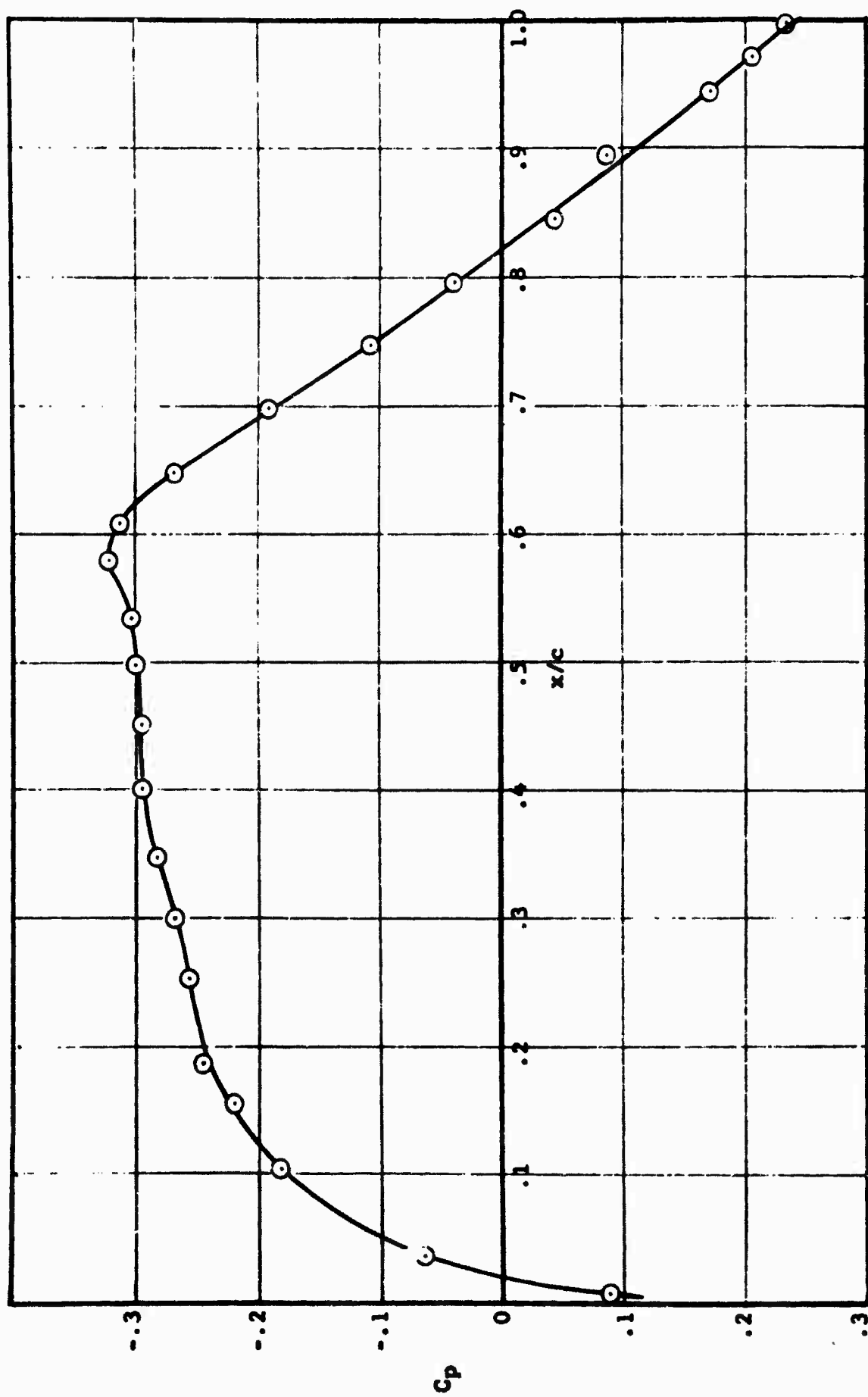
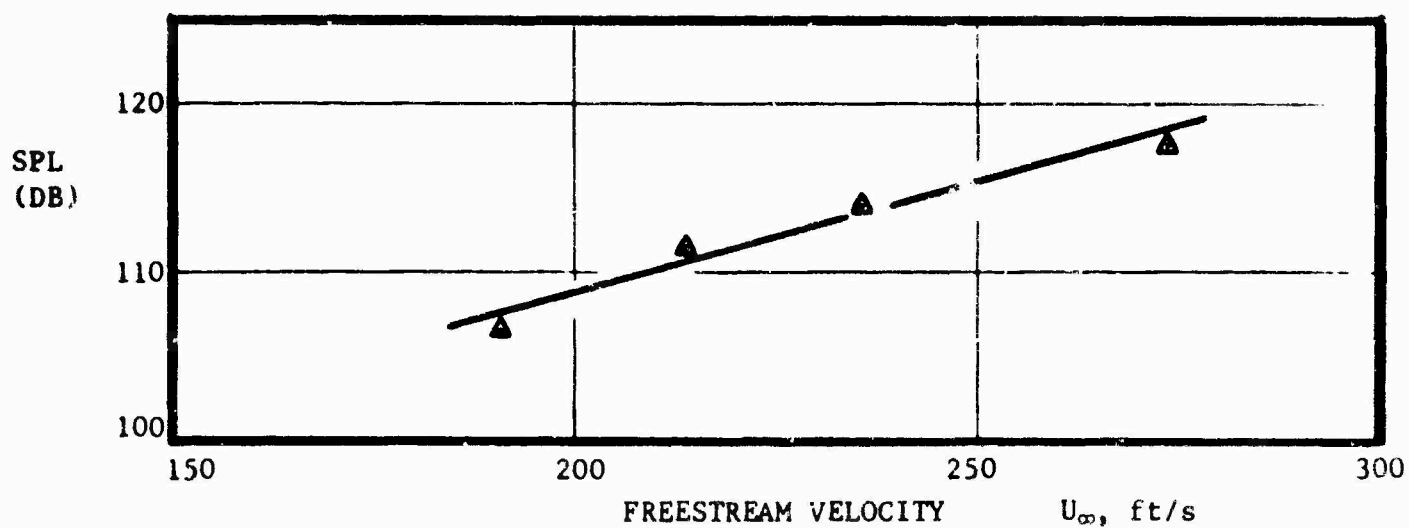
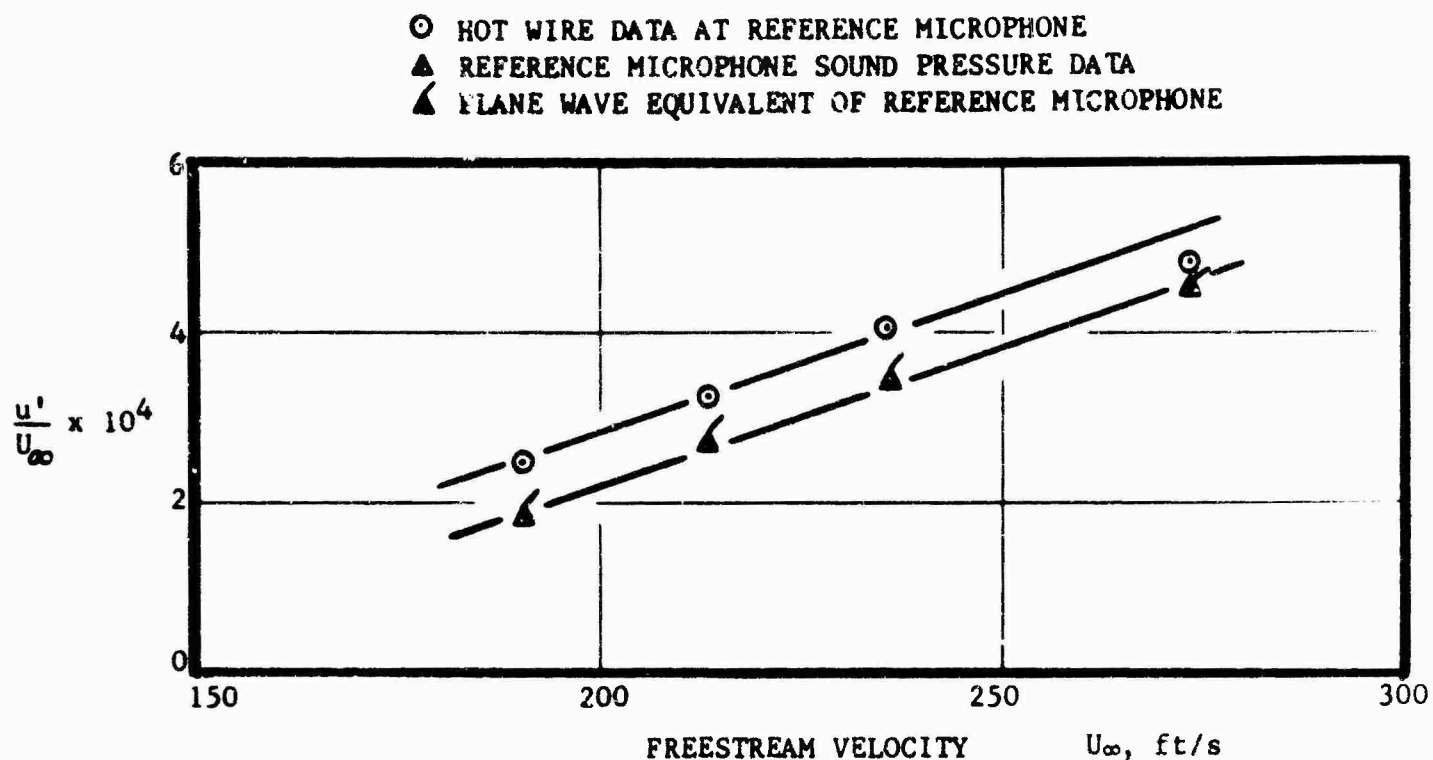


FIGURE 71  
 PRESSURE COEFFICIENT  $C_p$  VS CHORD  $x/c$   
 30° SWEEP Suction WING UNDER THE INFLUENCE OF SOUND  
 $\alpha = 0^\circ$



$K_c = 8.1 \times 10^6$	$9.1 \times 10^6$	$9.8 \times 10^6$	$11.2 \times 10^6$	~ 30° Swept Wing
$19.7 \times 10^6$	$22.1 \times 10^6$	$23.8 \times 10^6$		~ Thin Straight Wing

FIGURE 72  
 NORAIR 7- BY 10-FOOT WIND TUNNEL TURBULENCE AND NOISE LEVELS  
 WITH MODEL AND ACOUSTICAL WALL TREATMENT INSTALLED  
 30° SWEPT SUCTION WING UNDER THE INFLUENCE OF SOUND

⊙ REFERENCE MICROPHONE

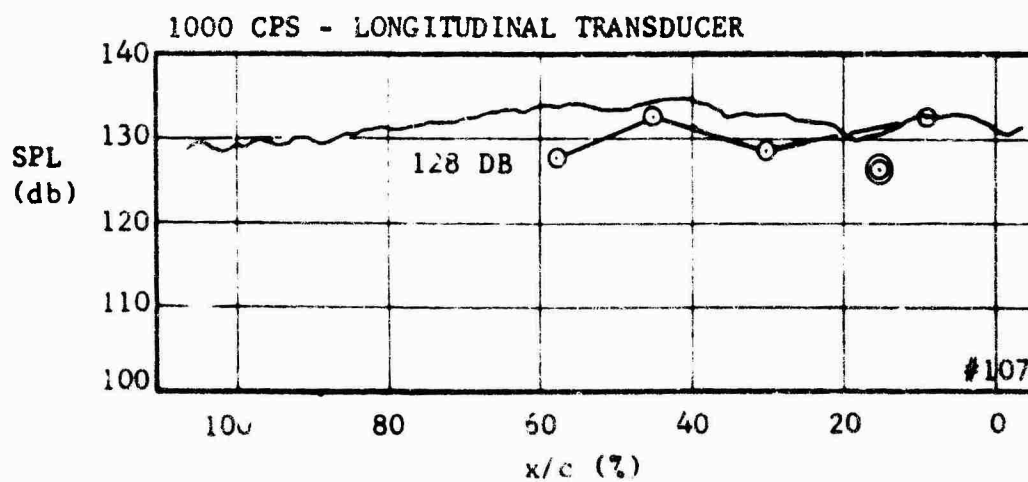
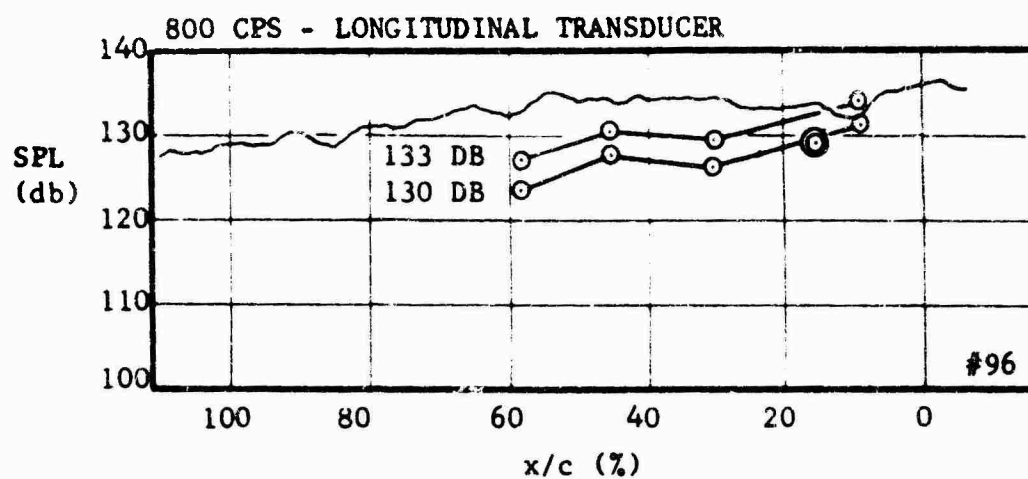
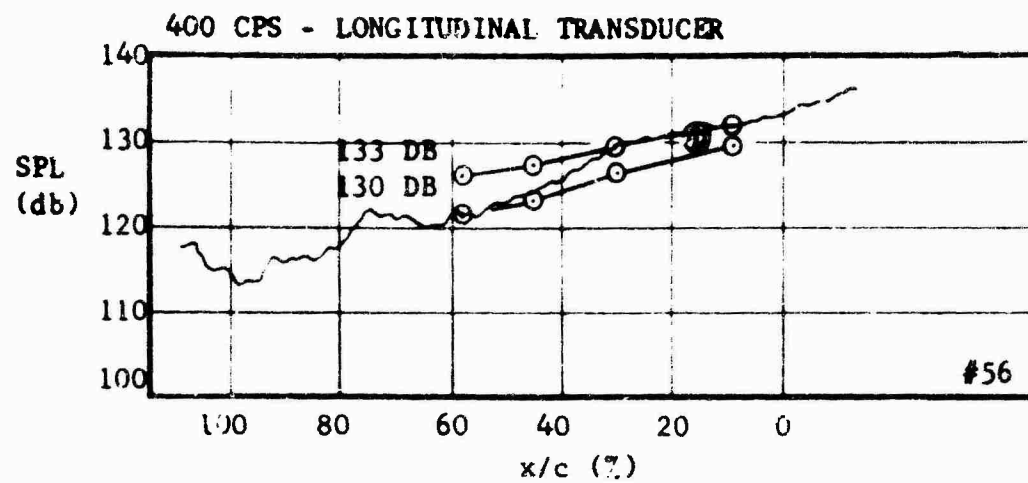
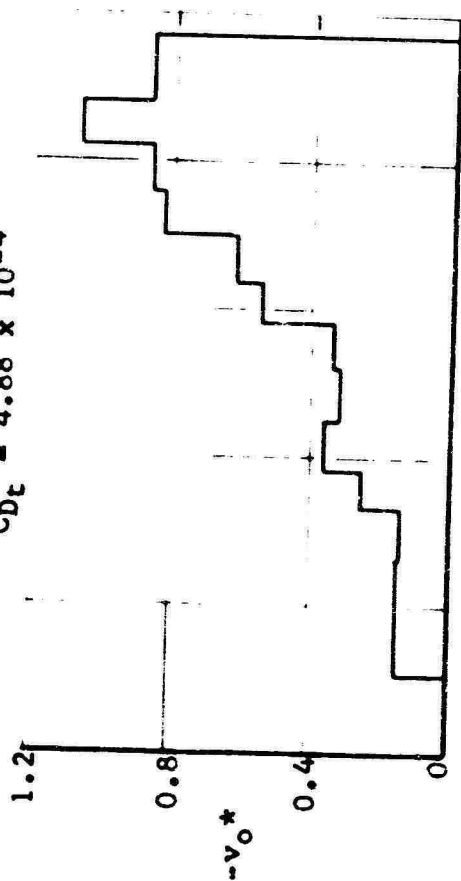


FIGURE 73  
COMPARISON OF SOUND FIELD TRAVERSES AT MIDSPAN  
6 INCHES AWAY FROM WING MAXIMUM THICKNESS,  $R_c = 9.6 \times 10^6$   
(WITH HOT WIRE READINGS AT EDGE OF  
BOUNDARY LAYER,  $R_c = 8.1 \times 10^6$ )

Minimum Drag Suction, No Sound

Run 117,  $C_Q = 1.26 \times 10^{-4}$

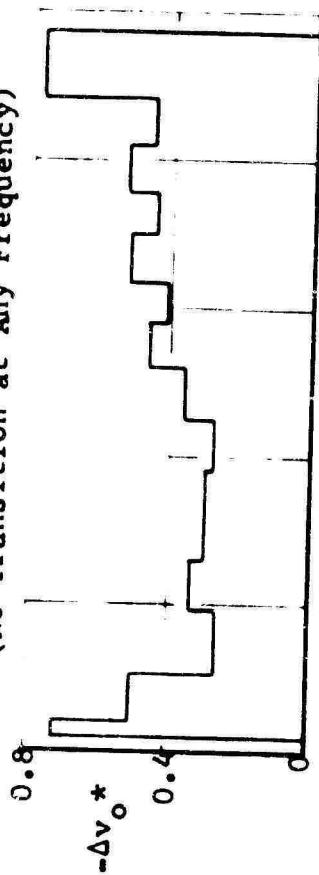
$C_{D_t} = 4.88 \times 10^{-4}$



Additional Suction for No Transition at  
150/300 cps, 131 db, Run 127,

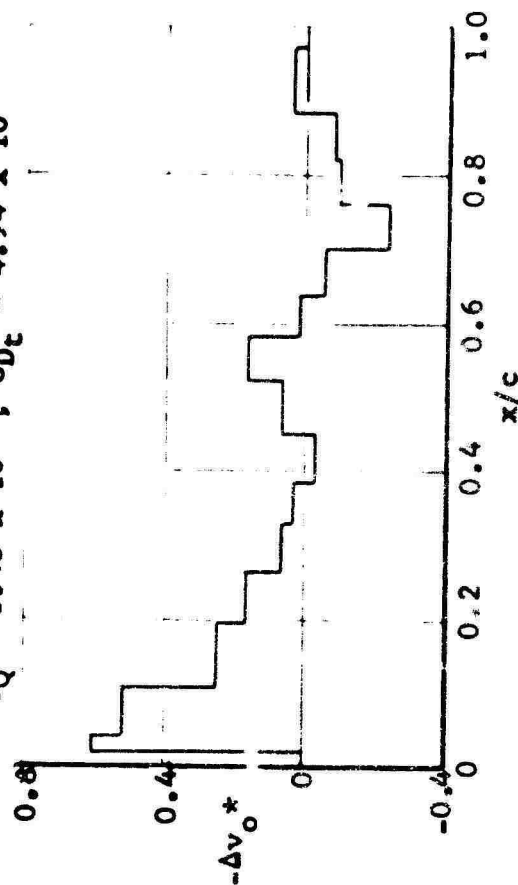
$C_Q = 2.46 \times 10^{-4}$ ,  $C_{D_t} = 5.90 \times 10^{-4}$

(No Transition at Any Frequency)



Additional Suction for No Transition at  
600/1200 cps, 125 db, Run 125,

$C_Q = 1.45 \times 10^{-4}$ ,  $C_{D_t} = 4.94 \times 10^{-4}$



Additional Suction for No Transition at  
300/600 cps, 128 db, Run 126,

$C_Q = 1.97 \times 10^{-4}$ ,  $C_{D_t} = 5.36 \times 10^{-4}$

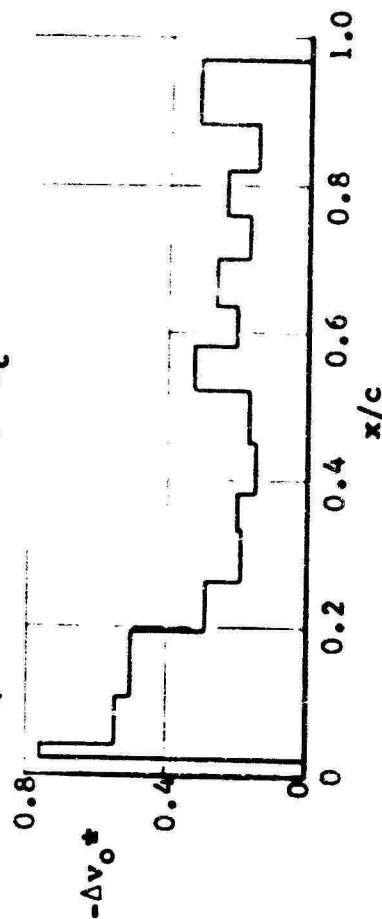
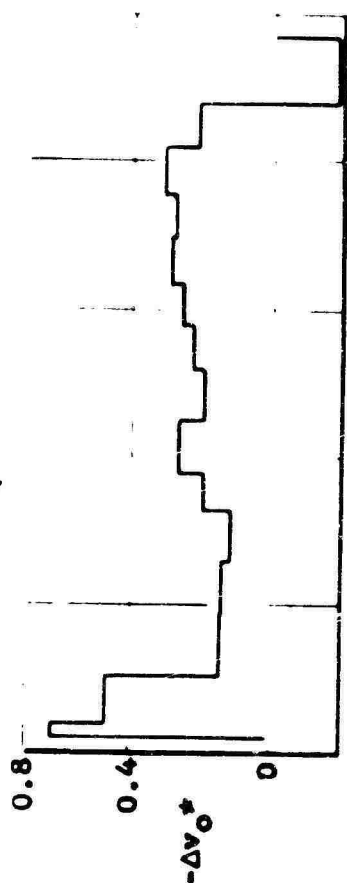
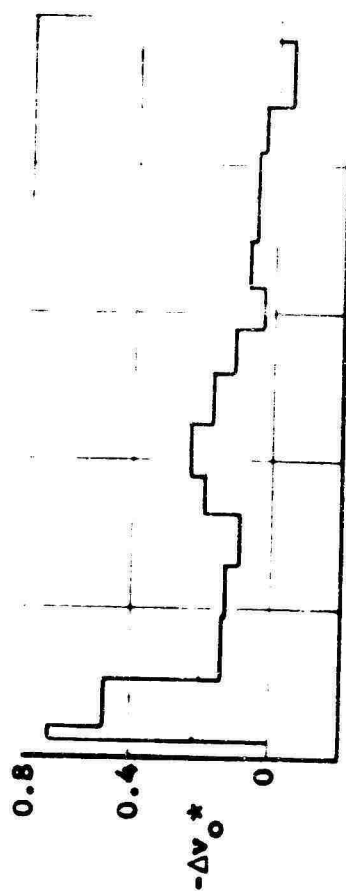


FIGURE 74 ADDITIONAL SUCTION,  $-\Delta v_o^*$ , REQUIRED TO MAINTAIN LAMINAR FLOW AT VARIOUS FREQUENCIES  
AND EXTERNAL SOUND PRESSURE LEVELS,  $R_c = 11.4 \times 10^6$

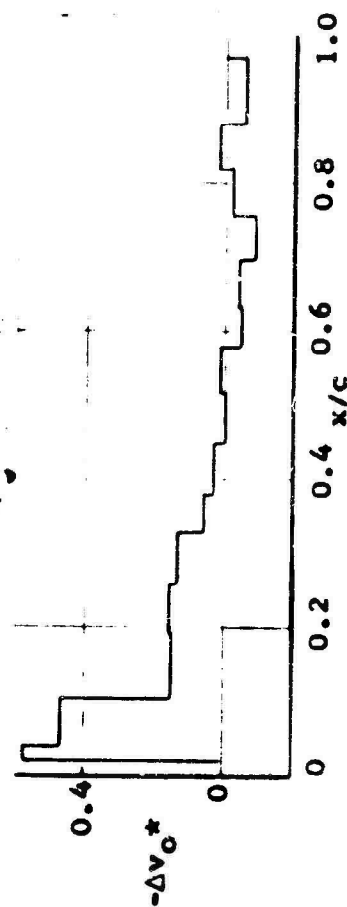
Additional Suction for No Transition at  
150/300 cps, 131 db, Run 132,  
 $C_Q = 1.77 \times 10^{-4}$



Additional Suction for No Transition at  
300/600 cps, 128 db, Run 131,  
 $C_Q = 1.61 \times 10^{-4}$

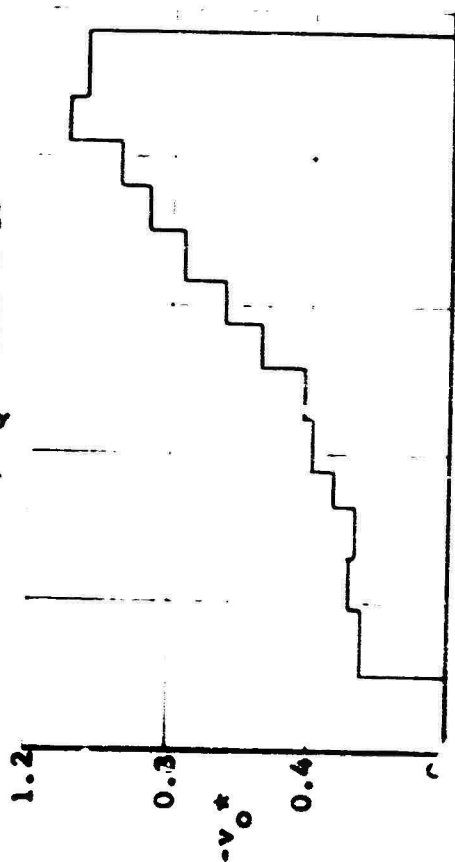


Additional Suction for No Transition at  
600/1200 cps, 125 db, Run 130,  
 $C_Q = 1.44 \times 10^{-4}$



Minimum Drag Suction, No Sound

Run 19,  $C_Q = 1.29 \times 10^{-4}$



Additional Suction for No Transition at  
Any Frequency, 131 db, Run 133,  
 $C_Q = 1.87 \times 10^{-4}$

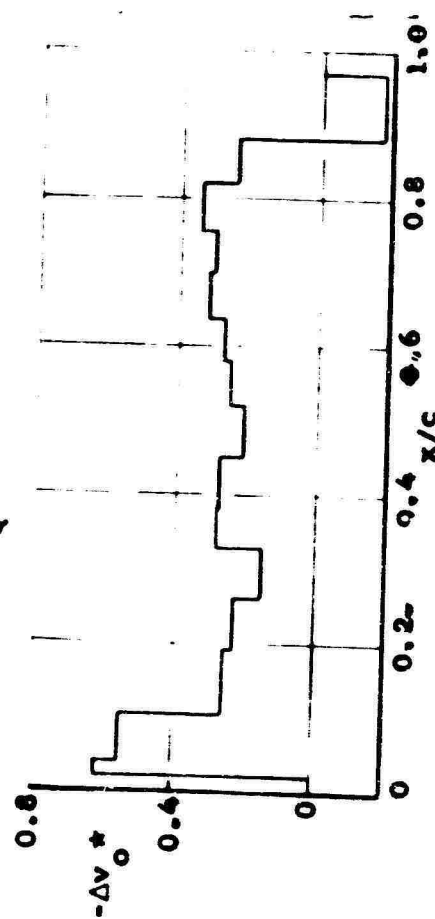


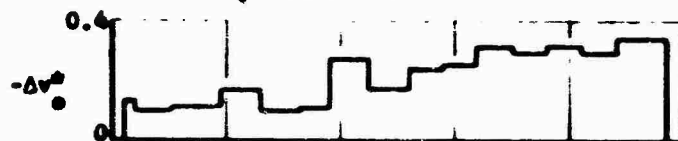
FIGURE 75 ADDITIONAL SUCTION,  $-\Delta v_o^*$ , REQUIRED TO MAINTAIN LAMINAR FLOW AT VARIOUS FREQUENCIES AND EXTERNAL SOUND PRESSURE LEVELS,  $R_c = 16.4 \times 10^6$



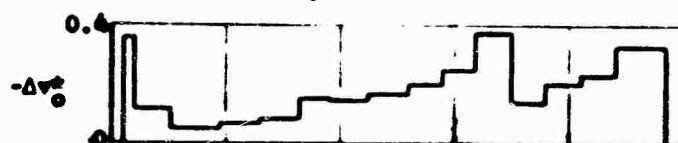
Minimum Drag Section, No Sound  
Run 104,  $C_Q = 1.17 \times 10^{-4}$



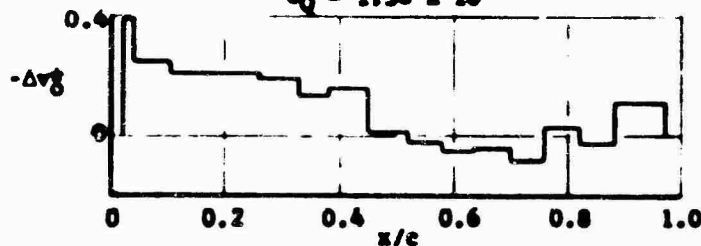
Additional Section for No Transition at  
267 cps, 135.5 db, Run 110  
 $C_Q = 1.03 \times 10^{-4}$



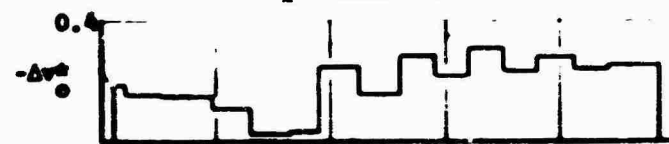
Additional Section for No Transition at  
443 cps, 131 db, Run 108  
 $C_Q = 1.36 \times 10^{-4}$



Additional Section for No Transition at  
810 cps, 130 db, Run 106  
 $C_Q = 1.36 \times 10^{-4}$



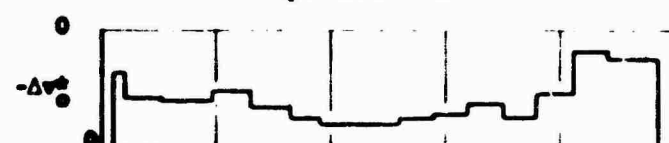
Additional Section for No Transition at  
150/300 cps, 130 db, Run 111,  
 $C_Q = 1.58 \times 10^{-4}$



Additional Section for No Transition at  
300/600 cps, 127 db, Run 112  
 $C_Q = 1.49 \times 10^{-4}$



Additional Section for No Transition at  
600/1200 cps, 125 db, Run 113  
 $C_Q = 1.53 \times 10^{-4}$



Additional Section for No Transition at  
Any Frequency, db, Run 114  
 $C_Q = 1.76 \times 10^{-4}$

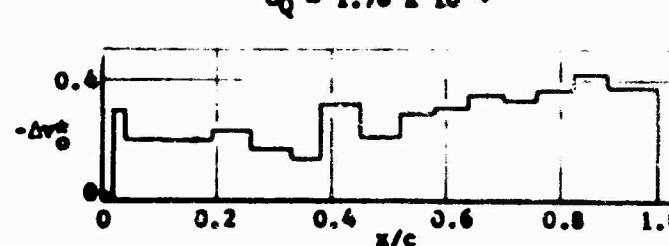
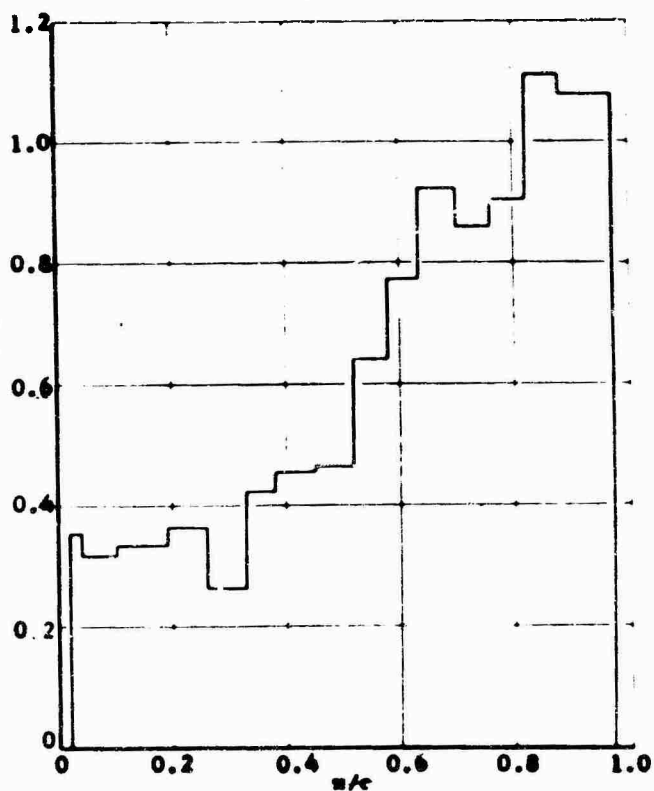
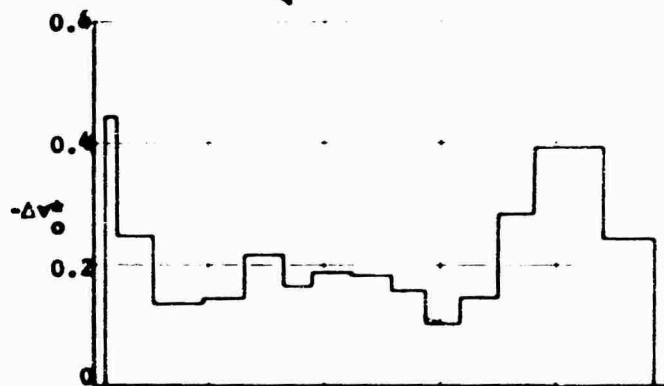


FIGURE 76 ADDITIONAL SUCTION  $-\Delta v_g$ , REQUIRED TO MAINTAIN LAMINAR FLOW AT VARIOUS FREQUENCIES AND EXTERNAL SOUND PRESSURE LEVELS,  $R_c = 20.2 \times 10^6$

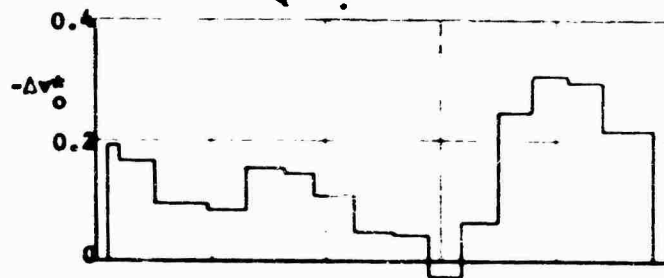
Minimum Drag Suction, No Sound  
Run 142,  $C_Q = 1.30 \times 10^{-4}$



Additional Suction for No Transition at  
150/300 cps, 130 db, Run 149,  
 $C_Q = 1.72 \times 10^{-4}$



Additional Suction for No Transition at  
300/600 cps, 128 db, Run 146,  
 $C_Q = 1.59 \times 10^{-4}$



Additional Suction for No Transition at  
600/1200 cps, 125 db, Run 147,  
 $C_Q = 1.54 \times 10^{-4}$

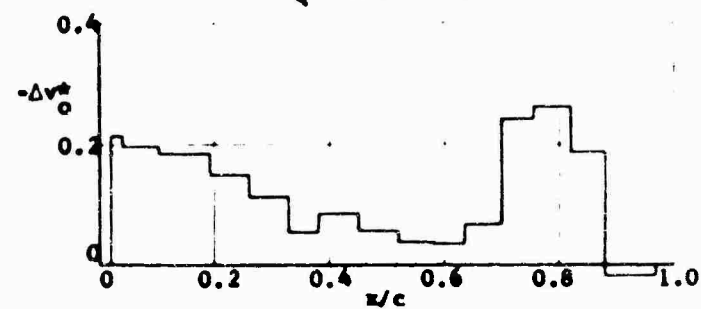


FIGURE 77 ADDITIONAL SUCTION,  $-\Delta v_0^*$ , REQUIRED TO MAINTAIN LAMINAR FLOW AT VARIOUS FREQUENCIES AND EXTERNAL SOUND PRESSURE LEVELS,  $R_c = 21.5 \times 10^6$

Run 117,  $C_Q = 1.26 \times 10^{-4}$ ;  $C_Q/C_{Q117} = 1.00$ ,  
 $C_{Dc} = 4.88 \times 10^{-4}$ ,  $C_{Dc}/C_{Dc117} = 1.00$

Run 129,  $C_Q = 1.44 \times 10^{-4}$ ;  $C_Q/C_{Q129} = 1.14$   
 $C_{Dc} = 4.90 \times 10^{-4}$ ,  $C_{Dc}/C_{Dc129} = 1.00$

Run 128,  $C_Q = 2.20 \times 10^{-4}$ ;  $C_Q/C_{Q128} = 1.75$   
 $C_{Dc} = 5.55 \times 10^{-4}$ ,  $C_{Dc}/C_{Dc128} = 1.13$

Run 127,  $C_Q = 2.46 \times 10^{-4}$ ;  $C_Q/C_{Q127} = 1.93$ ,  
 $C_{Dc} = 5.90 \times 10^{-4}$ ,  $C_{Dc}/C_{Dc127} = 1.81$

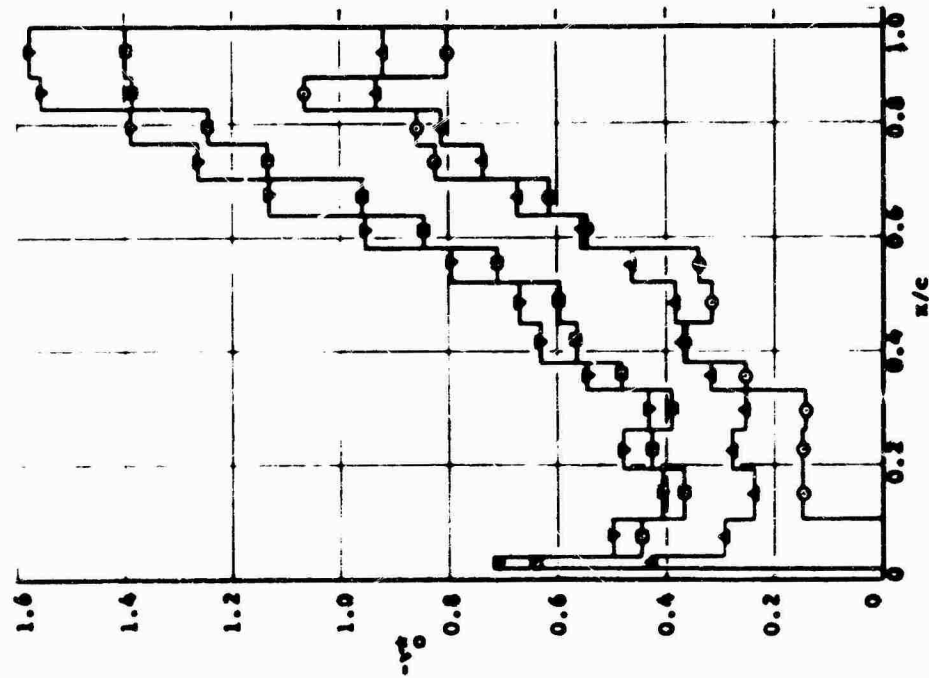
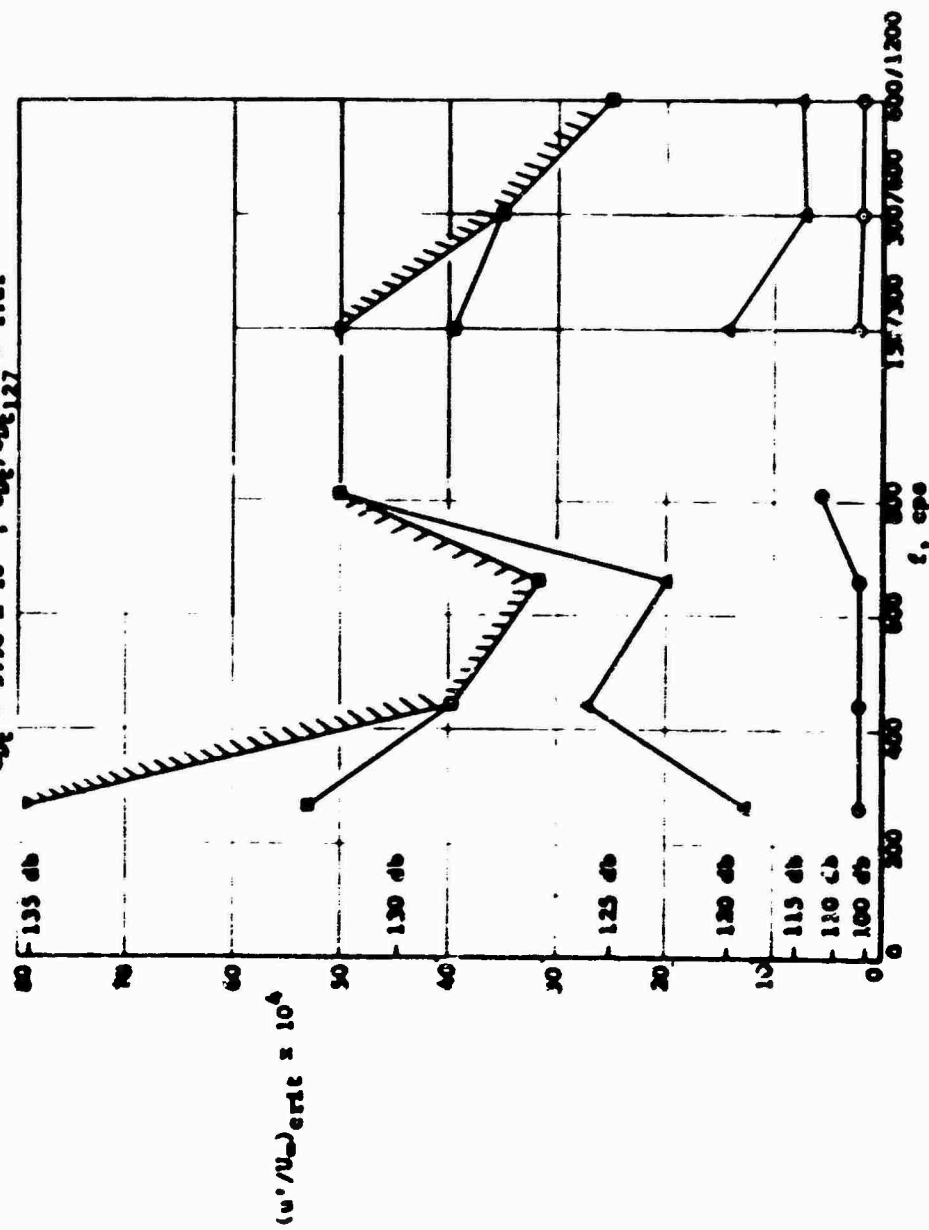


FIGURE 78 EFFECT OF VARIATION OF SUCTION LEVEL ON TRANSITION WITH EXTERNAL SOUND,  $R_c = 11.5 \times 10^6$

Run 134,  $C_Q = 1.15 \times 10^{-4}$ ,  $C_Q/C_{Q134} = 1.00$   
 Run 135,  $C_Q = 1.25 \times 10^{-4}$ ,  $C_Q/C_{Q135} = 1.09$   
 Run 136,  $C_Q = 1.36 \times 10^{-4}$ ,  $C_Q/C_{Q136} = 1.36$   
 Run 133,  $C_Q = 1.87 \times 10^{-4}$ ,  $C_Q/C_{Q133} = 1.63$

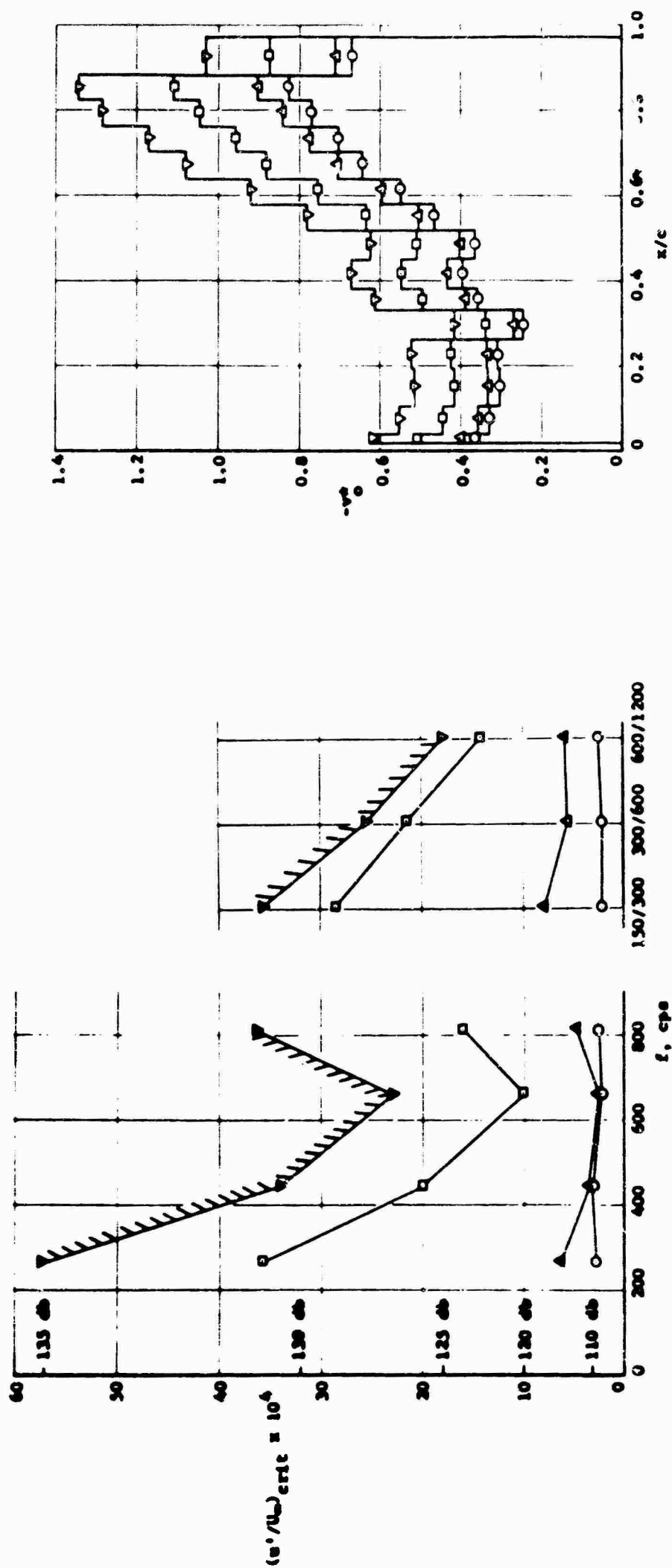


FIGURE 75 EFFECT OF VARIATION OF SUCTION LEVEL ON TRANSITION WITH EXTERNAL SOUND,  $R_c = 16.4 \times 10^6$

Run 152,  $CQ = 1.27 \times 10^{-4}$ ,  $CQ/CQ_{152} = 1.00$   
 Run 151,  $CQ = 1.46 \times 10^{-4}$ ,  $CQ/CQ_{151} = 1.13$   
 Run 150,  $CQ = 1.62 \times 10^{-4}$ ,  $CQ/CQ_{150} = 1.28$   
 Run 149,  $CQ = 1.72 \times 10^{-4}$ ,  $CQ/CQ_{149} = 1.35$

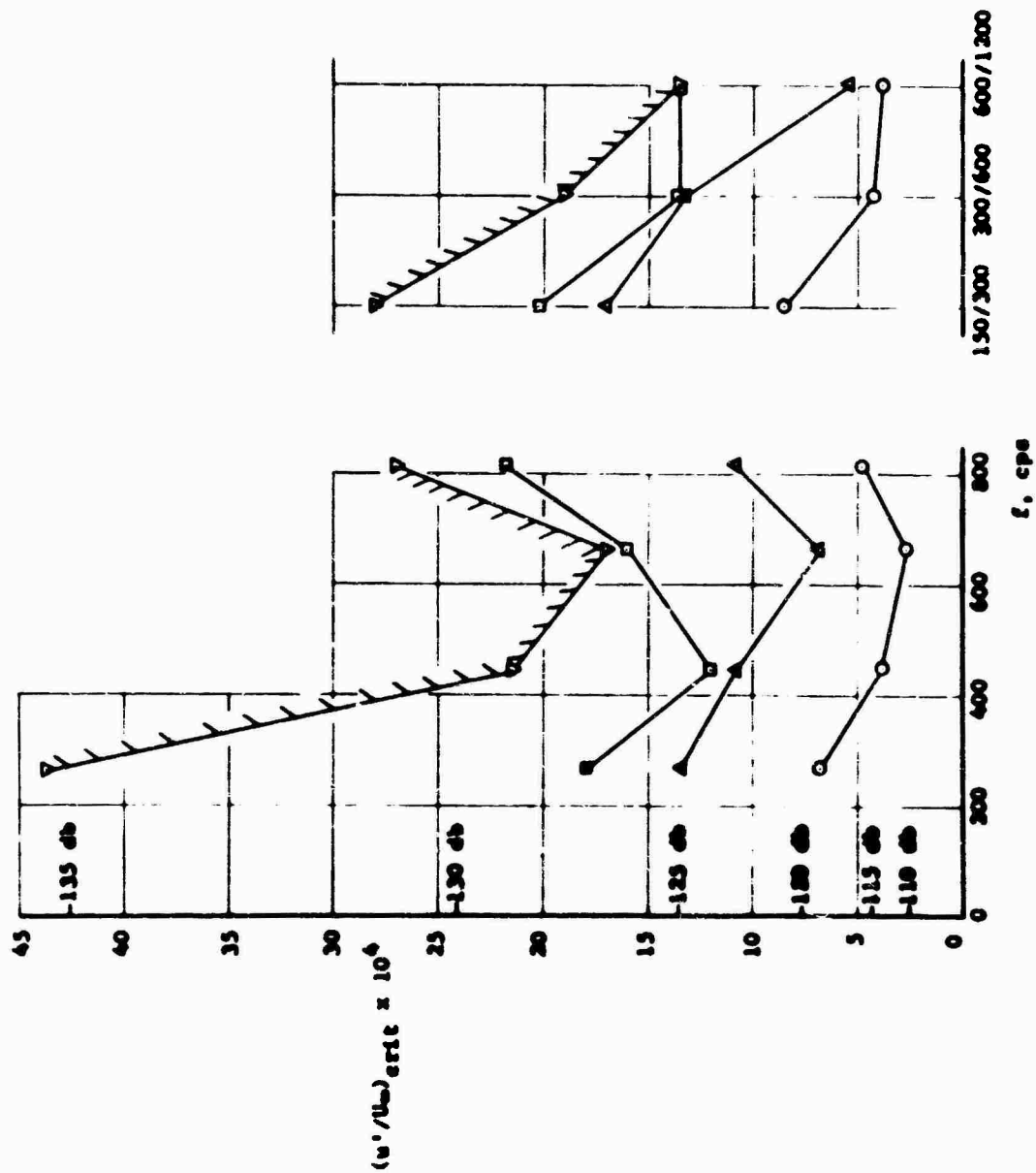
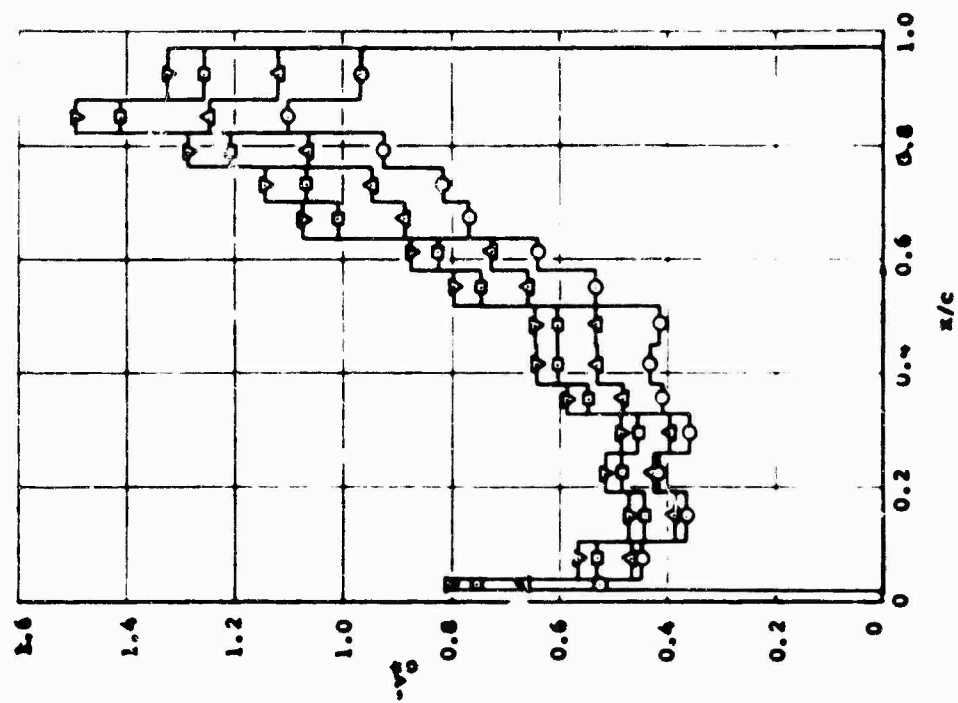


FIGURE 80 EFFECT OF VARIATION OF SUCTION LEVEL ON TRANSITION WITH EXTERNAL SOUND,  $R_c = 21.5 \times 10^6$



Run 122,  $C_Q = 1.11 \times 10^{-4}$ , Suction Starts at  $x/c = 0.106$   
 Run 123,  $C_Q = 1.14 \times 10^{-4}$ , Suction Starts at  $x/c = 0.020$

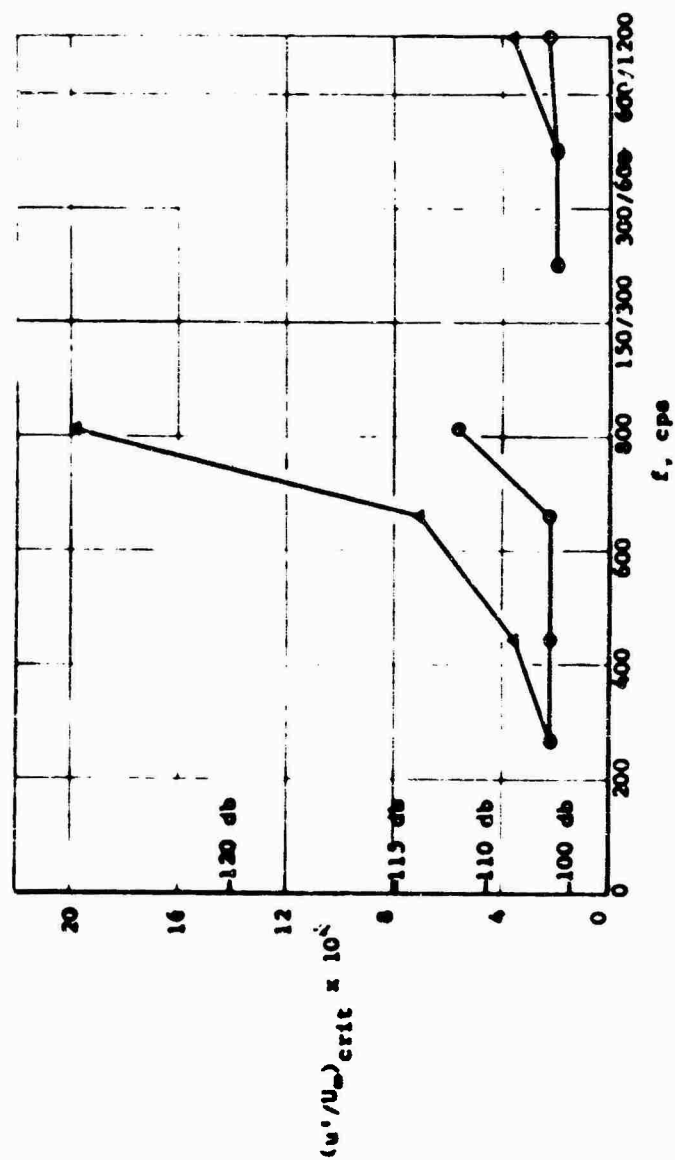
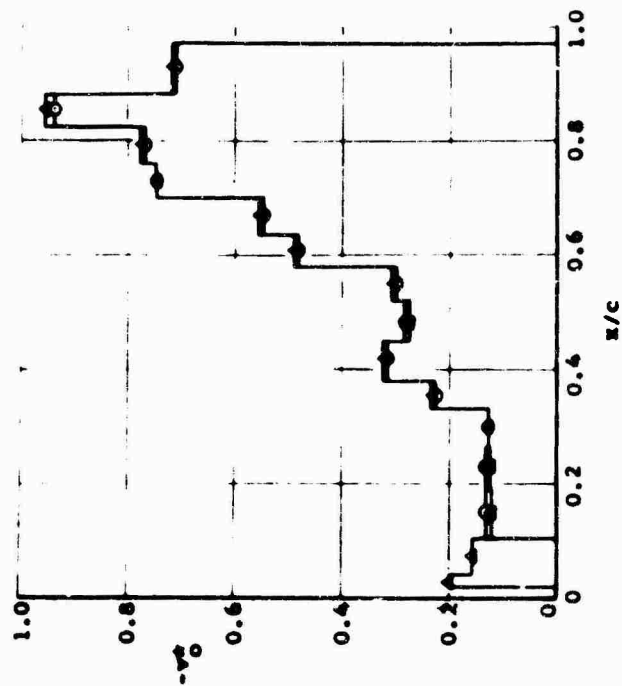


FIGURE 81 EFFECT OF FORWARD SUCTION ON TRANSITION WITH EXTERNAL SOUND,  $R_c = 11.5 \times 10^6$



Section Set for No Transition  
Open Static Location

$x/c = 0.002$   
 $x/c = 0.150$   
 $x/c = 0.464$   
 $x/c = 0.832$

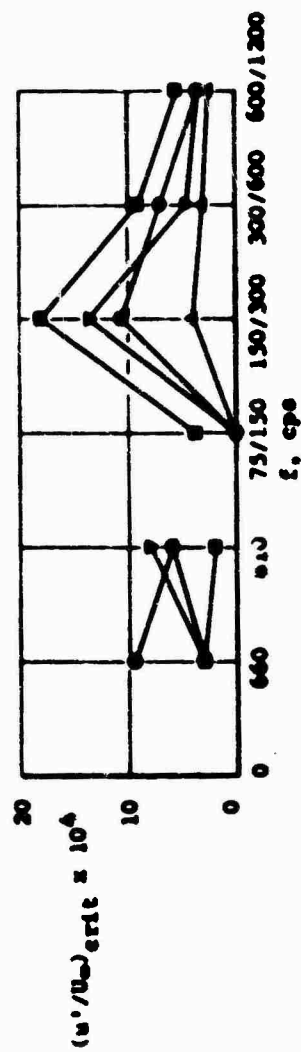
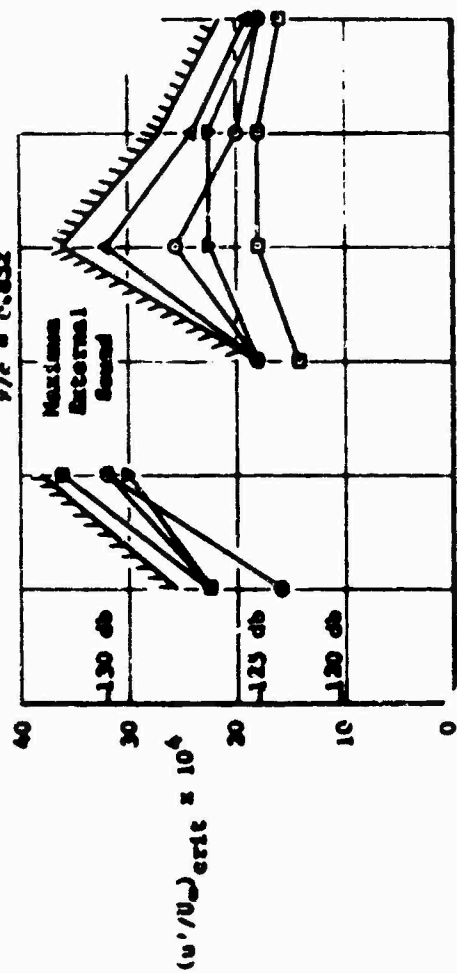
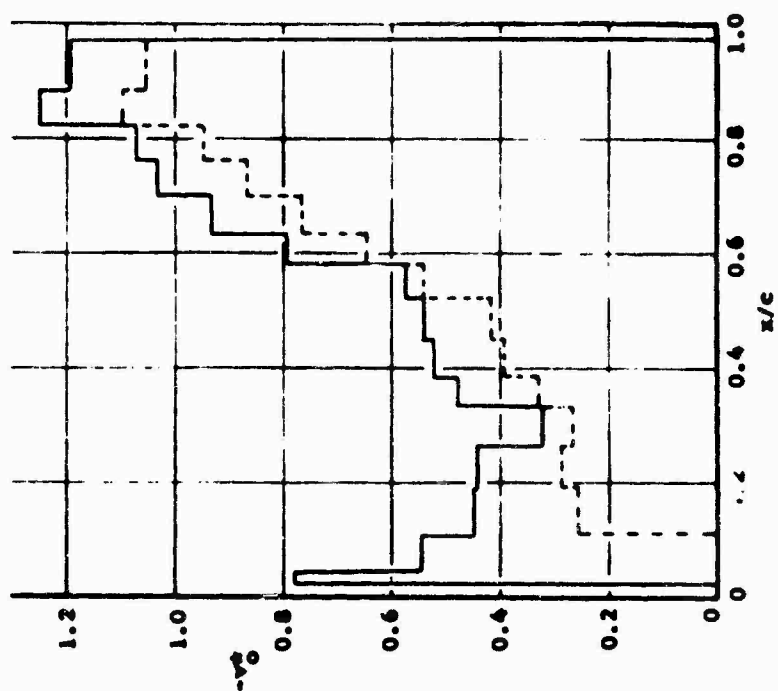


FIGURE 82 EFFECT OF SINGLE OPEN STATIC PRESSURE ORIFICE ON TRANSITION WITH EXTERNAL SOUND,  $R_c = 16.5 \times 10^6$

— No Transition Section (Run 96),  $C_Q = 1.72 \times 10^{-4}$   
 --- Minimum Drag Section (Run 19),  $C_Q = 1.29 \times 10^{-4}$



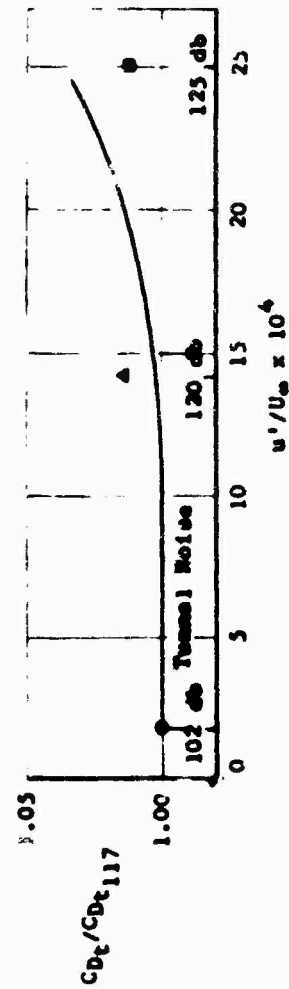
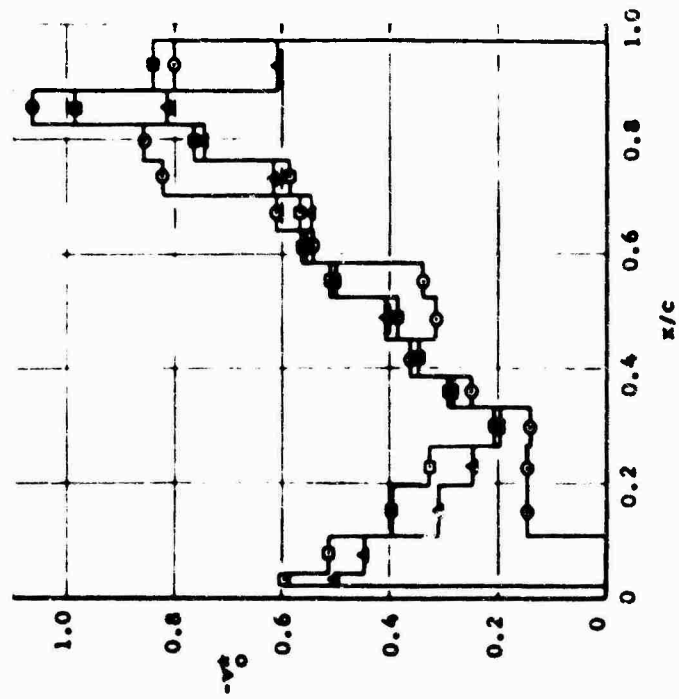
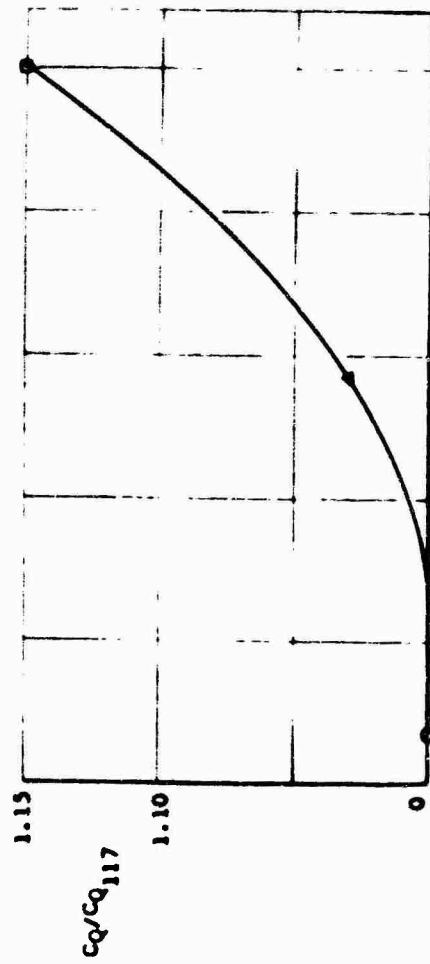


FIGURE 83 DRAG EFFECT OF INCREASING SUCTION QUANTITY TO MAINTAIN LAMINAR FLOW WITH EXTERNAL SOUND,  $R_c = 11.5 \times 10^6$



267 cps

Run 104,  $C_Q = 1.17 \times 10^{-4}$   
 Run 109,  $C_Q = 1.36 \times 10^{-4}$   
 Run 110,  $C_Q = 1.63 \times 10^{-4}$

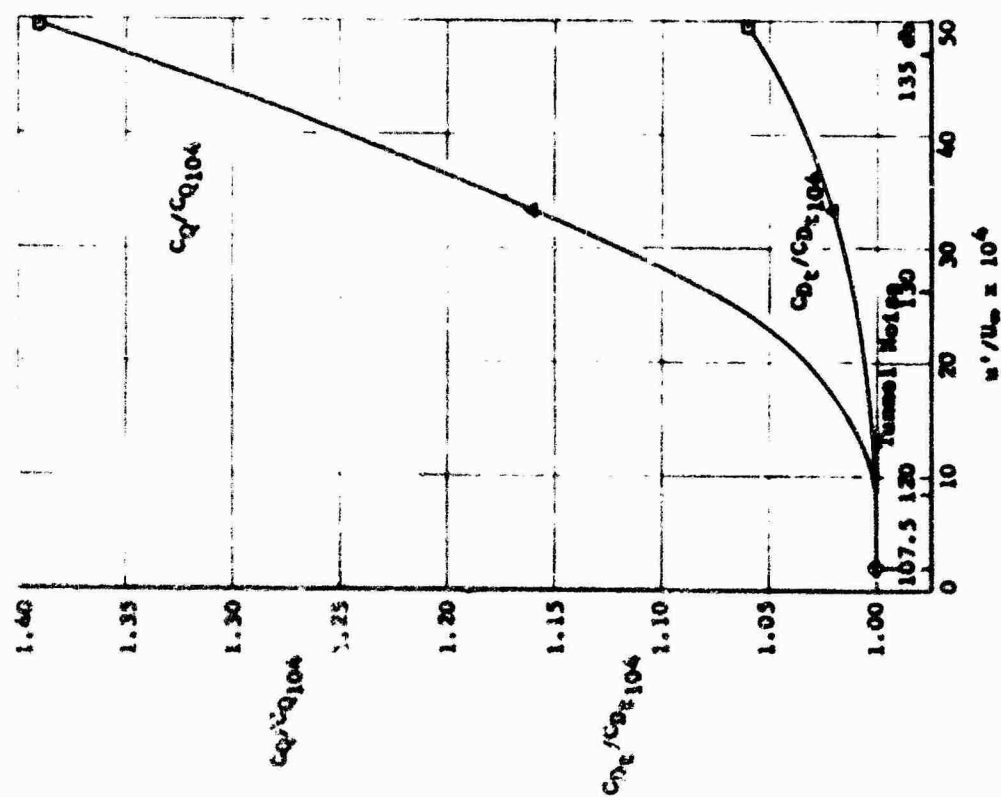
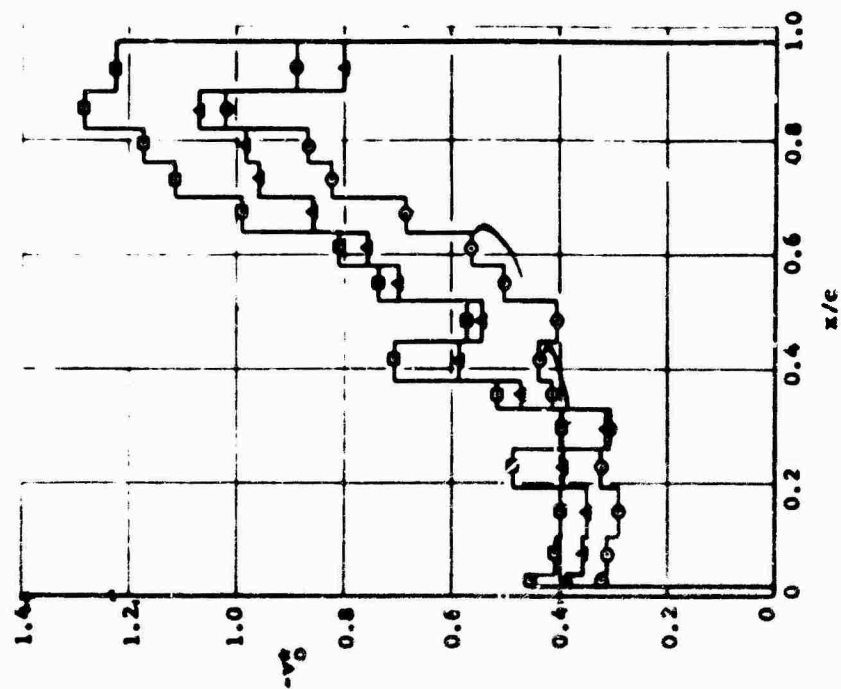


FIGURE 84 DRAG EFFECT OF INCREASING SUCTION QUANTITY TO MAINTAIN LAMINAR FLOW WITH EXTERNAL SOUND,  $R_c = 20.2 \times 10^6$



Runs 80-84, 660 cps,  $C_Q = 1.44 \times 10^{-4}$   
 Runs 75-79, 810 cps,  $C_Q = 1.36 \times 10^{-4}$

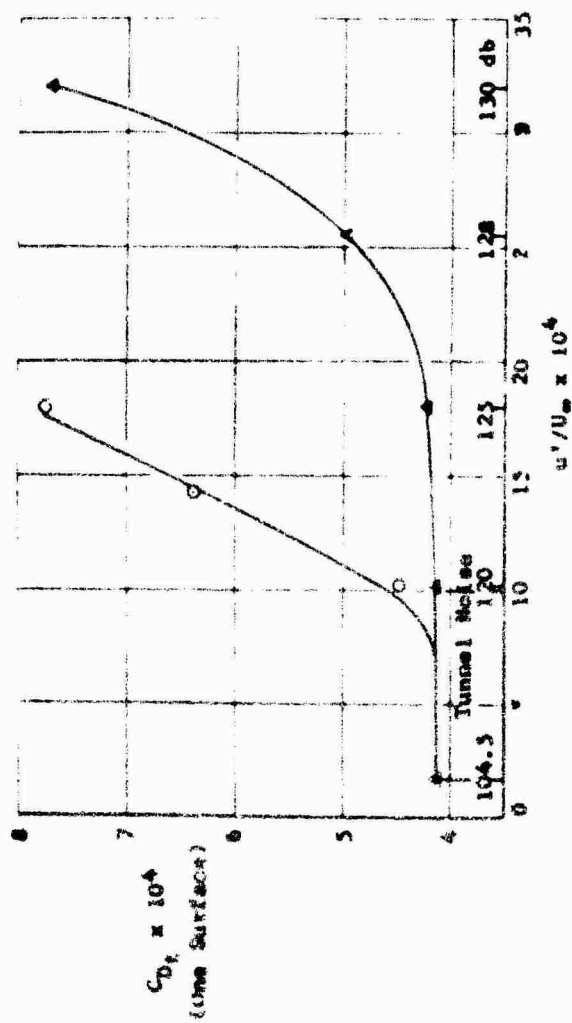
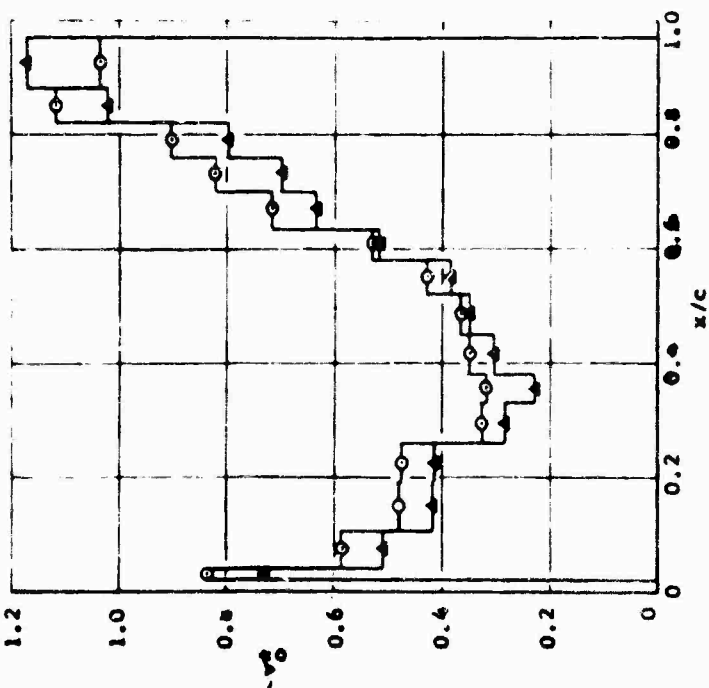


FIGURE 85 VARIATION OF TOTAL DRAG WITH EXTERNAL SOUND AT CONSTANT SUCTION QUANTITY,  $R_c = 16.5 \times 10^6$

663 cps

Runs 31-33,  $C_Q = 1.39 \times 10^{-4}$

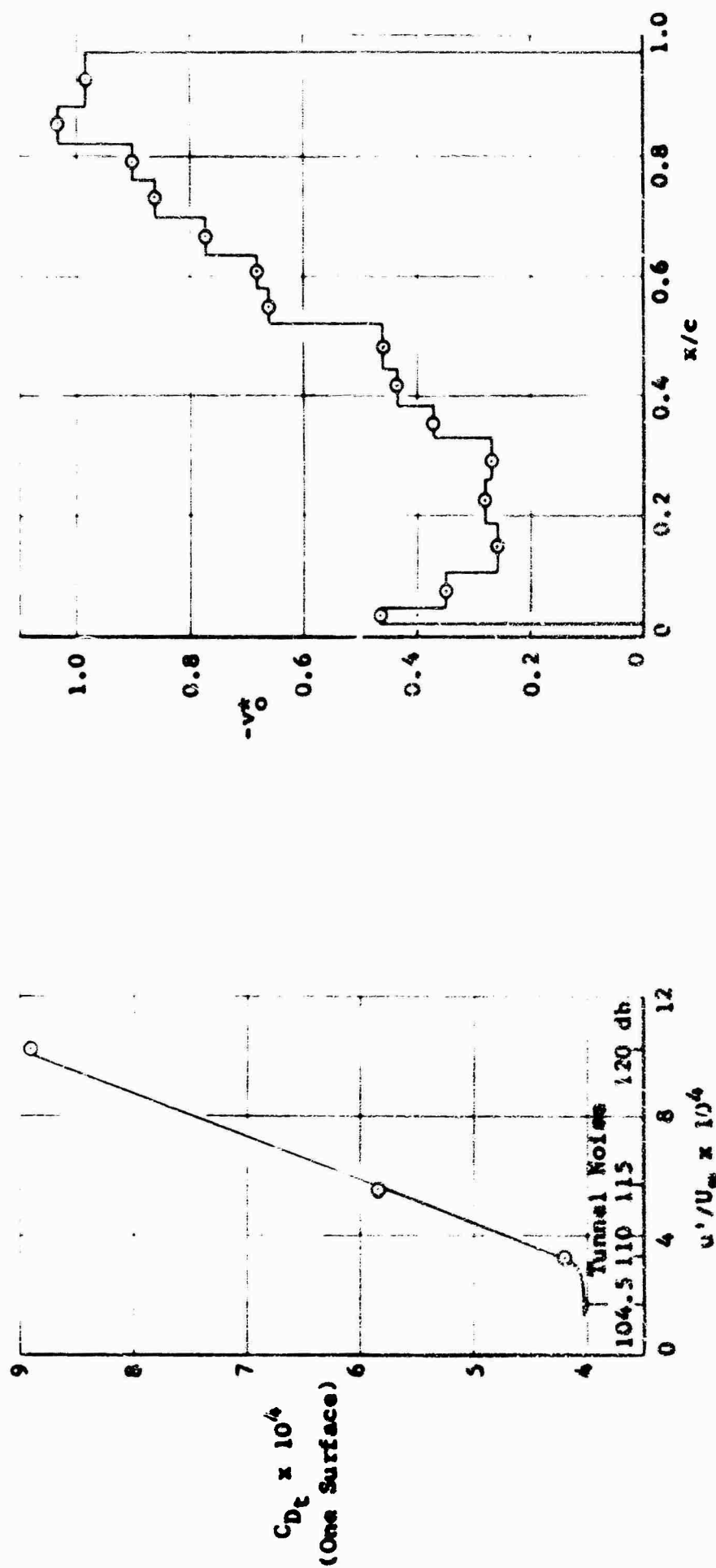


FIGURE 36 VARIATION OF TOTAL DRAG WITH EXTERNAL SOUND AT CONSTANT SUCTION QUANTITY,  $R_c = 16.5 \times 10^6$

Run 87-90, 442 cps  
Run 94-96, 150/300 cps  
Run 91-94, 300/600 cps

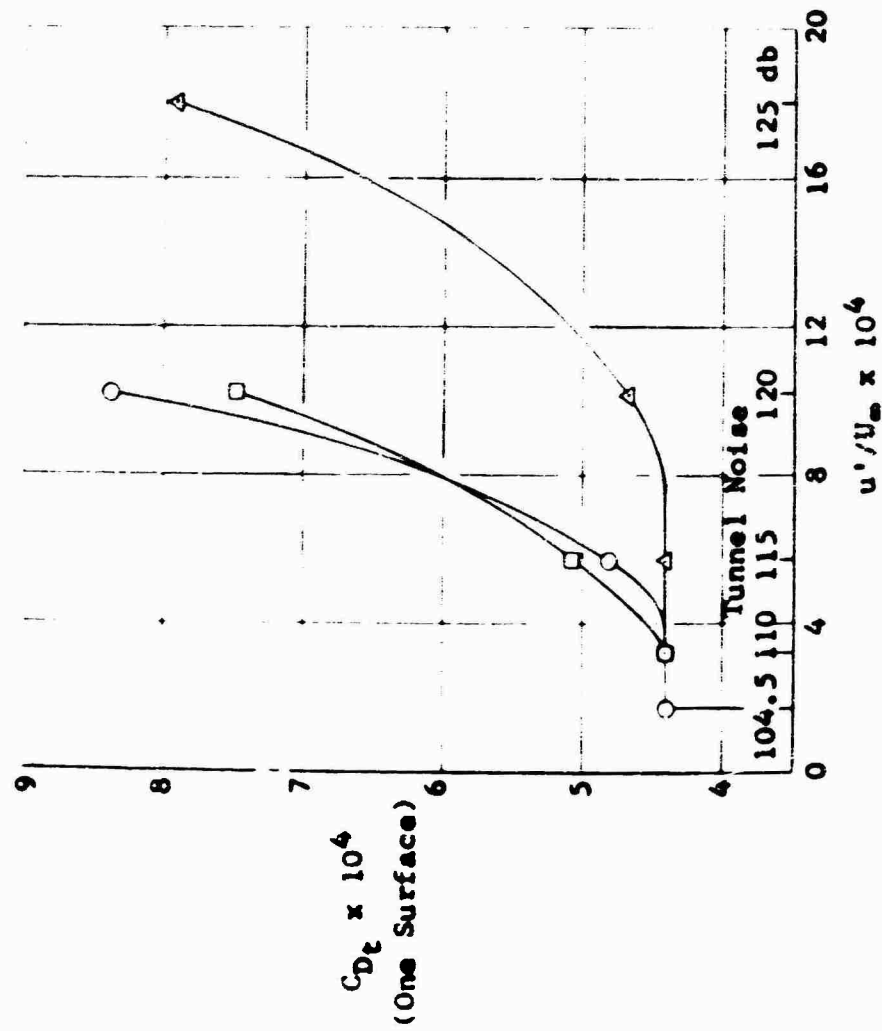
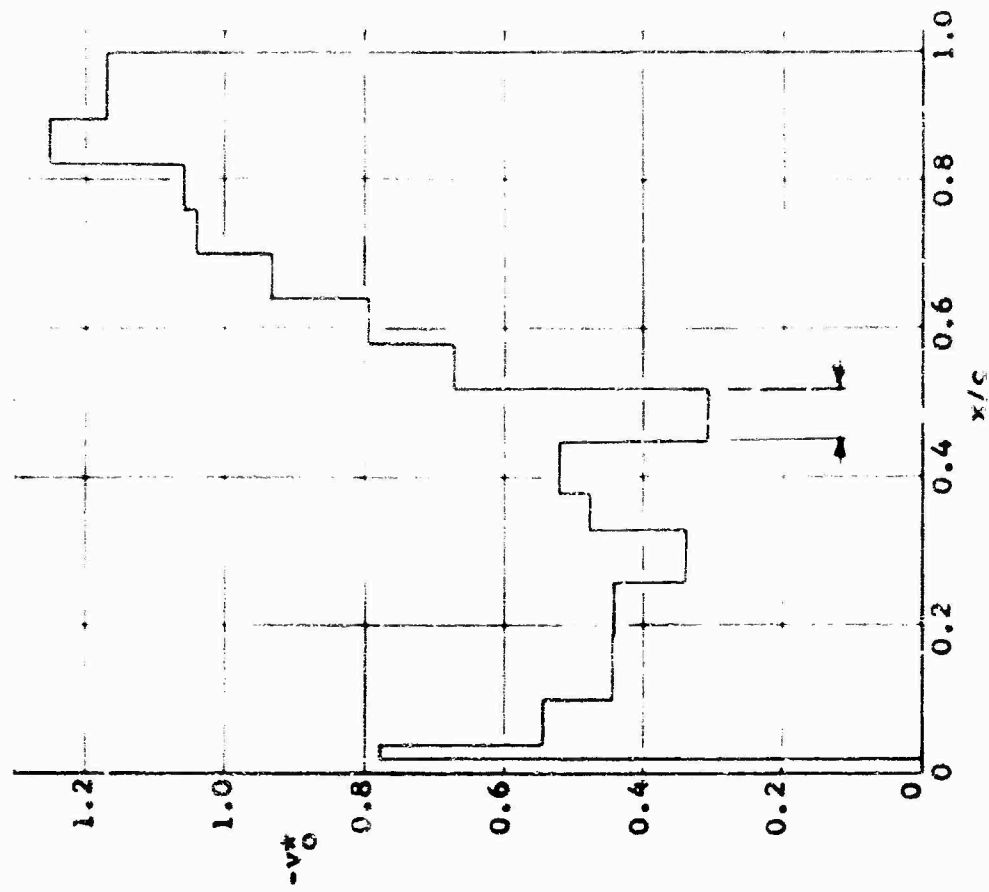


FIGURE 87 VARIATION OF TOTAL DRAG WITH EXTERNAL SOUND AT CONSTANT SUCTION QUANTITY  
(SUCTION LOW ON CHAMBER NO. 9,  $x/c = 0.45$  TO  $0.523$ ),  $R_c = 16.4 \times 10^6$



805 cps

Runs 60-64,  $C_Q = 1.37 \times 10^{-4}$

Runs 65-69,  $C = 1.37 \times 10^{-4}$

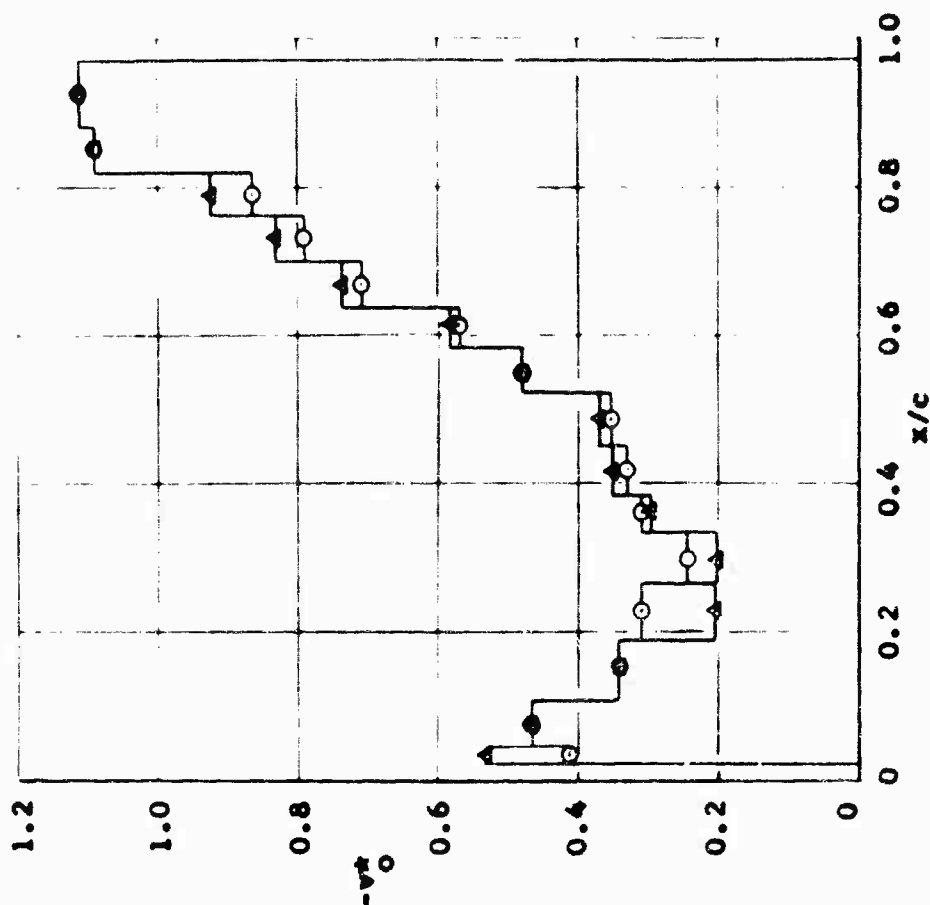
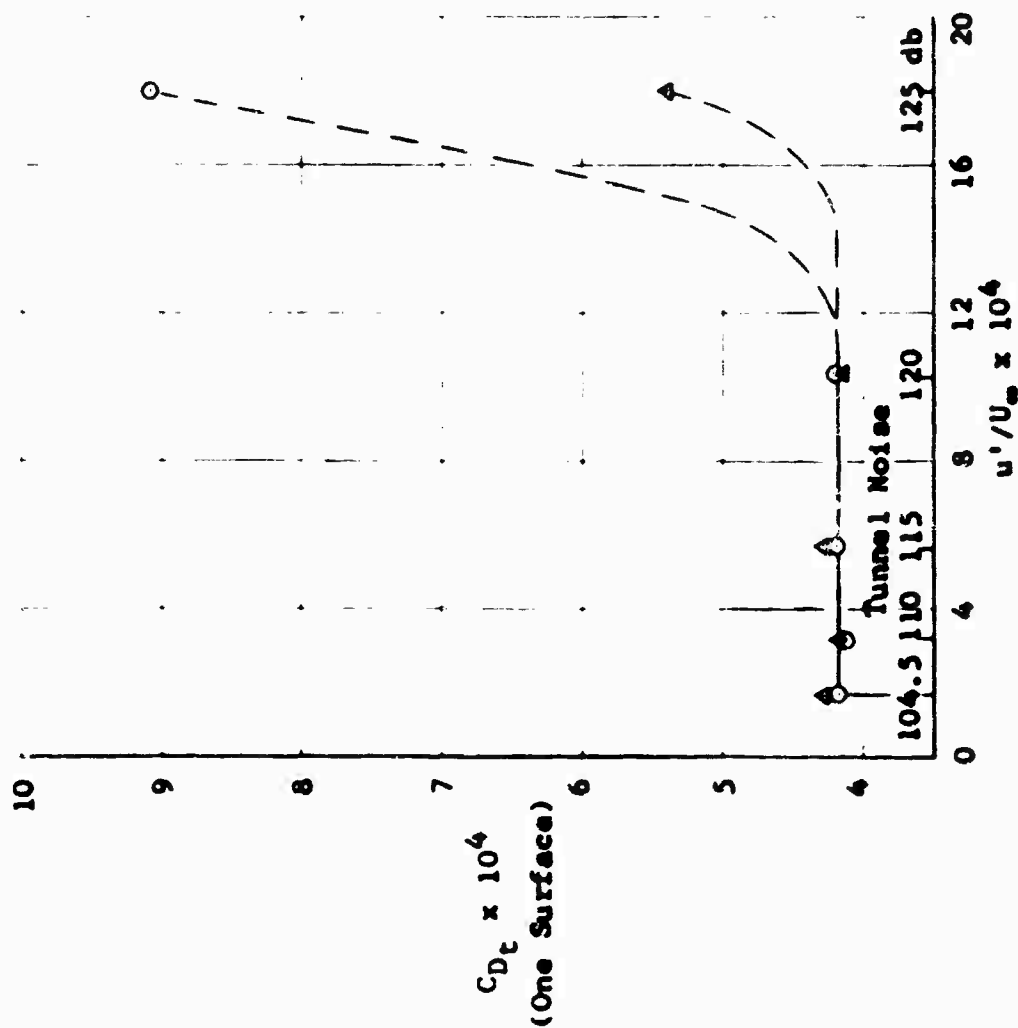


FIGURE 88 VARIATION OF TOTAL DRAG WITH EXTERNAL SOUND AT CONSTANT SUCTION QUANTITY

(STATICS OPEN BEHIND 40 PERCENT C),  $R_C = 16.4 \times 10^6$

$R_c = 11.5 \times 10^6$   
 $R_c = 16.4 \times 10^6$   
 $R_c = 20.2 \times 10^6$   
 $R_c = 21.5 \times 10^6$

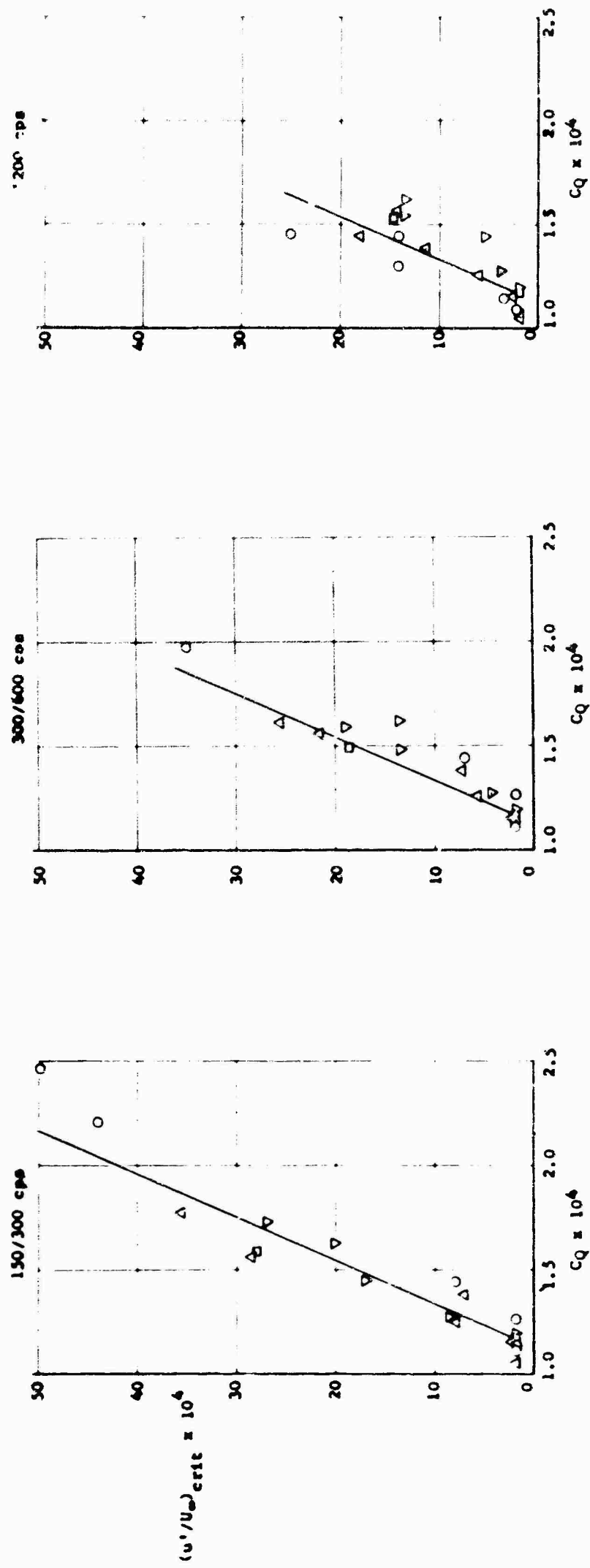


FIGURE 89 VELOCITY FLUCTUATION OF EXTERNAL SOUND FIELD TO CAUSE TRANSITION VS SUCTION QUANTITY AT VARIOUS CHORD REYNOLDS NUMBERS

LONGITUDINAL TRANSDUCER

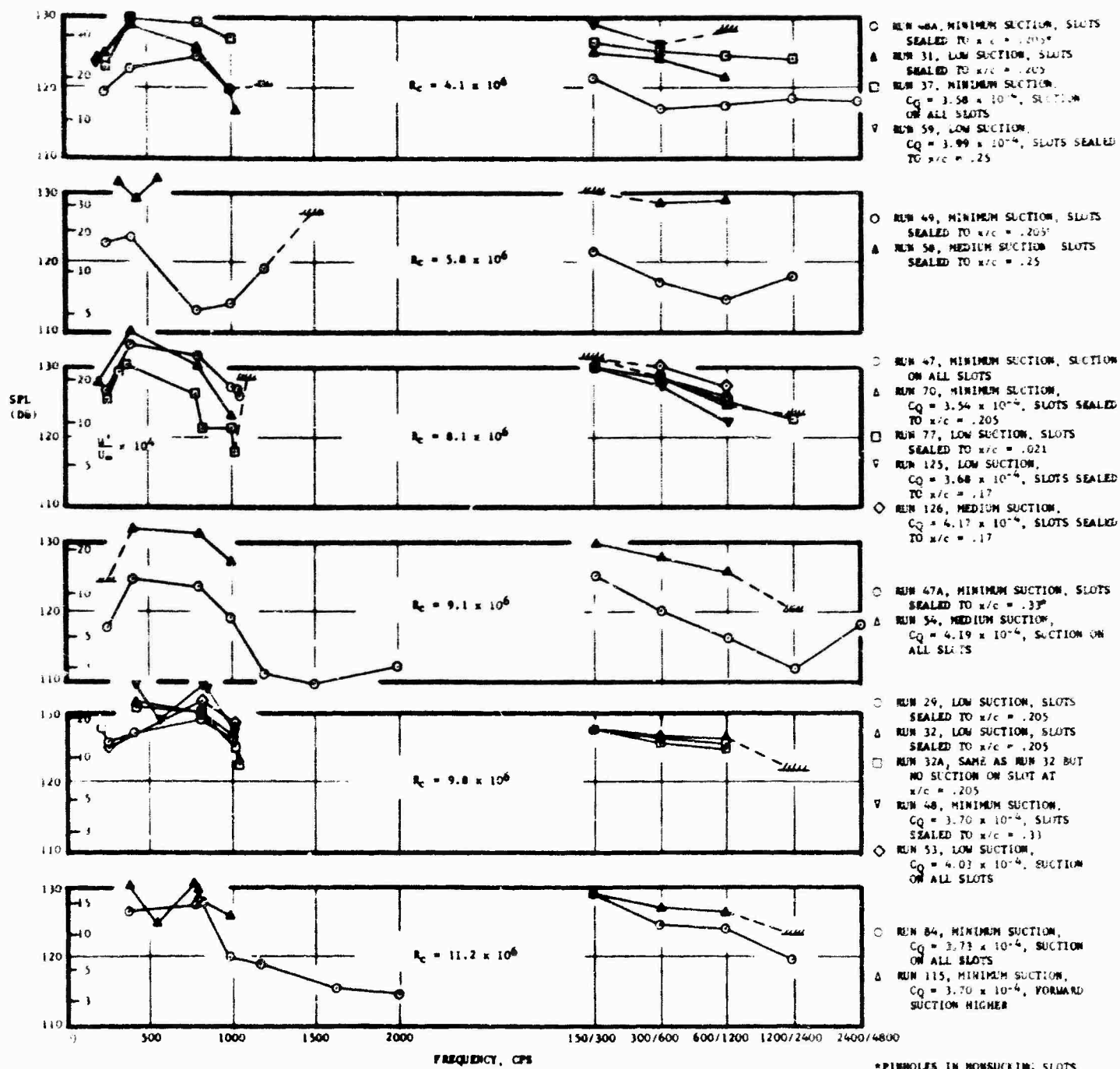


FIGURE 90

SOUND PRESSURE LEVEL FOR TRANSITION AS A FUNCTION OF FREQUENCY  
30° SWEEP SUCTION WING UNDER THE INFLUENCE OF SOUND

# TRANS-STATE SOUND

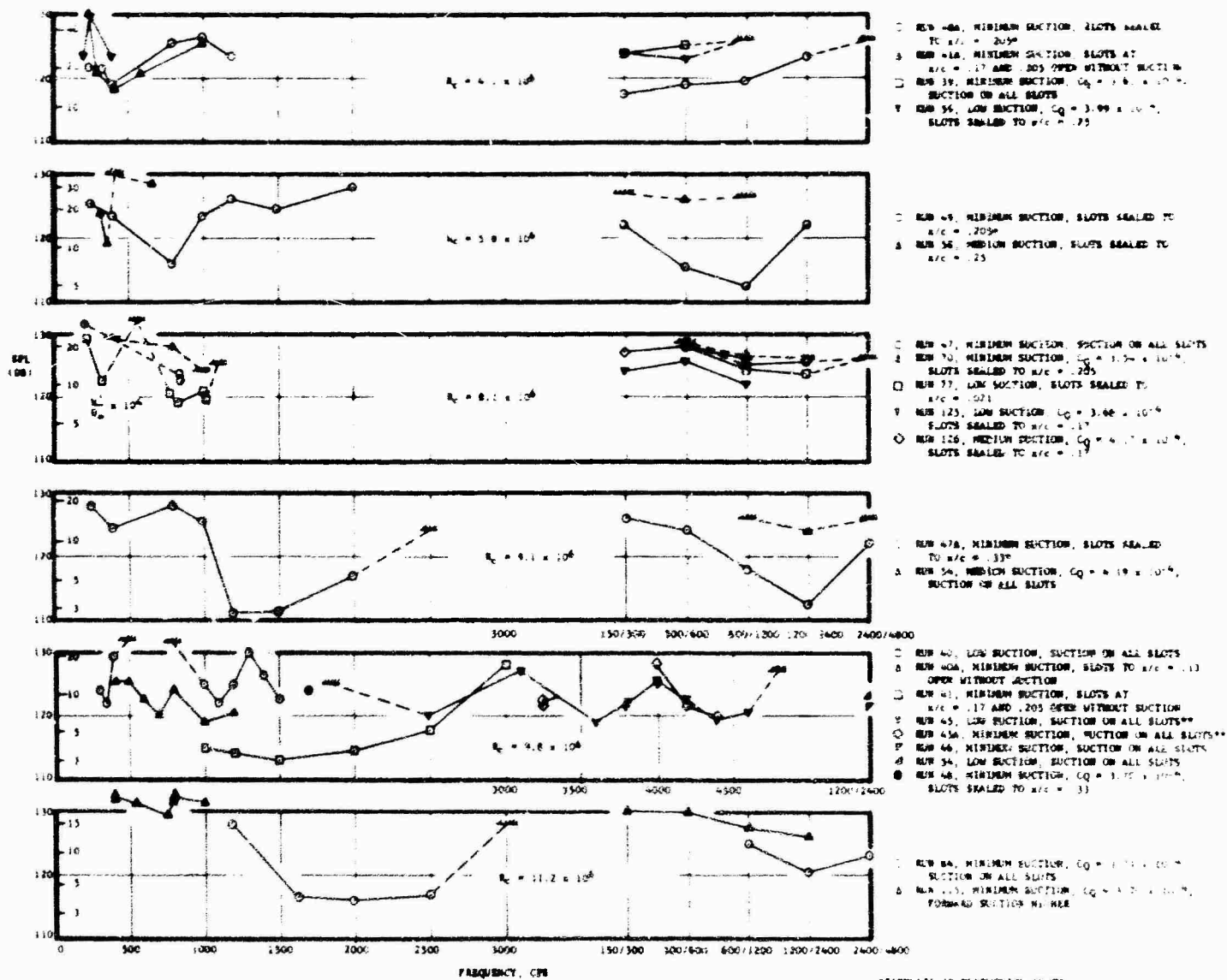


FIGURE 91

SOUND PRESSURE LEVEL FOR TRANSITION AS A FUNCTION OF FREQUENCY  
10<sup>3</sup> SWEEP SECTION WIND UNDER THE INFLUENCE OF SOUND

\*PINNULAE IN NONSWEEPING SLOTS  
\*\*FRONT STATIC PRESSURE (WIPES CLEANED), REAR STATIC PRESSURE (WIPES OPEN) (BUT NOT CLEANED) - NO TRANSITION UP TO THE MAXIMUM AVAILABLE SOUND LEVEL ABOUT 2000 CPS WITH REAR STATIC PRESSURE (WIPES OPEN)



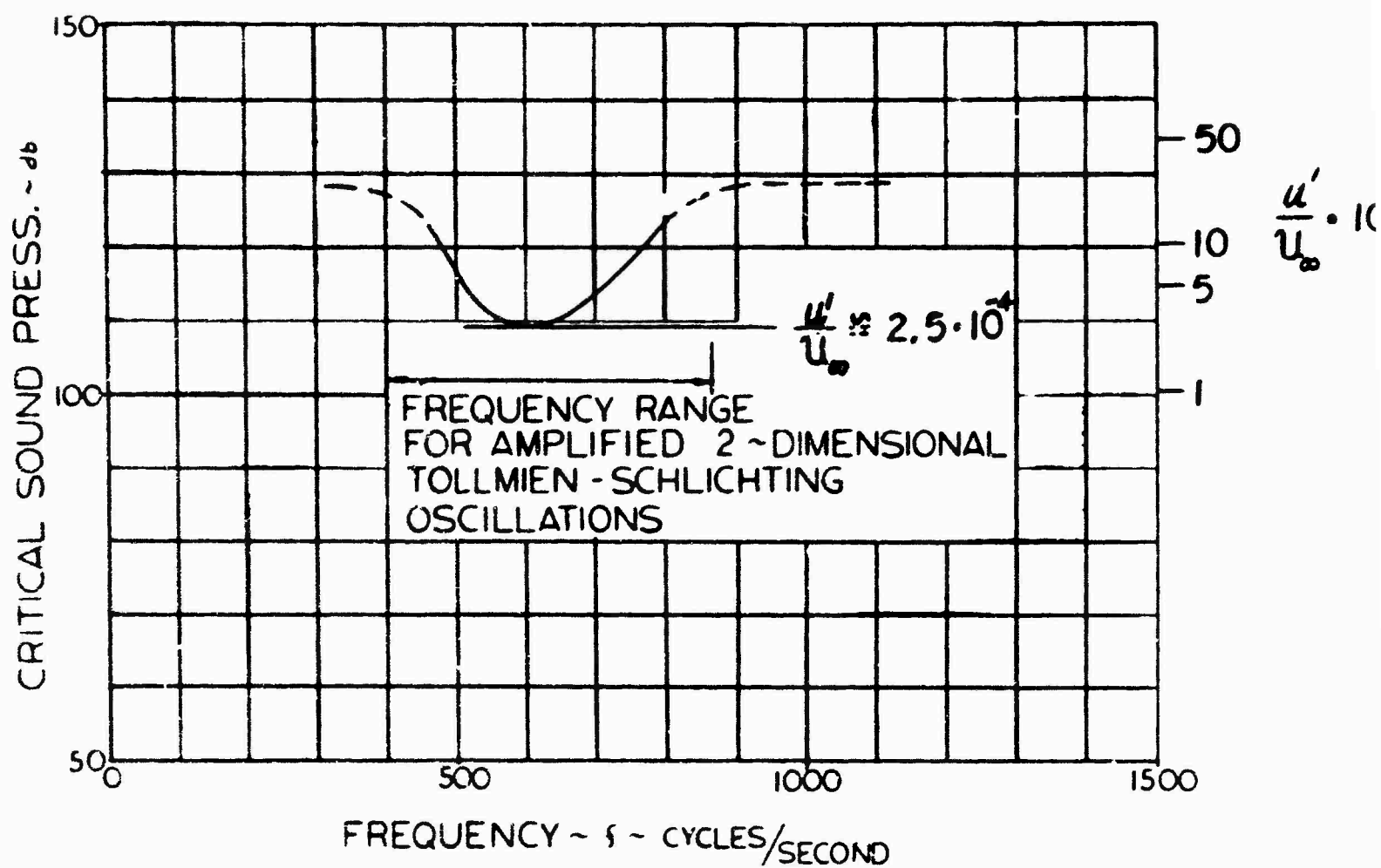


FIGURE 92

SOUND OF DISCRETE FREQUENCIES ALONG TUNNEL AXIS WITH SUCTION FROM 0.5c to 0.95c, FRONT SLOTS AND STATIC PRESSURE ORIFICES SEALED.  
(No suction upstream of 0.5c)  $R_c = 7 \times 10^6$

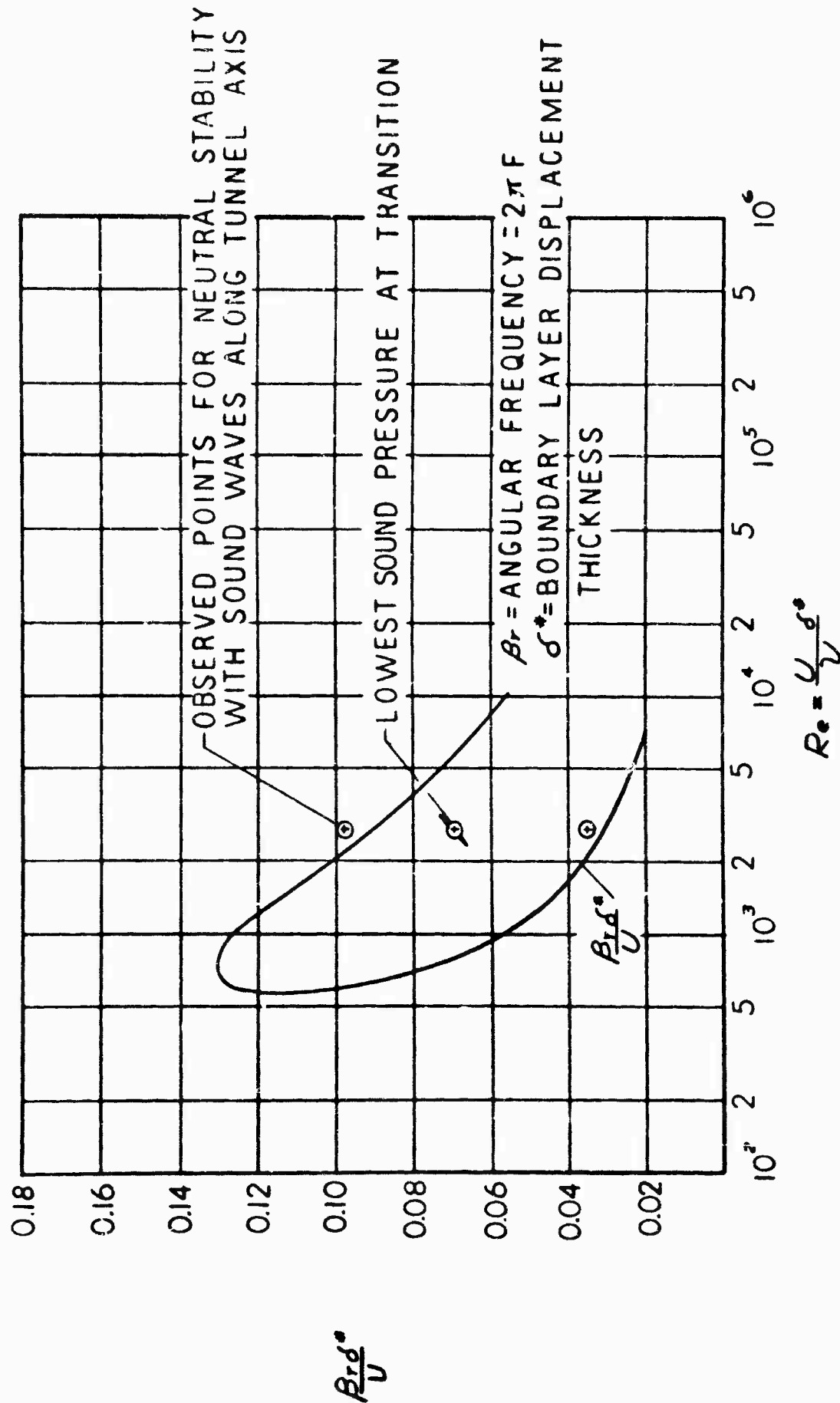


FIGURE 93

TOLLMJEN-SCHLICHTING INSTABILITY AGAINST 2 DIMENSIONAL DISTURBANCES (DISTURBANCE WAVE FRONTS ALONG WING SPAN)

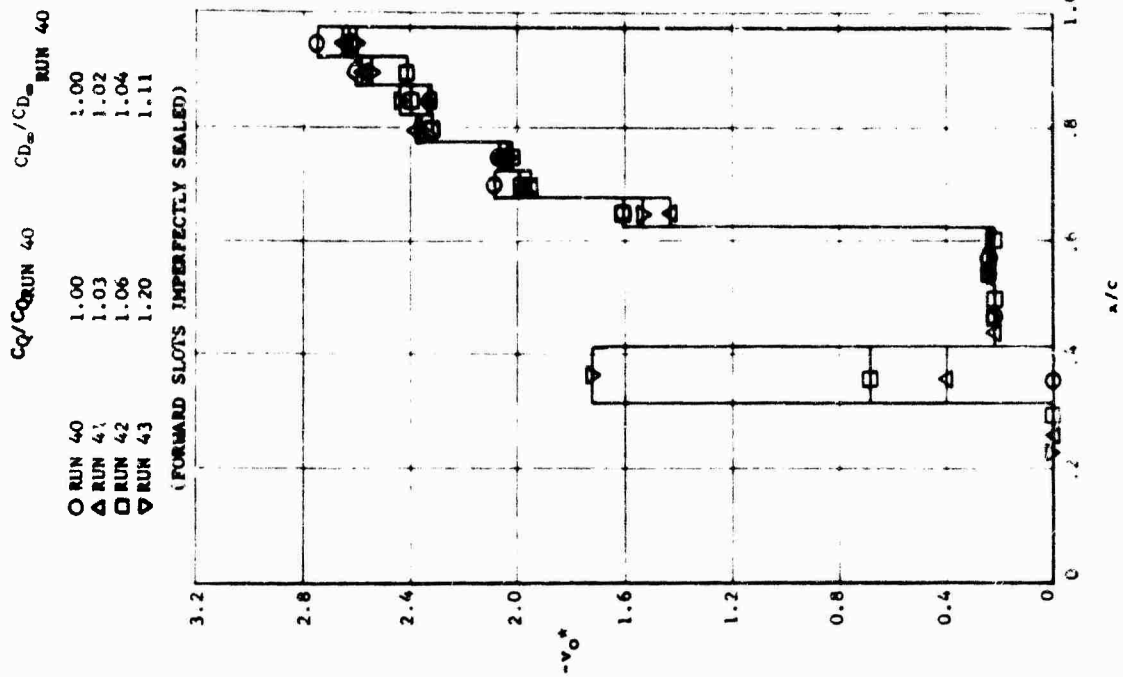
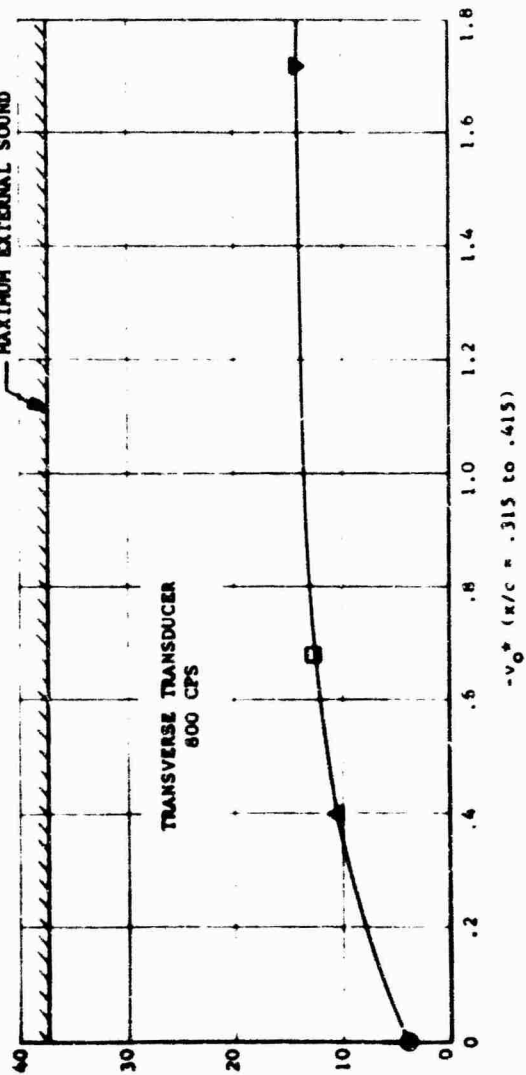
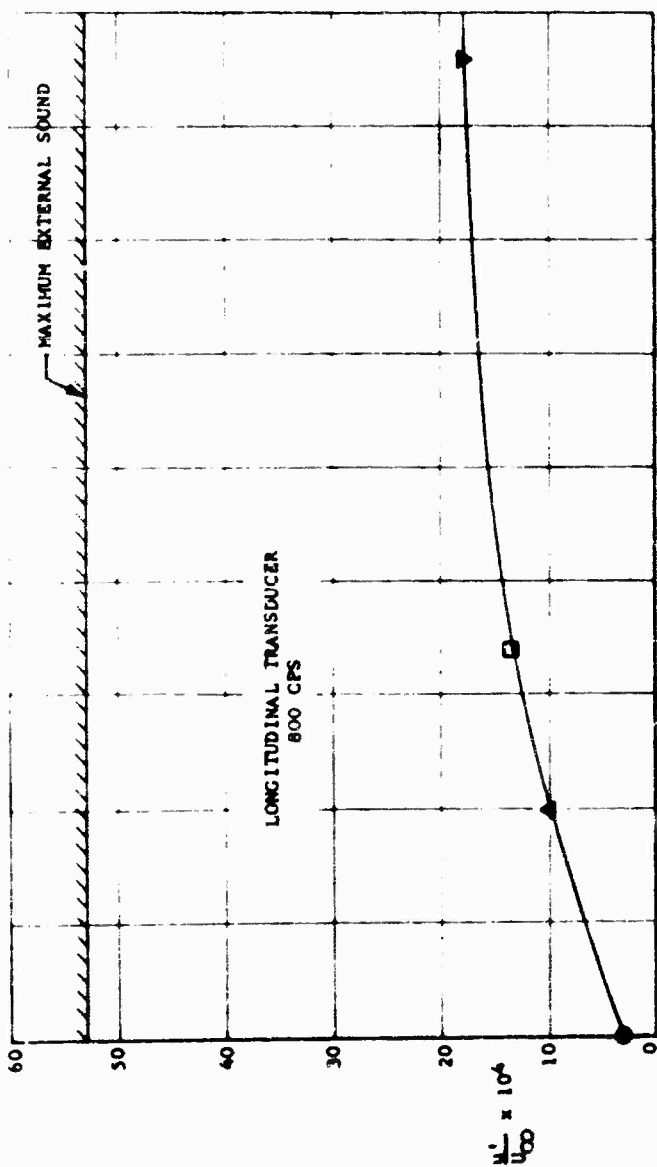


FIGURE 94

TRANSITION LIMIT WITH INCREASING SUCTION ON ONE CHAMBER  
30° SWEEP SUCTION WING UNDER THE INFLUENCE OF SOUND  
 $R_c = 5.8 \times 10^6$

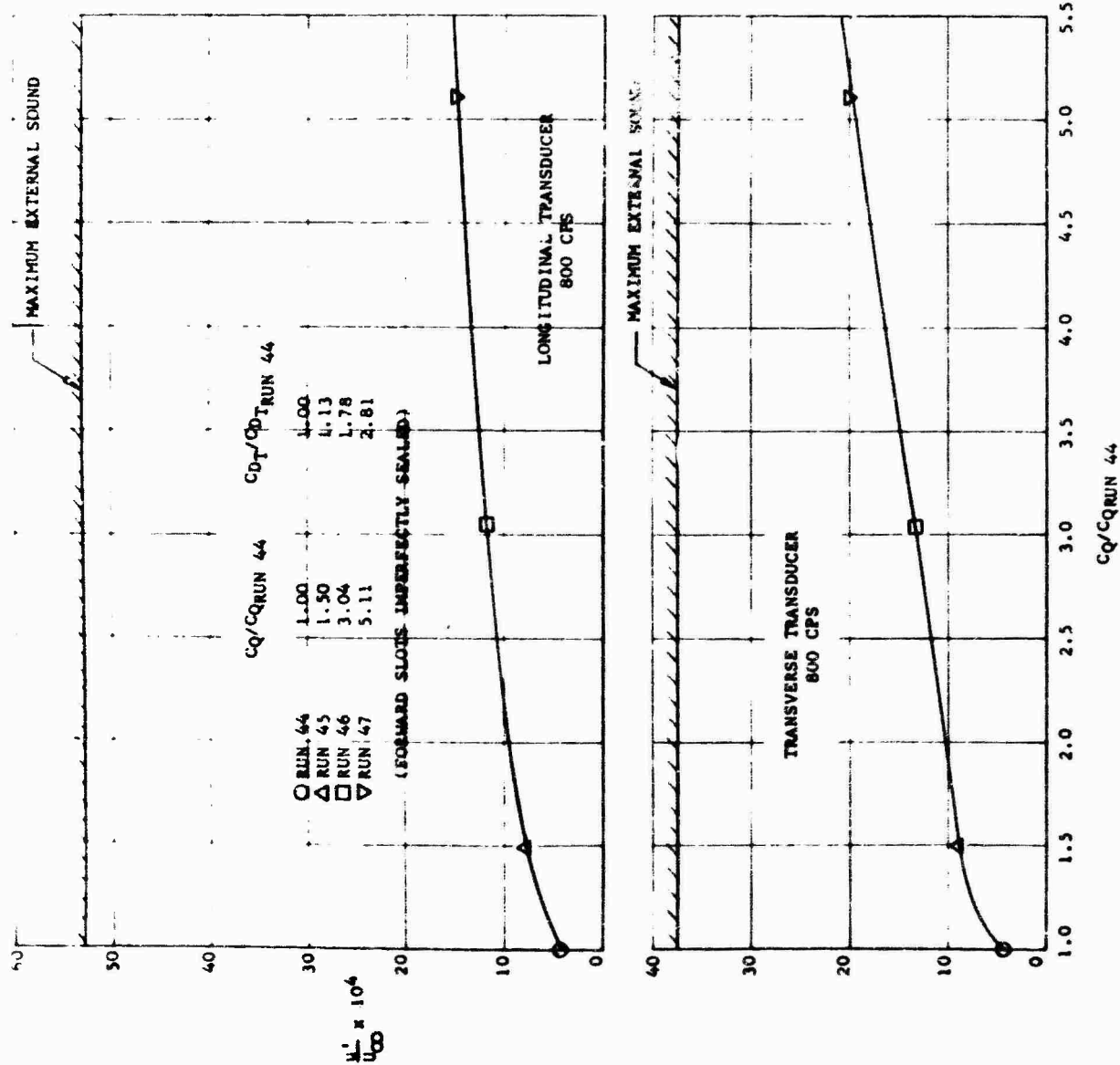
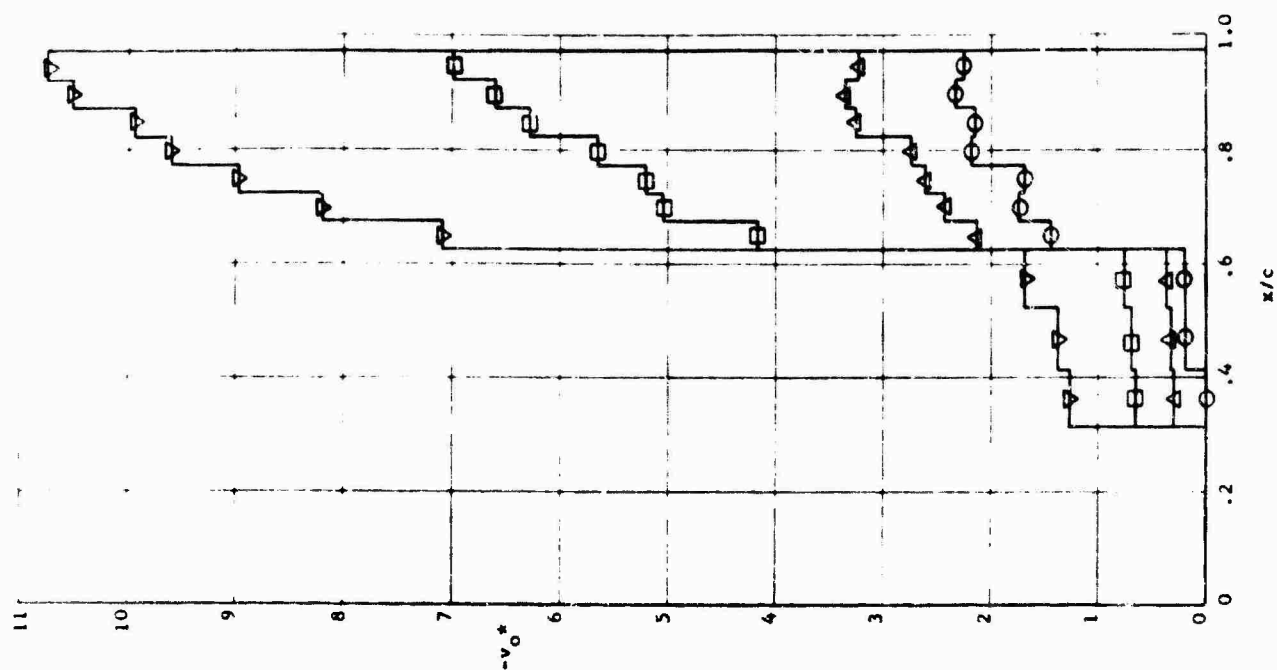
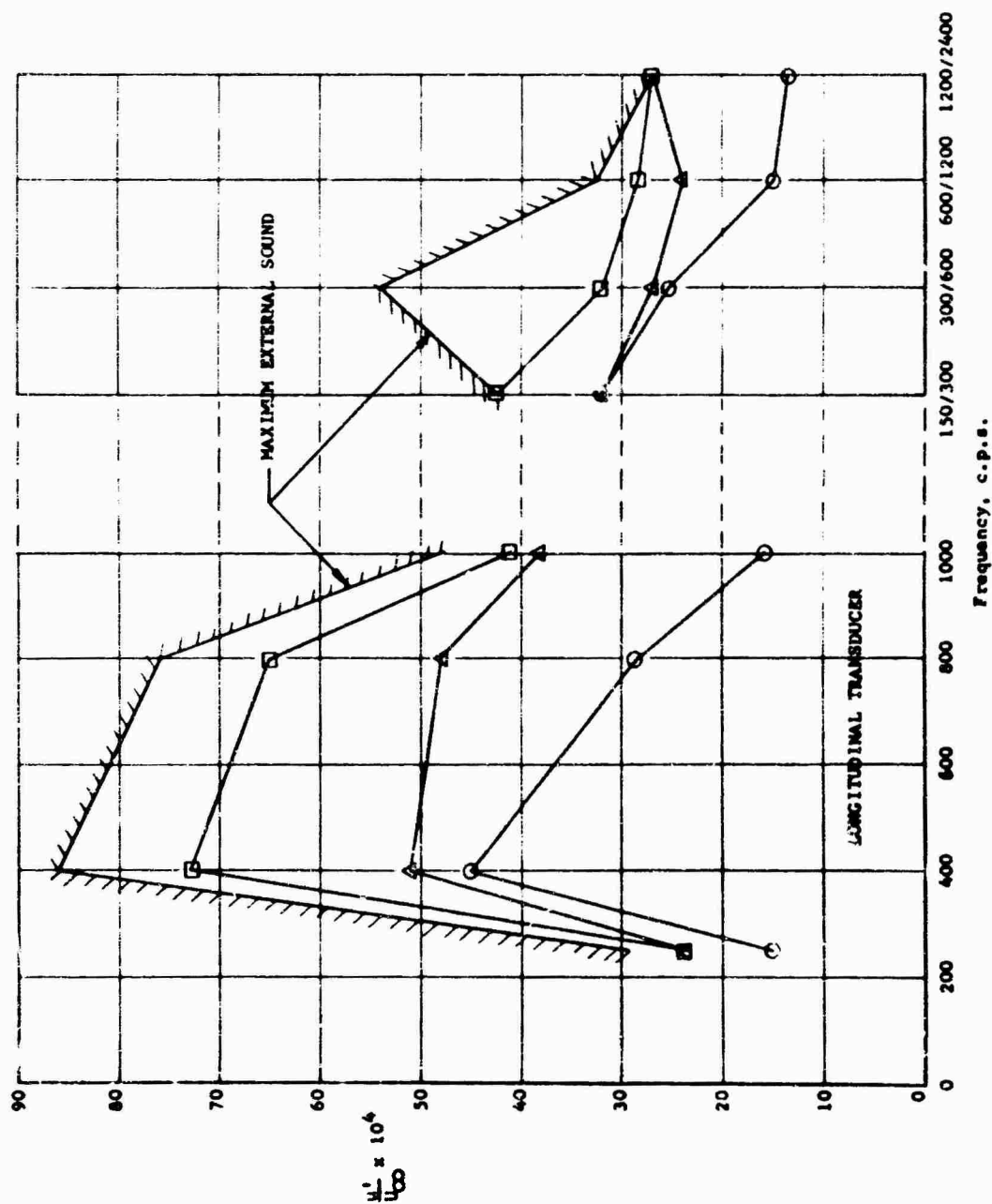


FIGURE 95  
TRANSITION LIMIT WITH INCREASING SUCTION LEVEL  
30° SWEEP SUCTION WING UNDER THE INFLUENCE OF SOUND  
 $R_c = 5.8 \times 10^6$



$C_D/C_{D_{RUN\ 36}}$   
 RUN 36 1.00  
 RUN 37 1.13  
 RUN 38 1.22  
 $C_{D_{max}}/C_{D_{RUN\ 36}}$   
 RUN 36 1.00  
 RUN 37 1.05  
 RUN 38 1.09  
 (STATIC PRESSURE ORIFICES OPEN)

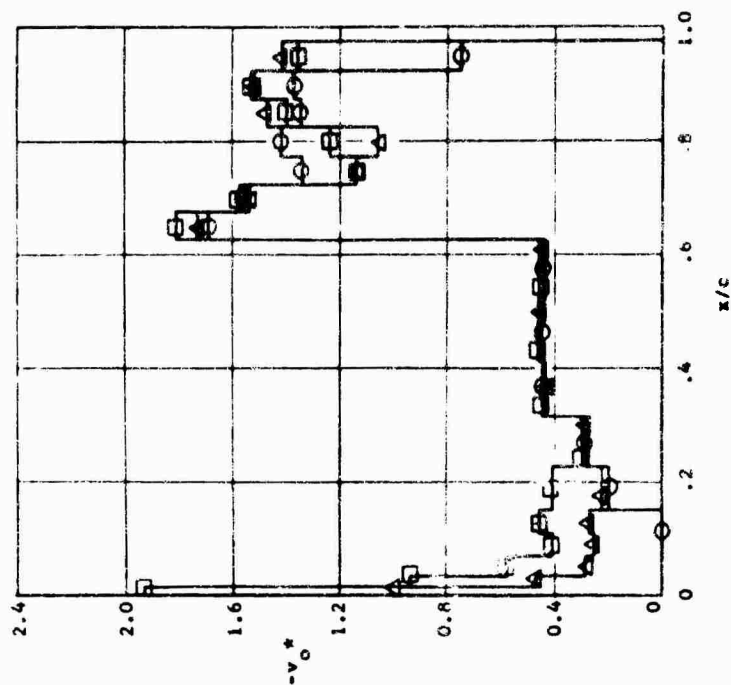


FIGURE 96  
 TRANSITION LIMIT WITH INCREASING FORWARD SUCTION  
 300 SWEET SUCTION WING UNDER THE INFLUENCE OF SOUND  
 $R_c = 4.1 \times 10^6$

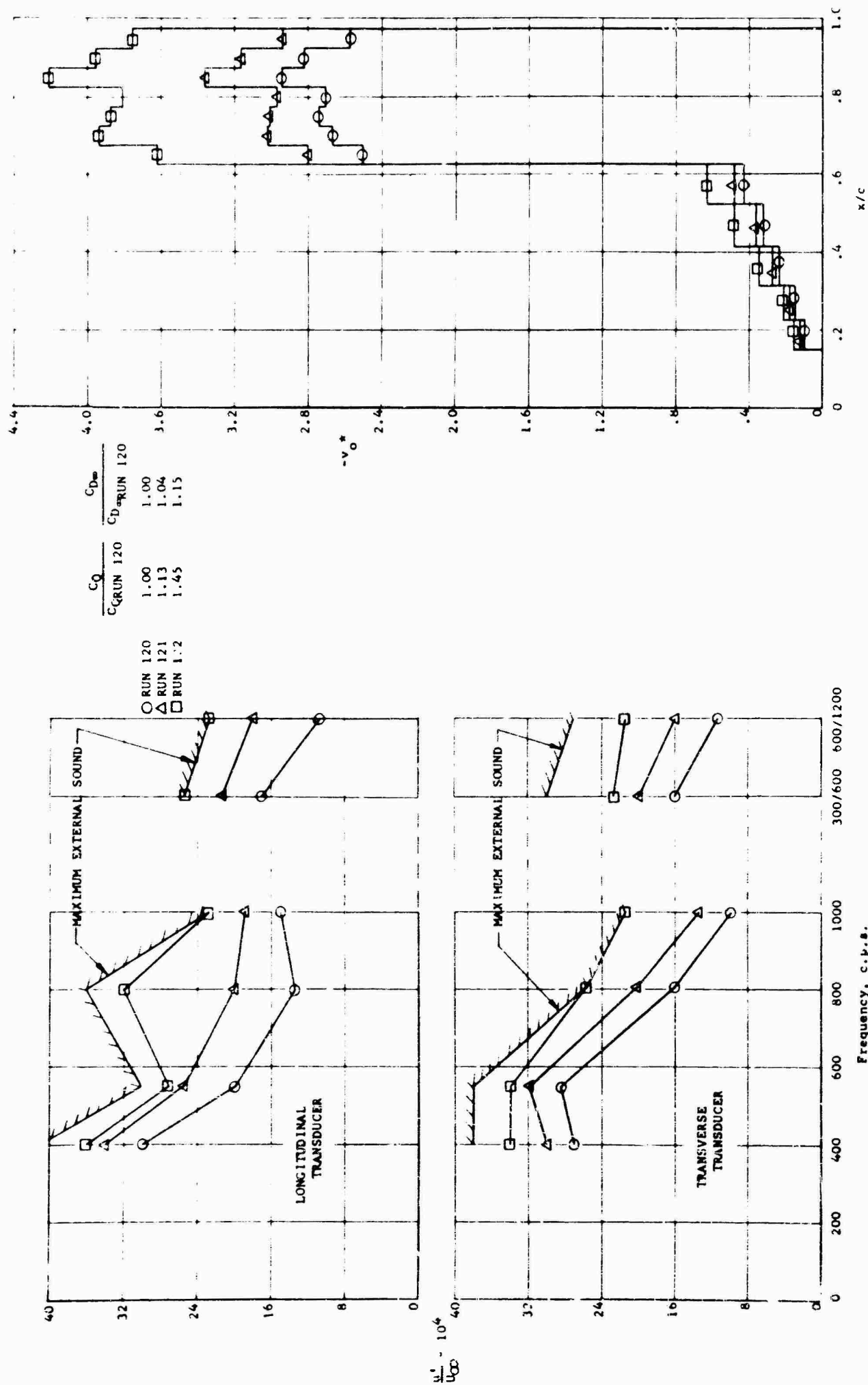
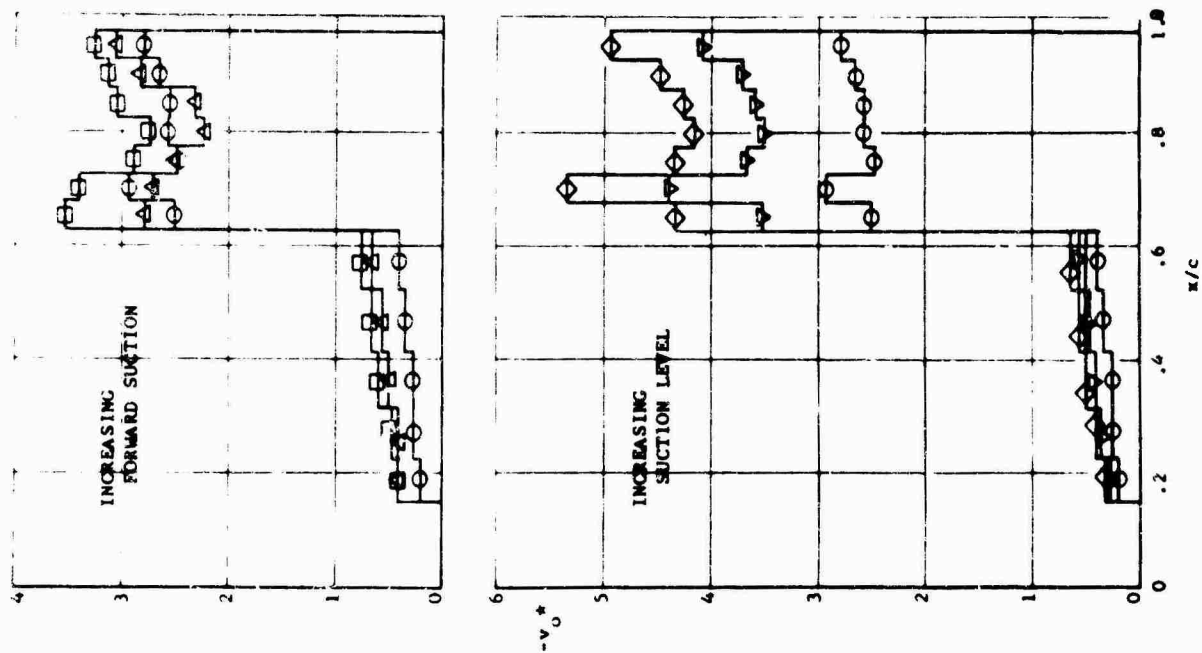
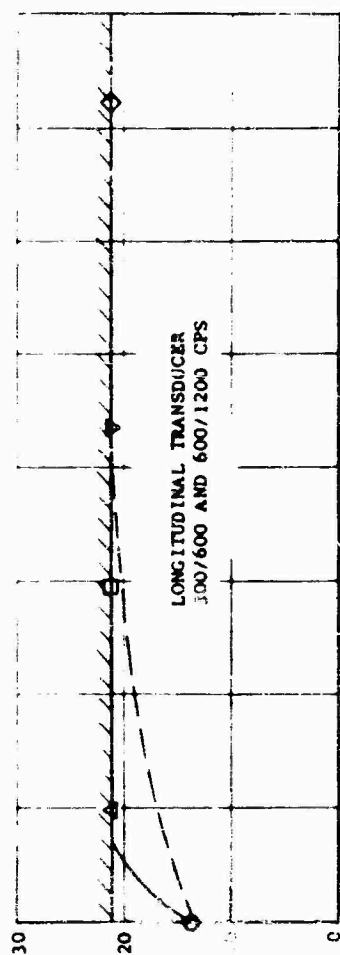


FIGURE 97  
TRANSITION LIMIT WITH INCREASING SUCTION LEVEL  
30° SWEEP SUCTION WING UNDER THE INFLUENCE OF SOUND  
 $R_c = 8.1 \times 10^6$



- RUN 130
- △ RUN 128
- RUN 133
- ▽ RUN 131
- ◇ RUN 132

- INCREASING FORWARD SUCTION
- - - INCREASING SUCTION LEVEL
- /// MAXIMUM EXTERNAL SOUND



$\frac{u'}{u_0} \times 10^4$

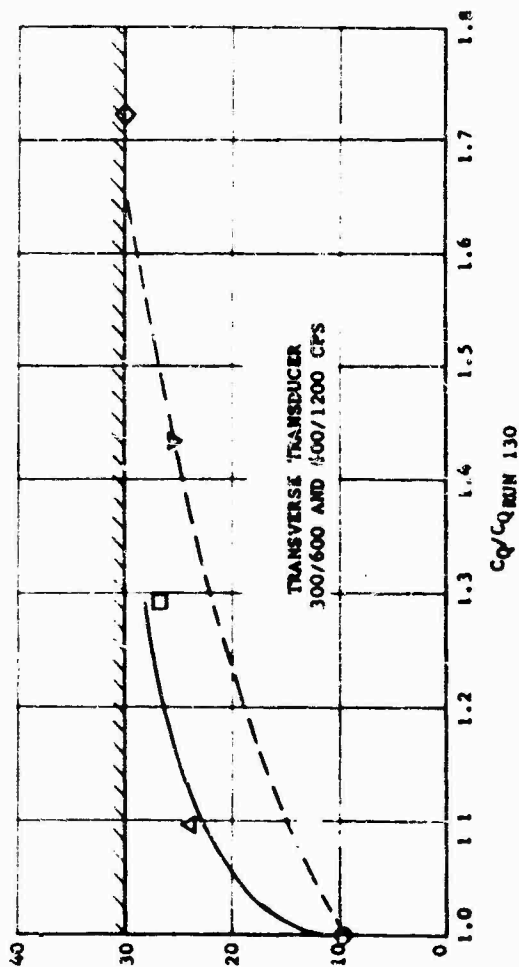


FIGURE 98  
TRANSITION LIMIT WITH INCREASING FORWARD SUCTION AND INCREASING SUCTION LEVEL  
30° SWEPT SUCTION WING UNDER THE INFLUENCE OF SOUND  
 $\alpha_c = 9.8 \times 10^6$

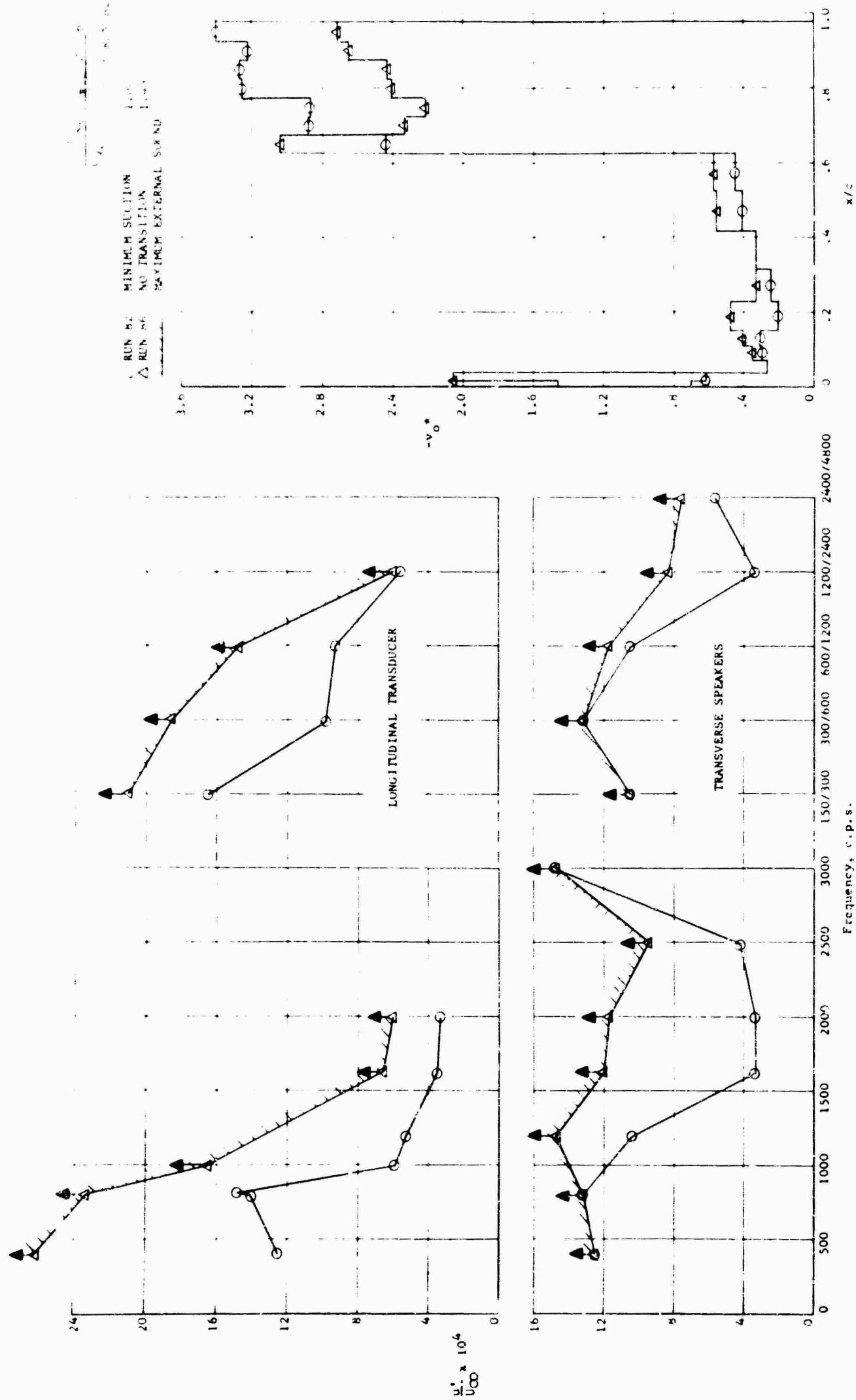
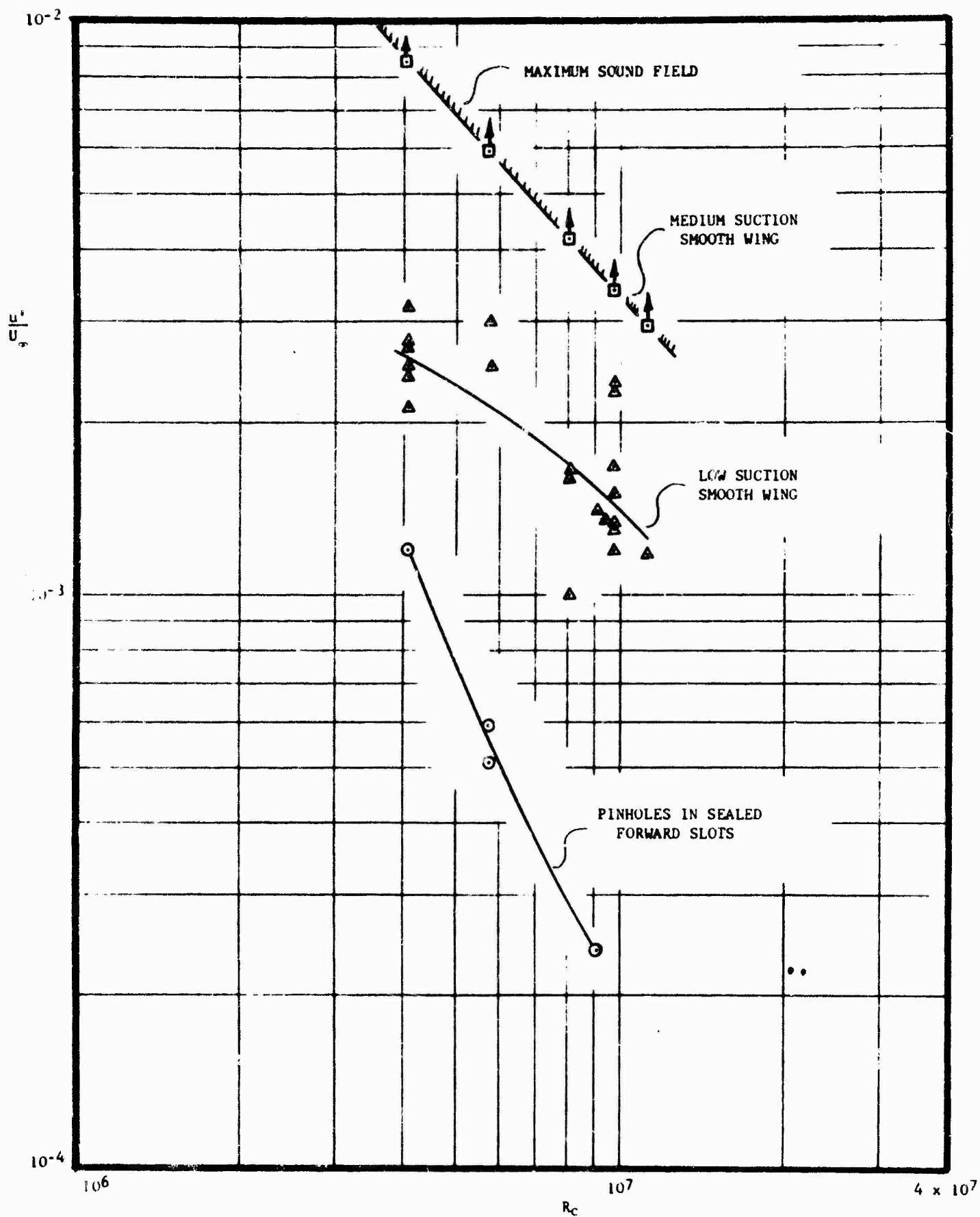


FIGURE 99  
TRANSITION LIMIT WITH INCREASING FORWARD SUCTION  
300 SWEEP SUCTION WING UNDER THE INFLUENCE OF SOUND  
 $P_c = 11.5 \times 10^6$





**FIGURE 100**  
 VELOCITY FLUCTUATION,  $\frac{u'}{U_\infty}$ , FOR TRANSITION WITH SMOOTH WING AND  
 PINHOLE IMPERFECTIONS AS A FUNCTION OF CHORD REYNOLDS NUMBER  
 30° SWEEPED SUCTION WING UNDER THE INFLUENCE OF SOUND

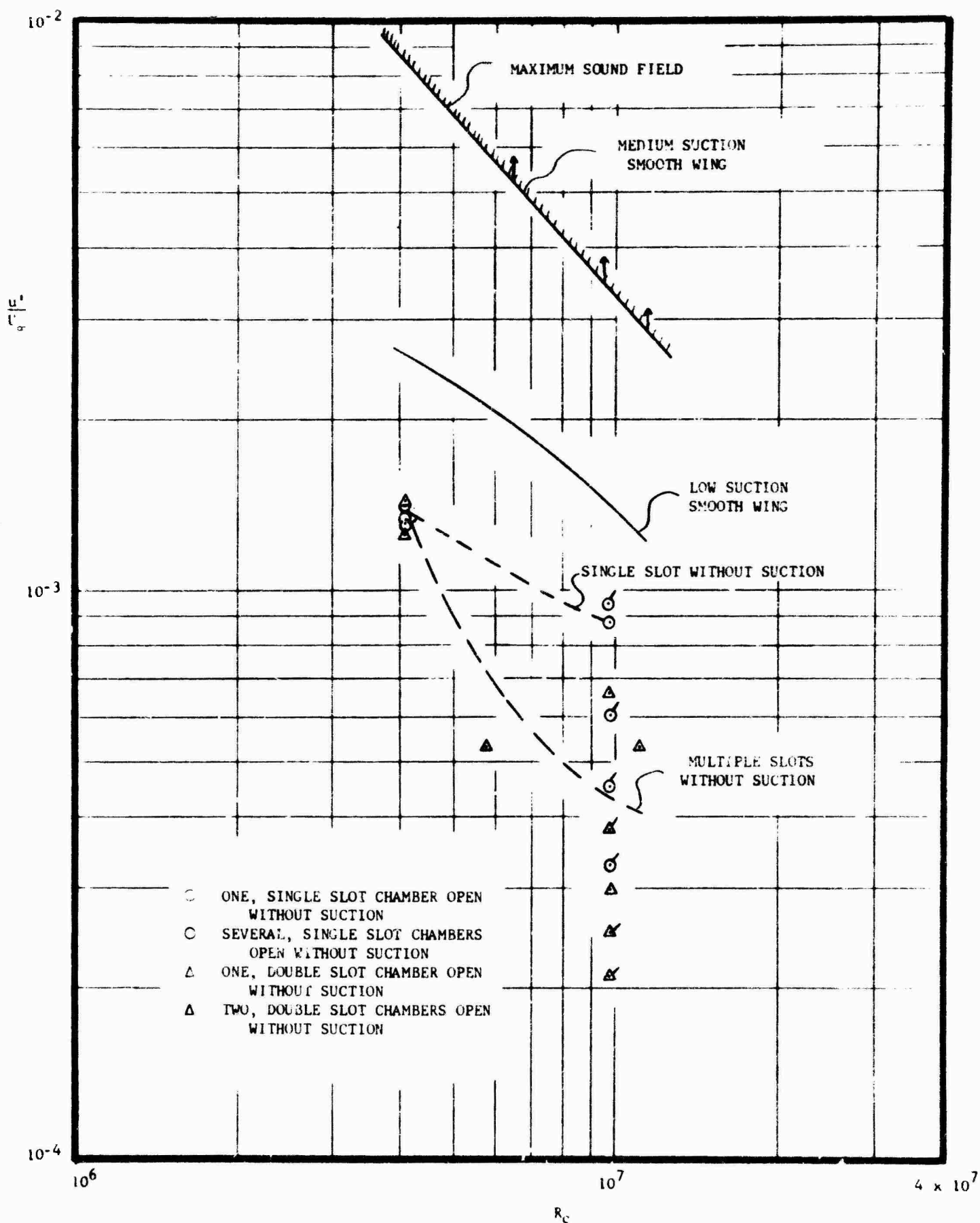


FIGURE 101

VELOCITY FLUCTUATION,  $\frac{u'}{U_\infty}$ , FOR TRANSITION WITH SINGLE AND MULTIPLE SLOTS OPEN WITHOUT SUCTION AS A FUNCTION OF CHORD REYNOLDS NUMBER  
30° SWEEP Suction WING UNDER THE INFLUENCE OF SOUND

FIGURE 103

TRANSITION SHOWN BY NAPHTHALENE SPRAY TECHNIQUE  
TRANSVERSE, TRANSDUCER, 122 DB, 800 CPS,  $R_c = 11.2 \times 10^6$ ,  
WEDGE AT 17% C FROM UNSEALED STATIC PRESSURE AT 3.7% C, RUN 532

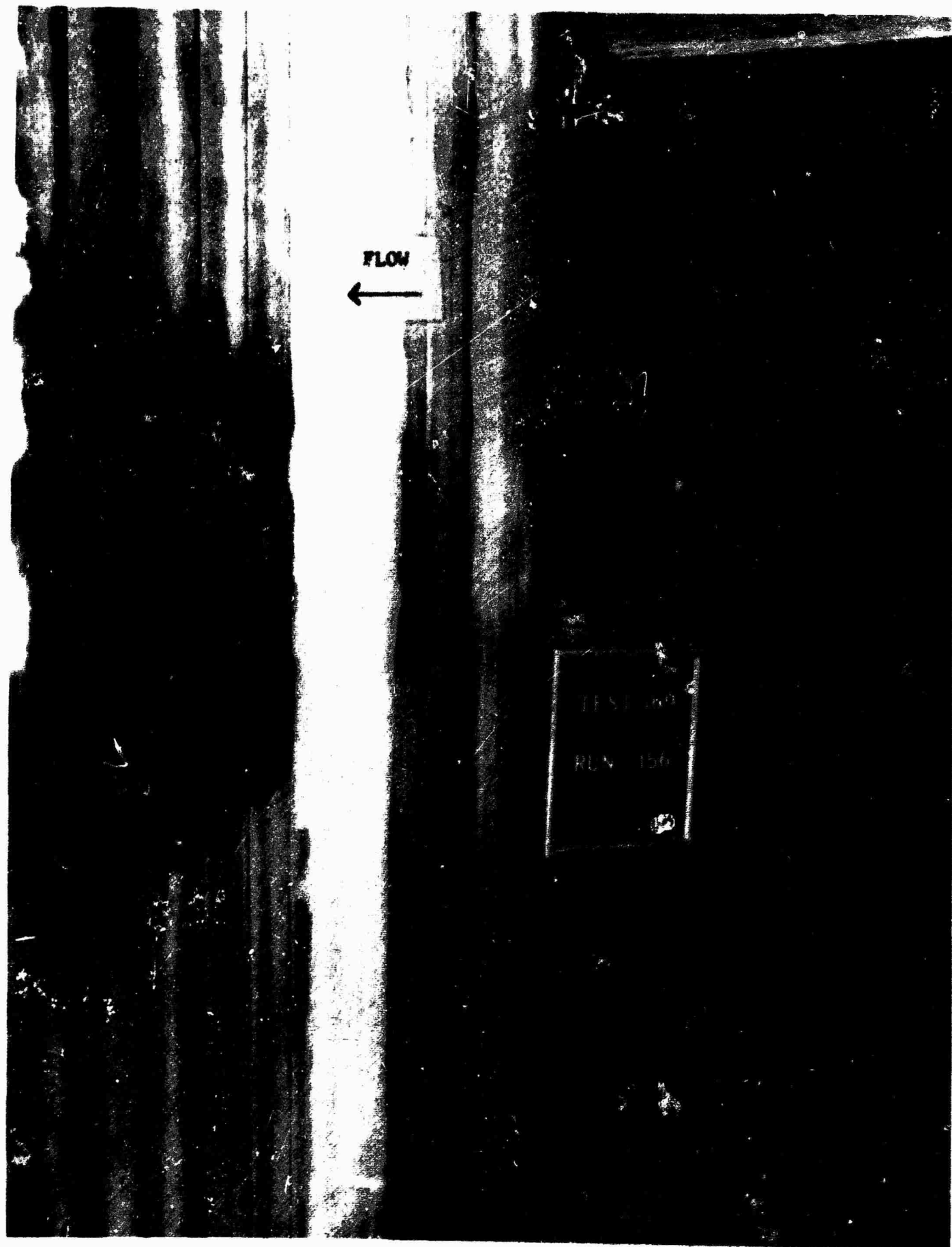


FIGURE 102 TRANSITION

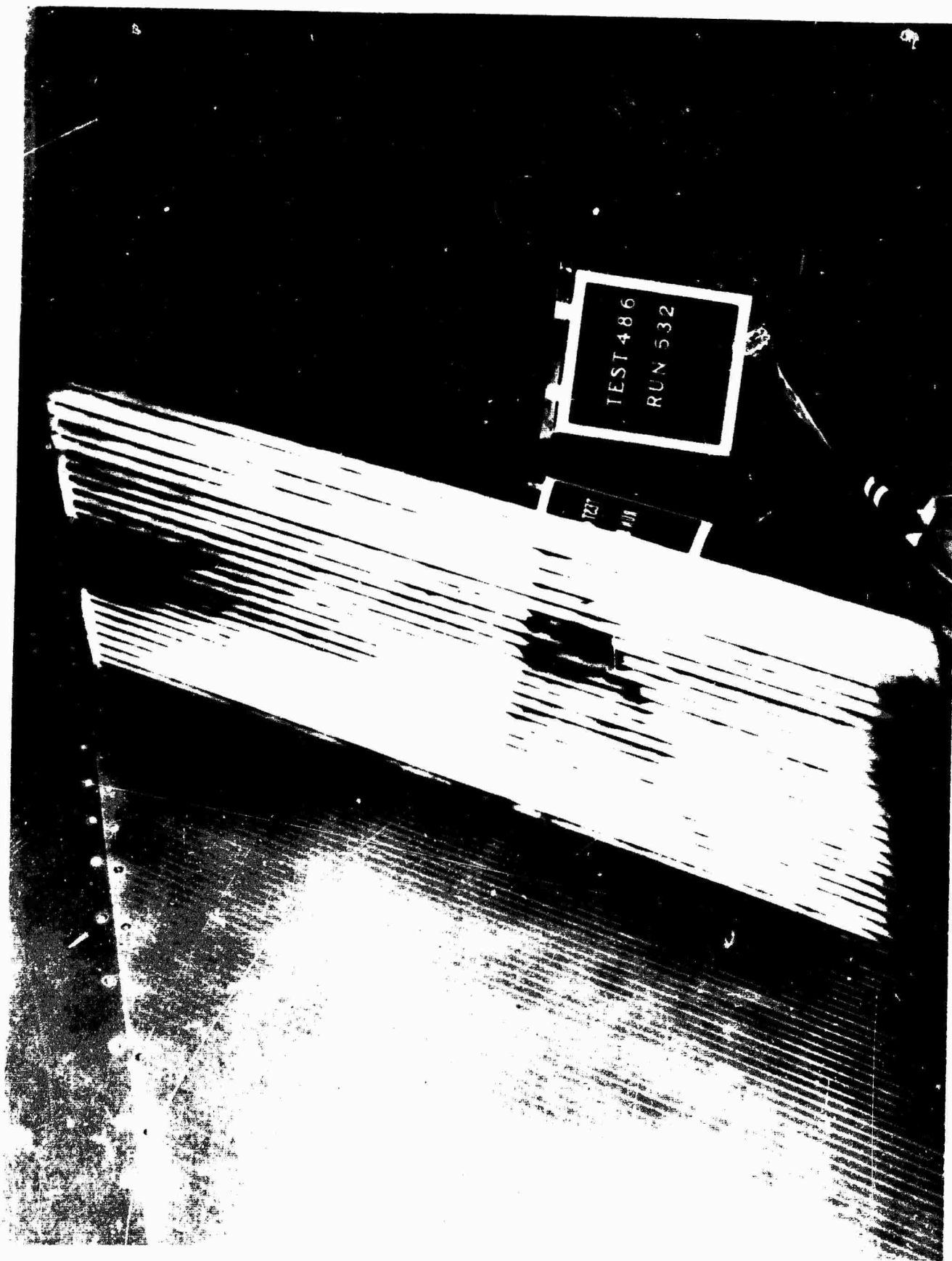


FIGURE 103

TRANSITION SHOWN BY NAPHTHALENE SPRAY TECHNIQUE  
TRANSVERSE, TRANSDUCER, 122 DB, 800 CPS,  $R_c = 11.2 \times 10^6$ ,  
WEDGE AT 17% C FROM UNSEALED STATIC PRESSURE AT 3.7% C, RUN 532



FIGURE 104  
TRANSITION SHOWN BY NAPHTHALENE SPRAY TECHNIQUE  
LONGITUDINAL, TRANSDUCER, 115 DB, 800 CPS,  $R_c = 5.8 \times 10^6$ ,  
WEDGES AT 30% C TOP AND AT 35% C BOTTOM FROM  
IMPERFECTLY SEALED FORWARD SLOTS, RUN 221



FIGURE 105  
TRANSITION SHOWN BY NAPHTHALENE SPRAY TECHNIQUE  
TRANSVERSAL, SPEAKERS, 127 DB, 200 CPS,  $R_c = 4.1 \times 10^6$ ,  
STRIATIONS AT 45 AND 49% C, RUN 292



FIGURE 106  
TRANSITION SHOWN BY NAPHTHALENE SPRAY TECHNIQUE  
TRANSVERSE, SPEAKERS, 121 DB, 365 CPS,  $R_c = 5.8 \times 10^6$ ,  
STRIATIONS AT 46 AND 50% C, RUN 315



FIGURE 107  
TRANSITION SHOWN BY NAPHTHALENE SPRAY TECHNIQUE  
TRANSVERSE, SPEAKERS, 129.5 DB, 667 CPS,  $R_c = 5.8 \times 10^6$ ,  
STRIATIONS AT 63 AND 67% C, RUN 304





FIGURE 108

TRANSITION SHOWN BY NAPHTHALENE SPRAY TECHNIQUE  
LONGITUDINAL, TRANSDUCER, 133 DB, 400 CPS,  $R_c = 4.1 \times 10^6$ ,  
TRANSITION AT 46% C TOP AND AT 49% C BOTTOM, RUN 286

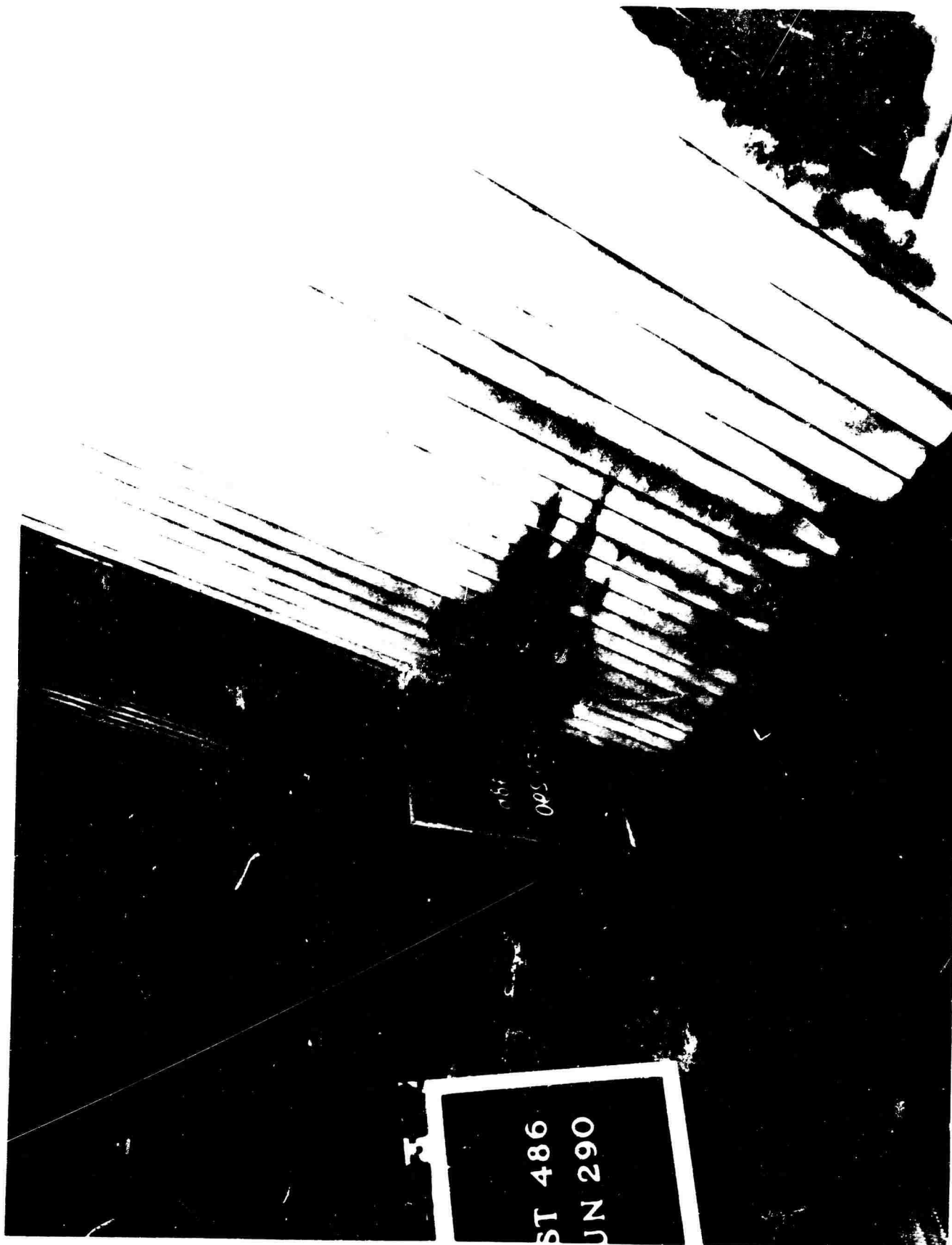


FIGURE 109  
 TRANSITION SHOWN BY NAPHTHALENE SPRAY TECHNIQUE  
 TRANSVERSE, SPEAKERS, 125 DB, 400 CPS,  $R_c = 4.1 \times 10^6$ ,  
 STRIATIONS AT 45 AND 56% C, RUN 290

TRANSITION AT 34% C, RUN 999  
TRANSITION AT 9% C, RUN 447

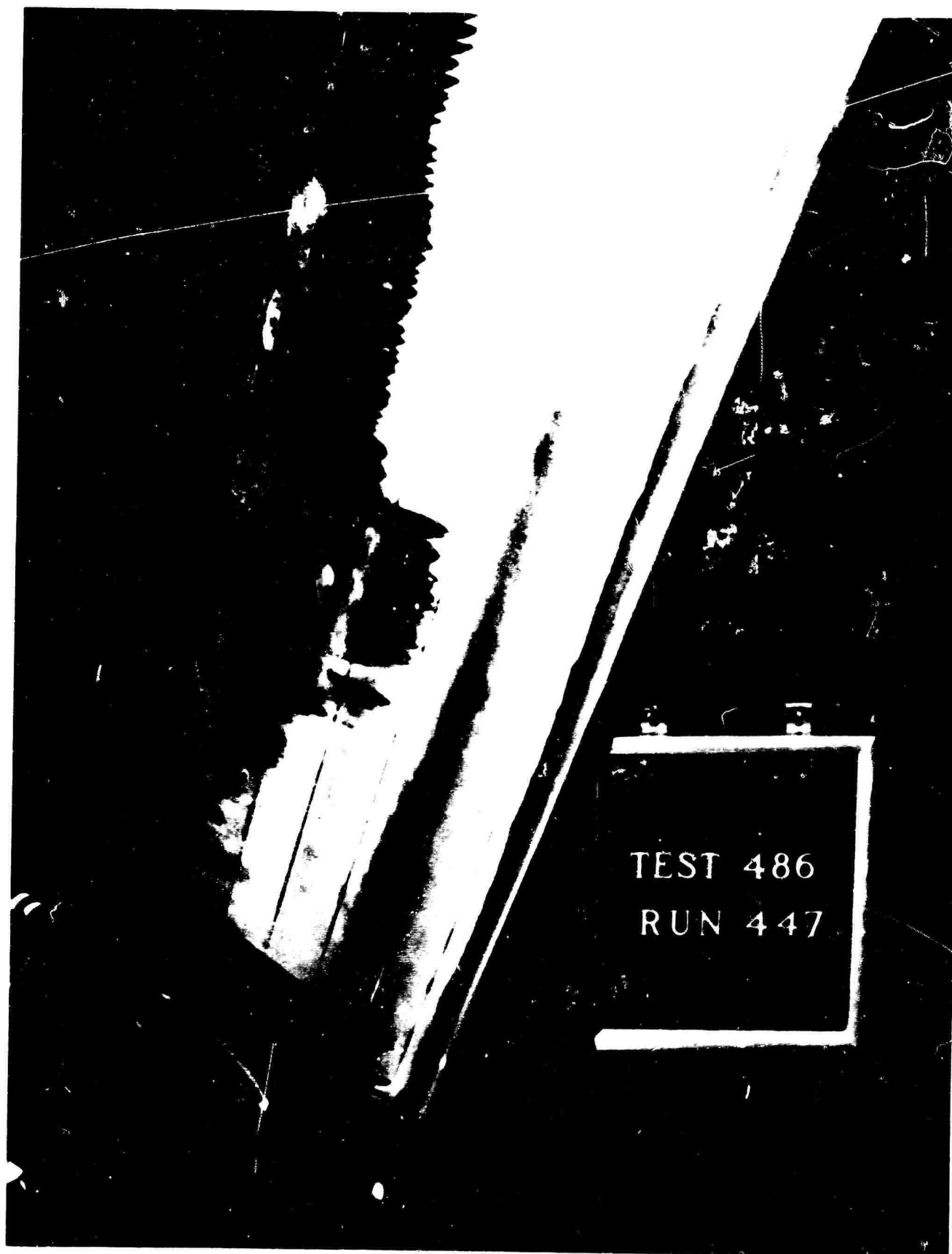


FIGURE 110  
TRANSITION SHOWN BY NAPHTHALENE SPRAY TECHNIQUE  
LONGITUDINAL, TRANSDUCER, 128.5 DB, 1000 CPS,  $R_c = 8.1 \times 10^6$ ,  
TRANSITION AT 9% C, RUN 447

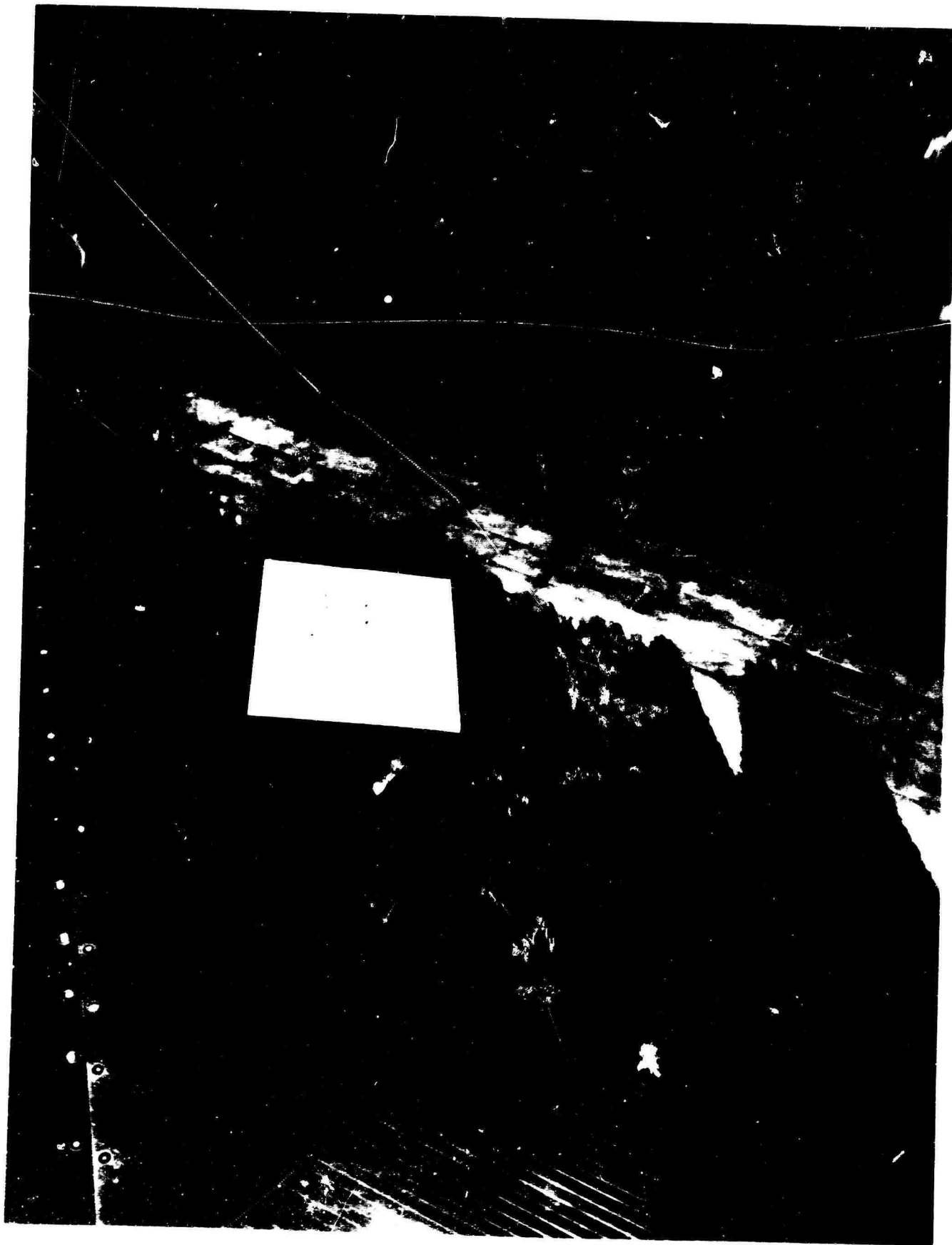


FIGURE 111  
TRANSITION SHOWN BY NAPHTHALENE SPRAY TECHNIQUE  
TRANSVERSE, TRANSDUCER, 130 DB, 1000 CPS,  $R_c = 8.1 \times 10^6$ ,  
TRANSITION AT 34% C, RUN 999



FIGURE 112  
TRANSITION SHOWN BY NAPHTHALENE SPRAY TECHNIQUE  
TRANSVERSE, TRANSDUCER, 130 DB, 1000 CPS,  $R_c = 8.1 \times 10^6$ ,  
TRANSITION AT 34% C, RUN 999



FIGURE 113  
TRANSITION SHOWN BY NAPHTHALENE SPRAY TECHNIQUE  
LONGITUDINAL, TRANSDUCER, 130 DB, 1000 CPS,  $R_c = 8.1 \times 10^6$ ,  
TRANSITION AT 68% C, RUN 474



FIGURE 114  
 TRANSITION SHOWN BY NAPHTHALENE SPRAY TECHNIQUE  
 LONGITUDINAL, TRANSDUCER, 134.5 DB, 781 CPS,  $R_c = 8.1 \times 10^6$ ,  
 TRANSITION AT 70% C, RUN 460

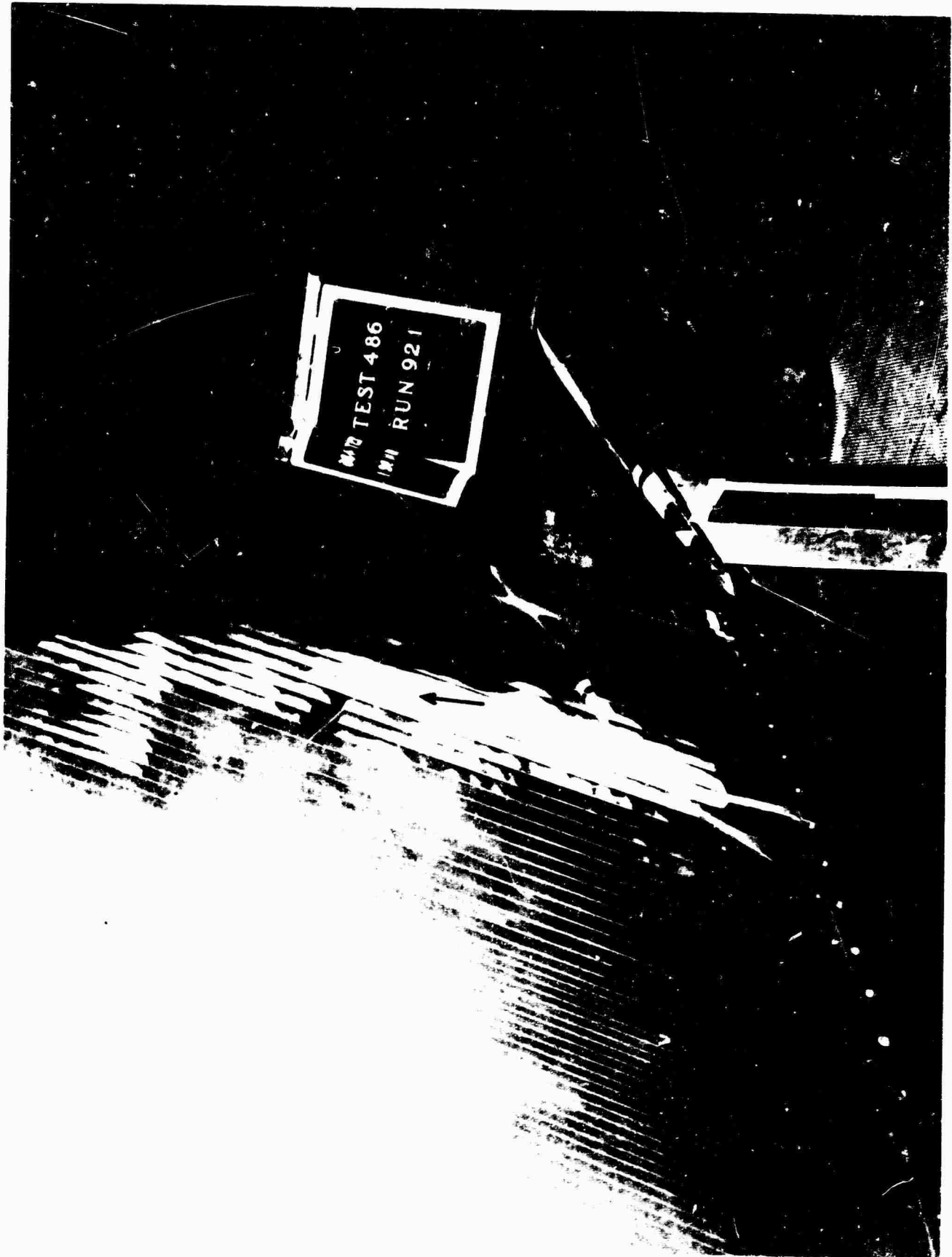


FIGURE 115

TRANSITION SHOWN BY NAPHTHALENE SPRAY TECHNIQUE  
LONGITUDINAL, TRANSDUCER, 125 DB, 800 CPS,  $R_c = 8.1 \times 10^6$ ,  
TRANSITION AT 50% CHORD, RUN 921





FIGURE 116  
TRANSITION SHOWN BY NAPHTHALENE SPRAY TECHNIQUE  
LONGITUDINAL, TRANSDUCER, 127 DB, 800 CPS,  $R_c = 8.1 \times 10^6$ ,  
TRANSITION AT 49% C, RUN 920



FIGURE 117  
TRANSITION SHOWN BY NAPHTHALENE SPRAY TECHNIQUE  
LONGITUDINAL, TRANSDUCER, 130 DB, 800 CPS,  $R_c = 8.1 \times 10^6$ ,  
TRANSITION AT 48% C, RUN 919

STRIATIONS AT 63 TO 66% C ABOVE, STRIPES AT 44 TO 49% C  
BELOW, RUN 335

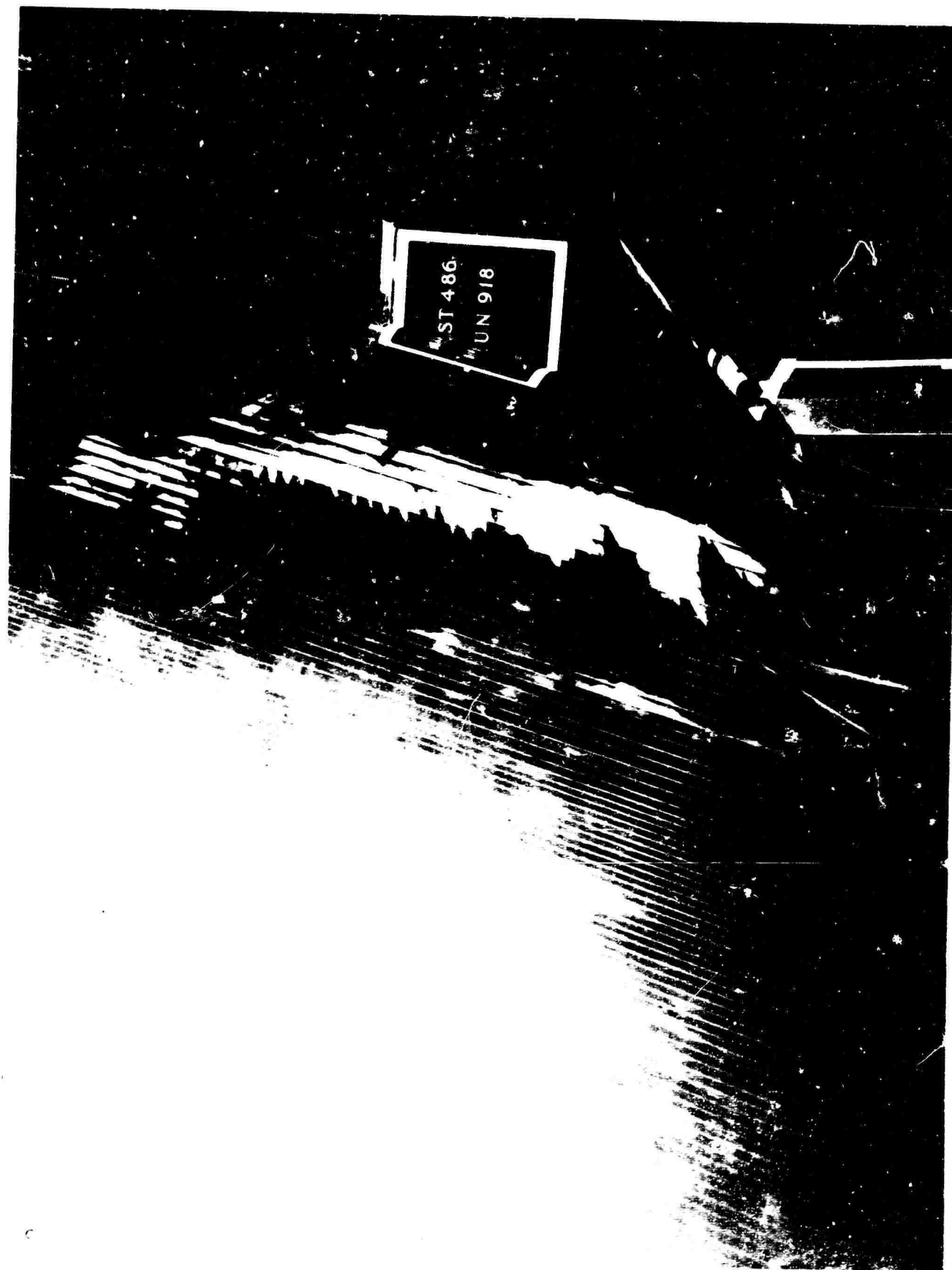


FIGURE 118

TRANSITION SHOWN BY NAPHTHALENE SPRAY TECHNIQUE  
LONGITUDINAL, TRANSDUCER, 133 DB, 800 CPS,  $R_c = 8.1 \times 10^{-3}$ ,  
TRANSITION AT 44% C, RUN 918



FIGURE 119

TRANSITION SHOWN BY NAPHTHALENE SPRAY TECHNIQUE  
LONGITUDINAL, TRANSDUCER, 134 DB, 785 CPS,  $R_c = 8.1 \times 10^6$ ,  
STRIATIONS AT 63 TO 66% C ABOVE, STRIPES AT 44 TO 46% C  
BELOW RUN 335

TRANSVERSE SPEAKERS, 118 DB, 365 CPS,  $R_c = 5.8 \times 10^6$ ,  
1/2-INCH STREAKS AT 75 TO 100% C, RUN 316

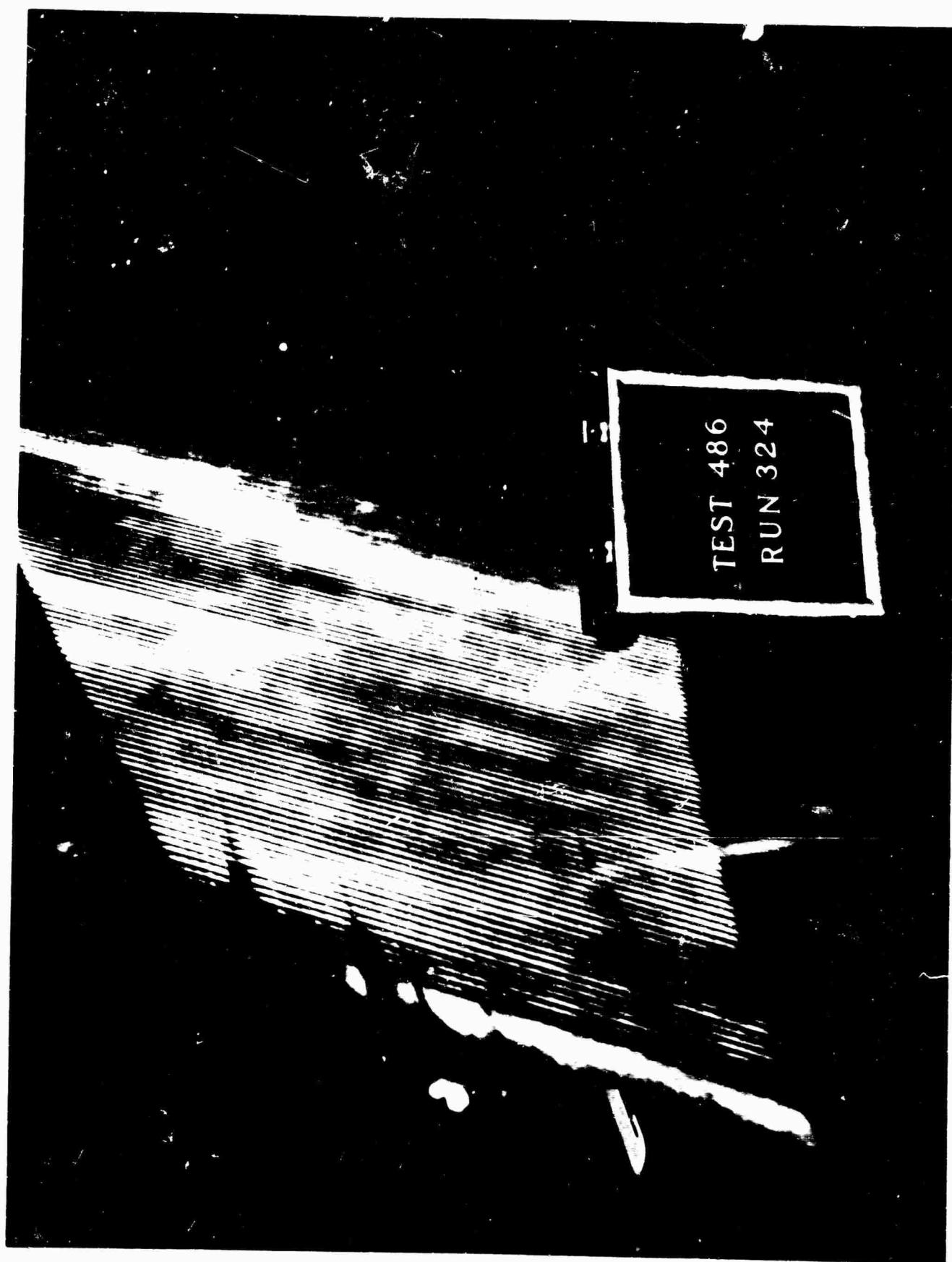


FIGURE 120  
TRANSITION SHOWN BY NAPHTHALENE SPRAY TECHNIQUE  
TRANSVERSE SPEAKERS, 117 DB, 365 CPS,  $R_c = 5.8 \times 10^6$ ,  
1/2-INCH STREAKS AT 75 TO 100% C, RUN 324

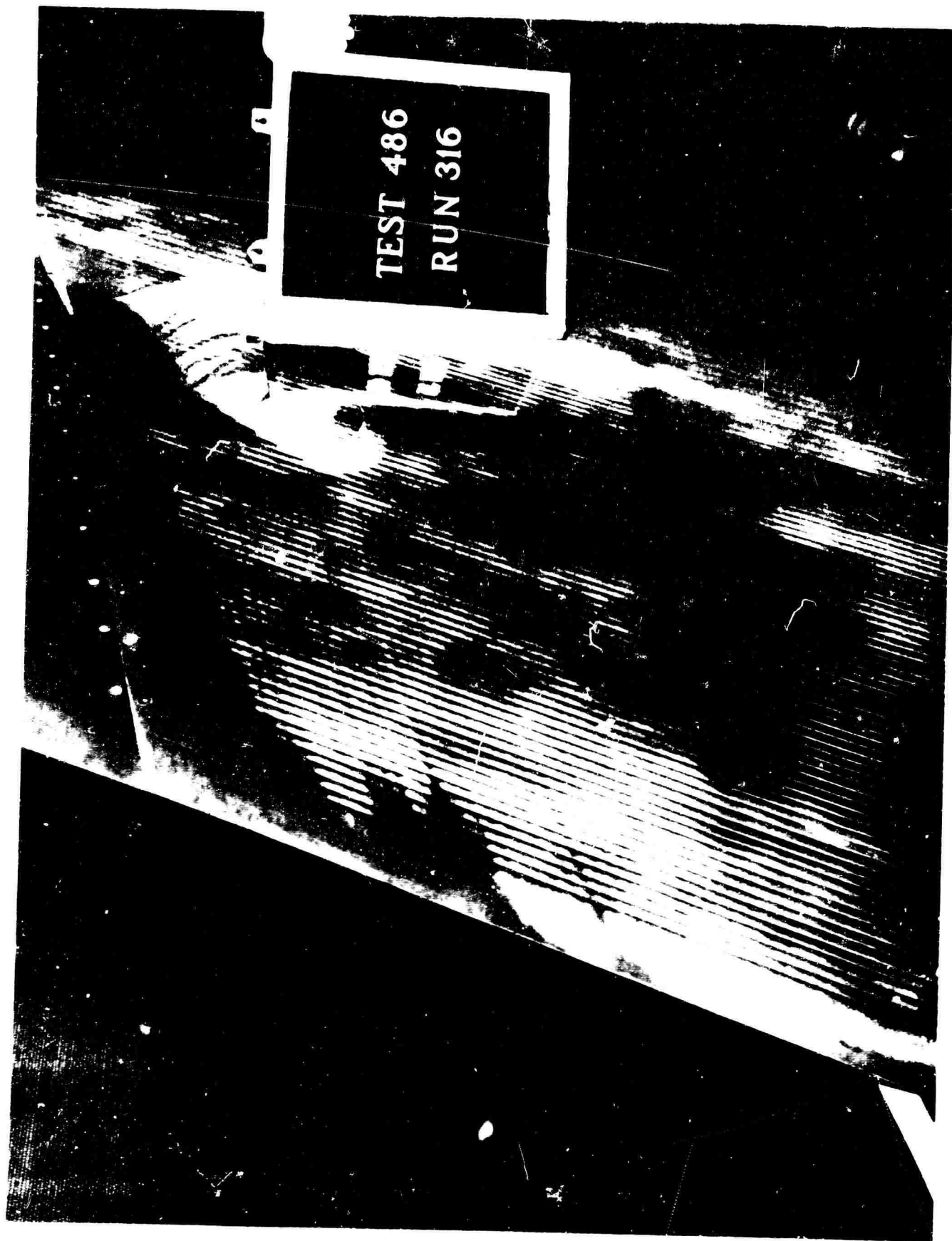


FIGURE 121

TRANSITION SHOWN BY NAPHTHALENE SPRAY TECHNIQUE  
TRANSVERSE, SPEAKERS, 118 DB, 365 CPS,  $R_c = 5.8 \times 10^6$ ,  
1/2-INCH STREAKS AT 75 TO 100% C, RUN 316

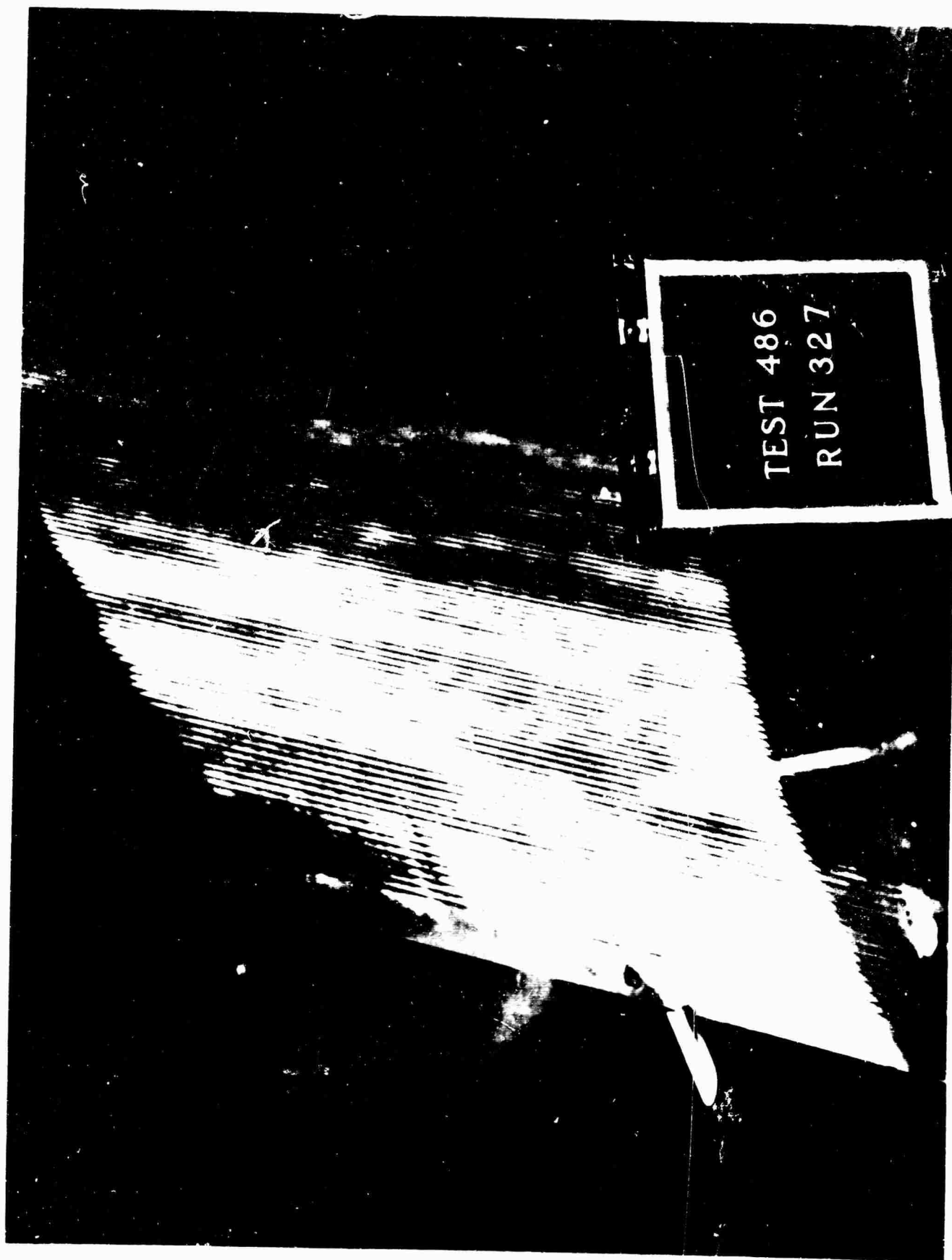


FIGURE 122  
TRANSITION SHOWN BY NAPHTHALENE SPRAY TECHNIQUE  
NO SOUND INPUT,  $R_c = 5.8 \times 10^6$ , 1/2-INCH STREAKS AT  
75 TO 100% C, RUN 327



FIGURE 123  
TRANSITION SHOWN BY NAPHTHALENE SPRAY TECHNIQUE  
TRANSVERSE, SPEAKERS, 121 DB, 365 CPS,  $R_c = 5.6 \times 10^6$ ,  
TRANSITION AT 50% C AND 1/2-INCH STREAKS, RUN 315



$R_c = 5.8 \times 10^6$ , TRANSITION AT  $63^\circ C$ , RUN 310



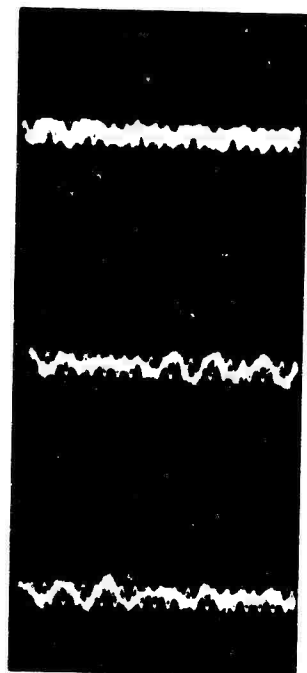
FIGURE 124  
TRANSITION SHOWN BY NAPHTHALENE SPRAY TECHNIQUE  
NO SOUND INPUT,  $R_c = 8.1 \times 10^6$ , TRANSITION AT  $90$  TO  
 $94^\circ C$  (COMING FROM STREAKS) RUN 453



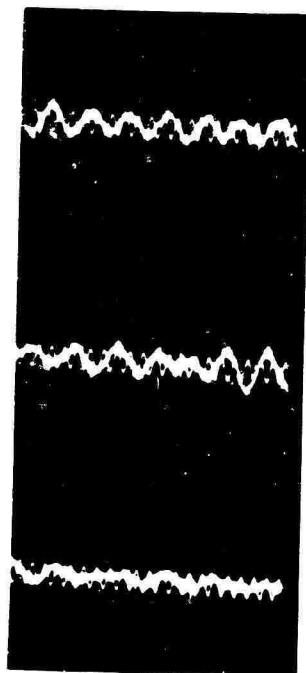
FIGURE 125  
TRANSITION SHOWN BY NAPHTHALENE SPRAY TECHNIQUE  
LONGITUDINAL, TRANSDUCER, 129 DB, 300/600 CPS,  
 $R_C = 5.8 \times 10^6$ , TRANSITION AT  $63^\circ \text{C}$ , RUN 310



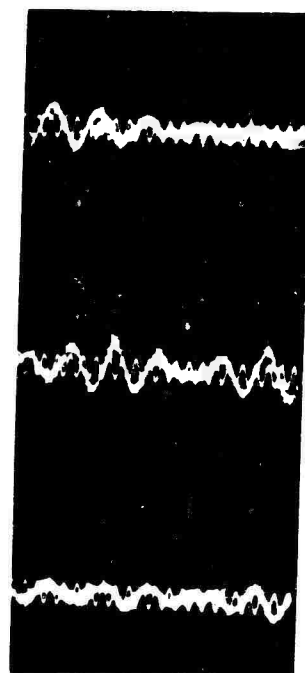
FIGURE 126  
TRANSITION SHOWN BY NAPHTHALENF PRAY TECHNIQUE  
LONGITUDINAL, TRANSDUCER, 134 DB, 800 CPS,  $R_c = 8.1 \times 10^6$ ,  
TRANSITION AT 6 TO 9% C, RUN 455



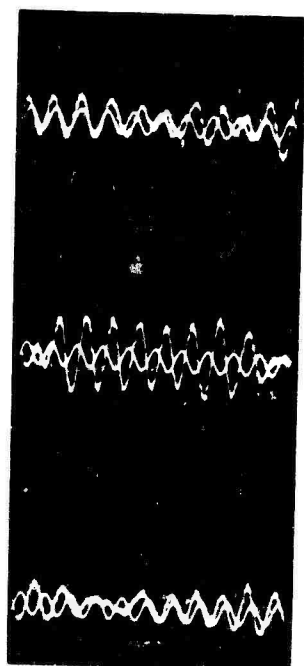
$R_c = 8.4 \times 10^6$   
 $x/c = 0.114$   
 $f \approx 330 \text{ cps}$



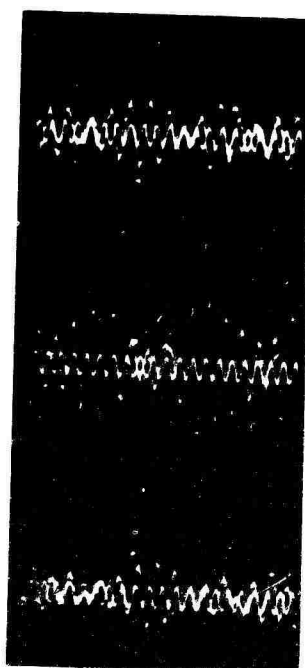
$R_c = 8.4 \times 10^6$   
 $x/c = 0.129$   
 $f \approx 320 \text{ cps}$



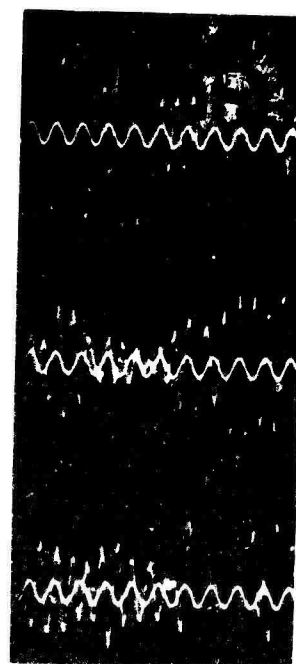
$R_c = 8.4 \times 10^6$   
 $x/c = 0.157$   
 $f \approx 310 \text{ cps}$



$R_c = 11.5 \times 10^6$   
 $x/c = 0.157$   
 $f \approx 445 \text{ cps}$



$R_c = 14.2 \times 10^6$   
 $x/c = 0.114$   
 $f \approx 750 \text{ cps}$



$R_c = 16.4 \times 10^6$   
 $x/c = 0.114$   
 $f \approx 850 \text{ cps}$

FIGURE 127 TOLLMIEN-SCHLICHTING BOUNDARY LAYER OSCILLATIONS,  
 NO APPLIED SUCTION, NO APPLIED SOUND,  $y = 0.018 \text{ INCH}$

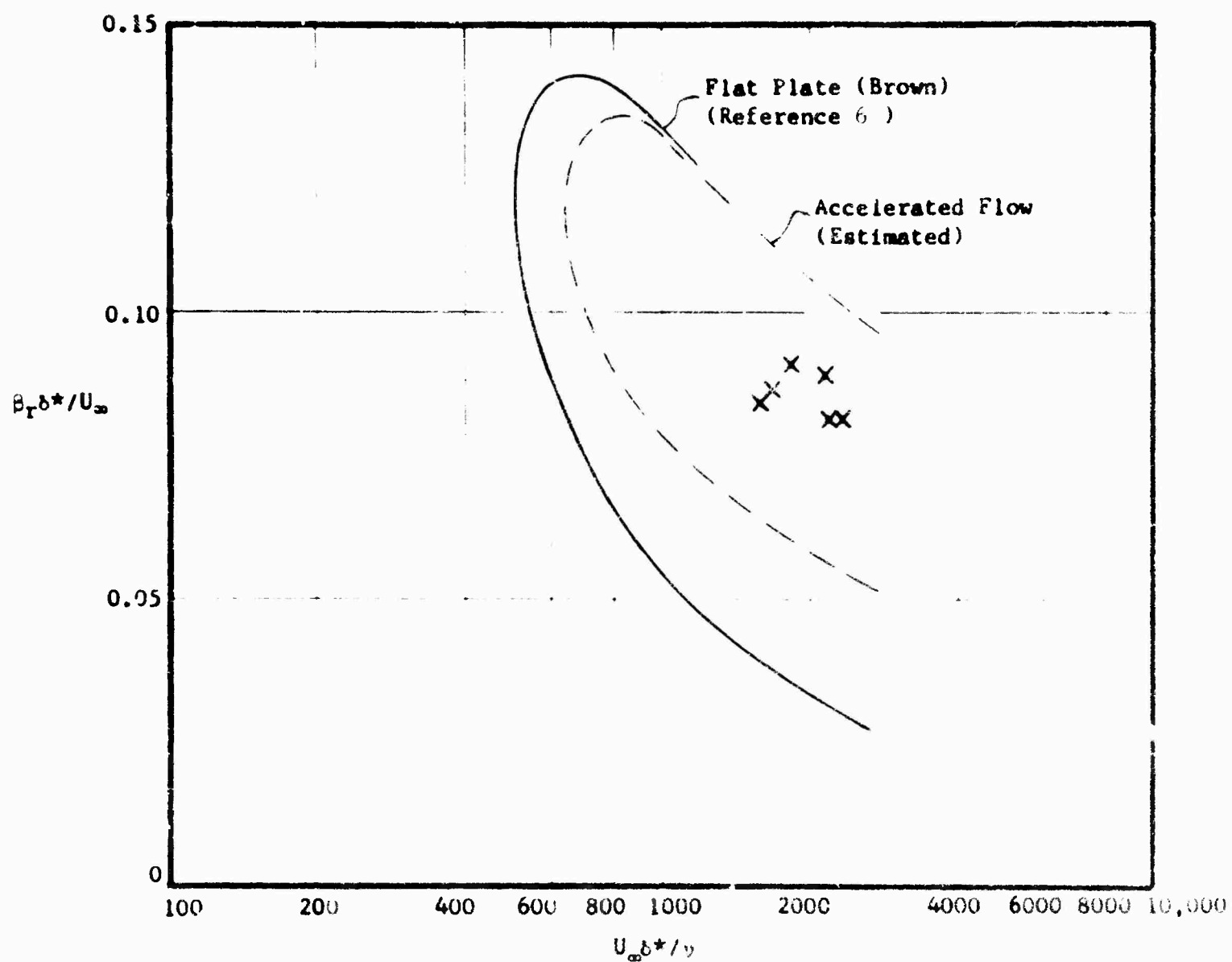
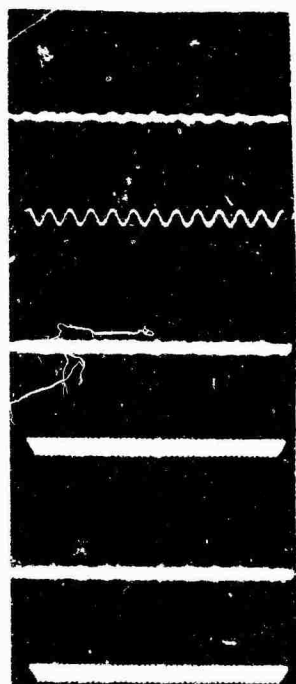


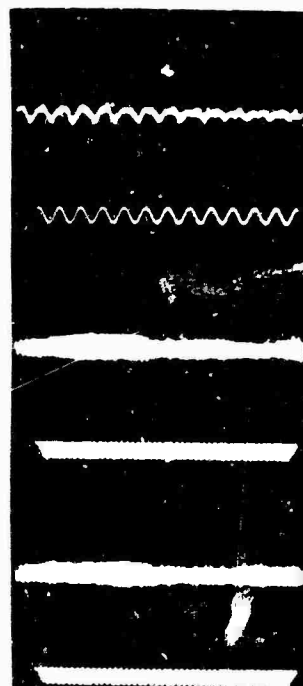
FIGURE 126 NONSUCTION AMPLIFIED OSCILLATION FREQUENCY DEPENDENCE



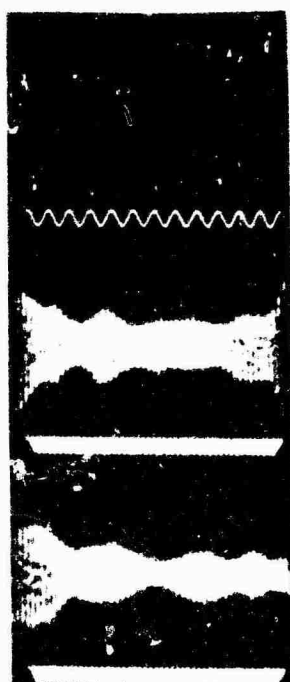
$x/c = 0.465$



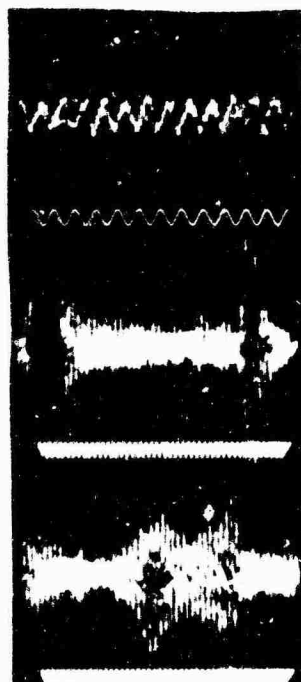
$x/c = 0.554$



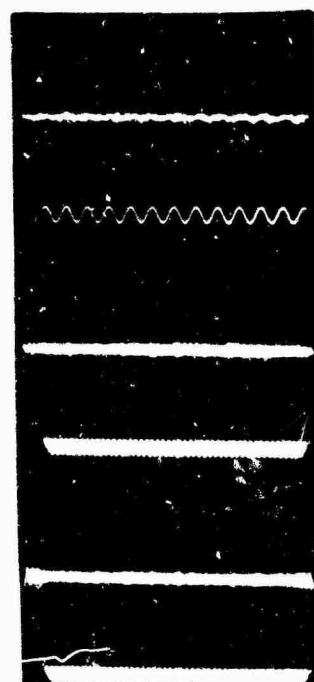
$x/c = 0.596$



$x/c = 0.621$

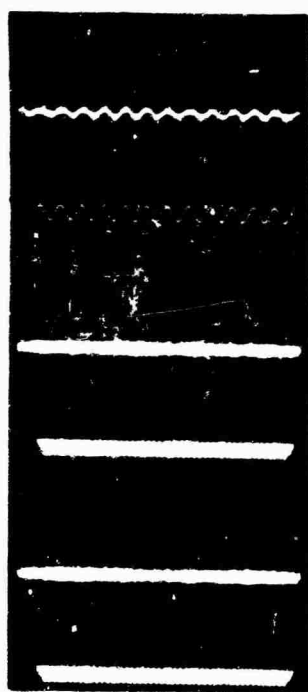


$x/c = 0.663$



$x/c = 0.748$

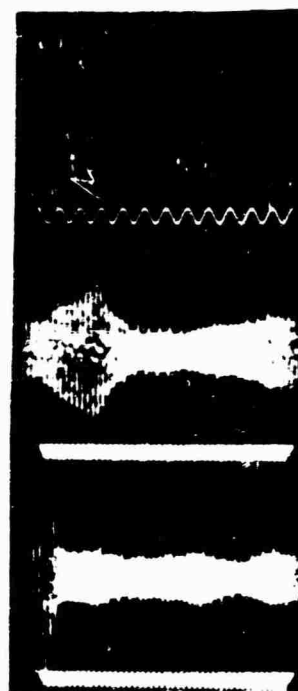
FIGURE 109 CHORDWISE HOT WIRE TRAVERSE, SPL = 105 DB,  $f = 248$  CPS,  
 $R_c = 14.2 \times 10^6$ ,  $y = 0.073$  INCH



$x/c = 0.465$



$x/c = 0.554$



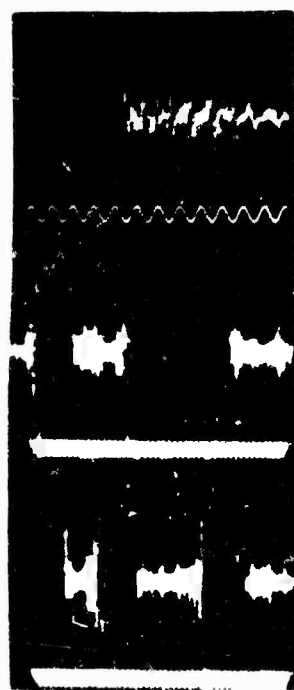
$x/c = 0.596$



$x/c = 0.621$

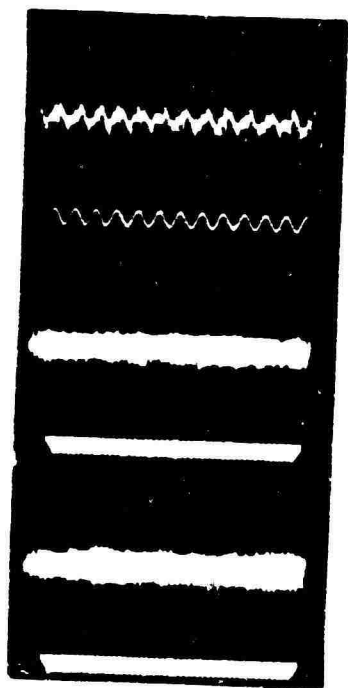


$x/c = 0.663$

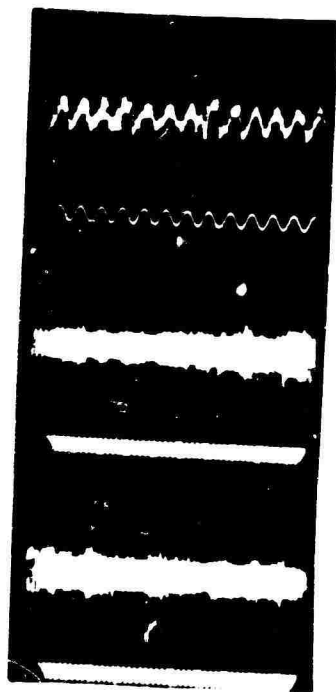


$x/c = 0.748$

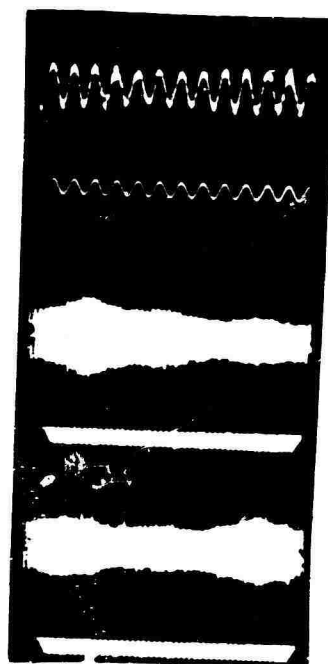
FIGURE 130 CHORDWISE NOT WIRE TRAVERSE, SPL = 110 DB,  $f = 248$  CPS,  
 $Re = 14.2 \times 10^6$ ,  $y = 0.073$  INCH



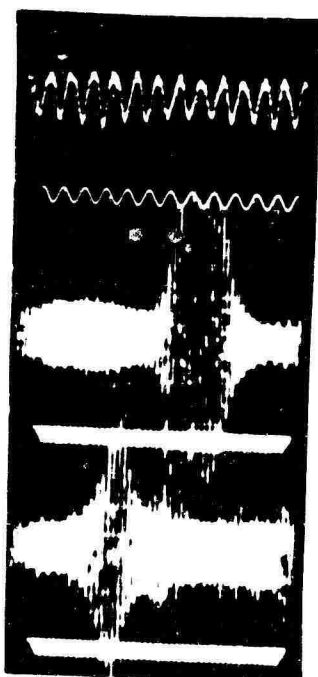
$x/c = 0.465$



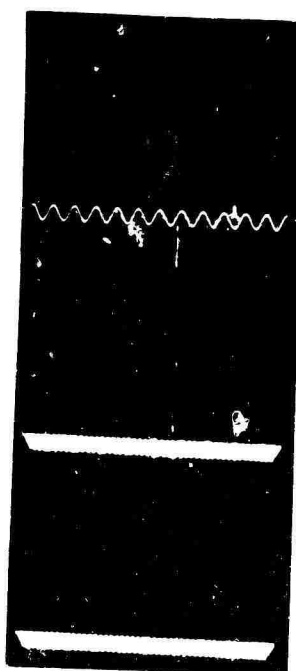
$x/c = 0.507$



$x/c = 0.554$



$x/c = 0.596$



$x/c = 0.621$

FIGURE 131 CHORDWISE HOT WIRE TRAVERSE, SPL = 115 DB,  $f = 248$  CPS,  
 $R_e = 14.2 \times 10^6$ ,  $y = 0.073$  INCH



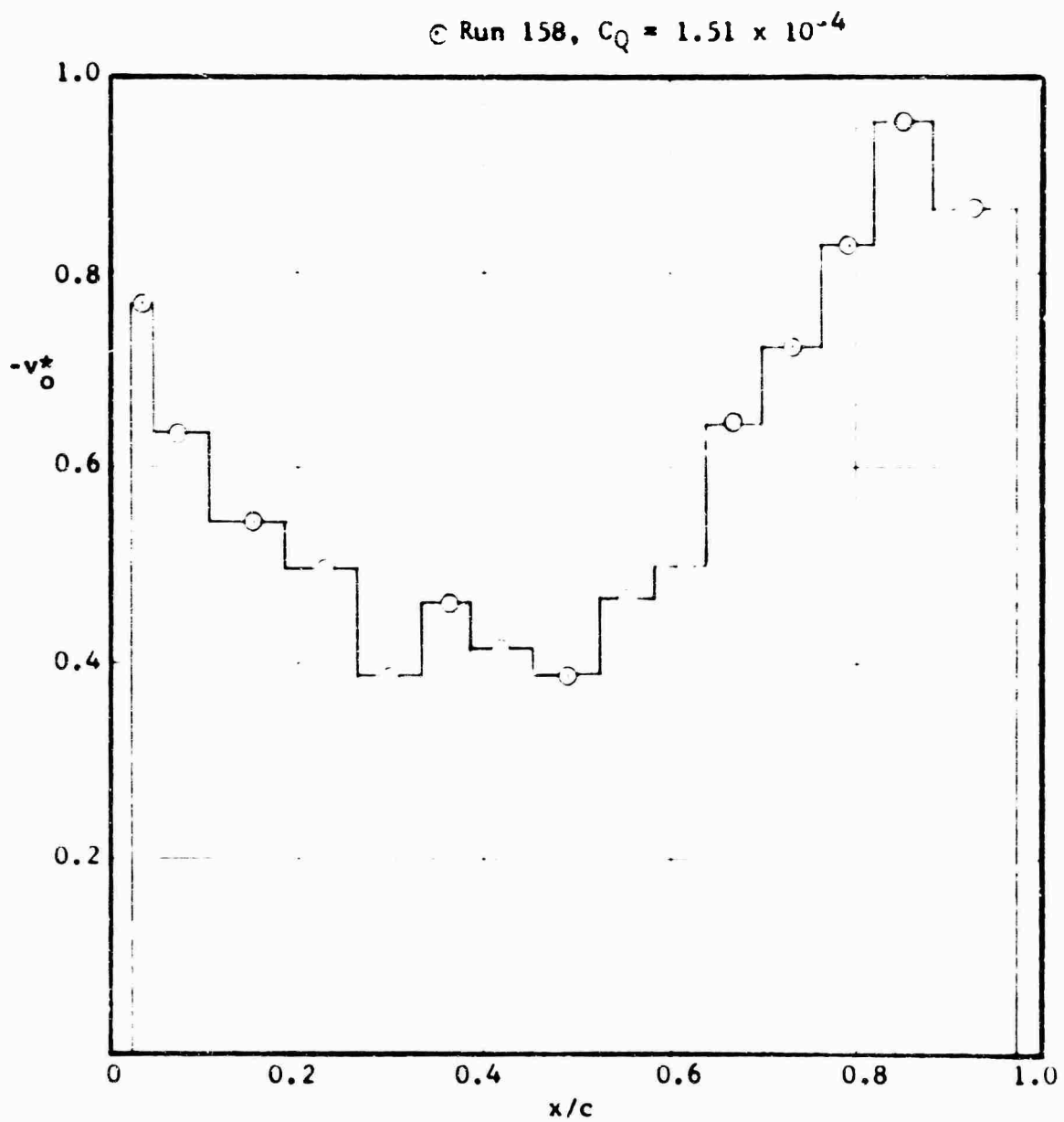


FIGURE 132 CHORDWISE SUCTION DISTRIBUTION

○ 105 db  
 △ 110 db  
 □ 115 db  
 ▽ 120 db

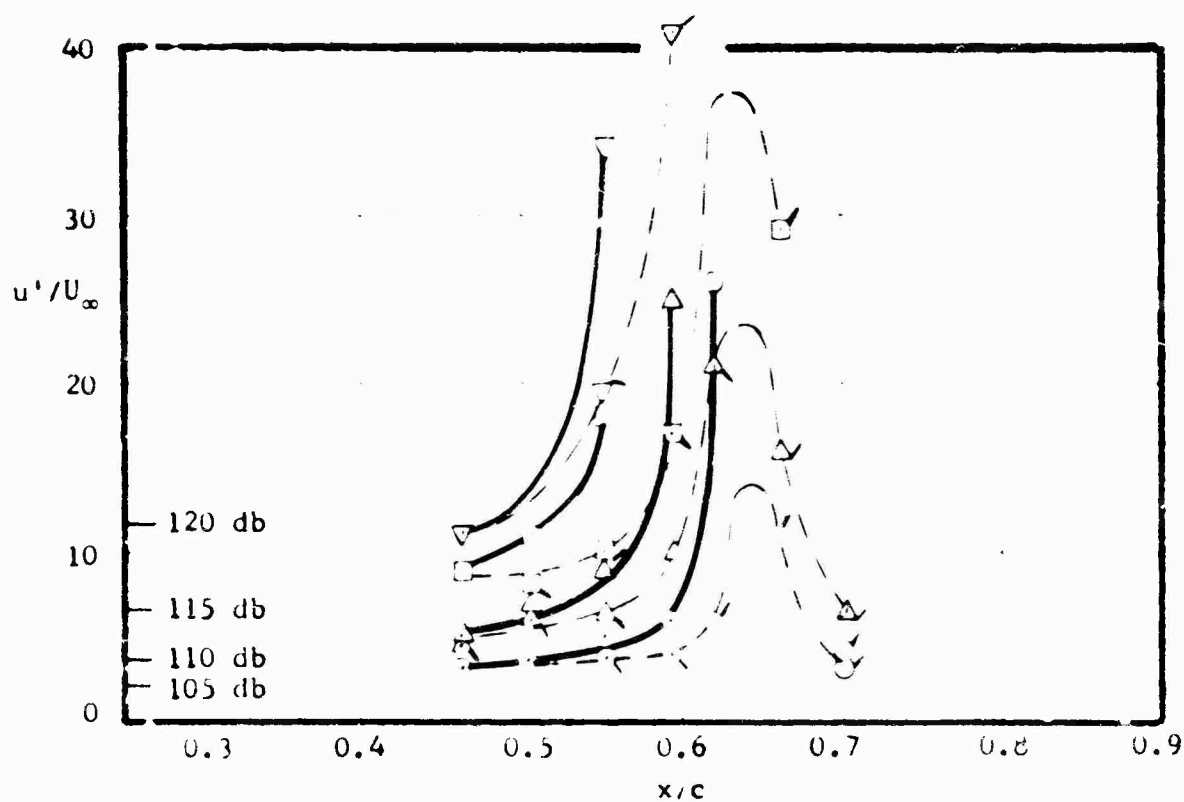


FIGURE 13. BOUNDARY LAYER FLUCTUATIONS AT VARIOUS CHORD LOCATIONS,  
 $f = 248$  CPS,  $R_c = 14.2 \times 10^6$ , PROBE AT  $y = 0.073$  INCH

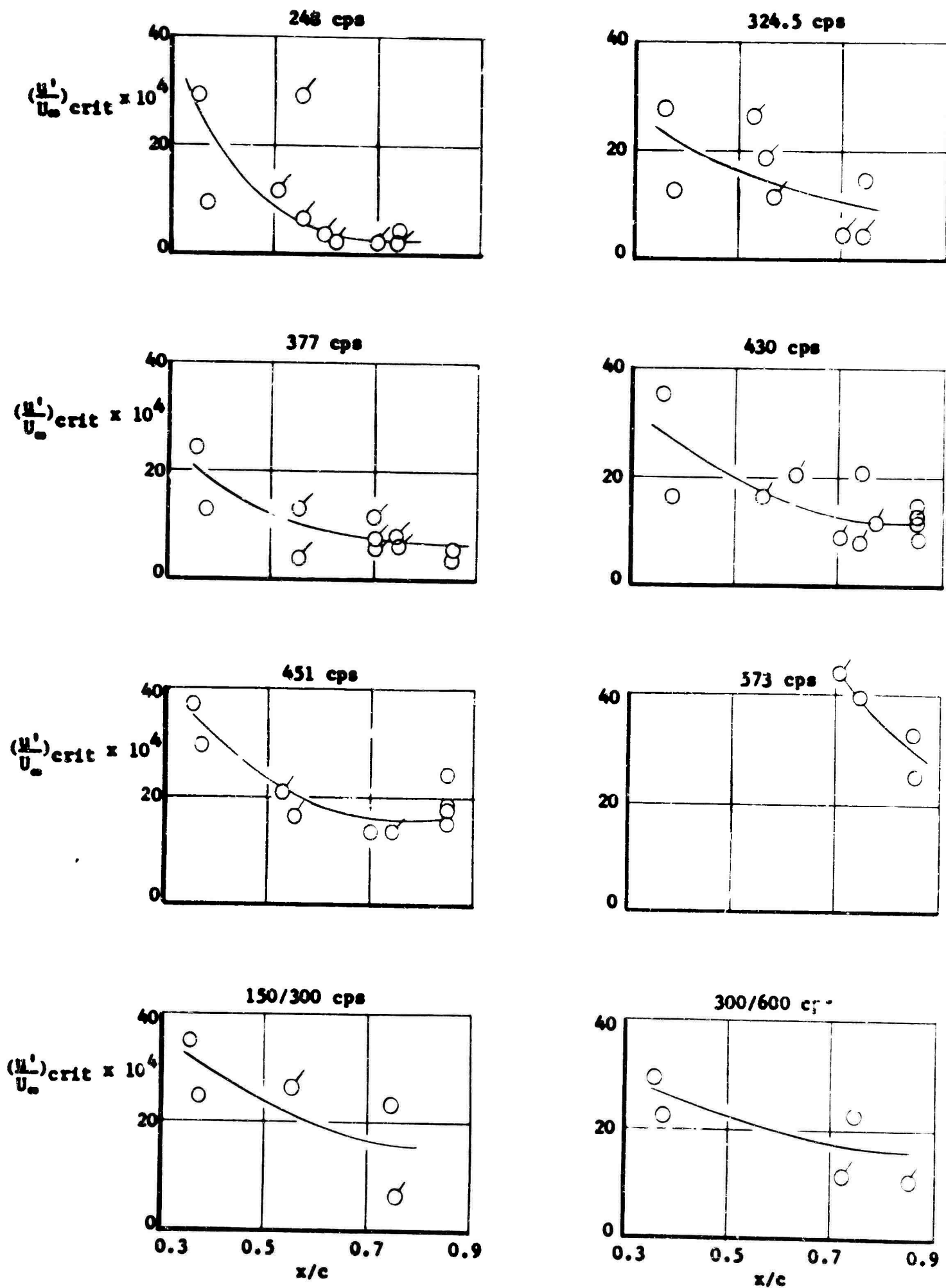


FIGURE 134 EXTERNAL SOUND LEVEL TO CAUSE TRANSITION AS A FUNCTION OF CHORD,  $R_c = 14.2 \times 10^6$

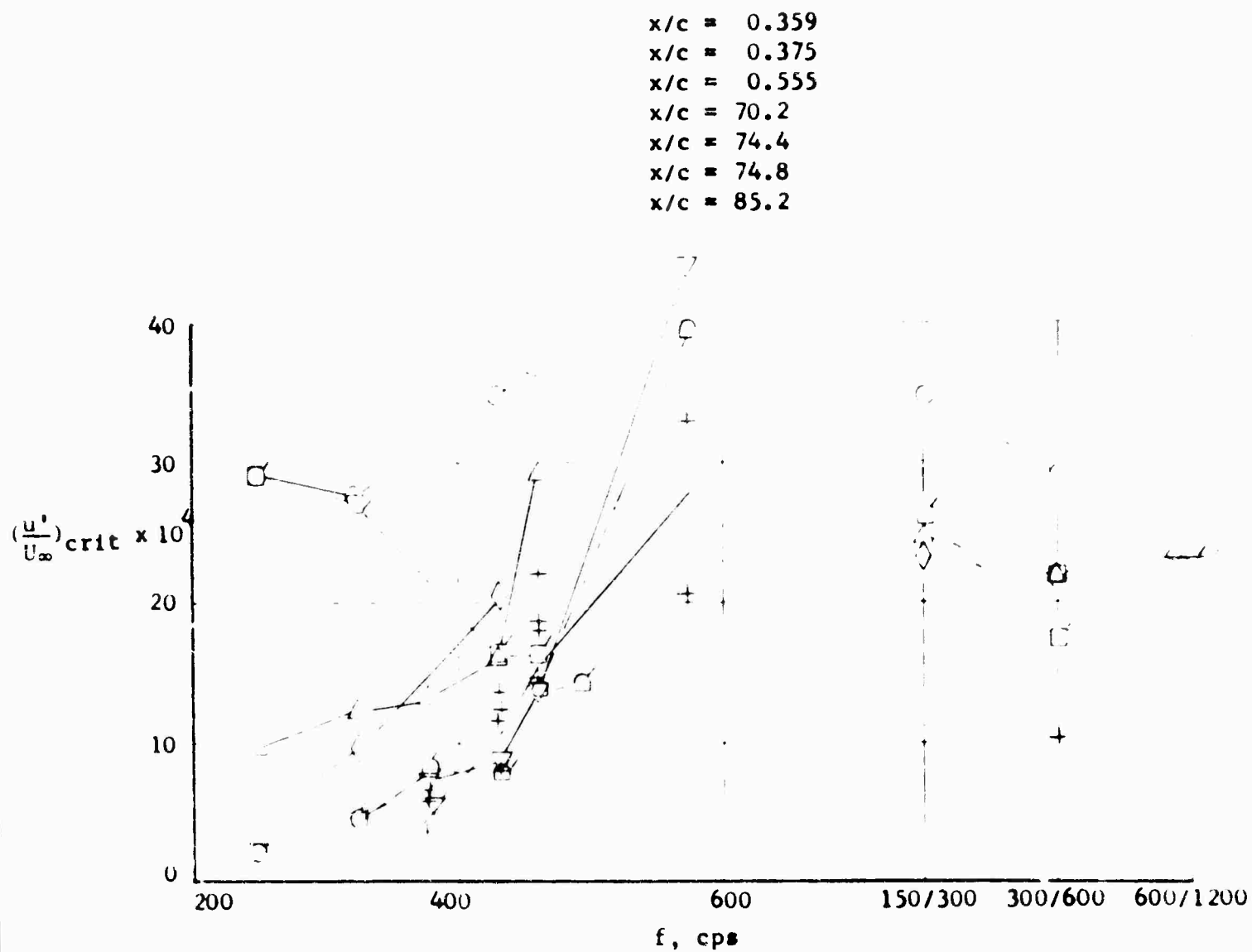


FIGURE 1 - EXTERNAL SOUND LEVEL TO CAUSE TRANSITION AT VARIOUS CHORDWISE STATIONS AS A FUNCTION OF FREQUENCY,  
 $R_c = 14.2 \times 10^6$

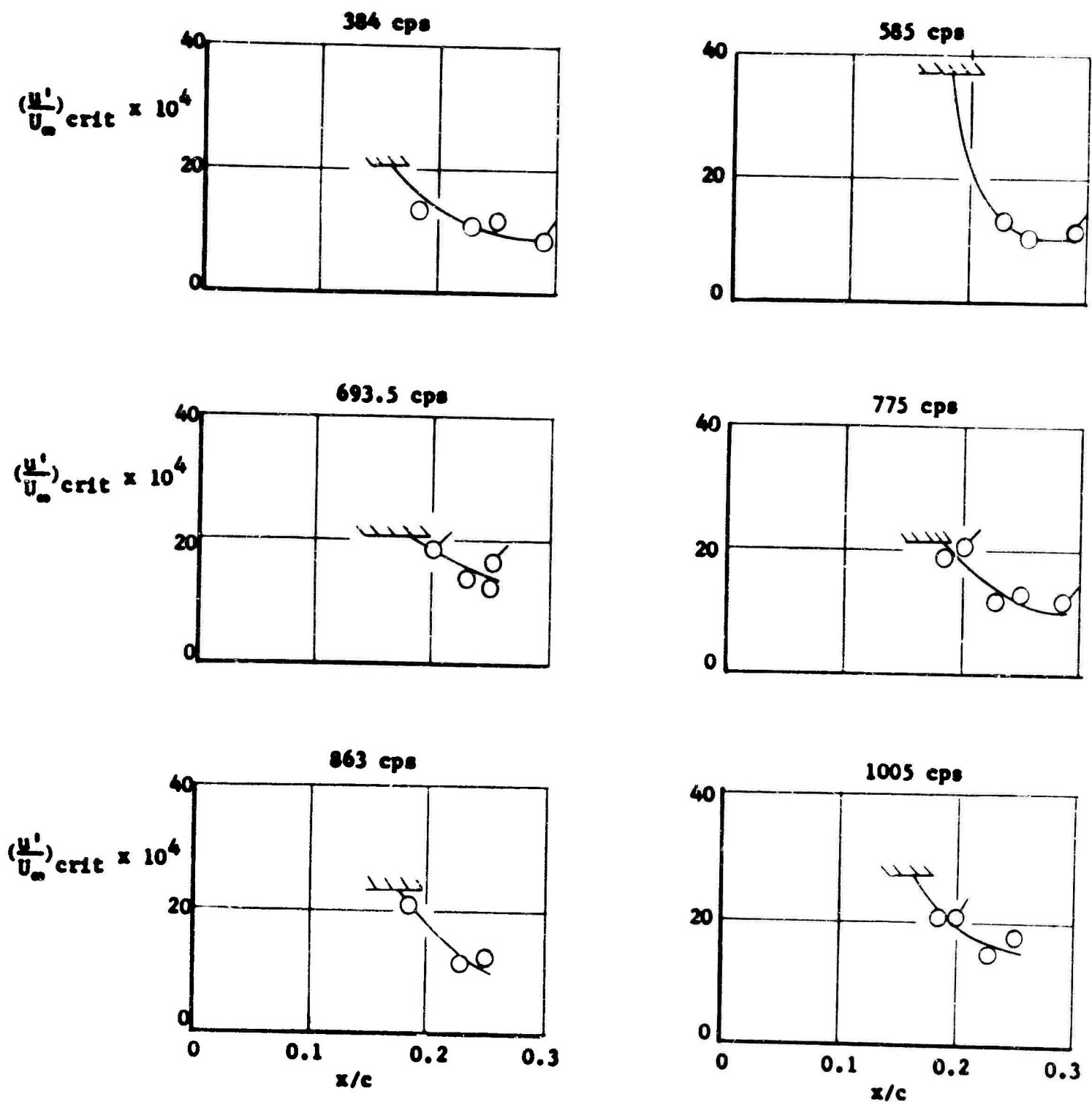


FIGURE 136 EXTERNAL SOUND LEVEL TO CAUSE TRANSITION AS A FUNCTION OF CHORDWISE LOCATION OF TRANSITION,  $R_c = 14.2 \times 10^6$

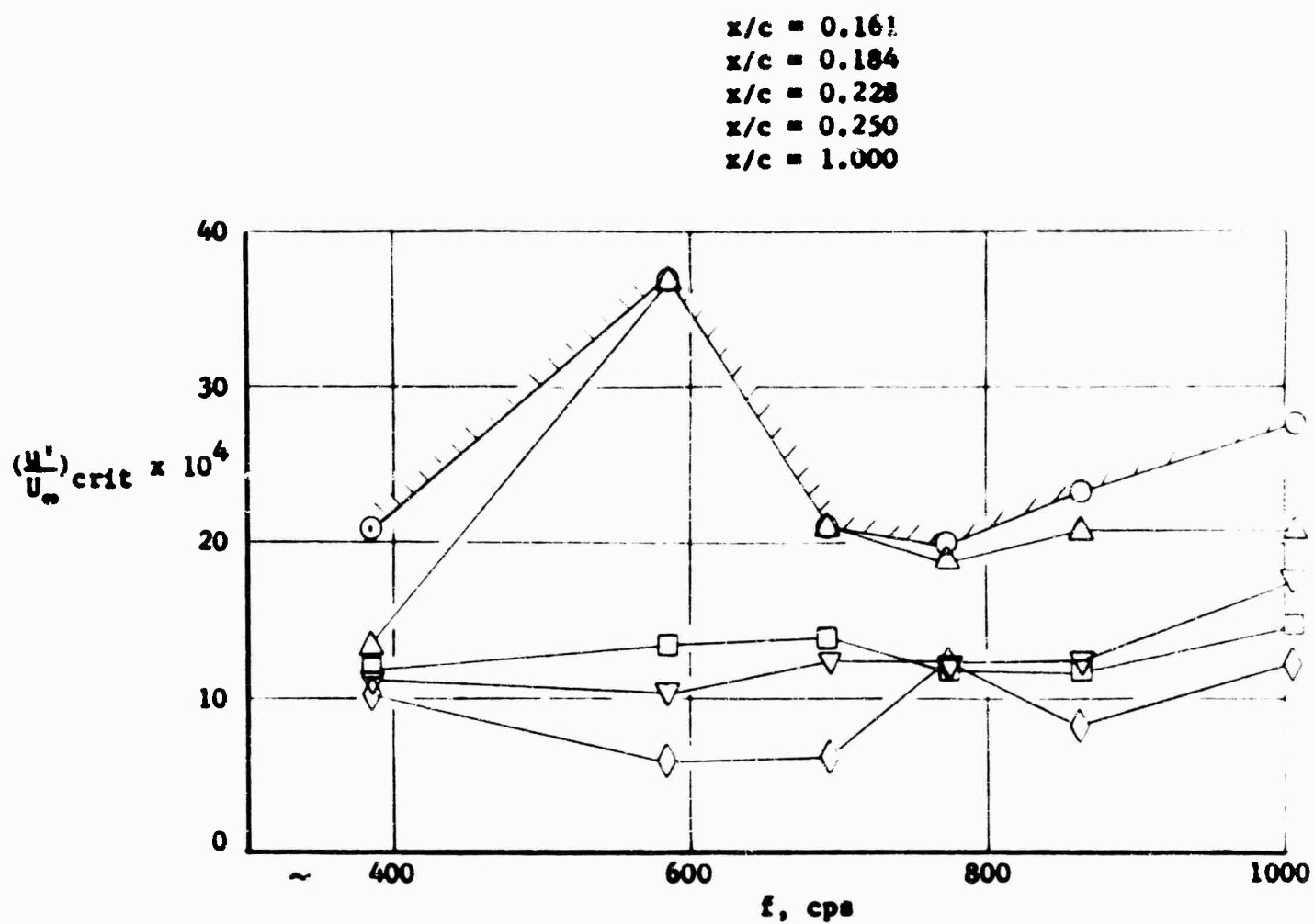
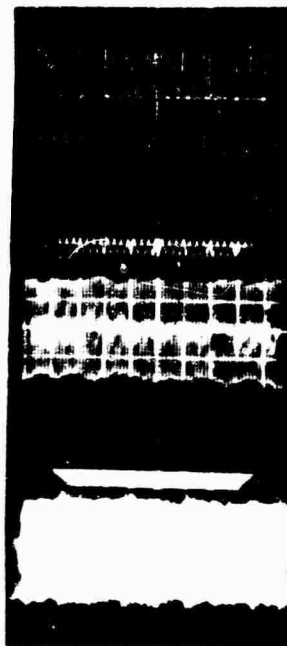


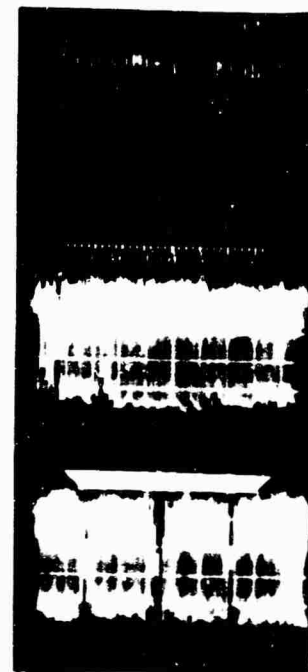
FIGURE 137 EXTERNAL SOUND LEVEL TO CAUSE TRANSITION AS A FUNCTION OF FREQUENCY,  $R_c = 14.2 \times 10^6$



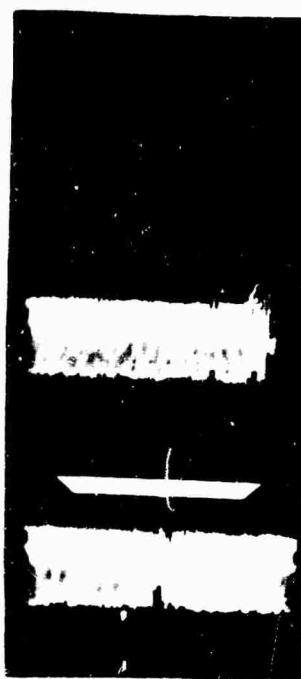
$x/c = 0.092$



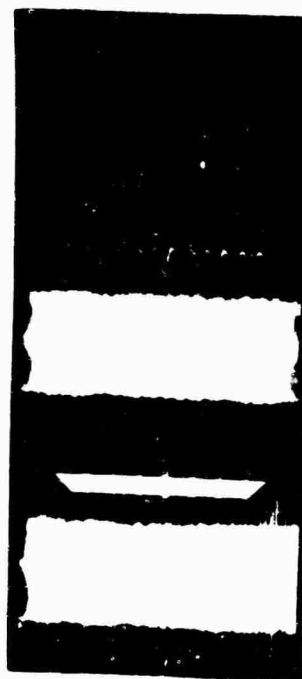
$x/c = 0.121$



$x/c = 0.156$



$x/c = 0.198$



$x/c = 0.246$



$x/c = 0.288$

FIGURE 138 CHORDWISE HOT WIRE TRAVERSE, SPL = 120 DB,  $f = 775$  CPS,  
 $R_e = 14.2 \times 10^6$ ,  $y = 0.044$  INCH

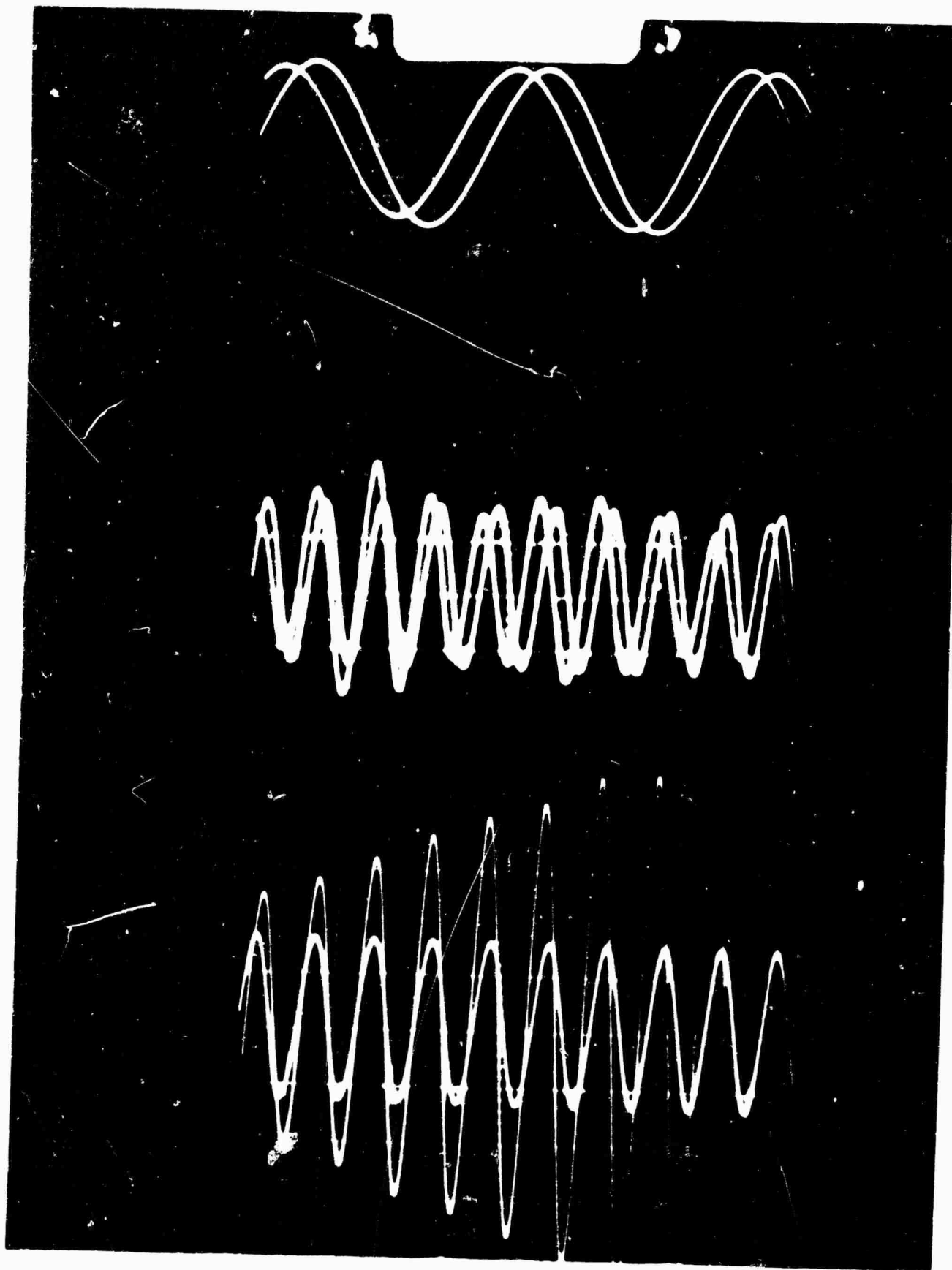


FIGURE 139  
OSCILLOSCOPE PHOTOGRAPH OF HOT WIRE SIGNAL SUPERIMPOSED  
ON REFERENCE SIGNAL FOR  $u'$  WIRE AT 55° C IN A 449 CPS  
SOUND FIELD; 125 DB TOP, 126 DB MIDDLE, 127 DB BOTTOM  
(SWEEP CHANGED BETWEEN TOP AND MIDDLE TRACES)



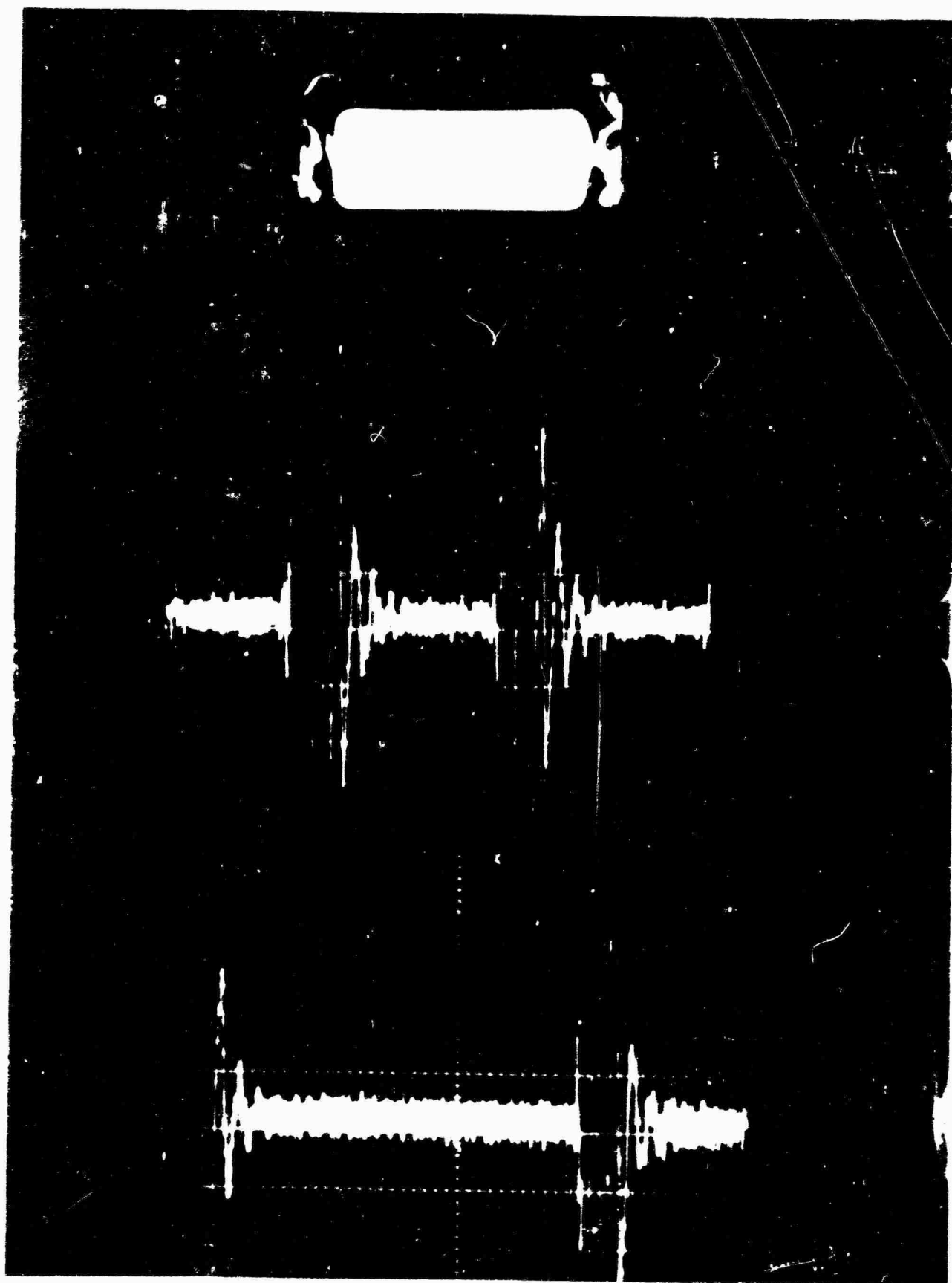


FIGURE 140  
OSCILLOSCOPE PHOTOGRAPH OF HOT WIRE SIGNAL FOR G' WIRE  
LOCATED AT 90° C IN 449 CPS, 130 DB SOUND FIELD (TRACE  
FROM LEFT TO RIGHT)

LONGITUDINAL TRANSDUCER  
LOW SUCTION (RUN 120)

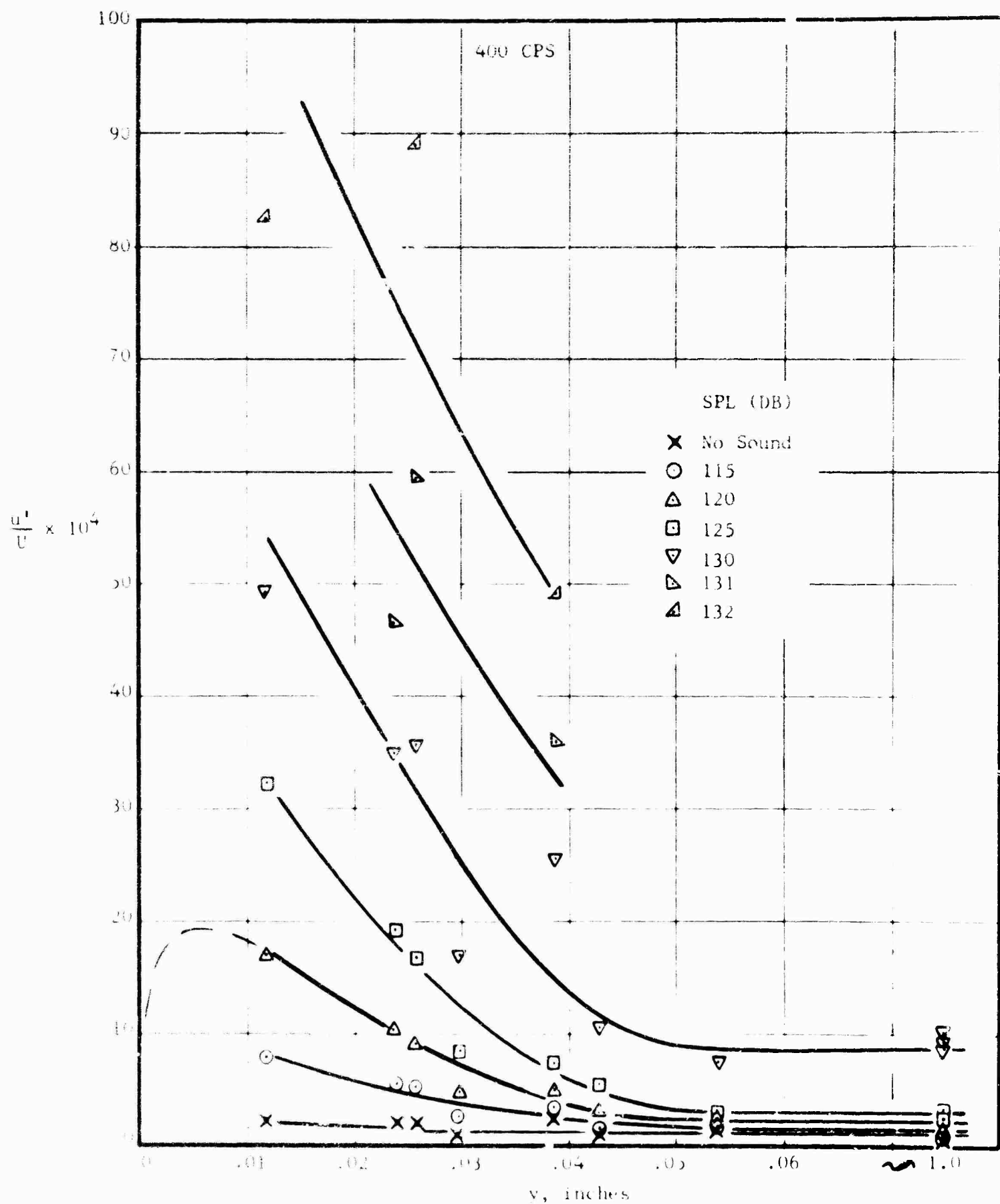


FIGURE 1-1  
LONGITUDINAL VELOCITY FLUCTUATIONS AT 45° CHORD  
TOP SWEEP SUCTION WING UNDER THE INFLUENCE OF SOUND  
 $Re = 8.1 \times 10^6$

Run 205,  $C_Q = 1.12 \times 10^{-4}$ ,  $C_Q/C_{Q205} = 1.00$   
 Run 206,  $C_Q = 1.25 \times 10^{-4}$ ,  $C_Q/C_{Q206} = 1.12$   
 Run 207,  $C_Q = 1.59 \times 10^{-4}$ ,  $C_Q/C_{Q207} = 1.42$

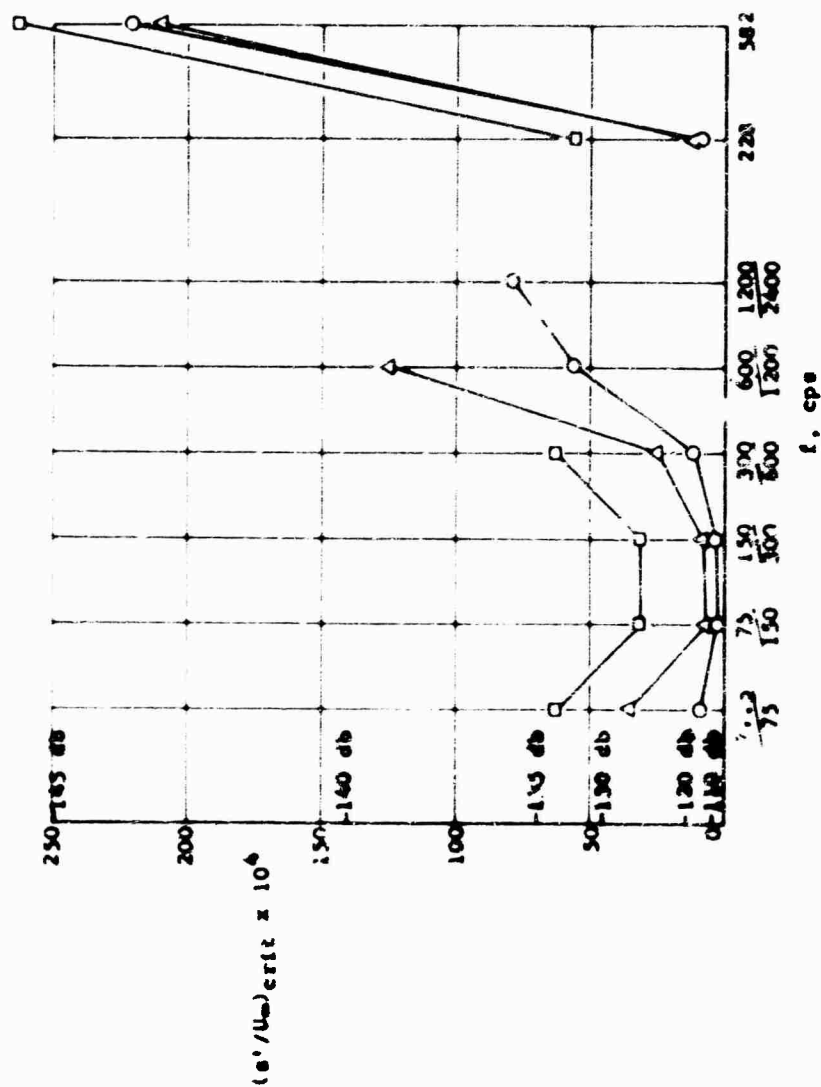
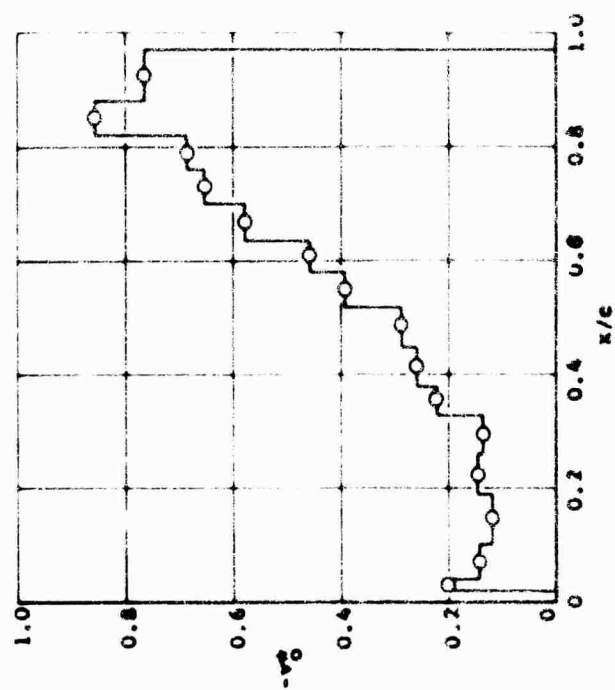


FIGURE 142 EFFECT OF SUCTION LEVEL INCREASE ON TRANSITION WITH INTERNAL SOUND,  $R_c = 11.5 \times 10^6$



Run 192,  $C_Q = 1.22 \times 10^{-4}$ ,  $C_Q/C_{Q192} = 1.00$   
 Run 193,  $C_Q = 1.32 \times 10^{-4}$ ,  $C_Q/C_{Q193} = 1.08$   
 Run 194,  $C_Q = 1.49 \times 10^{-4}$ ,  $C_Q/C_{Q194} = 1.22$   
 Run 195,  $C_Q = 1.64 \times 10^{-4}$ ,  $C_Q/C_{Q195} = 1.34$

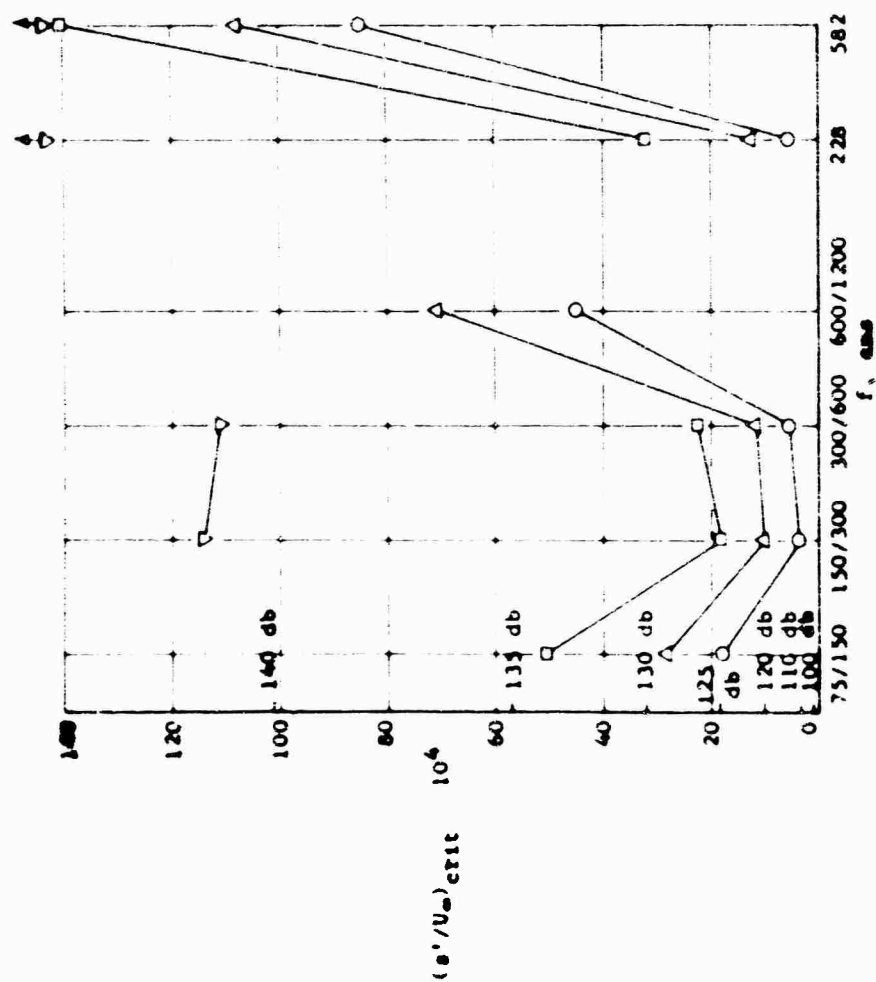
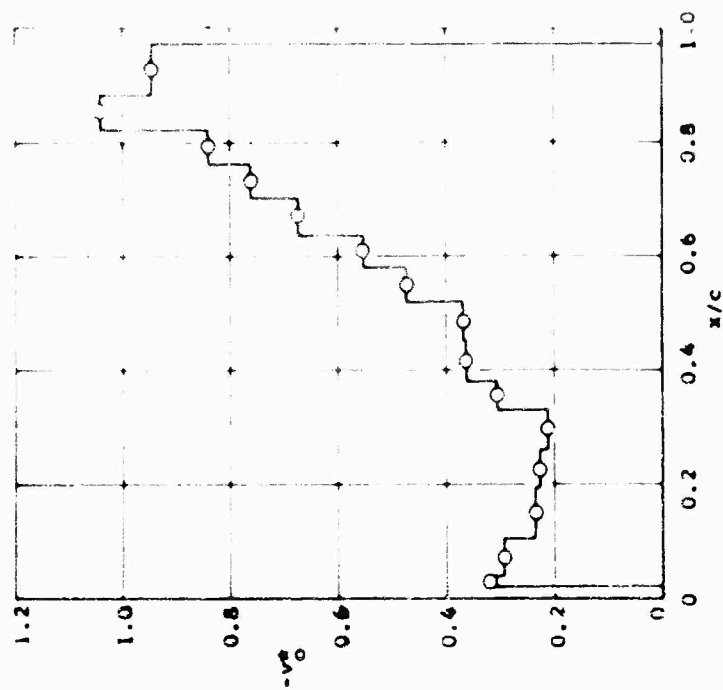


FIGURE 1-3 EFFECT OF INCREASING SUCTION LEVEL ON TRANSITION WITH INTERNAL SOUND,  $R_c = 16.4 \times 10^6$



Run 212,  $C_Q = 1.15 \times 10^{-4}$ ,  $C_Q/C_{Q212} = 1.00$   
 Run 241,  $C_Q = 1.21 \times 10^{-4}$ ,  $C_Q/C_{Q241} = 1.05$   
 Run 213,  $C_Q = 1.29 \times 10^{-4}$ ,  $C_Q/C_{Q213} = 1.10$   
 Run 214,  $C_Q = 1.34 \times 10^{-4}$ ,  $C_Q/C_{Q214} = 1.33$

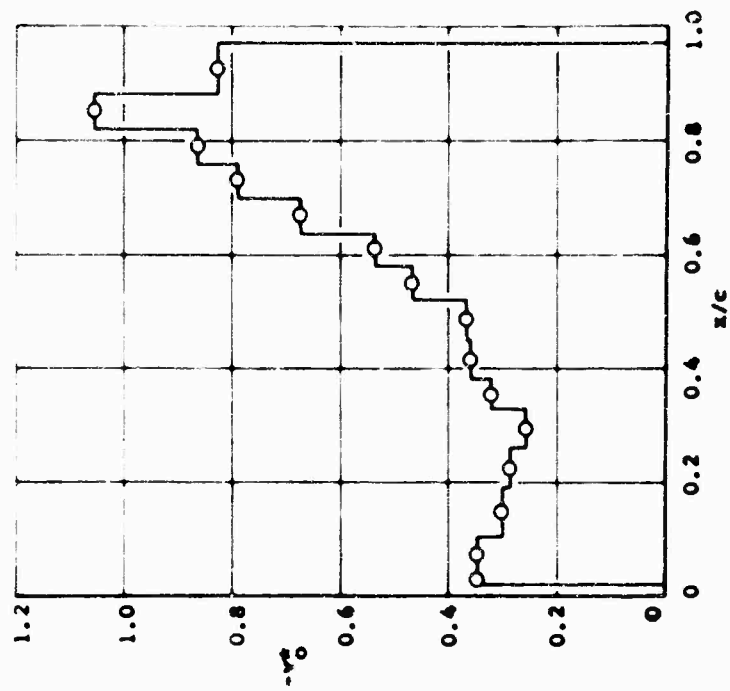
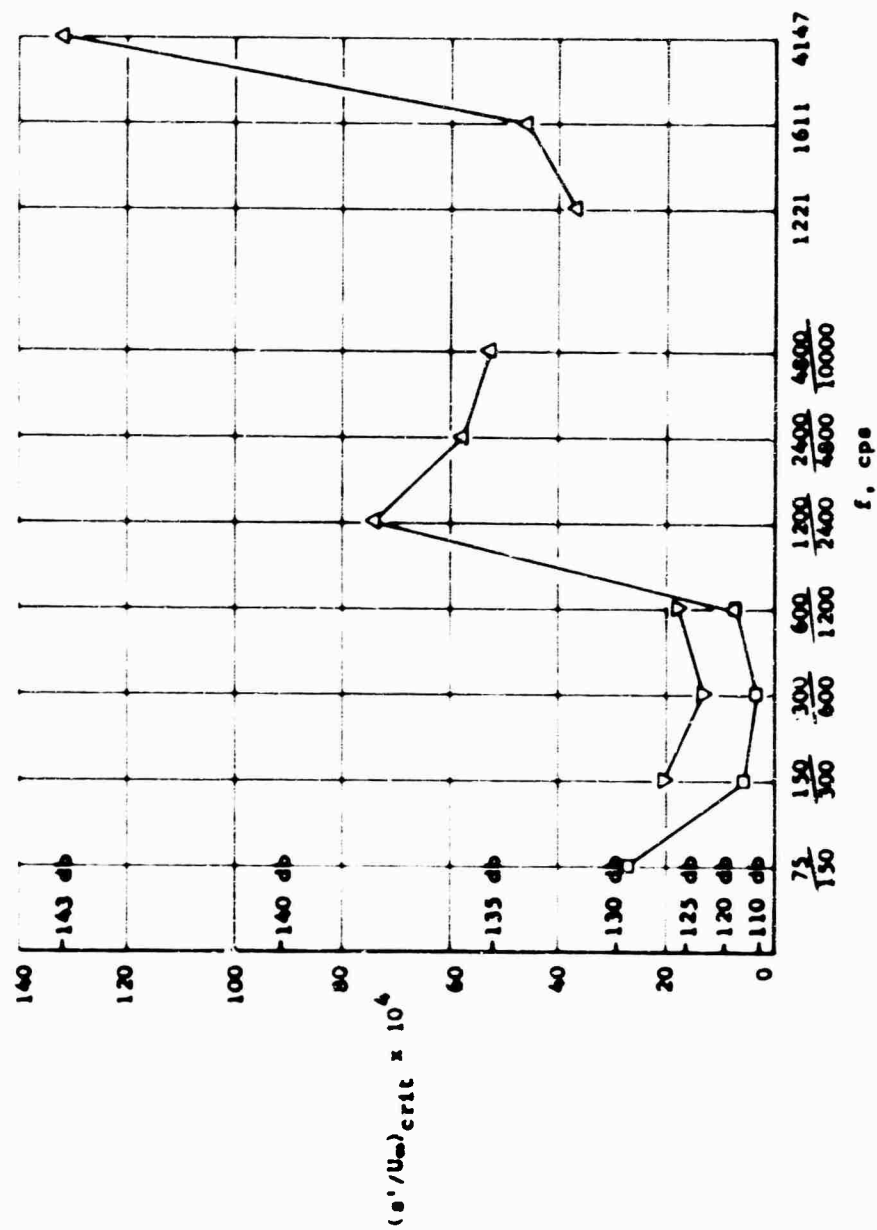


FIGURE 144 EFFECT OF INCREASING SUCTION LEVEL ON TRANSITION WITH INTERNAL SOUND,  $R_c = 18.9 \times 10^6$

Run 198,  $C_Q = 1.32 \times 10^{-4}$ ,  $C_Q/C_{Q198} = 1.00$   
 Run 203,  $C_Q = 1.33 \times 10^{-4}$ ,  $C_Q/C_{Q203} = 1.01$   
 Run 199,  $C_Q = 1.44 \times 10^{-4}$ ,  $C_Q/C_{Q199} = 1.09$   
 Run 200,  $C_Q = 1.58 \times 10^{-4}$ ,  $C_Q/C_{Q200} = 1.20$   
 Run 202,  $C_Q = 2.49 \times 10^{-4}$ ,  $C_Q/C_{Q202} = 1.89$

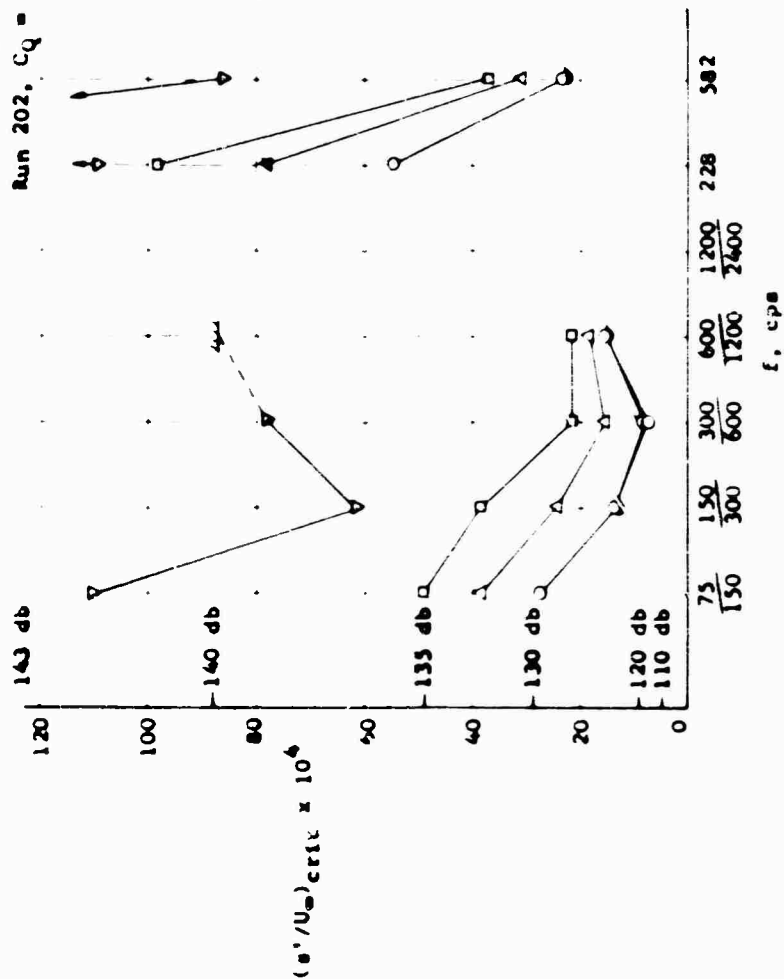
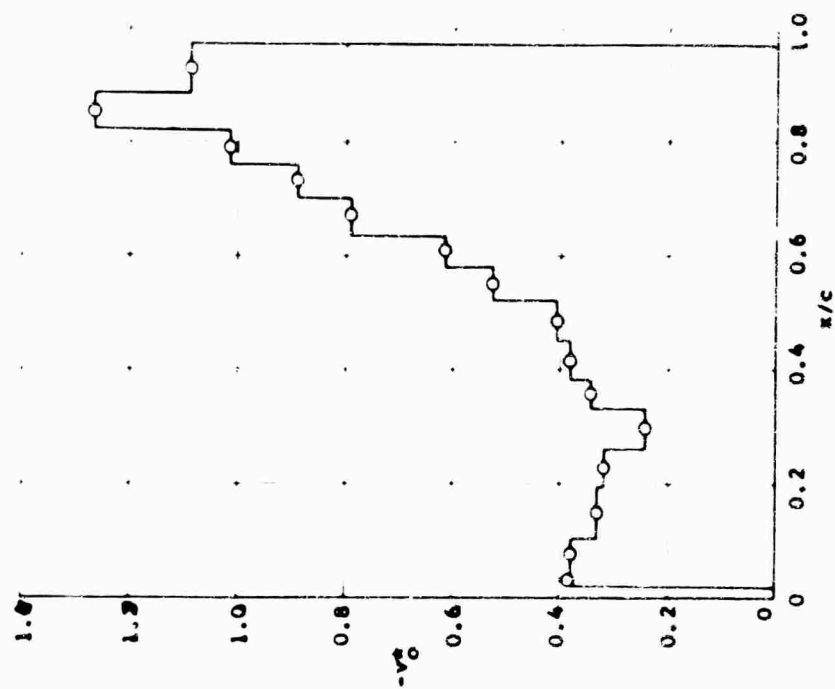


FIGURE 145 EFFECT OF SUCTION LEVEL INCREASE ON TRANSITION WITH INTERNAL SOUND,  $R_c = 19.3 \times 10^6$

Run 192,  $C_Q = 1.22 \times 10^{-4}$ ,  $C_Q/C_{Q192} = 1.00$   
 Run 196,  $C_Q = 1.34 \times 10^{-4}$ ,  $C_Q/C_{Q196} = 1.10$   
 Run 197,  $C_Q = 1.45 \times 10^{-4}$ ,  $C_Q/C_{Q197} = 1.19$

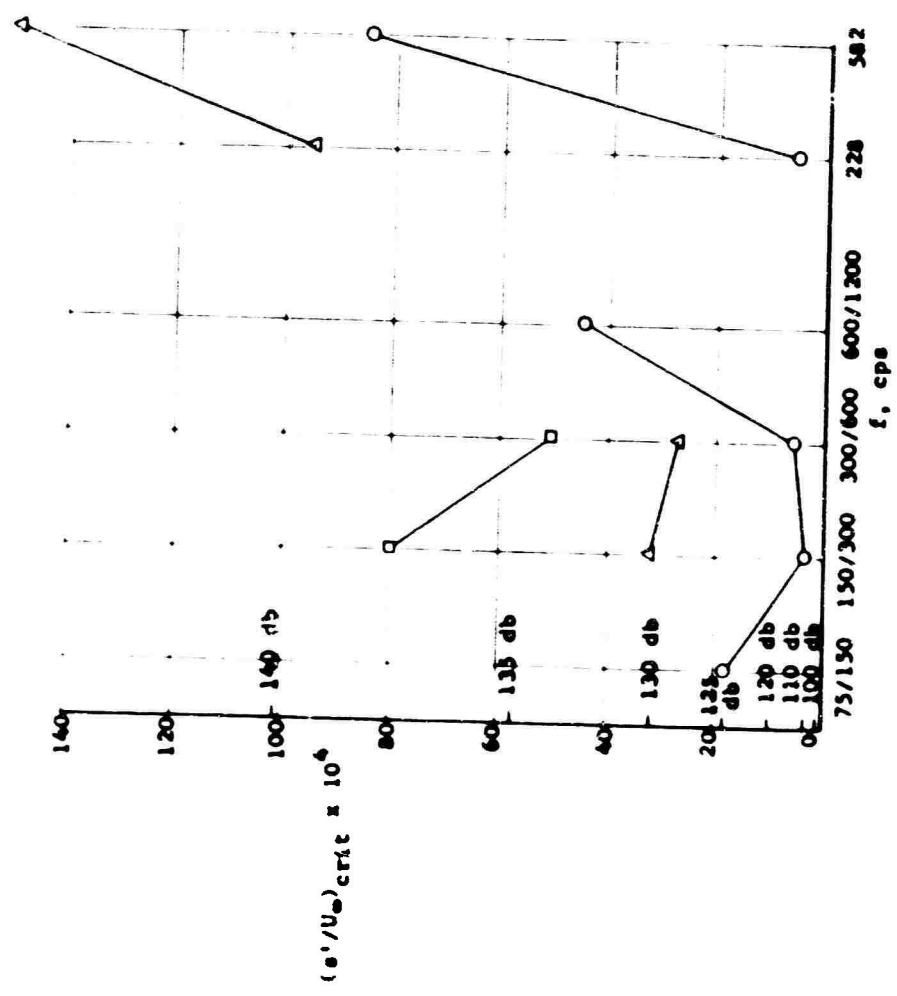
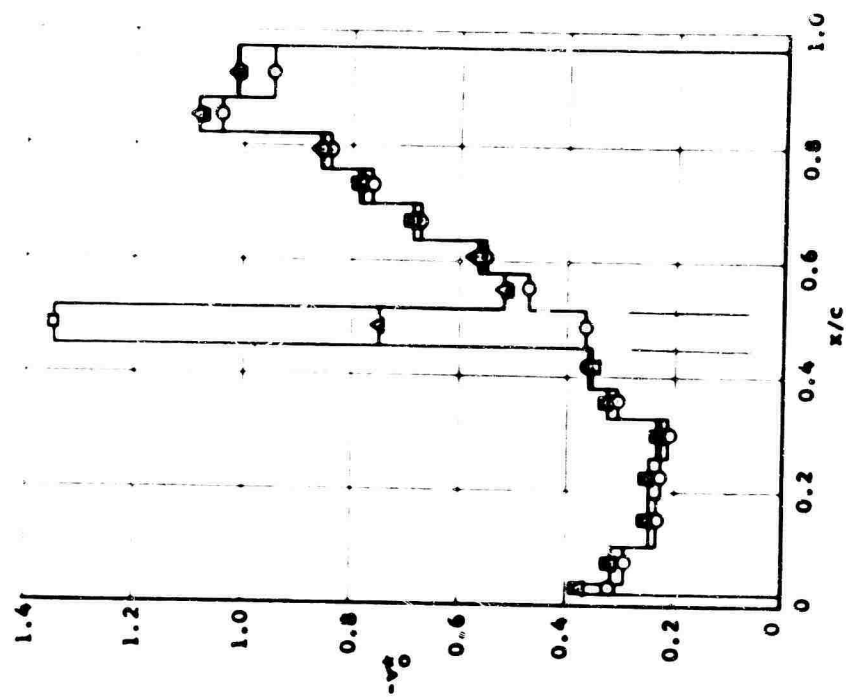


FIGURE 146 EFFECT OF LOCAL SUCTION INCREASE ON TRANSITION WITH INTERNAL SOUND,  $R_c = 16.4 \times 10^6$



Run 198,  $C_Q = 1.32 \times 10^{-4}$ ,  $C_Q/C_{Q198} = 1.00$   
 Run 204,  $C_Q = 1.36 \times 10^{-4}$ ,  $C_Q/C_{Q204} = 1.03$

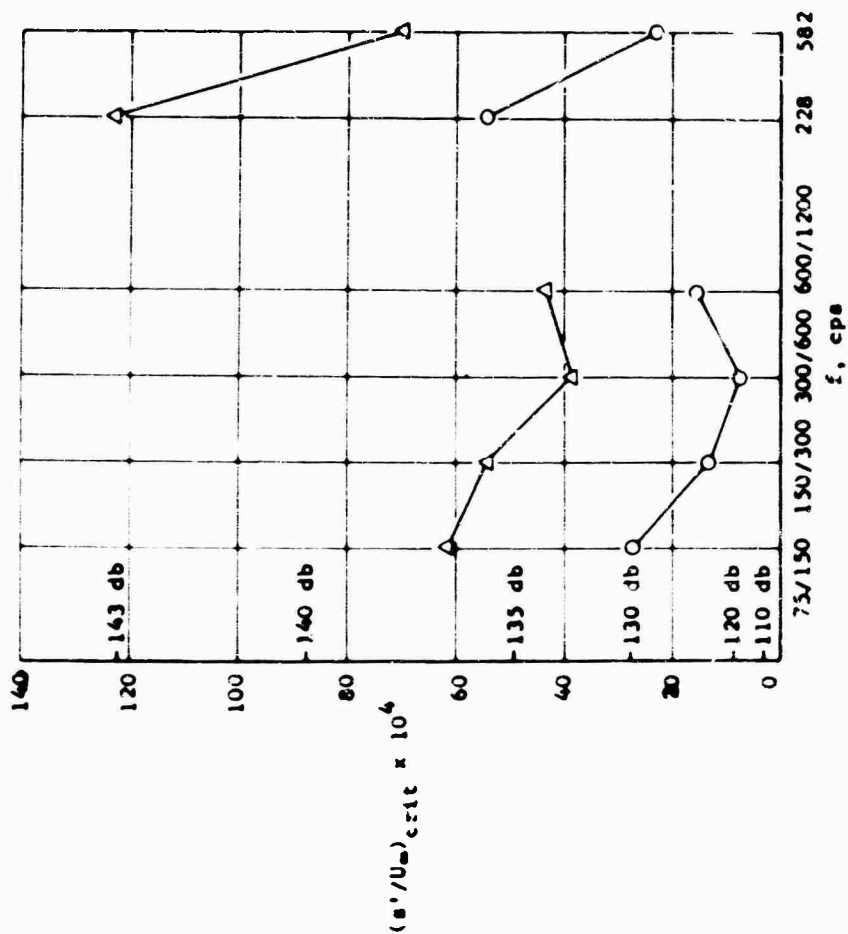
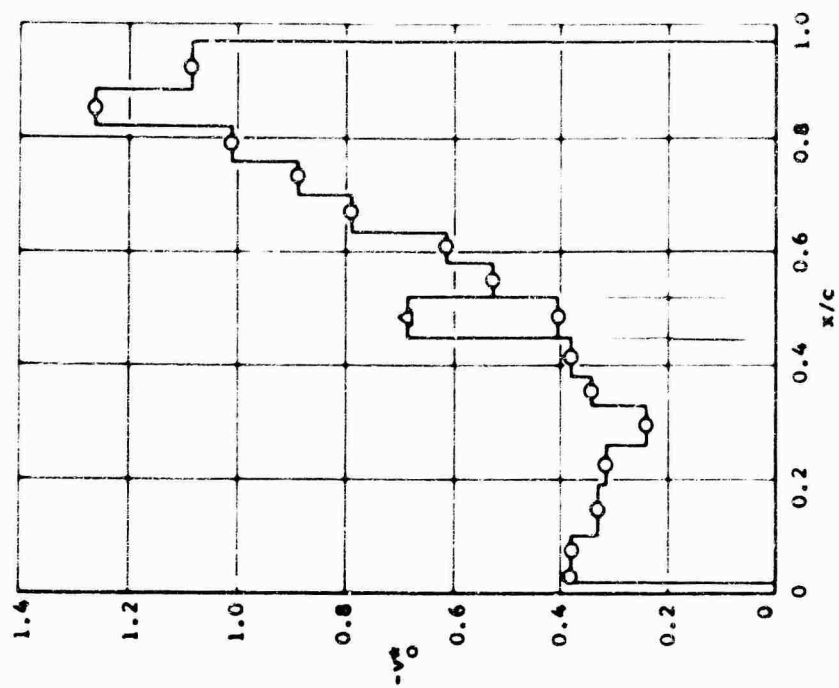


FIGURE 147 EFFECT OF LOCAL SUCTION INCREASE ON TRANSITION WITH INTERNAL SOUND,  $R_c = 19.3 \times 10^6$





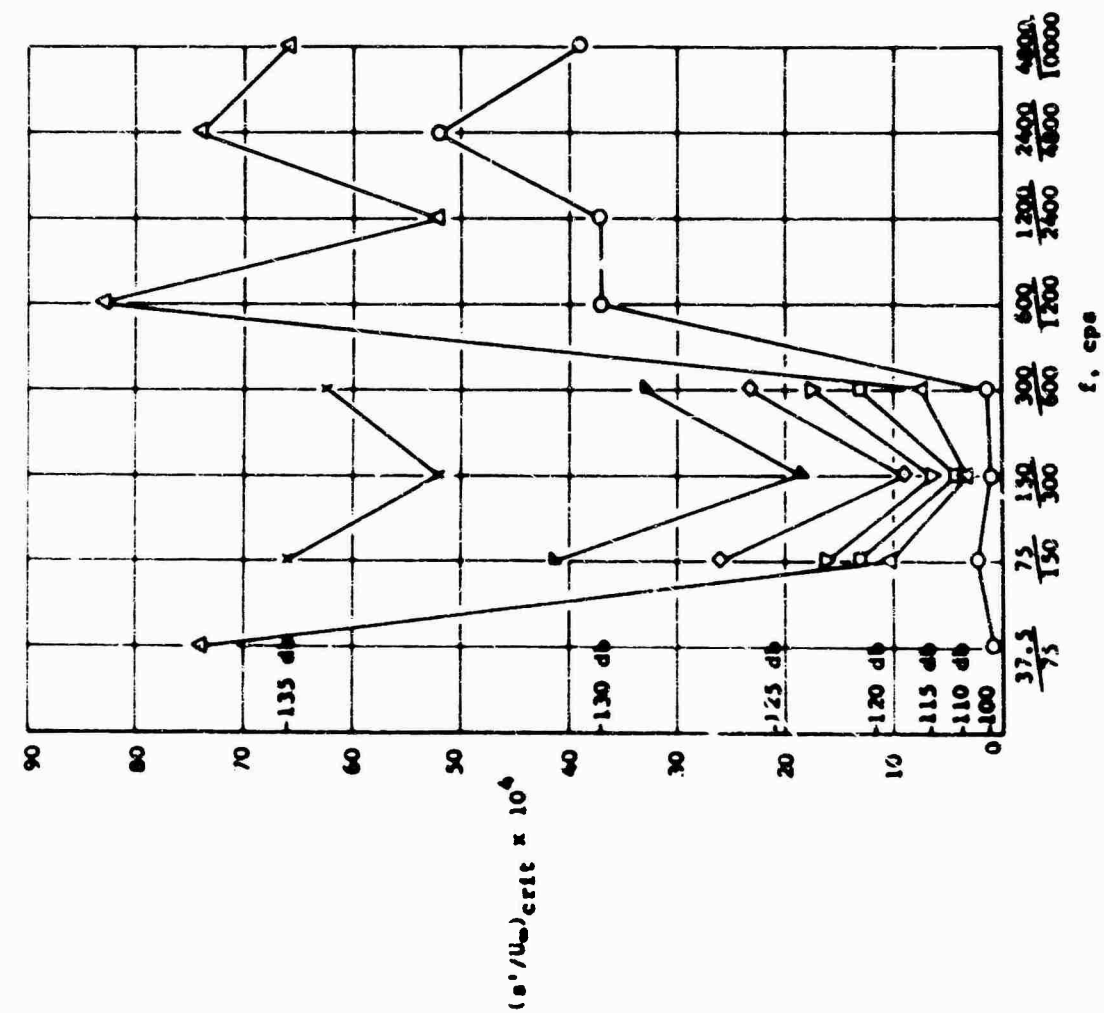
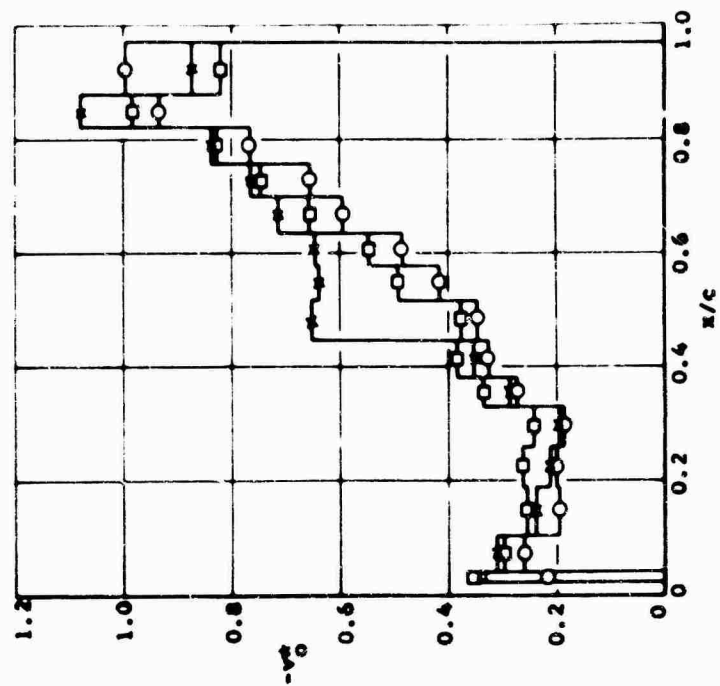


FIGURE 148 EFFECT OF SUCTION ON TRANSITION WITH INTERNAL SOUND,  $R_c = 14.2 \times 10^6$

Run 243,  $C_Q = 1.20 \times 10^{-4}$ ,  $C_Q/C_{Q243} = 1.00$   
 Run 244,  $C_Q = 1.32 \times 10^{-4}$ ,  $C_Q/C_{Q244} = 1.10$   
 Run 187,  $C_Q = 1.28 \times 10^{-4}$ ,  $C_Q/C_{Q187} = 1.07$   
 Run 191,  $C_Q = 1.31 \times 10^{-4}$ ,  $C_Q/C_{Q191} = 1.09$   
 Run 188,  $C_Q = 1.38 \times 10^{-4}$ ,  $C_Q/C_{Q188} = 1.15$   
 Run 189,  $C_Q = 1.52 \times 10^{-4}$ ,  $C_Q/C_{Q189} = 1.27$   
 Run 190,  $C_Q = 1.39 \times 10^{-4}$ ,  $C_Q/C_{Q190} = 1.16$



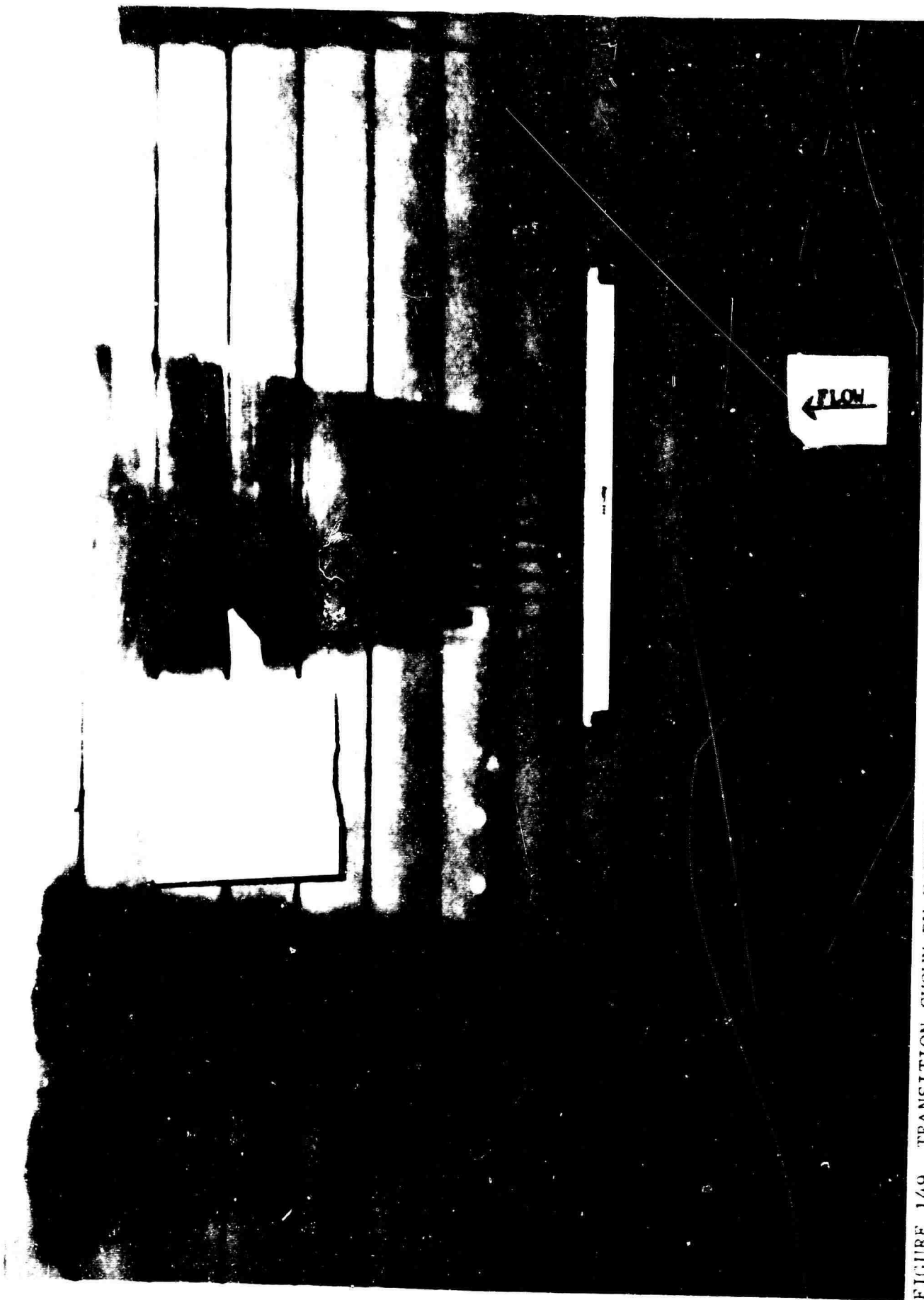


FIGURE 149 TRANSITION SHOWN BY NAPHTHALENE SPRAY TECHNIQUE, INTERNAL SOUND, 150 DB, 582 CPS,  
 $R_c = 11.5 \times 10^6$ , SUCTION RUN 205

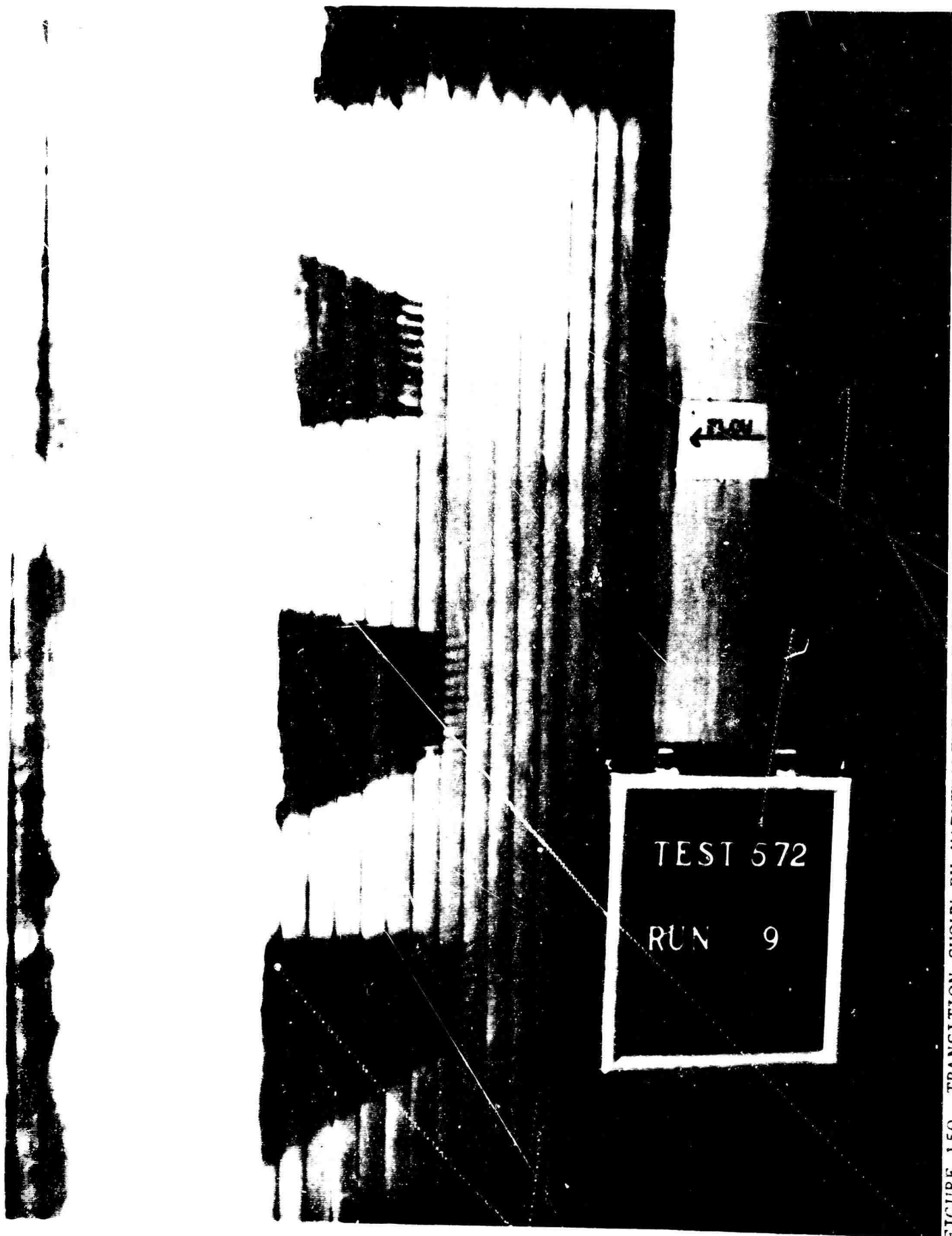


FIGURE 150 TRANSITION SHOWN BY NAPHTHALENE SPRAY TECHNIQUE. INTERNAL SOUND, 150 DB, 582 CPS

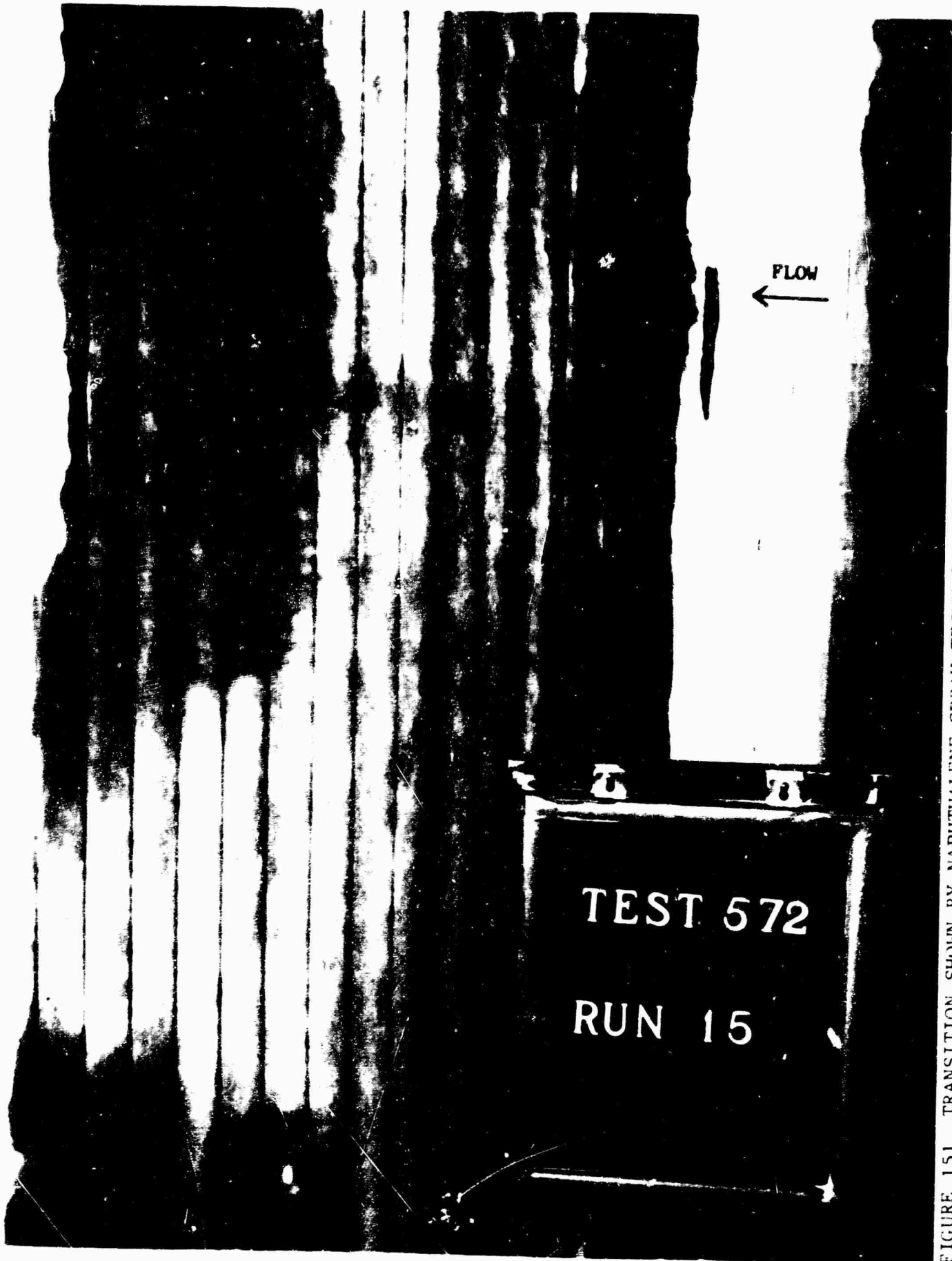


FIGURE 151 TRANSITION SHOWN BY NAPHTHALENE SPRAY TECHNIQUE, INTERNAL SOUND, 146 DB, 200 CPS,  
 $R_c = 11.5 \times 10^6$ , SUCTION RUN 205, TRANSITION AT 50% CHORD, RUN 15

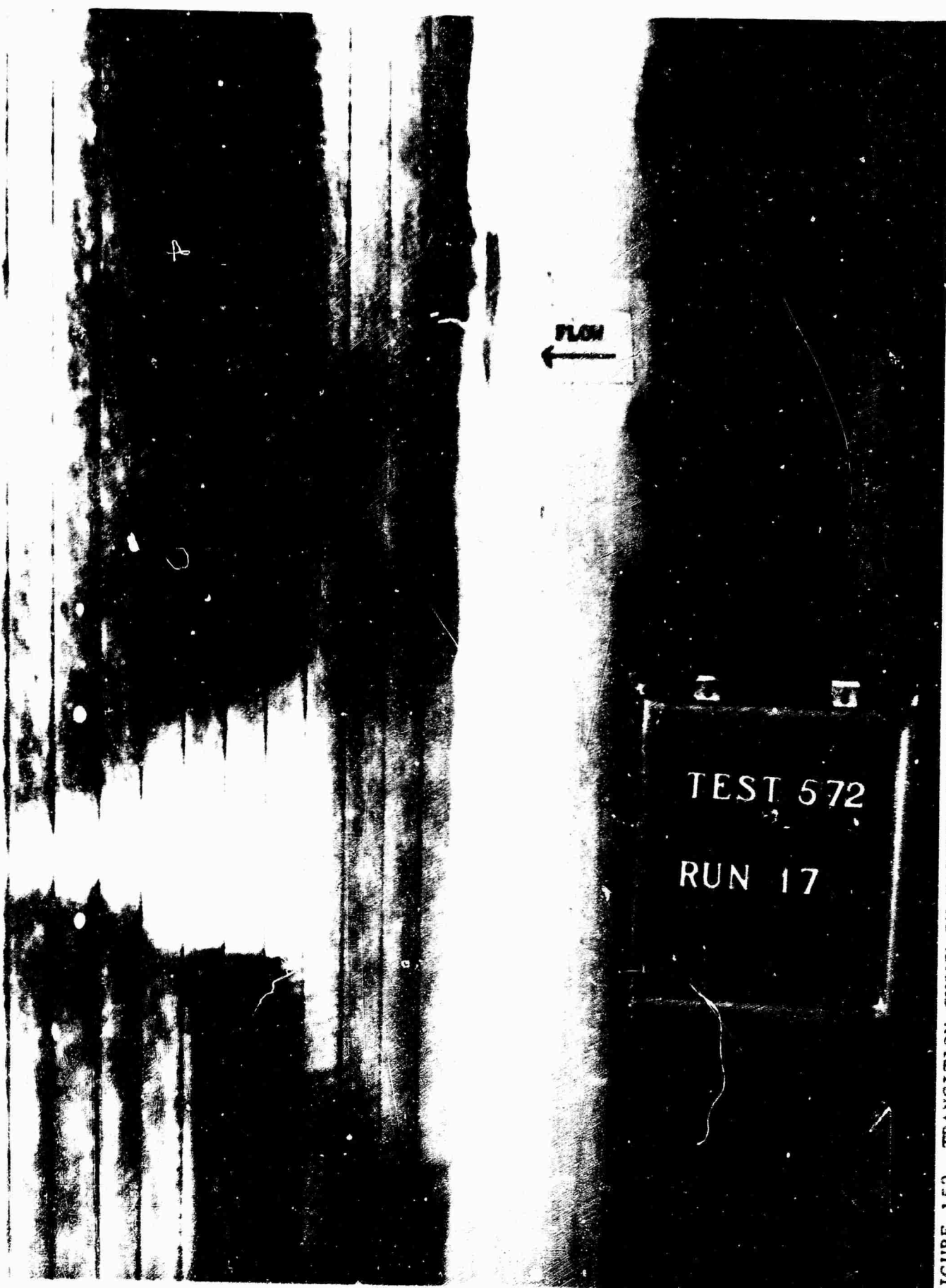


FIGURE 152 TRANSITION SHOWN BY NAPHTHALENE SPRAY TECHNIQUE, INTERNAL SOUND, 159 DB, 200 CPS,  
 $R_c = 11.5 \times 10^6$ , SUCTION RUN 205, TRANSITION AT ABOUT 45%, RUN 17

Run 228, No Vibration  
 Run 231, 10g at 100 cps  
 Run 218, 30g at 190 cps

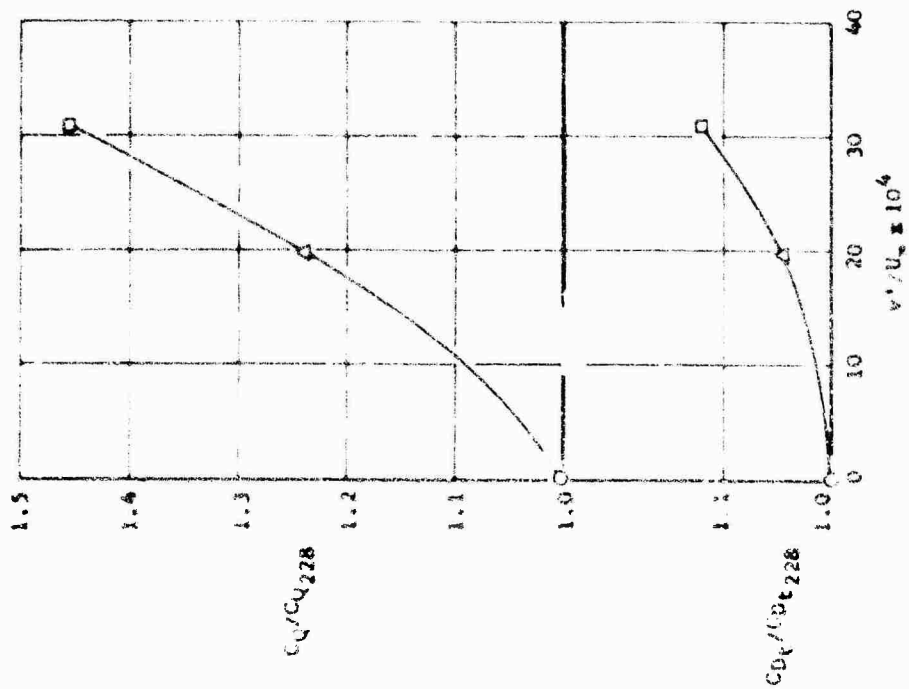
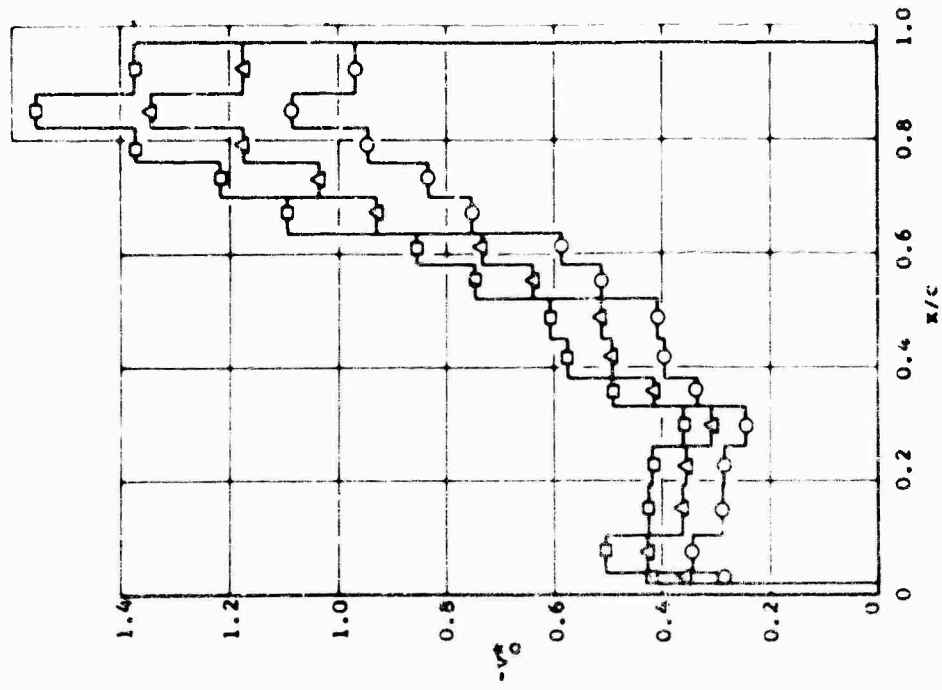


FIGURE 103 DRAG EFFECT OF INCREASING SUCTION LEVEL TO MAINTAIN LAMINAR FLOW WITH FORCED PANEL VIBRATION,  $R_c = 18.9 \times 10^6$



○ Run 9, No Vibration  
 △ Run 182, 22g at 190 cps  
 □ Run 183, 34g at 240 cps

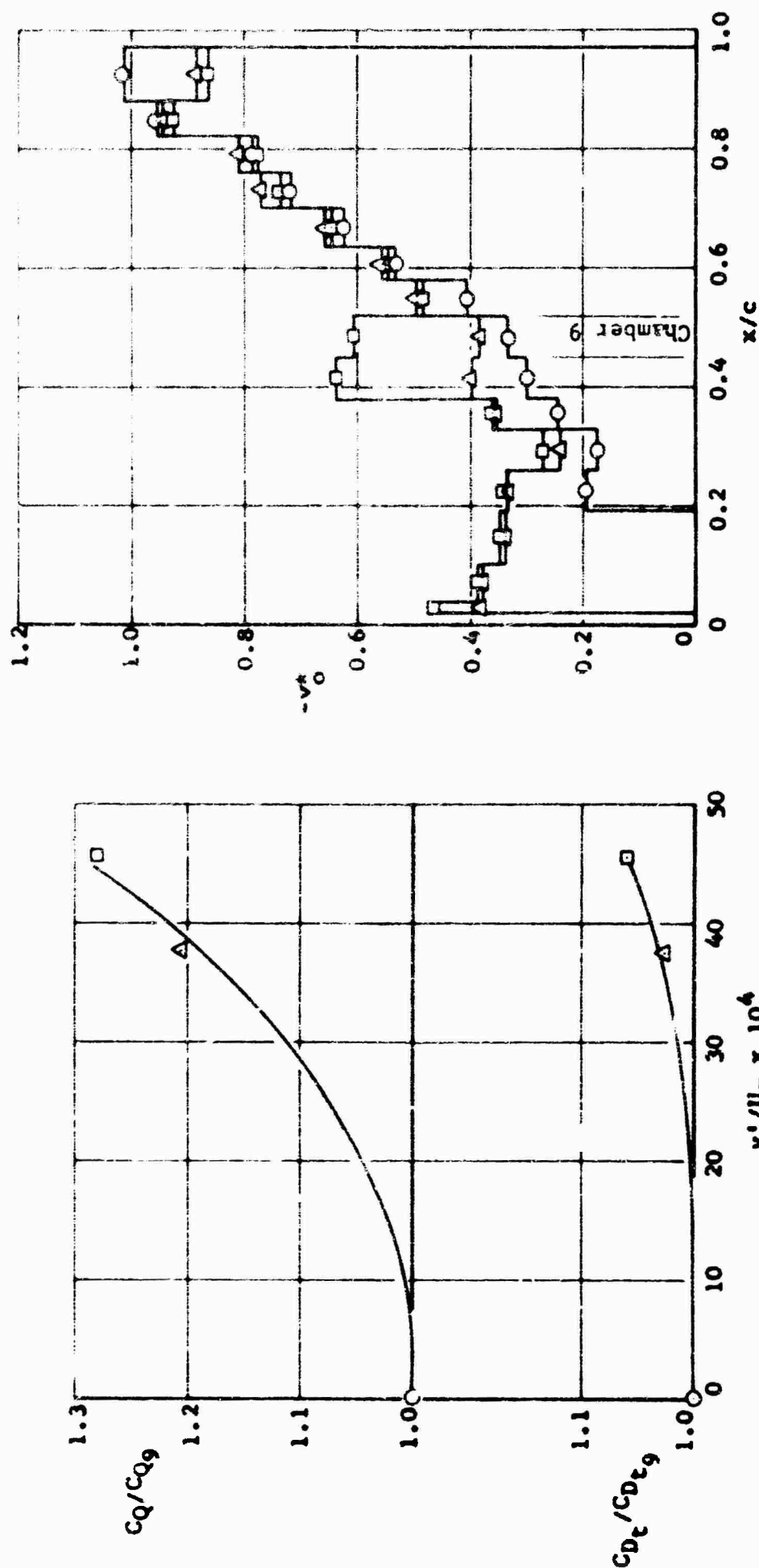


FIGURE 154 DRAG EFFECT OF INCREASING SUCTION LOCALLY TO MAINTAIN LAMINAR FLOW  
 WITH FORCED PANEL VIBRATION,  $R_c = 11.5 \times 10^6$

○ Run 244, No Vibration  
 △ Run 167, 21g at 190 cps  
 □ Run 166, 32g at 190 cps  
 Run 165, 43g at 240 cps

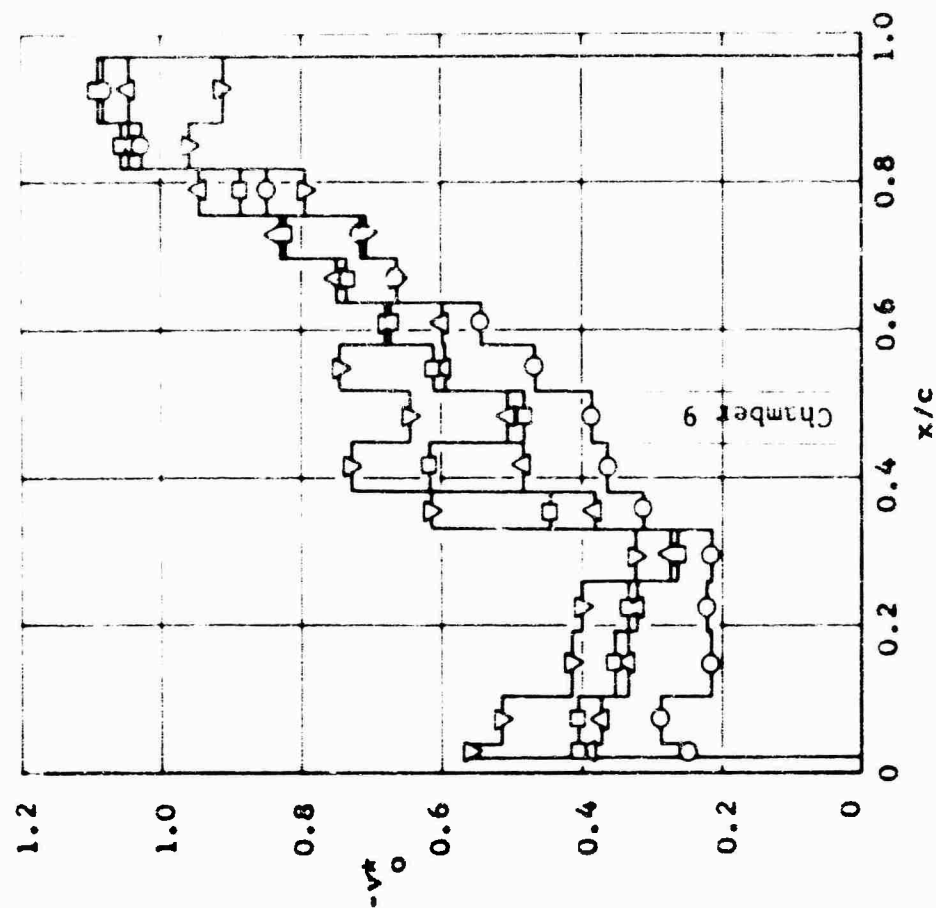
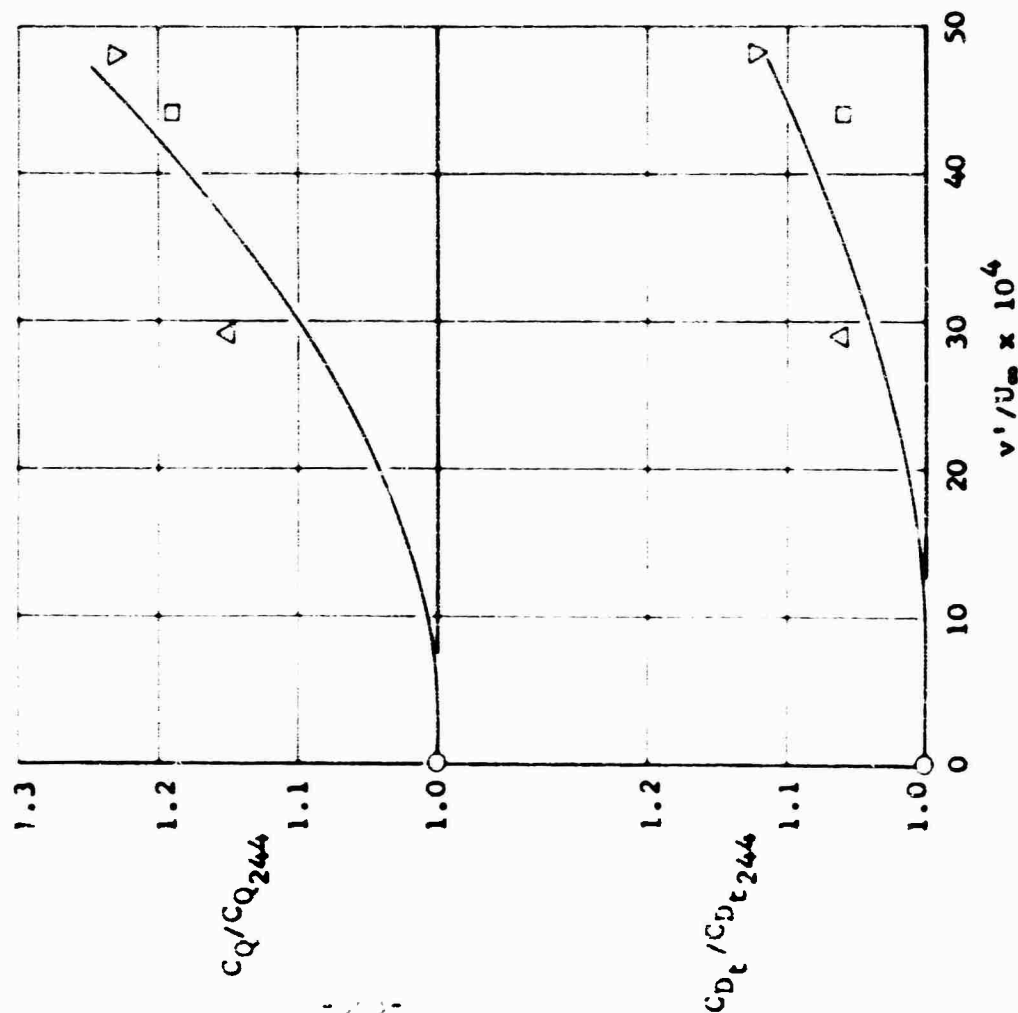


FIGURE 155 DRAG EFFECT OF INCREASING SUCTION LOCALLY TO MAINTAIN LAMINAR FLOW  
 WITH FORCED PANEL VIBRATION,  $R_c = 14.2 \times 10^6$



- Run 19, No Vibration  
 ▲ Run 184, 21.5g at 190 cps  
 □ Run 185, 35g at 240 cps

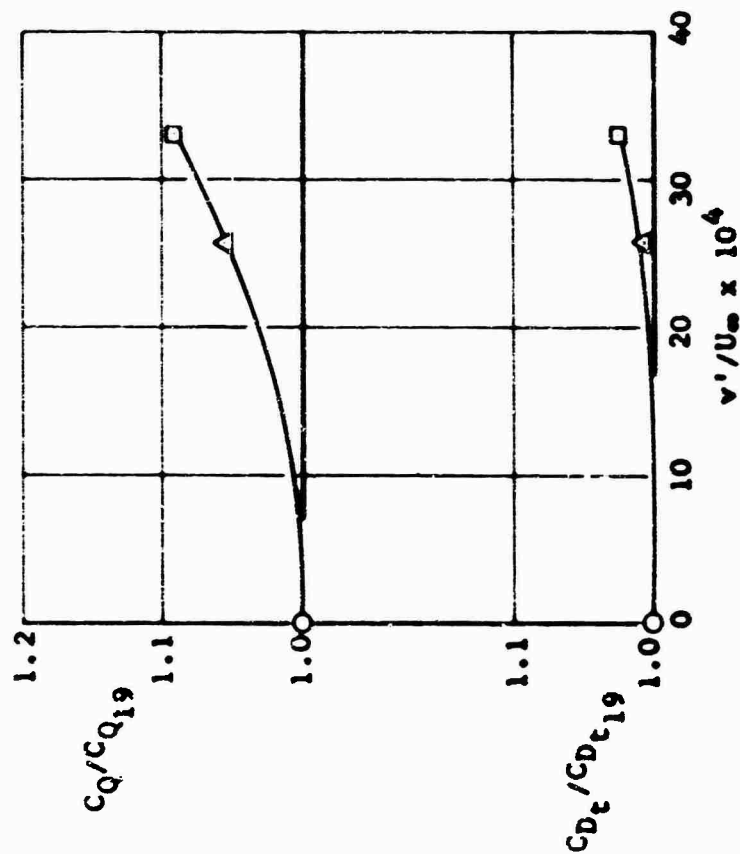
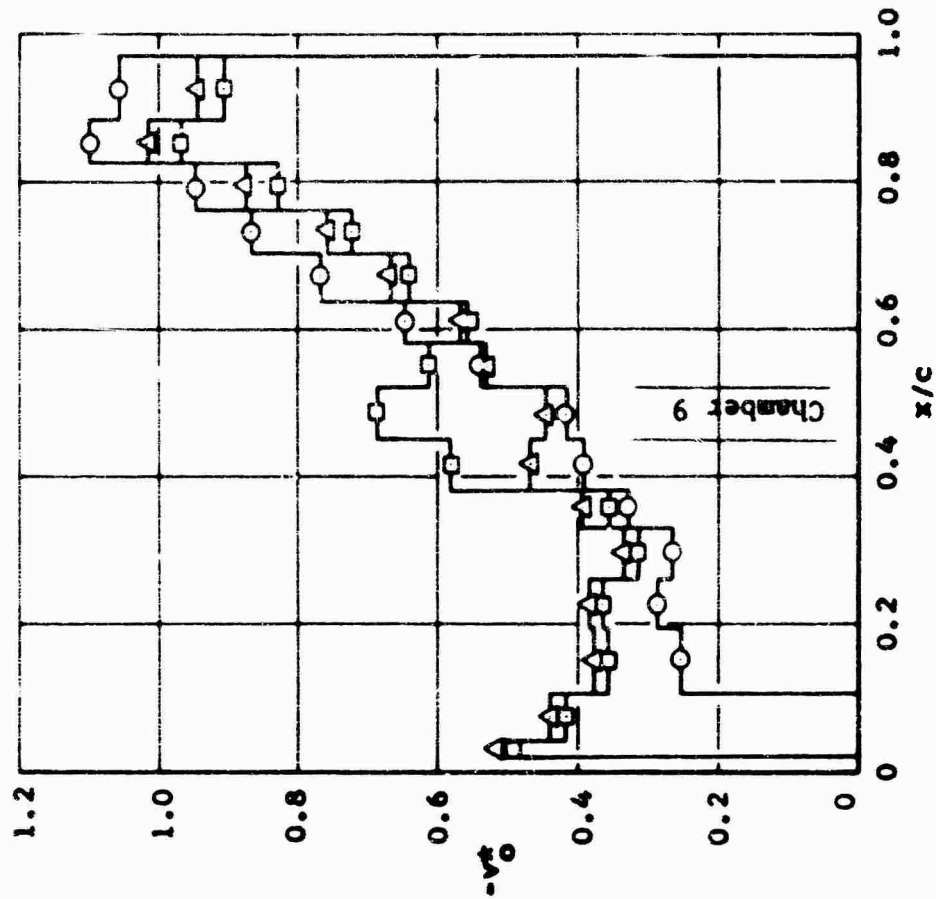


FIGURE 156 DRAG EFFECT OF INCREASING SUCTION LOCALLY TO MAINTAIN LAMINAR  
 FLOW WITH FORCED PANEL VIBRATION,  $R_c = 16.4 \times 10^6$

- Run 228, No Vibration
- △ Run 176, 20g at 190 cps
- Run 179, 21g at 190 cps
- ▢ Run 177, 32g at 240 cps
- Run 180, 33g at 240 cps
- Run 178, 46g at 240 cps

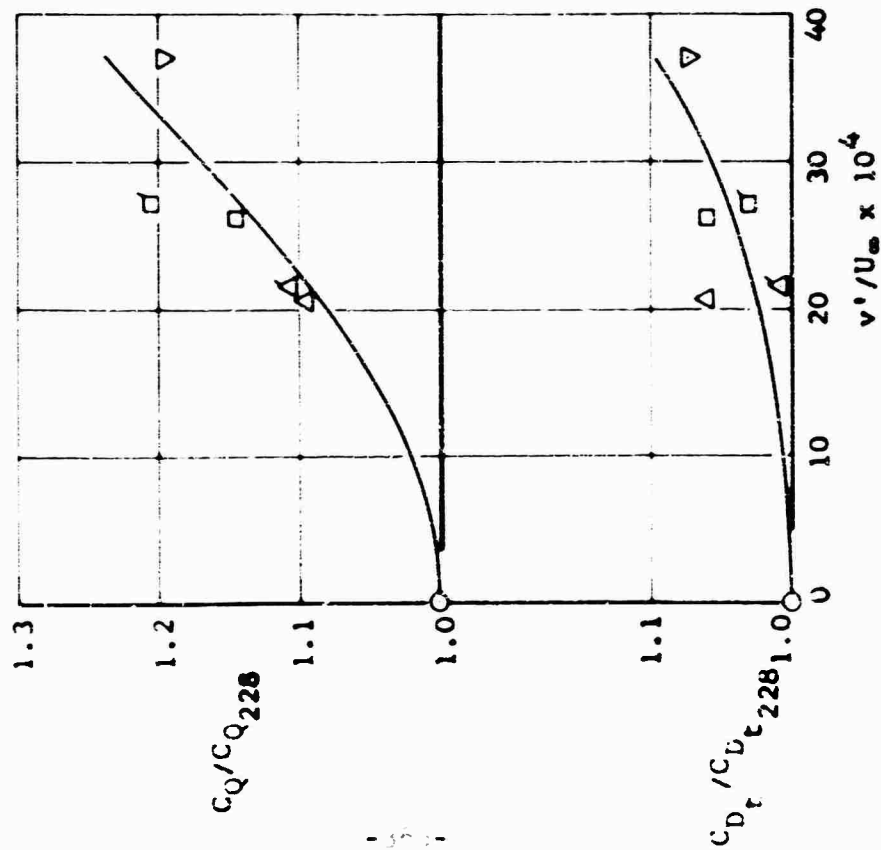
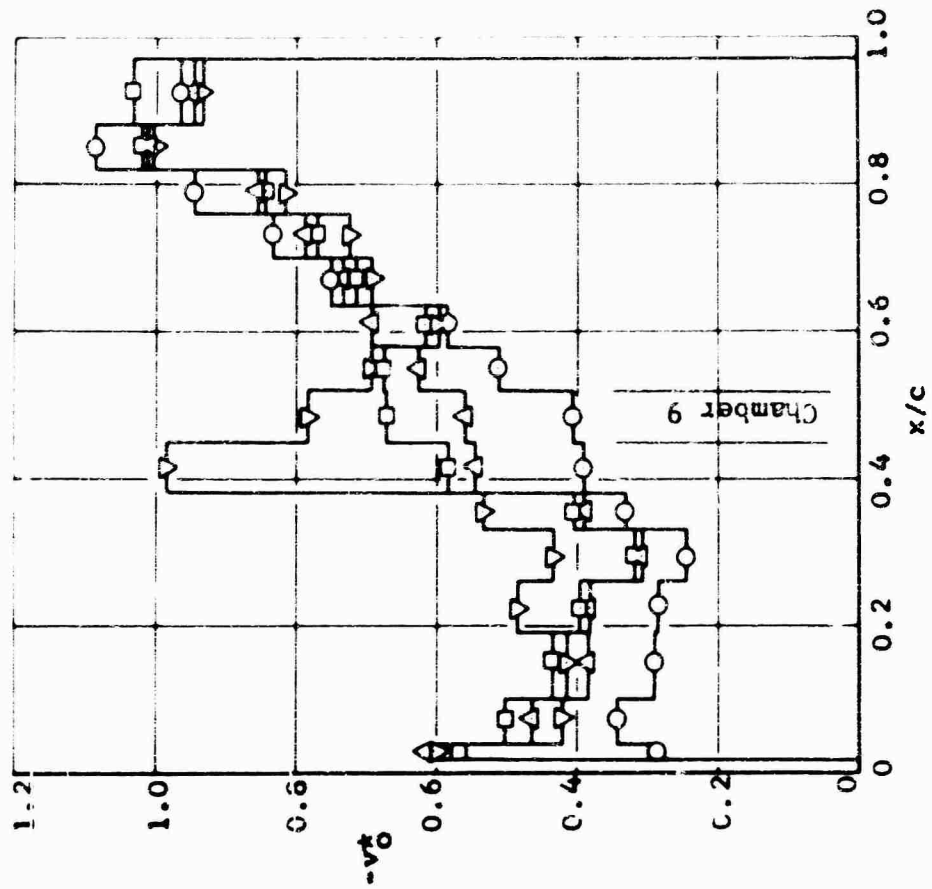


FIGURE 157 DRAG EFFECT OF INCREASING SUCTION LOCALLY TO MAINTAIN LAMINAR FLOW WITH FORCED PANEL VIBRATION,  $R_C = 18.9 \times 10^6$

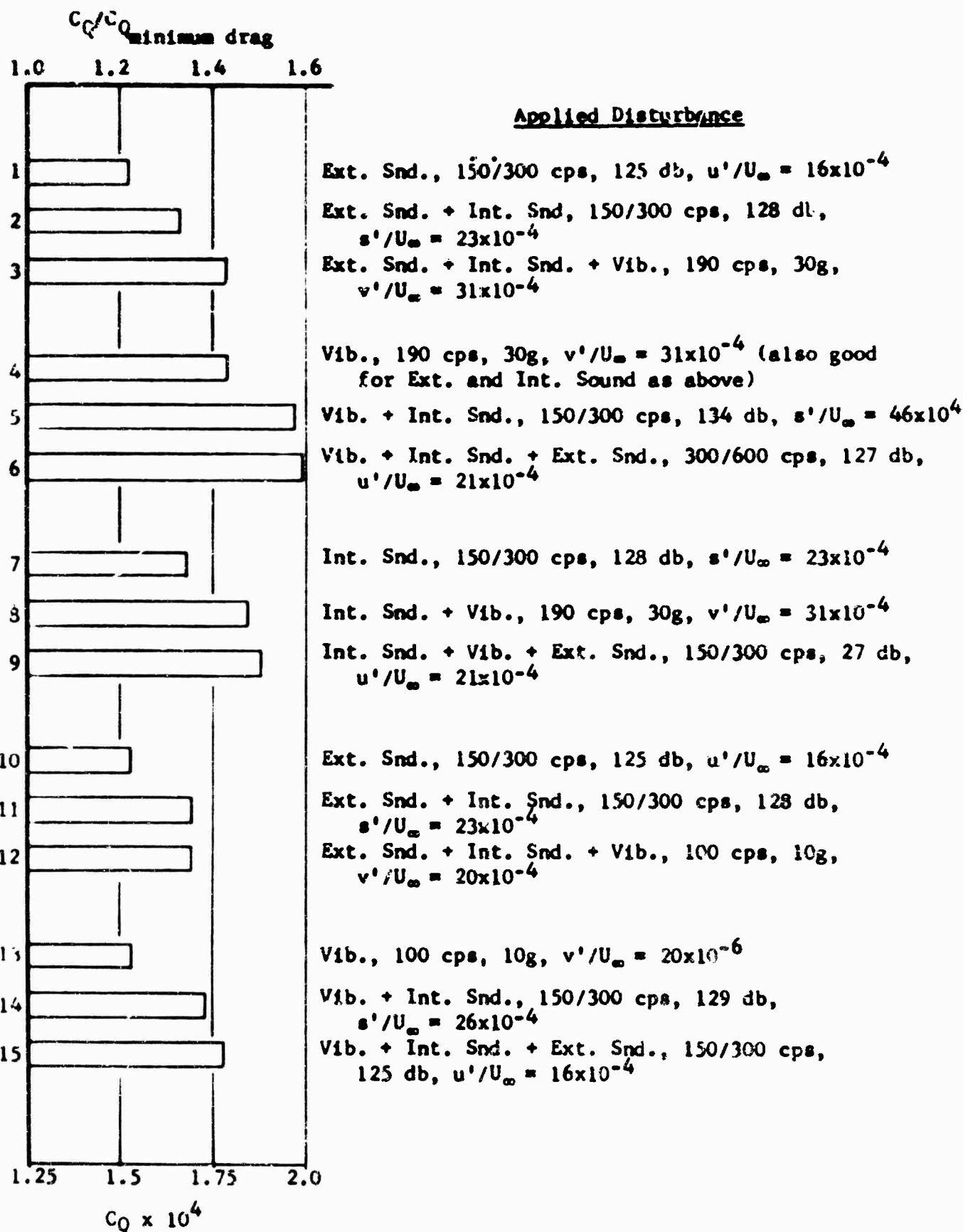


FIGURE 158 SUCTION REQUIREMENTS FOR LAMINAR FLOW WITH VARIOUS COMBINATIONS OF EXTERNAL SOUND, INTERNAL SOUND AND VIBRATION,  $R_c = 18.9 \times 10^6$

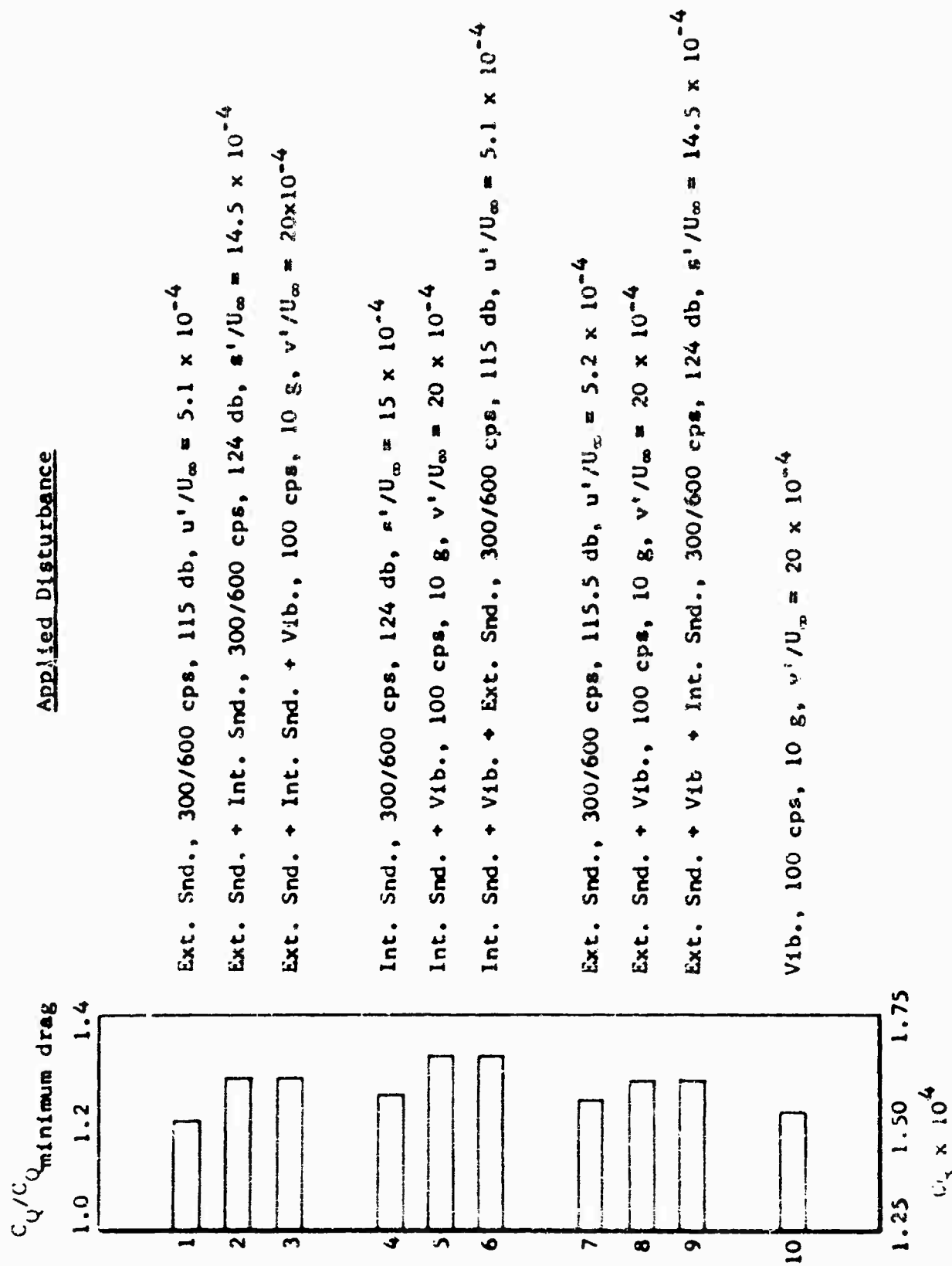
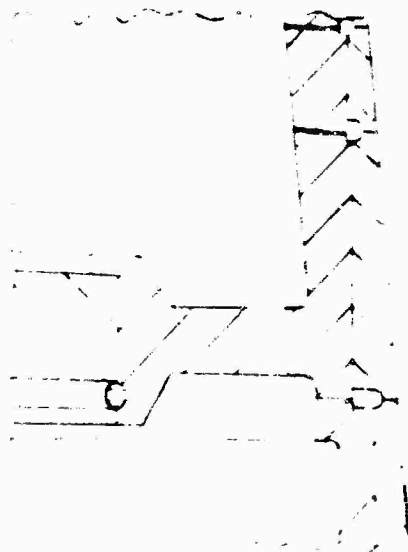
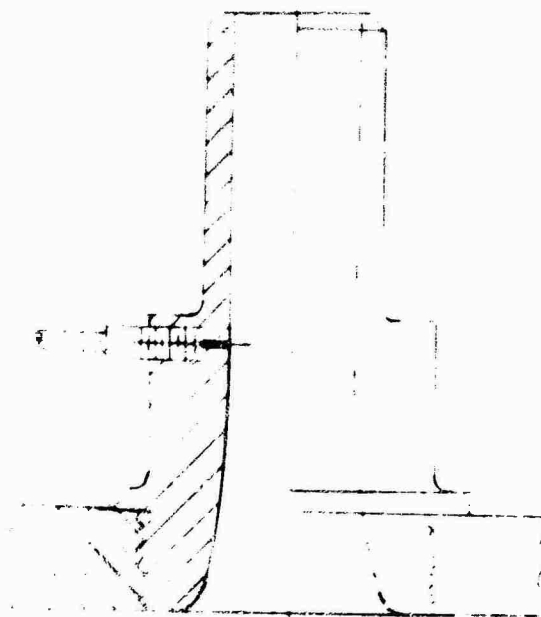


FIGURE 159 SUCTION REQUIREMENTS FOR LAMINAR FLOW WITH EQUAL STRENGTH COMBINATIONS OF EXTERNAL SOUND, INTERNAL SOUND AND VIBRATION,  $R_C = 18.9 \times 10^6$



Schematic View Showing Typical Bulkhead  
Installation and Details of Suction Slot,  
Plenum Chamber and Suction Flow Metering Holes



Schematic View of Typical Flow  
Measuring Nozzle Installation



FIGURE 160

MODIFIED SEARS-HAACK BODY OF REVOLUTION

MODEL CROSS SECTION WITH DETAILS OF SUCTION SLOTS

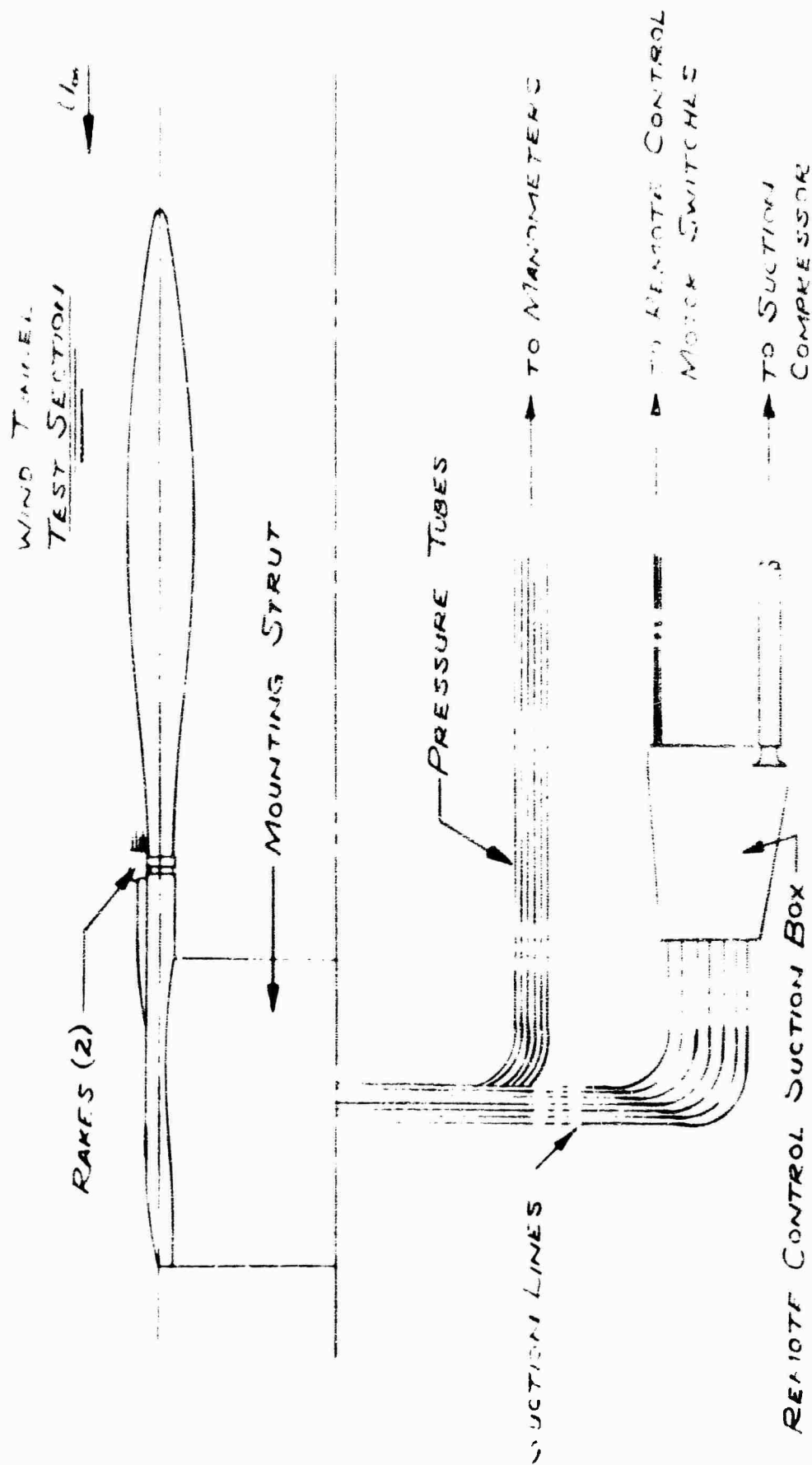


FIGURE 161

MODIFIED SEARS-HAACK BODY OF REVOLUTION

INSTALLATION DRAWING

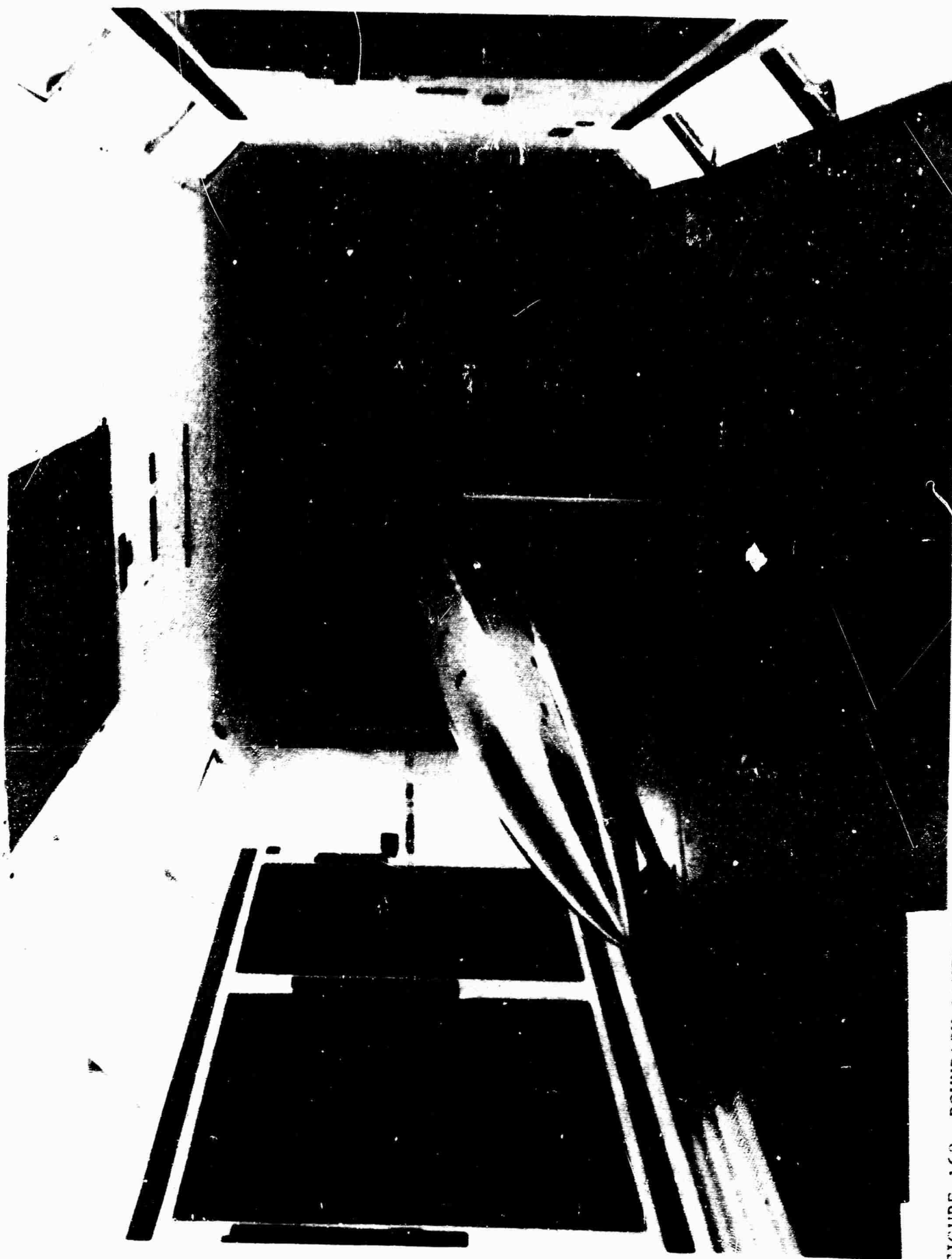


FIGURE 162 BOUNDARY LAYER CONTROL SEARS-HAACK BODY OF REVOLUTION



FIGURE 163 BOUNDARY LAYER CONTROL SEARS-HAACK BODY OF REVOLUTION



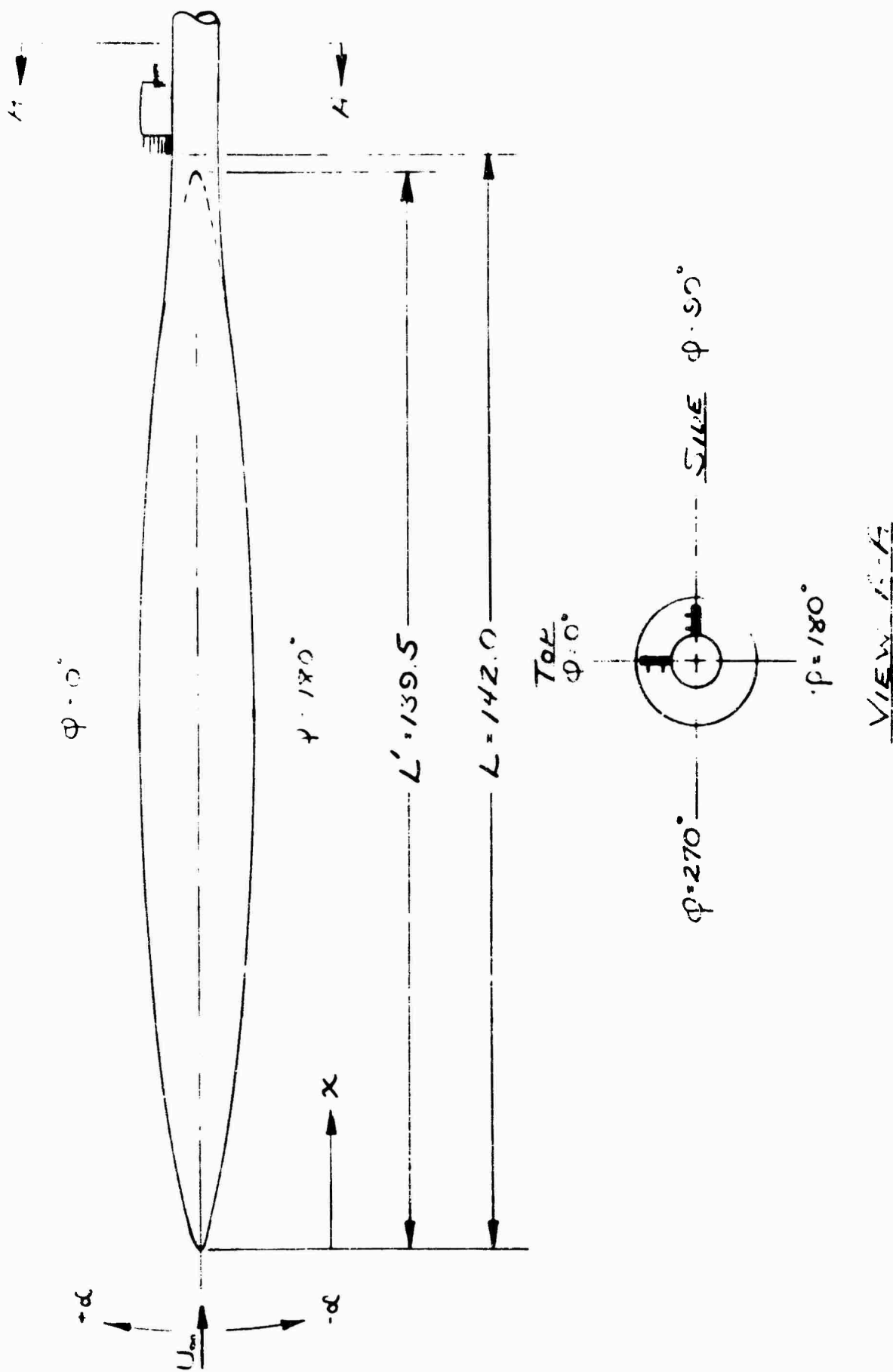


FIGURE 164

MODIFIED SEARS-HAACK BODY OF REVOLUTION

COORDINATE SYSTEM

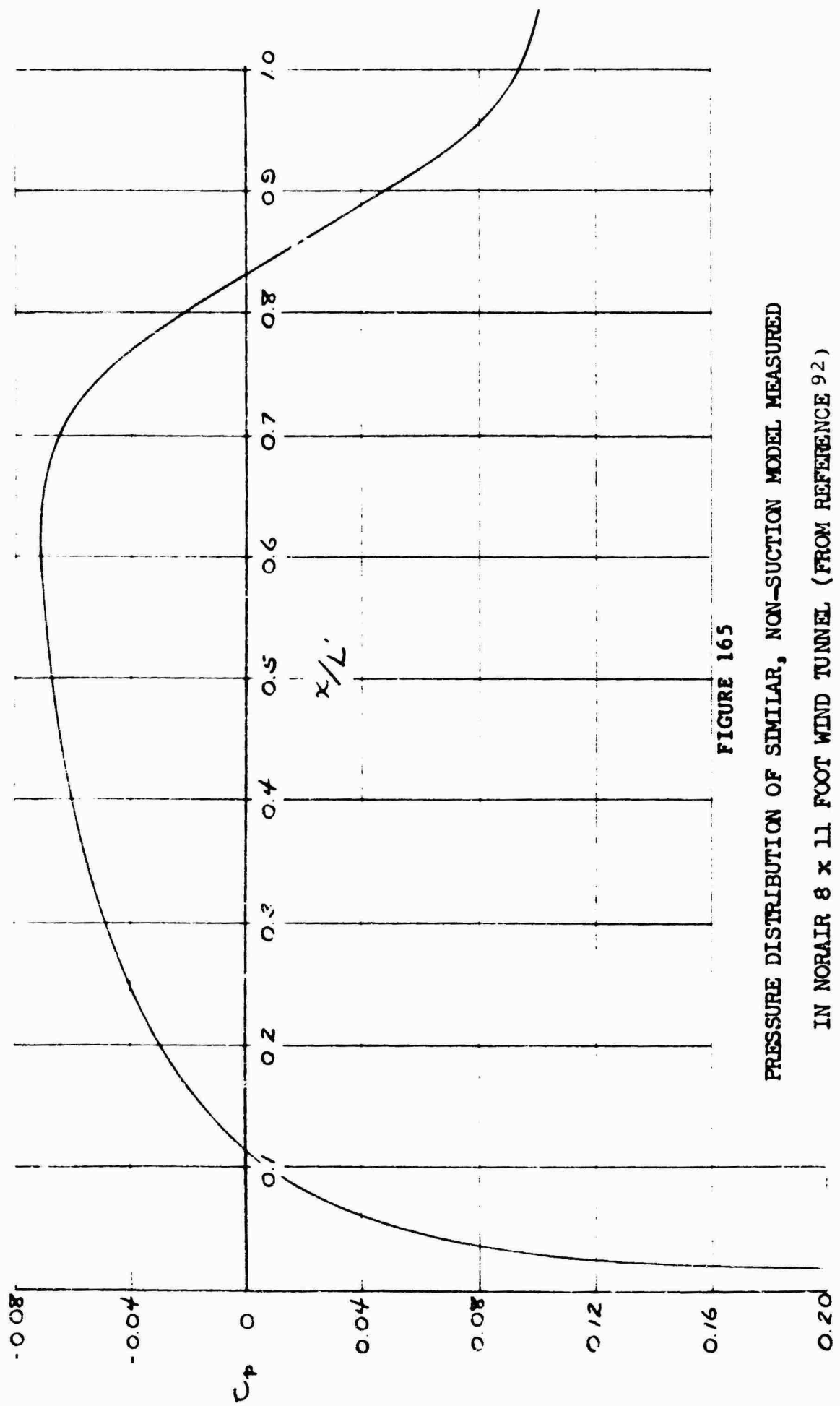
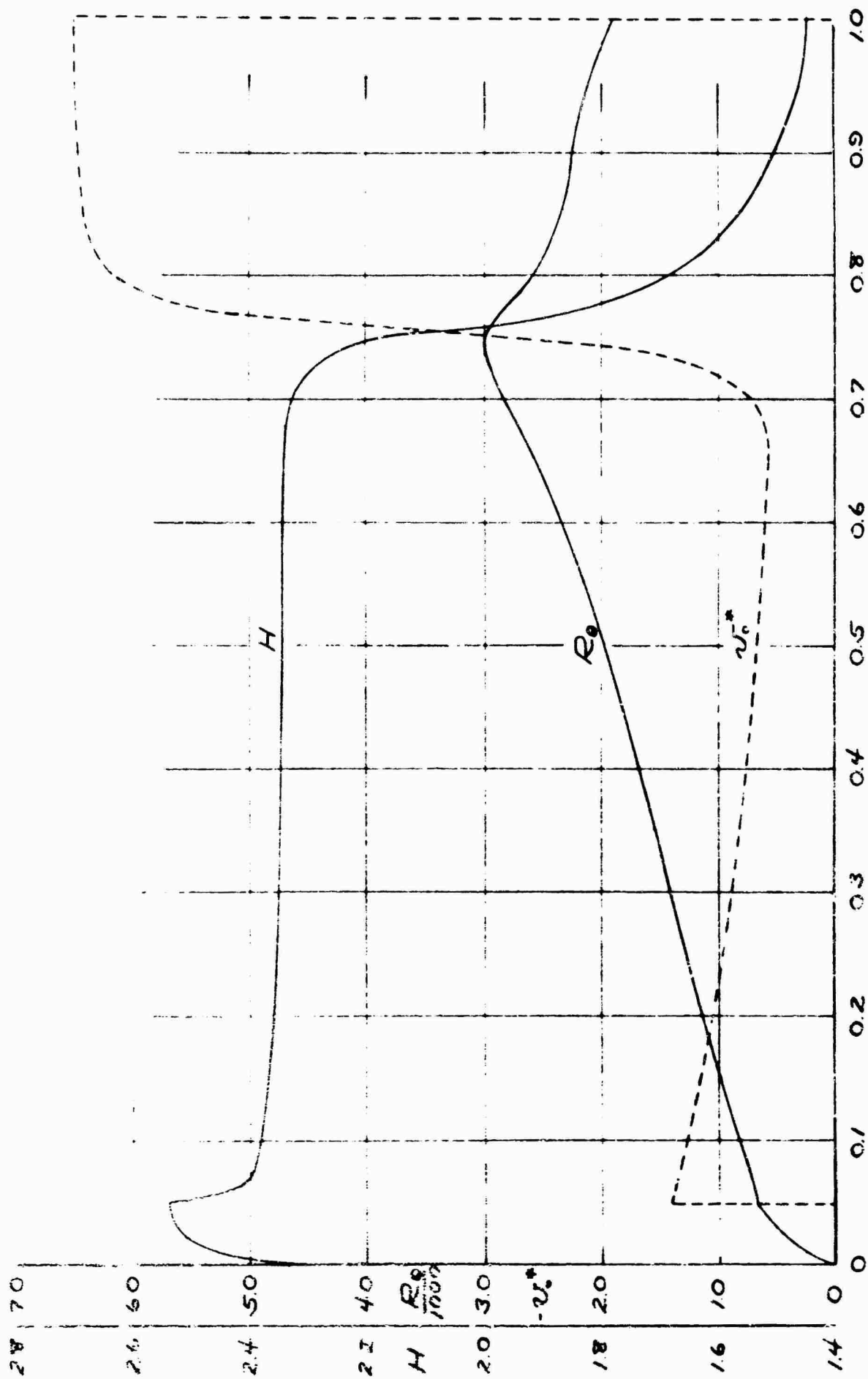


FIGURE 165

PRESSURE DISTRIBUTION OF SIMILAR, NON-SUCTION MODEL MEASURED

IN NORAIR 8 x 11 FOOT WIND TUNNEL (FROM REFERENCE 92)



$x/L'$

FIGURE 166

DESIGN AREA SUCTION VELOCITY DISTRIBUTION AND THEORETICAL

BOUNDARY LAYER DEVELOPMENT

$$R_L = 4.9 \times 10^6$$

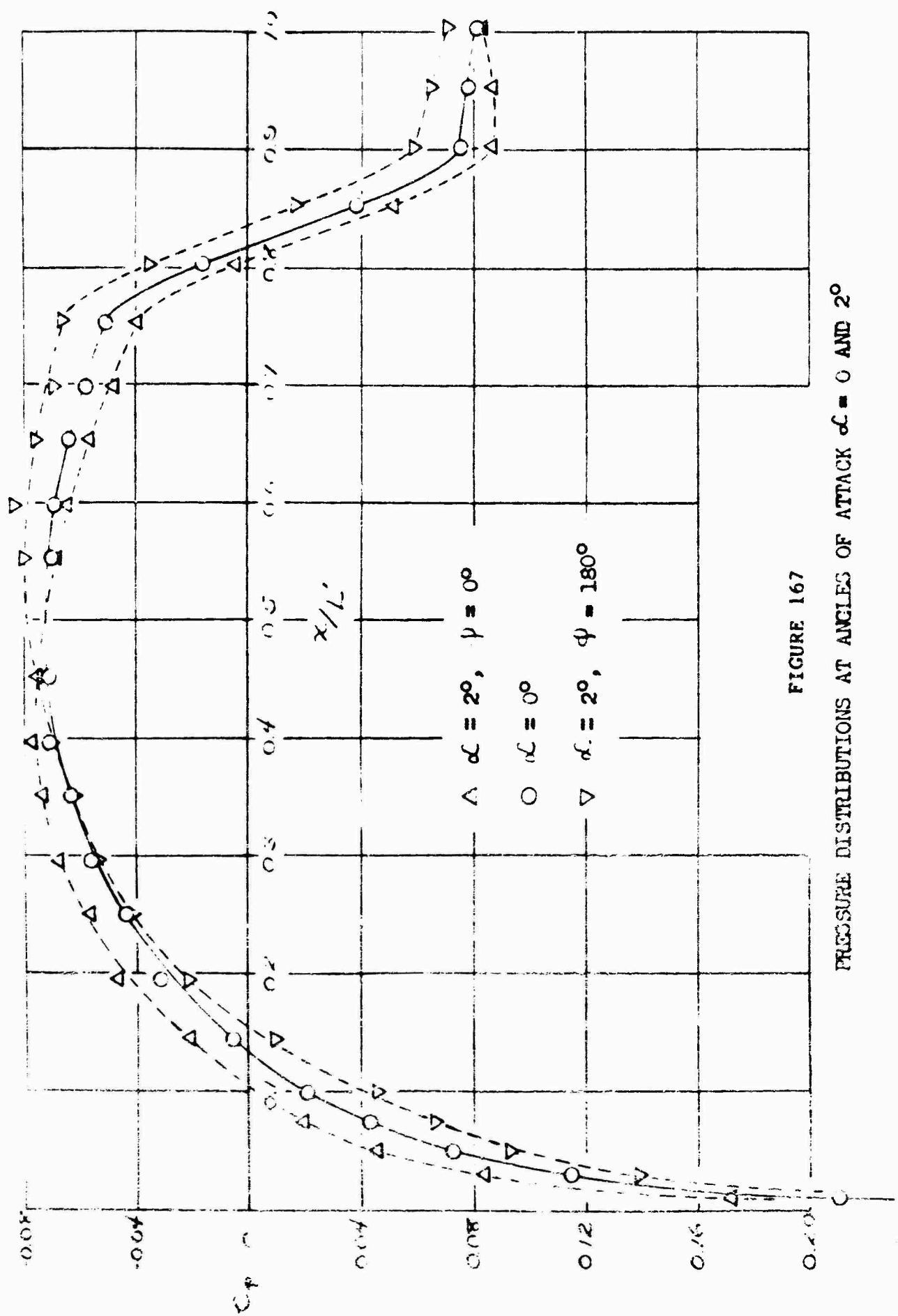


FIGURE 167

PRESSURE DISTRIBUTIONS AT ANGLES OF ATTACK  $\alpha = 0$  AND  $2^\circ$

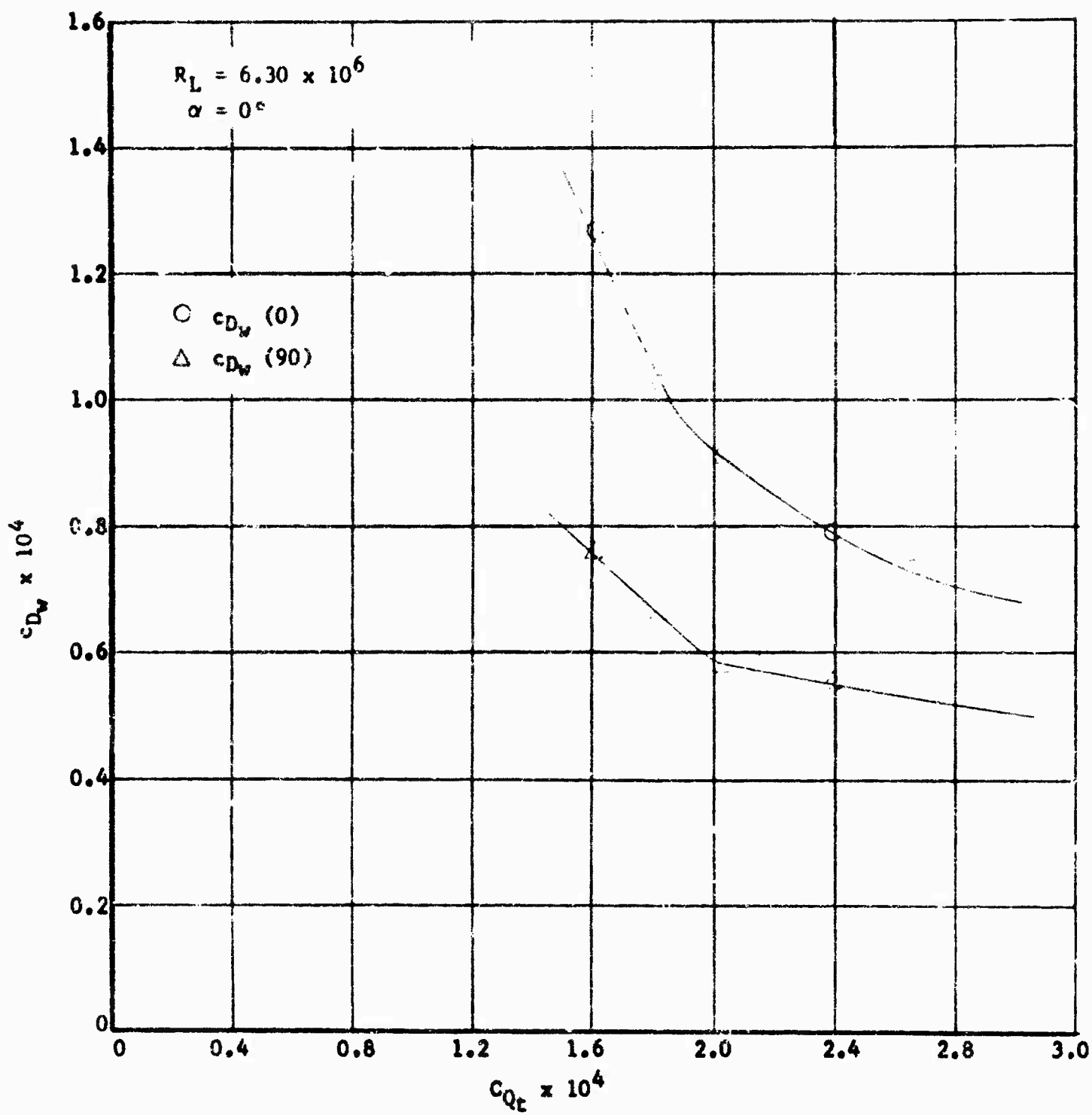


FIGURE 168 PARTIAL DRAG  $c_{D_w}$  VERSUS SUCTION QUANTITY  $C_{Q_t}$  FOR VARIOUS REYNOLDS NUMBERS  $R_L$  AND ANGLES OF ATTACK  $\alpha$

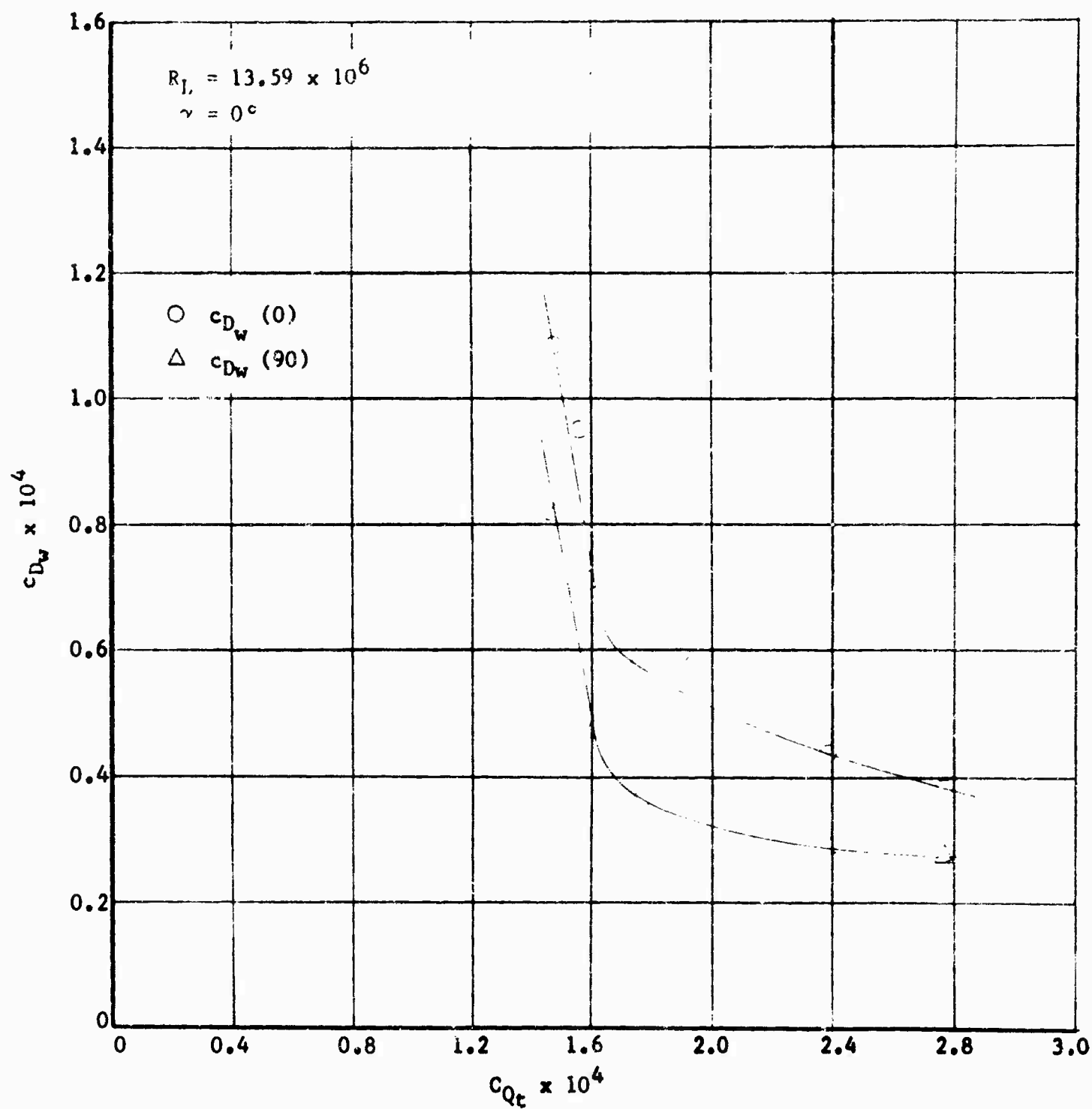


FIGURE 169 PARTIAL DRAG  $c_{D_w}$  VERSUS SUCTION QUANTITY  $C_{Q_t}$  FOR VARIOUS REYNOLDS NUMBERS  $R_L$  AND ANGLES OF ATTACK  $\alpha$

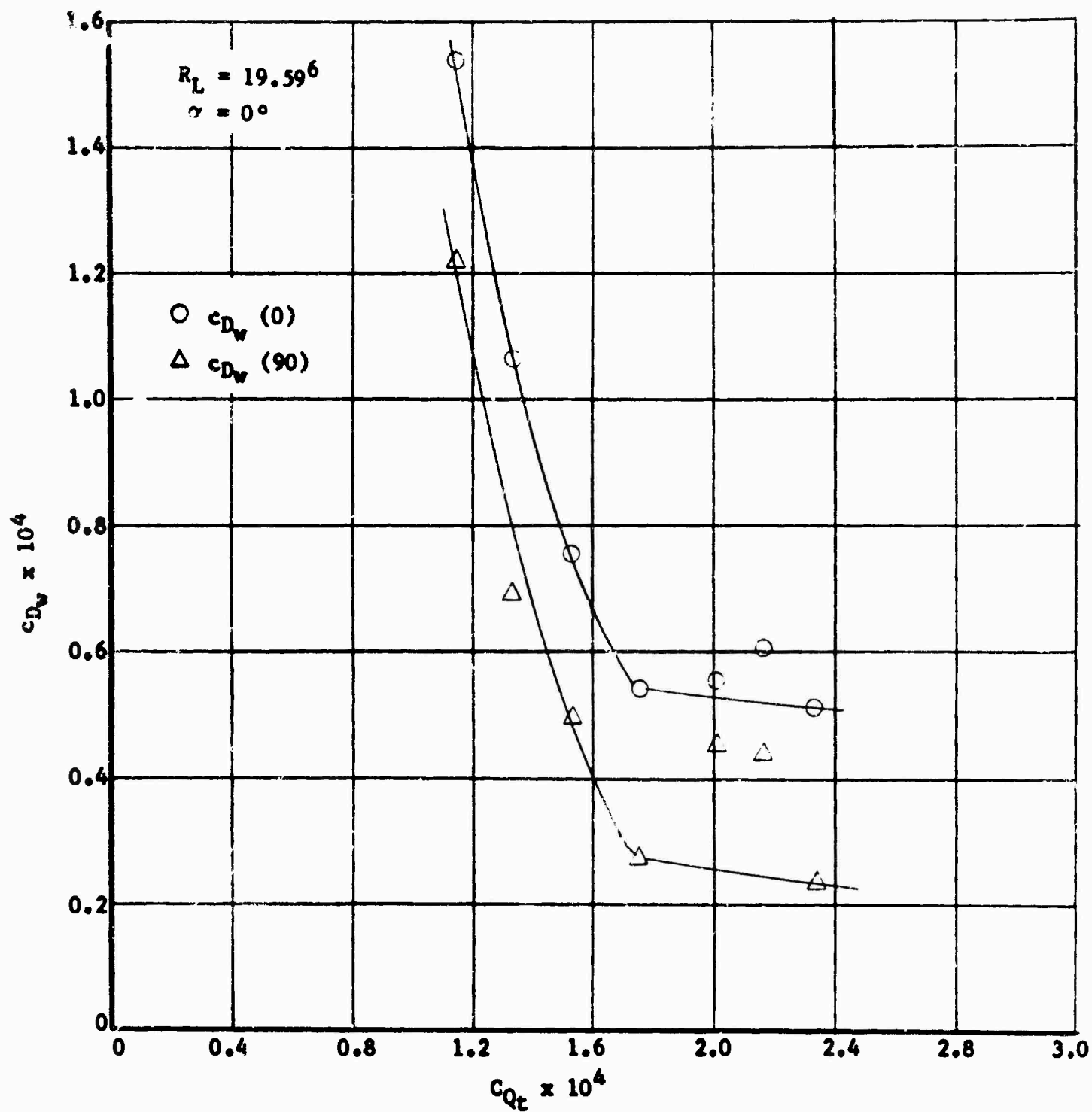


FIGURE 170 PARTIAL DRAG  $c_{D_w}$  VERSUS SUCTION QUANTITY  $C_{Q_t}$  FOR VARIOUS REYNOLDS NUMBERS  $R_L$  AND ANGLES OF ATTACK  $\alpha$

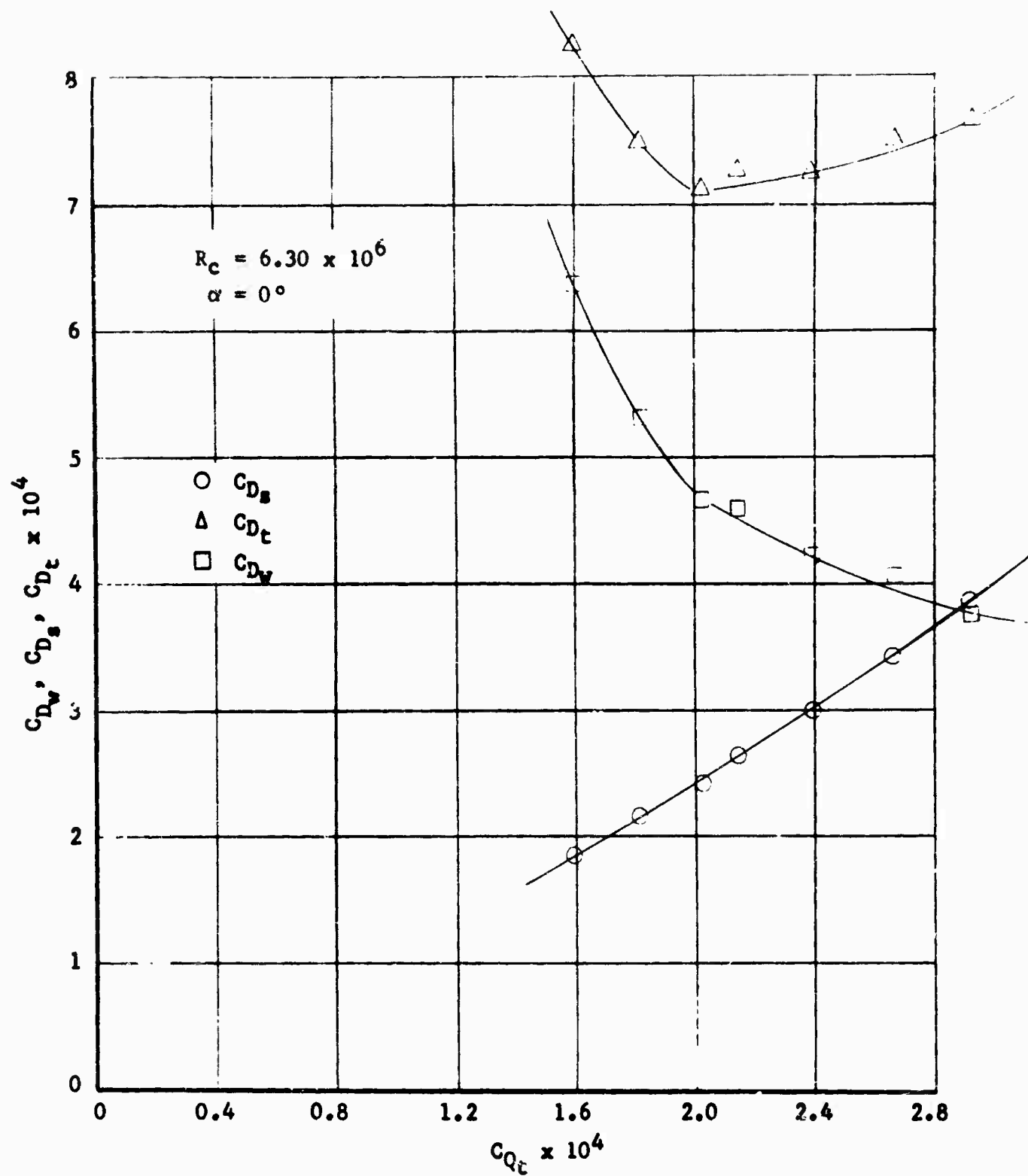


FIGURE 171 DRAG  $C_D$  VERSUS SUCTION QUANTITY  $C_{Q_t}$  FOR VARIOUS REYNOLDS NUMBERS  $R_c$  AND ANGLES OF ATTACK  $\alpha$



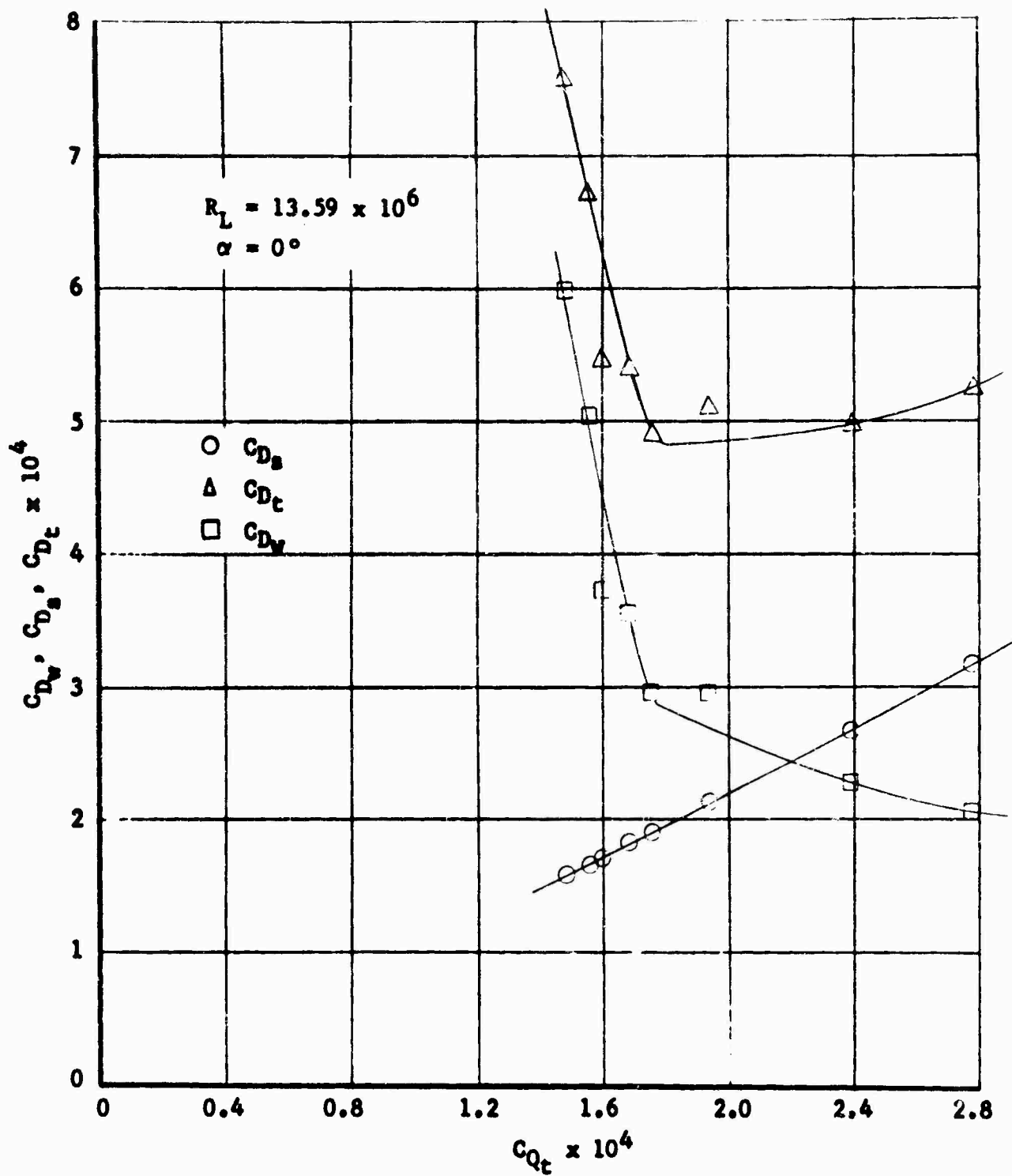


FIGURE 172 DRAG  $C_D$  VERSUS SUCTION QUANTITY  $C_{Q_t}$  FOR VARIOUS REYNOLDS NUMBERS  $R_c$  AND ANGLES OF ATTACK  $\alpha$

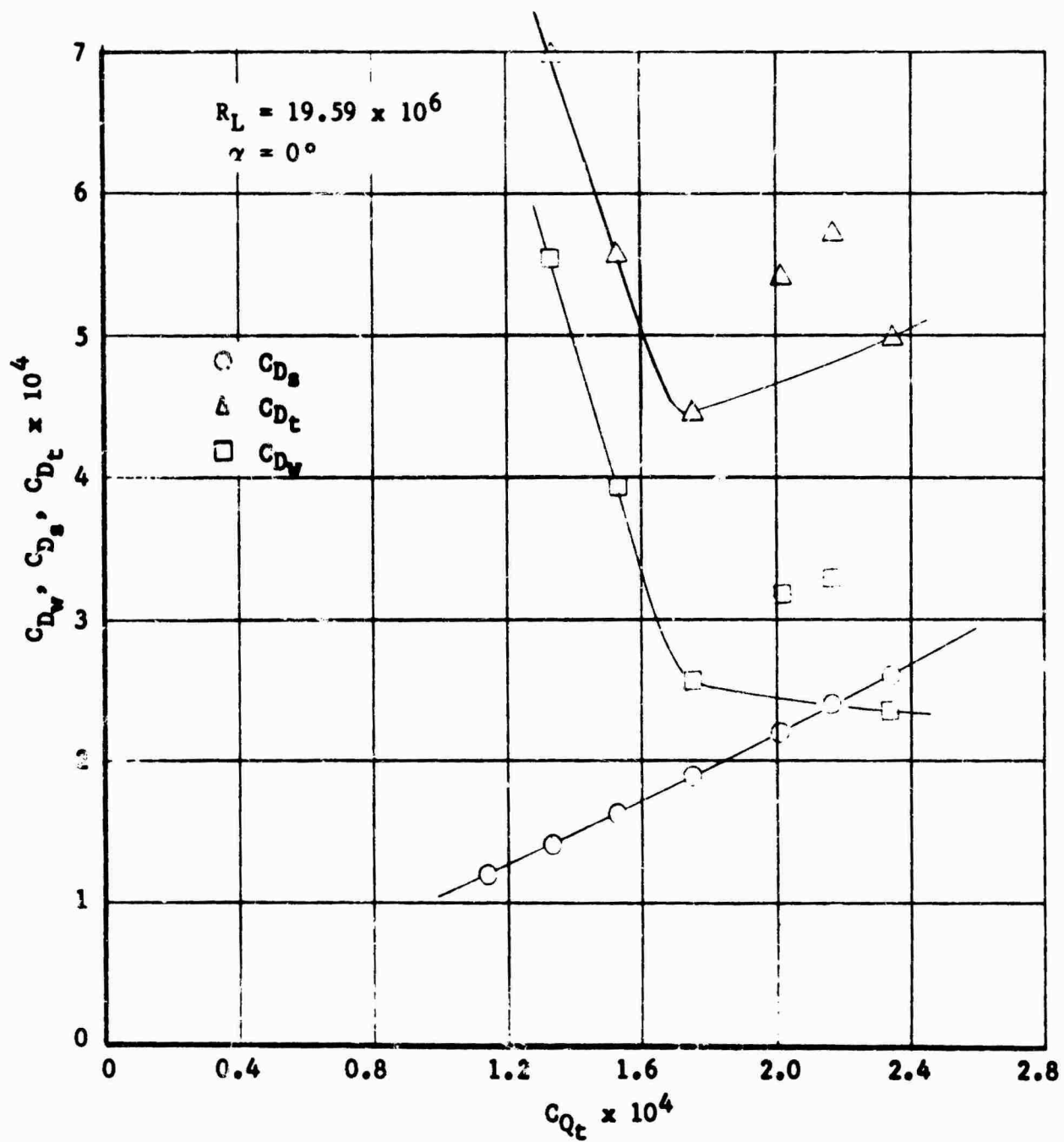


FIGURE 173 DRAG  $C_D$  VERSUS SUCTION QUANTITY  $C_{Qt}$  FOR VARIOUS REYNOLDS NUMBERS  $R_c$  AND ANGLES OF ATTACK  $\alpha$

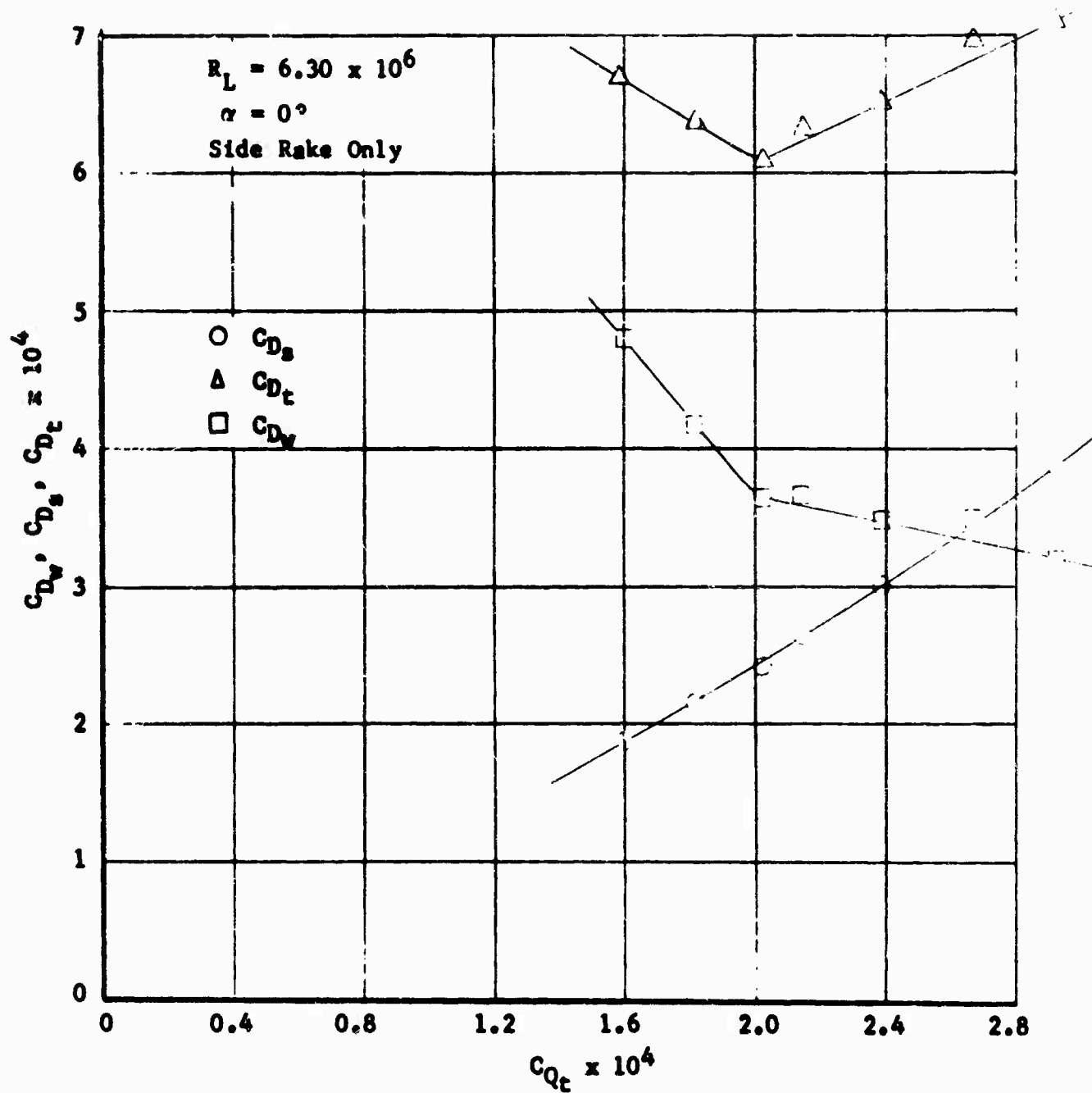


FIGURE 174 DRAG  $C_D$  VERSUS SUCTION QUANTITY  $C_{Q_t}$  FOR VARIOUS REYNOLDS NUMBERS  $R_c$  AND ANGLES OF ATTACK  $\alpha$

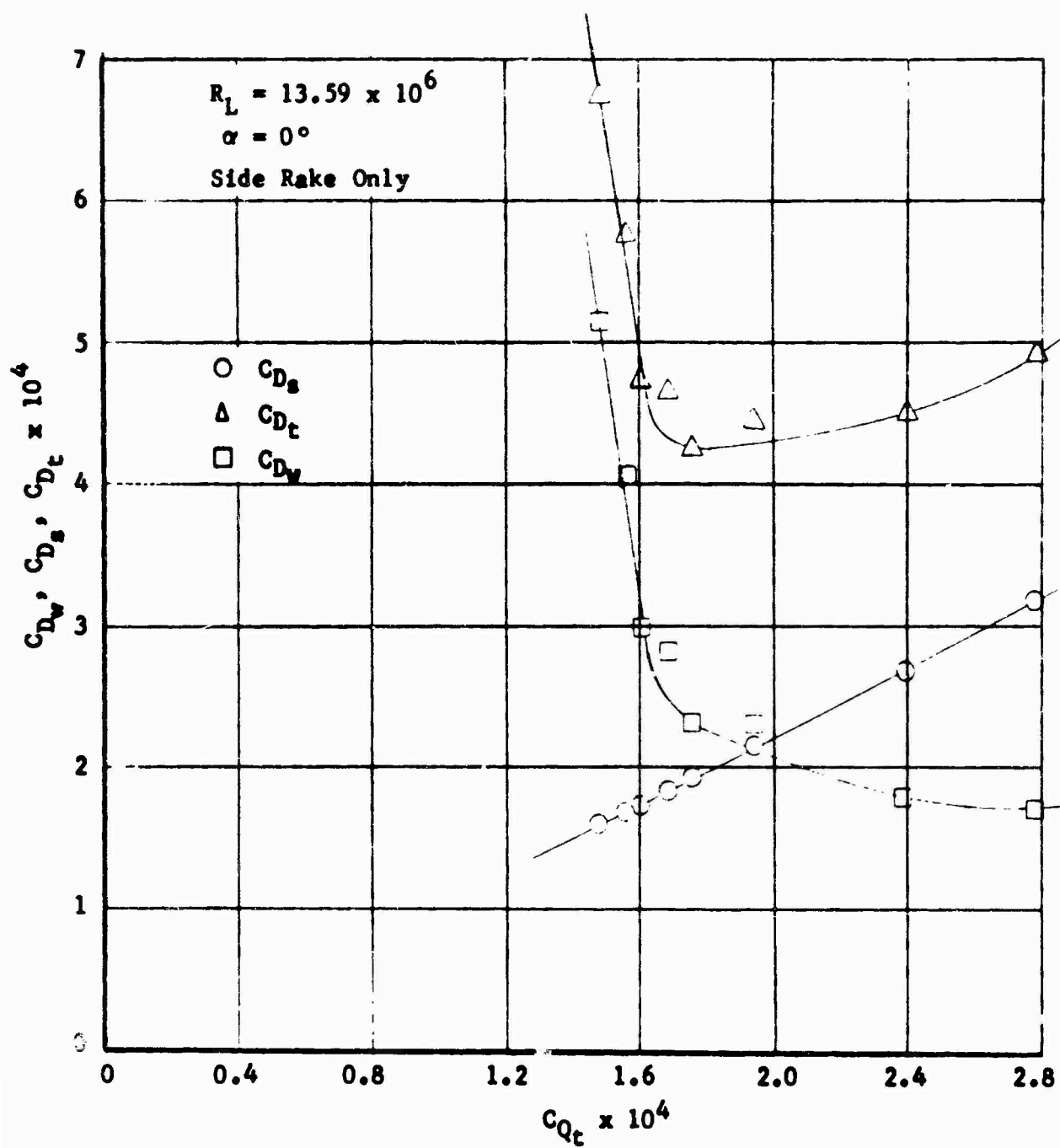


FIGURE 175 DRAG  $C_D$  VERSUS SUCTION QUANTITY  $C_{Qt}$  FOR VARIOUS REYNOLDS NUMBERS  $R_c$  AND ANGLES OF ATTACK  $\alpha$

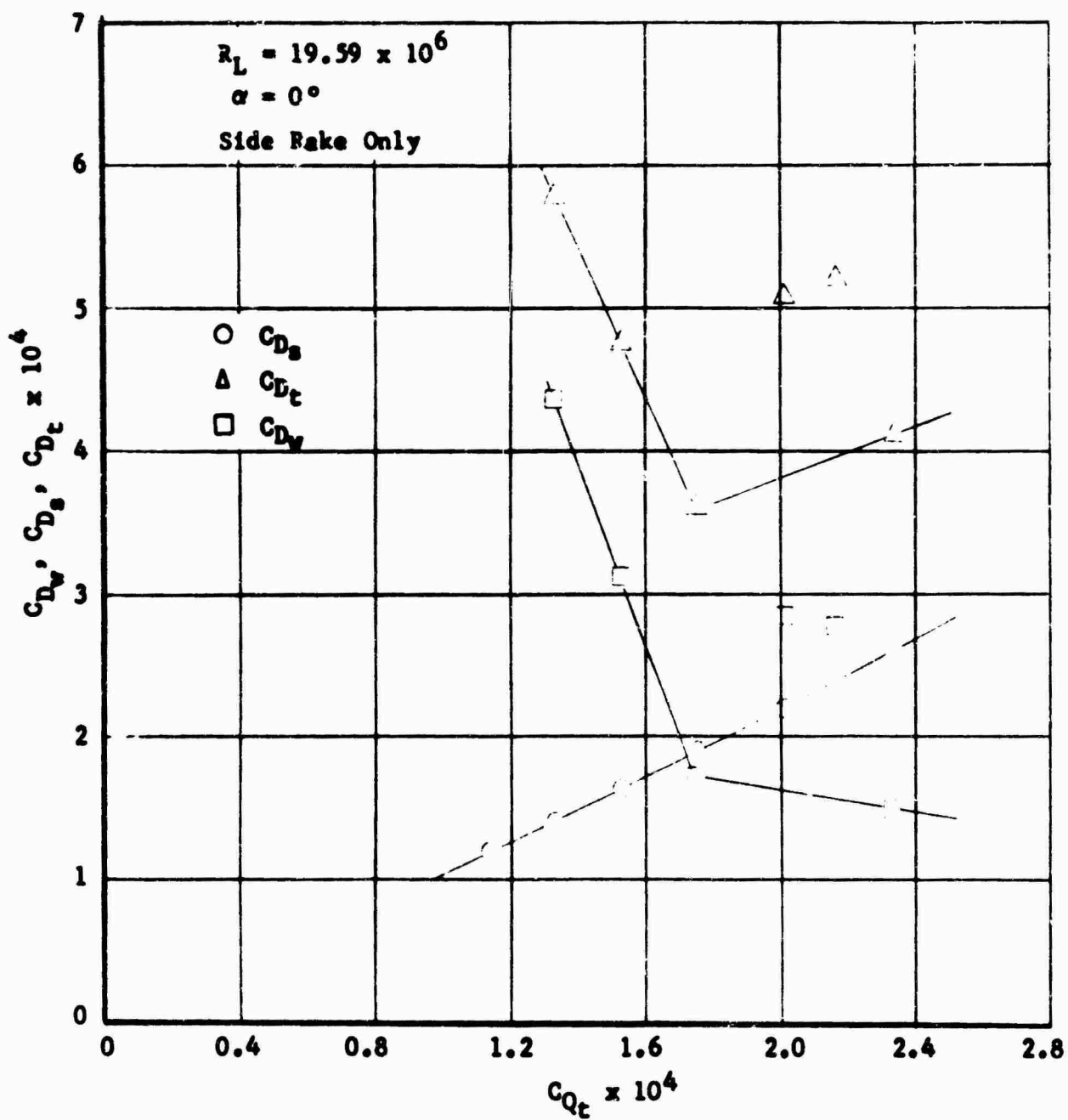


FIGURE 176 DRAG  $C_D$  VERSUS SUCTION QUANTITY  $C_{Qt}$  FOR VARIOUS REYNOLDS NUMBERS  $R_c$  AND ANGLES OF ATTACK  $\alpha$

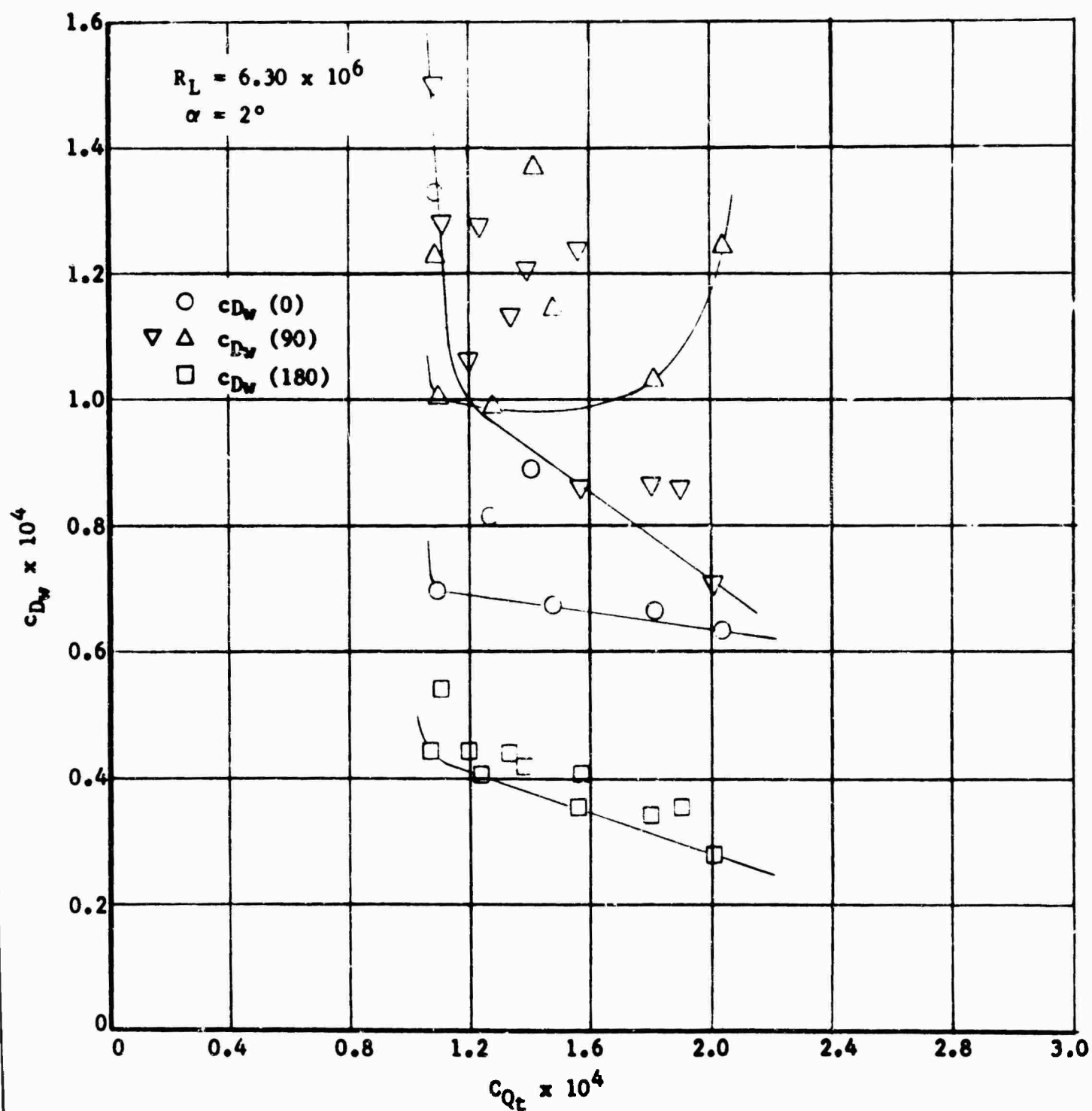


FIGURE 177 PARTIAL DRAG  $c_{D_w}$  VERSUS SUCTION QUANTITY  $C_{Q_t}$  FOR VARIOUS REYNOLDS NUMBERS  $R_L$  AND ANGLES OF ATTACK  $\alpha$

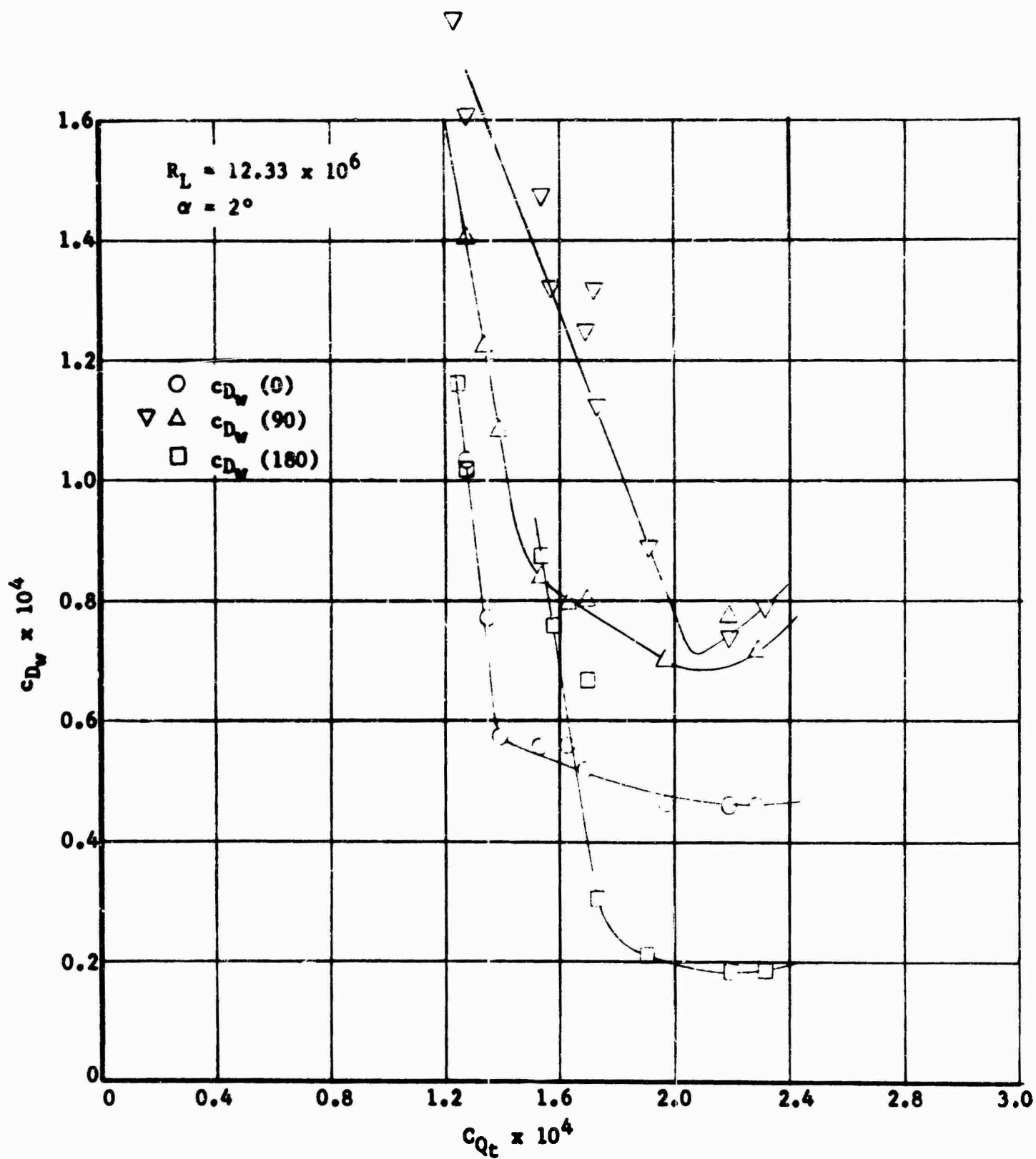


FIGURE 178 PARTIAL DRAG  $c_{D_w}$  VERSUS SUCTION QUANTITY  $C_{Q_t}$  FOR VARIOUS REYNOLDS NUMBERS  $R_L$  AND ANGLES OF ATTACK  $\alpha$

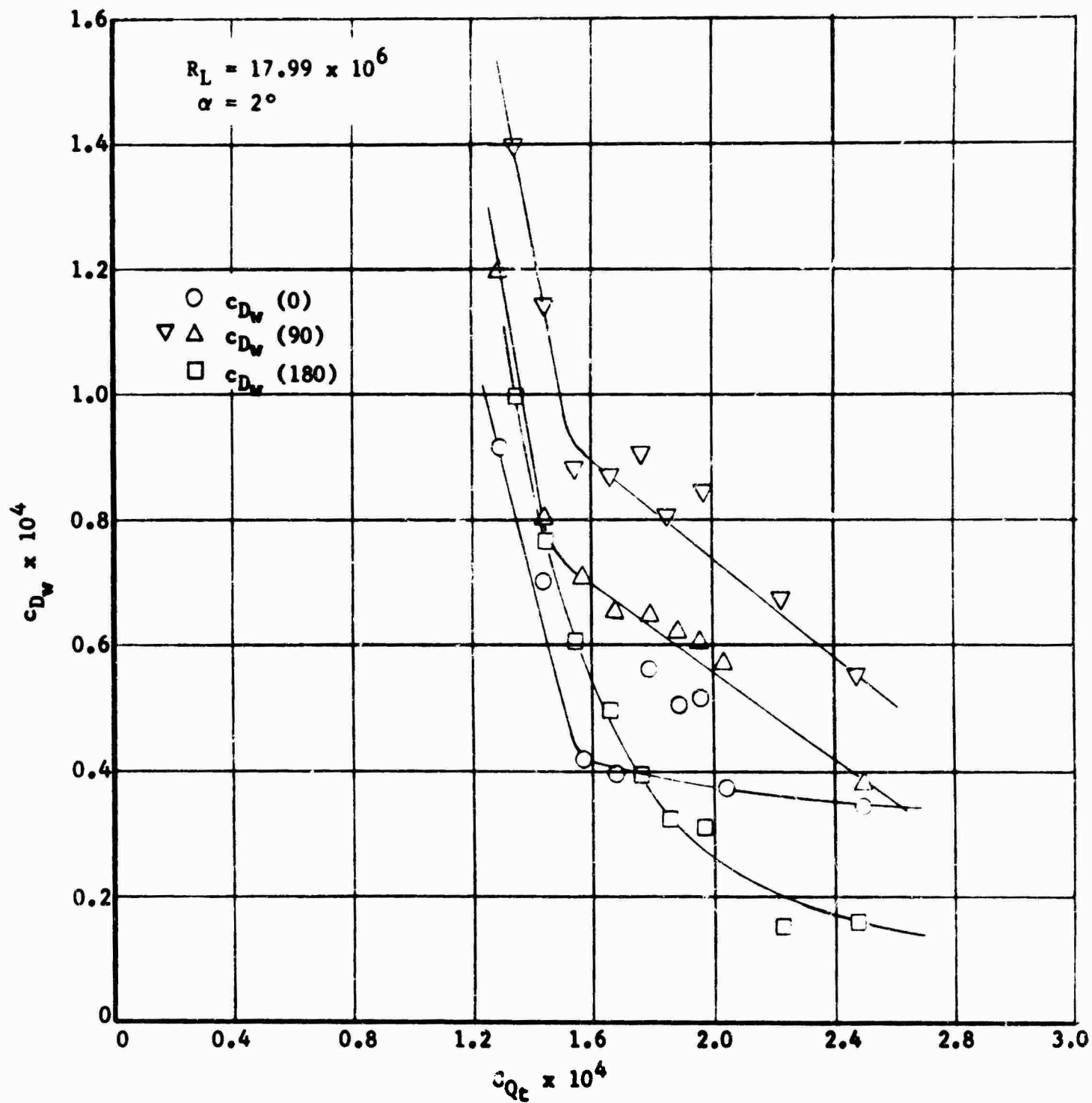


FIGURE 179 PARTIAL DRAG  $c_{D_w}$  VERSUS SUCTION QUANTITY  $C_{Q_c}$  FOR VARIOUS REYNOLDS NUMBERS  $R_L$  AND ANGLES OF ATTACK  $\alpha$



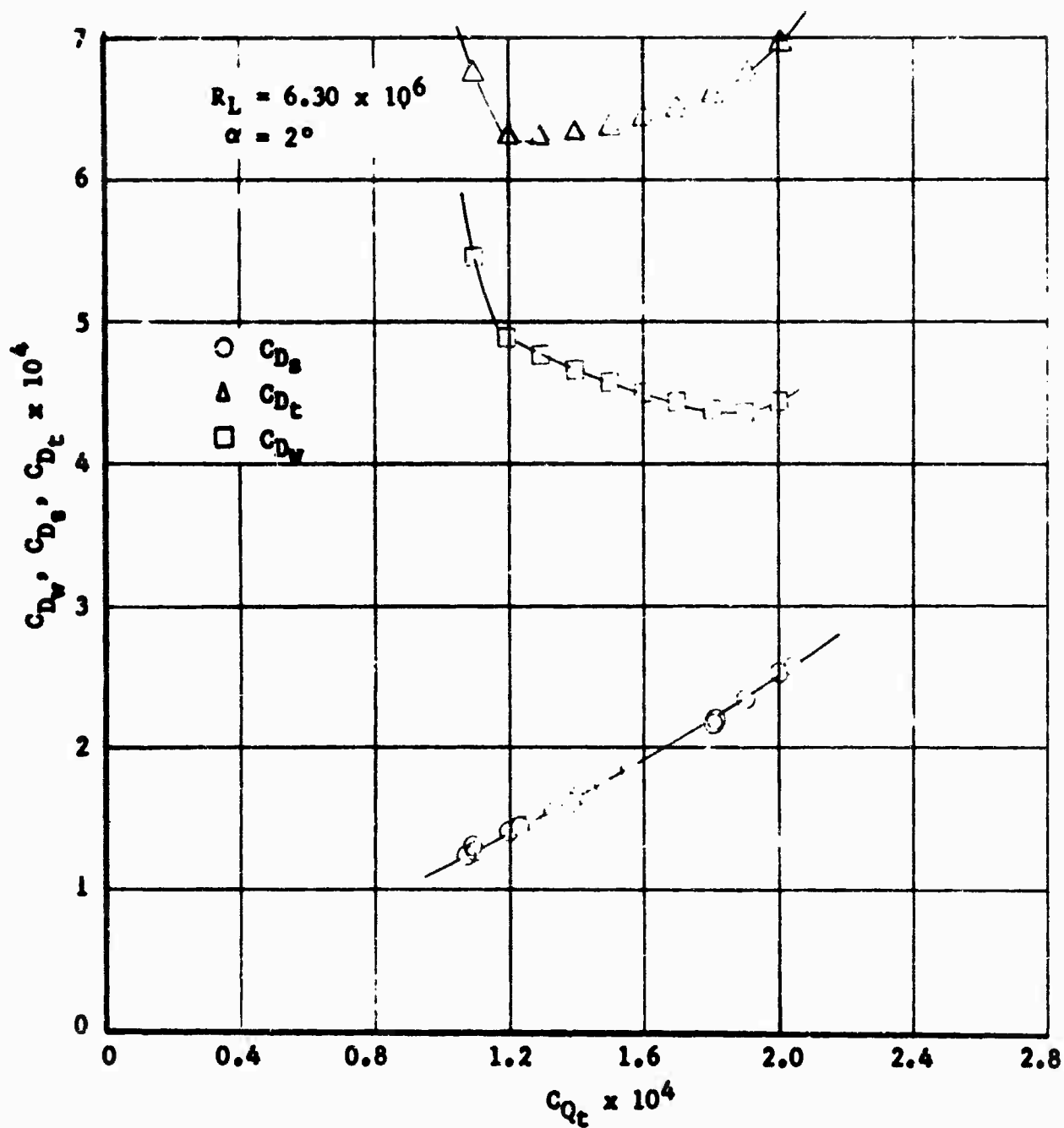


FIGURE 180 DRAG  $C_D$  VERSUS SUCTION QUANTITY  $C_{Qt}$  FOR VARIOUS REYNOLDS NUMBERS  $R_c$  AND ANGLES OF ATTACK  $\alpha$

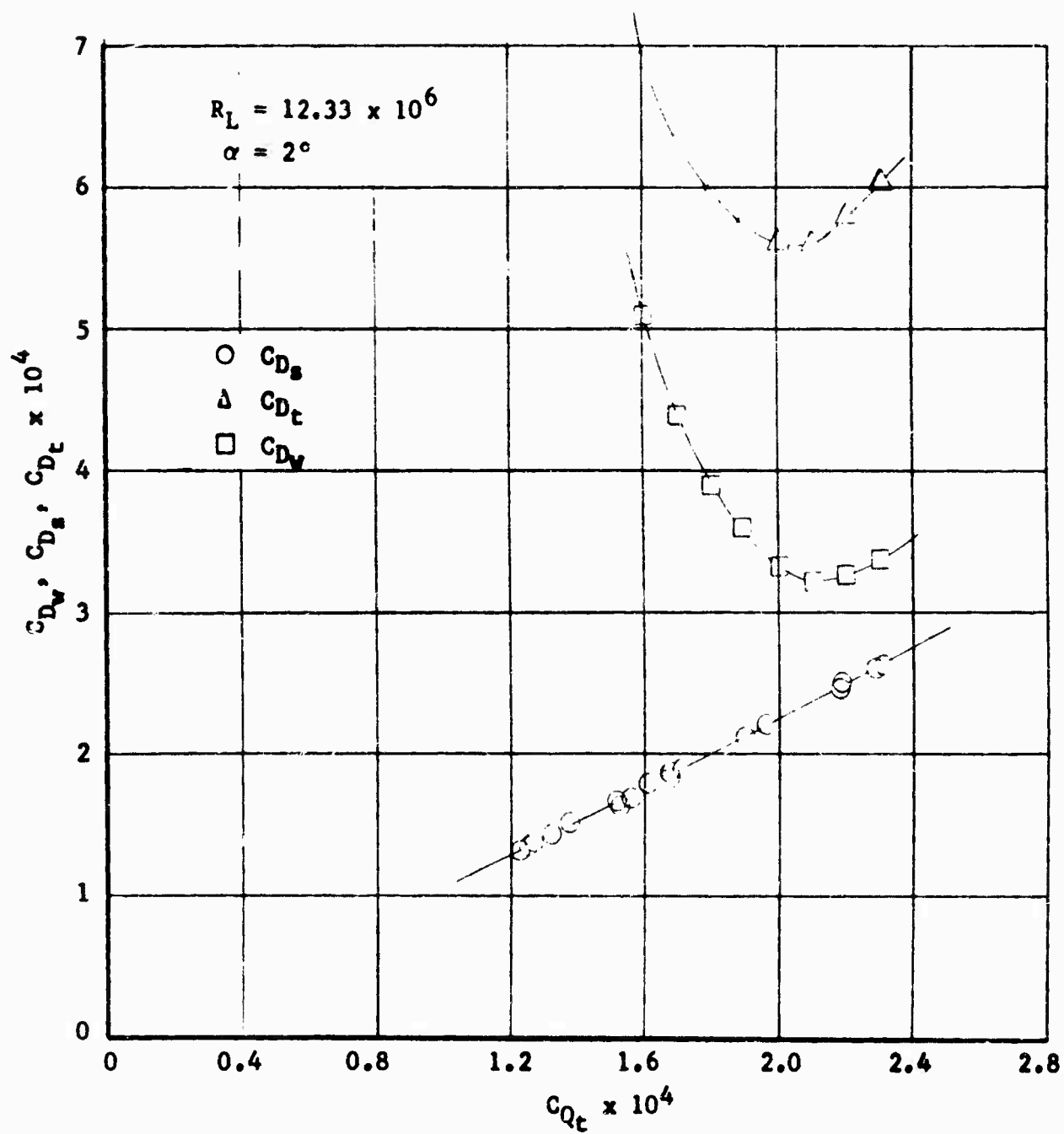


FIGURE 181 DRAG  $C_D$  VERSUS SUCTION QUANTITY  $C_{Q_t}$  FOR VARIOUS REYNOLDS NUMBERS  $R_c$  AND ANGLES OF ATTACK  $\alpha$

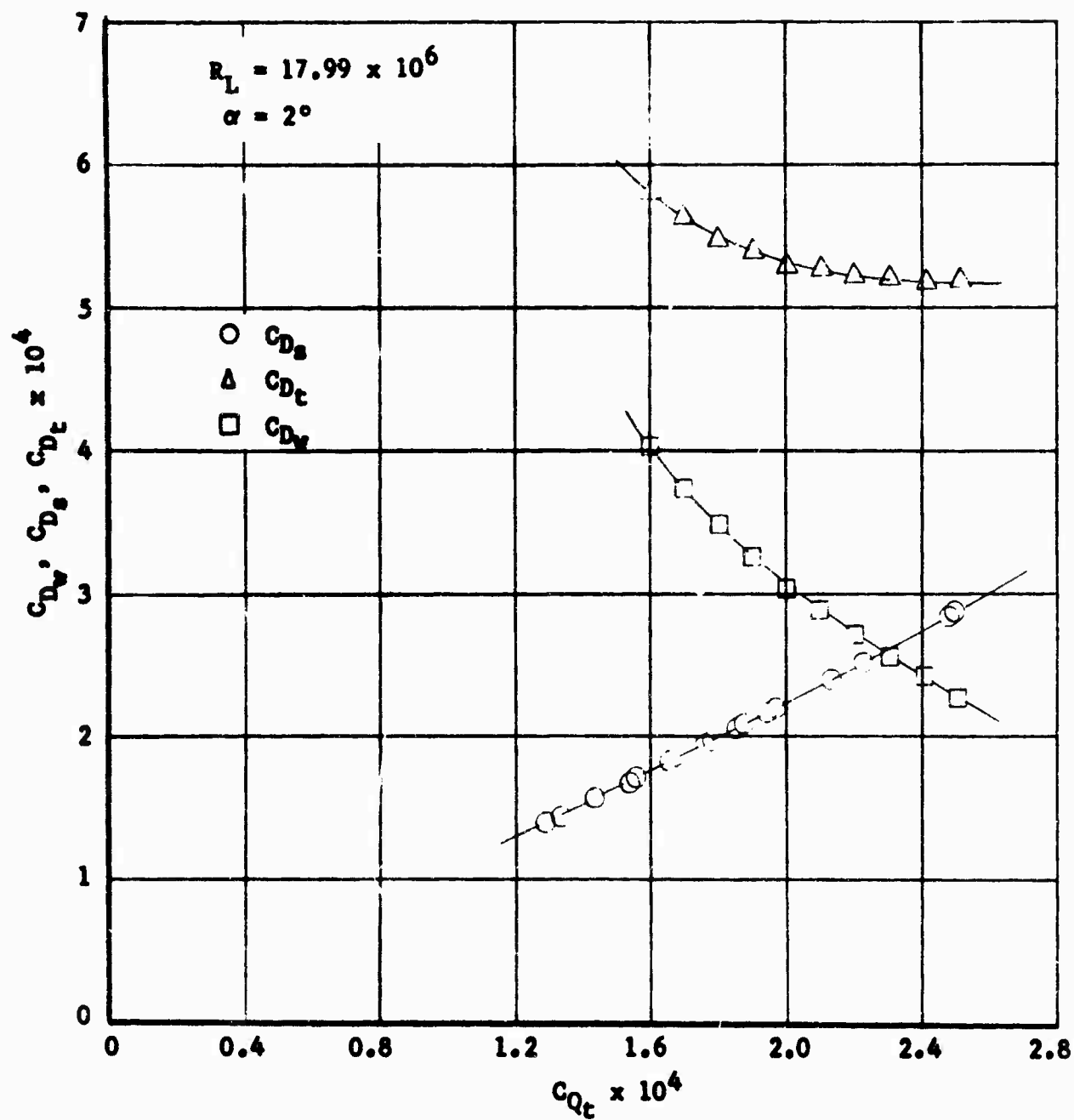


FIGURE 182 DRAG  $C_D$  VERSUS SUCTION QUANTITY  $C_{Qt}$  FOR VARIOUS REYNOLDS NUMBERS  $R_c$  AND ANGLES OF ATTACK  $\alpha$

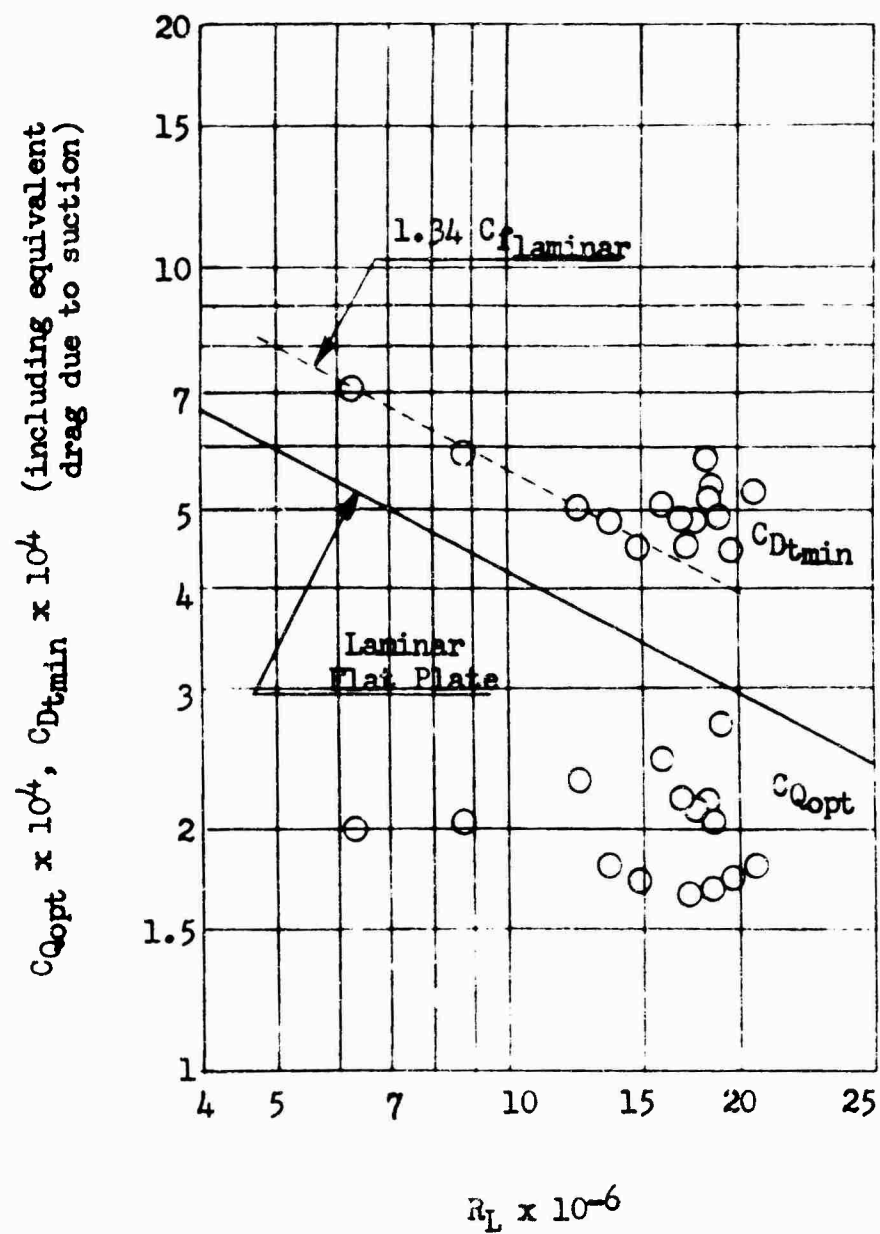


FIGURE 183

VARIATION OF MINIMUM EQUIVALENT TOTAL DRAG  $C_{Dtmin}$   
AND SUCTION COEFFICIENT AT MINIMUM EQUIVALENT TOTAL DRAG  $C_{Qopt}$  WITH  
LENGTH REYNOLDS NUMBER  $R_L$ ,  $\alpha = 0^\circ$

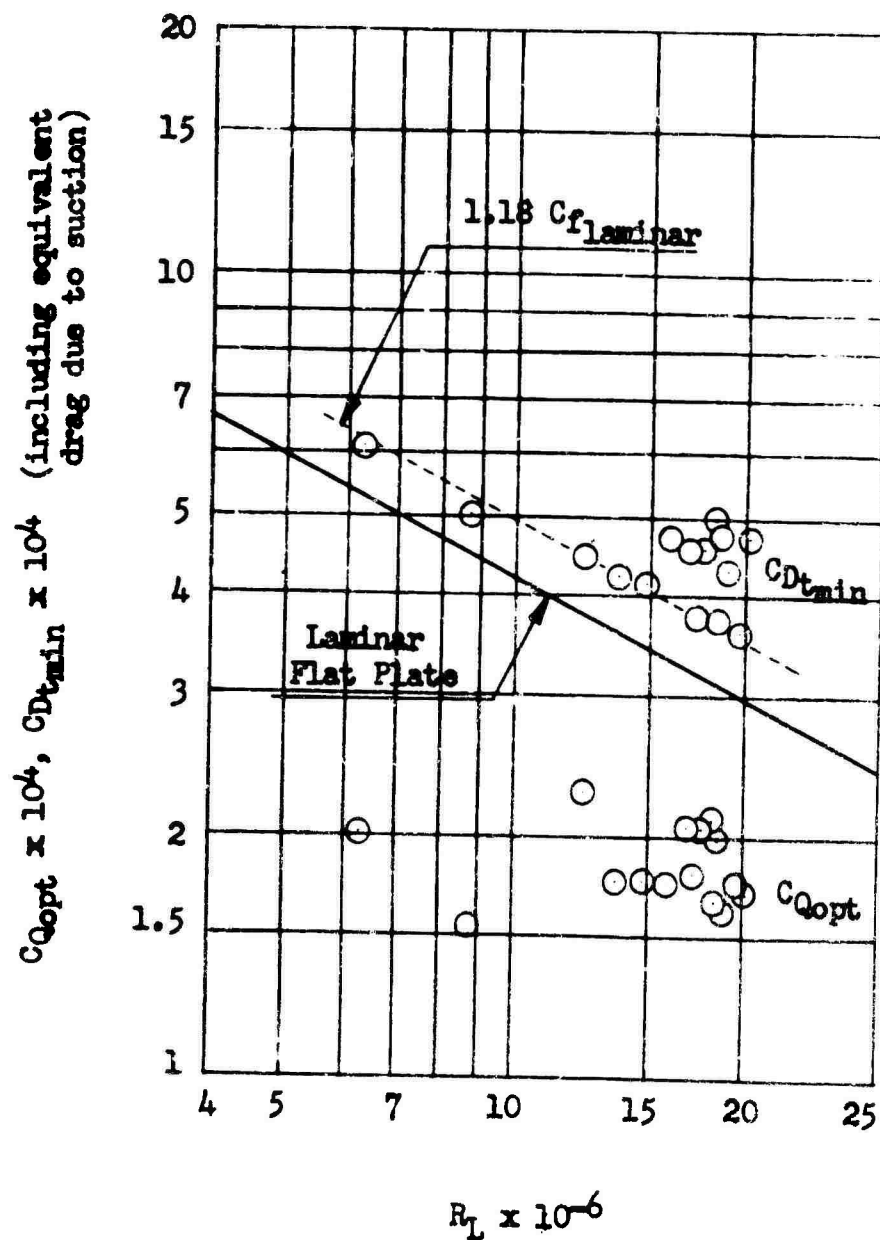


FIGURE 184

VARIATION OF MINIMUM EQUIVALENT TOTAL DRAG  $C_{Dtmin}$   
 AND SUCTION COEFFICIENT AT MINIMUM EQUIVALENT TOTAL DRAG  $C_{Qopt}$   
 WITH LENGTH REYNOLDS NUMBER  $R_L$ ,  
 $\alpha = 0^\circ$ , SIDE RAKE DATA ONLY

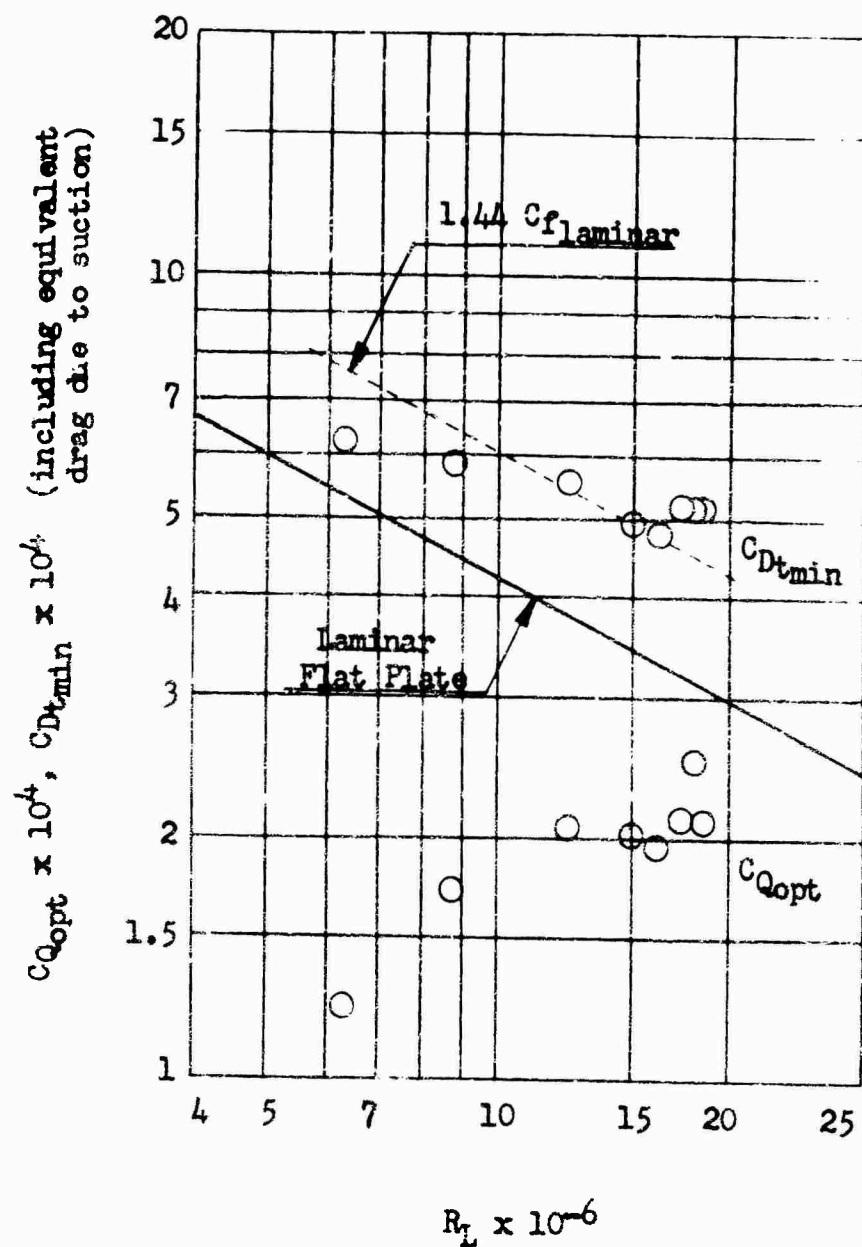


FIGURE 185

VARIATION OF MINIMUM EQUIVALENT TOTAL DRAG  $C_{D_{tmin}}$   
AND SUCTION COEFFICIENT AT MINIMUM EQUIVALENT TOTAL DRAG  $C_{Q_{opt}}$   
WITH LENGTH REYNOLDS NUMBER  $R_L$ ,

$$\alpha = 2^\circ$$

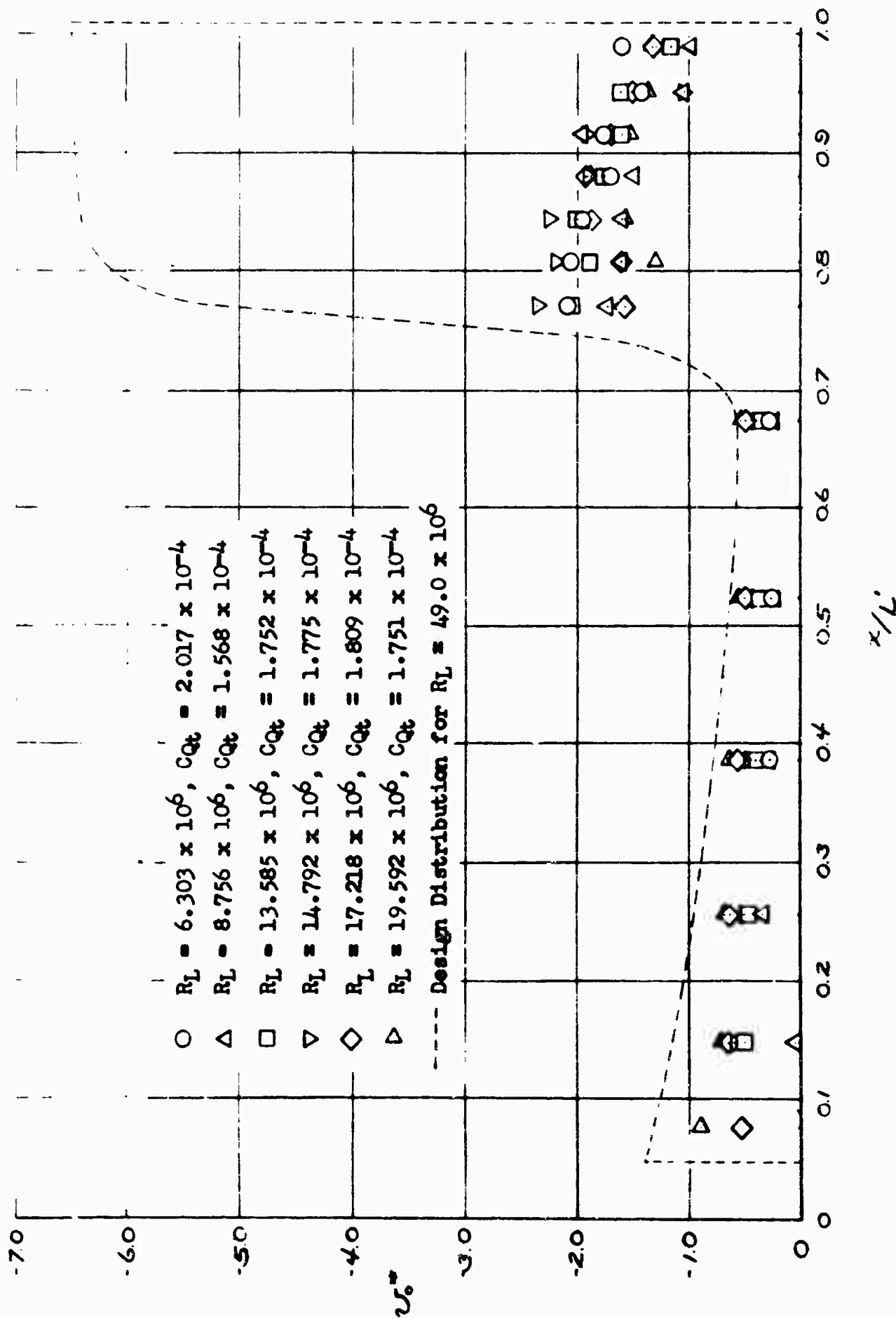


FIGURE 186

LENGTHWISE DISTRIBUTION OF EQUIVALENT AREA SUCTION VELOCITY  $v_o^*$   
 FOR SEVERAL REYNOLDS NUMBERS  $R_L$  COMPARED TO  
 DESIGN SUCTION VELOCITY DISTRIBUTION

TOP RAKE

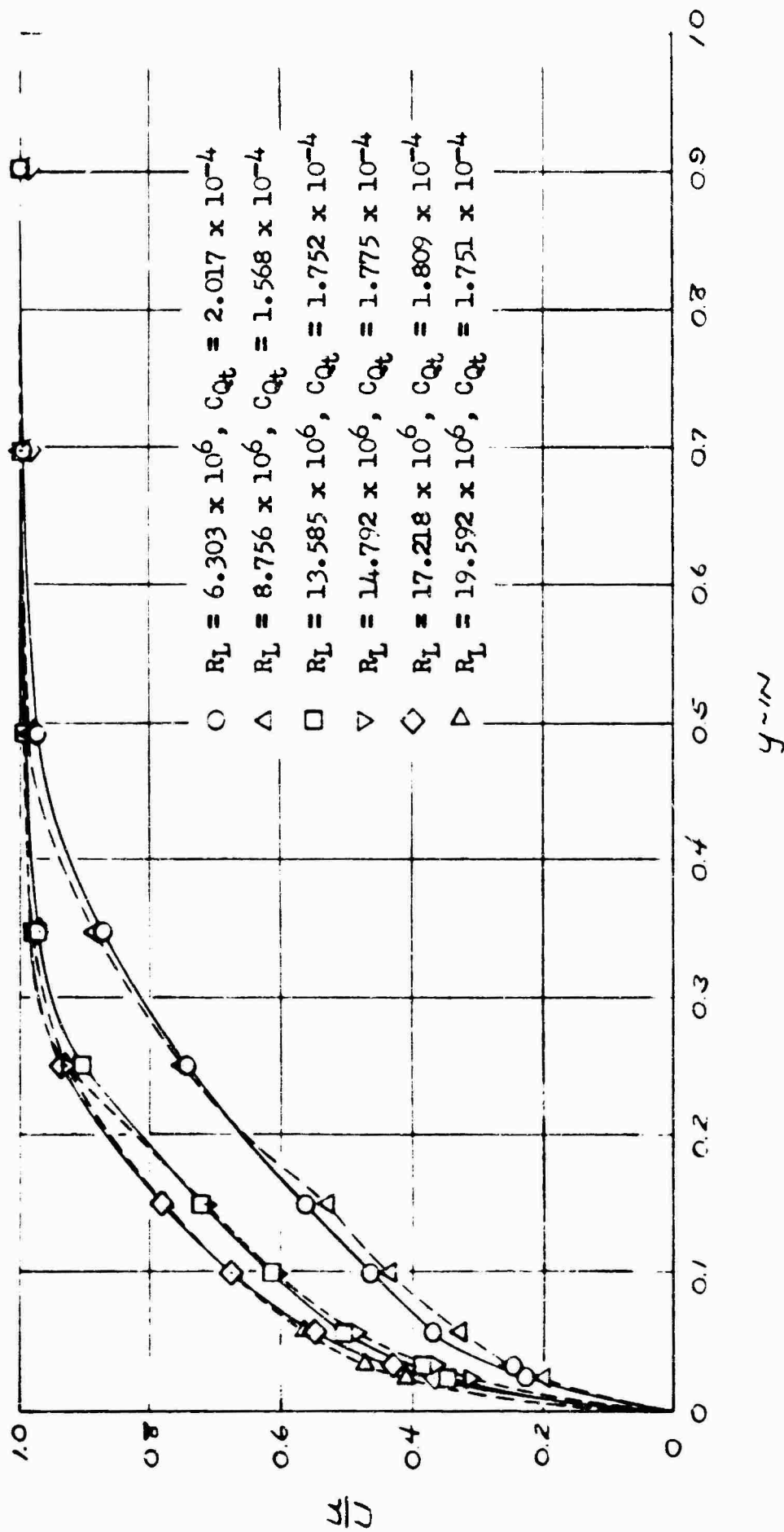


FIGURE 187a

BOUNDARY LAYER VELOCITY PROFILES MEASURED NEAR MINIMUM

EQUIVALENT TOTAL DRAG  $C_{D_{min}}$  AT SEVERAL REYNOLDS NUMBERS  $R_L$ ,

$\alpha = 0^\circ$



# SIDE RAKE

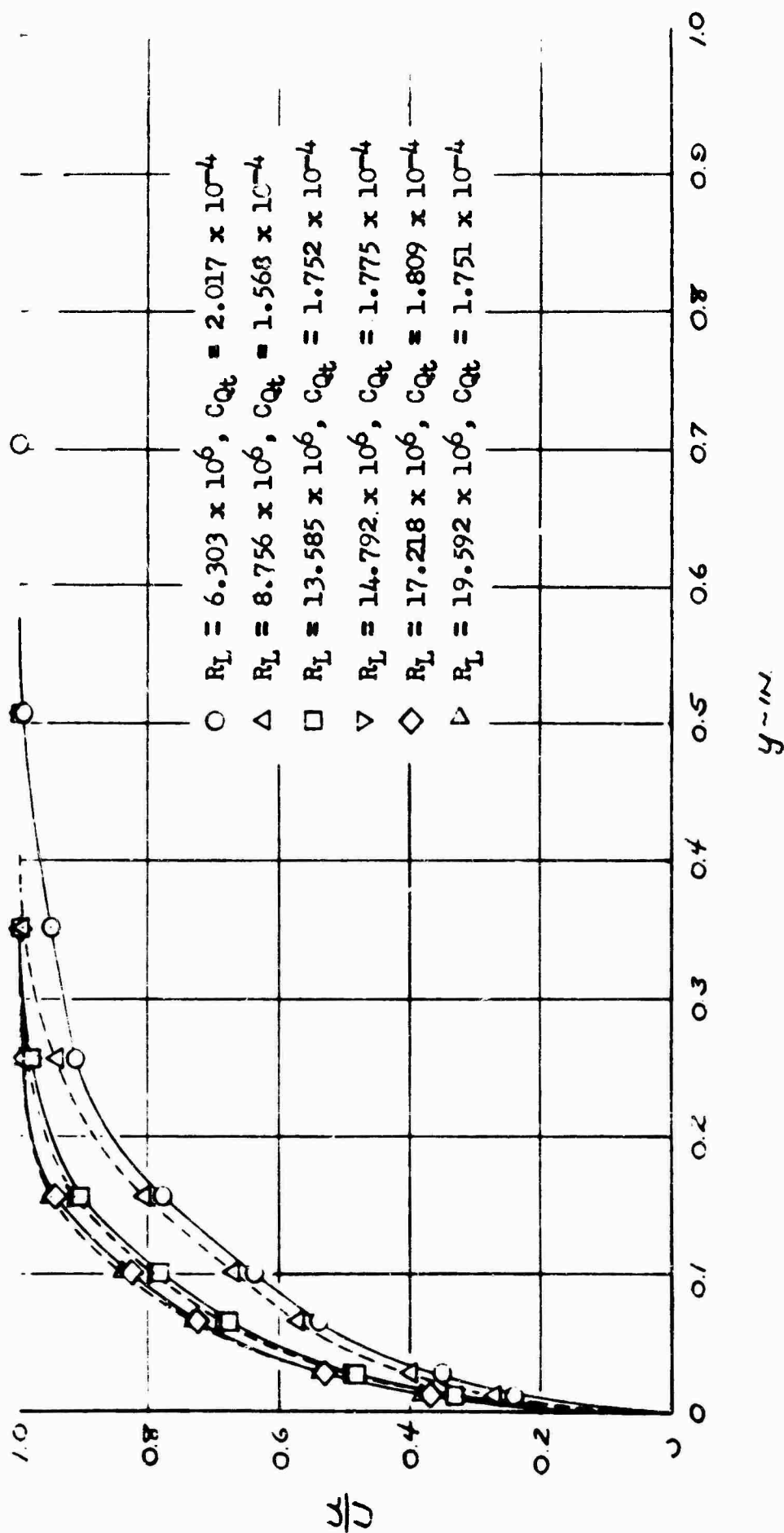


FIGURE 187b

BOUNDARY LAYER VELOCITY PROFILES MEASURED NEAR MINIMUM

EQUIVALENT TOTAL DRAG  $C_{Dt_{min}}$  AT SEVERAL REYNOLDS NUMBERS  $R_L$ ,

$\alpha C = 0^\circ$

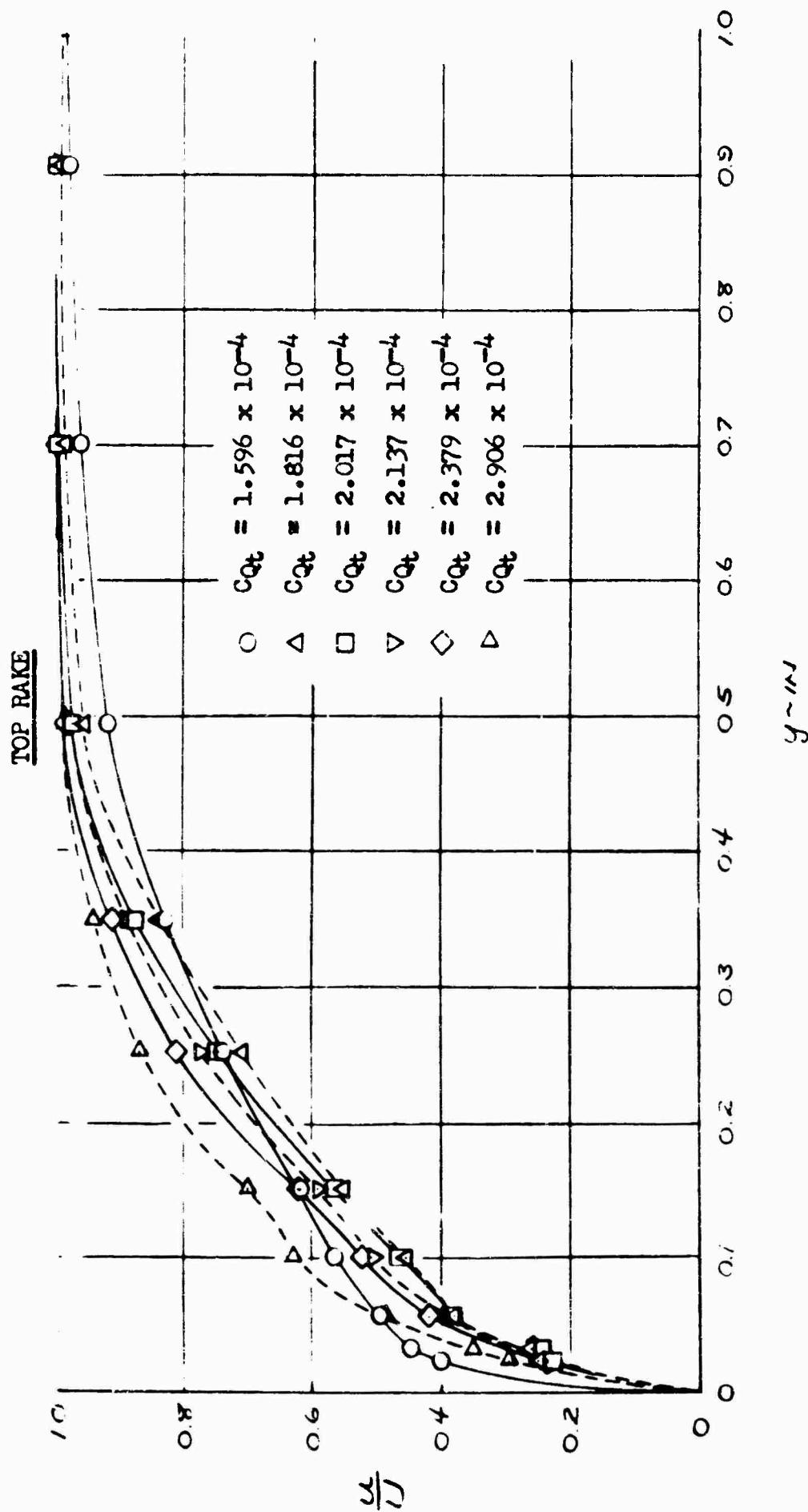


FIGURE 188a

VARIATION OF AFT END BOUNDARY LAYER VELOCITY PROFILE

WITH SUCTION COEFFICIENT  $C_{Qt}$

$$R_L = 6.303 \times 10^6$$

$$\alpha = 0^\circ$$

SIDE RAKE

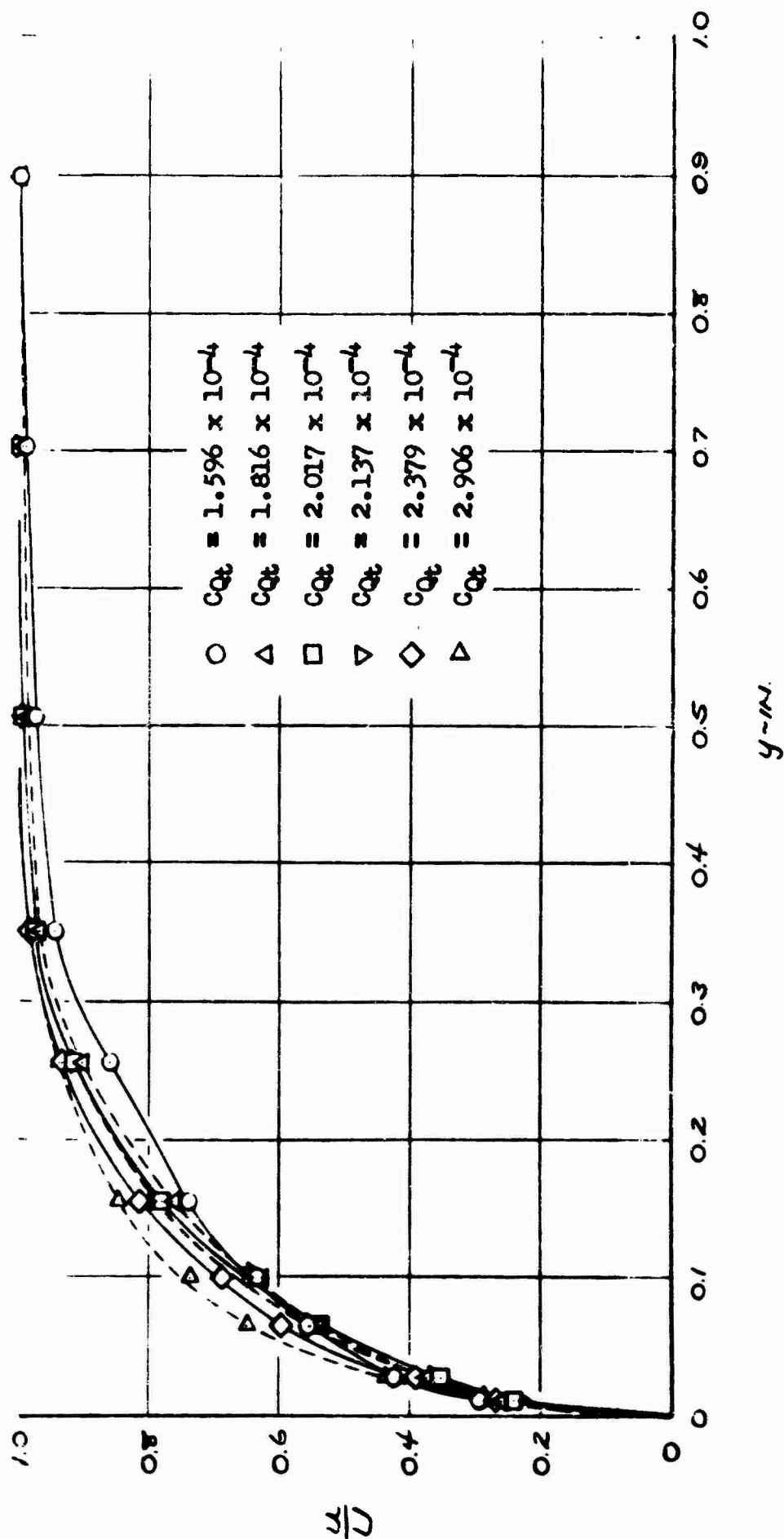


FIGURE 188b  
 VARIATION OF AFT END BOUNDARY LAYER VELOCITY PROFILE  
 WITH SUCTION COEFFICIENT  $C_{Qt}$

$$R_L = 6.303 \times 10^6$$

$$\alpha = 0^\circ$$

TOP RAKE

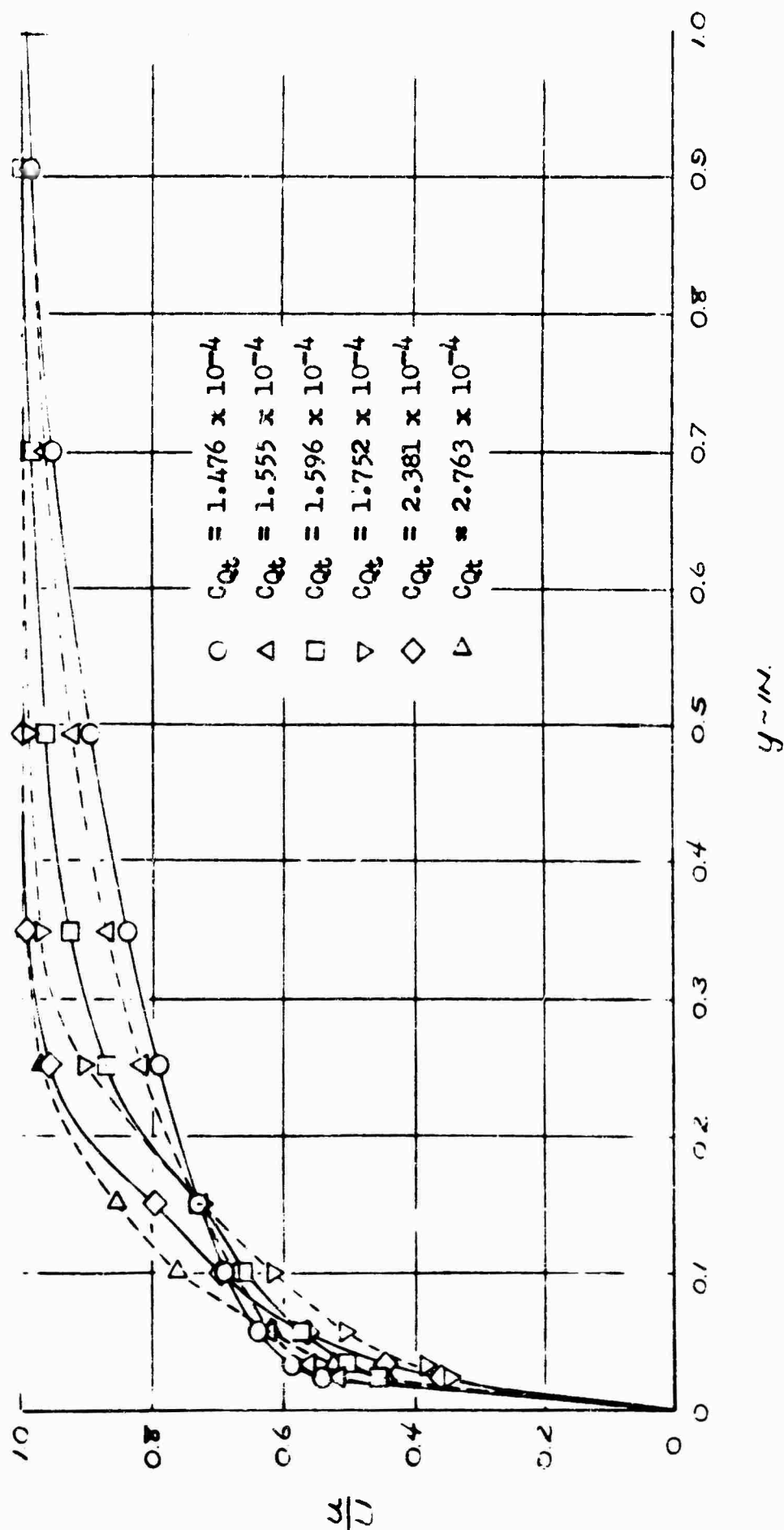


FIGURE 189a

VARIATION OF AFT END BOUNDARY LAYER VELOCITY PROFILE

WITH SUCTION COEFFICIENT  $C_{Qt}$

$R_L = 13.585 \times 10^6$

$\alpha = 0^\circ$

SIDE RAKE

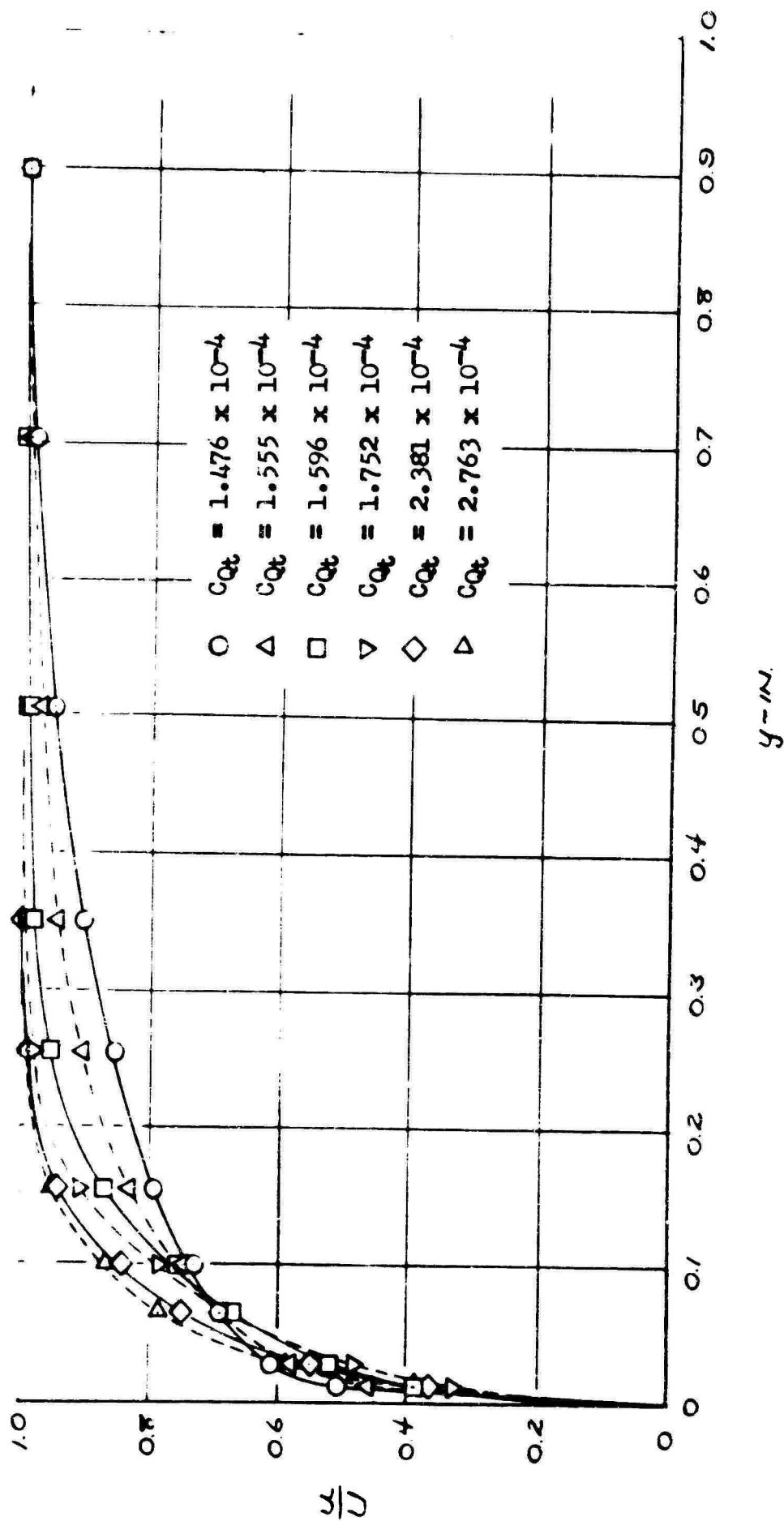


FIGURE 189b

VARIATION OF AFT END BOUNDARY LAYER VELOCITY PROFILE

WITH SUCTION COEFFICIENT  $C_{Qt}$

$$R_L = 13.585 \times 10^6$$

$$\alpha = 0^\circ$$

TOP RAKE

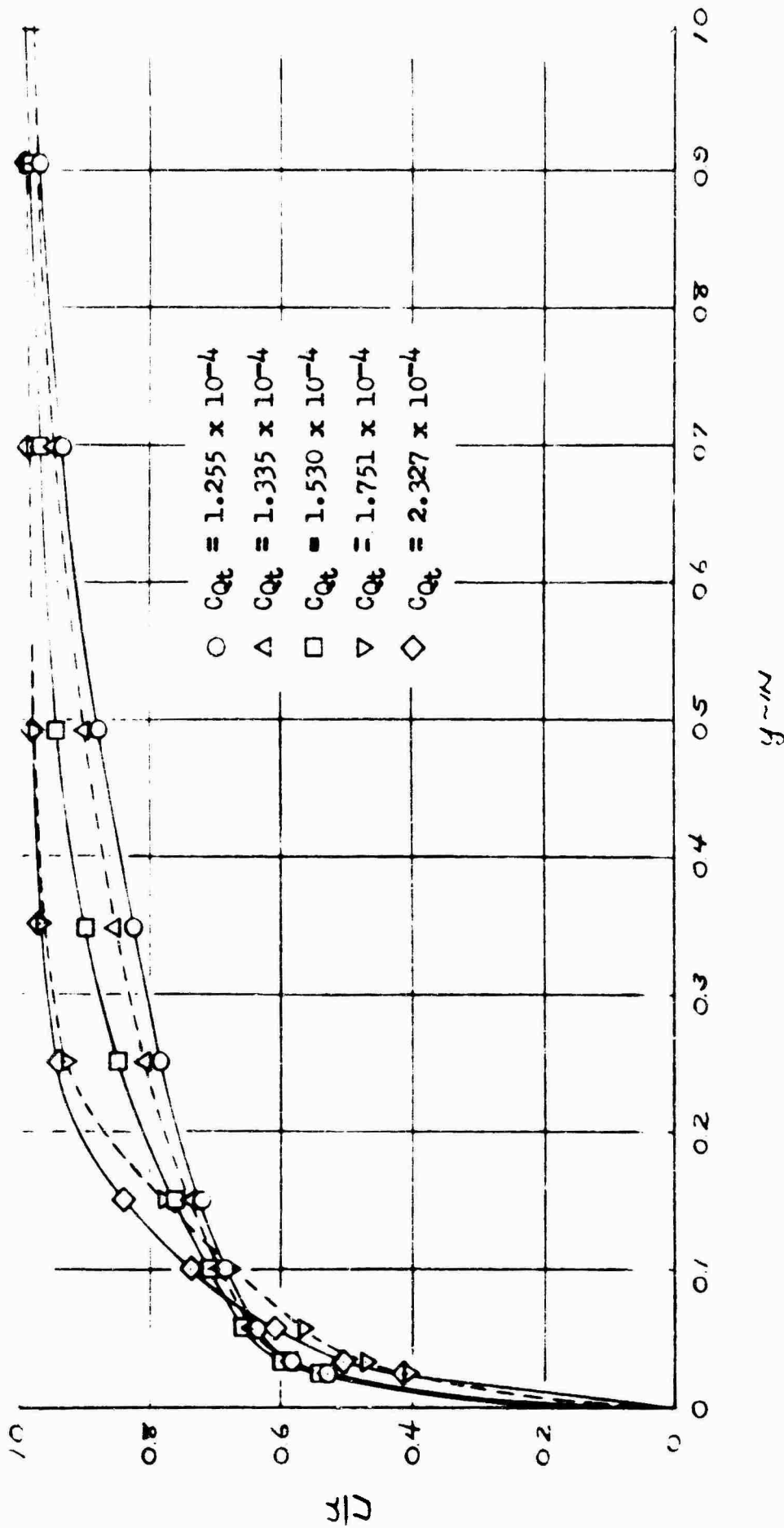


FIGURE 190a

VARIATION OF AFT END BOUNDARY LAYER VELOCITY PROFILE

WITH SUCTION COEFFICIENT  $C_{Qt}$

$R_L = 19.592 \times 10^6$

$\alpha = 0^\circ$

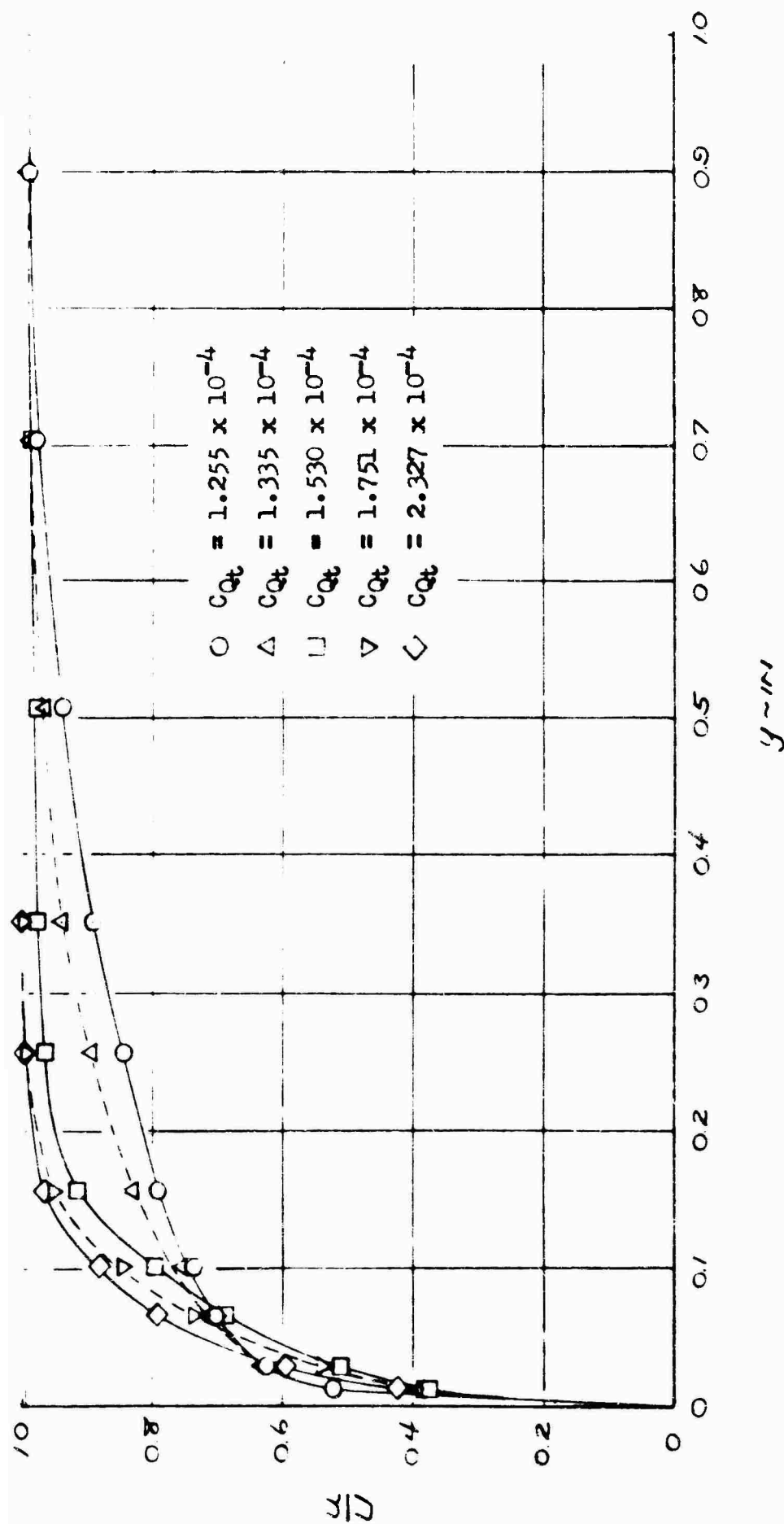


FIGURE 190b

VARIATION OF AFT END BOUNDARY LAYER VELOCITY PROFILE

WITH SUCTION COEFFICIENT  $C_{Qt}$

$$R_L = 19.592 \times 10^6$$

$$\alpha = 0^\circ$$

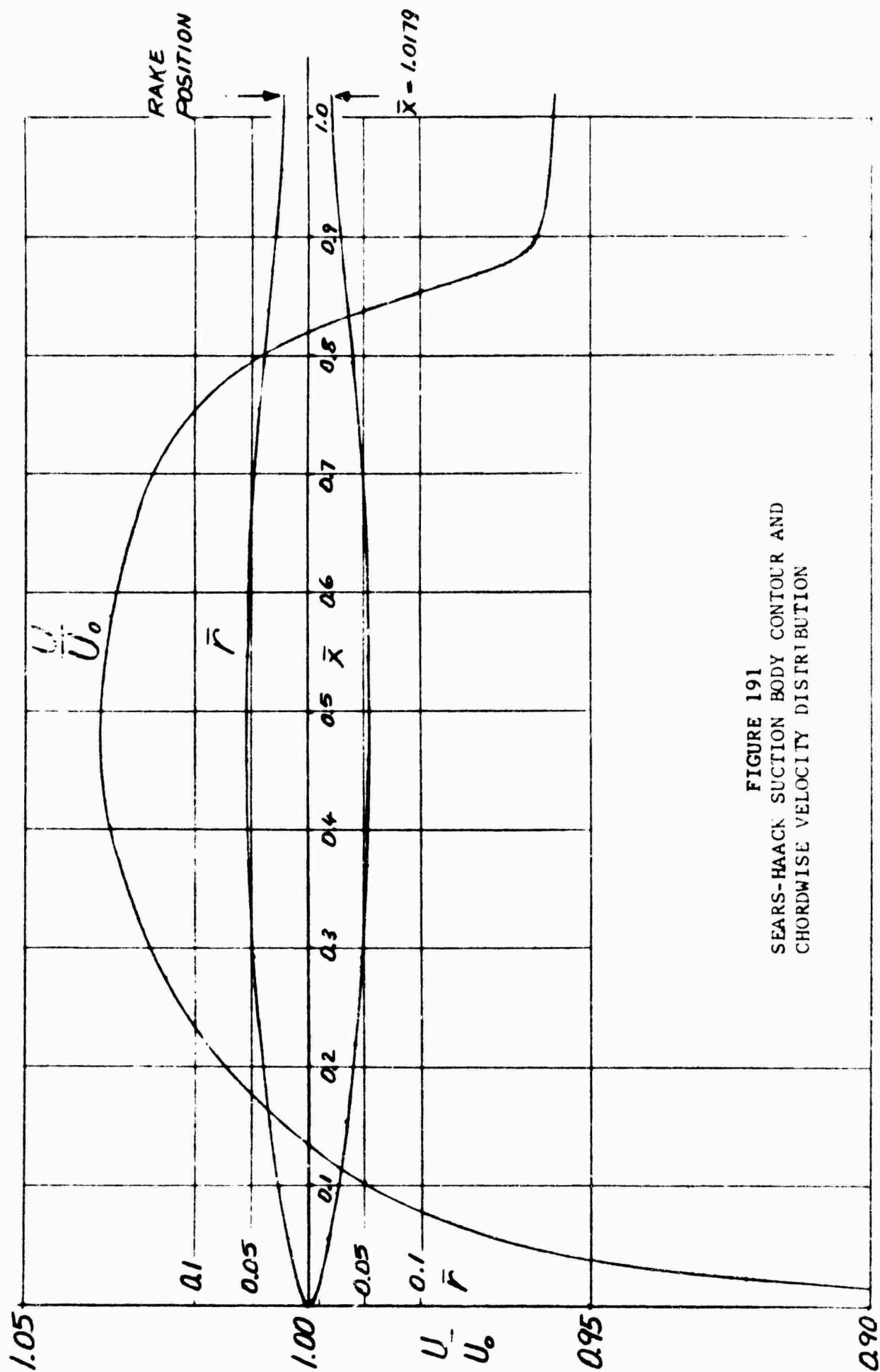


FIGURE 191  
SEARS-HAACK SUCTION BODY CONTOUR AND  
CHORDWISE VELOCITY DISTRIBUTION



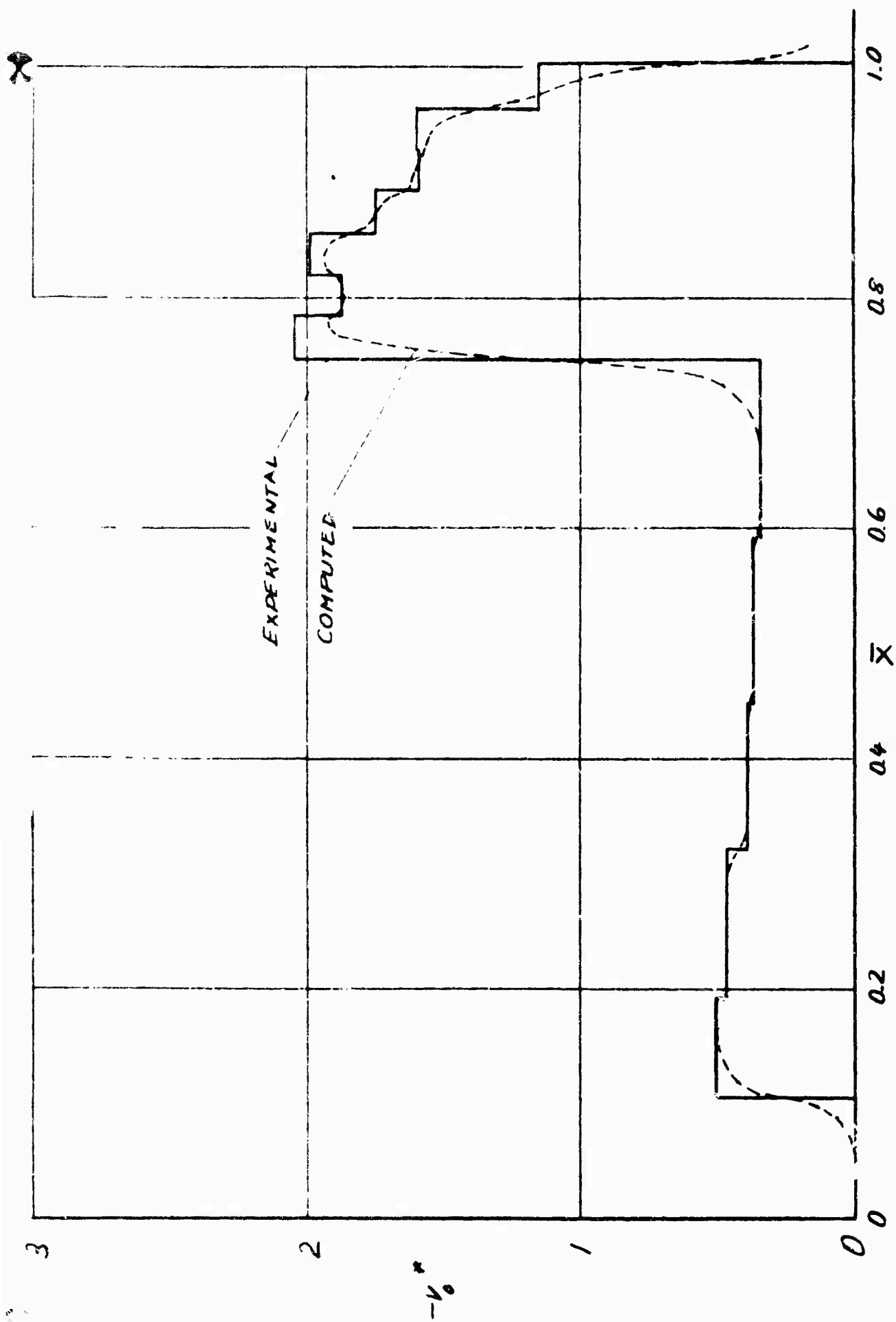


FIGURE 192  
COMPARISON OF EXPERIMENTAL AND  
ANALYTICAL CHORDWISE SUCTION INFLOW  
VELOCITY DISTRIBUTION FOR RUN NUMBER 66

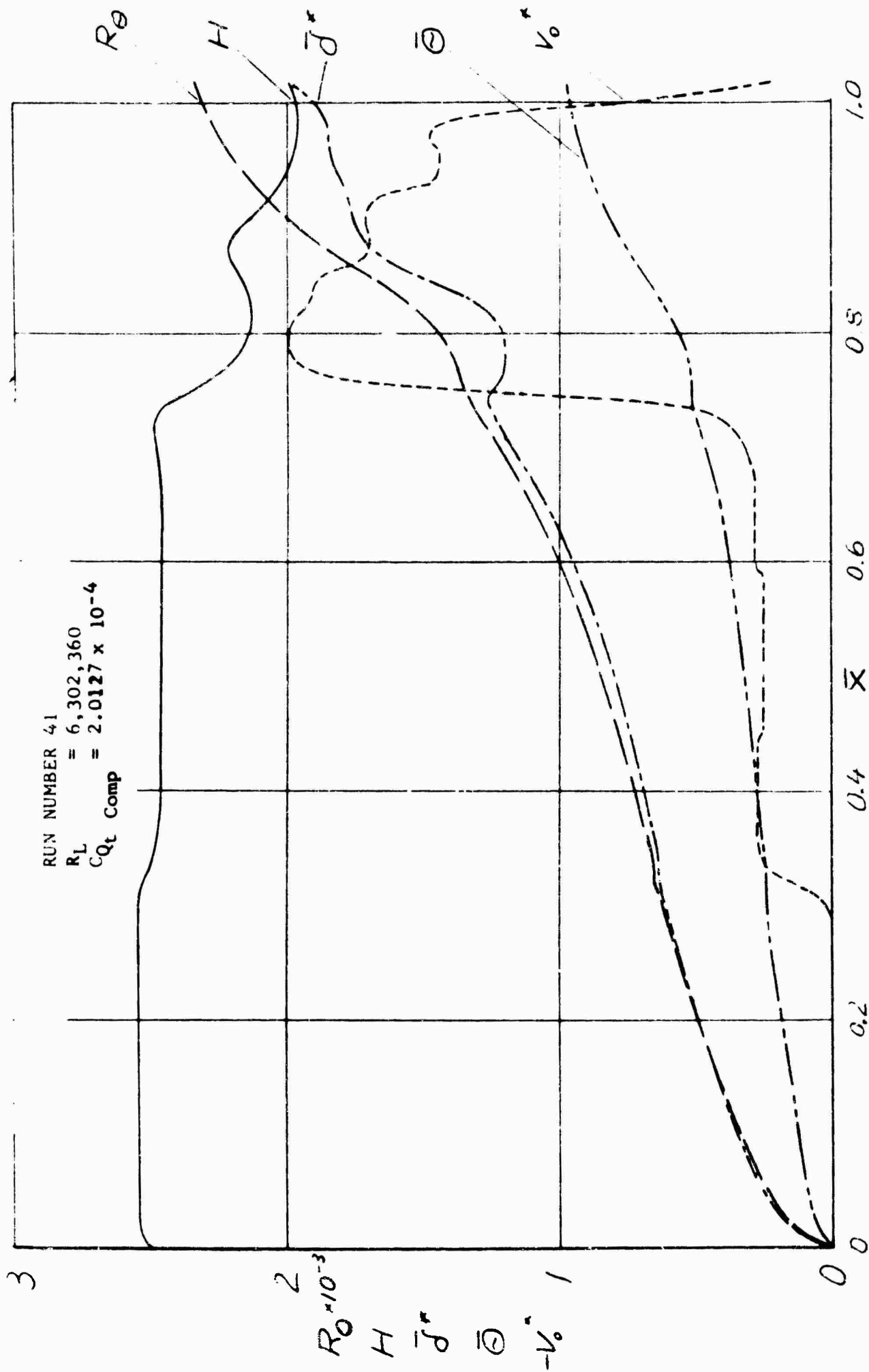


FIGURE 193  
 VARIATION OF DISPLACEMENT THICKNESS  $\delta^*$ , MOMENTUM THICKNESS  $\theta$ ,  
 SHAPE PARAMETER  $H$ , MOMENTUM THICKNESS REYNOLDS NUMBER  $R_\theta$   
 AND NONDIMENSIONAL SUCTION INFLOW VELOCITY  $V_0^*$  WITH CHORD

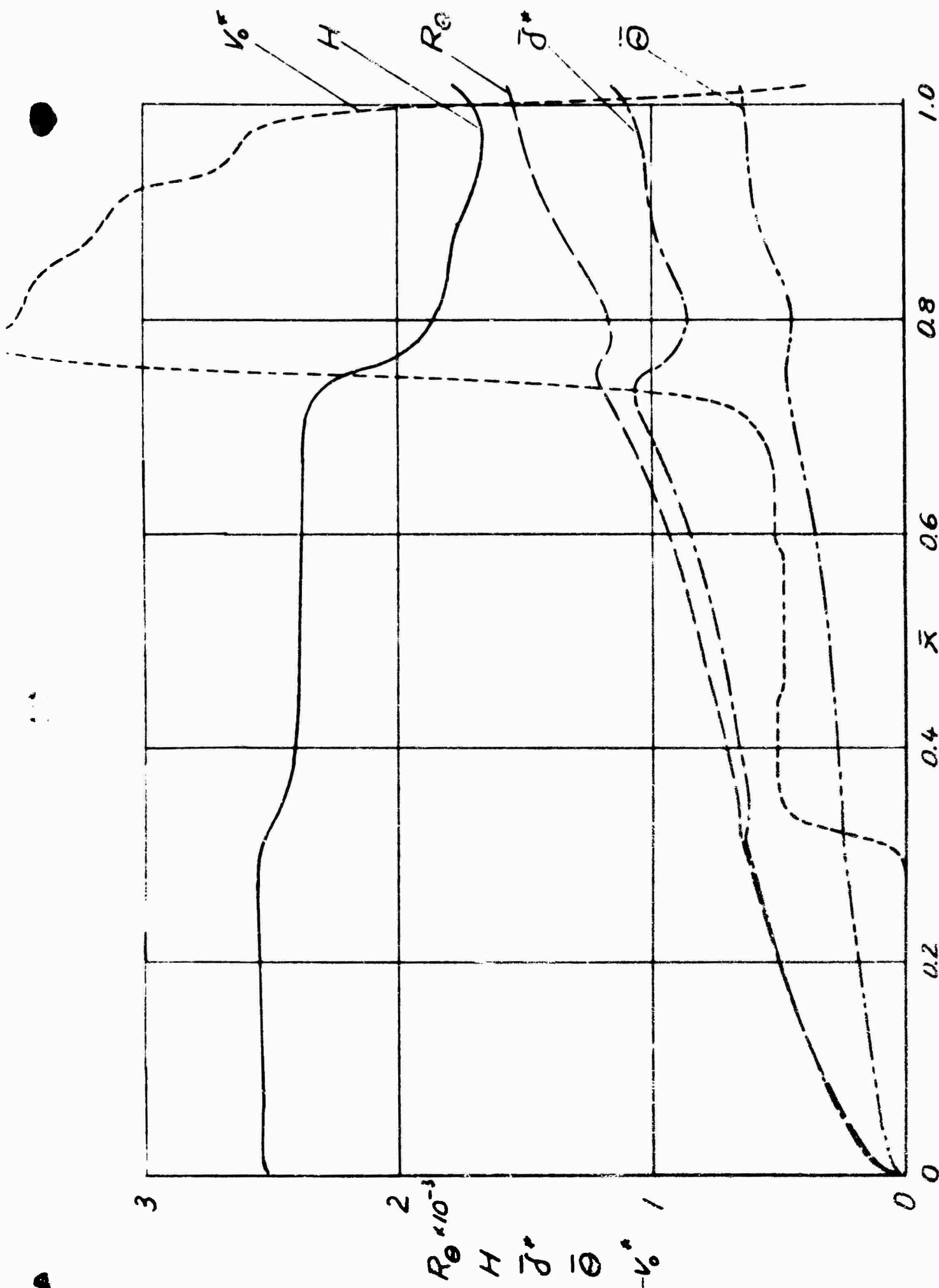


FIGURE 194  
 VARIATION OF DISPLACEMENT THICKNESS  $\delta^*$ , MOMENTUM  
 THICKNESS  $\delta$ , SHAPE PARAMETER  $H$ , MOMENTUM THICKNESS  
 REYNOLDS NUMBER  $R_\theta$  AND NONDIMENSIONAL SUCTION INFLOW  
 VELOCITY  $v_o^*$  WITH CHORD

RUN NUMBER 46  
 $R_L = 6.337,120$   
 $C_{Qt \text{ Comp}} = 3.6608 \times 10^{-4}$

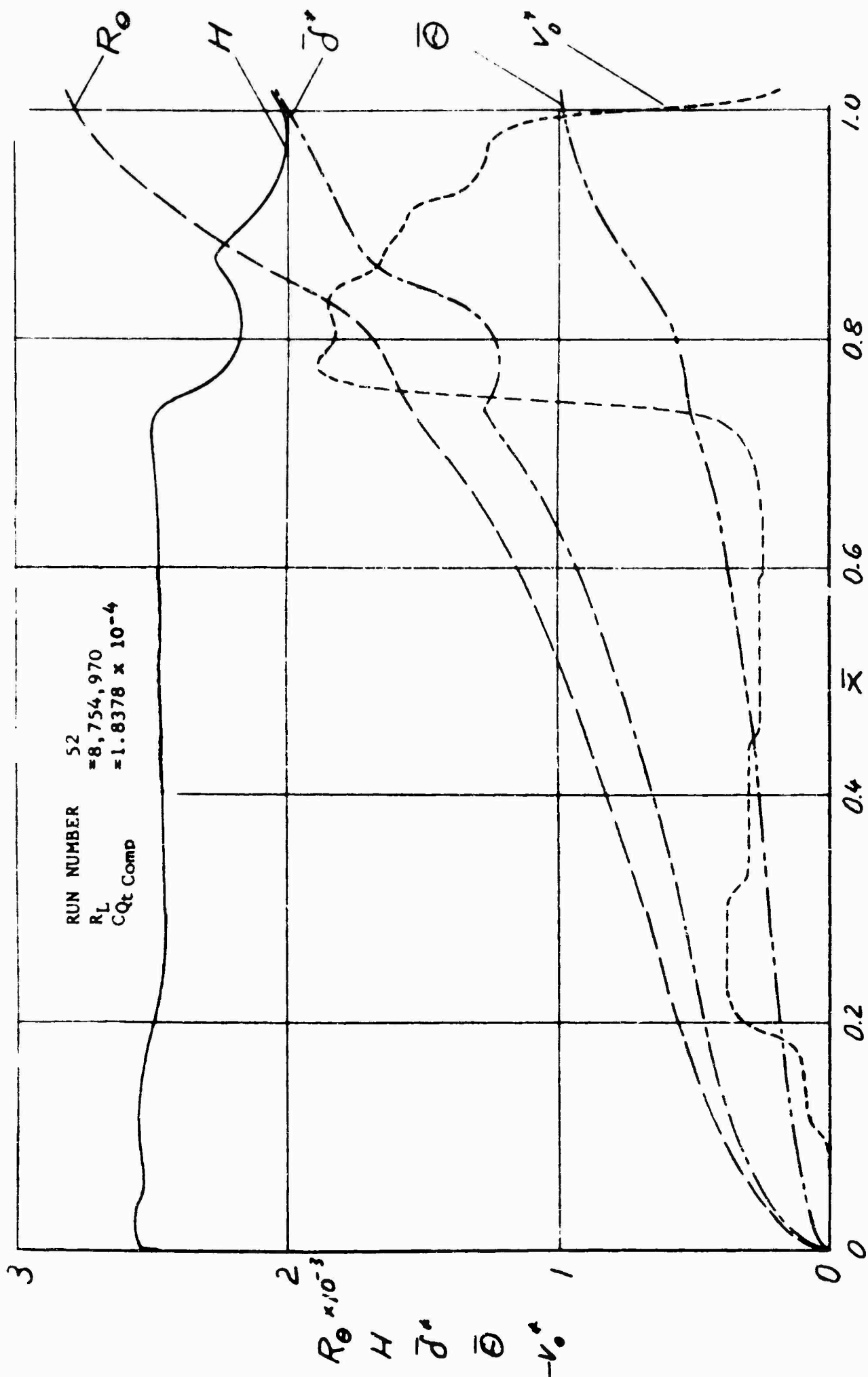


FIGURE 195  
 VARIATION OF DISPLACEMENT THICKNESS  $\delta^*$ , MOMENTUM THICKNESS  $\Theta$ , SHAPE PARAMETER  $H$ , MOMENTUM THICKNESS REYNOLDS NUMBER  $R_\Theta$  AND NONDIMENSIONAL SUCTION INFLOW VELOCITY  $v_0^*$  WITH CHORD

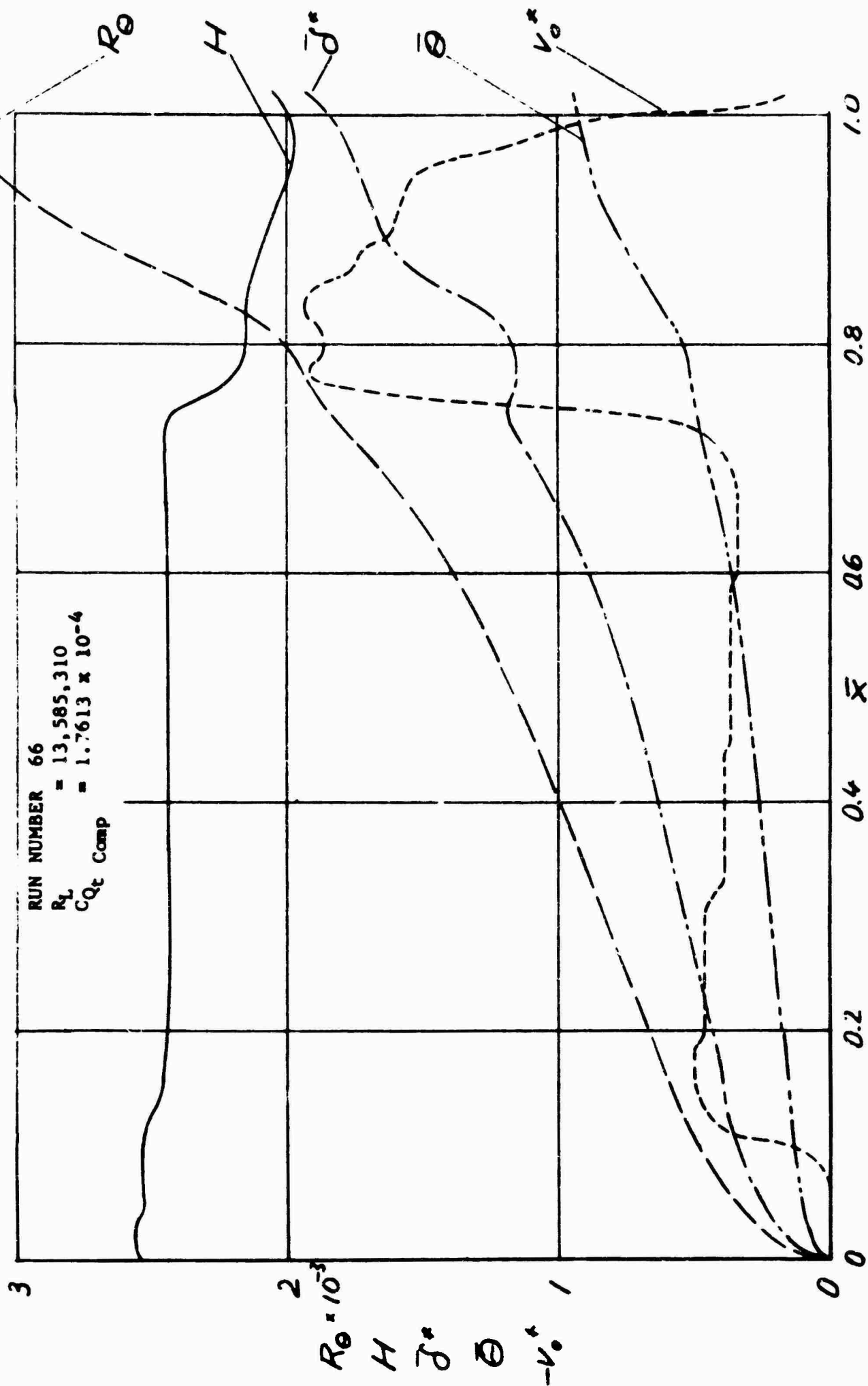


FIGURE 196  
 VARIATION OF DISPLACEMENT THICKNESS  $\delta^*$ , MOMENTUM THICKNESS  $\theta$   
 SHAPE PARAMETER  $H$ , MOMENTUM THICKNESS REYNOLDS NUMBER  $Re$   
 AND NONDIMENSIONAL SUCTION INFLOW VELOCITY  $v_o^*$  WITH CHORD

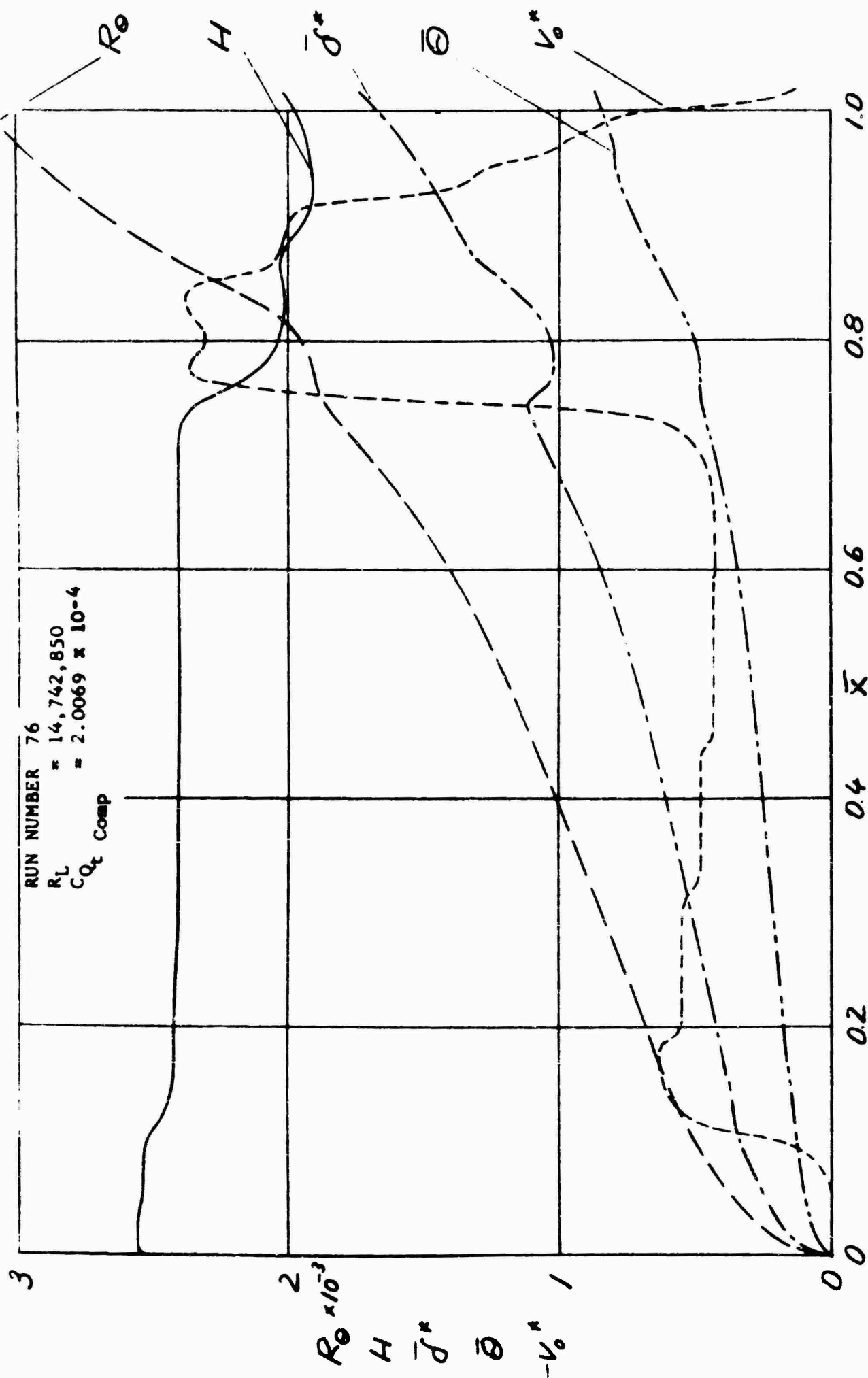


FIGURE 197  
 VARIATION OF DISPLACEMENT THICKNESS  $\delta^*$ , MOMENTUM THICKNESS  $\bar{\theta}$ ,  
 SHAPE PARAMETER  $H$ , MOMENTUM THICKNESS REYNOLDS NUMBER  $R_\theta$   
 AND NONDIMENSIONAL SUCTION INFLOW VELOCITY  $V_\theta^*$  WITH CHORD

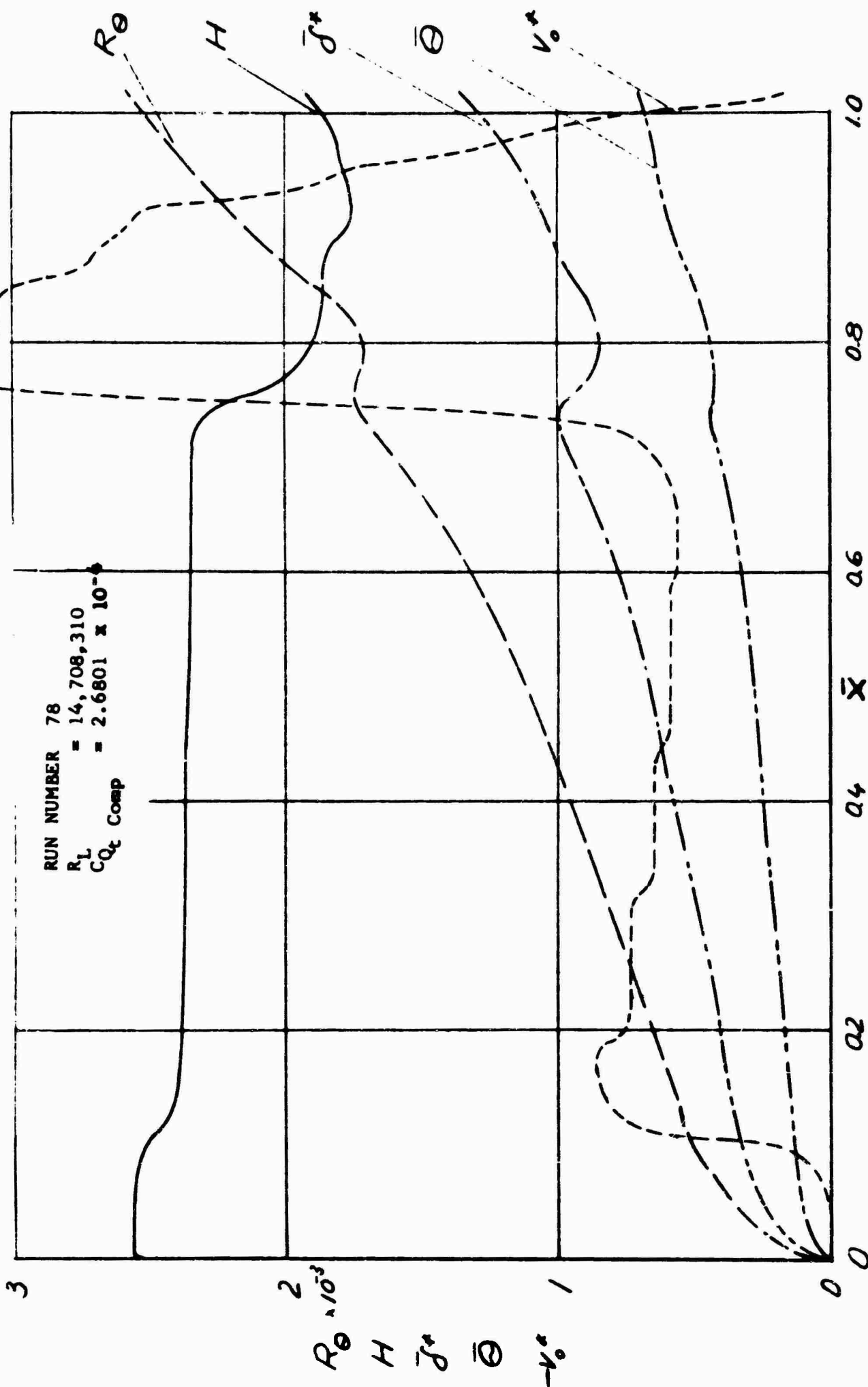


FIGURE 198  
 VARIATION OF DISPLACEMENT THICKNESS  $\delta^*$ , MOMENTUM THICKNESS  $\theta$ , SHAPE PARAMETER  $H$ , MOMENTUM THICKNESS REYNOLDS NUMBER  $R_\theta$  AND NONDIMENSIONAL SUCTION INFLOW VELOCITY  $v_0^*$  WITH CHORD

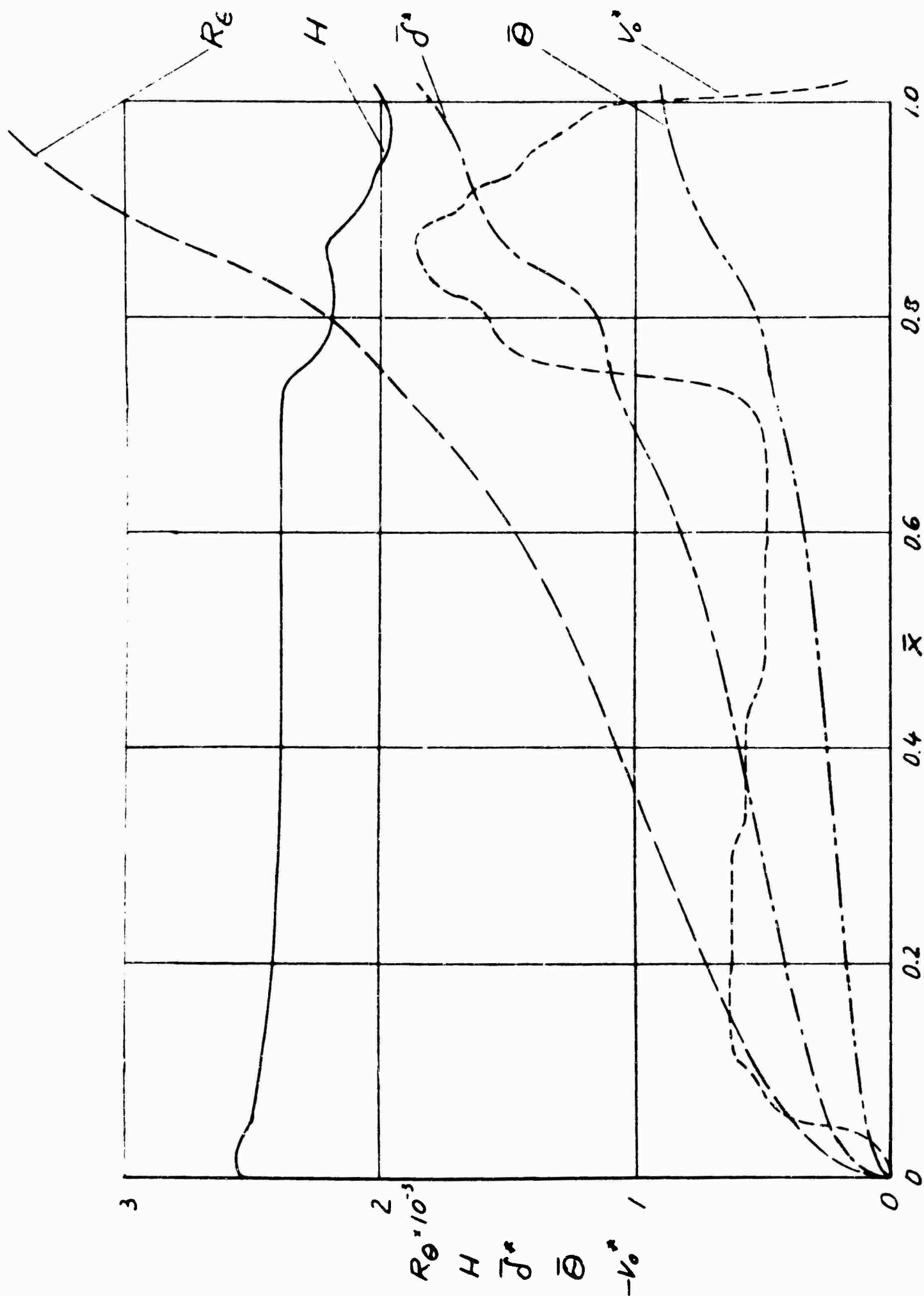


FIGURE 199  
 VARIATION OF DISPLACEMENT THICKNESS  $\bar{\delta}^*$ , MOMENTUM THICKNESS  $\bar{\theta}$ ,  
 SHAPE PARAMETER  $H$ , MOMENTUM THICKNESS REYNOLDS NUMBER  $R_{\theta}$  AND  
 NONDIMENSIONAL SUCTION INFLOW VELOCITY  $v_0^*$  WITH CHORD

RUN NUMBER 397  
 $R_L = 17,228,480$   
 $C_{Q_t} \text{ Comp} = 1.8237 \times 10^{-4}$



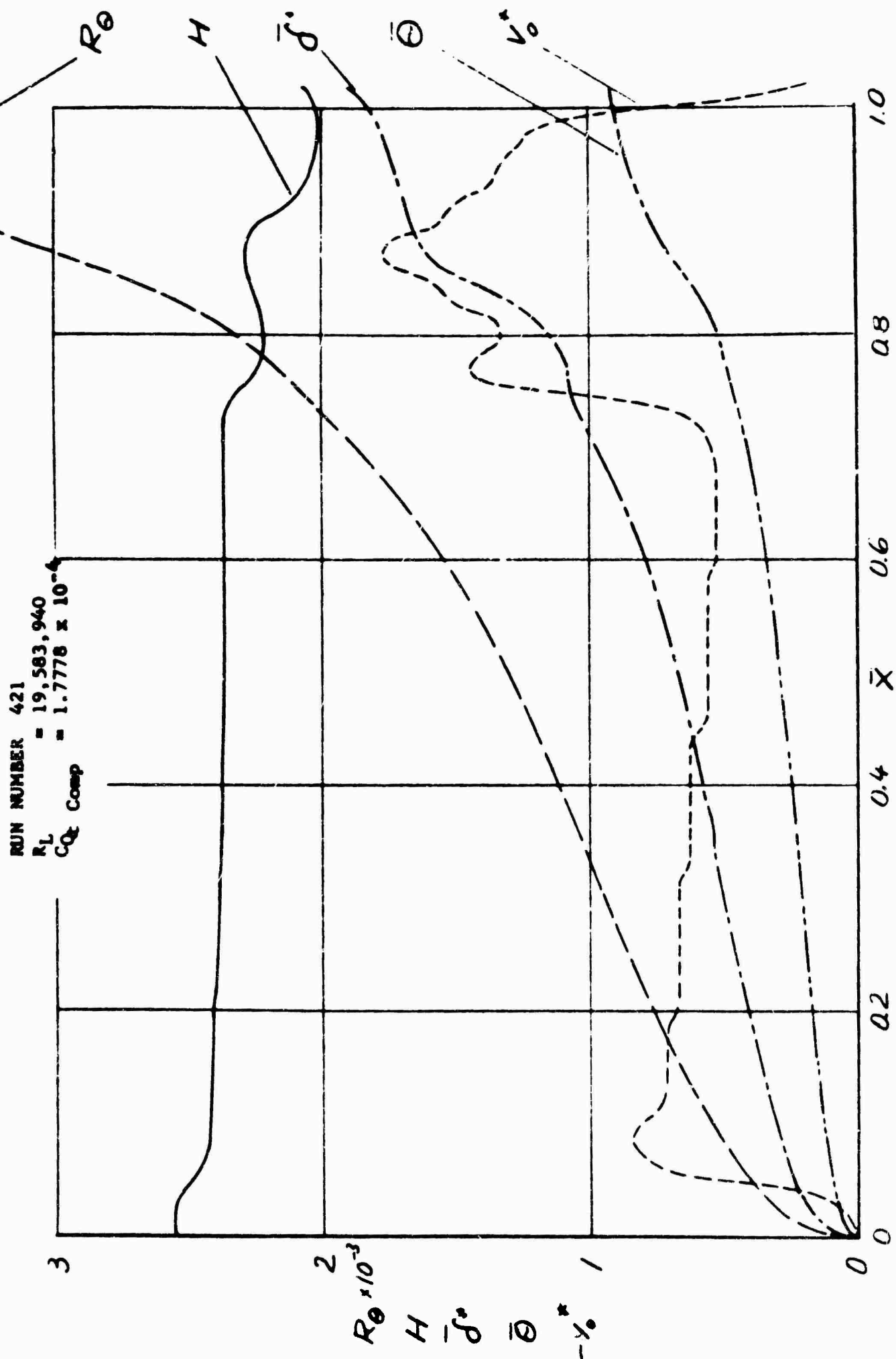


FIGURE 200  
 VARIATION OF DISPLACEMENT THICKNESS  $\delta^*$ , MOMENTUM THICKNESS  $\theta$ ,  
 SHAPE PARAMETER  $H$ , MOMENTUM THICKNESS REYNOLDS NUMBER  $R_\theta$  AND  
 NONDIMENSIONAL SUCTION INFLOW VELOCITY  $v_0^*$  WITH CHORD

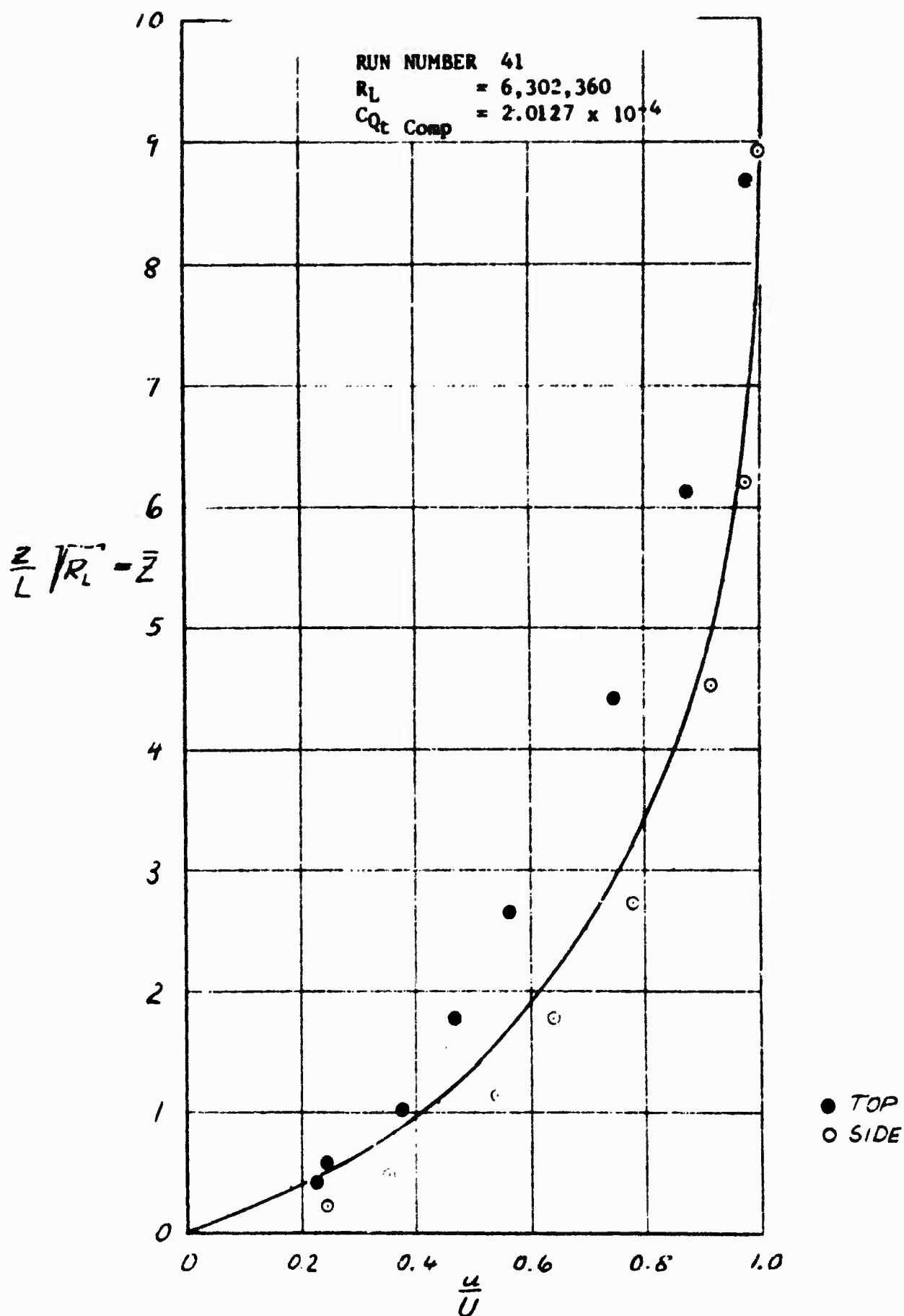


FIGURE 201  
 COMPARISON OF MEASURED AND CALCULATED  
 BOUNDARY LAYER VELOCITY PROFILES AT  
 THE RAKE POSITION

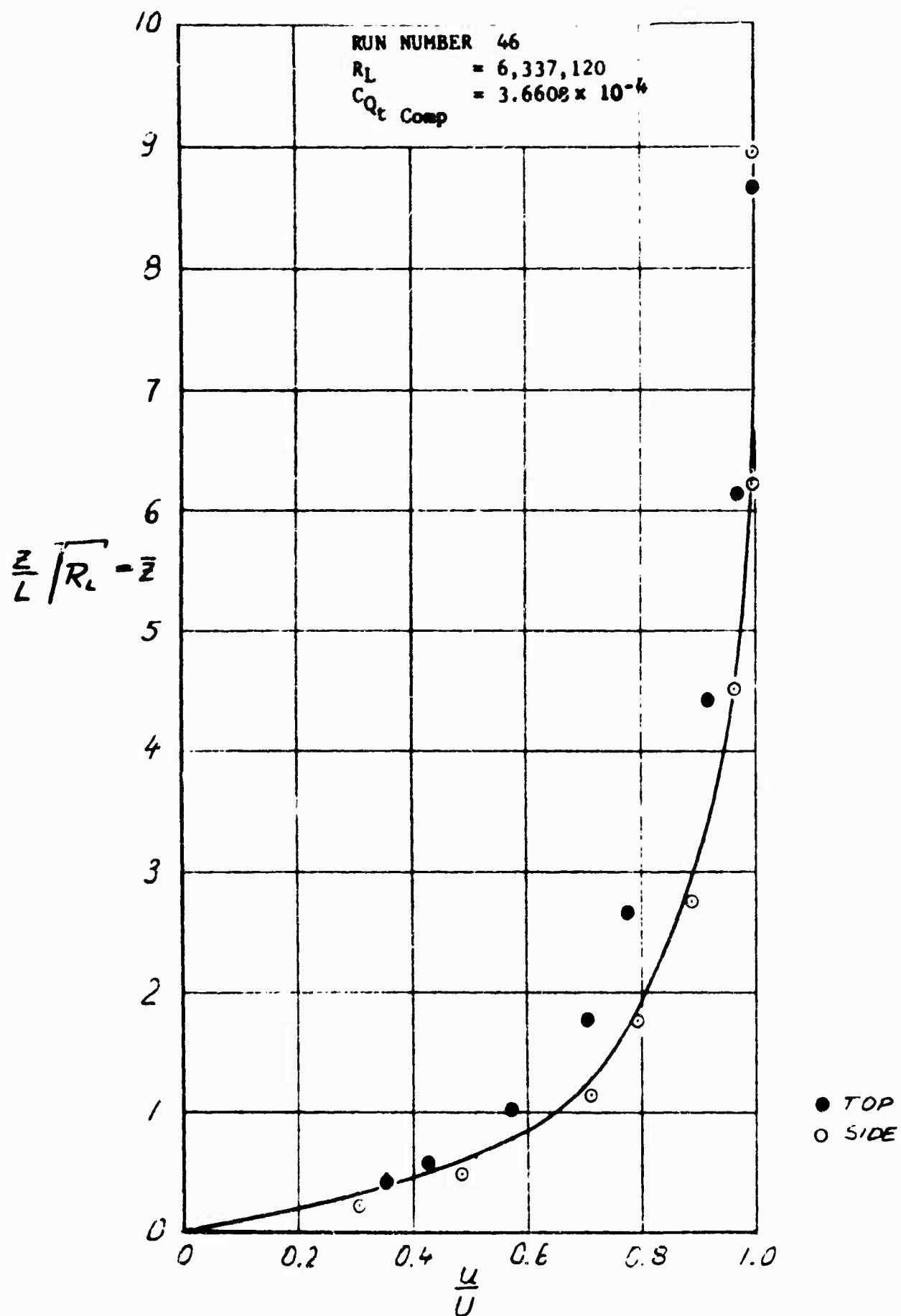


FIGURE 202  
 COMPARISON OF MEASURED AND CALCULATED  
 BOUNDARY LAYER VELOCITY PROFILES AT  
 THE RAKE POSITION



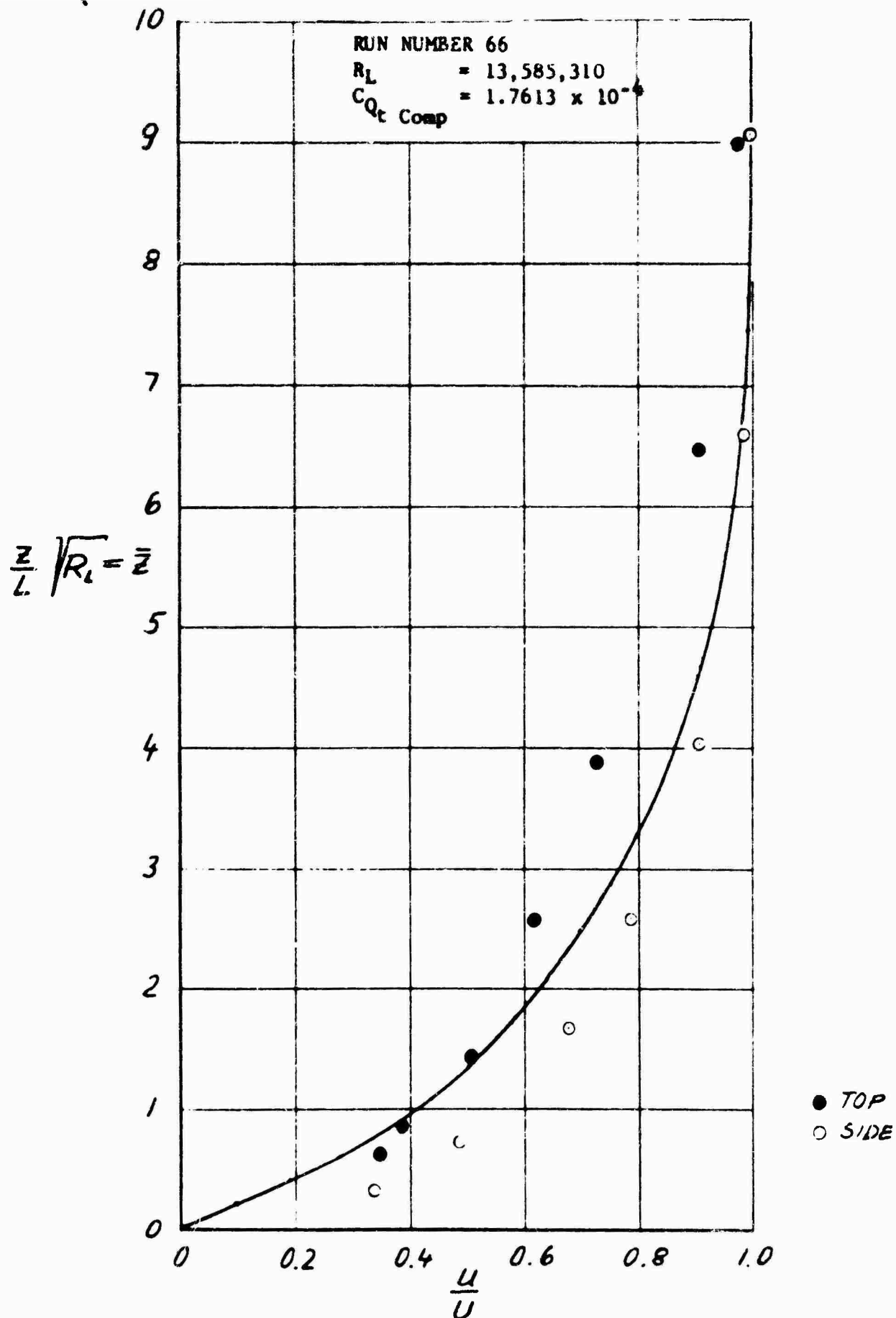


FIGURE 204  
 COMPARISON OF MEASURED AND CALCULATED  
 BOUNDARY LAYER VELOCITY PROFILES AT  
 THE RAKE POSITION

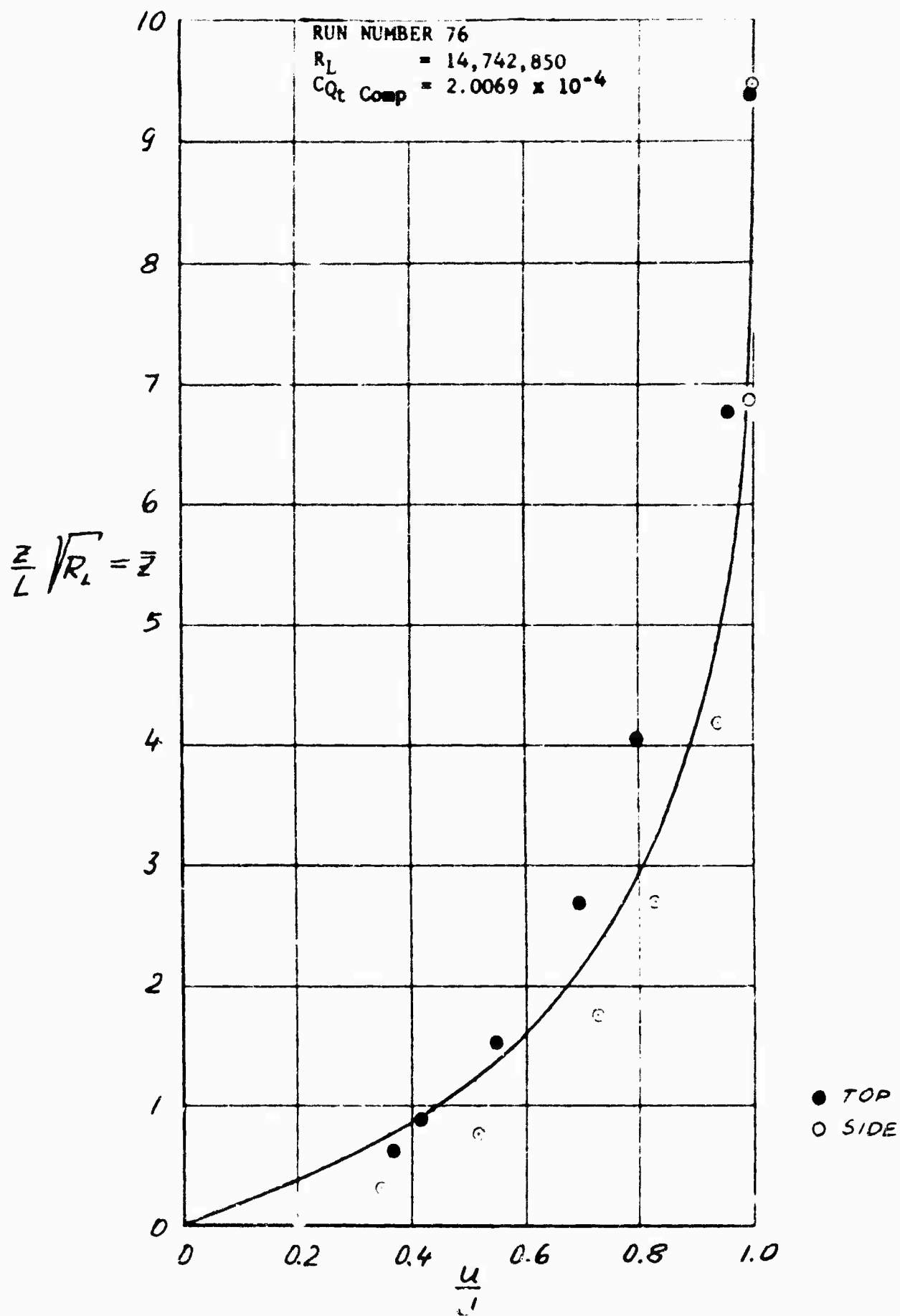


FIGURE 205  
 COMPARISON OF MEASURED AND CALCULATED  
 BOUNDARY LAYER VELOCITY PROFILES AT  
 THE RAKE POSITION

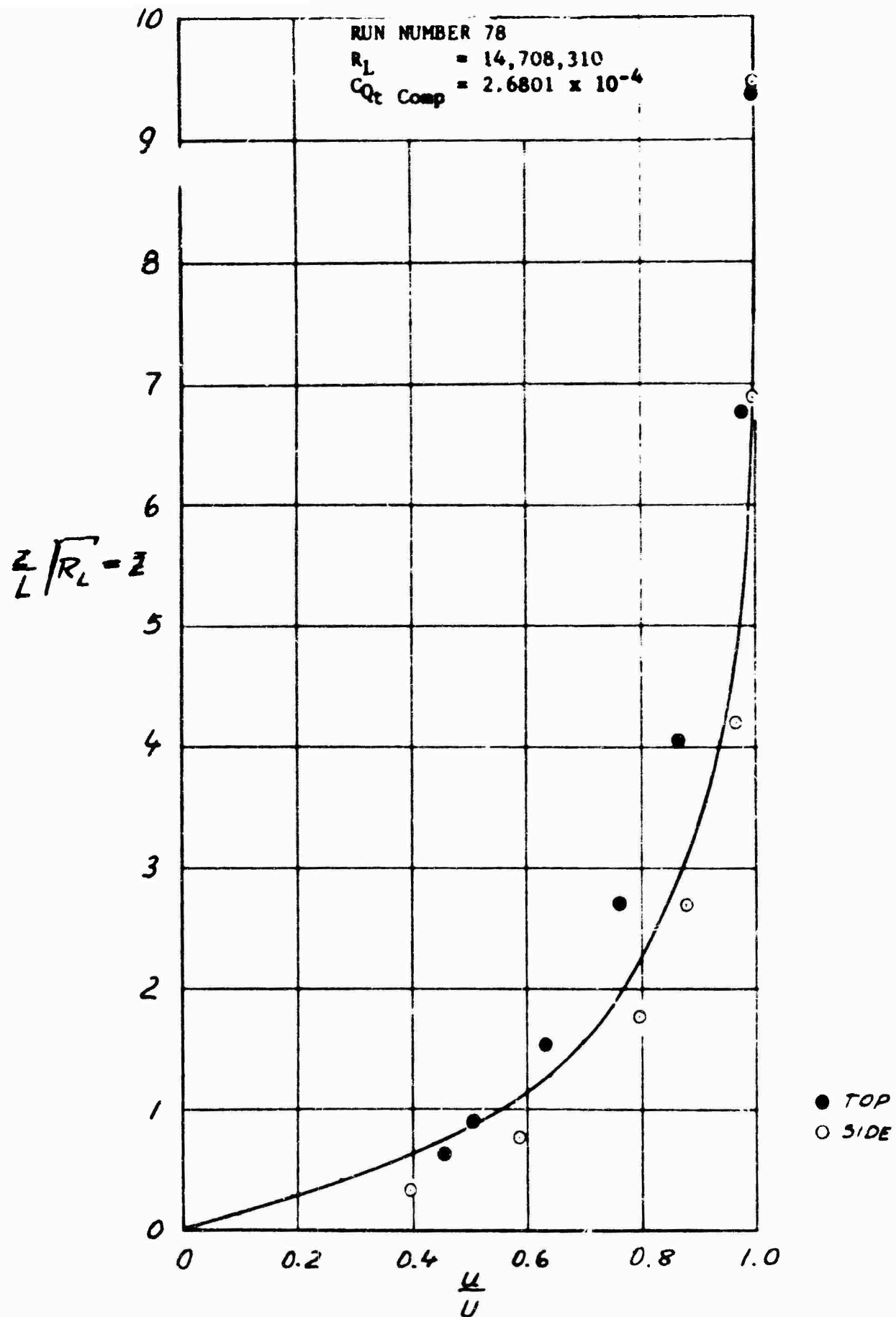


FIGURE 206  
 COMPARISON OF MEASURED AND CALCULATED  
 BOUNDARY LAYER VELOCITY PROFILES AT  
 THE RAKE POSITION

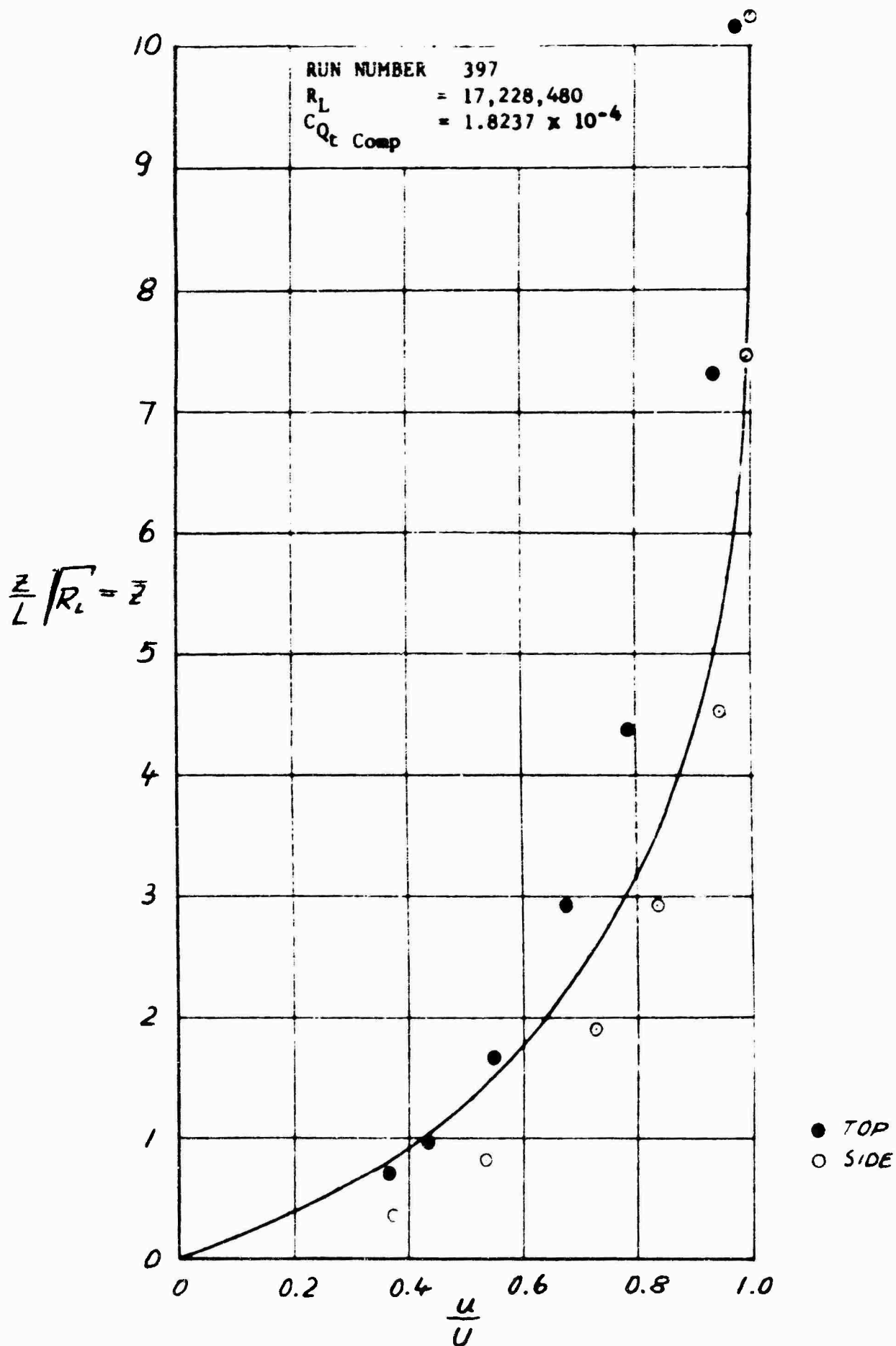


FIGURE 207  
 COMPARISON OF MEASURED AND CALCULATED  
 BOUNDARY LAYER VELOCITY PROFILES AT  
 THE RAKE POSITION



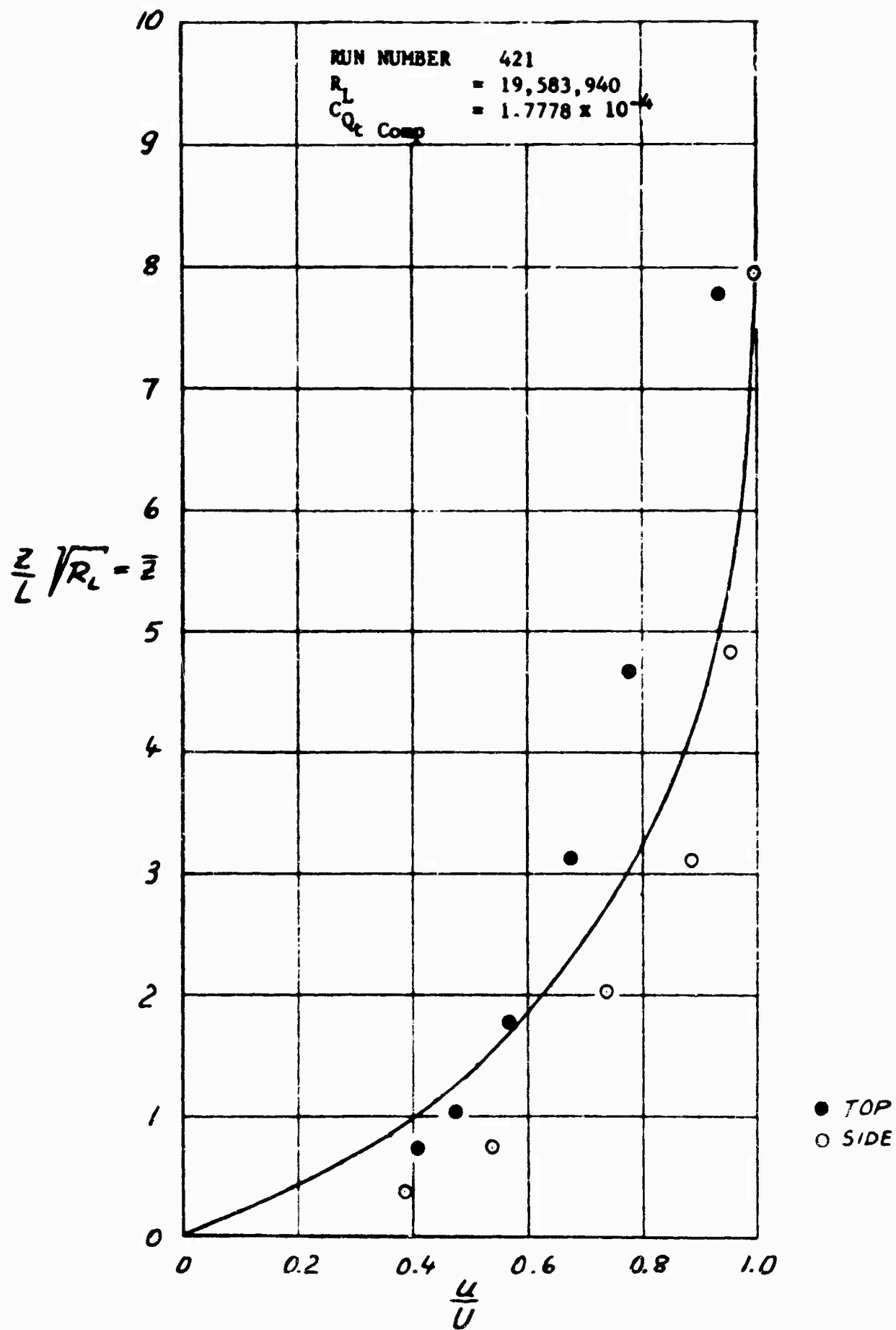


FIGURE 208  
 COMPARISON OF MEASURED AND CALCULATED  
 BOUNDARY LAYER VELOCITY PROFILES AT  
 THE RAKE POSITION

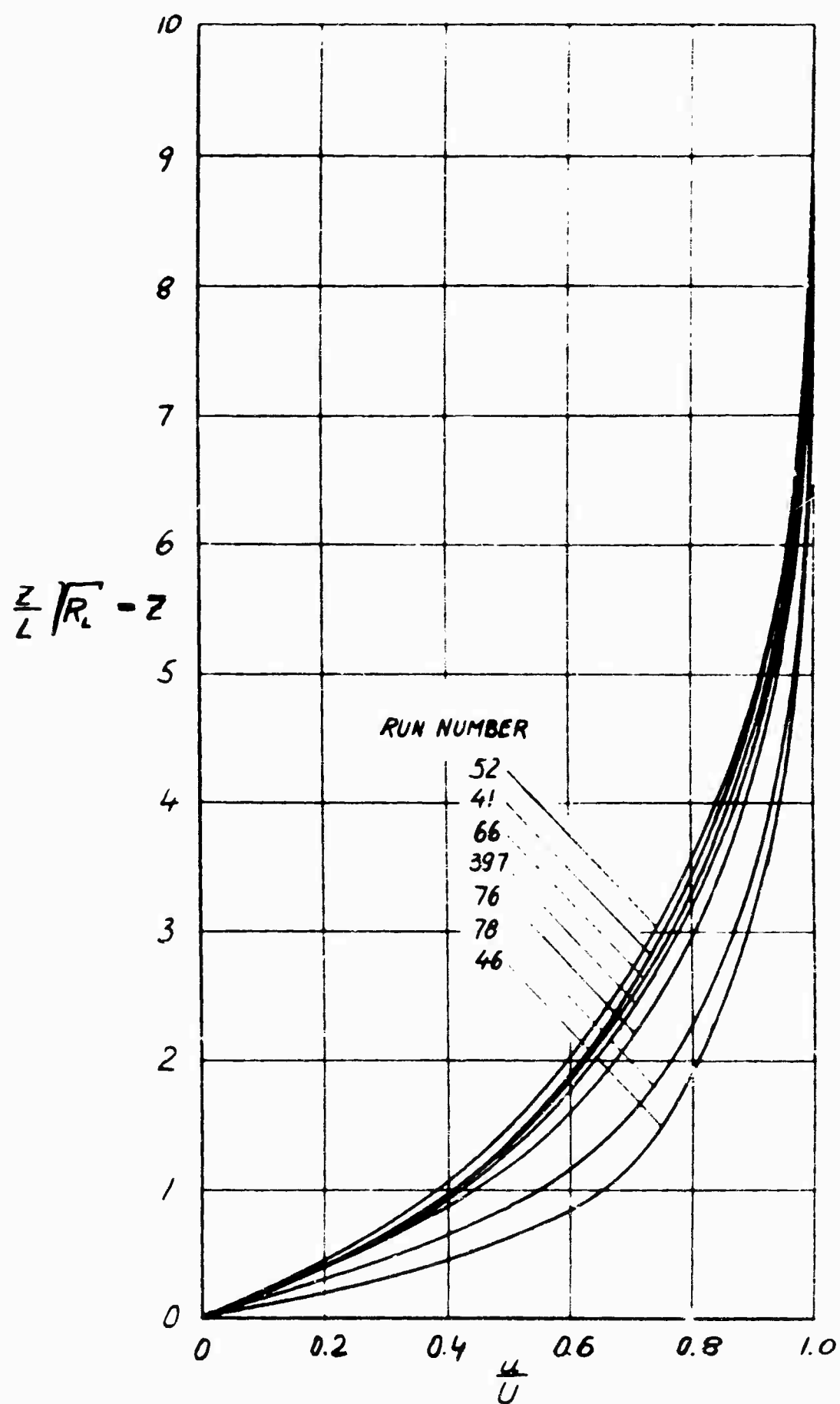


FIGURE 209  
 COMPARISON OF COMPUTED BOUNDARY LAYER VELOCITY  
 DISTRIBUTIONS AT THE RAKE POSITION

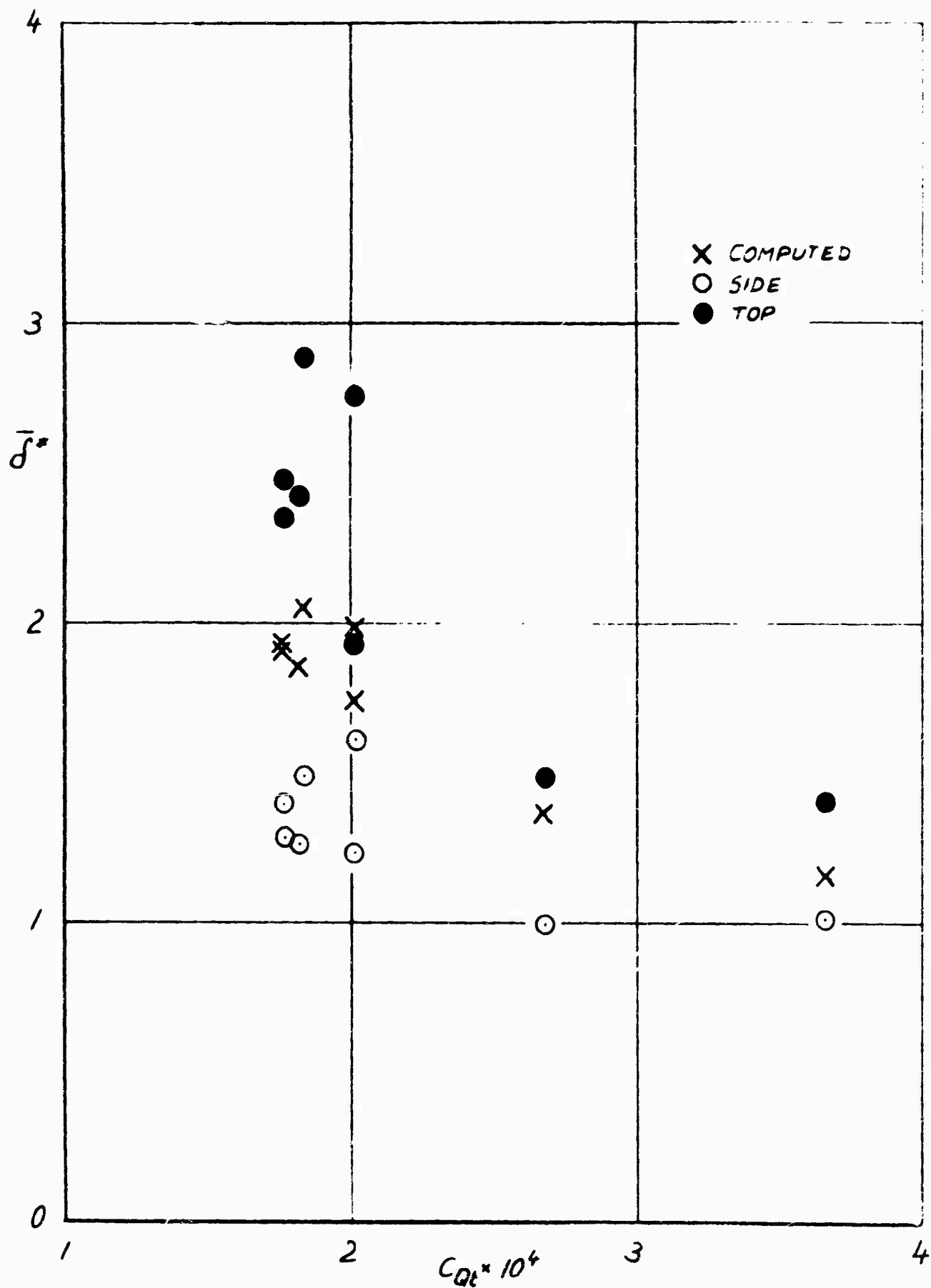


FIGURE 210  
VARIATION OF EXPERIMENTAL AND COMPUTED DIS-  
PLACEMENT THICKNESS  $\delta^*$  AT THE RAKE POSITION  
WITH TOTAL SUCTION FLOW COEFFICIENT  $C_{Qt}$

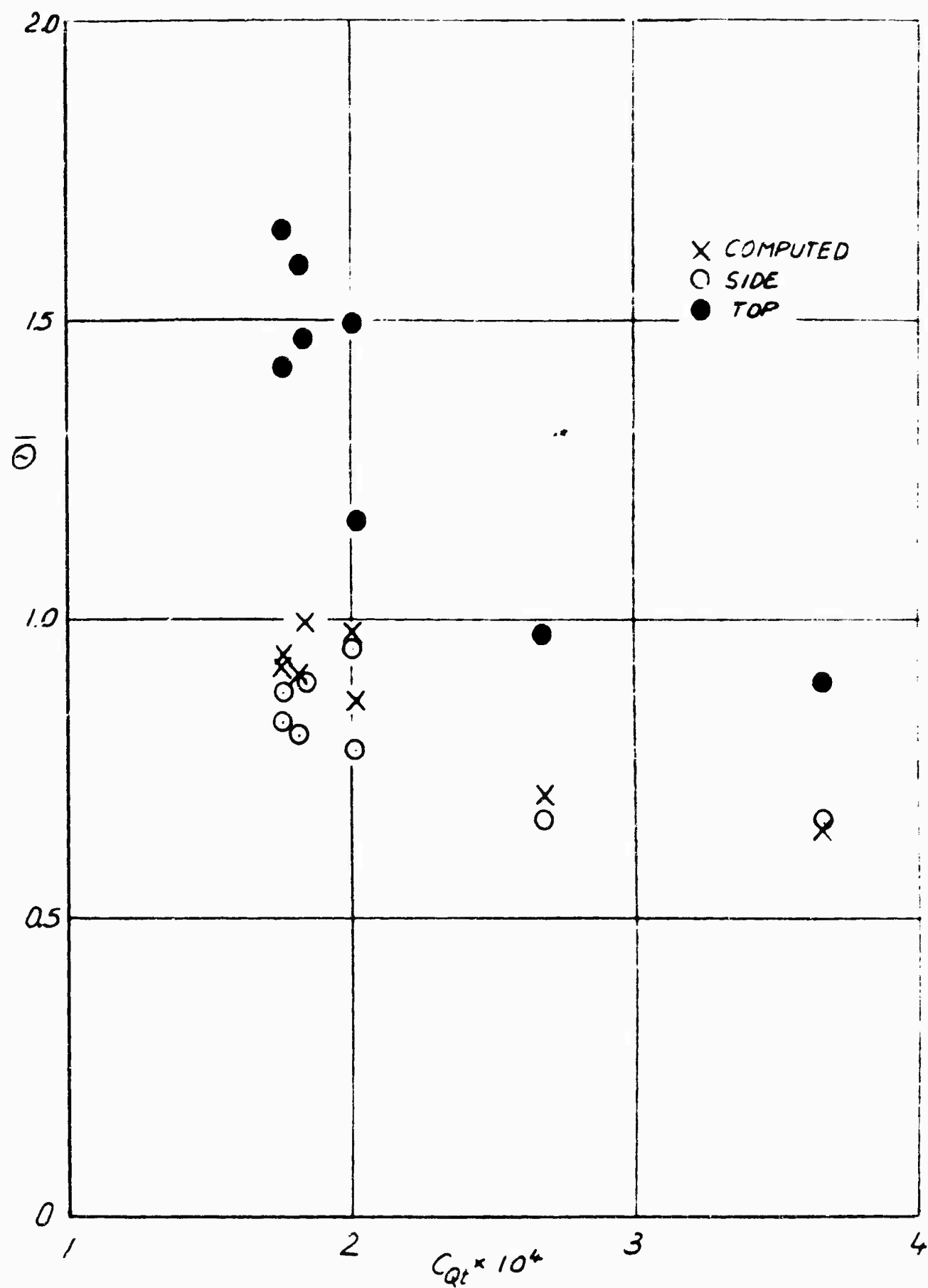


Figure 211  
 VARIATION OF EXPERIMENTAL AND COMPUTED  
 MOMENTUM THICKNESS  $\bar{\theta}$  AT THE RAKE POSITION  
 WITH TOTAL SUCTION FLOW COEFFICIENT  $C_{Qt}$

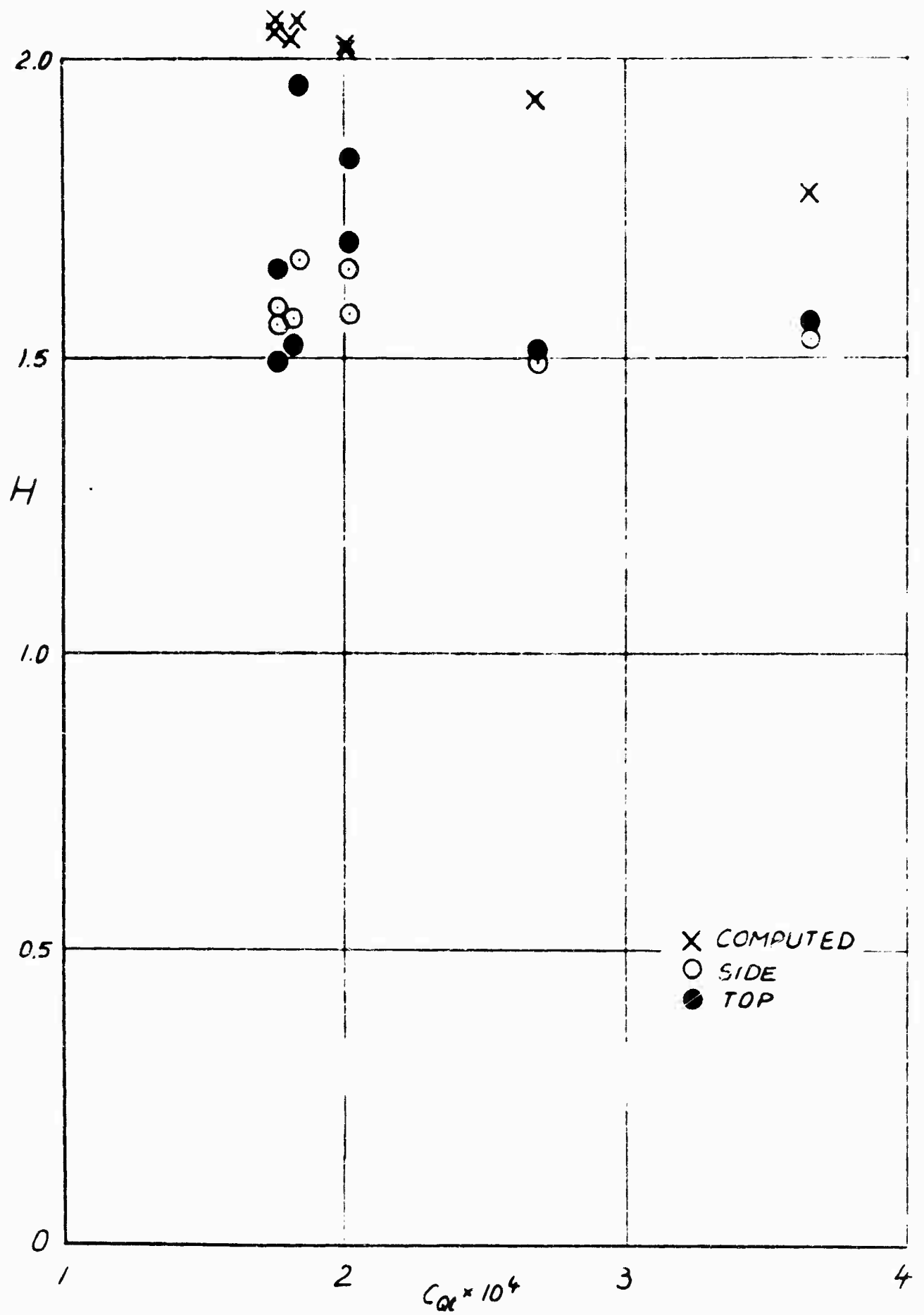


FIGURE 212  
VARIATION OF EXPERIMENTAL AND COMPUTED SHAPE PARAMETER  $H$  AT  
THE RAKE POSITION WITH TOTAL SUCTION FLOW COEFFICIENT  $C_{at}$

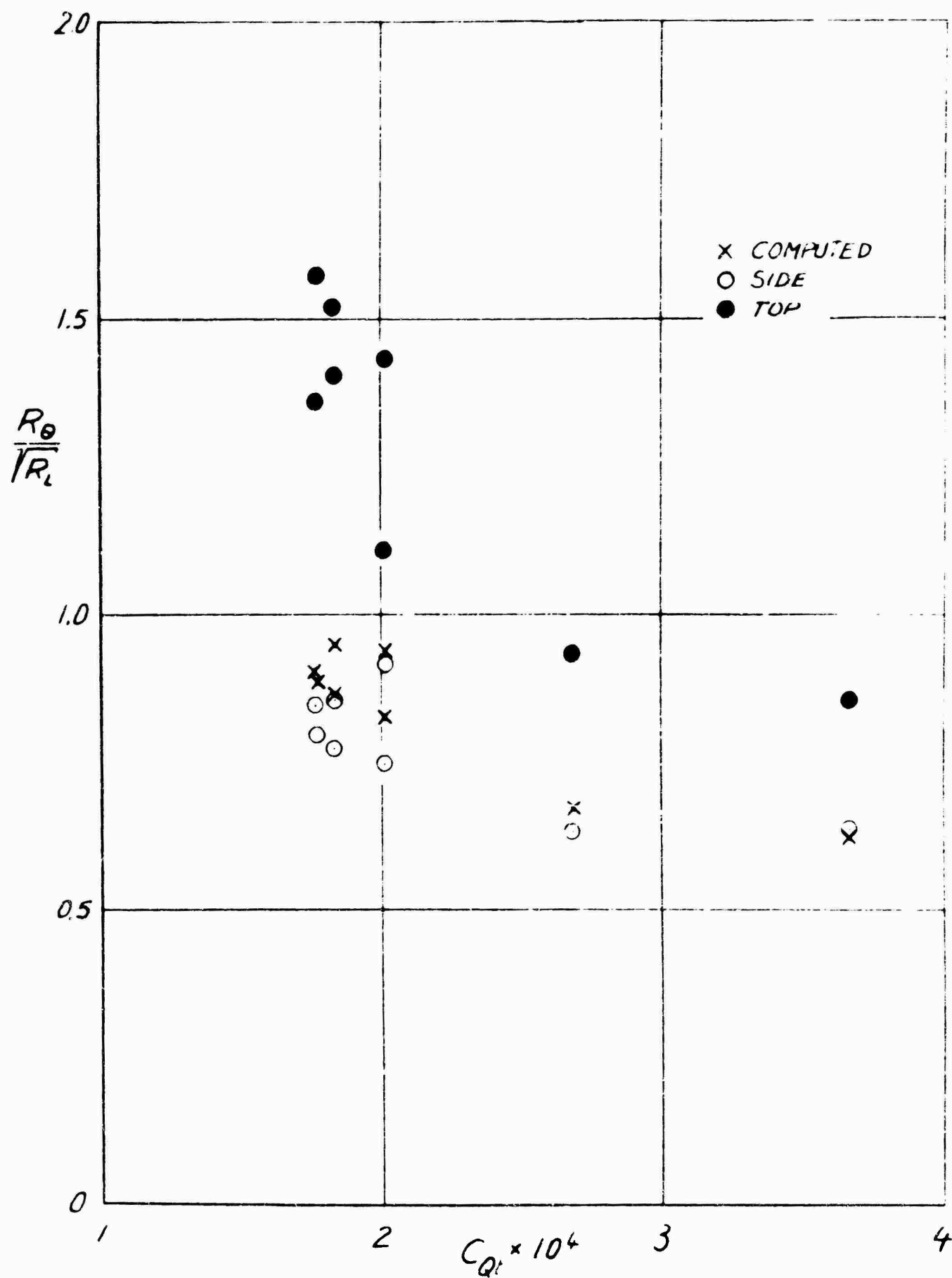


FIGURE 213  
 VARIATION OF EXPERIMENTAL AND COMPUTED  
 $\frac{R_0}{\sqrt{R_1}}$  AT THE RAKE POSITION WITH TOTAL  
 SUCTION FLOW COEFFICIENT  $C_{Q_1}$

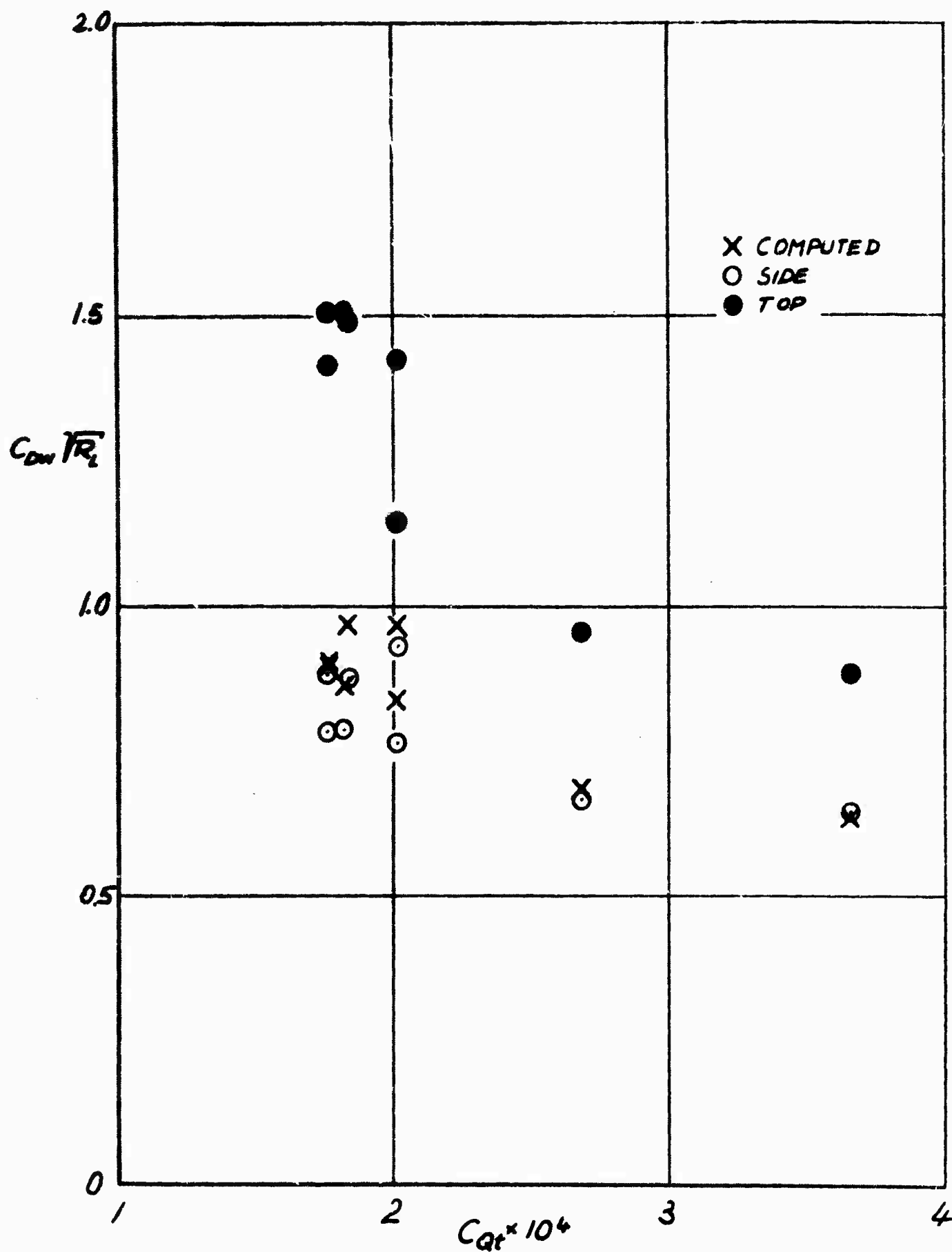


FIGURE 214  
 VARIATION OF EXPERIMENTAL AND COMPUTED  
 $C_{Dn} \sqrt{R_L}$  AT THE RAKE POSITION WITH TOTAL  
 SUCTION FLOW COEFFICIENT  $C_{Qt}$

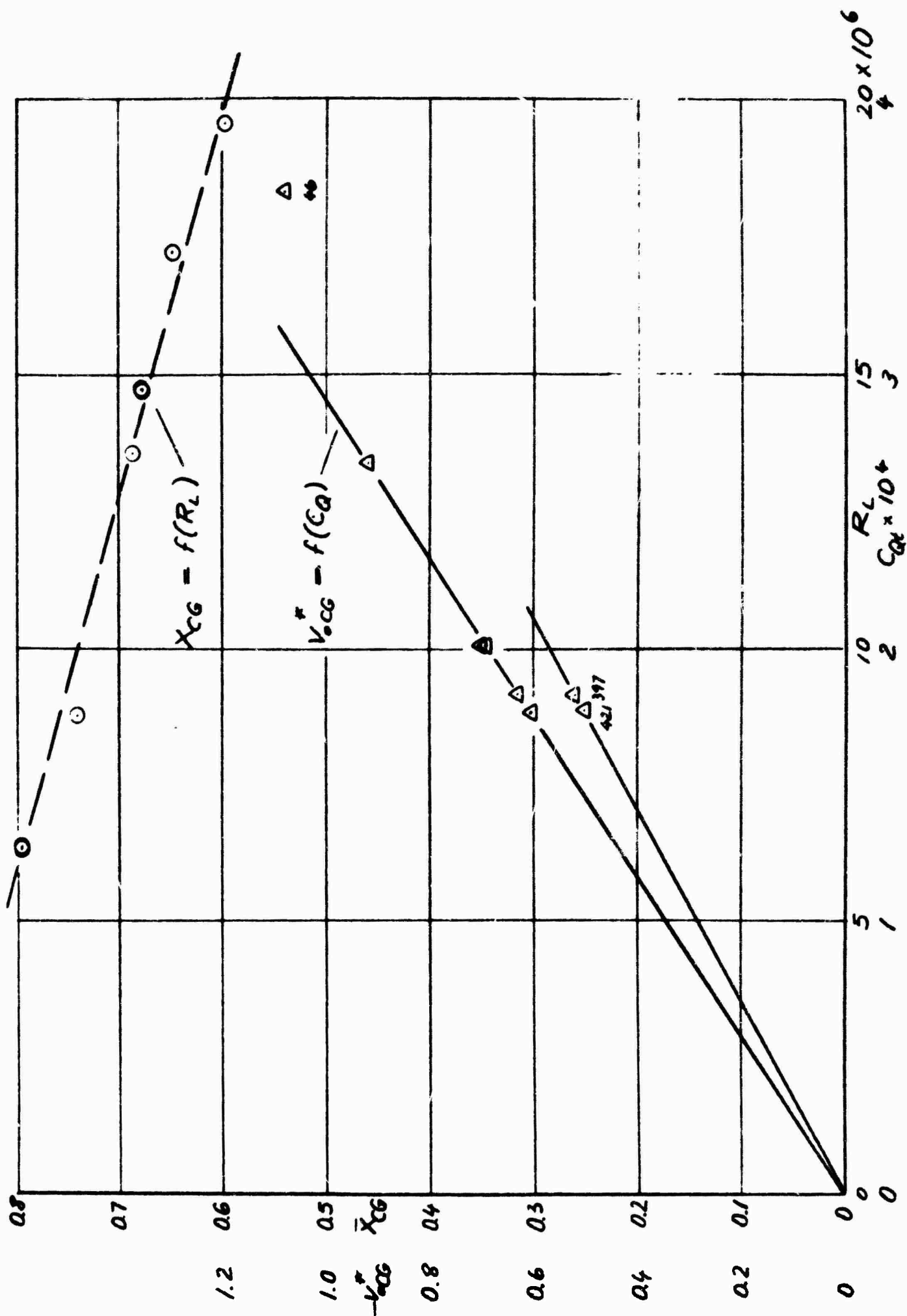


FIGURE 215  
VARIATION OF CENTER OF GRAVITY POSITION OF SUCTION INFLOW VELOCITY DISTRIBUTION WITH LENGTH REYNOLDS NUMBER  $R_L$  AND TOTAL SUCTION FLOW COEFFICIENT  $C_{Qt}$